Cultural Heritage Conservation and Environmental Impact Assessment by Non-Destructive Testing and Micro-Analysis

Edited by

René Van Grieken & Koen Janssens
Department of Chemistry, University of Antwerp, Belgium

A.A. BALKEMA PUBLISHERS LEIDEN / LONDON / NEW YORK / PHILADELPHIA / SINGAPORE

Also available as a printed book
see title verso for ISBN details

CULTURAL HERITAGE CONSERVATION AND ENVIRONMENTAL IMPACT ASSESSMENT BY NON-DESTRUCTIVE TESTING AND MICRO-ANALYSIS

Cultural Heritage Conservation and Environmental Impact Assessment by Non-Destructive Testing and Micro-Analysis

Edited by

René Van Grieken & Koen Janssens
Department of Chemistry, University of Antwerp, Belgium

A.A. BALKEMA PUBLISHERS LEIDEN / LONDON / NEW YORK / PHILADELPHIA / SINGAPORE

This edition published in the Taylor & Francis e-Library, 2005.

"To purchase your own copy of this or any of Taylor & Francis or Routledge's collection of thousands of eBooks please go to www.eBookstore.tandf.co.uk."

Copyright © 2005 Taylor & Francis Group plc, London, UK

All rights reserved. No part of this publication or the information contained herein may be reproduced, stored in a retrieval system,or transmitted in any form or by any means, electronic, mechanical, by photocopying, recording or otherwise, without written prior permission from the publisher.

Although all care is taken to ensure the integrity and quality of this publication and the information herein, no responsibility is assumed by the publishers nor the author for any damage to property or persons as a result of operation or use of this publication and/or the information contained herein.

Published by: A.A. Balkema Publishers, a member of Taylor & Francis Group plc
www.balkema.nl and www.tandf.co.uk

ISBN 0-203-97078-0 Master e-book ISBN

ISBN 90 5809 681 5 (Print Edition)

Cultural Heritage Conservation and Environmental Impact Assessment by Non-Destructive Testing and Micro-Analysis – Van Grieken & Janssens (eds)
© 2005 Taylor & Francis Group, London, ISBN 90 5809 681 5

Table of Contents

Preface VII

Quantitative analysis of ancient metal artefacts by means of portable energy-dispersive x-ray fluorescence spectrometers: a critical review 1
G.E. Gigante, S. Ridolfi, P. Ricciardi & M. Colapietro

Effects of the cultural environment 11
P. Brimblecombe

Non-destructive testing by the Rp method of bronze monuments: three case studies 19
G. D'Ercoli, G. Guida, M. Marabelli & V. Santin

A study of artists' materials based on Raman spectroscopy and total-reflection x-ray fluorescence analysis (TXRF) 27
P. Vandenabeele & L. Moens

Microfocus x-ray computed tomography (mCT) for archaeological glasses 37
H. Roemich, E. López, F. Mees, P. Jacobs, E. Cornelis, D. Van Dyck & T. Doménech Carbó

How diagnostic technologies contribute to the interpretation of the Byzantine icons 49
Y. Chryssoulakis & S. Daniilia

NDT and planning on historic buildings and complexes for the protection of cultural heritage 67
A. Moropoulou, N.P. Avdelidis & E.T. Delegou

Modern and ancient glass in the polluted atmosphere. What is the prevailing phenomenon? Leaching, corrosion, soling, encrusting …? 77
R.A. Lefèvre, A. Chabas, I. Munier & T. Lombardo

Non-destructive ion beam techniques for the depth profiling of elements in Amerindian gold jewellery artefacts 91
G. Demortier & J.-L. Ruvalcaba-Sil

Investigation of a novel conservation procedure for historical documents 101
E. Bulska & B. Wagner

Can x-ray computed tomography contribute to cultural heritage and stone conservation through the non-destructive monitoring of deterioration and restoration processes? 117
P. Jacobs & V. Cnudde

Microclimate measurements in the Cour Marly, Louvre Museum 127
D. Camuffo, A. Bernardi, F. Becherini, E. Pagan & R.A. Lefèvre

Innovative techniques for the characterisation of the encrustation on Pentelic marble from the Parthenon 135
P. Maravelaki-Kalaitzaki

New insights on the chemical nature of stone yellowing produced after laser cleaning 149
M. Gaviño, B. Hermosin, V. Vergès-Belmin, W. Nowik & C. Saiz-Jimenez

Dyes and pigments: ten open questions for conservation science 159
N.S. Baer

Analysis of paint layers by light microscopy, scanning electron microscopy and synchrotron induced x-ray micro-diffraction 171
B. Hochleitner, M. Schreiner, M. Drakopoulos, I. Snigireva & A. Snigirev

From Giotto to De Chirico: analysis of paintings with portable EDXRF equipment 183
R. Cesareo, A. Castellano, G. Buccolieri, S. Quarta, M. Marabelli, P. Santopadre, M. Ioele, G.E. Gigante & S. Ridolfi

Corrosion of bronze in outdoor environments 197
S.I. Sherwood

Endangered glass objects identified by ion beam analysis 211
C. Neelmeijer & M. Mäder

Trace elements fingerprinting using accelerators and ICP-MS: circulation of gold from the 6th century BC to the 12th century AD 223
M.F. Guerra

Assessment of air pollutant levels in some European museums and churches 245
V. Kontozova, Z. Spolnik, A. Worobiec, R. Godoi, R. Van Grieken, F. Deutsch & L. Bencs

A survey of the recent use of x-ray beam methods for non-destructive investigations in the cultural heritage sector 265
K. Janssens

Author index 309

Appendix 311

Cultural Heritage Conservation and Environmental Impact Assessment by Non-Destructive Testing and Micro-Analysis – Van Grieken & Janssens (eds)
© 2005 Taylor & Francis Group, London, ISBN 90 5809 681 5

Preface

The idea for this book was conceived during the "art2002" conference, i.e. the 7th International Conference on Non-destructive Testing and Microanalysis for the Diagnostics and Conservation of the Cultural and Environmental Heritage, which was organised by the editors of this book and their co-workers in Antwerp, Belgium, on June 2–6, 2002. It took place under the auspices of Istituto Centrale del Restauro and the AIPnD (Associazione Italiana Prove non Distruttive Monitoraggio Diagnostica) in Italy, and the University of Antwerp. Earlier conferences in this series on non-destructive testing and microanalysis for cultural heritage took place in Rome (1999 and 1984), Budapest (1996), Berlin (1994), Viterbo (1992), Perugia (1988).

In "art2002", ca. 200 papers were presented; some 85 were more general and strategy-oriented while 115 included the use of analytical techniques for characterisation of cultural heritage artefacts or materials. Among the analytical contributions at the conference, 63 employed one or more x-ray based or related technique (such as x-ray fluorescence analysis, scanning electron microscopy, proton induced x-ray emission, x-ray diffraction, x-ray absorption spectroscopy, total-reflection x-ray fluorescence and x-ray micro-tomography), while 28 made use of infra-red spectroscopy, 14 used Raman microscopy, 12 used visible light spectrometry or reflectometry and 6 employed gas chromatography coupled to mass spectrometry.

Among the speakers were 22 invited keynote lecturers and invited plenary lecturers, from 10 European countries and from the USA. This book contains contributions by these invited lecturers (in the chronological order of their lectures during the conference) and, in addition, a contribution by each of the two editors. The invited lecturers had all been chosen for their individual reputation and the quality of their research, but also because they represented a field deemed important by the organisers of the conference. Except for two, all of them decided to contribute to this book. Hence, this book can be assumed to cover in a balanced way the areas that are relevant and important in the state-of-the-art non-destructive testing and microanalysis in the realm of cultural heritage, with respect to the diagnostics and conservation strategies as well as to the technical analysis aspects, and, within the latter, with emphasis on the analysis techniques as well as on the different materials of cultural heritage value.

For the study, the conservation and the restoration of materials and artefacts of cultural-historical value, there is a well-defined need for methods that are able to provide information on the chemical composition of selected parts of cultural heritage artefacts and materials in order to elucidate their provenance, the state of alteration (on the surface and/or internally) of objects as a result of exposure to particular environmental conditions and the effectiveness of conservation and restoration strategies during and after application. The ideal analysis methods to provide such information for such artefacts should be universal (so that by means of a single instrument, many materials and objects of various shapes and dimensions can be examined), sensitive (so that object grouping and other types of provenance analysis can be done by means of trace-element and trace-component fingerprints) and of multi-elemental or multi-compound nature (so that in a single measurement, information on many elements and compounds is obtained simultaneously and that also information is obtained on elements and compounds which were not initially thought to be relevant to the investigation). Most of all, however, the techniques should be fully or nearly non-destructive, i.e., respecting the physical integrity of the object. It is obvious that valuable artefacts can normally only be investigated when the analysis does not result in any (visible) damage to be object under examination, which remains aesthetically unimpaired. Recently, partially driven by the increasing importance of high-tech materials of complex micro structural nature and as a result of miniaturisation of instrument components, a number of portable and microscopic versions of established

analytical methods have come into existence. Portable methods are well suited for inspection and/or analysis of objects of great cultural value as measurements can be made on site, thus eliminating the need to move the objects out of their normal surroundings (e.g., a museum or an archaeological site). Micro-analysis methods that can examine only a microscopic part of an object have recently beam booming; they are always (nearly) non-destructive and they yield valuable information on different parts (laterally or in-depth) of a heterogeneous work of art.

Non-destructive and micro-analytical techniques thus represent today an essential tool in both the diagnostics and conservation of cultural heritage items and they help to facilitate the choice of the most efficient interventions.

Hence the present book should be of relevance to material scientists and analytical chemists as well as to art historians, conservators and archaeologists, who have often received a formation of which the technical aspects are not extensive enough to allow them to absorb the above-mentioned state-of-the-art innovations from the dispersed literature. Advanced collaboration between these groups guarantees that general historic and ethnic information and physical and chemical characteristics of cultural heritage items and historical monuments will optimally be taken into account, to the benefit of our common cultural patrimony.

We gratefully acknowledge all the invited authors for their valuable and interesting contributions.

René Van Grieken,
Koen Janssens
Department of Chemistry,
University of Antwerp,
Belgium

Cultural Heritage Conservation and Environmental Impact Assessment by Non-Destructive Testing and Micro-Analysis – Van Grieken & Janssens (eds)
© 2005 Taylor & Francis Group, London, ISBN 90 5809 681 5

Quantitative analysis of ancient metal artefacts by means of portable energy-dispersive x-ray fluorescence spectrometers: a critical review

G.E. Gigante, S. Ridolfi & P. Ricciardi
Dipartimento di Fisica, Università degli Studi di Roma "La Sapienza", Roma, Italy

M. Colapietro
Dipartimento di Chimica, Università degli Studi di Roma "La Sapienza", Roma, Italy

ABSTRACT: Field portable energy-dispersive x-ray fluorescence (FP-EDXRF) spectrometers are becoming a standard tool for non-destructive analysis of metals. This article discusses the major issues related to the infield use of such equipments. The quantitative analysis of alloys is in principle possible with some restrictions due to the measuring conditions. The difficulties for a quantitative analysis and some evaluation of instrumental error are presented. Finally, the possibility to use such systems for the assay of ancient gold artefacts is shortly discussed.

1 INTRODUCTION

Quantitative analysis by means of FP-EDXRF spectrometers is becoming a very common and powerful tool in the investigation on ancient metal artefacts; its use, however, opens some methodological problems that are worthwhile discussing because they are in some aspects object of controversies (Van Grieken & Markowicz 1993, Cesareo et al. 2000, Marucco & Stankiewicz 1998).

The metal artefacts and, more in general, materials connected to the metallurgical activity are present in large amounts in museums and scientific collections all over the world. The use of this large experimental material is an important prospective for the archaeometallurgist, who needs experimental verification of his theoretical hypothesis (Giardino 1998). Unfortunately these materials cannot be moved from museums and sites were they are stored, because of conservation and safety reasons. The use of movable instrumentation, i.e. that can be used at the museum (or in site), can solve this problem, creating however new issues concerning its correct use and limitations.

The large use of portable systems is a general trend in all technological areas and, in part, in research (Sackett & Martin 1998). Their practical and economical advantages are evident, allowing, thanks to a greater level of automation, to reduce expenses for personnel and materials and to increase responsiveness. This has been true also in the field of conservation and, in a lesser extent, in archaeometry, in which the principal advantage resides in the possibility to perform a greater number of measurements, thus investigating a large number of different artefacts or performing many measurements on the same one.

The most common disadvantage is the larger risk of obtaining less accurate results (and a lower reproducibility level), due to the fact that the procedures can be better controlled in laboratory. Another point to remark is the need to employ well skilled personnel and a well scheduled plan of work, since the risk to do many useless measurements is larger when using simple instruments as are frequently the portable ones.

The traditional laboratory procedures operate in a remote mode: sampling and analysis phases are well separated in time and in space; the only unwanted consequence of this is to underestimate experimental conditions that could influence the results of the analysis (e.g. contamination, unknown microstructure, etc.). With a mobile system, the above mentioned phases take place in the same site, and frequently within a very short time. This fact can help the use of a more flexible

and effective measurement program, especially when the degree of automation of the instrument is very high.

In the case of a non-destructive measurement some additional problems arise, mainly coming from the potential inhomogeneity of the artefact structure and matrix. In the case of FP-EDXRF spectrometers, these limitations are mainly connected to the finite penetration of emitted x-rays and to the changes in the geometrical efficiency that can hardly be taken fixed when the artefact is examined in a non-destructive way (Gigante & Cesareo 1998).

There have been many important developments in the construction of FP-EDXRF instrumentation in the last decade, mainly due to the availability of small and portable x-ray tubes and non-cryogenic detectors similar, in performance, to the traditional cryogenic ones (Cesareo et al. 1992, Cesareo 2000).

Another remarkable contribution to the in-field use of the EDXRF technique has been the development of software specifically engineered for in-situ acquisition and data analysis, and further data managing.

2 DETERMINATION OF METAL ALLOYS COMPOSITION THROUGH XRF ANALYSIS

The determination of metal alloys composition is one of the most significant problems in which XRF techniques have successfully been employed. The principles on which these techniques are based are the following:

(a) The elements constituting the alloy produce one (or more) x-ray emissions within the energy range the spectrometer can analyse
(b) The spectrum of the exciting source is well known
(c) The coefficients describing absorption and subsequent emission of x-rays by the metallic sample are known (fundamental parameters)
(d) The approximation of infinite thickness sample is fulfilled
(e) The detector's physical efficiency and the spectrometer's geometrical efficiency can be determined
(f) The sample has a perfectly smooth surface; thus the geometry of the measurement can be taken fixed.

Under these hypotheses it is possible to reduce the analytical problem to the solution of a system of non linear equations, using an iterative procedure. These equations describe the functional relationship existing between the measured quantities, i.e. the relative intensities of the different elements' peaks, and the weight fraction of each element constituting the alloy. The equation for each element is:

$$I_i = I_0 G K_i A_i w_i$$

with

$$K_i = \tau(E_0)\,(1-\frac{1}{J_i})\omega_i f_i \varepsilon_i \qquad (1)$$

and with

$$A_i = (\mu(E_0)\operatorname{cosec}\,\psi_1 + \mu(E_i)\operatorname{cosec}\,\psi_2)^{-1}$$

with:
f_i: probability of emission of the line
G: geometrical efficiency of the spectrometer
I_0: intensity of the incident beam

J_i: jump ratio
N: number of elements in the sample
w_i: weight fraction of the i-th element
ε_i: detector's efficiency for the emitted photons' energy E_i
$\tau(E)$: partial absorption coefficient for the photoelectric effect
ω_i: fluorescence yield
$\mu(E)$: mass absorption coefficient of the sample for the energy E
$\mu_\iota(E)$: mass absorption coefficient of the i-th element for the energy E
ψ_1 and ψ_2: angles of incidence and emission
with

$$\mu = \sum_{j=1}^{N} \mu_j \; w_j \qquad (2)$$

In the above list of parameters, some coefficients are known with a good degree of approximation, such as the absorption coefficients; some others depend on the spectrometer, such as angles and efficiencies. These last ones can only be determined approximately when the sample does not have a smooth and flat surface or the pointing device is not accurate enough. The search for a solution of the system is made through the above mentioned iterative method that allows a quick determination of the best possible w_i, taking into account that the measured intensities (or intensities ratios) are affected by a statistical error and the given parameters are known with an uncertainty. This produces systematic biases on the values. Using a set of reference samples it is possible to determine the best value for the empirical parameters (x-ray tube intensity and geometrical and detection efficiency) (Piorek & Pasmore 1993). It is worth noting that the above equations are for a monochromatic exciting source; the use of a polychromatic beam, as is that generated by an x-ray tube, implies integration on energy spectrum of the source. The determination of the error produced by the application of the iterative method become consequently more complex, and the error itself can be considered as the result of two contributions. The first one is due to fluctuations in the beam intensity integral (and it can be treated as due to the fluctuations of a monochromatic source), the second is due to the shift in the exciting spectrum caused by variations in the voltage applied.

It is possible to use the ratios of the peak areas relative to that of the major alloy constituent. In this way it is implicit the assumption that the sum of the weight fractions equals unity.

Similar approaches to quantitative analysis are commonly found in environmental sciences; i.e. in the field of quantitative evaluation of heavy metals, systems have been developed which yield satisfactory results in the process of soil control. With the scope of such controls, some procedures have been outlined that give way to results which are retained trustworthy, in the typical working conditions of the field. Similarly, there are systems available for the analysis of metal in the industry (Metorex); in this case also standard procedures have been defined.

All of these systems imply the possibility of obtaining satisfactory quantitative results with the use of radioisotopic sources, which do present an intrinsic stability.

3 INSTRUMENTATION

A typical FP-EDXRF spectrometer is mainly composed of:

- an x-ray tube
- an x-ray detector with its electronics
- a multichannel analyser.

We have experienced a rapid evolution of these components in the last decade, starting from the developments of HgI_2 x-ray detectors in the early nineties of the last century (Cesareo et al. 1992). Now the situation seems to be going toward a stabilisation with a landscape of possible choices that fulfil the peculiar requirements of principal applications offering suitable solutions.

Table 1. Characteristics of small-size, portable x-ray tubes according to the element or elements to be analysed.

Element interval	Anode material	Anode voltage (kV)	Current (mA)	X-ray spectrum and peak/ BS* ratio
Sodium–chlorine	Calcium (K-lines)	8–10	0.1–1	3.7 keV peak BS (≈1/1)
Sodium–chlorine	Tungsten (L-lines)**	13–15		8.4, 9.7 and 11.3 keV peaks
Potassium–yttrium (K-lines) Cadmium–uranium (L-lines)	Molybdenum (K-lines)	30	0.1–1	17.5 keV peak BS (≈0.2/1)
Potassium–barium (K-lines) Heavy elements (L-lines)	Tungsten (K-lines)	40	0.1–1	Practically only BS

* Bremsstrahlung.
** Possibly with a transparent anode.

3.1 *X-ray tubes*

A great variety of x-ray tubes of various types (maximum voltage, current, anode), sizes and cost are currently available for EDXRF analysis, depending on the problem, and more specifically on the element or elements to be analysed. Leaving out analysis of traces, which requires high-current tubes with proper secondary targets, low-power x-ray tubes (with selected anodes) are generally adequate. They may be chosen primarily as a function of the atomic number of the elements to be analysed. Table 1 gives a survey of useful EDXRF tubes (Oxford, EIS) for analysis of any element.

A low size, low power W-anode x-ray tube working up to 50 kV, 0.1–0.3 mA is adequate for analysis of all elements of interest in any matrices with the exception of trace elements. Working at low voltages (15–20 kV) and at high voltages (35–40 kV) respectively, this tube is able to excite low atomic number elements such as S and Cl, or elements from Ca to Pb. In Figure 1 is shown a small x-ray tube with its pointing device (two collimated laser beams) which helps the user in the localization of the excitation area.

The advantage in using an x-ray tube, rather than a sealed radioisotopic source, is in the possibility to collimate the beam in a small area. A capillary collimator can also be employed in conjunction with the x-ray tube, to collimate the beam into sub mm^2 areas.

3.2 *X-ray detectors*

The typical, high-resolution x-ray detector was traditionally the nitrogen cooled Si or Ge detector, with an energy resolution of about 150–200 eV at 5.9 keV.

In the last decade, small size thermoelectrically cooled semiconductor detectors have become available, such as HgI_2, Si-PIN, SDD and CZT (Cesareo et al. 1992, Huber et al. 1995, Fiorini et al. 1997).

These detectors are cooled to about $-30°C$ by means of a Peltier circuit, and are contained in small size boxes also including a high quality preamplifier and the Peltier circuit.

- HgI_2 detectors were the first to be constructed, and currently have an energy resolution of about 180–200 eV at 5.9 keV, and an efficiency of about 100% in the whole range of x-rays.
- Si-PIN detectors, with a Si thickness of 300 μm, exhibit an energy resolution of 160–200 eV, and are useful up to about 30 keV, because the efficiency is decreasing at energy larger than 15 keV, due to the limited thickness.
- SDD (Si-drift) detectors have a Si thickness of 300 μm, and an energy resolution of about 150 eV at 5.9 keV. They are able to work also at high counting rates.
- CZT detectors have a thickness of 2 mm and an efficiency of about 100% in the whole x-ray range. The energy resolution is about 300 and 700 eV at 5.9 and 59.6 keV, respectively.

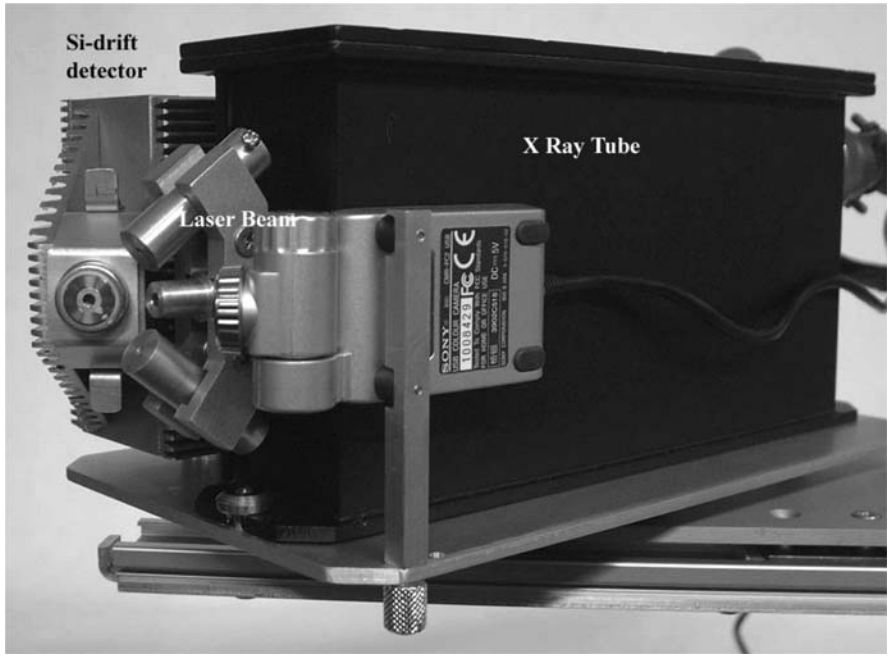

Figure 1. FP-EDXRF instrumentation (EIS s.r.l., Rome, Italy): detector, x-ray tube and pointing device.

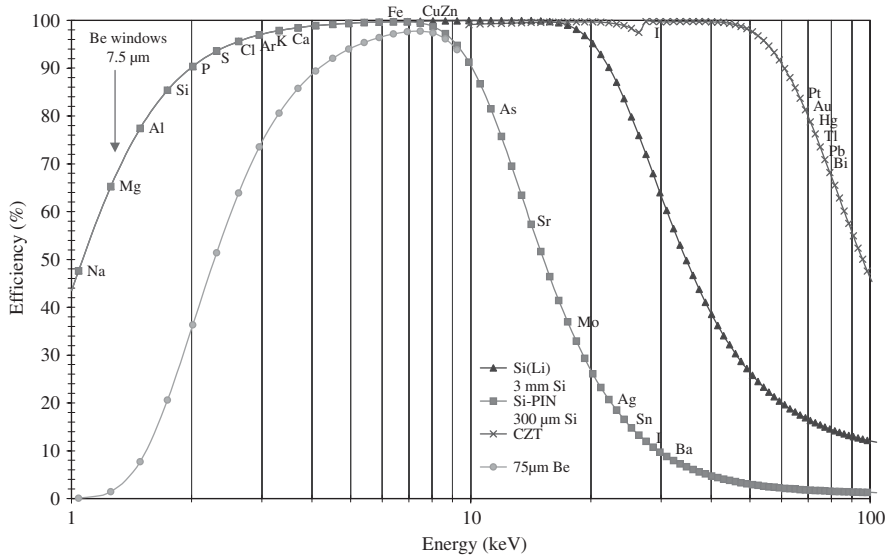

Figure 2. Efficiency of Si(Li), Si-PIN and CZT detectors.

In Figure 2, the efficiency of a Si(Li) detector is compared with that of two thermoelectrically cooled detectors: (a) a 300 µm thick Si detector (SDD or Si-PIN), (b) a 3 mm thick CdZnTe detector.

A summary of the useful Peltier-cooled detectors is given in Table 2.

Table 2. Comparison between the performance of various x-ray detectors: Si(Li), HPGe, Si-PIN, HgI_2, and SDD having an area of 10, 30, 7, 5 and 3.5 mm^2 respectively.

	Si(Li)	HPGe	Si-PIN	HgI_2	Si-drift
Energy resolution (FWHM at 5.9 keV)	140	150	170	200	155
Useful energy range (keV)	1–50	1–120	2–25	2–120	2–25
Efficiency*	0.008	0.025	0.0055	0.004	0.003
Shaping time (μs)	6–12	6	12	12	2
Cooling system	Liquid nitrogen	Liquid nitrogen	Peltier	Peltier	Peltier

* At 1 cm from a point source.

4 POSSIBLE EXPERIMENTAL ERRORS AND THEIR RELEVANCE IN EDXRF MEASUREMENTS

One of the basic aspects of a campaign of measurements is the possibility to indicate the precision of the results, which is associated with the statistical dispersion that one finds when considering the results of multiple measures. One also needs to investigate the accuracy of the data and, consequently, the reproducibility of the experimental procedure.

There are several possible causes of errors in an EDXRF measurement, namely the statistical error (due to the physical processes of spectrum generation in the tube and of signal formation in the detector), the calibration error (which produces a systematic rather than a randomly distributed effect), errors due to inhomogeneities in the object in analysis, and more errors associated with the measuring system as a whole. The latter are due to instrumental instabilities and to the geometry of the measure, which greatly affects the results, especially when dealing with artefacts having a rough surface.

An experimental evaluation of some of these errors has been made by estimation of the statistical spread of the results of some sets of N = 10 measurements on a metal foil made of 95% Au and 5% Ag; each set of measures was characterized by the sources of errors it could possibly be affected by, and the error was calculated as:

$$S = \sqrt{\frac{1}{N-1}\sum_{i=1}^{N}(x_i - \bar{x})^2} \tag{3}$$

where x_i is the result of the i-th measurement, and $\bar{x}$ is the average of the 10 results.

In order to better evaluate the effect of each kind of error, the different sources have been divided as follows:

1. Instrumental error, due to:
   a. Detector
   b. X-ray tube
2. Measurement error, due to:
   a. Geometry
   b. Calculation procedures
   c. Sample inhomogeneity

It is therefore possible, in principle, to calculate the total error as the quadratic sum of the errors due to each possible source:

$$\sigma^2_{total} = \sigma^2_a + \sigma^2_b + \ldots \tag{4}$$

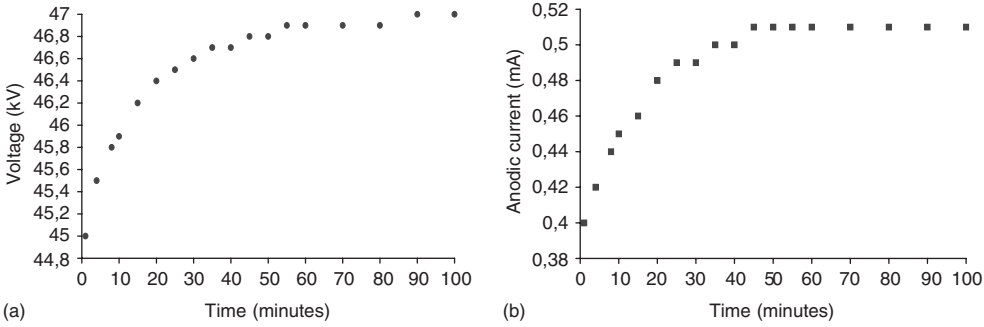

Figure 3. Behaviour of the tube's characteristics during the first 100 minutes after it has been turned on. (a) Voltage ($\tau = 21.5\ s^{-1}$), (b) Anodic current ($\tau = 13.8\ s^{-1}$).

The above relation holds only when the contributing errors are independent. Using an FP-EDXRF spectrometer, this condition is not fulfilled, especially for the instrumental causes of error. In this case, the evaluation of the contribution of each source of error can be done only by looking at its effect on the overall error, taking into account that the statistical error sets a lower limit to the precision obtainable.

4.1 *Instrumental error*

As for the detector, it induces a statistical error due to the Poissonian process of formation of the signal in the detector itself; the relative uncertainty has been found to be $\sigma/N = 1/\sqrt{N}$, where N is the net area of the peak of interest (which was either Ag Kα or Au Lα in our experiment). The relevance of the counting statistics in terms of resulting error leads to the choice to make long measures (600 s each) in order to enhance the importance of other sources of error.

The x-ray tube can be used in optimal conditions of stability by starting the first measurement about an hour after the system has been turned on; this lets the tube's voltage and current both reach an "equilibrium" value and drastically reduces fluctuations of the measured spectra (see Figs 3a, b).

The instability introduced by the shut-down of high tension is usually less relevant because the current flows continuously in the filament. An error can be induced by the inertia with which the maximum voltage is reached when the tube is turned on again; it is thus advisable to wait a few seconds before starting another measurement. The overall error associated to measurement affected by both the detector and the tube's instabilities has been found to lie in the range 0.5–3.0% of the weight fraction (calculated from the measured peak areas through the fundamental parameters approach).

4.2 *Measurement error*

The geometry of the measurement, if considered fixed, induces a systematic bias on the results. On the other hand, repositioning of the sample has a direct effect on the spread of the results; if done with a certain care, repositioning does not greatly influence the overall error which still lies in the range 0.5–3.0% of the weight fraction. A less careful (manual) repositioning causes the error to be for the most part due to geometry; its overall value varies greatly and goes up to about 20% of the weight fraction. The latter is the case when one can choose to calculate the concentration of each element in the alloy using the peak ratios, i.e. the ratios between the net areas of the peaks of interest and the area of a peak chosen as a "reference" (typically the Au Lα for gold alloys). The use of peak ratios allows to diminish the dependence on the geometrical factor and thus to reduce the influence of repositioning, yielding errors smaller than about 3.0% on the weight fraction.

The error induced by calculation procedures is not easy to quantify. It can usually be included in the calibration error, due to the setting that is systematically made before a series of measurements, by using some reference samples. An experimental verification of the variations in the values of the

calibration parameters in repeated measures during a few days has shown that the relative variation is no greater than about 1.5%.

The most significant uncertainty in the quantitative measurement of an alloy's composition during in field measures is obviously induced by the sample itself, which can be inhomogeneous and/or present surface deformations and corrosion layers.

5 MINIMUM DETECTABLE LIMITS OF SILVER AND COPPER IN GOLD ALLOYS

The minimum detectable limit (MDL) of Ag and Cu in a gold alloy has been calculated using the following expression:

$$\mathrm{MDL} = \frac{3\sigma_B}{\mathrm{dN}/\mathrm{dC}} \tag{5}$$

with σ_B = experimental error on the background, and dN/dC = detection sensibility; this last quantity is estimated by use of a linear fit on a set of 5 data relative to standards containing different concentrations of Ag, Cu and Au. Our portable system yields the following results: $\mathrm{MDL_{Ag}} = 0.061\%$ and $\mathrm{MDL_{Cu}} = 0.12\%$.

6 GOLD ASSAYING

Gold assaying by means of non-destructive XRF provides users with a real alternative to traditional gold assaying techniques. The results shown above confirm the possibility to obtain an accuracy of a few tenths of a percent relative to the weight fraction in optimal working conditions, i.e. when the surface of the sample is uniform and smooth. Moreover, the MDLs are satisfactory enough for archaeometric purposes in the case of major alloy constituents. This opens realistic perspectives for field portable analysis of ancient gold artefacts. A campaign on prehistoric jewellery in the Messenian region of the Peloponnesus is under way, in co-operation with Greek researchers. Although not yet published, the results obtained show how it is really possible to use portable systems for this kind of analysis (see Fig. 4).

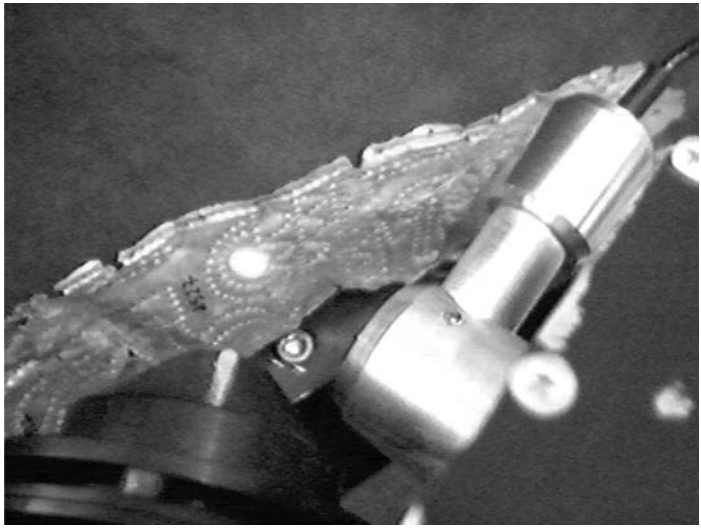

Figure 4. The FP-EDXRF spectrometer during the measurements on Messenian gold artefacts in the 2002 campaign.

7 CONCLUSIONS

A critical analysis of the errors of field portable spectrometers has shown how simple experimental devices make it possible to reach a level of precision better than 3% on the calculated weight fractions.

It has been proven valid a method for the correction of the geometrical efficiency errors, based on the use of a reference peak and the peak ratios.

The errors due to the use of a low power x-ray source, such as those currently available, do not set a strict limit to the possibility of obtaining good precisions. The many measurements made (whose results are partly reported in this article) have shown how, by using some care, the error due to source fluctuations is comparable if not negligible with respect to the statistical one, in most common experimental conditions, in which short counting times can be employed.

Our statement is confirmed by a careful analysis of the results obtainable with portable XRF systems operated with radioisotopic sources, which do not yield significantly better results.

In this review of the possible obtainable results it is worth underlining that the error introduced by the sample itself, due to its inhomogeneities and surface deformation, cannot be easily quantified. In many experimental conditions, such as those of non-destructive analysis, the latter is probably the most relevant source of error.

REFERENCES

Cesareo, R., Gigante, G.E., Iwanczyk, J.S. & Dabrowsky, A. 1992. The use of HgI_2 detectors for XRF analysis in archaeometry. *Nuclear Instruments and Methods in Physics Research* A 322: 583–590.

Cesareo, R., Gigante, G.E., Castellano, A. & Iwanckyk, J.S. 2000. Portable systems for Energy dispersive x-ray fluorescence analysis. In R.A. Meyers (ed.), *Encyclopedia of Analytical Chemistry*: 13327–13338. Chichester: John Wiley & Sons.

Cesareo, R. 2000. X-ray physics: interaction with matter, production, detection. *Rivista del Nuovo Cimento* 7 EIS srl. via Silvani, Rome, Italy.

Fiorini, C., Kemmer, J., Lechner, P., Kromer, K., Rohde, M. & Schulein, T. 1997. A new detection system for x-ray microanalysis based on a silicon drift detector with Peltier cooling. *Rev. of Scientific Instr.* 68: 2461.

Giardino, C. 1998. *I metalli nel mondo antico. Introduzione all'archeo-metallurgia*. Bari: Laterza.

Gigante, G.E. & Cesareo, R. 1998. Non destructive analysis of ancient metal alloys by in situ EDXRF transportable equipment. *Radiation Physics and Chemistry* 51: 689–700.

Huber, A.C., Pantazis, J.A. & Jordanov, V. 1995. High performance, thermoelectrically cooled x-ray and gamma ray detectors. *Nucl. Instr. and Meth.* B 99: 665–668.

Marucco, A. & Stankiewicz, W. 1998. Development of an XRF spectrometry analytical method for gold determination in gold jewellery alloys. *Gold Technology* 24: 1–22.

Metorex. www.metorex.fi

Oxford Analytical Systems Division. 275 Technology Circle, Scotts Valley, Ca 95066 USA.

Piorek, S. & Pasmore, J.R. 1993. Standardless, in situ analysis of metallic contaminants in the natural environment with a PC-based, high resolution portable x-ray analyzer. *Third International Symposium on Field Screening Methods for Hazardous Waste and Toxic Chemicals, Las Vegas, Nevada*.

Sackett, D. & Martin, K. 1998. EPA Method 6200 and Field Portable X-ray Fluorescence. *A presentation developed for the EPA Technology Innovation Office and On-Site In-Sights Workshops for innovative field characterization technologies.* http://www.environmental-center.com/articles/article1198/article1198.htm

Shefsky, S. 1997. Comparing field portable x-ray fluorescence to laboratory analysis of heavy metals in soil. *International Symposium of Field Screening Methods for Hazardous Wastes and Toxic Chemicals*, in www.Niton.com

Van Grieken, R. & Markowicz, A.M. 1993. *Handbook of X-ray Spectrometry*. *Practical Spectroscopy Series* 14. New York: Marcel Dekker Inc.

Cultural Heritage Conservation and Environmental Impact Assessment by Non-Destructive Testing and Micro-Analysis – Van Grieken & Janssens (eds)
© 2005 Taylor & Francis Group, London, ISBN 90 5809 681 5

Effects of the cultural environment

Peter Brimblecombe
School of Environmental Sciences, University of East Anglia, Norwich, UK

ABSTRACT: Preventive conservation has focused attention on the importance of the cultural environment in controlling damage to our artistic heritage. Despite extensive monitoring of the museum environment and increasingly accurate measurement of the damage to the surfaces of objects, the link between environment and the damage it causes is not always fully explored. This paper will examine the way in which environmental factors are linked to damage and the how they can be related to the formulation of standards and guidelines. Studies of the thermodynamics and mechanisms of damage can aid decisions about the level and frequency of intervention.

1 PREVENTIVE CONSERVATION

Preventive conservation has become a dominant strategy in the management of cultural heritage over the last few decades. The American Institute for Conservation of Historic and Artistic Works (AIC) defines this as "the mitigation of deterioration and damage to cultural property through the formulation and implementation of policies and procedures for the following: appropriate environmental conditions; handling and maintenance procedures for storage, exhibition, packing, transport, and use; integrated pest management; emergency preparedness and response; and reformatting/duplication."

Despite the importance assigned to this approach, recent surveys show that, in terms of financial expenditure, most museums still spend more on restoration and intervention than they do on preventive conservation. This may, of course simply reflect that restoration is a costly business, but it does serve as a reminder that preventive conservation is a critically important tool. In a recent European Preventive Conservation survey (Putt 2001), it appeared that museums were "consistently acting on the 'traditional' concerns of relative humidity, temperature, light, operation of heating and air conditioning. On the other hand, other physical aspects of care, such as disaster preparedness, pollution and pest management, receive much less attention."

So while it is possible that insufficient attention focuses on pollution or pest management, it is clear that the environment is a key focus of preventive conservation.

An inherent supposition of preventive conservation is that an appropriate environment will mitigate deterioration and damage to cultural property. This is perhaps reasonable, but the difficulties of defining such environments are a much more troublesome. There is a further issue in that there are now many measurements of the climate and chemistry of the cultural environment. Yet although these often provoke comment on the way the environments might relate to damage, the links are more often supposition than observation. Rather than list the work of others I will simply note my own guilt in this matter as reflected in a series of papers undertaken within a European Commission funded project on the museum environment (e.g. Brimblecombe et al. 1999). This paper is an attempt to explore the nature of the link of conservation of materials to the cultural environment.

2 ENVIRONMENT AND DAMAGE

It often seems that the origin of this separation between the cultural environment and damage is caused by the way in which environment is treated in classic texts (e.g. Appelbaum 1991, Thomson

1978) or indeed the AIC definition above. Environmental factors are typically separated out and treated one by one, with separate section of books devoted to each. Such an approach is useful and instructive, but it risks obscuring our prime interest in damage to heritage. In addition it draws attention away from some of the underlying characteristics of damage to cultural materials. It for instance plays down the synergisms that seem inherent between many of the environmental factors.

Additionally a single environmental factor such as high relative humidity can cause a number of types of degradation that are inherently distinct e.g. high humidity may cause both warping (a physical change) and yet again it can induce rusting in metals. The gas–metal reactions that lead to tarnish or corrosion products are often enhanced by the presence of water (adsorbed molecules or liquid), i.e. synergisms.

If we turn this conventional approach around and focus on the damage itself a different, though instructive, view emerges. We can list the various types of damage (as done in Table 1) to include such as: erosion, chemical attack, mechanical stress.

However we can categorize damage into even broader classes by considering the mode in which it occurs.

Impulsive processes: Perhaps the most obvious class of damage is the impulse (Koestler et al. 1994), which one might think of as dropping an object on the floor. This is also characteristic of extreme events such as earthquake, fire or war. In these cases we need to be concerned with the probability of the event occurring (Baer 1991, Benarie & Druzik 1992).

Dose processes: These processes are typical of a more gradual deterioration. The damage is proportional to the dose, which is typically dose is regarded as the product of concentration, or flux, and exposure time.

Cyclic processes: In the context of damage to cultural objects this rate of change generally relates to cyclic changes, such as the number of freeze thaw cycles a wet stone can be take through before a given amount of damage occurs. In general, mechanical and physical damage appears to most often result from cyclic changes in environmental factors. Wear, such as damage to the binding of a book can also be a function of the number of times it is opened and closed (duty cycles). However it may also be necessary to consider the amplitude of the cycles and their frequency. Because, although not necessarily relevant in the conservation context, if the frequency of the imposed cycle became very high there might not be enough time for heat to dissipate and mechanical failure could occur in fewer duty cycles than at lower frequencies. On the other hand in archives where a book is opened very infrequently, other degradation processes may have set in and cause catastrophic failure to ensue after only a few duty cycles.

These three categories impulse, dose and cycles/change may not be the only ones and indeed others such as the logarithmic Arrhenius relationship for thermal degradation may be proposed. It is not my intention to be complete here, but rather to draw attention to the implication of such broad modes of damage to the way in which we limit it.

The impulse is a probabilistic factor. However we only take precautions against highly probably events if they cause significant damage. Thus the damage caused by a gamma particle from decay of a potassium-40 atom in glass is highly probable. We would expect about twenty radio active decays a second in a piece of medieval window glass. However as each decay only places 2.2×10^{-13} J in the material, imposing an insignificant risk. Risk analysis generally sees the imposed risk as a product of probability event and impact of the event. Thus a meteorite impact could completely destroy a collection, but the probability is low (although increasingly governments have been concerned with such risks and methods of aversion). However, fire, theft, earthquakes are almost as destructive, yet their risks are so much more probable that we work harder to mitigate against them.

Dose is often lowered by decreasing the intensity of the factor. However, it is also possible to lower the time of exposure (especially in the case of light). Intensity can be decreased thorough the use of filters which reduce intensity (in the case of light) or concentration or flux (e.g. in the case of air pollutants).

Cyclic processes are frequently buffered. This is an attempt to change the amplitude of the change in temperature or humidity, and in modern times there has been an attempt, often criticised, to regulate through active control (i.e. HVAC systems). Alternatively there are attempts in some

Table 1. Some important factors affecting the degradation of items of cultural value (Brimblecombe 1994). The bold text marks principal factors.

Process	Environmental factors	Damage function	Materials affected	Observed impact and examples
photo-degradation	**light**, chemicals humidity	dose law	dyes, organic substances	fading, color and chemical change
erosion	polishing, dust, air and water movement	dose law	solids	loss of surface detail, scratches in "bright work", furniture etc.
soiling	**dust**, humidity, electrical charge, air flow, thermophoresis, photophoresis,	**dose law**, deposition velocity	most surfaces, but geometry and surface texture and composition may be important	blackening, loss of contrast, changes in color
chemical attack	**trace gases**, light, humidity, air flow, catalytic particles	dose law deposition velocity	tarnishing of metals corrosion of materials weathering of stone	rusting of ferrous metals, patina formation, weathering of glass stone, discoloration of dyes...
hydration	**humidity**, chemicals on surface, temperature	dose law	surface corrosion	enbrittlement of glass, bronze disease
freezing	temperature, water	cycles	porous materials	mechanical failure of stone
crystallisation stress	salts, water	cycles	porous materials	mechanical failure of stone
chemical transformation stress	**pollutants**, notably SO_2 for stone	dose	solid reactions with large volume changes	sulphation of stone, exfoliation
dissolution	water flow, solutes	dose	reactive solids	loss of surface detail
hygrometric stress	humidity	cycles	composite and organic materials	swelling, warping of canvases loss of paint
biodegradation	**organisms**, humidity, optimal high temperature and radiation. Low ventilation	seasonal cycles, population	substrates with nutrients and water	mould, lichen growth – loss of detail, dissolution, mechanical, failure
differential thermal expansion	temperature	cycles, spatial differentials	composites or large objects	mechanical failure e.g. shedding of photographic film
wear, fatigue, collapse	mechanical stress, vibration	duty cycles and their amplitude	stressed parts	hinges, delicate solid objects
radiation damage	ionising radiation	dose law	solids at high dose	discoloration, transformation
thermal decomposition	temperature	Arrhenius law	thermally unstable	chemical changes, degradation, materials e.g. cellulose nitrate

cases to reduce frequency, i.e. the number of duty cycles can be reduced by limiting the use of a fragile book.

These all remain broad conceptual elements and are hardly relating the environment to real damage.

3 MONITORING CULTURAL ENVIRONMENTS

Monitoring or measurements within cultural environments continue to be important. However, they need to be properly focussed on the causes of damage. This problem may be illustrated by considering chemical change, which is often induced through corrosion, oxidation or air pollution. In the case of air pollution there is often a problem because monitoring has focussed on those gases harmful to human health. In heritage protection the focus should be towards those gases that damage materials. However the heritage field is small, so instrument makers have designed equipment for monitoring gases harmful to human health, often with high time resolution.

Because objects accumulate pollutant damage over long periods of time, we are usually more concerned with high sensitivity, rather than high time resolution. Outdoor monitoring equipment adapted for museum studies, can be insensitive, and focus on relevant to general urban air quality issues. The health focus had led to a pre-occupation with SO_2, NO_2 and O_3, along with hydrocarbons and even occasionally carbon monoxide. There is a tendency to monitor those things that are easy to measure rather than those that are recognised as potentially damaging. Thus there are few systematic measurements of nitric acid, sulphides, organic acids and even where there is a strong desire to focus on specific and relevant gases, they are not always known. Wool was often thought to be a source of hydrogen sulphide in museums, but at room temperature wool appears to release carbonyl sulphide and only small amounts of hydrogen sulphide (Brimblecombe et al. 1992). This general failure to be able to define the cultural environment can make it difficult to link environment and damage.

4 MECHANISMS AND MODELS

Mechanistic concepts form an important way to relate environment and damage. Although these thermodynamic, kinetic and other theoretical approaches have been used, they are perhaps less common than their utility would seem to provoke.

Thermodynamics has been useful in exploring the process of degradation of damage to stone and metals (e.g. Livingston 1991, Raychaudhuri & Brimblecombe 2000, Zhang-yue 1989). Recent work on the Vasa has highlighted the usefulness of this approach through Pourbaix diagrams to understand the production of sulphuric acid in the wood (Sandstrom et al. 2002). Raychaudhuri & Brimblecombe (2000) have used thermodynamic arguments to unravel the problems of a wide spread concern about the damage to lead and calcareous materials by formaldehyde in museums. Laboratory studies suggested lead was relatively insensitive to formaldehyde. Damage might arise through adjunct formic acid, but formates were often absent from damaged items. Our work suggested that significant lead corrosion was found only when formaldehyde was in oxidizing atmospheres. In the absence of oxidants such as hydrogen peroxide there was only the merest tarnish even at high humidity. This suggested that oxidation is an important control on corrosion by formaldehyde. Although the oxidation leads to formic acid the thermodynamically stable products were basic lead carbonates, plumbonacrite, $Pb_{10}(CO_3)_6(OH)_6O$ and hydrocerussite, $Pb_3(CO_3)_2(OH)_2$ and not always lead formates.

Kinetics may also give an insight into the way in which materials degrade. Recently we have explored the kinetics of SO_2 and NO_2 oxidation in materials. The Vasa studies highlighted the importance of iron in catalyzing the oxidation of SO_2 to sulphuric acid as did our earlier studies which hinted at the importance of metals in the degradation of leather and parchment (Bowden & Brimblecombe 2000). However subsequent studies suggest that in leather unless the metals are at

very high concentrations, they may be bound to protein, and not especially effective as catalysts (Bowden & Brimblecombe 2003).

5 THRESHOLDS

Another key argument in the heritage field that frequent provokes a great deal of argument is the existence or absence of thresholds. Formally a threshold would be a concentration or flux that resulted in no damage. In the health field there are long arguments as to whether the dose and response extends to zero or some small harmless value of dose.

There are similar fundamental limits set by thermodynamics for the damage to materials (Brimblecombe 1994). Gas–solid reactions set pressures below which the reaction will not occur. This is largely driven by the fact that solids are taken as standard states in thermodynamics and set to unity. However often when one examines the thermodynamics of many systems, only extremely low concentrations, far lower than that encountered in the unpolluted atmosphere, yield no reaction. Nevertheless there are some systems, such as that of the lead formates, where gas phase concentrations (i.e. of formic acid) could be low enough to cause no damage (Raychaudhuri & Brimblecombe 2000).

There are however more realistic thresholds. In a practical sense we should consider operational thresholds. This can be thought of in two ways:

1. We could consider these as concentrations where the rate of damage from the pollutant becomes less significant than damage by other mechanisms.
2. Alternatively, it could be the concentration where survival time is sufficient.

These approaches need to address difficult philosophical questions about what is an acceptable degree of damage to a cultural item or a reduction in its lifetime. They often raise considerable passion. In both health and cultural heritage thresholds are often objected to on the basis that they become interpreted as permission to pollute.

6 STANDARDS

One of the hopes long entertained in the conservation field is the ability to set guidelines values for parameters in indoor and outdoor environments. Such conditions once met, it is hoped will ensure a long life for the object of interest. Indeed one has to accept that rational sets of guidelines would be a most useful asset to the conservator, even if only to allow prediction of the likely rate of deterioration in a given situation (Brimblecombe 1994).

They do allow well-informed management decisions. Yet it is surprising how few standards appear to be constructed in this way. Relative humidity after getting off to a rather arbitrary choice of 50% now seems to be more clearly addressed, but notably continues to be expressed as a value and a range. It would seem more sensible, as it is a cyclic process, to set standards in terms of frequency and amplitude in addition to the mean. In the case of exposure to light there is a clear attempt to relate the light exposure to fading. However some most inexplicable concerns seem to be raised about very brief exposures to short exposures to electronic flash, that I confess I do not understand. However, I note a recommendation that the safest lighting for photographing textiles is electronic flash, because despite high output of UV and IR in the flash are of very short duration (Swann 1998).

Not so for air pollutants, looking at available recommendations (Blades et al. 2000), they seem quite arbitrary, often appearing to be based on what is technically feasible rather than an analysis of damage to materials. It is possible to attempt an estimate of appropriate standards based on an analysis of a very long-term (60-year) exposure of cultural items. This has been done for book-binding leathers exposed to low concentrations of sulphur dioxide and basing the standard on the

serviceability (to avoid the difficult consideration cultural worth) of the bindings (Brimblecombe 1998).

Tétreault (1999) has argued for a best knowledge rather than best technology approach and in particular has promoted a notion of *no observable adverse effect level* (NOAEL) and a *no observable adverse effect dosage* (NOAED). It is argued that this can use the increasing amount of data on the interaction between materials and pollutants in museums and simulated museum environments. Such data helps to narrow the range of critical levels of pollutants.

However, difficulties still remain. The case of lead corrosion and formaldehyde treated above reminds us of the complexity. Formaldehyde proved to be a precursor and not the corrosive agent, which makes setting formaldehyde concentration standards for museums of little value. It is not the concentration of formaldehyde that is important, but rather it's potential to oxidize to formic acid. This potential is not easy to evaluate.

The form of air pollution standards is important because the concentration/time dependent model used for health protection is not suitable. It may be that the critical loads adopted for acid rain damage to ecosystems is more relevant. The issue is complicated by: problems with pollutant identification, damage issues, and the number of targets, timescales, accumulation and synergisms. In the case of outdoor pollution we should consider the basis of 96/62/ec air pollution standards, which derive from:

- "limit values… based on findings of international scientific groups…" as in position papers
- "reference methods… specified"
- "other techniques beside direct measurement" indicative monitoring
- "preliminary representative data"
- a cost benefit analysis.

Such an approach has been hard to adopt for the cultural heritage because the 96/62/ec regulations typically derive from scientific findings in position papers. Even for a well-known material like building stone, knowledge is often so patchy, that justifying a heritage standard is difficult. There are often no specified reference methods. Cost benefit analysis has been done for the architectural heritage, but less commonly for museum collections, particularly in relation to air pollution because outdoor air pollution seems such an uncontrollable externality.

Cultural heritage is not at all like the protection of human health from air pollutants. In the case of human health the interaction is limited to a single species. The protection of cultural heritage involves protecting an enormous range of different materials. This makes it more akin to an ecosystem or a zoo, than a human population or a city. It may well be that some of the novel techniques such as neural networks or fuzzy logic (Fisher 2003) offer ways forward in understanding that problem.

7 REGULATION

The idea of regulation to given standards seem to lie at the heart of preventive conservation and to provide enhanced protection. They are also useful in:

- creating uniformity
- spreading the load
- offering justified goals
- offering peace of mind
- creating a sense of professionalism.

There are many critics of environmental norms. Faith in guidelines should not be used to shift responsibility for heritage to the architect or engineer. Sometimes environmental norms can lead poorly justified over-protection, on the basis that it minimises the amount of understanding required. One can go even further and take a cynical view of regulation and see pollution control as linked

to the accretion of regulatory power by government agencies. In the heritage field one should note that:

- external agencies keen to regulate
- cultural ministries at a national level have typically been weak
- European Commission keen to regulate heritage as shown in EC 62/96 and CAFÉ
- HVAC engineers often favour regulation of the museum environment.

A further problem is the cost of regulation. It is important to recognise that the cost of regulation is usually dispersed away from the regulatory agency, which may gain financially through licences, validation etc. This can be seen in urban air pollution issues where the costs of monitoring and enforcement are typically shifted to local authorities or adoption of control devices often borne by industrial/consumer – a frequent source of complaint.

Much needs to be done and we have a lot to learn. However, we may need to remind ourselves that standards offer no panacea for heritage!

ACKNOWLEDGEMENTS

Some of the ideas developed here benefited from funding under the EU Projects AER ENV4-CT95-0088 and IMPACT EVK4-CT2000-00031.

REFERENCES

Appelbaum, B. 1991. *Guide to Environmental Protection of Collections* Madison CT: Sound View Press

Baer, N. S. 1991. Assessment and management of risks to cultural property. In N. S. Baer, C. Sabbioni & A. I. Sors (eds) *Science, Technology and European Cultural Heritage*, pp. 27–36. Oxford: Butterworth-Heinemann

Benarie, M. & Druzik, J. R. 1992. Entropy and risk assessment of cultural heritage conservation. *European Cultural Heritage Newsletter on Research* 6: 14–17

Blades, N., Oreszczyn, T., Bordass, B. & Cassar, M. 2000. *Guidelines on Pollution Control in Museum Buildings* London: Museum Practice, Museums Association

Bowden, D. & Brimblecombe, P. 2000. Scanning electron microscopy of sulfur profiles in parchment. *Journal of the Society of Leather Technologists and Chemists* 84: 177–186

Bowden, D. & Brimblecombe, P. 2003. Oxidation of sulfur dioxide in colligenaceous materials. *Studies in Conservation* (prepared for submission)

Brimblecombe, P. 1990. Composition of museum atmospheres. *Atmospheric Environment* 24B: 1–8

Brimblecombe, P. 1994. The balance of environmental factors attacking artifacts. In W. Krumbein, P. Brimblecombe, D. E. Cosgrove & S. Staniforth (eds) *Durability and Change: The Science, Responsibility, and Cost of Sustaining Cultural Heritage*, pp. 67–79. Chichester: John Wiley and Sons

Brimblecombe, P. 1998. Pollution studies. In R. Larsen (ed.) *Deterioration and Conservation of Vegetable Tanned Leather, Protection and Conservation of the European Cultural Heritage*, pp. 25–31. Copenhagen: Royal Danish Academy of Fine Arts

Brimblecombe, P., Blades, H., Camuffo, D., Sturaro, G., Valentino, A., Gysels, K., Van Grieken, R., Busse, H.-J., Kim, O., Ulrych, U. & Wieser, M. 1999. The indoor environment of a modern museum building, the Sainsbury Centre for Visual Arts, Norwich, UK, *Indoor Air* 9: 146–164

Brimblecombe, P., Shooter, D. & Kaur, A. 1992. Wool and reduced sulphur gases in museum air. *Studies in Conservation* 37: 53–60

Fisher, B. 2003. Fuzzy enviromental decision making: applications to air pollution. *Atmospheric Environment* 37: 1865–1877

Koestler, R. J., Brimblecombe, P., Camuffo, D., Ginell, W. S., Graedel, T. E., Leavengood, P., Petushkove, J., Steiger, M., Urzi, C., Verges-Belmin, V. & Warscheid, T. 1994. How do external environmental factors accelerate change. In W. Krumbein, P. Brimblecombe, D. E. Cosgrove & S. Staniforth (eds) *Durability and Change: The Science, Responsibility, and Cost of Sustaining Cultural Heritage*, pp. 149–163. Chichester: John Wiley and Sons

Livingston, R. A. 1991. Influence of the environment on the patina of the statue of liberty. *Environmental Science and Technology* 25: 1400–1408

Putt, N. 2001. The Road to Vantaa: The European Preventive Conservation Strategy Project. In N. Putt & H. Hayhä (eds) *European Preventive Conservation Strategy, A Project Report*, pp. 23–37. Vantaa: EVTEK Institute of Art and Design

Raychaudhuri, M. & Brimblecombe, P. 2000. Formaldehyde oxidation and lead corrosion. *Studies in Conservation* 45: 226–232

Sandstrom, M., Jalilehvand, F., Persson, I., Gellus, U. G., Frank, P. & Hall-Roth, I. 2002. Deterioration of the seventeenth-century warship Vasa by internat formation of sulphuric acid. *Nature* 415: 893–896

Swann, J. 1998. *Guidelines for Costume* ICOM

Tetreault, J. 1999. Standards Levels of Pollutant in Museums: Part II. In A. W. Brokerhof (ed.) *Indoor Air Pollution: Detection and Prevention, Presentation Abstracts and Additional Notes*, Amsterdam: Instituut Collectie Nederland

Thomson, G. 1978. *The Museum Environment*. London: Butterworth

Zhang-yue, L. 1989. Thermodynamic analysis of marble deterioration in the atmosphere. *Water, Air and Soil Pollution* 48: 417–422.

Cultural Heritage Conservation and Environmental Impact Assessment by Non-Destructive Testing and Micro-Analysis – Van Grieken & Janssens (eds)
© 2005 Taylor & Francis Group, London, ISBN 90 5809 681 5

Non-destructive testing by the Rp method of bronze monuments: three case studies

G. D'Ercoli, G. Guida, M. Marabelli & V. Santin
Istituto Centrale per il Restauro, Roma, Italy

ABSTRACT: Three case studies are illustrated on the application of an electrochemical non-destructive method, the measurement of polarization resistance, for checking the rate of corrosion and for planning and controlling the restoration procedures of bronze monuments.

1 INTRODUCTION

The restoration of bronze monuments requires a project of measurements, mainly non-destructive, with the aim of verifying the state of conservation, both of the surface and of the metallic structure, and of controlling the electrochemical corrosion rate of the alloy before and after restoration.

A first example of this methodological approach is represented by the research carried out on the monument "Il Perseo e la Medusa" (Fig. 1) of Benvenuto Cellini, exposed outdoors, under the "Loggia dei Lanzi" in Florence.

The following controls have been carried out:

- Energy dispersive fluorescence x-ray of the alloy
- Metallographic analysis

Figure 1. Perseo. Measurements during the maintenance project.

Figure 2. Dying Horse. Rai building. Roma.

– IRS of the patinas and sediments
– Measurement of corrosion rate
– Spectrophotometric control of the surface
– Ultrasonic controls of the structure
– Analysis of the clay core.

Quite the same approach has been followed for other two artefacts, the modern monument "Dying Horse" (Fig. 2) of Francesco Messina in Rome and the archaeological "Dancing Satyr" from Mazara del Vallo in Sicily.

2 MEASUREMENTS

Only at the end of the research mentioned above the intervention on the Florentine bronze statue has been carried out; in particular the measurement of the electrochemical corrosion rate has supported the resolution of maintaining the restored monument outdoors.

The measurement of the wet corrosion rate quoted above (D'Ercoli et al. 1997), based on the polarization resistance (Rp), needs particular attention and the checking with other parallel methods; in fact the method records the very small shift of potential due to the application of an external known current impulse and then calculates the Rp and the corrosion rate of the alloy.

The results are influenced by the thickness and composition of the patinas, by their porosity and permeability, by the possible presence of salts catalysts of corrosion, and by the composition and phase structure of the alloy.

It is also fundamental to ascertain composition and thickness of outer layers of coatings and/or sediments-encrustations. Furthermore, composition and other chemical-physical characteristics of the patinas and encrustations will depend strictly on the surface orientation to the rain water, to the sun radiation, to the moisture absorption and finally to the dry and wet deposition of air dispersed pollution agents.

Table 1. Wet corrosion rate (micrometers/y) of "Perseo" surface inside and outside areas washed with deionised water.

Area	Patina color	No of measurements outside	Mean value of corrosion rate	No of measurements inside	Mean value of corrosion rate
P-S1	Dark grey	10	6.8	7	8.5
P-S2	Black	7	0.4	6	0.3
	Black	16	0.2		
P-S3	Dark grey	5	0.6	5	0
P-S4	Green/grey	9	1.6	6	1.5
	Green/grey	21	1.0		
P-S5	Dark grey	8	1.1	5	0.7
	Dark grey	27	4.7		
M-S6	Dark grey	3	0.4	5	0.2
	Dark grey	5	2.1		
P-N7	Black	13	0.3	4	0.3
	Black	15	0.1		
P-W8	Green/blue	5	22.0	6	19.3
P-N9	Green/black	5	0.8	5	0.3
	Green/black	10	0.5		
P-N10	Clear green	17	6.1	5	70.0
	Clear green	13	3.2	5	12.8
	Clear green			3	4.7
M-N11	Clear green	15	66.1	3	215
	Clear green	7	69.4	7	171
	Clear green	7	72.0	3	96.0
M-N12	Green	8	10.6		
	Green	5	13.6	5	45.6
	Green	19	4.7	8	11.0
M-W13	Green/grey	13	19.3	5	29.6
	Green/grey	15	13.6	4	7.4
S-E14	Black	8	0.2	8	0.2
M-S15	Dark grey	5	5.2		
M-E16	Dark grey	6	9.7	Before washing	
	Dark grey	7	84.9	During washing	
	Dark grey	5	16.8	After washing	
P-E17	Green/grey	6	1.4		
P-E18	Dark grey	24	3.5		

Legends

P = Perseo
M = Medusa and the Cloth
N = North exposure (generally washed)
S = South exposure (generally sheltered)
E = East exposure (not washed, but the Sword)
W = West exposure (washed)

An example of this complex study is represented by the survey on the Perseo monument (D'Ercoli et al. 2001, Santamaria & Marabelli 2001); the highest polarization resistance has been measured in the areas covered by an ancient compact and adherent black coating, while inversely a marked rate of corrosion is exhibited by surfaces with thin patinas, reach of copper sulphates, continuously leached by rain water. Finally, areas covered by encrustations, sheltered by the architecture of the Loggia, have normally a reduced corrosion rate (Table 1).

An totally different example is offered by the modern monument "The Dying Horse", of Francesco Messina, in Rome (D'Ercoli et al. 2002). This modern monument was finished with an artificial patina very thin, probably obtained with a chemical reagent containing chlorine.

Therefore, the corrosion rate is everywhere very high (Table 2), and the patina is thin, porous, not sheltering and reach of sulphates and chlorides. The most delicate phase of

Table 2. Wet corrosion rate (micrometers/y) of the “Dying Horse”, in different areas.

Patina color	Area	No of measures	Min–Max	Mean value of corrosion rate
Light green	Fore left knee	6	80–290	145
Light geodetic drips	Rear left leg	3	110–640	300
Light geodetic drips	Rear left leg	5	310–640	426
Black geodetic drips	Rear left leg	6	110–180	137
Light geodetic drips	Rear left leg	7	470–620	523
Black geodetic drips	Rear left thigh and buttock	8	70–140	105
Light grey	Back	8	180–390	241
Light grey	Back	9	110–400	241
Light geodetic drips	Chest and fore left leg	8	240–330	286
Black geodetic drips	Chest and fore left leg	8	13–60	23
Grey	Fore right leg	8	350–480	420
Grey green	Chest	9	440–640	522
Brown geodetic drips	Belly, right flank	7	80–350	166
Brown geodetic drips	Belly, right flank	6	180–210	195
Brown geodetic drips	Belly, right flank	9	200–240	212

Figure 3. Dancing Satyr.

restoration has been the application of the protective coating, a double layer formulation (acrylic copolymer/microcrystalline wax).

Finally it is worth-while to mention the very complex survey for an archaeological statue “The Dancing Satyr”, rescued from the sea, near Mazara del Vallo, in Sicily (D’Ercoli et al. 2003).

The control of the corrosion rate has been particularly difficult, for the presence of sea encrustations and corrosion products with thickness, adhesion and cohesion very different from point to point and with areas sometimes sheltered by the encrustations, damaged by pitting corrosion (Fig. 3) (Table 3).

Table 3. Wet corrosion rate (microns/y) of the “Dancing Satyr”, in different areas.

Patina color	Type of patina	Area	No of measures	Min–Max	Mean value of corrosion rate
Dark brown	Rust sediment and calcareous encrustation on corrosion products	Left temple, neck, right shoulder	12	0.4–20	14.4
Green	Corrosion products and calcareous encrustation	Right thigh	9	2.0–30	12.3
Green	Corrosion products	Right buttock	9	38–84	73.3
Green	Corrosion products with paratacamite	Left thigh	11	74–680	1030
Green	Corrosion products with paratacamite	Left shoulder	5	14–780	376
Grey green	Calcareous encrustation	Right buttock	6	2.2–10	6.1
Grey green	Corrosion products and calcareous encrustation	Left buttock	12	7.4–400	96.6
Green	Corrosion products with paratacamite	Left thigh	22	2–180	56.4
Green	Corrosion products with paratacamite	Left thigh	3	1760–>2000	1840
Grey green	Corrosion products and calcareous encrustation	Right thigh	5	56–86	69.6
Green yellow	Corrosion products, calcareous encrustation and mud sediment	Right buttock	11	8–78	48.5
Black	Carbonaceous sediment and calcareous encrustation on corrosion products with paratacamite	Left buttock	5		>2000
Black	Carbonaceous sediment and calcareous encrustation on corrosion products (probable paratacamite)	Left flank	23	20–1260	305
Black	Carbonaceous sediment and calcareous encrustation on corrosion products	Waist-rear	5	38–66	54.0
Black	Carbonaceous sediment and calcareous encrustation on corrosion products	Left thigh	5	50–200	121
Brown	Corrosion products with calcareous encrustation and mud sediment	Back-middle	5	14–18	18.4
Brown	Calcareous encrustation and mud sediment on corrosion products	Back-middle	5	140–160	148
Brown	Discontinuous calcareous encrustation on corrosion products (probable paratacamite)	Left shoulder	5	580–860	724

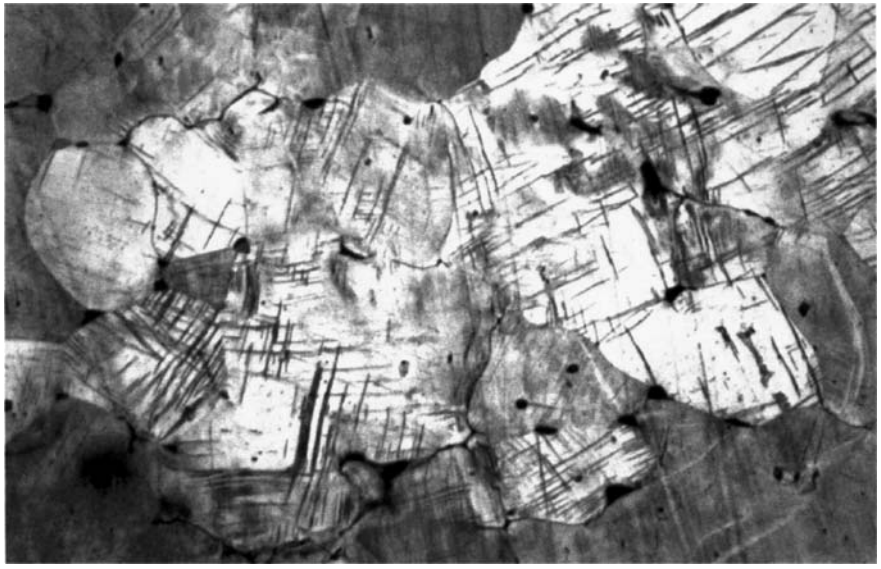

Figure 4. Perseo. Heavily worked microstructure (magnification 200×).

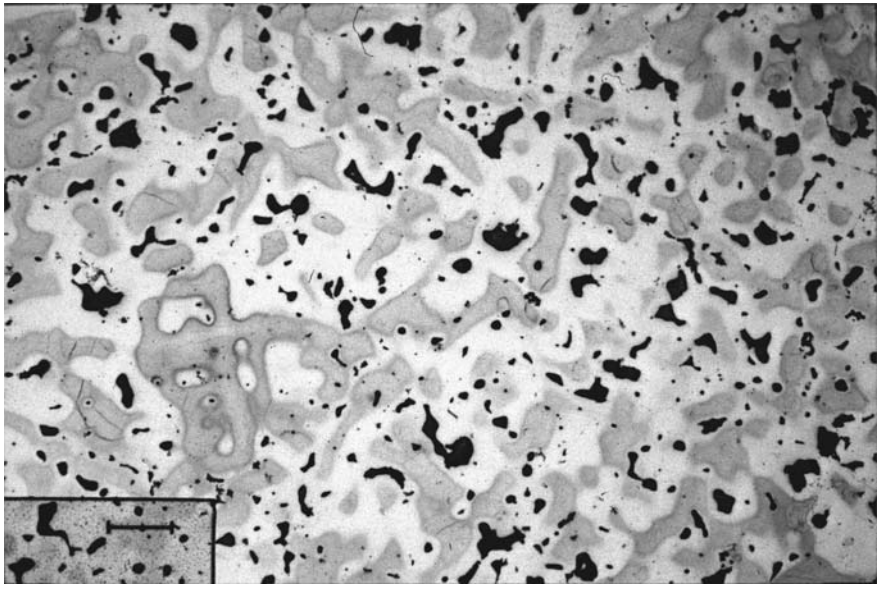

Figure 5. Dying Horse. Dendritic primary microstructure (magnification 100×).

The conclusion is that the archaeological bronzes constitute a very complex and variable situation, requiring repeated measurements at various cleaning levels, both mechanical and chemical.

Finally, metallographic analysis has been quoted between the methods adopted for the monument of the Perseo (Castellano et al. 2001).

This analysis, carried out on very small samples of the alloy, has allowed the study and documentation of the fine microstructure of the bronze, both for archaeometric and conservative purpose. Also a non-destructive metallographic examination has been applied, by using a video microscope

and special polishing micro tools. This examination has put in evidence a substantial difference in the structures of the Perseo and of the Dying Horse.

In fact, in the case of the Perseo, some areas of the surface have been heavily worked by Cellini and his assistants, not only for finishing and polishing the statue, but also for removing the outer blow-holes caused by a defective casting process (Fig. 4). On the contrary the statue of F. Messina exhibits a metallographic structure typical of a rough primary cast alloy, following the modern taste of the artist (Fig. 5).

3 CONCLUSIONS

The three monuments quoted above exhibit different corrosion rates, depending on the treatment of the surface and on the exposure to the outdoor climate and respectively to the marine environment. The Rp method represents a valuable, experimented procedure, which must be carried out with particular skillfulness, due to the complex and variable patina composition and surface structure.

The Laboratory of Chemistry of I.C.R. has worked in this field in the last forty years, with the aim of studying the ancient technological processes, directing diagnostic examination, documentation and restoration planning, and also supporting scientifically the final quality testing of the restoration procedure. It is a matter of fact that the Rp method plays in this field a special prominent role.

REFERENCES

Castellano, A., Cesareo, R., Cordaro, M., Gigante, G.E., Guida, G. & Marabelli, M. 2001. Indagini non-distruttive per il restauro del monumento bronzeo del Perseo di Benvenuto Cellini, Internal report. ICR, Roma.

D'Ercoli, G., Marabelli, M. & Santin, V. 1997. Monumenti bronzei: valutazione dello stato conservativo mediante la resistenza di polarizzazione. In Atti della LXIV Riunione, La scienza per i beni culturali: 225–233, 16–18 October 1997, Roma.

D'Ercoli, G., Marabelli, M. & Santin, V. 2001. Misure elettrochimiche per la salvaguardia del monumento del Perseo, Internal report. ICR, Roma.

D'Ercoli, G., Marabelli, M. & Santin, V. 2002. Il Cavallo Morente di Francesco Messina. Corrosimetria tramite misure della Rp, Internal report. ICR, Roma.

D'Ercoli, G., Marabelli, M. & Santin, V. 2003. Controllo elettrochimico della corrosione del bronzo "Satiro danzante" da Mazara del Vallo, Internal report. ICR, Roma.

Santamaria, U. & Marabelli, M. 2001. Analisi e caratterizzazione delle superfici corrose del monumento bronzeo "Il Perseo e la Medusa" di Benvenuto Cellini, Internal report. ICR, Roma.

Cultural Heritage Conservation and Environmental Impact Assessment by Non-Destructive Testing and Micro-Analysis – Van Grieken & Janssens (eds)
© 2005 Taylor & Francis Group, London, ISBN 90 5809 681 5

A study of artists' materials based on Raman spectroscopy and total-reflection x-ray fluorescence analysis (TXRF)

Peter Vandenabeele & Luc Moens
Ghent University, Laboratory of Analytical Chemistry, Ghent, Belgium

ABSTRACT: Raman spectroscopy and total-reflection x-ray fluorescence are used for the non-destructive molecular and elemental analysis, respectively, of artefacts. It appeared that the combination of both techniques offered a significant added value. The techniques were applied successfully to study pigments in medieval manuscripts and in Egyptian burial masks.

1 INTRODUCTION

During recent years, art analysis is becoming increasingly important, as (art-)historians, conservators and keepers increasingly request the application of scientific methods to answer questions concerning dating, provenance or authenticity of art objects. Next to the fundamental interest in the materials and techniques that the artists have been applying, their concerns involve the examination of interactions between different original materials and the reactions with the materials used for conservation treatments. Scientific studies can help in finding the origin of the degradation and may suggest new methods to slow down these detrimental processes.

Moreover, the spectroscopic examination of art objects may help in dating the artefact. Some pigments have well-described dates of first use and their identification is a way of dating the artefact *post quem*. A well-documented example is the invention of Prussian blue in 1704 by Diesbach in Berlin. Other materials are known to have disappeared, when they were substituted by other materials with better properties (e.g. better hiding power, colouring strength, lightfastness, lower price, less unhealthy, etc.). Their retrieval enables to date the artefact *ante quem*. A well-known example of this is the use of natural Indian yellow. This pigment was extracted from the urine of cows that were fed with mango leaves and the pigment consisted mainly of magnesium and calcium salts of euxantinic acid ($C_{19}H_{16}O_{11}Mg \cdot 5\,H_2O$). As this practice was very harmful for the animals – it caused kidney injuries and even their death – the production of the pigment was forbidden by law in 1900.

The discovery of anachronistic use of materials is an indication that the artwork has to be reattributed to another period of time or another geographic region, or it can be an indication for a forgery, since artists obviously cannot have used materials that were not available during their career. In these investigations, care has to be taken that no conclusions are drawn from the examination of restored areas.

If no anachronisms can be retrieved in the materials, another method may be used for the determination of the genuineness of a painted artefact. Comparing the pigments with the pigments that the same artist used in his other works may yield new indications. Inconsistencies might be a good indication for a falsification and further examinations may be considered. During the investigation of a painting that was attributed to Amadeo Modigliani certain pigments were found that were not observed in an extended set of paintings of the artist. Moreover, several pigments that were retrieved in all of these reference works were not present in the suspect artefact. This indication of forgery was confirmed later by a radiographic study of the painting technique of the

work. The strength of this method depends on the quality of the investigations and the extent of the set of reference paintings.

Large studies on the use and dissipation of certain materials and methods also provide information on ancient trade routes and on social, cultural and political interactions between groups of people. A typical example is the spread of lead-tin yellow type II ($PbSn_2SiO_7$) in the Low Countries at the beginning of the 14th Century: the pigment probably originated from Venice and Bohemian glass production.

In general, several analytical techniques are applied for the investigation of objects of art. In order to be qualified for this research, the methods have to meet several conditions. For the direct analysis of artefacts, the investigations have to be non-destructive. On the other hand, if sampling is needed, the examinations must be performed on small (micro-)samples. Depending on the questions to be answered, several methods have been applied for art investigation. Archaeometry profits from the continuous evolutions of analytical methods. Miniaturisation and the inherent decrease in sample consumption are typical examples of such improvements.

Certain methods, such as proton-induced x-ray emission (PIXE) and scanning electron microscopy, complemented with an energy-dispersive x-ray detection (SEM/EDX) allow the elemental composition of an artefact to be determined. The latter method shows an excellent lateral resolution. Another atomic spectroscopic method that is often used in this field to determine the elemental composition is x-ray fluorescence analysis (XRF). Infra-red (IR) and Raman spectroscopy on the other hand reveal molecular information. The high lateral resolution and the absence of sample preparation are highly favourable properties of micro-Raman spectroscopy (MRS). Separation methods, such as gas chromatography (GC), liquid chromatography (LC) and electrophoresis, are also applied in art analysis, mainly for the analysis of organic material, such as binding media.

Often the art scientist has to perform an analysis on request of an (art-)historian, keeper or conservator. In this interdisciplinary field of interest, for the sake of the preservation of the artefact, it is of high importance that there is a good communication between the team members and that the aims and objectives are clearly and well defined. Depending on the research questions, the appropriate analytical technique has to be selected.

When planning the examination of an object of art, the risk of damaging the artefact during spectroscopic investigation should be considered. Although most analytical methods that are applied to art analysis are non-destructive or at least their sample consumption is minimal, it should be considered that all manipulations of the artefact inherently include a certain risk of damage. In general the methods can be divided in two groups: methods that require no sample and techniques requiring a micro sample.

The first group of techniques is called non-destructive, which is an advantage in this field. A disadvantage is that the artefact or the analytical equipment should be brought together and therefore the development of transportable analytical devices is of high importance. When starting the investigation, the analyst has to consider possible long-term effects of the action. One way of classifying direct, non-destructive methods is by distinguishing imaging techniques, spatially resolved analytical techniques and surface analysis.

The second approach consists of sampling the artefact before analysis. Care has to be taken to limit the damage as much as possible, while the sample on the other hand has to be representative. Moreover, during the sampling procedure, transport to the laboratory and, if necessary, sample preparation contamination has to be avoided. Among the analytical techniques that require sampling, distinction can be made depending on whether the sample is destroyed ('consumed') during the analysis or not.

In this work micro-samples are used and two sensitive analytical methods are applied that provide complementary information. These methods have no sample consumption, allowing to perform all the investigations on the same samples. Total-reflection x-ray fluorescence analysis (TXRF) quantitatively reveals the elemental composition ($Z > 14$) of the sample, while micro-Raman spectroscopy (MRS) provides molecular information on the different components of the same sample.

In this chapter a short overview of these two micro-analytical techniques will be provided and then several examples of this approach will be given.

2 METHODS

2.1 *Total reflection x-ray fluorescence analysis (TXRF)*

Total reflection x-ray fluorescence analysis has successfully been applied to the microanalysis of, among others, environmental samples, forensic samples, biological tissues and artefacts.

After passing a quartz-reflector, acting as a low-pass filter, the primary x-ray beam is sent to an optically flat sample carrier under a very small angle (typically $<0.1°$). As a consequence of this special geometric arrangement, total external reflection occurs, causing a doubling of the fluorescence signal of the sample grains and drastically reducing the spectral background. The element-specific fluorescence x-rays are recorded by a LN cooled semiconductor detector, which is positioned in 90° geometry relative to the incident beam. As the sample consists of very small amounts of material, spread on the sample carrier, no matrix effects are observed and the relative amounts of the detected elements can be calculated directly from the signal intensities, using element-specific sensitivities. As for minute samples from artefacts no absolute sample mass is known (estimated to be less than 0.1 μg), only relative amounts of the detected elements can be given.

2.2 *Raman spectroscopy*

Recently, Raman spectroscopy is increasingly applied for the investigation of artefacts. The Raman effect was predicted in 1923 by Smekal and was for the first time observed by C.V. Raman in 1928. For these experiments he used sunlight. Later mercury arch lamps were involved and pure liquids were examined, requiring 600 ml of liquid and 24 hours accumulation time to record a spectrum. Due to instrumental innovations (e.g. the introduction of lasers, charge-coupled device (CCD) detectors, Fourier-transform (FT) instrumentation, …) sample requirements and accumulation times drastically decreased and Raman spectroscopy became increasingly important in molecular spectroscopy. Raman spectroscopy became accessible to research groups, performing molecular analysis in different domains, such as pharmaceutical analysis, semiconductor research, geological applications, biochemistry, etc. This evolution made that the instrumentation became available as well for other applications, such as art analysis. Recently, an increasing number of research groups are experiencing the advantages of applying Raman spectroscopy for the molecular investigation of art and antiquities. Results have been presented in areas as, among others, pigment analysis of wall paintings, manuscripts, easel paintings, glass and porcelain analysis, biomaterials (such as resins and binding media), corrosion products, etc.

The Raman effect may be considered as an inelastic scattering of electromagnetic radiation. The large majority of the scattered radiation has the same frequency as the incident (laser-)beam. This is called Rayleigh scattering. Only a very minute number of photons have a higher (Stokes Raman scattering) or a lower (Anti-Stokes Raman scattering) wavelength as the incident photons. The energy-shift is proportional to the vibrational frequency of a Raman active molecular vibration in the sample. Raman band positions are thus dependent on the strength of the bond and on the reduced mass of the constituting atoms.

Recently, different approaches to perform direct, non-invasive Raman analysis became available. Small objects can easily be positioned on the microscope table of a Raman microscope. Results have been published on the Raman analysis of porcelain cards and on the investigation of glazed medallions. Another approach consists of the use of a tilted microscope, which allows positioning the artefact in front of the microscope. Examples have been published on the use of fibre optics instrumentation for Raman investigations. Nowadays, miniaturisation of the method allows the construction of mobile spectrometers, which can be transported to the museum site, to perform the Raman analysis *in situ*.

Table 1. Overview of some pigments and their TXRF key-elements.

Vermilion	HgS	Hg	Lead white	$2PbCO_3 \cdot Pb(OH)_2$	Pb
Realgar	As_2S_3	As	Titanium white	TiO_2	Ti
Hematite	Fe_2O_3	Fe	Permanent white	$BaSO_4$	Ba
Red lead	Pb_3O_4	Pb	Massicot	PbO	Pb
Azurite	$CuCO_3 \cdot Cu(OH)_2$	Cu	Lead-tin yellow	$Pb_2SnO_4 \cdot Sn_2SiO_7$	Pb + Sn
Smalt	Co-glass	Co	Chrome yellow	$2PbSO_4 \cdot PbCrO_4$	Pb + Cr
Prussian blue	$Fe_4[Fe(CN)_6]_3$	Fe	Yellow ochre	$Fe_2O_3 \cdot nH_2O$	Fe

3 SELECTED TOPICS

In the next paragraphs this approach will be illustrated by means of two examples. First this combined approach is applied on the analysis of mediaeval manuscripts. It is shown that, by using both techniques, it is possible to go beyond simple pigment identification, but that some details on the manufacturing of these artefacts can be obtained. The second example shows the results of the analysis of Egyptian burial masks, where besides of pigment identification, some degradation phenomena were observed.

3.1 *The analysis of mediaeval manuscripts by TXRF and MRS*

Mediaeval manuscripts have been examined on several occasions. MRS has frequently been used for the identification of pigments. Elemental analytical methods are able to identify the pigments by means of key-elements: these are elements, or combinations of elements that are specific for a certain pigment. An overview of some important pigments and their key-elements is given in Table 1.

The combined method approach – using TXRF and MRS – has successfully been applied for the investigation of the breviarium Mayer van den Bergh, a marvellously illuminated manuscript, dating from the beginning of the 16th Century. By using the TXRF key elements, it was possible to identify most inorganic pigments. However, in some cases micro-Raman spectroscopy had to complete the investigation, for instance to differentiate between red lead (Pb_3O_4), massicot (PbO, orthorombic) and litharge (PbO, tetragonal) or to discriminate between several green copper containing pigments.

On the other hand, TXRF could provide quantitative information on the relative amounts of elements (main elements as well as impurities) that were present in the samples. It has been demonstrated that this information, in combination with the knowledge of the pigments present, could be of help for the discrimination between several artists or workshops that have contributed to the production of this manuscript.

Another example of using both techniques for the analysis of mediaeval manuscripts has been performed on the study of the Mercatellis manuscripts. Raphael de Mercatellis (1437–1508) was a natural son of Philips the Good and was born in Bruges in a Venetian family of merchants.

He studied theology at the university in Paris and became a Benedictine monk in the abbey of St. Peter (Ghent). Later he became abbot of the St. Peter's abbey in Oudenburg and at that time he started to establish his library (Fig. 1).

In contrast to other bibliophiles of the time, the Mercatellis-collection contained manuscripts in Latin, covering a broad range of subjects. Besides works on theology or canon law, the library contained treatises on astronomy, mathematics and medicine. Although book printing had already been invented at the time, Raphael de Mercatellis ordered manuscripts.

One of the manuscripts even is a hand-made copy of a work printed before. Some Mercatellis manuscripts have been examined with micro-Raman spectroscopy and total-reflection x-ray fluorescence. All the samples from the manuscripts contained a considerable amount of calcium. This was ascribed to the original preparation of the parchment. From the Raman investigations it was clear that calcium was present as chalk ($CaCO_3$) as well as gypsum ($CaSO_4 \cdot 2H_2O$).

Figure 1. Illustration from the Mercatellis manuscripts, showing a huge collection of books on the background. The large books were preserved in a vertical position and had ornaments in metal, in order to protect them. (This figure is presented in the signature in colours, at the end of this volume, Appendix, pg. 313)

The red samples contained vermilion (HgS) and some samples in addition to this also contained red lead (Pb_3O_4). The green pigment in one of the Mercatellis manuscripts had a similar spectrum as a synthetic basic copper sulphate. Further examinations of the synthetic basic copper sulphate showed a similar x-ray diffraction pattern as the green mineral brochantite ($Cu_4SO_4(OH)_6$). The ink samples from the manuscripts showed, after TXRF investigation a significant amount of iron. By using micro-Raman spectroscopy, the presence of iron-gall ink could be readily observed. By performing Raman investigations on the samples, it was possible to conclude that in the Mercatellis manuscripts only azurite ($2CuCO_3 \cdot Cu(OH)_2$) was used as a blue pigment.

Next to the identification of the pigments based on the key-elements, TXRF also provides the (inorganic) impurity pattern of the paint. This research focuses on the study of the dissimilarities between the samples taken from a single manuscript. In the Mercatellis-manuscript 'Expositio problematum Aristotelis' (Ghent University Library Ms. 72), the acanthus borders may be distinguished on stylistic grounds into 3 different groups. The difference between the first two groups is minimal. In order to examine whether or not this can be confirmed by TXRF, micro-samples were taken from the blue acanthus borders. By comparing the relative amounts of the non-pigment elements Fe, Zn, As, Ca and Pb, it was possible to differentiate between the three groups. A similar classification was found when comparing the blue samples of the acanthus borders as well as when looking at the blue initials.

3.2 *A combined method approach for the analysis of Egyptian burial masks*

Two Egyptian burial masks have been examined by using Raman spectroscopy as well as Total-reflection x-ray fluorescence analysis. In ancient Egypt, mummification has been applied during ca. 3000 years, and during an important part of this period, burial masks were in vogue. These masks were usually made by using linen, stiffened with plaster that was subsequently painted. They usually served as an identification of the mummies and their lustre was an expression of the importance of the person as well as of the craftsmanship of the manufacturer.

By using TXRF it was possible to obtain indications for most of the pigments in these masks. The white areas had Ca as key element, indicating the presence of calcium carbonate ($CaCO_3$) of gypsum ($CaSO_4 \cdot 2H_2O$). The green area contained a lot of copper, indicating the presence of a

green copper pigment, while the sample of the guilding of one of the masks contained ca. 10% (w/w) gold. The blue area contained Cu, indicating the presence of either azurite or Egyptian blue, while the red sample contained Hg, key element of vermilion (HgS) and Fe, the key element for hematite (Fe_2O_3). For the black areas, only non-characteristic elements were detected, which might originate from impurities in the paint. Carbon is not detected by TXRF. In a beige sample large amounts of Ca, As, S and Fe are retrieved, which are characteristic for the presence of chalk or gypsum, yellow ochre and an As containing pigment, probably realgar or orpiment. Orpiment is yellow arsenic(III) sulphide (As_2S_3), while realgar is the orange arsenic(II) sulphide (As_4S_4).

Micro-Raman spectroscopic examination confirms the findings of TXRF. The red sample contains grains of vermilion and hematite. Small traces of realgar were retrieved in these samples as well. The examination of the green sample with MRS, by using a T80 nm laser, does not yield a sufficiently intense Raman spectrum, due to absorption of the red laser by the green pigment grains. Fluorescence on the other hand caused difficulties for the identification of the blue copper containing pigment. Although this is not a positive identification, this finding confirms the suspicion that Egyptian blue has been applied. Indeed, due to fluorescence, no reference samples of this material could be obtained by using a 780 nm laser, while the other antique blue copper pigment, azurite, yields a prominent Raman spectrum. Black samples contain carbon black. The white areas of one of the masks were painted by using chalk, while on the other mask gypsum was applied. These materials can easily be distinguished by their Raman spectrum: the symmetrical stretch of the CO_3^{2-} ion is located at 1086 cm^{-1} in $CaCO_3$, while the symmetrical stretch of the SO_4^{2-} ion in gypsum is found at 1008 cm^{-1}.

By close examination of the beige sample, and in accordance to the TXRF results, revealed the presence of Chalk and limonite. Besides of these materials, some yellow particles gave rise to an unknown Raman spectrum, clearly different from the reference spectra of realgar or orpiment. Since there was a considerable amount of As detected by TXRF, it was expected that these grains were As containing. Therefore, an extensive literature search was performed, and it turned out that the Raman spectrum of these grains corresponds with pararealgar, a yellow photo degradation product of realgar, that was characterised by Roberts et al. in 1980. Clark and Gibbs showed that pararealgar has been applied aside of orpiment in a 13th Century manuscript and they suggest that the illuminators at that time might intend to use pararealgar and that they could distinguish between both of these yellow materials. The evolution of the Raman spectra during the fotodegradation of realgar is shown in Figure 2.

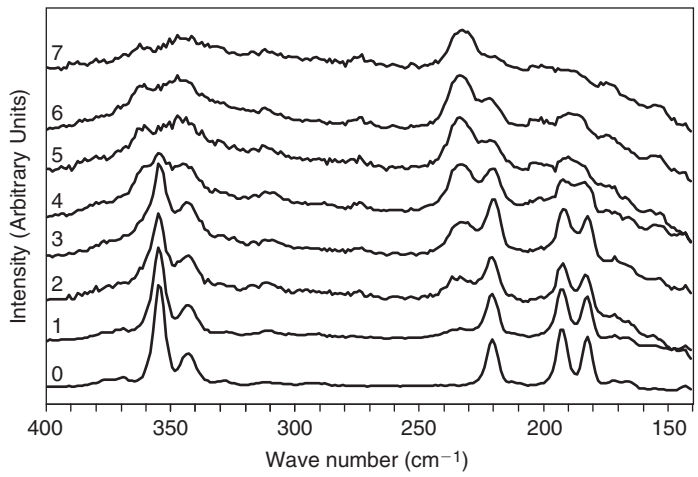

Figure 2. Photo-degradation of realgar: Raman spectra of a sample of realgar after 0 till 7 times 24 hours exposure to UV radiation.

As a consequence of these findings, some new (art-)historical questions rise. For instance, one can wonder whether this pararealgar was applied as such, or whether the degradation took place on the artefact. If the assumption is made that pararealgar was applied as such – considering the storage conditions of these masks (in the dark) and the retrieval of realgar in the red areas – the art-historical question remains whether the antique Egyptians intended to use pararealgar or that they used it mistakenly instead of orpiment.

4 CONCLUSIONS

It was shown that Raman spectroscopy and total-reflection x-ray fluorescence (TXRF) analysis both can be applied for the non-destructive analysis of artefacts. Raman spectroscopy is able to provide a molecular spectrum of the individual pigment grains in a micro sample of the artefact. TXRF on the other hand gives the relative amounts of the elements that are present in the same sample. Moreover, the examples in this work illustrate that the combination of these techniques is able to extract more information from these samples. When applying both techniques on the analysis of mediaeval manuscripts, it is possible to obtain an insight into the different craftsmen or workshops that manufactured this work of art. During the analysis of the Egyptian burial masks, it is demonstrated that pigments may be identified, even so well as degradation phenomena may be studied. Especially in this case, the interaction between conservators, art-historians and keepers on the one hand and the analysts on the other hand is illustrated: the first group comes with some questions to the analysts, who try to answer their problems. But during their research, new aspects of the artists' materials are found such as the identification of pararealgar, creating new questions that need further (art-)historical inquiries.

ACKNOWLEDGEMENTS

The authors wish to acknowledge the fund for scientific research-Flanders (F.W.O.-Vlaanderen) and the research council of Ghent University (BOF-UGent) for their financial support. P.V. is especially grateful to the F.W.O.-Vlaanderen for his post-doctoral fellowship.

REFERENCES

Adams, F., Adriaens, A., Aerts, A., De Raedt, I., Janssens, K. & Schalm, O., 1997. *Journal of Analytical Atomic Spectrometry*, 12, 257–265.

Adriaens, A., 1996. *Mikrochimica Acta*, 124, 89–98.

Al-Kofahi, M.M., Al-Tarawneh, K.F. & Shobaki, J.M., 1997. *X-Ray Spectrometry*, 26, 10–14.

Baer, N.S., Joel, A., Feller, R.L. & Indictor, N., 1986. Indian Yellow, In: *Artists' Pigments. A Handbook of their History and Characteristics*. Vol. 1, R.L. Feller (ed.), Cambridge: National Gallery of Art, Cambridge University Press.

Bouchard, M. & Smith, D.C., 1999. In: GeoRaman '99 – 4th International conference on Raman Spectroscopy Applied to the Earth Sciences, 31 June 9–11th 1999, Valladolid: GeoRaman '99 Abstracts. Special publication, Valladolid: Universidad de Valladolid press.

Cahill, T.A., Kusko, B. & Schwab, R.N., 1981. Nuclear Instruments and Methods, 181, 205–208.

Ciliberto, E. & Spoto, G. (eds), 2000. Modern Analytical Methods in Art and Archaeology, Chemical Analysis Series, Vol. 155, New York: John Wiley and Sons.

Clark, R.J.H., Cridland, L., Kariuki, B.M., Harris, K.D.M. & Withnall, R., 1995. Synthesis, structural characterisation and Raman Spectroscopy of the inorganic pigments lead tin yellow types I and II and lead antimonate yellow: their identification on medieval paintings and manuscripts, *J. Chem. Soc. Dalton Trans*. 16, 2577–2582.

Coupry, C., Lautié, A., Revault, M. & Dufilho, J., 1994. Contribution of Raman spectroscopy to art and history, *Journal of Raman Spectroscopy*, 25, 89–94.

Clark, R.J.H., 1995. *Chemical Society Reviews*, 187–196.
Dekeyzer, B., Vandenabeele, P., Moens, L. & Cardon, B., The Mayer van den Bergh Breviary (Ghent-Bruges Early 16th c.) Hands and Pigments, Conference Proceedings Colloque XII pour l'etude du dessin sous-jacent et de la technologie dans la peinture – La peinture dans les Pays-Bas au 16e siecle. Pratiques d'atelier. Infrarouges et autres methodes d'investigation, Bruges 11–13 September 1997.
Derbyshire, A. & Withnall, R., 1999. *J. Raman Spectrosc*. 30, 185–188.
De Reu, M., Van Hooydonk, G., Vandenabeele, P., Moens, L., von Bohlen A. & Klockenkämper, R., 1999. *Scriptorium*, 53, 357–372.
Derolez, A., The Library of Raphael de Marcatellis, Abbot of St. Bavon's, Ghent (1437–1508), E. 1979. Ghent: Story-Scientia Ltd.
Devos, W., Archaeometrische toepassing van totale reflectie XRF, INAA en ICP-MS, Ph.D. 1996. Thesis Ghent University.
De Benedetto, G.E., Catalano, F., Sabattini, L. & Zambonin, P.G., 1998. *Fresenius' Journal of Analytical Chemistry*, 362, 170–175.
Derbyshire, A. & Withnall, R., 1999. *Journal of Raman Spectroscopy*, 30, 185–188.
Espadaler, I., Sistach, M.C., Cortina, M., Eljarrat, E., Alcatraz, R., Cabanas J. & Rivera J., 1998. *Applied Spectroscopy*, 52, 5, 713–716.
Gardiner, D.J. & Graves, P.R., 1989. *Practical Raman Spectroscopy*, Berlin: Springer Verlag.
Henry C., Analytical Chemistry, 69, 309A–313A, 1997. In: I.R. Lewis & H.G.M. Edwards (eds), *Handbook of Raman Spectroscopy*, New York: Marcel Dekker, Inc., 2001.
Klockenkämper, R., Total reflection x-ray analysis, *Chemical Analysis Series*, Vol. 140, John New York: Wiley and Sons, 1997.
Klockenkämper, R. & von Bohlen, A., 1996. *X-Ray Spectrom*. 25, 156–162 (1996).
Learner T., *Spectroscopy Europe*, 8/4, 14–19.
Moens, L., Devos, W., Klockenkämper, R. & von Bohlen, A., 1995. *J. Trace and Microprobe Techniques*, 13, 119–139.
Moens, L. & Vandenabeele, P., 2002. Pigments and binders, a study of artists' materials based on Raman spectroscopy and total-reflection x-ray fluorescence analysis (TXRF), R. Van Grieken, K. Janssens, L. Van 't dack & G. Meersman (eds). *Conference proceedings on Art 2002, 7th international conference on non-destructive testing and microanalysis for the diagnostics and conservation of the cultural and environmental heritage, Antwerp: University of Antwerp.*
Moens, L., Devos, W., Klockenkämper, R. & von Bohlen, A., 1994. *Trends in Analytical Chemistry*, 13/5, 198–205.
Moens, L., Devos, W., Klockenkämper, R. & von Bohlen, A., 1995. *J. Trace and Microprobe Techniques*, 13, 119–139.
Prange, A., Reus, U., Bödekker, H., Fisher, R. & Adolf, F.P., 1995. *Anal. Sci.* 11, 483–487.
Punyadeera, C., Pillary, A.E., Jacobson L. & Whitelaw G., 1997. *X-Ray Spectrometry*, 26, 249–256.
Smith, D.C., Bouchard, M. & Lorblanchet M., 1999. *Journal of Raman Spectroscopy*, 30, 347–354.
Smith, D.C., 2000. Techne Sci. Service Hist. Art Civil. 11, 69.
Vallance, S.L., 1997. *The Analyst*, 122, 75R–81R.
Vandenabeele, P. (ed.), 2004. Journal of Raman Spectroscopy: Special Issue: Raman Spectroscopy in Art and Archaeology, W. Kiefer (ed. in chief), 35 (8/9).
Vandenabeele, P., Wehling, B., Moens, L., Dekeyzer, B., Cardon, B., von Bohlen, A. & Klockenkämper, R., 1999. *The Analyst*, 124, 169–172.
Vandenabeele, P. & Moens, L., 2000. Micro-Raman spectroscopy applied to the investigation of art objects, In: D.L. Andrews, T. Asakura, S. Jutamulia, W.P. Kirk, M.G. Lagally, R.B. Lal & J.D. Trolinger (eds), *Proceedings of SPIE Vol.4098, Conference proceedings Raman spectroscopy and light scattering technologies in materials science the International symposium on Optical science and technology, San Diego*, 301–310.
Vandenabeele, P., Wehling, B., Moens, L., Dekeyzer, B., Cardon, B. von Bohlen, A. & Klockenkämper, R., 1999. *The Analyst*, 124, 169–172.
Vallance, S.L., 1997. *The Analyst*, 122, 75R–81R.
Vandenabeele, P., Verpoort, F. & Moens, L., 2001. *Journal of Raman Spectroscopy*, 32; 263–269.
Vandenabeele, P., Weis, T.L., Grant, E.R. & Moens, L.J., 2004. *Analytical and Bioanalytical Chemistry*, 379, 137–142.
Vandenabeele, P., von Bohlen, A., Moens, L., Klockenkämper, R., Joukes, F. & Dewispelaere, G., 2000. *Analytical Letters*, 33/15, 3315–3332.
Vandenabeele, P., Wehling, B., Moens, L., Dekeyzer, B., Cardon, B., von Bohlen, A. & Klockenkämper, R., 1999. *Analyst*, 124, 169–172.

Van Hooydonk, G., De Reu, M., Moens, L., Van Aelst, J. & Melis, L., 1998. *Eur. J. Inorg. Chem*., 639–644.
von Bohlen, A., Devos, W., Moens, L. & Klockenkämper, R., 1994. *Restauro* 5/94, 328–330.
von Bohlen, A., Klockenkämper, R. & Tölg, G., 1987. *Fresenius Z. Anal. Chem*. 331, 2551–2555.
Wagner, B., Garbos, S., Bulska, E. & Hulanicki, A., 1999. *Spectrochimica Acta Part B* 54, 797–804.
Wehling, B., Vandenabeele, P., Moens, L., Klockenkämper, R., von Bohlen, A., Van Hooydonk, G. & De Reu, M., 1999. *Mikrochim. Acta*, 130, 253–260.
Weser, U., Kaup, Y., Etspuler, M., Koller, J. & Baumer U., 1998. *Analytical Chemistry*, 70, 511A–516A.

Cultural Heritage Conservation and Environmental Impact Assessment by Non-Destructive Testing and Micro-Analysis – Van Grieken & Janssens (eds)
© 2005 Taylor & Francis Group, London, ISBN 90 5809 681 5

Microfocus x-ray computed tomography (mCT) for archaeological glasses

H. Roemich & E. López
Fraunhofer-Institut fuer Silicatforschung (ISC), Bronnbach-Branch, Germany

F. Mees & P. Jacobs
Ghent University, Belgium

E. Cornelis & D. Van Dyck
University of Antwerp, Belgium

T. Doménech Carbó
Polytechnical University of Valencia, Spain

ABSTRACT: Glasses may develop thick corrosion layers during exposure in the soil. Corroded pieces are extremely fragile and require special conservation treatments. For the characterization of the morphology and the thickness of the degradation layer mainly scanning electron microscopy (SEM) is used. The preparation of samples to study cross-sections is invasive. As part of an EC-project, microfocus x-ray computed tomography (mCT) was optimized for heavily corroded glasses. The mCT device, equipped with a microfocus x-ray source and a CCD camera, is capable of achieving a high resolution. The corrosion layers have a lower attenuation for x-rays than the unaltered glass, resulting in contrasting grey values in the images obtained. The interpretation of the images was achieved by calibrating the method with artificially corroded model glasses and selected originals. With mCT, small fragments can be characterized non-destructively and their internal features and external morphology can be visualized as 3D model.

1 THE RESTORATION AND CONSERVATION OF ARCHAEOLOGICAL GLASS: A CHALLENGE

1.1 *Background*

Glass objects have been produced for more than 5.000 years, in Europe since about 3.000 years. They were made both for daily use and for artistic purposes. Historic glasses – especially those originating from antiquity and the Middle Ages – are mostly retrieved from archaeological excavations. The largest part is represented by vessel glass and glass jewels, rarely found as entire pieces but mostly as fragments (Newton & Davison 1989, Knight 1996).

Outstanding objects are presented in museums or private collections. The rearrangement of fragments to form a complete object is often not successful. These pieces are stored in depots and are available for scientific investigations upon request.

1.2 *Glass corrosion in the soil*

Glass corrosion is defined as the reaction of the surface with aqueous solution or with air humidity. This process is strongly influenced by the pH of the aqueous medium. In high alkaline solutions the glass network is attacked which leads to its dissolution. The acidic attack can be described as an ion-exchange of protons and network modifier ions (e.g. potassium). In addition, molecular water

diffuses into the glass. A surface layer with a low content of network modifier ions is formed which is called "gel layer" (Clark & Zoitos 1992, Roemich 1999a, 1999b).

In principle, the silica-rich gel-layer can reach a thickness of more than 200 μm and can act as a protective barrier against further attack on the bulk glass. However, temperature and humidity changes may cause shrinkage of this layer, leading to micro-cracks. The increased surface area continues to react with water, losing its contact to the bulk and causing it to flake off.

During atmospheric corrosion, e.g. of medieval window glass, the leached components can react with acidic gases such as CO_2, or SO_2, to form their respective salts (Newton & Davison 1989, Roemich 1999a, 1999b). These corrosion products may be soluble and be washed off the surface by rain. If they have low solubility in water (e.g. gypsum) they build up a crust, enclosing dirt or dust particles.

The degradation mechanism of glass in the soil is a complex sequence of glass dissolution, glass leaching and precipitation of secondary deposits. The degradation rate depends on the burial environment: water, acidity and alkalinity, redox-potential, the presence of salts, oxygen, complexing agents and organisms, as well as temperature (Roemich, in press, Roemich & López 2002).

1.3 *Degradation phenomena*

In general, archaeological glass finds exhibit more complex and different damage phenomena than window glass from the Middle Ages exposed to atmospheric weathering (Newton & Davison 1989, Roemich 1999). Lamellar corrosion layers and local pitting are two examples of heavy damage observed for excavated glass. Corrosion in the soil may lead to a destabilization of valuable originals, extensive loss of original material or to the complete destruction of the object.

Based on previous investigations it is expected that the thickness of the gel-layer and the corrosion crust will range between 10 and 100 μm and will reach several hundreds of μm in extreme cases. In addition, cracks and pores may determine the morphology of the degradation layer. Darkening effects, caused by the migration of trace elements from the soil into the glass or by the change of oxidation state of coloring components may occur, which leads to severe problems during restoration (Newton & Davison 1989, Roemich et al. 1998, López et al. 2002).

1.4 *Characterization of corroded glasses*

The thickness and structure of the gel-layer and the crust characterize the corrosion state of glass objects. Infrared (IR) spectroscopy (in transmission mode), an ideal method to measure the water content of slightly corroded slices of model glasses, is not applicable to original glasses (Roemich 1999a, 1999b). By light microscopy or scanning electron microscopy (SEM) information on the surface can be gathered. Depth profiles are obtained by analysing cross sections with microprobes, SIMS or SEM-EDX/WDX. XPS, a technique widely used for surface analysis, involves etching steps to obtain depth profiles. Examples of other techniques that allow depth profiling are dynamic SIMS and Rutherford Backscattering Spectroscopy.

The most efficient methods are destructive, because of the way samples have to be prepared, because they operate under high vacuum which alters the water-containing gel-layer during the measurement, or due to the nature of the technique. Therefore, they are applied only selectively and mostly on small pieces or edges which might not be representative for the entire object.

1.5 *Request for non-destructive analysis*

Within the same batch of excavated glasses, the corrosion state of pieces and fragments can be very different. During the restoration campaign all segments should be treated individually, according to their degree of deterioration. This is not possible if nearly all segments have to be analyzed by destroying part of the object.

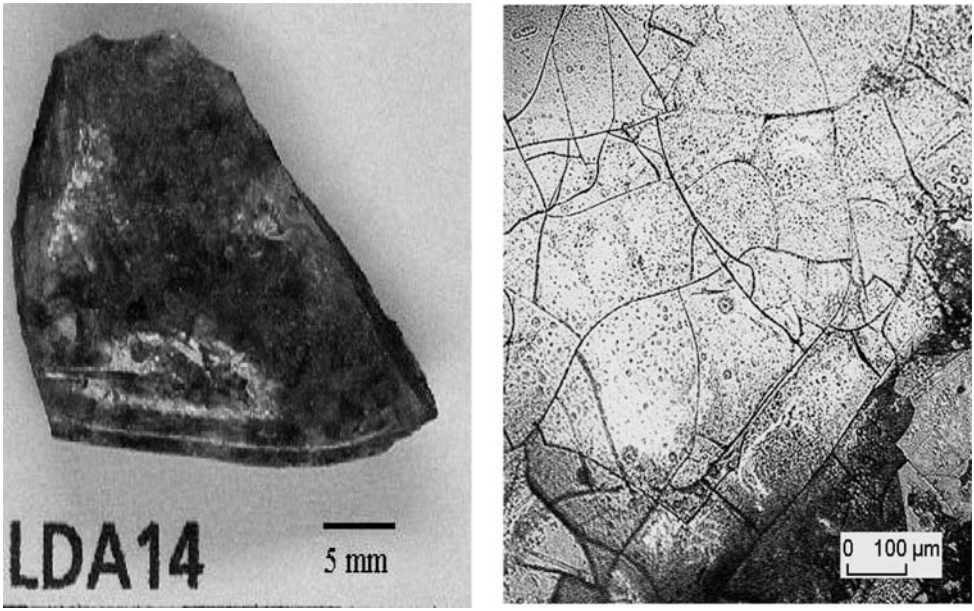

Figure 1. Original glass (sample number: LDA14), Middle Ages, excavated near Ulm, Germany. Left: Overview; the original green colour is not visible. The surface is covered by a brownish corrosion layer. Right: Light microscopy; micro-cracks are covering the surface, which appears slightly iridescent.
(This figure is presented in the signature in colours at the end of this volume, Appendix, pg. 313)

One crucial factor after excavation is cleaning of fragile glass surfaces. Also consolidation and conservation materials and methods play an important role in long-term preservation of archaeological glass. In general, there is an increasing need for conservation methods, which are tailored and tested for their specific use on archaeological glasses. For this purpose non-destructive analytical techniques, which may allow monitoring of the restoration/conservation procedure step by step and non-destructively are requested by all experts in this field.

X-ray computed tomography provided a promising new approach for non-destructive analysis, since the material contrast of partly corroded glasses seemed appropriate for CT measurements.

1.6 *Selection of samples*

In order to demonstrate the range of applications of mCT, glass segments with different composition and different corrosion states were examined. Most original glasses were provided by excavations in Spain (Almoina, Paterna, Manises, all in the region of Valencia). To expand the range of interesting corrosion phenomena, originals from Germany, the Netherlands and the UK were included. Selected examples are shown in Figures 1 to 5.

However, the development of a new analytical method relies on reference materials, which can be used for calibrating the new technique and for comparison with the results obtained by other methods. Systematic variations of glass composition and laboratory simulation of well-defined corrosion layers were necessary to obtain a broad variety of test samples (Roemich 1999). An example is given in Figure 6.

In the simulation experiments, model glasses with a high potassium content were used because they react rapidly under corrosive environments. Figure 6 shows damage phenomena obtained by artificial weathering in a climate chamber.

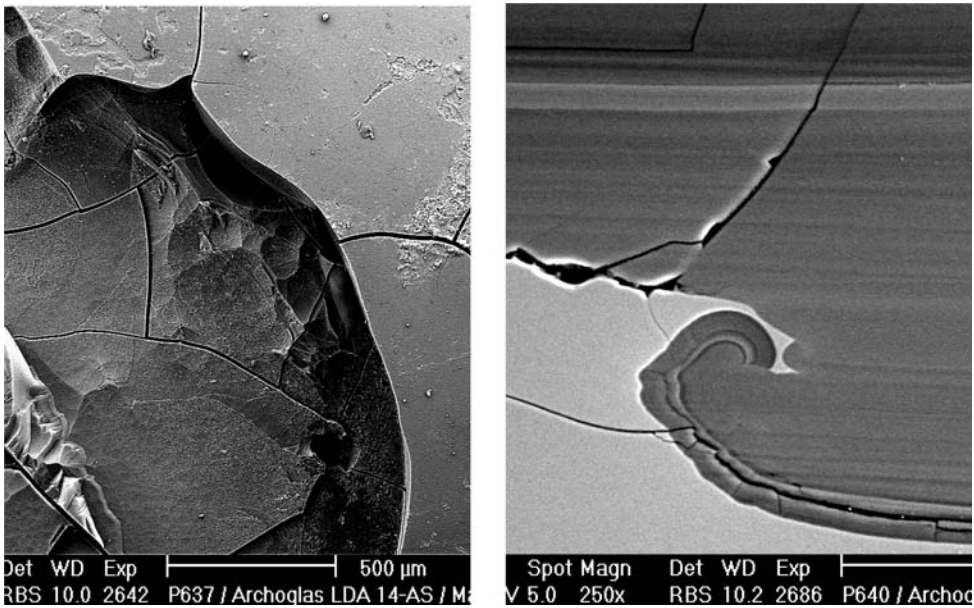

Figure 2. Original glass (sample number: LDA14), Middle Ages, excavated near Ulm, Germany. Left: SEM (surface); micro-cracks are visible, part of the surface is peeling off. Right: SEM (cross-section); the corrosion layer has a laminated structure, which varies in thickness.

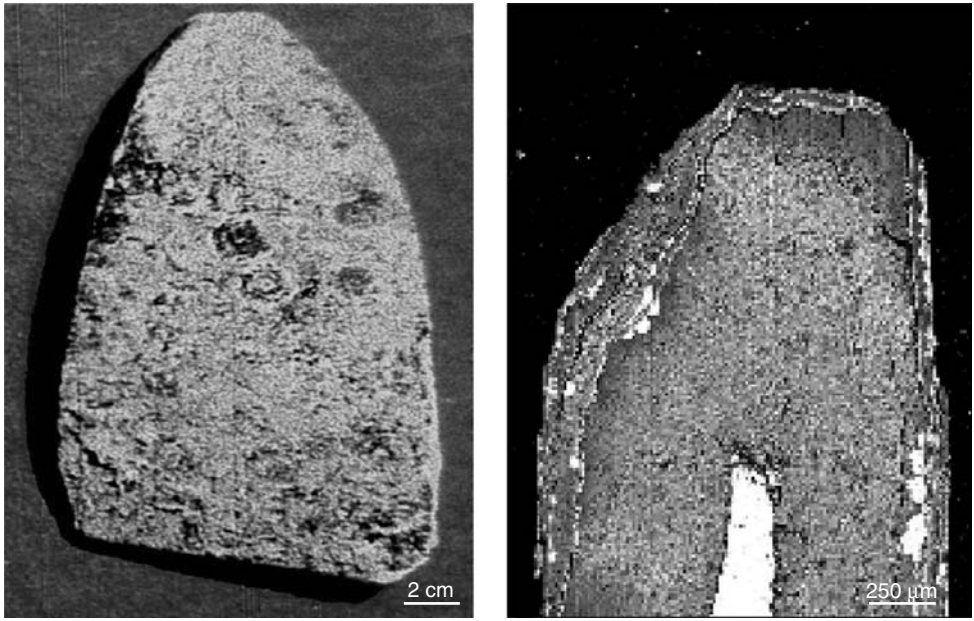

Figure 3. Original glass (sample number: F8 – 6), Middle Ages, excavated in Almoina (Valencia), Spain. Left: Overview; the external layer is opaque, which makes the fragment non-transparent. Right: SEM (cross-section); the thickness of the corrosion layer ranges between 100 and 400 µm, the remaining non-corroded bulk glass is about 100 µm thick.
(This figure is presented in the signature in colours at the end of this volume, Appendix, pg. 314)

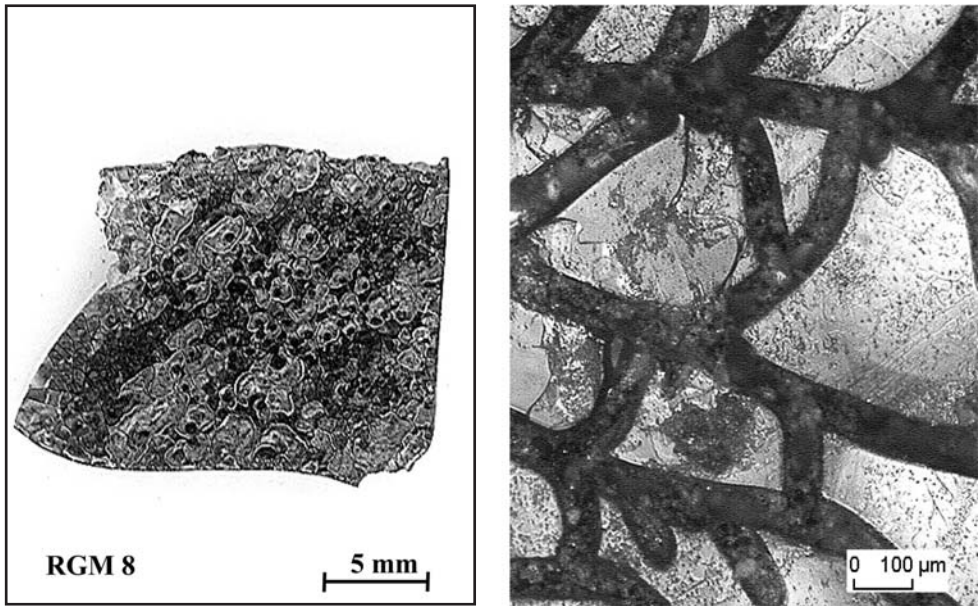

Figure 4. Original glass (sample number: RGM8), Middle Ages, excavated in Cologne, Germany. Left: Overview; the fragment seems to be completely corroded.
Right: Light microscopy; large cracks are covering the surface, which appears opaque.
(This figure is presented in the signature in colours at the end of this volume, Appendix, pg. 314)

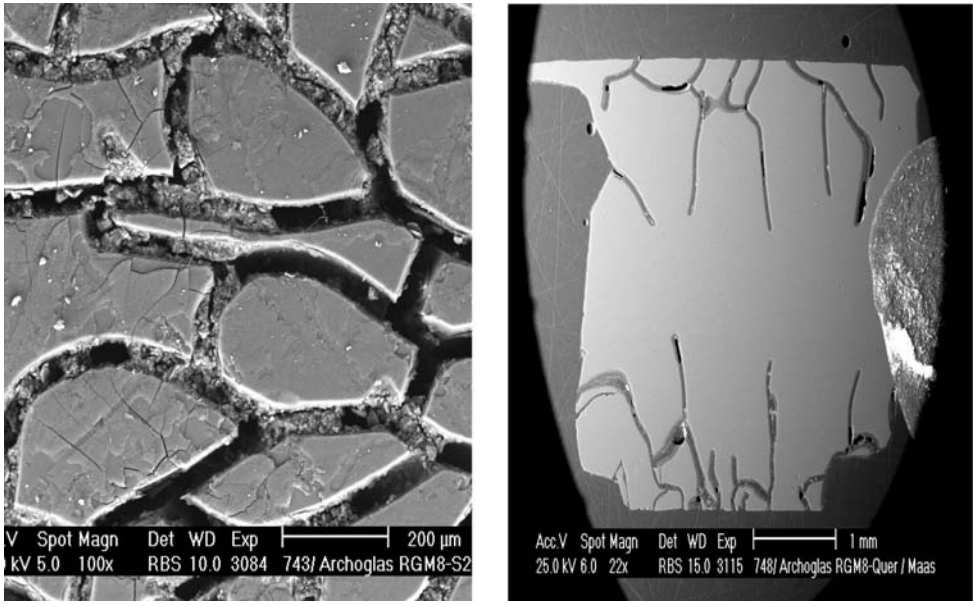

Figure 5. Original glass (sample number: RGM8), Middle Ages, excavated in Cologne, Germany. Left: SEM (surface); the network of cracks covers the surface, but it is not clear how the cracks are connected with each other. Right: SEM (cross-section); detail of the network of cracks, penetrating deep in the sample.

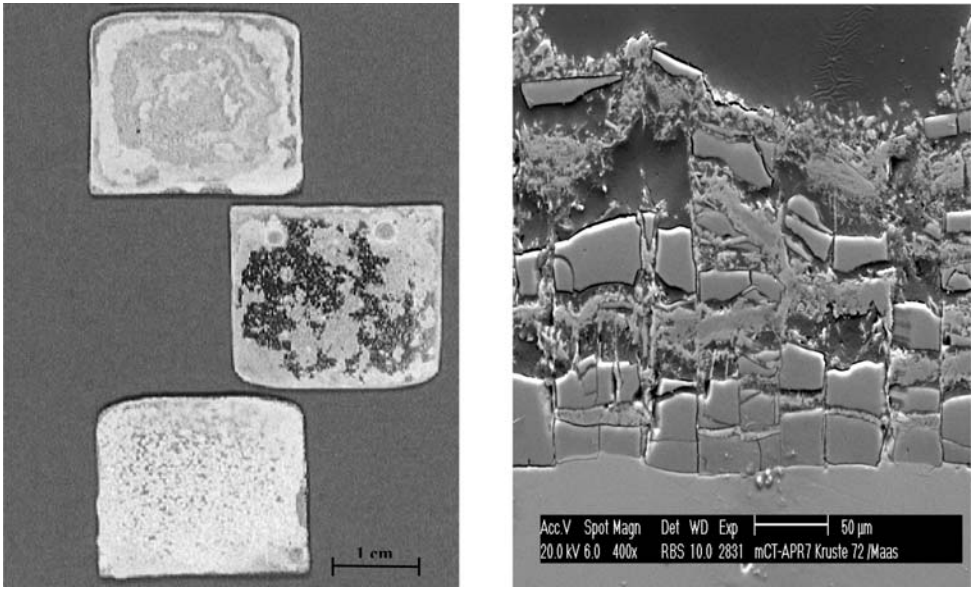

Figure 6. Model glasses with corrosion crusts. Left: Overview; model glasses with different chemical composition, after artificial weathering in a climate chamber. Right: SEM (cross section); gel-layer and corrosion products after accelerated weathering (left sample shown in overview).

2 MICROFOCUS X-RAY COMPUTED TOMOGRAPHY (mCT)

2.1 *The analytical background*

In medicine, tomographic research methods have already been used for nearly three decades. Procedures like nuclear magnetic resonance imaging or x-ray computed tomography (CT) are firmly established nowadays and provide information about the internal structure of parts of the human body, which cannot be obtained by other methods with a comparable information (Kak & Slaney 1999).

X-ray computed tomography is not only used for medical applications but also for materials research. The technique is based on recording the attenuation of the x-ray beam for different orientations of the sample relative to a central rotation axis. Information that is contained in these 1D or 2D projections is then used to reconstruct cross-sections perpendicular to the axis of rotation, showing patterns of variations in attenuation values. These patterns are determined by variations in density and composition. A reconstruction is typically calculated for sets of parallel slices, which can be used to create 3D models of selected classes of objects (see Figure 7).

2.2 *The application of CT for the protection of cultural heritage*

CT investigations, mainly using conventional medical scanners, have been used as part of a number of studies in the field of cultural heritage, e.g. to monitor moisture distributions in building stone samples (Jacobs et al. 1995, De Cleene 1996, Jacobs et al. 1997, Jacobs 2002) and for the study of sculptures. The resolutions obtained range between 0.1 to 1.0 mm. For the analyses of altered glass a resolution of 10 to 20 µm is required, implying the improvement of the analytical resolution by one or two orders of magnitude.

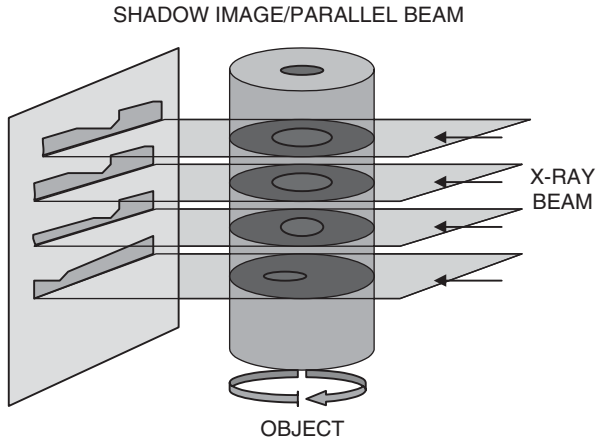

Figure 7. Schematic representation of the CT-principle.

2.3 *mCT equipment and measurements*

For this study a SKYSCAN 1072 Desktop x-ray Micro-tomograph with a 130 kV micro-focus x-ray source was used. The detector in this system is a CCD camera, coupled to a scintillator, producing 12 bit images of 1024 by 1024 pixels. The field of view of the camera is 2.5 by 2.5 cm.

During acquisition, x-ray radiographs are recorded for different angles during step-wise rotation between 0 and 180 degrees around a vertical axis. The most important acquisition parameters are voltage, magnification, frame averaging (which specifies the number of exposures made for each position of the sample), random movement (between successive exposures) and the use of hardware filters (to reduce beam hardening artifacts).

The reconstruction of horizontal cross-sections by a convoluted back-projection involves the use of beam hardening and misalignment corrections, and the selection of an interval for conversion to a 256 grey level scale.

mCT images commonly contain artifacts, which disturbs their appearance and hinders quantitative analysis. They can be reduced or eliminated by an appropriate choice of settings for the acquisition and reconstruction parameters.

During the project an optimal scanning procedure was developed. Two settings of parameters were defined, for low magnification and for high magnification. A normalization procedure was also developed, using a specific model glass as a reference, to obtain identical grey values for the same material in images produced by different scans.

2.4 *Interpretation of grey values*

A series of glasses with different compositions was measured to determine the range of grey values for non-corroded glass. As expected, the strongest attenuation was observed for glasses containing lead. Bulk material of "SiO_2", prepared by the sol-gel process, was resolved as a compound with very weak attenuation. All other glasses yielded values between those two extremes.

3 RESULTS AND INTERPRETATION

3.1 *Selected results*

Figure 8 shows an mCT image of a model glass for which the characterization by SEM is presented in Figure 6. It is obvious that the corrosion layer, which is a mixture of gel-layer material and corrosion products, is resolved as bright area (weak attenuation) covering the bulk glass, which

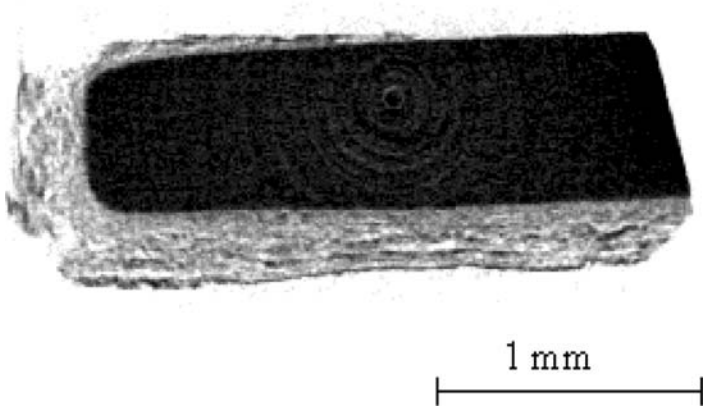

Figure 8. mCT image of a model glass (sample kc2) (one side of the sample was protected during weathering).

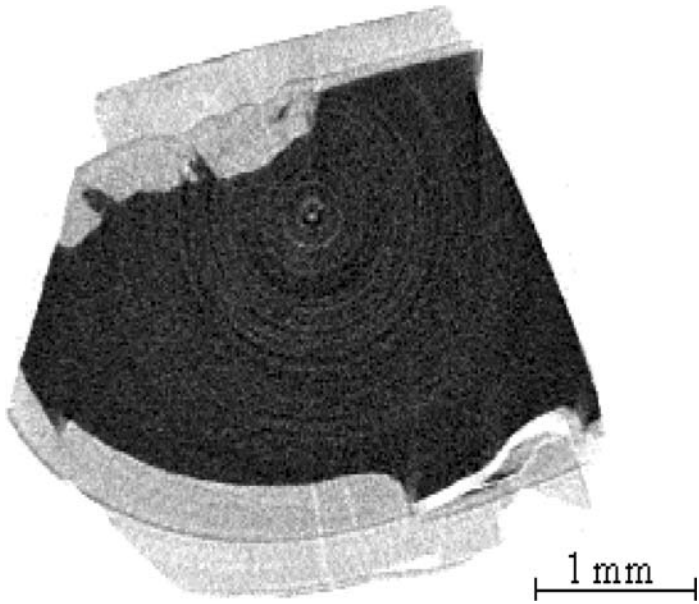

Figure 9. mCT image of the original glass LDA14.

appears darker in contrast (stronger attenuation). The thickness of the corrosion layer can be estimated by SEM to be about 150 μm. The mCT-image confirms this finding, which means that the material contrast detected by SEM and by mCT are comparable.

For the original glass LDA14, the laminated corrosion layer was characterized by SEM (Figure 2) and estimated to have a thickness between 100 and 400 μm. The corresponding mCT-image (Figure 9) confirms this result. However, it should be noted that the laminated substructure visible in SEM images can not be resolved by mCT.

The medieval glass F8 – 6 is even more corroded than LDA14, leaving only some unaltered bulk glass in the core of the sample (SEM in Figure 3). The mCT-image in Figure 10 gives a clear contrast between corroded layer and bulk glass. CT analysis also allows 3D-reconstruction of the sample and visualization of the inhomogeniety of the corrosion.

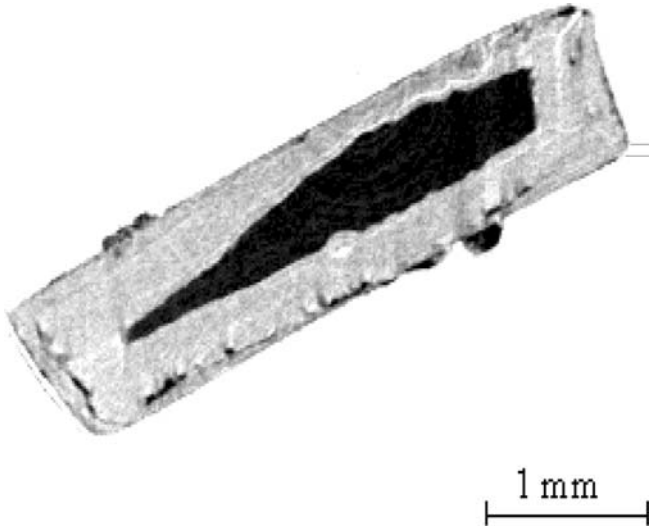

Figure 10. mCT image of the original glass F8 – 6.

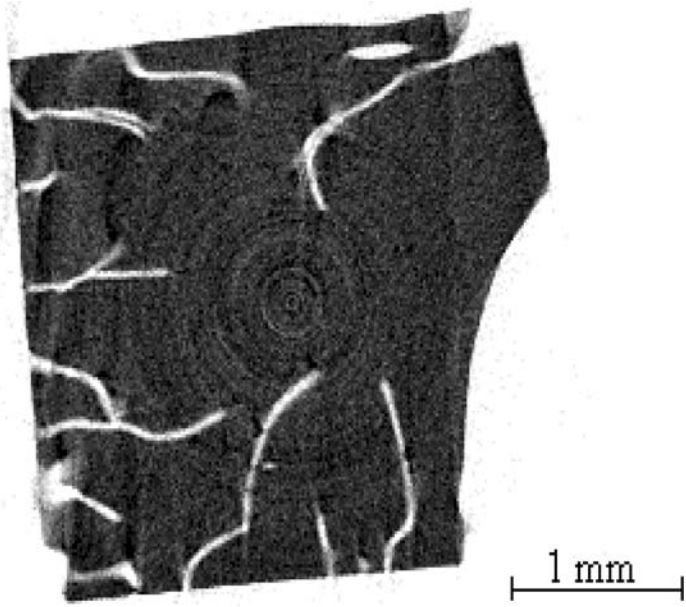

Figure 11. mCT image of the original glass RGM8.

For the glass sample RGM8 a network of cracks was detected by SEM (see Figure 5). A similar structure is revealed by mCT (Figure 11). By image-processing the grey values for the cracks can be separated from the bulk to visualise the network as a 3D model, which is presented in Figure 12.

4 SUMMARY AND PERSPECTIVE

An appropriate mCT scanner has been standardized for the study of archaeological glass. The applicability of mCT for the detection of corrosion layers was demonstrated for a wide range of

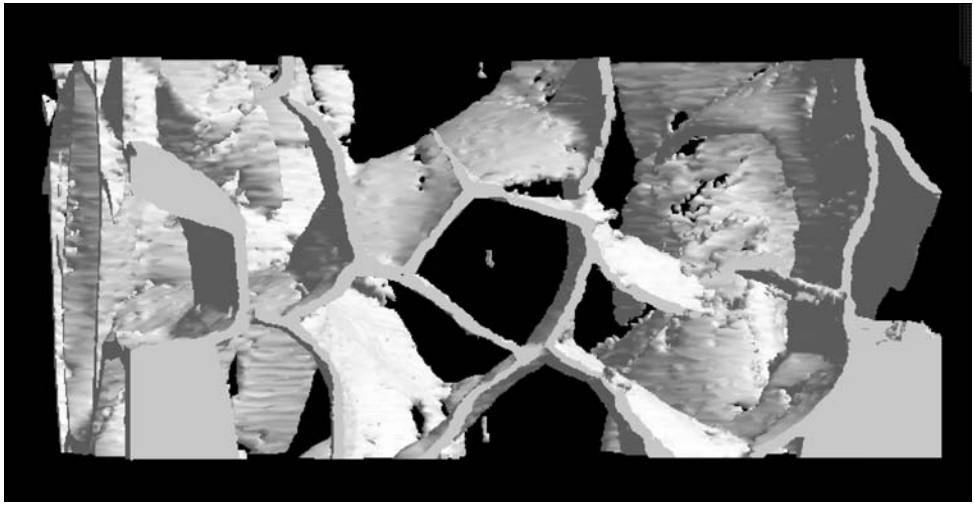

Figure 12. 3D reconstruction of the network of cracks in sample RGM8 (obtained by processing of mCT images). Image width: 3 mm.

examples (reference samples and original glasses). mCT analysis supplied results comparable to SEM with respect to the thickness of the corrosion layer, which was resolved normally as an area with lower attenuation values than the bulk glass.

For this publication only selected results of the project can be presented. The results of further examinations are submitted for publication (Roemich et al., in press), or will be presented elsewhere. The achievements of the project are summarized in the final report (Roemich 2002).

The mCT scanner used in this study is appropriate to detect corrosion layers thicker than 10 μm. Higher resolutions might be achieved in the future, when new generations of cameras and improved data processing are available.

The protection of cultural heritage can be considered as an extremely promising new field for the application of CT, since more than in any other domain of applied science non-destructive analytical methods are required. More common analytical techniques like Scanning Electron Microscopy (SEM) or most other methods for the characterization of material compositions require sample preparations, which are invasive with respect to the original material.

With mCT, original fragments can be examined non-destructively in their original state.

ACKNOWLEDGEMENTS

The development of a high-resolution desk-top tomograph has been carried out within the framework of an EC-funded project ("Monitoring the corrosion state of glass objects by optimised micro computerised x-ray-Tomography", SMT4-CT98-2261). The Fraunhofer Institut für Silicatforschung (ISC) acted as co-ordinator of the project, providing a rich and long experience in analyses and conservation research of historical glass. The other participants were CT experts from Belgium (University of Antwerp and Ghent University), the company Skyscan as manufacturer of the mCT device (Antwerp, Belgium) and the Polytechnical University of Valencia (Spain) as specialist on archaeological glasses.

The Ceramic Museum of Manises, the National Museum of Ceramic "Gonzáles Marti", the Archaeological Museum of Paterna and the Archaeological site of l'Almoina in Valencia (Spain) have provided most of the original glass samples for this project. The two glass fragments form Germany originate from the Römisch-Germanisches Museum der Stadt Köln and from the Landesdenkmalamt Baden-Württemberg, Stuttgart.

REFERENCES

Clark, D.E. & Zoitos, B. K. 1992. Corrosion testing and characterisation. In D.E. Clark & D.K. Zoitos (eds), *Corrosion of glass, ceramics and ceramic superconductors*. New Jersey: Noyes publications: 51–124.

Jacobs, P. 2002. Can x-ray computer tomography contribute to cultural heritage and stone conservation through the non-destructive monitoring of deterioration and restoration process? In R. Van Grieken, K. Janssens, L. Van't dack, & G. Meersman (eds), *Non-destructive Testing and Microanalysis for the Diagnostics and Conservation of the Cultural and Environmental Heritage Proc. Intern. Symp., Antwerp. 2–6 June 2002*, Antwerp: University of Antwerp.

Jacobs, P., Sevens, E. & Kunnen, M. 1995. Principles of computerised x-ray tomography and applications to building materials. *The Science of the Total Environment* 167: 161–170.

Jacobs, P., Sevens, E. & Kunnen, M. 1996. Computerized x-ray tomography (CT): a potential non-destructive research tool for building stone characterisation. In de Cleene M. (ed), *Interactive physical Weathering and Bioreceptivity Study on Building Stones, Monitored by Computerized X-Ray Tomography (CT) as a Potential Non-Destructive Research tool. Protection and Conservation of the European Cultural Heritage*. Research Report No. 2, Brussels: European Commission, 207–252.

Jacobs, P., Sevens, E., Vossaert, P. & Kunnen, M. 1997. Non-destructive monitoring of interactive physical and biological deterioration of building stones by computerized x-ray tomography. In P. Marinos, G. Koukis, G. Tsiambaos & G. Stournaras (eds). *Engineering Geology and the Environment*. Rotterdam: Balkema 3163–3168.

Kak, A.C. & Slaney, M. 1999. *Principles of Computerized Tomographic Imaging.* New York: IEEE Press.

Knight, B. 1996. Excavated window glass: a neglected resource? In A. Roy and P. Smith (eds), *Archaeological Conservation and its Consequences*. London: IIC, 99–104.

López, E., Roemich, H., Cornelis, E., Tennent, N.H. & Jacobs, P. 2002. Special corrosion phenomena on glass objects. *Proceedings of the conference "Hyalos-Vitrum-Glass"*, *Rhodes*: 251–255.

Newton, R. & Davison, S. 1989. *Conservation of Glass*. London: Butterworths.

Roemich, H. 1999a. Historic glass and its interaction with the environment. In N. Tennent (ed.), *The Conservation of Glass and Ceramics.* London: James & James: 5–14.

Roemich, H. 1999b. Laboratory experiments to simulate corrosion on stained glass windows. In N. Tennent (ed.), *The Conservation of Glass and Ceramics.* London: James & James: 57–65.

Roemich, H. (ed.) 2002. *Monitoring the Corrosion State of Glass Objects by Optimized Micro-computed X-Ray-Tomography.* Final Report, EC contract SMT4-CT98-2261.

Roemich, H., Aerts, A., Janssens, K. & Adams, F. 1998. Simulation of corrosion phenomena of glass objects on model glasses. In M.K. Choudhary, N.T. Huff & C.H. Drummond (eds), *Proceedings of XVIII International Congress on Glass, San Francisco 5–10 July 1998*, published on CD-ROM, American Ceramic Society.

Roemich, H., Gerlach, S., Mottner, P., Mees, F., Jacobs, P., Van Dyck, D. & Doménech, T. In press. Results from burial experiments with simulated medieval glasses. *Proceedings of the MRS Fall Meeting Symposium II.*

Roemich, H. & López, E. 2002. Research on corrosion phenomena of archaeological glass. *Proc. of the conference "Hyalos-Vitrum-Glass". Rhodes*: 241–247.

Cultural Heritage Conservation and Environmental Impact Assessment by Non-Destructive Testing and Micro-Analysis – Van Grieken & Janssens (eds)
© 2005 Taylor & Francis Group, London, ISBN 90 5809 681 5

How diagnostic technologies contribute to the interpretation of the Byzantine icons

Y. Chryssoulakis
National Technical University of Athens, Chemical Engineering Department, Athens, Greece

Sister Daniilia
"Ormylia" Art Diagnosis Centre, Sacred Convent of the Annunciation, Ormylia, Chalkidiki, Greece

ABSTRACT: The authors of the present study try to offer answers about the contribution of the modern, sophisticated technologies to an engagement with the intrinsic spiritual message that is expressed through Byzantine iconographic tradition.

The extensive examination of three great fresco ensembles created between 1295 AD, and 1557 AD supplied a large volume of information about the drawing, the colour, the working materials and the process of rendering the painting. The fact that these details demonstrate both the particular characteristics that concern each fresco ensemble independently and those that create relationships among them, led us to speculate on the relationship between the "code" underlying the manner of painting Byzantine icons and the spiritual message that they express.

1 INTRODUCTION

There follow a number of conclusions from the experimental measuring and observing of artistic works using non-destructive and sampling microanalytical methods of analysis. These are accompanied by certain truths, fundamental values and rules from the teaching of Christ or from other equivalent sources of the same mystical tradition.

Three great fresco ensembles were studied:

- the Church of the Protaton, painted by Manuel Panselinos (1295 AD),
- the wall-paintings of St Nicolas Anapausas, Meteora, painted by Theophanes the Cretan (1525 AD) and
- the wall-paintings of the Transfiguration of the Saviour, Dousikon, painted by Tzortzis (1557 AD).

The first attempt made in approaching and studying this authentication was based on:

- the results of the application of the interpretative, analytical methods of infrared reflectography, the measurement of colour, optical microscopy, and μFTIR and μRaman spectroscopies,
- the understanding of the theology of icons as recorded by the great Fathers of the Church, and
- the interpretations of contemporary theologians and researchers of Byzantine icons and of Byzantine art in general.

After the bloody period of iconoclasm, the Seventh Ecumenical Council (837 AD) defined the principles relating to the dogma of the veneration of icons. The icon is given a position at the same level as the word of the Gospel: "The word and the icon profess and manifest one another" (Canon, 1986). "That which the word conveys through the ear is what painting manifests silently through the icons" (Basil 1999).

Iconography, an art that evolved on the walls of churches, constitutes an integral element in the liturgical life of the Church. Using its own language, it summons the faithful to approach the divine world and to be initiated into the mystery of eternity through a mysterious encounter with God.

The defender, par excellence, of the veneration of icons, Saint John of Damascus, writes characteristically: "I do not venerate matter, but rather I venerate the Creator of matter, who for my sake became material and deigned to dwell in matter, who through matter effected my salvation" (John 1989).

Using this matter, iconographers are called not merely to please the observer at an aesthetic and psychological level, but chiefly to convey the experience of the one being observed, who has been transfigured by uncreated light.

The present study makes use of the results of the aforementioned methods. They concern:

– the drawing,
– the working materials (pigments and binders) and
– the process of making the harmony of colours.

2 THE DRAWING

An application of the technology of infrared reflectography to examine the wall paintings of Manuel Panselinos in the Athonite Church of the Protaton revealed the drawing of the figures.

The elements which characterise his painting are the following:

– the expanse of light, clear outlines and limited shadings
– the dynamism and simplicity of the drawing
– the freedom of design and the certainty of final brush strokes
– the richness of expression

These elements are not merely the product of the artist's enormous technical talent. By adhering at the same time to the traditional rules of Byzantine art, he achieved something begotten only by a person with deep personal experience, whereby the shapes, colours and lines conform to what they express.

2.1 *The expanse of light, clear outlines and limited shadings*

Light here does not follow the laws of physical optics, but free from their constraints, it presents the iconic figures incorruptible and ever existing-gleaming from their inner radiance (Fig. 1 and 2).

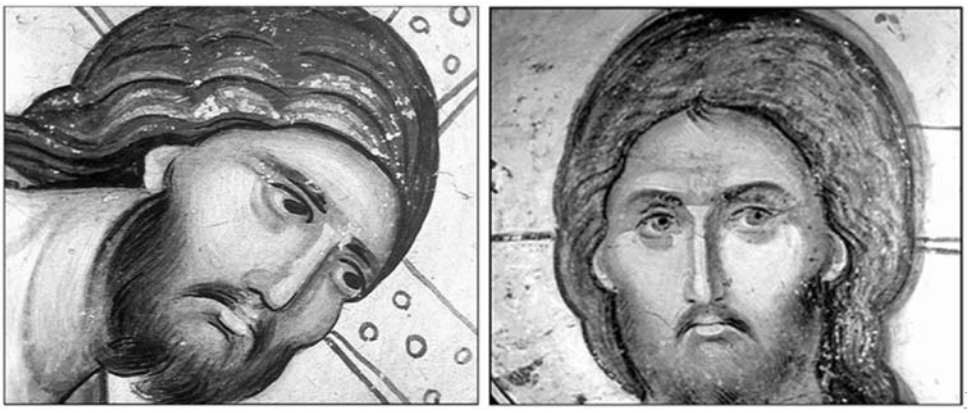

Figure 1. Infrared reflectograms at 1800 nm. *Left*: Resurrection of the Christ (detail of His Head), *Right*: Christ Enthroned (detail of His Head).

This stable, centripetal illumination stems from the presupposition of the existence of being, which exists precisely because it shares in divine light. The significance, however, is not how much light there is in an icon, but how it illuminates figures, so that the light gives them being.

In this are also included the clear outlines of the figures with their rudimentary shadings. Each figure, unique and unconfused with the others, possesses its own space, thereby symbolising the independent spiritual domain which was carved out for it by the Creator within the abundant light of His kingdom – a light which leaves behind it no shadows. Everything is absorbed, baptised in the light.

2.2 *The dynamism and simplicity of the drawing*

The apparent formalism, expressed in the austerity and the simplicity of the schematised lines, expresses the striving for ascesis, for inner orderly conduct and the attitude of prayer before God (Uspensky 1992). The iconographer, using the medium of matter, is called to portray the incorruptible bodies of the Saints (Fig. 3 and 4).

This is what the icon wishes to express with its articulation and simplicity of lines and outlines. The outer harmony and peace of the iconic figure, who is a type and manifestation of victory over man and over the world's inner dissension and chaos, express inner order and harmony.

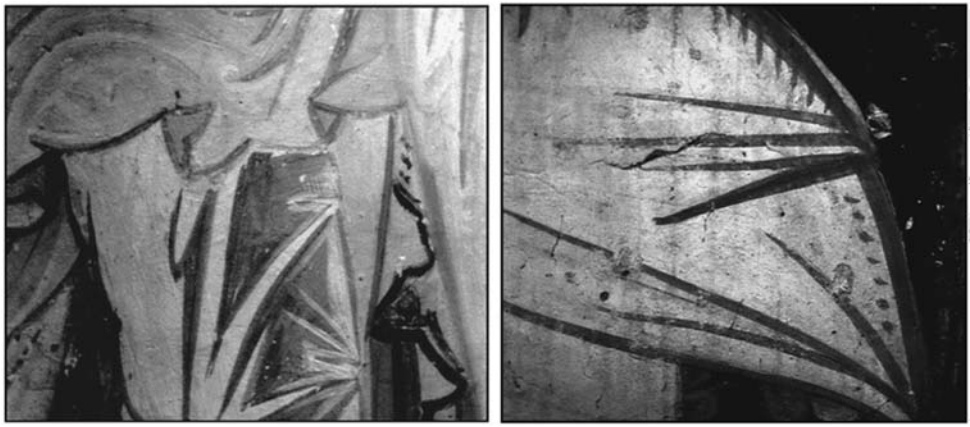

Figure 2. Infrared reflectograms at 1800 nm. Details of garments.

Figure 3. Infrared reflectograms at 1800 nm. *Left*: Head of St Luke, *Right*: Head of St Mercurius.

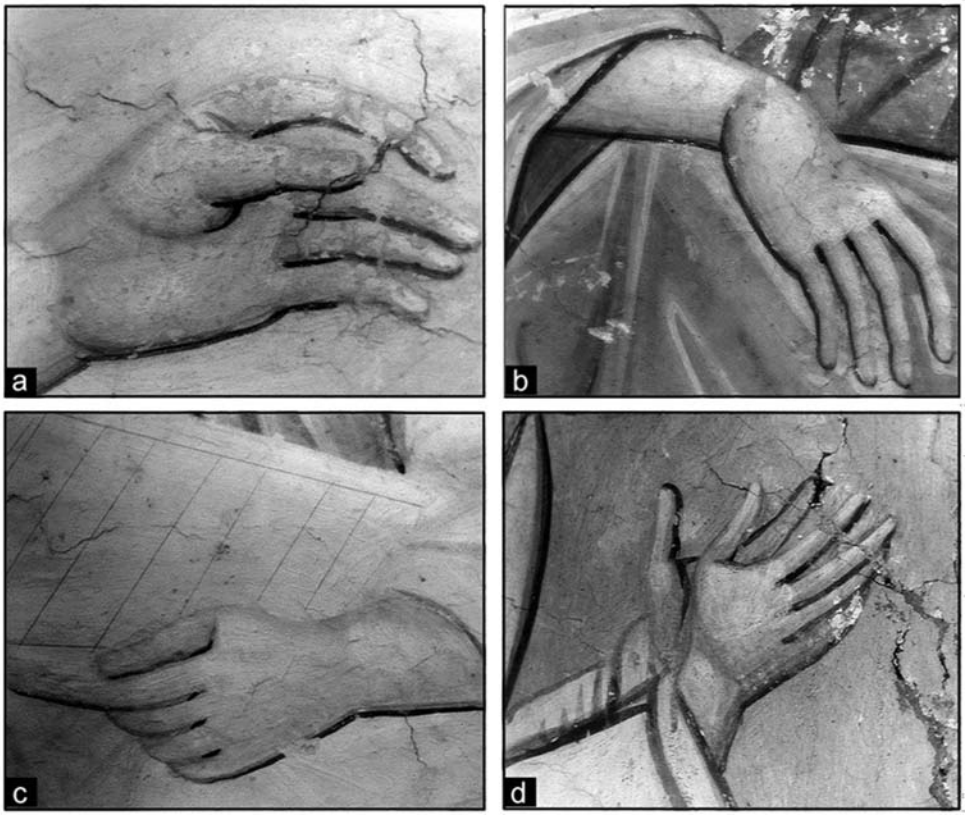

Figure 4. Infrared reflectograms at 1800 nm. *a*, *b*: Hands of St John the Theologian, *c*: Left hand of St Prochorus, *d*: Hands of St Peter.

2.3 *The freedom of design and the certainty of final brush strokes*

The use of initial drawing incisions (Fig. 5) was observed chiefly in the clothing, which bear a dark underlay. Plotted by colour and brush, the initial drawing is impossible to trace, although it must exist on the final coating of the plaster.

The assumption that it is there, even as a rudimentary sketch, is supported by the discovery of very small changes ("pentimenti") in only two of the more than one hundred (100) infrared reflectograms that were selectively taken (Fig. 6).

However, this design was not revealed, first because of the use of pigments with a low absorbance of infrared rays, and secondly because of its coating by final dark brushstrokes, where use was made of carbon black (high absorbance) pigments.

Indicative of the great talent of the particular artist (Manuel Panselinos) is the extraordinary freedom of design. This shows that the personality of each iconographer is not disregarded. On the contrary, his technical ability, his natural gifts and uniqueness, play their part in the rendering of expression. While the iconographer is not simply a copier, the projection of his personality, however, is subdued and discreet. Just as the priest celebrates with specific words and always with the same material objects, so also does the iconographer constantly follow the laws of tradition in his painting: the design, the materials, the formation; since the spiritual experience of the tradition's essence is unchanging.

In this way it is possible to regard the icon as a service, an expression of the experience of the Saints of the Church – not an isolated conception or view of an autonomous painter offering mere

Figure 5. Entrance of the Mother of God into the Temple. Detail of the Virgin. Infrared reflectogram at 1800 nm.

Figure 6. The Ressurection. Detail of the Christ's right foot. Infrared reflectogram at 1800 nm.

aesthetic satisfaction as opposed to spiritual uplift or participation in the light of God. Beauty in the Church means holiness-participation in divine beauty – not beauty for its own sake, since "flesh and blood cannot inherit the kingdom of God" (Corinthians 1957).

2.4 *The richness of expression*

The figures' entire expression is concentrated in the face – though chiefly in the eyes (Fig. 7 and 8). According to the Scriptures, "the eye is the lamp of the body" (Matthew 1957). The transmission of the iconic persons' spiritual life, with their fixed, piercing, yet withdrawn eyes, expresses the unusual power and authority of the spirit over the body, which remains motionless so that man may hear the revelations of God. It is there that the joy of having achieved a higher spiritual life overflows. It is this inner man that the Byzantines were interested in portraying, though at the same time preserving also the true characteristics of each physiognomy, now bathed in perpetual light where is the true life.

Figure 7. The Entrance of the Mother of God into the Temple (details of the faces). Infrared reflectograms at 1800 nm.

Figure 8. Sts John the Theologian and Prochorus (details of their faces). Infrared reflectograms at 1800 nm.

3 THE WORKING MATERIALS (PIGMENTS AND BINDERS) AND THE PROCESS OF MAKING

The observation, under a polarising optical microscope, of a representative number of samples from the fresco ensembles of the aforementioned monuments, when combined with the application of the μFTIR and μRaman spectroscopic methods of analysis, brought to light the composition of the working materials, the way in which the colour layers were superimposed, the manner of blending the pigments in the different colour mixtures, and their grain size; that is to say, the complete process of the artistic structure.

Although the wall paintings of the three monuments belong to different periods and were produced by different artists, there appear great similarities which may be summarised according to the following characteristics.

3.1 *A small and specific number of pigments*

When painting the great fresco ensemble of the Church of the Protaton, Manuel Panselinos used only ten pigments (Table 1).

For his wall paintings of the Katholikon of the Monastery of St Nicolas Anapausas, Meteora, Theophanes the Cretan used the same pigments but also malachite, while warm ochre and caput mortuum are absent. We encounter the same pigments in the wall paintings of the Katholikon of the Dousikon Monastery, painted by Tzortzis.

The earth pigments mixed with limewater to which was added a small amount of egg as a binding medium, were applied on a carefully prepared damp lime plaster. Dry plaster artwork was also completed using the same binding method.

These materials (pigments and binders), above all, represent the mineral and animal kingdom. Their contribution to the painting of holy icons is a symbol of the organic unity of man with the created kingdom that surrounds him.

The earthly origin of pigments is reminiscent of the creation of man "out of earth" who, however, was renewed and was made incorruptible through the work of Christ on earth.

All the colours of nature have a unique and independent harmony and sweetness. By virtue of these pure colours with which the walls of the churches were painted, Byzantine artists succeeded in conveying this elevated chromatic harmony.

3.2 *The use of pure pigments presenting low-hiding thickness values on the underlay paint layers and the simplicity of mixtures*

Strictly speaking, the use of pure pigments for applying underlay paint layers is typical. According to the type of pigment, the thickness of the coating is relatively low and fluctuates between 10 and

Table 1. Pigments used by Manuel Panselinos.

Name	Composition
Yellow ochre	$Fe_2O_3 \cdot H_2O$, clay
Warm ochre	$Fe_2O_3 \cdot H_2O$, clay
Red ochre	Fe_2O_3
Caput mortuum	Fe_2O_3
Cinnabar	HgS
Minium	Pb_3O_4
Green earth	$K[(Al^{III}, Fe^{III})(Fe^{II}, Mg^{II})], (AlSi_3,Si_4)O_{10}(OH)_2$
Azurite	$2CuCO_3^{-} \cdot Cu(OH)_2$
Calcium carbonate	$CaCO_3$
Carbon black	C

15 μm. When pure pigments are used, without admixtures, they give off all their luminosity, while, at the same time, the thinly-applied coating offers high transparency. Hence, the final result creates the impression that the figures in their entirety are illuminated by an interior light that penetrates through their existence. When, however, in order to convey the colour of the underlay, the pigments used are mixed with the white of lime, then this same white offers the desired luminosity with its own light.

This transparency and lucidity of the underlay paint layers of Byzantine icons, in conjunction with the use of pure pigments, symbolises the purity and the clarity of the Saints' body and the purification of the mind and of the heart, achieved through the labours of fasting and prayer.

The use of lime white, either as a binding agent for the basic pigments that convey the gradations of the highlights of the faces and of the clothing, or as pure white, plays a special role in the transmission of light in Byzantine icons.

3.3 *Clarity in the stratigraphy of the highlights and of the shadows*

Stratigraphy in Byzantine icons is characterised by sparseness and clarity. Each new gradation is superimposed one above the other, in such a way that its manner of application can be differentiated.

Table 2. Pigments and layer structure of the scene "Entry of the Mother of God into the Temple" (Figure 9), Protaton, Mount Athos.

Paint area	Layer structure and pigments detected
Halo	Yellow ochre
Background	i. lime and carbon black, ii. carbon black and lime, iii. azurite
Earth surface	i. lime and carbon black, ii. carbon black and lime, iii. green earth
Blue garments	Underlay: i. lime and carbon black, ii. carbon black and lime, Light: azurite Shadows: carbon black
Red garments	Underlay: red ochre 1st light: cinnabar, 2nd light: minium Shadows: red ochre and carbon black
Orange garments	Underlay: warm ochre Lights: warm ochre and lime, Highlight: lime Shadows: red ochre
Yellow garments	Underlay: yellow ochre Lights: yellow ochre and lime or carbon black and lime, Highlight: lime Shadows: red ochre or yellow ochre and carbon black
Green garments	Underlay: green earth or green earth and lime or green earth and yellow ochre or carbon black and lime and green earth Lights: green earth and lime or green earth and yellow ochre and lime or carbon black and lime or yellow ochre and lime, Highlight: lime Shadows: green earth and carbon black or green earth and red ochre
Purple garments	Underlay: caput mortuum or caput mortuum and lime Lights: azurite or caput mortuum and lime or carbon black and lime or caput mortuum and carbon black and lime, Highlight: lime Shadows: caput mortuum or caput mortuum and carbon black
Flesh tones	Underlay: green earth and yellow ochre and grains of lime Flesh tones: yellow ochre and lime Highlights: lime Light transitory shade: green earth and lime and grains of yellow ochre Warm transitory shade: red and yellow ochre and/or cinnabar Shadows: i. red ochre, ii. red ochre and carbon black

As a rule, the number of highlights or shadings is confined to two gradations which are applied to the underlay paint layer, there being no confusion between them. However, there are cases where their number may be reduced in one gradation (Table 2).

In the majority of instances, the highlights are rendered using a mixture of the basic colour of the underlay with lime white. The latter adds additional thickness to the colour layers (Fig. 10). But when lime white is not to be found in the highlights, as for example in red and purple-blue coloured clothing, the pigments are used in their pure form (Fig. 11).

The purity and accuracy of the manner of depiction, combined with the austerity and the laconism of the details, give a seal of authenticity to this divine art, as they do with all types of expression in the liturgical life in the Church: the homily, the hymnography, the music.

Figure 9. The Entrance of the Mother of God into the Temple. Manuel Panselinos, 1295 AD.
(This figure is presented in the signature in colours at the end of this volume, Appendix, pg. 315).

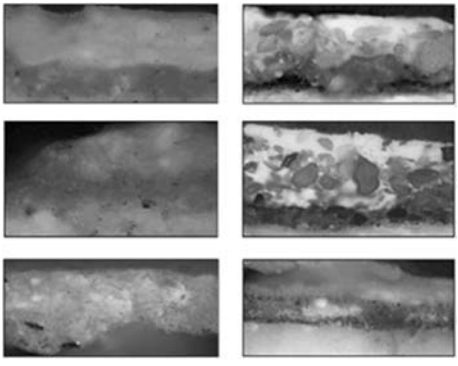

Figure 10. Gradual mixing of lime white with the basic colour of underlay in order to achieve highlights gradations.
(This figure is presented in the signature in colours at the end of this volume, Appendix, pg. 315).

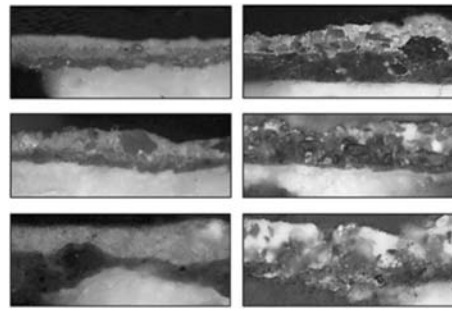

Figure 11. The use of cinnabar, minium and azurite as highlights.
(This figure is presented in the signature in colours at the end of this volume, Appendix, pg. 315).

4 THE HARMONY OF THE COLOURS

In this research two systems of colour measurement and representation were used: the CIE L*a*b* (and L*a*b* CMC) and the x, y, Y (CIE 1931), as well as diagrams of the reflectance factor (R%) versus the wavelength (λ).

Looking at the results from studying the three aforementioned monuments (belonging to different styles and different artists), we were able to discern the common characteristics of the three iconographers' "palette." The harmony that governs the entire colour range is of particularly great interest.

The technique of colour measurements aims:

4.1 *To determine the "palette" of the artists*

The illustration in the colour diagram a*b* of an adequate number of representative colour measurements from each fresco ensemble, reproduces and affirms precisely the "palette" of the three great artists.

The elements that determine the entire range of hues in a work of art are:

- the kinds of pigments used
- the artistic sensitivity of the artist (the harmony and blending of the pigments)
- the factor referred to as the Byzantine iconographic tradition.

Taking into consideration all the a*b* diagrams coming from the three monuments, we were able to demonstrate that there is a typical, common field where the greatest number of measurements of yellow, orange, red, mauve, grey-blue, and oil-green colourings is apportioned. This is essentially due to the common kinds of pigment used: yellow and red ochres, caput mortuum, cinnabar, green earth, azurite, carbon black, and white lime (Fig. 12).

Noteworthy divergences exist in the fields of blue and green. In the Protaton, malachite green was not used, whereas it was found to constitute a basic pigment in the artwork of the Anapausas and the Dousikon Monasteries. This is why there appear measurements in the green area of the diagrams pertaining to these two monuments.

The divergence in the field of blue is not due to the fact that a pigment other than azurite was used, but because the monuments of the 16th century have preserved this colour better (probably because less time has intervened).

In the field of yellow the small deviations are due on the one hand to the fact the Protaton used limonite as a yellow pigment, while Anapausas and Dousikon have yellow ochre, and on the other to the fact that at Dousikon gold leaf for the haloes was also used.

Generally speaking, it may be said that the colour fields in which the three great artists move are the same, but the nuances of each ensemble is affected by the artistic sensitivity of the artist and the stylistic current of the era. For this reason the affectations of the representations in monuments

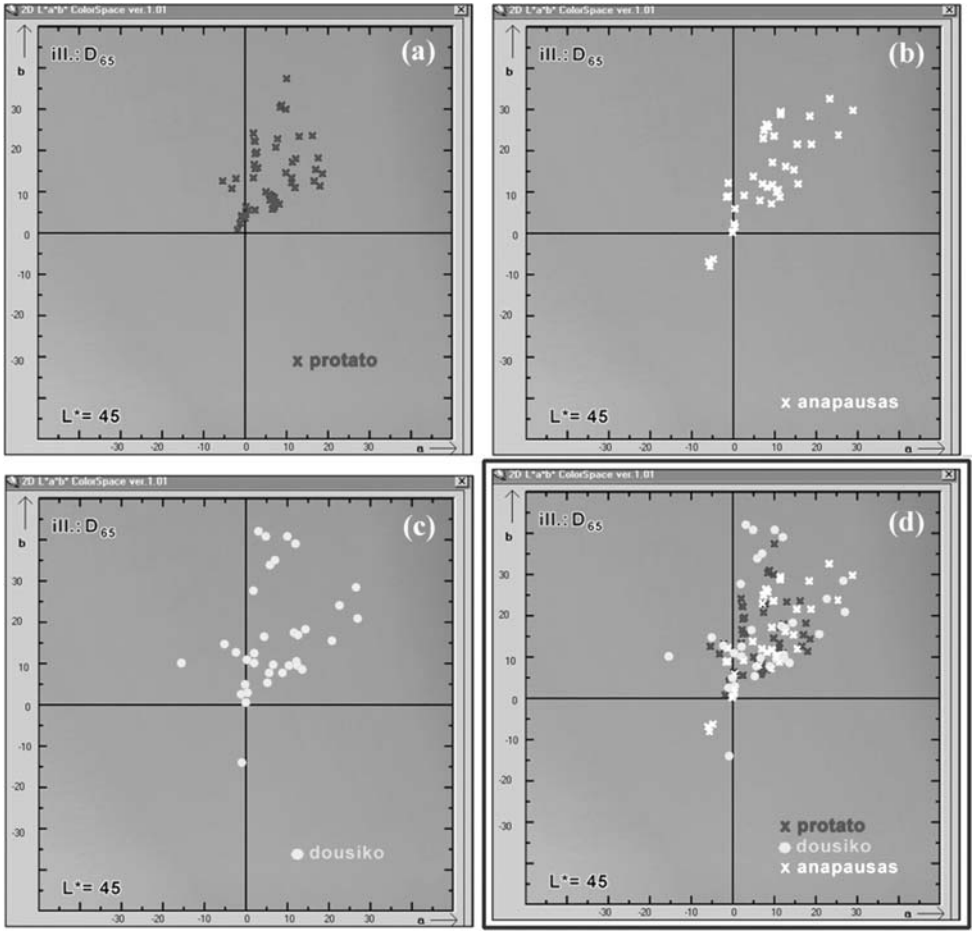

Figure 12. Colour diagram a*b*: Illustration of representative measurements taken from the three monuments. (a) Protato (b) Dousiko (c) Anapausas and (d) the three superimposed.

executed in the Cretan style (Theophanes, Tzortzis) are found to be mutually much nearer, than when compared with those of Panselinos.

The homogeneity of the colour field in which the painters of Byzantine icons move, testifies to their respect for this artistic tradition, as it evolved through the passage of the centuries. "Paint images using the colours passed down by tradition" exhorts St Symeon, Archbishop of Thessaloniki (Συμεών, 1994). And we do this not through blind obedience to certain rules, but because within the tradition we participate in the experience of sanctified iconographers, in the living experience of the Church.

To determine the characteristics of the various colours, such as their hue, saturation degree and brightness (luminance).

By arranging all of the colour measurements performed in a large number of scenes of the Protaton wall paintings, as shown in the composite colour diagram a*b*, we could see that the level of saturation of the hues and even that of the pure pigments is low (Fig. 13).

Without a doubt this fact is directly connected with:

– the kinds of pigments used
– the hiding thickness of the colour layers
– the manner of pigments blending.

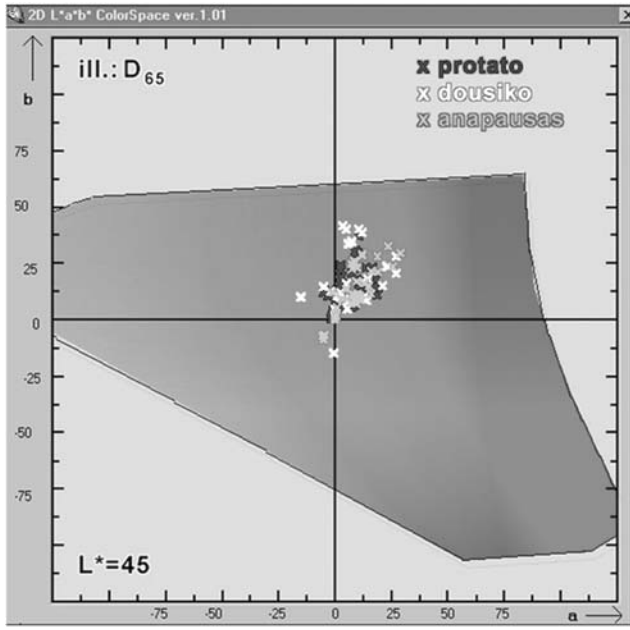

Figure 13. Colour diagram a*b*: Illustration of representative measurements taken from the three monuments (Protaton, Dousikon and Anapausas). The relatively low saturation level is apparent.
(This figure is presented in the signature in colours at the end of this volume, Appendix, pg. 316).

Bearing in mind that the blending of the pigments is simple (done chiefly by adding white or black), a decisive role is played by the fact that the pigments of Byzantine icons are earthy and as such are characterised by a soft and sweet tones.

In general, the ground tones of the garments are made of pure pigments. Nevertheless, the saturation level is relatively low, due to the nature and the earthen origin of these pigments. The lights' shadings are accomplished mainly by blending calcium white with the ground tone's colour. In cases of red and blue lights, the special pigments used in their pure form, are of relatively high saturation level and substitute the brightness of the white lights.

The graphic representation of the reflectance factor (R%) of the various colourings, versus the wavelength (λ), assisted in the derivation of results relative to the purity of the pigments used. For this to be better understood, in the same diagram the reference curve of the pure pigment is represented. The thickness of the pigment's coating, as given in the reference sample, is such that it does not permit the impact of the underlying preparation layer on the reflectance factor. In the diagram of the warm ochre, the first curve refers to the reflectance factor before cleaning test, while the second to the reflectance factor after cleaning test with distilled water. It becomes apparent that the soiled layer has suffered a significant loss of colour brightness, and this ought to be taken into consideration when making a comparison (Fig. 14).

As it appears from the diagrams, each hue reveals reflectance at the same wave length as that of the pure pigment (Fig. 15). The differences in the reflectance factor are due to:

- the layer of dirt which has settled on the painted surface
- the low hiding thickness of the colour layers of the frescos
- the natural or accidental admixtures of the grains of other pigments, and
- the probable existence of an underlying coloured layer "imprimatura", of a different hue, whose aim is to affect the final aesthetic result.

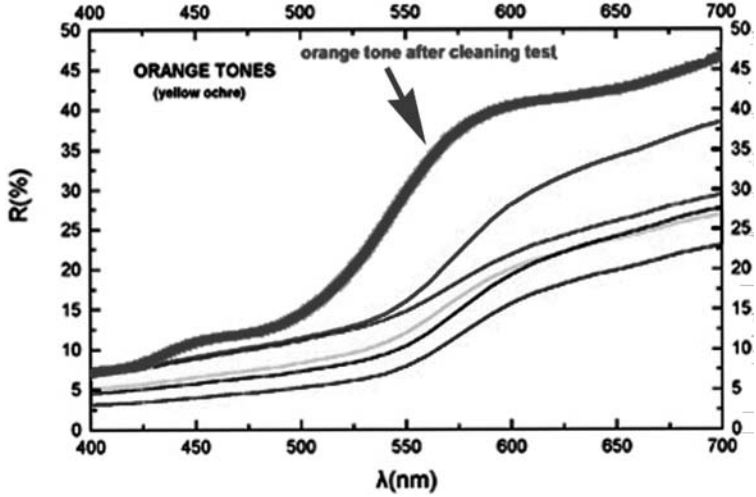

Figure 14. Graphical representation of the diffuse reflectance curve (R%) versus the wavelength (λ) of some hues of warm ochre before and after cleaning test. Measurements were taken on several positions of different thematic scenes from the Protaton Church.

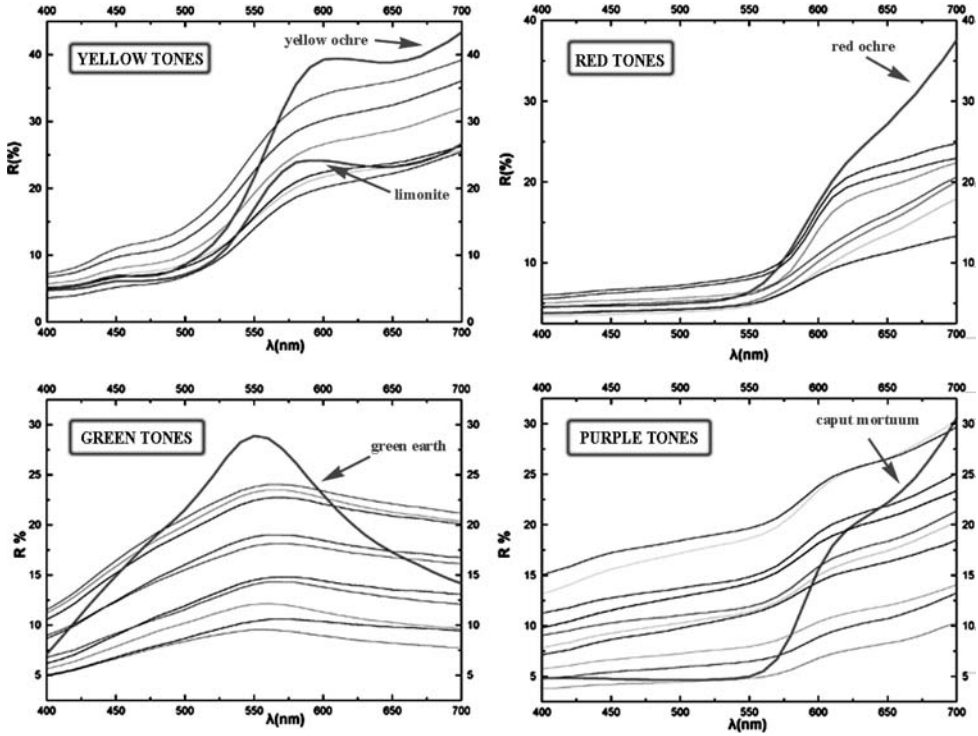

Figure 15. Graphical representation of the diffuse reflectance curve (R%) versus the wavelength (λ) of the representative measurements (yellow, red, green, purple) and of the respective reference curve of the pure pigment.

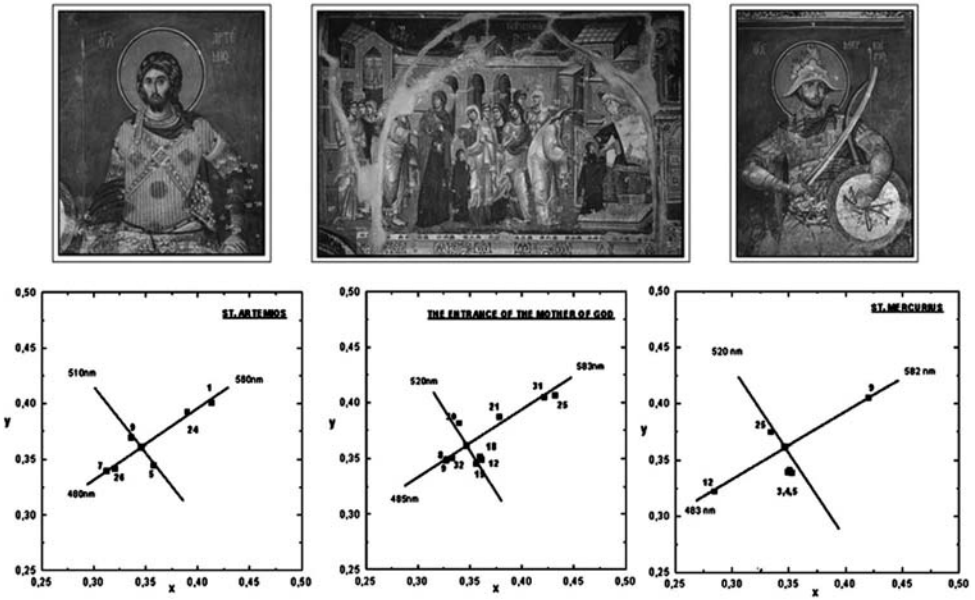

Figure 16. x, y chromaticity diagram (CIE 1931). Illustration of representative measurements of supplementary colours from isolated holy figures and from entire scenes of the Protaton church.
(This figure is presented in the signature in colours at the end of this volume, Appendix, pg. 316).

The results of this study, which has applied the technique of colour measurement, certify and complete the results concerning the purity, the transparency, and the brightness of the colour gradations on the frescos of the Protaton.

The "joy of colour" in Byzantine icons, which is manifested by the purity, the transparency and the brightness of the colour gradations, symbolises the inner beauty and purity.

The presence of specific colour hues in the "palette" of Byzantine iconographers is not incidental. Their selection is conditioned by their contribution to the intrinsic spiritual truths which are expressed through each colour. A first attempt at deciphering the colour symbolism in the Byzantine Iconographic Tradition is being made for the effective interpretation of these truths and messages.

In other words, while, for the Iconographer, the mystical relationship between an infinite number of fine shades and spiritual understandings is considered to be potentially recognisable, the faithful observer is often faced with difficulties in deciphering this particular correspondence.

4.2 *To express ideas on the harmony that governs the entire colour stimulation*

The graphic representation of measurements in the x, y diagram revealed the existence of complementary colourings (colour combinations), as much in isolated figures as with entire scenes. Great accuracy can be observed chiefly in the complementarity for mauve with green shades, and for the yellow with blue (Fig. 16).

The accurate harmony-complementarity of the shades with the combinations, which Panselinos executed, expresses the notion of "unity" as much in the iconic figures as also in the whole. Moreover, "with the use of complementary combinations there is lost the sense of the three-dimensional which is created even by the fundamental dialectical light-shadow, drawing-proplasmos-highlights, so that finally the representation is depicted as two-dimensional in a harmonic, chromatic relationship between the figure and the space around him" (Σκλήρη, 1992).

Especially, as far as faces are concerned, this is accomplished through the colour balance between the flesh tones and the surrounding lights.

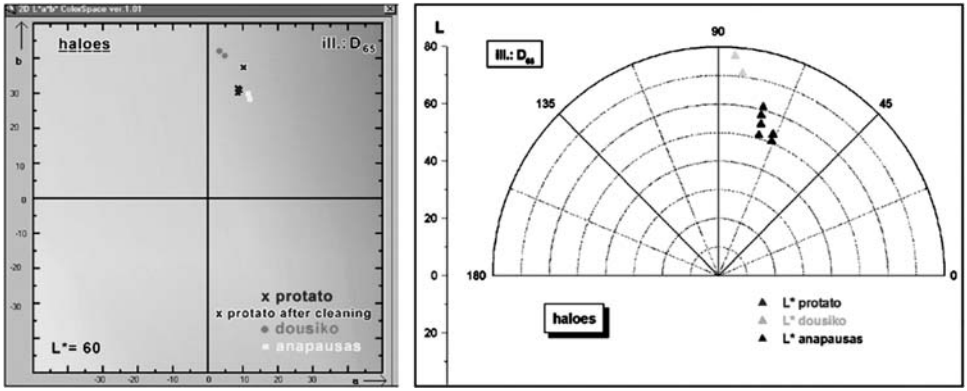

Figure 17. (a) Colour diagram a*b* : Illustration of representative measurements of the yellow halos from the two monuments Protato and Anapausas and of the gold halos from Dousikon. (b) Representation of the hue (h) of the same measurements versus luminance (L).

The harmonic relationship of the sky blue of the wall-paintings with the yellow of the haloes, symbolises the harmonic relationship of the renewed man with the new heaven of the kingdom of God. The yellow or the gold of the halo is symbolic of the brightness of holiness. According to Trubetskoy, "gold – the sun at its zenith – with the light that surpasses even the brightness of the sensible sun, because it symbolises the sun which never sets, God whose light is greater than the sun's" (Trubetskoy, 1991) (Fig. 17).

5 SYMBOLISM OF THE FUNDAMENTAL COLOURS

The following thoughts and data are submitted in the hope that they will assist in the essential reading and recognition of the message-colour selection code of communication in the Byzantine iconographic tradition.

5.1 *Blue, dark blue–violet*

That part of the visible spectral area occupied by the colours blue, dark blue and violet is characterised by the smallest wave-length values of the greatest frequency, effectiveness, and penetration: in other words, characteristics belonging to wisdom.

Of all colours, deep dark blue and violet are not only the most profound but also the most immaterial.

Violet expresses detachment and withdrawal from the material world and the soaring of the soul towards God.

Dark blue dominates in iconography because it is a sign of the mystery of Divine Life. It is the central colour of the mandorla in icons of the Transfiguration and of Christ in Glory. Furthermore, blue is most often the colour used for the vestment of the Pantocrator and the mantle of the Virgin.

5.2 *Green*

Green holds a central place in the solar spectrum. Counterbalancing the two extremes, it symbolises, from the left, wisdom (dark blue–violet) and from the right, love (red). In this way, it projects the understanding of the harmony manifested in humanity's two natures: wisdom and love, with the activated sense of justice and harmony.

As a colour that originates in the plant world and springtime, green symbolizes revival (more a regeneration of the spirit, which is the initiation into Truth, Awakening and, by extension, Hope). "Green" and "life" are two closely connected concepts.

5.3 *Yellow and gold*

Yellow is the colour of the sun and of gold. Gold is symbolic of the Word. Gold, Light, Word are three concepts knowingly undifferentiated in the collective subconscious of people.

In being unalterable, gold, therefore, represents for Christians eternal life, faith and above all Christ Himself: the Sun of Justice, the Light of the World, the Splendour of the rising sun.

Furthermore, gold itself is not one of the colours seen everyday in nature, hence, the gilt background of an icon creates a "space" against which bodies no longer need to conform to the elements either of scenery or architecture. Liberated from all that is terrestrial, they are spiritualised – transfigured in the golden light of eternity.

5.4 *Red and purple*

The colour red, being at the other end of the solar spectrum to dark blue and violet, has, in contrast with them, exactly their opposite qualities.

It symbolises munificence and the active offer of love, which, with an immediacy, unite men in precisely the same way as the colour red (the seat of love), assisted by the heart, nurtures with life and activates the tissues and the cells of the human body, thereby yielding its warmth.

A symbol of sacrifice and of altruism, red is an important colour in Christianity.

For the Byzantines, purple was the symbol of supreme power. Their emperors always wore purple, except when assisting at liturgical ceremonies when they dressed in white. It is noteworthy that Justinian's Code strictly forbade the sale or trading of purple dye and cloth outside Byzantium.

5.5 *Brown*

The colour of earth, clay and sod, brown is the outcome of a mixture of red, blue, green and some black. Brown is considered to be a symbol of poverty and humility (the latter word coming from the Latin, humus, meaning earth or soil) and conjures up a slow death to the world.

5.6 *Black and white*

Black and white are not colours in the literal sense. Both adjoin the chromatic representational domain of excitation colours in positions diametrically opposed to each other.

In this sense, white, expressing the Monad, the united whole of the colours of the solar spectrum, symbolises the entirety of knowledge, a knowledge final and perfect: Truth and Wisdom.

There can be no light brighter than white. Naturally, this "colour" symbolises light itself, light supreme, the utmost expression of colour. It constitutes, that is, the "colour" of the light of lucidity, integrity, purity and virginity, as well as the "colour" of joy and felicity.

Like white, black is both the absence of colour and at the same time the true embodiment all colours together. Symbolically, white represents the unity of light, while black is its denial.

Given that a black "colour" remains behind after combustion and follows the activity of transforming fire, it symbolises, as such, cleansing, receptivity and purification, which lead to the total metamorphosis proceeding to purity.

These few considerations may help us to appreciate the vast field of research associated with colours and their use in iconography. If we seem to have emphasized it unduly within the framework of this limited study, it is simply because we consider the subject to be of fundamental importance.

REFERENCES

Basil the Great. 1999. *Homily 19, on the 40 Martyrs, P.G.31:509A*. Αθήνα: Κέντρο Πατερικών Εκδόσεων.

Canon of the Seventh Ecumenical Council. 1986. Π*ρακτικά των Αγίων και Οικουμενικών* Συνόδων, τόμ. Γ′, *σελ.* 223–389. 'Αγιον 'Ορος: Καλύβη Τίμίου Προδρόμου Ι. Σκήτης Αγίας 'Αννης.

Holy Bible: I Corinthians 15:50. 1957. London: The British and Foreign Bible Society.

Holy Bible: Matthew 6:22. 1957. London: The British and Foreign Bible Society.
John of Damascus. 1989. *First Treatise in the Defense of Holy Icons, P.G.94:1245A*. Αθήνα: Κέντρο Πατερικών Εκδόσεων.
Trubetskoy, A. 1991. *Icons: Theology in color.* New York: Crestwood, St. Vladimir's Seminary Press.
Uspensky, L. 1992. *Theology of the Icon (Vol. I-II).* New York: Crestwood, St. Vladimir's Seminary Press.
π. Σκλήρη, Σ. 1992. *Εν εσόπτρω*. Αθήνα: Μιχαήλ Π. Γρηγόρης.
Συμεών Θεσσαλονίκης. 1994. '*Απαντα*, *P.G.155:113D*. Αθήνα: Κέντρο Πατερικών Εκδόσεων.

RELEVANT BIBLIOGRAPHY

Baggley, J. 1995. *Doors of Perception, Icons and their Spiritual significance.* New York: Crestwood, St. Vladimir's Seminary Press.
Bomford, D., Kirby, J., Leighton, J. & Roy, A. 1988. *Art in the Making Rembrandt.* London: The National Gallery.
Bomford, D., Kirby, J., Leighton, J. & Roy, A. 1989. *Art in the Making Italian Painting before 1400.* London: The National Gallery.
Cenini, C. 1960. *The Craftsman's Handbook*. New York: Dover Publications, Inc.
Dionysius of Fourna. 1996. *The Painter's Manual.* Torrance: Oakwood Publications.
Feller, R. 1986. *Artists' Pigments, Vol.1.* Washington: National Gallery of Art.
FitzHugh, E. 1997. *Artists' Pigments, Vol.3.* Washington: National Gallery of Art.
Florensky, P. 1996. *Iconostasis.* New York: Crestwood, St. Vladimir's Seminary Press.
Gettens, R. J. & Stout, G. L. 1966. *Painting Materials, A short encyclopedia*. New York: Dover Publications, Inc.
Itten, J. 1998. *ΗΤέχνη του Χρώματος*. Α*θήνα*: 'Ενωση Καθηγητών Καλλιτεχνικών Μαθημάτων.
Laurie, A. P. 1967. *The Painter's* M*ethods and Materials*. New York: Dover Publications, Inc.
Mayer, R. 1991. *The Artist's Handbook of Materials & Techniques.* London: Faber and Faber.
Quenot, M. 1992. *The Icon, Window of the Kingdom.* New York: Crestwood, St. Vladimir's Seminary Press.
Quenot, M. 1998. *Η Ανάσταση και η Εικόνα*. Κατερίνη: Τέρτιος.
Roy, A. 1993. *Artists' Pigments, Vol.2.* Washington: National Gallery of Art.
Sendler, E. 1999. *The Icon, Image of the Invisible.* New York: Oakwood Publications.
St. Dionisius the Areopagite. 1988. *Ecclesiastical Hierarchy*: *P.G*.3:*392A-472B.* Αθήνα: Κέντρο Πατερικών Εκδόσεων.
Thompson, D. V. 1956. *The Materials and Techniques of Medieval Painting*. New York: Dover Publications, Inc.
Uspensky, L. & Lossky, V. 1982. *The Meaning of Icons.* New York: Crestwood, St. Vladimir's Seminary Press.
Winfield, D. C. 1968. *Middle and later Byzantine Wall Painting Methods*. New York: Dumbarton Oaks Papers.
Αλεξοπούλου-Αγοράνου, Α. & Χρυσουλάκης, Ι. 1993. *Θετικές Επιστήμες και* '*Εργα* '*Τέχνης*. Αθήνα: Εκδόσεις Γκόνη.
Αγ. Διαδόχου Φωτικής. 1986. *Φιλοκαλία*, *τόμ. 9, 100 Γνωστικά Κεφάλαια*. Θεσσαλονίκη: Πατερικαί Εκδόσεις "Γρηγόριος ο Παλαμάς".
Ευδοκίμωφ, Π. 1993. *Η Τέχνη της Εικόνας*, *Θεολογία της Ωραιότητος*. Θεσσαλονίκη: Εκδόσεις Πουρνάρα.
Αγ. Μακαρίου Αιγυπτίου. 1970. Π*νευματικαί Ομιλίαι α′ – ν*', ΒΕΠ. Αθήνα: Αποστολική Διακονία.
Αγ. Μακαρίου Αιγυπτίου. 1971. Π*νευματικαί Ομιλίαι να′ – πε*', ΒΕΠ. Αθήνα: Αποστολική Διακονία.
Ζωγραφίδης, Γ. 1997. *Βυζαντινή Φιλοσοφία της Εικόνας*. Α*θήνα*: Ελληνικά γράμματα.
Κόντογλου, Φ. 1960. '*Εκφρασις της Ορθοδόξου Εικονογραφίας*. Αθήνα: Αστήρ.
Μιχελή, Π. 1972. *Αισθητική θεώρηση της Βυζαντινής Τέχνης*. Αθήνα: Κ. Τσιρόπουλος.

Cultural Heritage Conservation and Environmental Impact Assessment by Non-Destructive Testing and Micro-Analysis – Van Grieken & Janssens (eds)
© 2005 Taylor & Francis Group, London, ISBN 90 5809 681 5

NDT and planning on historic buildings and complexes for the protection of cultural heritage

A. Moropoulou, N.P. Avdelidis & E.T. Delegou
National Technical University of Athens, School of Chemical Engineering, Section of Materials Science & Engineering, Athens, Greece

ABSTRACT: Non-destructive testing and evaluation techniques, such as Digital Image Processing (DIP), Fiber Optic Microscopy (FOM), Infrared Thermography (IR-Thermo), Ultrasonic (US) measurements and Ground Penetrating Radar (GPR), were applied in the Materials Science & Engineering (MSE) laboratory, in the National Technical University of Athens (NTUA) in Greece, on advanced and historic materials concerning architectural surfaces and historic complexes for research purposes such as: (a) materials quality control, as well as for the technology assessment concerning the production of advanced materials, (b) environmental impact assessment – materials and weathering mapping, (c) evaluation of conservation materials compatibility and conservation interventions effectiveness on the scale of architectural surfaces and historic masonries, (d) strategic planning for the conservation interventions and (e) environmental management for the protection of cultural heritage. Finally, the integrated management of data by GIS on the buildings/complexes scale develops a planning methodology concerning proper, effective and compatible materials and techniques for conservation interventions.

1 INTRODUCTION

Non-destructive investigation techniques are largely used because of the outstanding advantages that they are capable to provide in a variety of applications, i.e. assess and preserve the longevity of materials, surfaces of architectural and artistic value, structures and historic complexes (Moropoulou et al. 1999). The combined use of non-destructive testing and evaluation (NDT & E) techniques can allocate, amongst others, information relating to mechanical properties, micro-structural characteristics, energy and mass transfer phenomena (i.e. moisture movement and evaporation). In particular, the application of NDT & E techniques such as DIP, FOM, IR-Thermo, US and GPR, when combined with laboratory investigation of critical parameters, can provide particular interpretation of the actual physico-chemical phenomena. Moreover, a Geographic Information System (GIS) can be used on the scale of historic buildings and/or large complexes, in order to manage a multidisciplinary database, including environmental, architectural, structural and materials data. In this work, non-destructive investigation techniques were used because of the outstanding advantages that they are able to provide in a variety of applications and especially for conservation purposes of historic monuments, where destructive sectioning is usually restricted or even prohibited.

2 EXPERIMENTAL TECHNIQUES

Non-destructive testing techniques are applied for the evaluation of historic and restoration mortars concerning their behaviour on the masonry level. DIP on historic architectural surfaces results on the characteristic distribution pattern of the weathering forms, when the micro-structural and

textural characteristics of weathered stone are used as interpretation criteria. Image classification in terms of damage intensity is possible in cases such as alveolar decay. The same processing distinguishes in general restoration materials as compatible or incompatible to their original ones. FOM allows for the observation of the building materials texture on site and permits their identification and classification to the various types of already studied historic materials. IR-Thermo allows for recording the thermal maps of the surfaces under study and provides information on the differential behaviour of the various materials on the masonry scale on the subject of the impact of the environmental factors and microclimatic variations on them (i.e. the water evaporation cycles are controlling the weathering effects in porous materials). US measurements allows for the comparative study of the outer (weathered) to the inner (sound) material layer and the various strength levels of the different building materials. A GPR system is used for determining the thickness, as long as there is a clear and adequate dielectric contrast among layers and so it is possible to pick up an echo (pulse echo approach) allowing the location of interfaces. The combined use of the above mentioned non-destructive testing (NDT) techniques leads to conclusions concerning:

a. The weathering depth and the damage level of ancient mortars by US measurements as classified per mortar type and microstructure observations by FOM.
b. The compatibility of restoration mortars and plasters with the original building unit on the historic masonry scale, such as:
   - Elastic module of the various types of historic and restoration mortars by US.
   - Physico-chemical behaviour of the capillary systems of the various building materials, governing the percolation and evaporation of salt solutions within the historic masonry by IR-Thermo.

DIP (Image Pro Software) operates on images (i.e. photographs, micrographs) converted into a complex of numerical data. The process in order to digitise the image, is usually carried out by means of a telecamera, consisting in the sampling of the function f(x,y) according to a square dot matrix and successive quantification of spatial samples codified in the binary system. DIP can be used for the mapping of the decay patterns on a historic structure (i.e. masonry).

FOM (Pico Scopeman – Moritex) can be applied in the field in several magnifications ($\times 25$, $\times 50$, $\times 100$, $\times 200$, $\times 600$). The images can then be stored in a video system and processed in the laboratory. Microscopic investigation of the materials, according to their surface morphology and texture can be achieved, using this technique.

IR-Thermo (AVIO Thermal Video System) measures the thermal radiation emitted by the material – structure being examined and renders the image of the surface area in colours, in relation to a temperature scale. Two thermographic systems are available; both of them are consisted of an infrared detector and a processor. The detector is constructed of either mercury-cadmium-telluride that gives a spectral response between 8 and 12 μm with a scan speed of 15 frames per second or indium-antimonite that gives a spectral response between 3 and 5.4 μm with a scan speed of 30 frames per second.

US measurements can provide information about the condition and strength of materials and so to assist in order to compare various materials (sound and weathered) within a structure. The system used consisted of a portable ultrasonic non-destructive indicating tester (PUNDIT 6) and a pair of transducers of various frequencies (54 KHz–1 MHz). The indirect method (arrangement of the transducers on the same surface of the material) is commonly used when applying in situ measurements.

GPR is an electromagnetic method, involving propagation of electromagnetic (EM) waves; Ramac-GPR system using antennas of various frequencies (100 MHz–1 GHz). The antenna transmits short pulses of electromagnetic energy, which they are reflected from interfaces in the material(s), due to the changes of the dielectric properties. GPR data are used for determining the thickness, as long as there is a clear and adequate dielectric contrast among layers and so it is possible to pick up an echo allowing the location of interfaces.

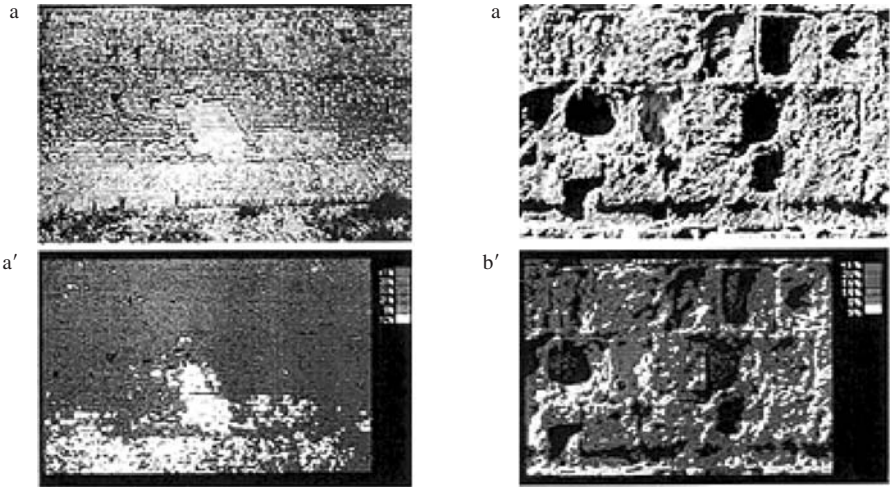

Figure 1. Digital images processing at the Medieval Fortifications of Rhodes.

3 RESULTS & DISCUSSION

Detailed materials mapping for the evaluation of conservation interventions compatibility, is presented in Figure 1. In particular, alveolar disease varying from disintegration to pitting, cavities, interconnected cavities and full face caves can be distinguished and quantified in images b, b′, whilst incompatible restoration materials, hard carbonate and biogenic crust, partial replacement by new incompatible building stones are introduced in images a, a′.

FOM can study the surface morphology before and after a cleaning intervention by indicating the cleaning method's abrasive levels or its selectivity (Moropoulou et al. 2002). In addition, after consolidation treatments, information concerning micro-structural modifications in porous materials, as well as the deposition mechanism of the applied materials, can be gathered (Moropoulou et al. 2000). A FOM investigation of the National Bank of Greece historic building in Nafplio (Fig. 2), after assessing the recent conservation interventions on marble and plasters, is presented. In particular, after the cleaning conservation interventions, some grey marble surfaces present partially detachment of authentic material, and totally discriminated boundaries of the coarse-grained calcite due to the development of intergranular fissures and calcite grains swelling (a). Respectively, some white marble surfaces demonstrate smoother areas, comparing to grey marble, although intergranular fissures of a finer-grained calcite were presented (d). Extensive orientated scratches are disclosed to many areas of grey (b) and white (h) marble surfaces, because of the rotary abrading tool application during the cleaning interventions. The developed unacceptable abrasion levels as well as the loss of authentic material prove the incompatibility of such "cleaning" methods. Moreover, black-grey crusts (e) and gluey depositions (f) remained on several white marble surfaces, whilst beige paint coating was spilled to marble areas that were next to plastered surfaces (h). Moreover, the detachment occurred at the interface of marble and repair putty, verifies the incompatibility of the used sealant: aesthetical incompatibility due to the colour and texture variance, as well as physico-chemical incompatibility due to the different thermal expansion coefficient and weathering susceptibility (c). Additionally, white marble surfaces disclose veins of iron oxides and hydroxides (g). The beige paint coating of plaster displays a fine smooth surface, since it was recently applied, and is classified to acrylic-based paints, because of its morphology (i). The thin white finish of acrylic putty (a white cement based material rich in PVAC), (j) exhibit a totally different texture comparing to the old thin white plaster finish (k), which is a lime mortar, as far as historic evidence is concerned. In particular, the old finish plaster is consisted of a white binder, coherent attached to the white and brownish aggregates (k), whilst the acrylic

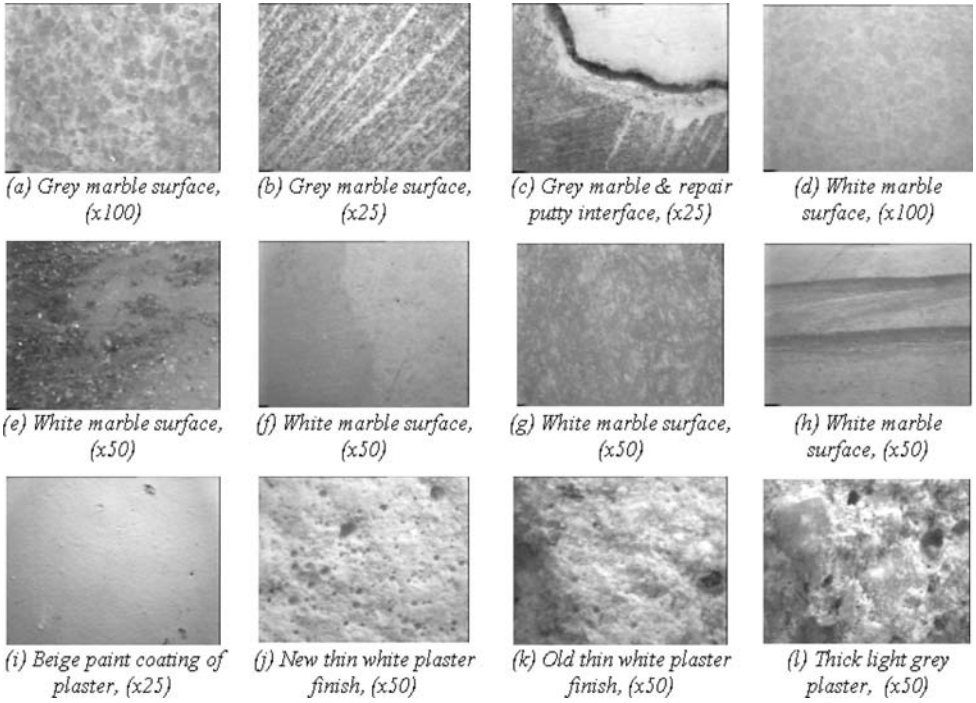

Figure 2. Nafplio's building – FOM investigation.

putty areas present extensively micro-pores and micro-craters, containing no aggregates (j). The physico-chemical incompatibility between the lime plaster finish and the acrylic putty, in terms of chemical and mineralogical composition, as well as microstructure, is profound. The putty was not only applied because of its function as a fine substrate for acrylic-based paints. It was also used for sealing micro-fissures, discontinuities and detachments of authentic material that occurred, after the utilisation of blowtorches (development of high temperatures irregular distribution) for the exterior paint coatings removal. Finally, the thick underlying plaster discloses light grey aggregates of fine and low granulation, whist the light grey binder is friable and unsound. Micro-fissures, micro-craters and micro-pores, demonstrate this lime mortar weathering (l).

IR-Thermo by the monitoring of consolidated porous stones during capillary rise tests (moisture) can assist in the interpretation of the physicochemical incompatibility that a consolidation material presents in relation to the stone (Fig. 3). Incompatible consolidation materials prevent the respiration behaviour of stone by constraining its water movement and vapour permeability. Due to the difference between the thermal diffusivities of consolidated and untreated stones, IR-Thermo could provide significant information with reference to the way the different consolidation materials – treatments have an effect on the moisture movement and/or deposits and consequently the respiration behaviour of the porous stones (Avdelidis et al. 2003).

The various consolidants used for the treatment of the porous stones behave in two different ways. The samples that were treated with prehydrolysed ethyl silicate with amorphous silica (CSPH2) and aqueous colloidal dispersion of silica particles (CSPL3) seem not to disrupt the capillary rise of water that occurs inside the pores. On the other hand, the acryl siliconic resin and the ethyl silicate, used respectively on treated samples CSEU1 and CSRP4, appear to obstruct the large pores of the stones, explaining the low water absorption percentage values presented in the graph as well as the obtained IR Thermo images.

Thermography provides visualisation of moisture (water movement) in porous materials; it monitors the water movement in porous stone and detects its impact by recording temperature variations

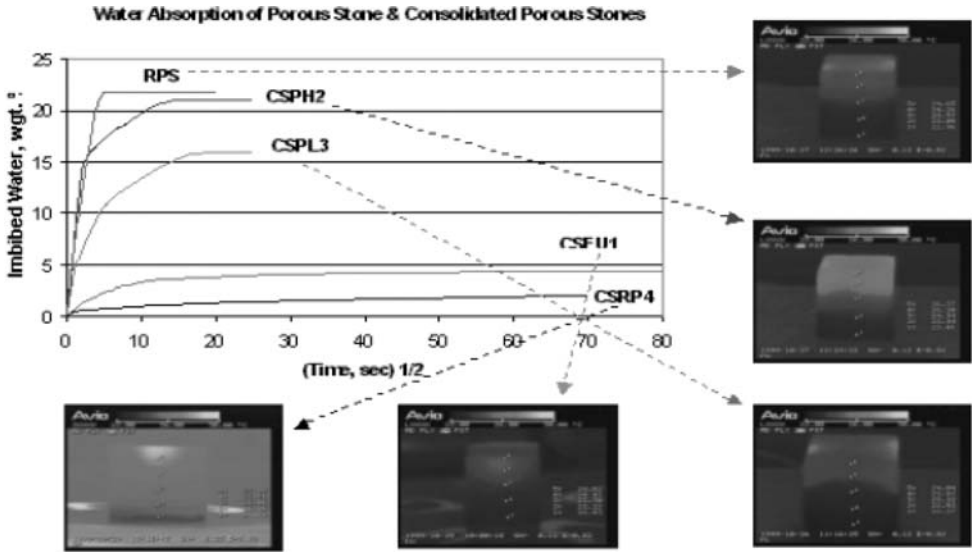

Figure 3. Water absorption curves and IR Thermo images during capillary rise tests.

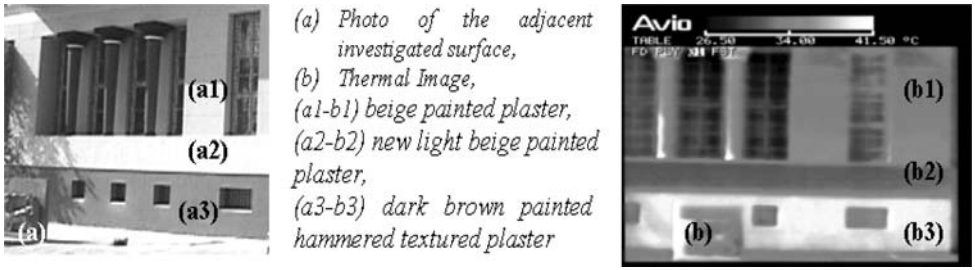

Figure 4. Nafplio's building – IR-Thermo investigation.

on the surface of the stones. The IR Thermo images obtained present such variations during the capillary rise tests.

Furthermore, in an investigation at the National Bank of Greece historic building in Nafplio (Fig. 4), IR-Thermo disclosed temperature readings and their distribution on the examined architectural surfaces by the rendering of different shades of grey. The investigation revealed that the beige painted lime plaster presents intermediate to low temperature values (a1-b1). This is attributed to moisture withholding deriving from the acrylic putty application (a cement based material rich in organic components) that prevents the respiration behaviour of the lime-plastered surfaces by constraining its water movement and vapour permeability. The respiration behaviour among cement, organic and lime-based materials varies because of the differences noticed not only in their chemical and mineralogical composition but also in their microstructure (i.e. total porosity, pore size distribution, pore radius).

Thus, there is different permeability among such materials leading to physicochemical incompatibility. The new light beige painted cement plaster, demonstrates the lowest temperature readings (a2-b2), since cement materials are hydrophilic, withholding moisture. Finally, the hammered plaster high temperatures (a3-b3), appear not only due to the plaster's superficial relief, but also because the plaster's moisture evaporation rate is not prevented, since acrylic putty was not applied.

US measurements can classify totally different types of materials within a structure, i.e. classification of plasters, according to their velocity readings. US measurements presented from the

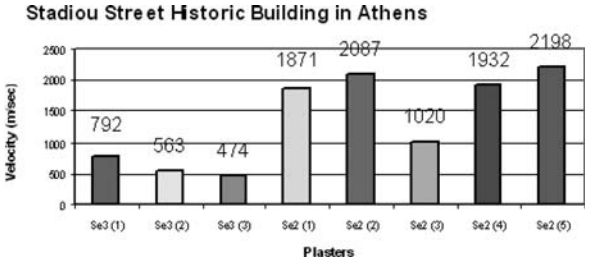

Se3 (1): Beige painted plaster, west façade, clay mortar
Se3 (2), Se3 (3): Beige painted plaster, north façade, clay mortar
Se2 (1), Se2 (2), Se2 (3), Se2 (4), Se2(5): Grey painted scratched plaster, west façade, cement mortar

Figure 5. Stadiou street historic building – US measurements.

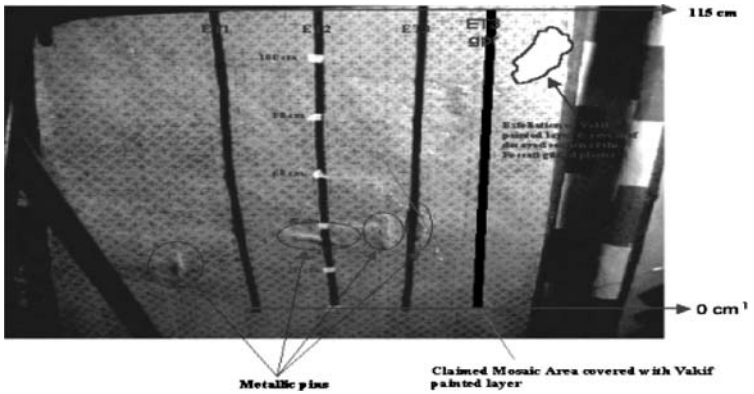

Figure 6. Photograph of the investigated area in the Hagia Sophia dome.

Stadiou street historic building in Athens can be classified into two groups (Fig. 5). The first one, displaying low ultrasonic velocities (Se3 (1), Se3 (2), and Se3 (3)) represents areas of the beige painted plaster, that is plastered surfaces of clay mortars. The second one, exhibiting higher velocities (Se2 (1), Se2 (2), Se2 (3), Se2 (4), and Se2 (5)), corresponds to the decorative scratched plasters that resemble stone finish (cement-based mortars). This classification derives from the totally different microstructure, mechanical properties, texture, chemical and mineralogical composition that totally different types of plasters (clay mortars and cement-based mortars) hold. The fact that the cement-based plasters demonstrate higher velocities comparing to the clay plasters is apparent. But what it was not prospective is the large declination presented. Clay plasters low velocities can be in general attributed to the reduced compactness of the material itself, but in this case are ascribed mainly to its weathered condition. The area of Se3 (1) measurement though is in better condition than the other two measured areas (Se3 (2) and Se3 (3)). The noted US velocities from areas of the decorative scratched plaster indicate the material's compactness, as well as, its sufficient conservation state. The relative high values verify a cement binder content. The area of Se3 (3) measurement though seems to be less compact and probably decayed due to the low velocity value recorded.

Major interventions in the past, in Hagia Sophia in Istanbul where different mosaic categories of invaluableness are presented, have caused aesthetic problems leading to some cases to severe damage of the mosaic. Such example is the intervention occurred in the early 1900's, under the General Directorate of Pious Foundations, mostly known as the "Vakif intervention". The plaster of this intervention was covered with an opaque yellow pigment in a glue medium. Stencil ornaments in pattern were applied on this yellow ground.

So, in this work, a plastered mosaic surface (characteristic Vakif intervention surface) in the Hagia Sophia dome is presented. The surface was situated between the 19th and the 20th rib at the northwest part of the dome, 16 metres from the centre of the dome. Figure 6 shows the examined

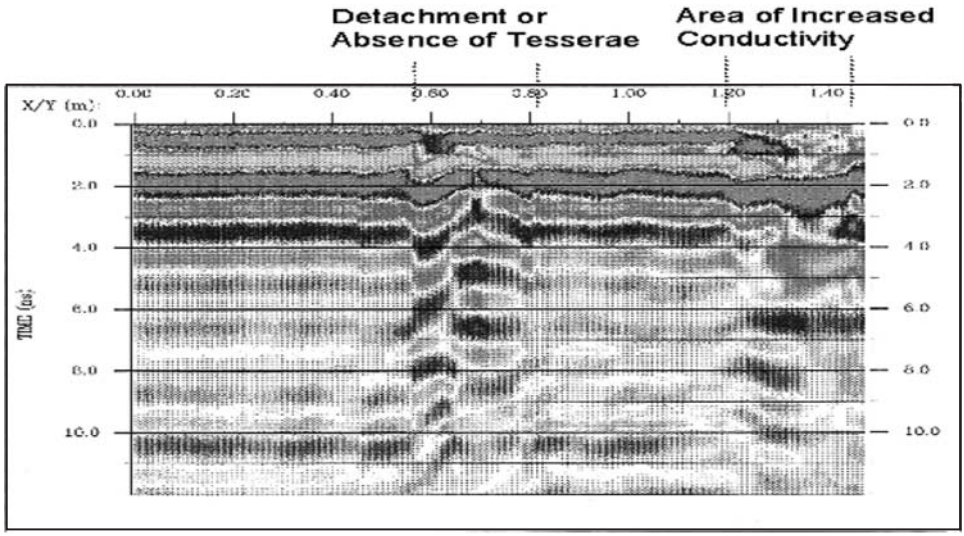

Figure 7. GPR measurement.

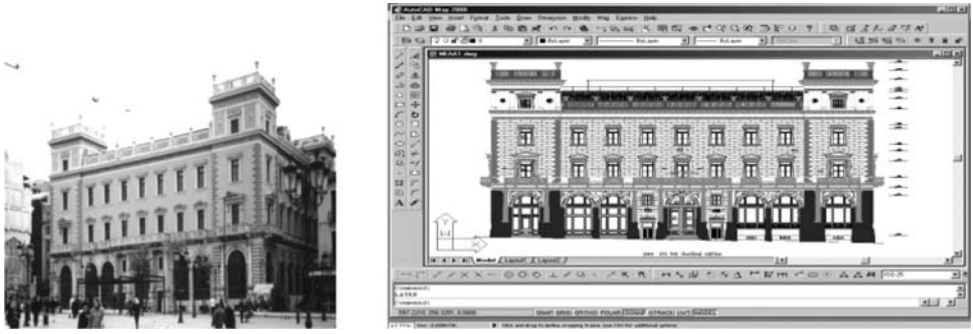

Figure 8. Photo and materials mapping using AutoCAD of the north façade of Mela Palace.

surface. GPR can reveal surfaces of plastered mosaics, in which areas of detached tesserae, as well as areas with moisture problems and presence of salts are displayed (Fig. 7). The boundaries of problematic areas are detectable, due to the differentiations of the EM waves transmission.

4 PLANNING OF HISTORIC BUILDINGS CONSERVATION INTERVENTIONS, USING INTEGRATED INFORMATION SYSTEMS

The architectural drawings of the Mela Palace historic building façades were created in AutoCAD (Michael 2001). These drawings function as the base map, where all the acquired non-destructive data can be recalled, since they are stored in a database. This integrated information system can be activated presenting all the available data of the investigated areas on screen. Therefore, the materials façades (i.e. stuccos, painted plastered surfaces, decorative plasters resembling edge cornered stones, white marble and grey marble surfaces) can be displayed on screen classified according to their architectural description and physico-chemical characteristics (Fig. 8).

Moreover, environmental impact assessment can be achieved through the management of DIP and IR Thermo images. Several pseudo colours (in a colour mode) or shades of grey (in black and

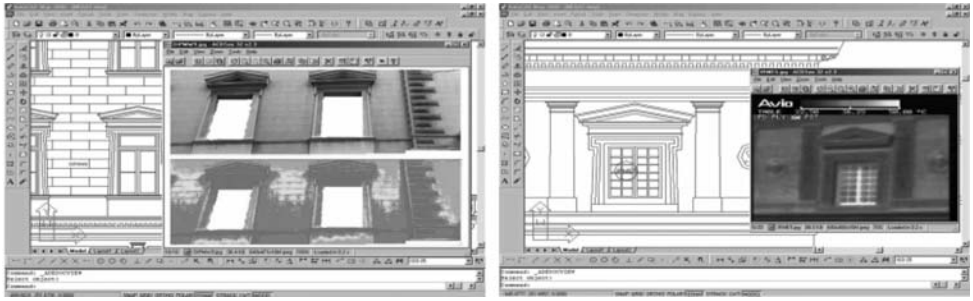

Figure 9. Decay mapping through NDT management (DIP and IR Thermo).

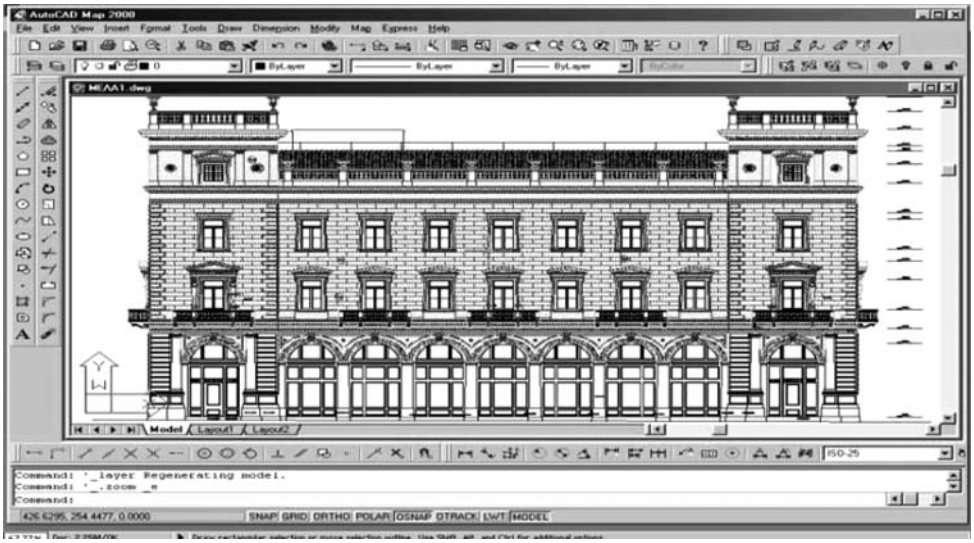

Figure 10. Planning of conservation interventions by the management of AutoCAD mapping results.

white format) through DIP images attribute the displayed decay patterns, whereas the IR Thermo images record the temperature distribution of the investigated surfaces (Fig. 9). In particular, the DIP image presents the painted plaster surfaces of the west façade, presenting with the different shades of grey the dust fall & black depositions area, the washed out surfaces, the blackish depositions and the firm painting. The IR Thermo image shows moisture deposits at the areas of decorative plasters, stuccos and pilasters comparing to the rest plastered area.

Finally, the management of the AutoCAD mapping results can achieve planning of conservation interventions. Thus, Figure 10 presents the areas where the removal of plaster's external paint, using a wet micro blasting method of 2.5 bar maximum pressure, is suggested, and the areas where a siloxane-based paint should be applied.

5 PRESERVATION PLANNING AS A TOOL FOR A SUSTAINABLE HISTORIC CITY: THE HISTORIC COMPLEX OF MEDIEVAL CITY OF RHODES

A Geographical Information System (GIS) can be used in order to manage a multidisciplinary database, including environmental, functional, materials and structural data (Moropoulou et al. 2001). Integrated environmental planning can be accomplished by the analysis of all the relevant

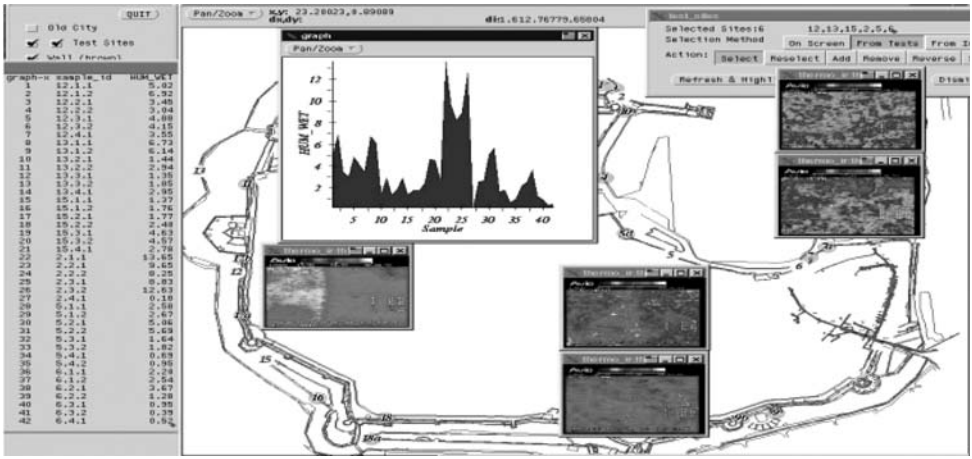

Figure 11. IR-Thermo images managed by GIS for the environmental impact assessment and related management concerning the planning of underground networks in the Medieval City of Rhodes.

data with the objective of eliminating the negative impact of the natural and artificial (man-made) environment on historic fortifications, with the purpose of preventing additional damage and preserving the compulsory conservation level – intensity, whilst the historic site is revitalised in the course of further treatments – uses and its role is reinforced. Finally, integrated management can be suggested in terms of preservation of historic sites as intervention to materials and structures (Fig. 11), urban planning and environmental management to eliminate environmental loads, as well as development and rehabilitation of the places – sites and buildings by introducing new uses (cultural and recreational activities and tourism).

6 CONCLUSIONS

The main objective of this work was to present the effectiveness of various NDT & E techniques in the investigation of historic structures. From the examples that were performed on the architectural surfaces of historic sites and buildings, it is deduced that the combined use of such techniques could provide considerable amount of information for the assessment of materials and techniques for the protection of cultural heritage. Furthermore, the integrated management of data by GIS on the buildings/complexes scale develops a planning methodology concerning proper, effective and compatible materials and techniques for conservation interventions.

ACKNOWLEDGEMENTS

Acknowledgements are attributed to geophysists A. Aggelopoulos and P. Karmis for the GPR measurement and analysis in Hagia Sophia, architect S. Michael for the AutoCad designs of the Mela Palace and engineer Th. Tsiourva and professor M. Koui for the results presented in the GIS section of this paper.

REFERENCES

Avdelidis, N.P., Moropoulou, A. & Theoulakis, P. 2003. Detection of water deposits and movement in porous materials by infrared imaging. *Journal of Infrared Physics & Technology* 44: 183–190.

Michael, S. 2001. Management and planning of conservation interventions concerning the facades of the National Bank of Greece neoclassical buildings in Athens and Piraeus. *Master Thesis*, NTUA, Greece.

Moropoulou, A., Koui, M., Avdelidis, N.P. & Achilleopoulos, N. 1999. NDT for materials quality control, environmental impact assessment and management of cultural heritage. *Journal of Insight* 41: 362–368.

Moropoulou, A., Koui, M. & Avdelidis, N.P. 2000. Infrared thermography as a NDT tool in the evaluation of materials & techniques for the protection of historic monuments. *Journal of Insight* 42: 379–383.

Moropoulou, A., Koui, M., Kourteli, Ch., Theoulakis, P. & Avdelidis, N.P. 2001. Integrated methodology for measuring and monitoring salt decay in the Medieval City of Rhodes porous stone. *Journal of Mediterranean Archaeology & Archaeometry* 1: 57–68.

Moropoulou, A., Delegou, E.T., Avdelidis, N.P. & Koui, M. 2002. Assessment of cleaning conservation interventions on architectural surfaces using an integrated methodology. In Vandiver, P. Goodway, M., Druzik, J.R & Mass, J.L (eds), *Materials Issues in Art and Archaeology VI: 69–76.* Pittsburgh: Materials Research Society.

Cultural Heritage Conservation and Environmental Impact Assessment by Non-Destructive Testing and Micro-Analysis – Van Grieken & Janssens (eds)
© 2005 Taylor & Francis Group, London, ISBN 90 5809 681 5

Modern and ancient glass in the polluted atmosphere. What is the prevailing phenomenon? Leaching, corrosion, soiling, encrusting . . .?

Roger-Alexandre Lefèvre, Anne Chabas, Isabelle Munier & Tiziana Lombardo
Laboratoire Interuniversitaire des Systèmes Atmosphériques (LISA), Université Paris, Créteil, France

ABSTRACT: Very few information is available concerning the composition of the atmosphere in the cities during past periods until Industrial Revolution but also concerning its action on ancient glass and stained glass. Nevertheless, the presence on stained glass of crusts containing wood debris (charcoal) indicates that this past atmosphere was loaded with particles originating from the combustion of wood. Leaching and corrosion currently observed on stained glass unsheltered from rain cannot easily be related to ancient phenomena because of the cumulative effects of modern pollution added to past effects.

In the modern cities, glass and stained glass suffer from the atmospheric pollution (gases, particles, rain), of which action extent depends mainly on glass composition: modern glass (Ca-Na-Si) is more durable than ancient one (Si-Ca-K).

Glass samples having the composition of ancient glass alter when exposed to modern air pollution: neocrystallisations appear depending in the first stages mainly on the composition of the glass (chlorides, nitrates, sulphates of K and Ca) and later mainly on the composition of the atmospheric pollutants (sulphate of Ca). This phenomenon leads to the growth of gypseous black crusts developed on stained-glass windows in the parts sheltered from rain. In parts unsheltered a leaching occurs.

On modern glass leaching is very weak and the prevailing phenomenon is soiling resulting from the sticking of coarse and fine particles when glass is sheltered from rain and from the remaining of fine particles when unsheltered.

1 INTRODUCTION: MEDIAEVAL GLASS, MODERN GLASS, AND ATMOSPHERIC POLLUTION

Glass is widely regarded as a non-weatherable material. Indeed many ancient glass artefacts arrive to us apparently intact; however, modern tools of investigation of material surfaces show that, if at the macroscopic scale the glass might seem to be intact; this is not the case at the microscopic level.

The principal factor in the decay of glass is *water*, which causes, when its pH is below 9, a superficial leaching of alkaline and alkaline earth elements called "modifiers" in the irregular network of SiO_4 tetrahedra (Verità 2001). As a result, a surface layer of hydrated amorphous silica develops being able often to act as a barrier against further propagation of the leaching in interior of the glass. In fact, it progresses essentially along fractures parallel or perpendicular to the glass surface (Libourel et al. 1994, Sterpenich & Libourel 2001). When the pH of the water is above 9, the network of the tetrahedra is destroyed and glass corrodes. In polluted atmospheric conditions, the pH of water is more often acid than basic and the leaching mechanism predominates. Its intensity depends mainly on the glass chemical composition: *ancient glasses*, in particular those of stained-glass windows, are generally potassium-rich and not highly resistant to weathering, whereas *modern ones*, being sodium-rich, are very durable.

This paper deals with the behaviour of ancient and modern glass in the ancient and modern atmospheres. The consistency of the observation and interpretation is obviously higher when considering modern glass in modern atmosphere than ancient glass in the ancient atmosphere. For ancient glass in the modern atmosphere the difficulty comes from the impossibility to separate the cumulative effects of the successive polluted atmospheres.

2 MEDIAEVAL GLASS IN MEDIAEVAL POLLUTED ATMOSPHERE

Whereas a lot of information is available concerning the atmosphere at the global scale during past periods, very few is displayed in the literature concerning the composition of the atmosphere in the cities before Industrial Revolution and concerning the action of this ancient atmosphere on glass and stained-glass. Nevertheless, witnesses of the effects of pre-industrial atmosphere on building façades which have been preserved, by a combination of circumstances (walling-up and/or burial) against the following industrial air pollution have been reported in Arles and Bologna (Ausset et al. 1998, Del Monte et al. 2001a), and Paris (Del Monte et al. 2001b). The presence of crusts containing wood debris on the stone surface demonstrates that the concentration of airborne dust particles in the atmosphere of the cities even before the Industrial Revolution was high enough to be responsible for darkening the façades and for the development of grey crusts. The nature of the particles (wood debris) and of the cement (mainly calcite with minor gypsum) present in these crusts reflects the nature of the predominant fuel (wood) as well as the nature of the dominant gaseous pollutant present in the atmosphere at the time of crust formation (i.e. CO_2 and minor SO_2 originating from wood combustion).

The presence of wood debris in crusts on ancient stained-glass has been reported in Tours on the Saint-Gatien Cathedral (Lefèvre et al. 1998) confirming the information obtained from stone: during the pre-industrial period a *soiling* followed by an *encrusting* existed in the parts of glass sheltered from rain. *Leaching* and *corrosion* currently observed on ancient glass and stained glass unsheltered from rain cannot easily be related to ancient phenomena because of the cumulative effects of modern pollution added to past effects.

3 MEDIAEVAL STAINED GLASS IN MODERN POLLUTED ATMOSPHERE

The main observable effects of modern air pollution on *mediaeval stained glass* are *leaching* and *corrosion* where unsheltered from acid rain and development of *sulphated black crusts* where sheltered.

Such gypseous crusts have been often observed on several ancient stained glass windows (Newton & Davison 1989), and extensively studied for the Tours Cathedral (Lefèvre 1998) and the Sainte-Chapelle in Paris (Lefèvre & Davison 1998, Munier & Lefèvre 2000) (Fig. 1). They can reach few millimeters thick and their color varies from white to dark with infinity of intermediate brown and gray. Their cement is mainly constituted by gypsum ($CaSO_4$, $2H_2O$); however syngenite ($K_2Ca(SO_4)_2 \cdot H_2O$) is also observed on potash-lime glass, as well as, sometimes, calcite ($CaCO_3$). Many particles of various chemical compositions, morphologies and origins are embedded in this matrix.

The study of medieval glass precious fragments was made it possible thanks to the development of electronic microscopy linked with an analytical system. In the case of the Sainte-Chapelle windows study (Munier et al. 2000a, 2000b), the stained-glass pieces had a sufficiently small size to be observed directly without specific preparation, except a light carbon coating easily removed during restoration. Besides, the superficial gypseous crusts were easily removed from the glass surface without damaging the original medieval surface, since they were generally poorly adhesive.

The medieval studied glasses had calco-potassic compositions with significant amounts of magnesium and phosphorous (Munier 2000b). The glass composition just below the surface was impoverished in potassium and in calcium, what indicates a noticeable lixiviation process. The glass surface was granular, fairly fractured and dotted with numerous pits (Fig. 2).

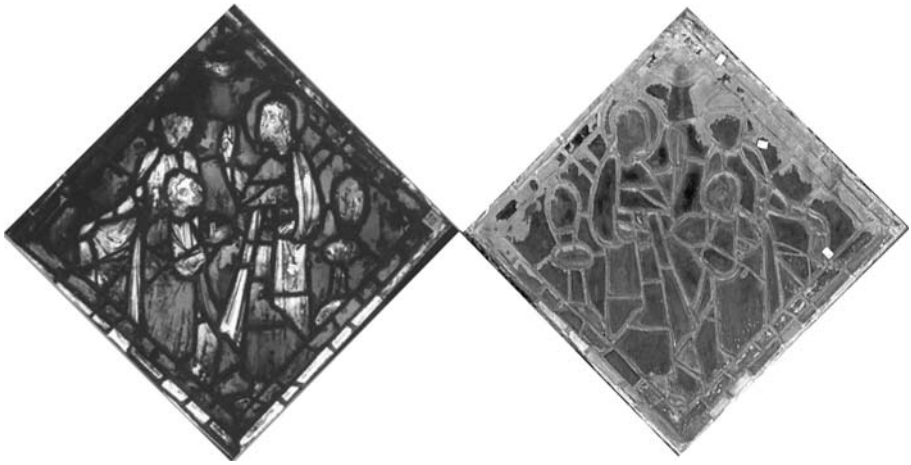

Figure 1. Saint John the Baptist stained glass of the Sainte-Chapelle in Paris (Window 102, panel 58). Left: viewed by transparency from the interior of the Chapel; Right: the same viewed from the exterior: gypsum black crusts develop in the parts sheltered from rain (mainly upper parts).
(This figure is presented in the signature in colours at the end of this volume, Appendix, pg. 317)

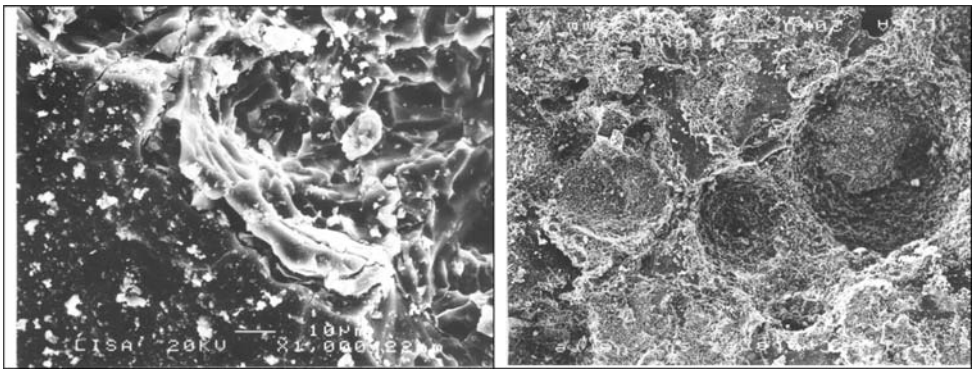

Figure 2. Sainte-Chapelle stained glass. Left: glass surface fractured and loss of glass fragment (upper-right); Right: pits observed on glass surface.

The superficial crust covered the sheltered area of the glass windows (upper part of the panels and near sealing leads). They were mainly constituted by gypsum with traces of calcite and quartz (SiO_2) (Munier 2000b). The gypsum was formed by small tangled acicular crystals (Fig. 3).

These crusts contained large amount of exogenous particles, which could be divided into three main categories: terrigenous, anthropic and biogenic. These particles had been accumulated into the crusts since their formation, which probably dated from 1936, date of the last stained-glass windows cleaning (Aubert et al. 1959).

The terrigenous category gathered calcic (calcite, dolomite), siliceous (quartz) and silico-aluminous (feldspars and clay minerals) particles. This category was the most important (∼65%) and correspond to the deposition of the mineral particles remobilized by human activity.

The anthropic particles (∼35%) were divided into metallic fragments (Fe, Pb, Ba . . .) and fly-ash. The most numerous observed fly-ash (more than 80%) was smooth and alumino-silicated, the porous (10%) and spongy (5%) fly-ash was carbon- and sulphur-rich, and rough surface metal-rich ones were less abundant (5%). All of these particles are of industrial origin: smooth surface fly-ash originates principally from coal combustion (and in a less extent from heavy-oil combustion), and

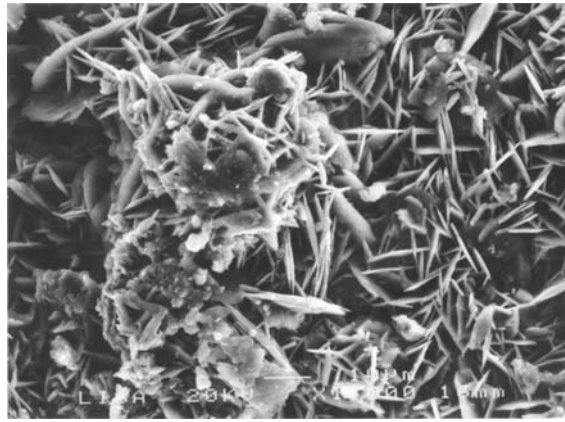

Figure 3. Gypseous crystals observed on the medieval stained glass of the Sainte-Chapelle.

porous and spongy fly-ash from combustion of heavy and light oil. Pollens and microorganisms essentially formed the last category.

Particles and cement of gypseous black crusts observed on glass surfaces are quite similar to those observed on stone. This is a clear evidence of the atmospheric origin of their constituents and their similar formation mechanisms: deposition and cementation of airborne particles.

4 MEDIAEVAL-LIKE LOW DURABLE MODEL GLASS IN MODERN POLLUTED ATMOSPHERE

To study the impact of the modern polluted atmosphere on glass, a lot of experiments have been recently performed either in the field (Woisetschlager et al. 1999, Schreiner & Schmitz 2000) or in climate chamber (Römich 2000, Boehm 1999). The glasses used in these studies are representative of sensitive mediaeval glass and contain significant amounts of potassium and calcium. These studies have showed that the formed alteration products have a chemical composition depending on the glass composition but also on the atmospheric gaseous composition.

A detailed study of two medieval-like glasses weathered in the polluted atmosphere of Paris have been then conducted in order to characterise the formation of a leached layer and of weathering products (Munier & Lefèvre 2000c, Munier et al. 2001, 2002), and the factors likely to influence it (Munier 2000b, Munier et al. 2002).

In this study two low-durability model glasses, rich in Ca-K and in Na-K, were exposed both unsheltered and sheltered from direct rain. So as to appreciate the seasonal influence, two series of samples were exposed: the first beginning in November 1997 and the second in May 1998. Parallel to the glass exposure, atmospheric data (temperature, relative humidity (RH)) and gaseous atmospheric content data (SO_2, NO_x) were collected.

The structure and the water content of the leached layers were studied through Infrared Spectroscopy (Del Monte & Rossi 1997). The alteration products were examined through Analytical Scanning Electron Microscopy (ASEM). So as to evaluate the quantity of neocrystallisations formed, a specific non-destructive analytical protocol, using Inductively Coupled Plasma – Atomic Emission Spectrometry (ICP-AES) and Ionic Chromatography (IC), was developed, allowing one to characterise and to quantify the ionic content of their water-soluble fraction (Munier et al. 2002).

The surface leached layer formed from the very beginning of the glass alteration. It is depleted of heavier atoms (K, Ca …) and/or enriched in lighter atoms or molecules (H^+, H_3O^+, H_2O …) (Fig. 4).

The water intake increased continuously during the glass samples exposure and was markedly more important for glasses exposed directly to the rain (Fig. 5). However, whatever the exposure

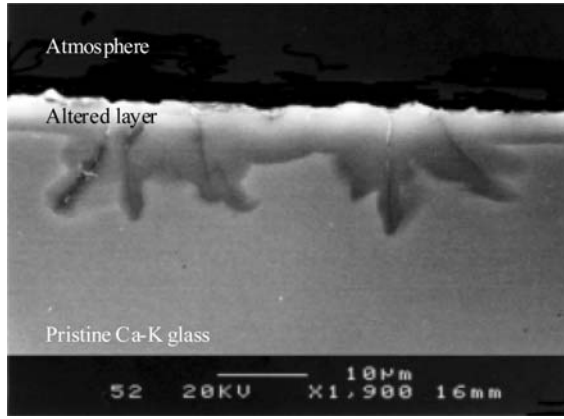

Figure 4. Polished cross-section of a November series Ca-K glass sample exposed 9 months to the rain (ASEM – backscattered electrons).

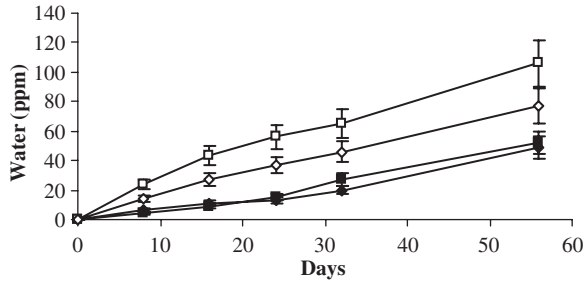

Figure 5. Water content (ppm) of the glass samples (November series) versus the exposure time (Ca-K glass sheltered (♦) and unsheltered (◊), and Na-K glass sheltered (■) and unsheltered (□)) (error = 15%).

mode, all the glass samples underwent a leaching process, even those undoubtedly sheltered. The observation of such alteration process on sheltered glasses underlines the noticeable influence of air humidity on glass weathering.

After few days, the development of neocrystallisations at the glass samples surface was observed. These neocrystallisations presented different shapes according to the chemical composition of the underlying glass (Fig. 6). With time, the dimension of the crystals and the surface fraction covered by deposit increase.

The chemical analysis of the neocrystallisations showed that their *cationic* content reflects the nature of the underlying glass mobile ions: on the Ca-K, glass they were rich in *Ca* and *K* and on the Na-K glass in *Na* and *K*. Their *anionic* part is characteristic of the atmospheric components: *sulphates*, *nitrates* and *chlorides* (carbonates being not analysed) as *major anions* and *formates*, *fluorides*, *nitrites* and *oxalates* as *minor anions*.

The *sulphates* were the major anions contained in neocrystallisations formed in the November series. Their amounts analysed on both glasses were greatly correlated (Fig. 7), indicating clearly that the nature of the glass substrate had a very small influence on the sulphates formation process, which then would probably mainly depend on atmospheric factors.

The main atmospheric factor likely to influence the sulphates formation is the atmospheric SO_2 content, of which amounts were markedly more important in November comparing to May. (Munier 2000c) In order to evaluate the influence of SO_2 content on the sulphates formation, the amounts of sulphates formed successively between two withdrawals were plotted versus the average of the atmospheric SO_2 content over the same period of time (Fig. 8). The correlation was quite good, indicating that sulphur dioxide seemed to favour the sulphates formation.

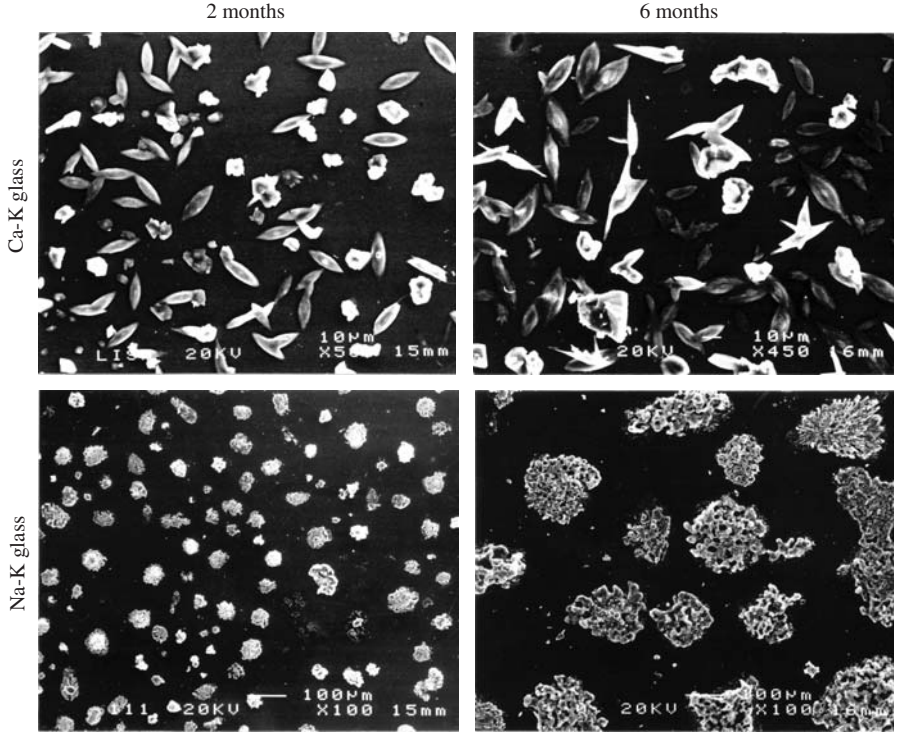

Figure 6. Neocrystallisations developed on Ca-K glass (top) and on Na-K glass (bottom) exposed two months (left column) and six months (right column) sheltered from direct rain.

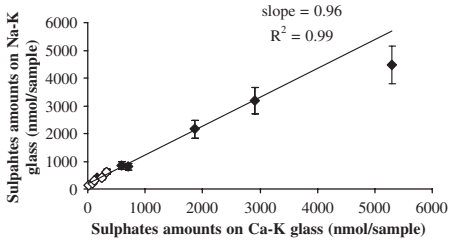

Figure 7. Correlation between the sulphates formed on sheltered Ca-K and Na-K glasses exposed from November 1997 (♦) and from May 1998 (◊).

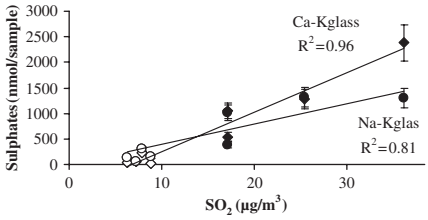

Figure 8. Correlations between the sulphates formed on sheltered Ca-K and Na-K glasses exposed from November 1997 (Ca-K: ♦, Na-K: ●) and from May 1998 (Ca-K: ◊, Na-K: ○) and SO_2 content.

Besides, the sulphates formed mainly at high relative humidity (>65%). The formation of sulphates when RH exceeded 65% could be due to a real influence of RH, which could have favoured the formation of a film of water on the glass surface (Munier et al. 2002), or to the influence of SO_2, or to both.

The *nitrates* amounts were always more important in May series than in the November series, on both glasses. In the May series, they were sometimes the most important analysed salts present on the glasses. When comparing both glasses, *nitrates* amounts were generally slightly more important on Na-K glass samples, and seemed to be slightly correlated ($r^2 = 0.63$). The nitrates formation depended thus partially on the underlying glass.

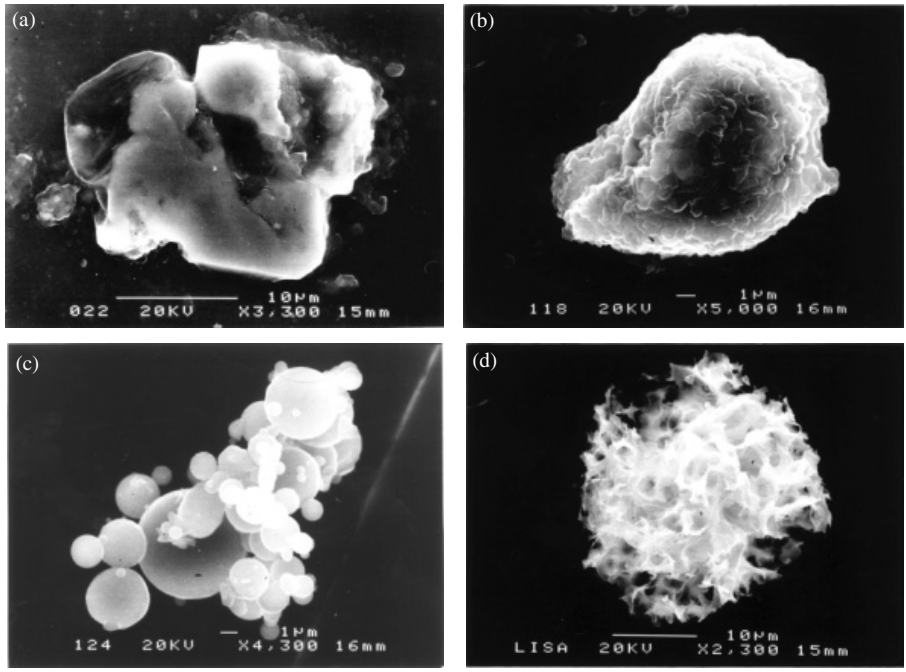

Figure 9. Particles settled on glass surface (a): NaCl crystals (Halite), (b): Ca-rich particle (Calcite), (c) Alumino-silicated smooth fly-ash, (d): carbonaceous spongy fly-ash.

A potential parameter which could also have influenced nitrates formation was a potential source of nitrates: $NO_x (= NO + NO_2)$. However, plotting the successive nitrates amounts, formed between two withdrawals, versus the mean NO_x atmospheric content over the same period, showed that they were not correlated. The source of the nitrates has to be searched among nitrogen-bearing species having high content during the May period, HNO_3 probably.

The nitrates amounts did not have a particular correlation with RH values measured during the exposure time (Munier et al. 2002). Thus, RH was not a limiting factor in the nitrates formation process on the exposed glass samples.

The comparison of ASEM and ICP-AES/IC (Munier 2000) analyses allowed one to estimate the possible *mineralogical species* forming the neocrystallisations:

- The *sulphates* formed on Ca-K glasses were likely constituted by *anhydrite/gypsum* ($CaSO_4/CaSO_4 \cdot 2H_2O$) and *syngenite* ($K_2Ca(SO_4)_2 \cdot H_2O$), and those developed on the Na-K glass samples by *thenardite/mirabilite* ($Na_2SO_4/Na_2SO_4 \cdot 10H_2O$) and *arcanite/mercallite* ($K_2SO_4/KHSO_4$).
- The encountered *nitrates* may probably be constituted by *niter* (KNO_3) on Ca-K glass and *soda-niter* ($NaNO_3$) on Na-K glass.
- The presence of *carbonates* remains difficult to confirm but they were probably present as *kalicinite* ($KHCO_3$) and *calcite* ($CaCO_3$) in the case of Ca-K glasses and as a mixture of sodium carbonates (*thermonatrite* ($Na_2CO_3 \cdot H_2O$), *natrite* ($Na_2CO_3 \cdot 10H_2O$), *trona* ($Na_3H(CO_3)_2 \cdot H_2O$), ...) in the case of the Na-K glass samples.

Numerous particles were observed on glass samples surface. In the case of samples exposed to the rain, the particles remained on the glass surface between two rain events. However, when atmospheric particles settled on sheltered glass surface, they were not washed away by the rain but were gradually incorporated into the growing neocrystallisations. Nevertheless, it was possible to observe them through ASEM (Munier 2000). The same categories as above are observed, as well as marine particles (*Halite* essentially) (Fig. 9).

In any cases, the influence of these particles is probably negligible by comparison with underlying glass with respect to the supply of cations to neocrystallisations, at least at the beginning of the alteration process.

On these mediaeval-like low-durable model glasses, exposed sheltered from the rain to the modern polluted atmosphere, the leaching process is at first predominant, leading to the development of neocrystallisations, of which chemical and mineralogical compositions reflect the glass but also the gaseous pollutants composition (i.e. sulphates and nitrates of Ca, Na, K).

However, since the glass alteration rate generally decreases sharply with time, the atmospheric contribution (gases and particles deposition) will become predominant and the influence of the underlying glass less marked (Grambow 1985). The most stable mineral phase (Gypsum) would then become the major phase and then a black gypsum crust would develop progressively, cementing deposited airborne particles, as it is observed on old stained-glass windows.

In unsheltered location, the neocrystallisations, developed between two rain events, as well as the deposited atmospheric particles will still be washed by the following rain and the leaching will remain the unique witness of the effect of the atmospheric pollution.

5 MODERN GLASS IN MODERN POLLUTED ATMOSPHERE

As written above, on low-durable mediaeval-like glasses exposed to atmospheric pollution a lot of weathering products form, resulting from interactions between gaseous pollutants, water and modifier cations of the glass network, hiding the mechanism and the effects of deposited atmospheric particulates, that means *soiling*. To study only the *soiling*, the choice of a soda-lime glass currently employed in the contemporary building façades and less sensitive to the weathering is therefore more adapted. In fact, soiling is the major problem arising with modern glass in modern polluted atmospheres.

Such a soda-lime glass was exposed, unsheltered and sheltered from rain, for up 2 years in the polluted atmosphere of Paris (Lombardo 2002) according to the exposition protocol described in (Chabas & Lefèvre 2002).

The loss or gain of matter was measured by glass weighing, before and after exposure. The ratio (final weight – initial weight)/sample surface (cm^2) of the glass is expressed versus time (Fig. 10). Sheltered glass shows a gain of weight versus time. Unsheltered glass shows a mass decreasing at the beginning of the exposure while after the 2nd month a mass gain is recorded.

The gain of weight of the sheltered glass is due to the accumulation of particles, which are not washed by rain. The loss of weight of the unsheltered glass indicates a competition between the

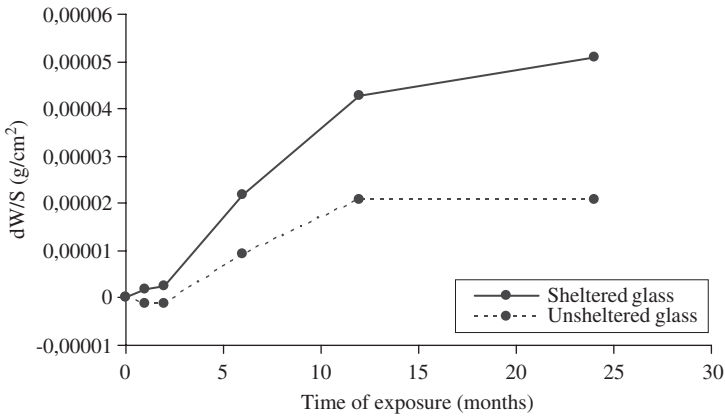

Figure 10. Weight variation (g/cm^2) of the sheltered and unsheltered Na-Ca glass during 2 years of exposure.

weak leaching of the glass and the deposited particles being not entirely washed by rain. After 2 months, the particles deposit is in dominant position.

The atmospheric particles deposited on the glass and on filters were characterised by Analytical Scanning Electron Microscopy. Magnification was adapted in order to study all particles, coarse (diameter $\geq 1\mu m$) and fine ($<1\ \mu m$). The percentage of the glass surface covered with all particles without distinction of their geochemical origin is calculated by Image Processing (Fig. 11).

For each exposure and each size category of particles, the percentage of covered surface increases versus time. The trend is in accordance with the gain of mass previously shown (Fig. 10). The more important percentage of covered surface for fine particles on the unsheltered glass can be explained with regards to the glass surface aspect and to the geochemical origin of particles. This possible origin can be determined according to the morphology, size, chemical composition of each particle analysed in randomly chosen areas. Five geochemical origins were attributed to particles: marine, terrigenous, anthropic, biogenic and undetermined.

Marine particles are cubic crystals of *halite* (NaCl) coming to Paris through oceanic western wind.

Terrigenous particles consist of silica (*quartz*), alumino-silicates (K and Na-Ca *feldspars* and *clay minerals*) and carbonates (*calcite*, *dolomite*) (Fig. 12) (with more or less S and Cl anthropic impurities). These particles can be strictly natural (soil dust) or coming from derived products (cement and concrete dust removal).

Anthropic particles are issued from man related activities and can be subdivided into many sub-categories:

- Fe, Ti or Al-rich irregular *metallic fragments* (Fig. 13) coming from rusted and painted structures.
- Smooth Si-Al *fly-ash* and carbonaceous spongy *fly-ash* issued from coal and heavy oil burning.
- S and Ca rich prismatic particles (probably *Gypsum*) (Fig. 14) which can be formed by evaporation of rain and fog droplets. S has an atmospheric origin (dissolution of SO_2). A very small part of Ca comes probably from the glass but the major part originates from the atmosphere (cement plants, industrial plants and coal combustion, works on buildings).
- C rich aggregates of nanospheres in cluster or in chain (with occasionally Cl and S) (Fig. 15) which are typical *soots* emitted from diesel, gasoline, kerosene and natural gas combustion. Often, these clusters lose their fresh and round aspect adsorbing water, salts and organic components. They form *aged soot clusters*. These particles are also present as isolated (Fig. 16), especially in fine particles category.
- *Biogenic particles* are spores and pollens (Fig. 17).
- At last, *undetermined species* are the category attributed to other particles.

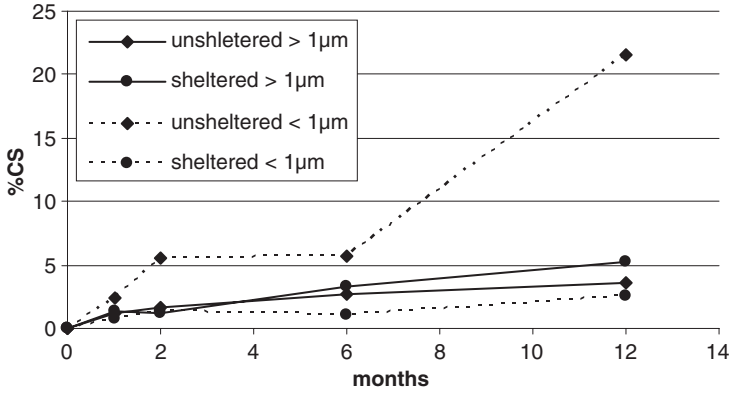

Figure 11. Evolution of the percentage of glass surface covered by particles (CS).

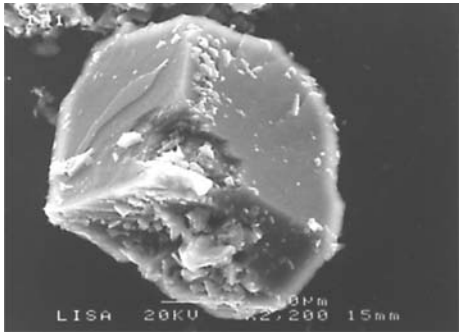

Figure 12. Ca-rich particles (probable calcite) of terrigenous origin observed on the sheltered Na-Ca glass.

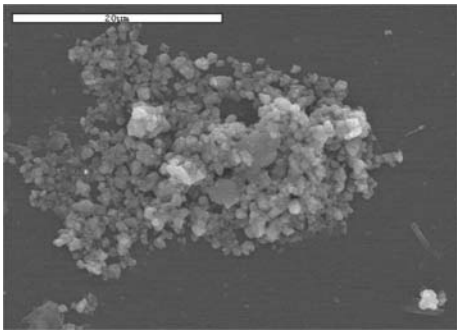

Figure 13. Irregular Fe-rich debris of anthropic origin present on the sheltered Na-Ca glass.

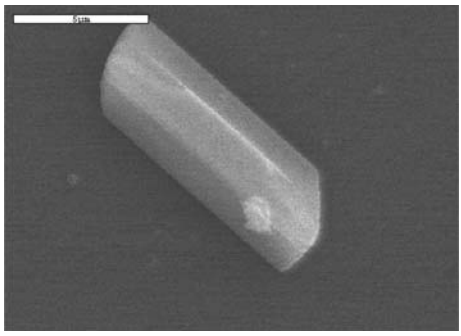

Figure 14. Gypsum prism of anthropic origin developed on the sheltered Na-Ca glass.

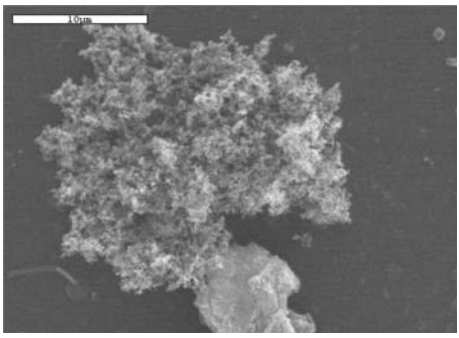

Figure 15. Cluster of soots of diesel exhausts observed on the sheltered Na-Ca glass.

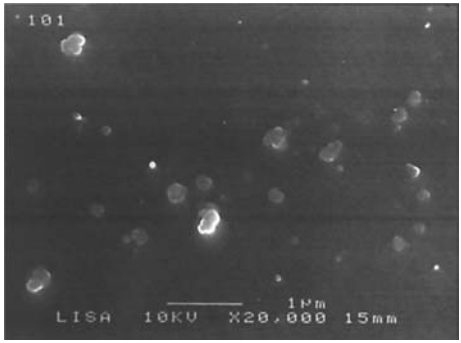

Figure 16. Isolated nanosoots present on the unsheltered Na-Ca glass.

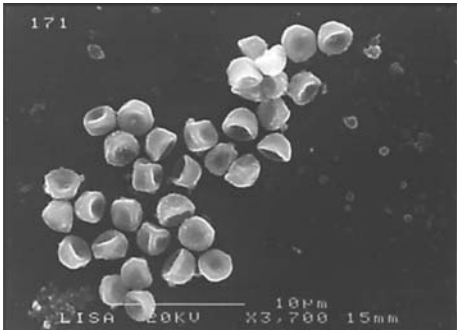

Figure 17. Biogenic particles deposited on the sheltered Na-Ca glass.

For **particles bigger than 1 µm** (Fig. 18), those of marine origin are very few numerous in the air and absent on glasses. Terrigenous particles are mainly represented in the air and on the unsheltered glass. The main important feature is that *anthropic particles are in dominant position in the air, on the sheltered glass and are well represented on the unsheltered glass*. Forming this

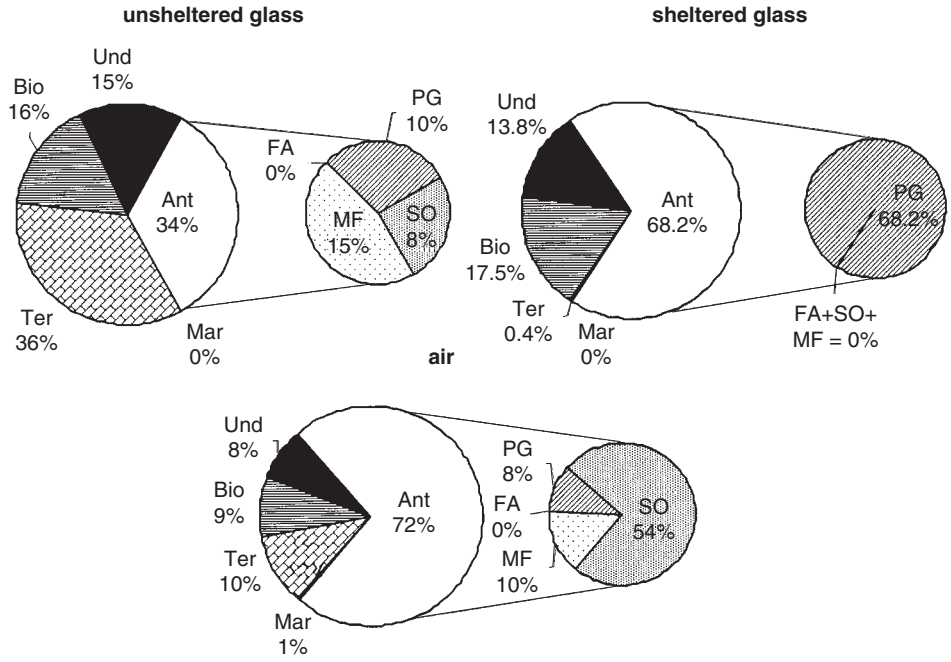

Figure 18. Mean percentage of the different categories of **particles ≥ 1 µm** on Na-Ca glasses (sheltered and unsheltered) and in the air of Paris after 1 year of exposure (Mar: marine; Ter: terrigenous; Ant: anthropic = MF (metallic fragment) + FA (fly-ash) + PG (prism of gypsum) + SO (soots); Bio: biogenic; Und: undetermined particles).

last category, metallic fragments are found in the air and on the unsheltered glass; fly-ash particles are absent; prisms of gypsum are present in the air and on glasses, especially on the sheltered one where they form the totality of the anthropic category; soots were recognized in the air and on the unsheltered glass. Biogenic category is present in the air and on glasses.

Some interpretations can be proposed for coarse particles. The non-dominance of anthropic particles on the unsheltered glass is in disagreement with previous study (Chabas & Lefèvre 2002). This is due to a competition with terrigenous particles induced by important restoration works occurred near the exposure site during the field experiment. These particles, very coarse in size, fall down by sedimentation more easily on the unsheltered glass than on the sheltered. If there is no rain, they can accumulate on the unsheltered glass.

Among the anthropic category, the absence of fly-ash, replaced by abundant soots shows the change of particulate pollution during the last decades. The predominance of gypsum on sheltered glass indicates the occurrence of condensation phenomenon from air humidity and fog which favours the crystallization of gypsum. This film of water and salt could mask the other particles and especially soots.

Considering **particles smaller than 1 µm**, only anthropic category is mainly represented (≥98%). Inside this category, some rare prisms of gypsum are present, mainly on sheltered glass. This confirms the phenomenon of condensation previously seen with coarse particles. But 90% of the deposit is formed by carbon-rich nano-soots. The accumulation of these particles is so important that a continuous carpet-like layer is formed progressively on the glass (Fig. 19). The higher percentage of covered surface for unsheltered glass is perhaps due to the absence of the thin film of condensation, because washed by rain, and which persists on the sheltered glass, hiding the carpet-like layer of nano-soots.

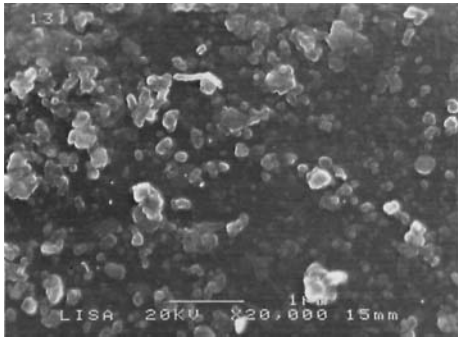

Figure 19. Unsheltered Na-Ca glass exposed 12 months: a carpet-like soot layer covers continuously the surface.

6 CONCLUSION: WHAT IS THE PREVAILING PHENOMENON? LEACHING, CORROSION, SOILING, ENCRUSTING …?

Concerning the *mediaeval glass in the mediaeval polluted atmosphere* only an *encrusting* is supposed to have existed because the crusts contain good tracers of the past atmosphere: debris of charcoal, and because the same phenomenon is well documented on stone at the same time. Possible leaching and corrosion are very difficult to demonstrate because of the impossibility to discriminate them from those dating from modern period.

The *mediaeval stained glass* is subject of *leaching, corrosion and encrusting* in the *modern polluted atmosphere* because very sensitive due to its chemical composition generally potash-lime silicated.

The exposure of *mediaeval-like low-durable model glass* to the polluted atmospheric environment involves the development of *neocrystallisations* on the surface. At the beginning of the experiment the mineralogical nature of these neocrystallisations depends strongly on the chemical composition of the underlying glass, which interacts by the release of specific cations. Their formation process depends also on gaseous pollutants. The development of sulphates is thus favoured by high SO_2 content and high relative humidity. The atmospheric contribution becomes predominant with time and gypsum becomes the major phase: a *gypsum crust* containing airborne particles, particularly anthropic, develops progressively like on stone in areas sheltered from rain. Thus, the neocrystallisations can be interpreted as the *embryonic phase* of sulphated crusts.

The main damage caused by the atmospheric pollution to *modern calco-sodic durable glass* is mainly aesthetic: it consists of *soiling* due to the synthesis and the remaining of gypsum, and by the deposition and the remaining of soot-particles at the glass surface, also in the parts unsheltered from rain. This last location is a paradox, which calls for the need of continuous and often expensive cleaning operations. That is why self-cleaning glass is the purpose of research at present time. On the other hand, *leaching* of modern calco-sodic glass is an insignificant phenomenon, without any observable consequence in the short term.

REFERENCES

Aubert, M., Grodecki, L., Lafond, J. & Vernier, J. 1959. Les vitraux de Notre Dame et de la Sainte Chapelle de Paris. *Corpus Vitrearum Medii Aevi, France, Vol 1,* Paris: Caisse Nationale des Monuments Historiques, Centre National de la Recherche Historique.

Ausset, P., Bannery, F., Del Monte, M. & Lefèvre, R. 1998. Recording of pre-industrial atmospheric environment by ancient crusts on stone monuments, *Atmos. Environ.*, 32, 2859–2863.

Boehm, T. 1999. The influence of temperature, relative humidity and SO_2 concentration on weathering of glass. *Proceedings of the 5th International Conference of European Society of Glass Science and Technology, Prague*, CD-ROM.

Cachier, H. 1998. Carbonaceous combustion aerosols, In R.M. Harrison and R. Van Grieken (eds) *Atmospheric Particles*, Chichester: John Wiley and Sons, 295–348.
Chabas, A. & Lefèvre, R. 2002. Soiling of soda-lime float glass in the polluted atmosphere of Paris, *Glass Technology*, 43C, 79–83.
Del Monte, M. & Rossi, P. 1997. Fog and gypsum crystals on building materials. *Atmospheric Environ.*, 31, 1637–1646.
Del Monte, M., Forti, P., Ausset, P., Lefèvre, R. & Tolomelli, M. 2001a. Air pollution records on selenite in the urban environment, *Atmos. Environ.*, 35, 3885–3896.
Del Monte, M., Ausset, P., Lefèvre, R. & Thiébault, S. 2001b. Evidence of pre-industrial air pollution from the Heads of the Kings of Juda Statues from Notre-Dame in Paris, *Sci. Total Environ.*, 273, 101–109.
Grambow, B. 1985. A general rate equation for nuclear waste glass corrosion, *Scientific Basis for Nuclear Waste Management VIII, Materials Research Society Symp. Proc.*, 44, 15–27.
Lefèvre, R., Grégoire, M., Derbez, M. & Ausset, P. 1998. Origin of sulphated grey crusts on glass in polluted urban atmosphere: the stained-glass windows of Tours Cathedral (France). *Glass Sci. Technol., Glastech. Ber*., 71, 3, 75–80.
Libourel, G., Barbey, P & Chaussidon, M. 1994. L'altération des vitraux, *La Recherche*, 262, 168–188.
Lombardo, T. 2002. Mécanismes d'altération du verre calco-sodique en atmosphère urbaine polluée, *Thesis of the University of Paris XII – Val de Marne*, 239 pg.
Munier, I. & Lefèvre, R. 2000a. Comparison of the particles and cements of sulphated crusts from stained-glass, lead and stone of the Sainte-Chapelle in Paris, Seville: 5th International Symposium on the Conservation of Monuments in the Mediterranean Basin, 36.
Munier, I. 2000b. Impact de la pollution atmosphérique urbaine sur l'altération de verres modèles de faible durabilité, *Thesis of the University of Paris XII – Val de Marne*, 417 pg.
Munier, I. & Lefèvre, R. 2000c. New crystallisations developed on low-durability glasses exposed to the atmospheric pollution in Paris, *Riv. Sperim. Vetro, Murano-Venice,* 30, 6, 127–130.
Munier, I., Lefèvre, R.-A. & Losno, R. 2001. Atmospheric factors influencing the formation of neocrystallisations on low-durability glass exposed to urban atmosphere, XIXth International Congress on Glass, Edinburgh, 11–12.
Munier, I., Lefèvre, R. & Losno, R. 2002. Atmospheric factors influencing the formation of neocrystallisations on low-durability glass exposed to urban atmosphere, *Glass Technology*, in press.
Munier, I., Lefèvre, R, Geotti-Bianchini, F. & Verità, M. 2002. Influence of polluted urban atmosphere on the weathering of low-durability glasses, *Glass Technology*, in press.
Newton, R. & Davison, S. 1989. *Conservation of Glass*, London: Butterworth Heinemann, 318 pg.
Römich, H. 2000: Simulation of corrosion phenomena of historical glasses: an update. *Riv. Sperim. Vetro*, *Murano-Venice,* 6, 9–14.
Schreiner, M. & Schmitz, I. 2000. Surface analytical investigations on naturally weathered medieval stained glass, *Riv. Sperim. Vetro*, *Murano-Venice*, 6, 15–22.
Sterpenich, J. & Libourel, G. 2001. Medieval stained glass windows: a physical and chemical characterisation of alteration, *Science and Technologies of the Materials and of the Environment for the Protection of Stained Glass and Stone Monuments,* European Commission Research report n° 14, 171–180.
Verità, M., 2001. Glass, its nature, properties and deterioration mechanisms, *Science and Technologies of the Materials and of the Environment for the Protection of Stained Glass and Stone Monuments,* European Commission Research report n° 14, 29–39.
Woisetschläger, G., Dutz, M. & Schreiner, M. 1999. Evaluation of the weathering progress on naturally weathered potash-lime-silica glass with medieval composition by scanning electron microscopy (SEM). *Proceedings of the UN/CE Workshop on Quantification of Effects of Air Pollutants on Materials*, *Berlin*, 27–36.

Cultural Heritage Conservation and Environmental Impact Assessment by Non-Destructive Testing and Micro-Analysis – Van Grieken & Janssens (eds)
© 2005 Taylor & Francis Group, London, ISBN 90 5809 681 5

Non-destructive ion beam techniques for the depth profiling of elements in Amerindian gold jewellery artefacts

Guy Demortier
LARN, Facultés Universitaires Notre-Dame de la Paix, Namur, Belgium

José-Luis Ruvalcaba-Sil
Department of Physics, UNAM, Mexico city, Mexico

ABSTRACT: The study of complex materials (non homogeneous matrices containing medium and/or heavy atoms as major elements) by PIXE requires the tailoring of the experimental set up to take into account the high x-ray intensity produced by these main elements present at the surface, as well as the expected low intensity from other elements "buried" in the substrate. Additionally, high Z matrices have a high x-ray absorption capability and are not always homogeneous. The non-homogeneity may be, on the one hand, a layered structure (which is uneasy to profile by Rutherford Backscattering Spectroscopy (RBS) if the material contains elements of neighbouring masses or if the layered structure extends on several microns). PIXE measurements at various incident energies (and with various projectiles (p, d, He_3, He_4)) are then an alternative method to overcome those difficulties. The use of special filters to selectively decrease the intensity of the most intense x-ray lines, the accurate calculation of the characteristic x-ray intensity ratios ($K\alpha/K\beta$, $L\alpha/L\beta$) of individual elements, the computation of the secondary x-ray fluorescence are amongst the most important parameters to be investigated in order to solve these difficult analytical problems. Examples of Cu, Ag and Au based alloys with various coatings as encountered in Amerindian metallurgy are discussed. Special application to Pre-Hispanic gold jewellery has been developed. Amerindian goldsmiths have indeed used original techniques to manufacture and to gild ornaments and artefacts. Gold metallurgy in ancient America was mainly a surface technology. Surface studies of artefacts from various regions of Pre-Hispanic South America were carried out using proton milli- and microbeams (from 1 mm down to 10 μm diameter). Outstanding aspects about the metallurgical processes involved in the gilding of the artefacts have been established.

1 NON-VACUUM EXPERIMENTAL ASSEMBLY FOR PIXE

PIXE is extensively used for archaeological purposes in a non-vacuum geometry. The experimental arrangement of the target site is presented in Figure 1. The incident proton beam (generally 2.8 to 3 MeV) crosses a foil of Al (12 μm thick) through a carbon collimator (diameter: 500 μm) before reaching the sample situated at 1 cm from this exit foil. The size of the beam at the target site increases up to 700 μm due to angular straggling in air. The Si(Li) detector is generally set at 135° with respect to the incident proton beam. The material of the carbon collimator plays the role of an x-ray absorber of all elements present on (and in) the Al foil.

Sometimes, a second Si(Li) detector is used to monitor the incident proton beam by detection of the Ar x-rays induced in the air in a narrow region (5 mm long) between the target and the sample. Another way to monitor the incident beam is to use a Ge(Li) detector collecting γ-rays from the Al exit foil (883, 1013 and 1778 keV).

Multi-elemental analysis by PIXE is often to be accommodated for very different counting rates in various x-ray peaks. The use of filters, to selectively reduce the most intense characteristic x-rays

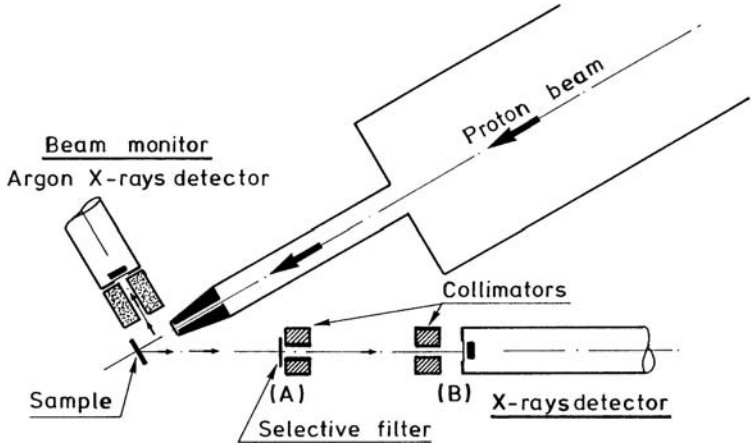

Figure 1. The non-vacuum PIXE set up.

of some major element of the matrix is sometimes compulsory. The best choice of the filters and their thicknesses is to be decided in each case.

The size and the position of the filters may give rise to interferences from secondary x-rays. The filter is ideally put at mid-distance between the target and the detector on a collimator (1 cm thick aluminium drilled with a 4 mm hole). This collimator limits the incident x-ray flux on the filter. A second collimator, in front of the detector, defines the detection solid angle. The effect of various geometries for the filter position was described in a previous work : the best solution is achieved with the minimum sizes of the filters and of the collimators.

2 DEPTH PROFILING BY PIXE

PIXE is probably the most popular ion beam technique for non-destructive analysis of archaeological artefacts. Generally, for elemental analysis, it is assumed a priori that the material is homogeneous and that therefore the relative intensities of characteristic x-ray lines may be quantitatively related to the actual composition. This composition is obtained by comparison with known homogeneous reference samples irradiated in the same geometrical situation.

Very often, the analysis is routinely performed at one single proton energy. Analyses of ancient objects, using various methods often give rise to discrepancies between analytical results. These differences are generally attributed to the lack of local homogeneity, or to the presence of corrosion or patina at the surface. However, the possibility of corrosion products or patina is unlikely for gold artefacts. Nevertheless, we have demonstrated that, for gold jewellery items of Mesoamerican origin, the assumption of homogeneity in depth may not be valid and that discrepancies between results of different origins may be understood in terms of depth profiles.

Gold jewellery of Columbia and Peru were often made with tumbaga, a gold-silver-copper alloy containing, in the bulk, a large proportion of copper. Improper preservation of such artefacts would show a visible alteration of the surface by burial over a long period of time due to the transformation of copper in copper oxides. These oxides may be eliminated by a mechanical or a light chemical process but these processes would completely modify the relative local concentrations. These local modifications could easily be observed using a scanning PIXE microprobe.

The ancient pre-columbian goldsmiths were aware of the imperfect preservation of tumbaga and they experimented with procedures leading to the removal of the excess of copper at the surface by various recipes. In this way, they produced artefacts with a colour very close to that of pure gold. Improvements include two aspects: i) the aesthetic of the artefact is increased as colour became

closer to the colour of pure gold; ii) the material had a better resistance to corrosion and a lower melting point for the purpose of casting.

The copper depletion and the consequent gold enhancement at the surface may be identified by traditional methods like RBS, but the quantitative analysis of the depth profiles of copper, silver and gold is not easily determined by this way. In this case, PIXE at various energies (e.g. from 600 keV to 3 MeV) or with various incidences angles of the proton beam with respect to the irradiated surface of the jewellery item may give quantitative depth profiling.

3 SELECTION OF AMERINDIAN ARTEFACTS

The gold pendant of Figure 2 was discovered in Oaxaca, Mexico. It corresponds to the late post-classic period (1500 A.D.). It was non destructively analysed at the Pelletron laboratory of the IFUNAM at the University of Mexico.

Results of non-vacuum PIXE analyses of the various parts of the pendant are given in Table 1. The bells of the pendant have lower concentrations of gold than the other parts of the artefact, but in some regions of them (impacts 7–8, 13–15), the amounts of gold are higher and quite similar to the rest of the pendant.

It is observed that the alloy composition is rich in gold but is not uniform in the rest of the pendant (feathers and main body). There is a clear difference of colour between the bells and the other pendant regions.

The object has been irradiated with protons of energy ranging from 1.3 to 3 MeV and the relative intensities of the signals of Cu and Au have been measured. For impact n°40, results at 3 MeV could be compatible with a uniform distribution of Au, Ag and Cu in the whole depth at respectively 68%, 12% and 20%. When the same region is analysed at lower proton energies, the calculation

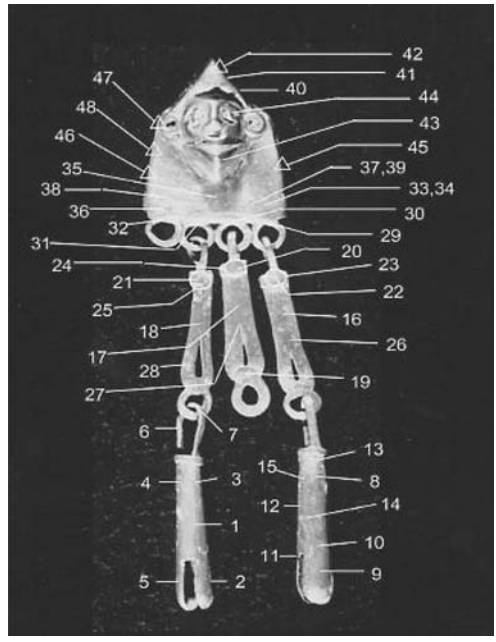

Figure 2. Eagle warrior pendant (San Francisco Caxonos, Oaxaca, 1500 AD, length: 8.0 cm). Oaxacas's Regional Museum, Mexico.
(This figure is presented in the signature in colours at the end of this volume, Appendix, pg. 317)

Table 1. Eagle warrior pendant – Oaxaca. Concentrations in % by weight.

Impact	Cu	Ag	Au	Impact	Cu	Ag	Au
Bell 1				*Feathers*			
1	35.0	10.0	55.0	24	25	9.0	66.0
2	35.5	9.0	55.5	25	28.5	8.0	63.5
3	35.5	10.5	58.0	26	17.0	9.5	72.5
4	36.5	10.2	52.8	27	27.0	8.1	64.9
5	36.5	10.2	53.3	28	17.5	10.0	72.5
6	35.0	10.3	54.7	*Main body*			
Bell 2				29	24.5	9.0	66.5
7	14.5	14.5	71	30	28.0	9.8	62.2
8	13	14.5	72.5	31	25.5	9.5	65.0
9	34	11.5	54.5	32	24.5	9.9	65.6
10	31	11.0	58.0	33	25.5	10.1	64.4
11	35	8.0	57.0	34	26.5	9.7	63.8
12	36	11.2	52.8	35	29.5	9.0	61.5
13	14.5	13.5	72.0	36	26.0	9.5	65.5
14	14	13.5	72.5	37	19.0	10.0	71.0
15	17	13.0	70	38	23.0	10.5	66.5
Feathers				39	19.5	11.0	69.5
16	13	11.0	76	40	20.0	12.0	68
17	19	9.5	71.5	41	29.5	9.6	60.9
18	16	10.0	74	42	25.5	7.5	67
19	19	9.7	71.3	43	34.5	8.0	57.5
20	23	9.0	68.0	44	28.0	14.5	57.5
21	20	12.3	67.7	45	31.0	9.7	59.3
22	23	9.9	67.1	46	28	9.0	63.0
23	27	10.0	63.0	47	30.5	7.5	62.0

Table 2. Apparent elemental composition (with the hypothesis that the material is homogeneous) of the middle region of the warrior pendant as a function of the proton energy beam. Concentrations in weight %.

	Apparent elemental composition		
Proton beam energy (MeV)	Cu	Ag	Au
3.0	20.0 ± 1.0	12.0 ± 0.6	68.0 ± 2.0
2.6	20.0 ± 1.0	12.0 ± 0.6	68.0 ± 2.0
2.2	18.0 ± 0.9	12.0 ± 0.6	70.0 ± 2.1
1.7	15.5 ± 0.8	12.0 ± 0.6	72.5 ± 2.2
1.3	13.0 ± 0.7	12.0 ± 0.6	75.0 ± 2.3

of concentrations, assuming a homogeneous distribution in the bulk, gives completely different results.

If we suppose that the material is homogeneous in the depth, the apparent gold content increases when the proton energy decreases (Table 2). The reason is that the material is not homogeneous with respect to its depth. For 1.3 MeV protons, the analysed layer is about 30% of the one analysed with 3 MeV protons, and then more sensitive to the surface concentration. Measurements at 1.3, 1.7, 2.2, 2.6 and 3 MeV have been performed to give the actual distribution of Au and Cu in four

Table 3. Elemental depth profile determined by PIXE at various proton energies. Concentration in weight %.

Layer	Thickness (μm)	Elemental composition		
		Cu (%)	Ag (%)	Au (%)
1	1.0	–	–	100 ± 3
2	0.7	10.0 ± 0.5	5.0 ± 0.3	85.0 ± 2.6
3	0.5	20.0 ± 1.0	10.0 ± 0.5	70.0 ± 2.1
4	0.5	35.0 ± 1.8	10.0 ± 0.5	55.0 ± 1.6
5	Bulk	50.0 ± 2.5	10.0 ± 0.5	40 ± 1.2

Figure 3. Mesoamerican pectoral (Columbia) (500–1500 A.D.). Weight: 37.3 gr; volume: 2.65 cm^3. (This figure is presented in the signature in colours at the end of this volume, Appendix, pg. 317)

successive layers and also the bulk concentration (Table 3). Similar results have been found for the feathers and also in the bells. Then, the variations observed for the elemental composition by PIXE at 3 MeV at the impacts points are due to the thickness of the gold enriched surface. A depletion gilding process was applied to enrich the surface of gold in a depth up to 5 μm.

A pectoral of Mesoamerican origin (Fig. 3) is made of a metal sheet not uniform in thickness (0.18 to 0.35 mm). PIXE analyses at one single proton energy (2.2 MeV) give copper, silver and gold values reported in Table 4, indicating that the material is quite homogeneous laterally. Several analyses at various proton energies, but at the same impact clearly indicate (Table 5) that the copper content apparently increases when the proton energy is increased. These values obtained by postulating a homogeneous composition, is a proof that the bulk contains more copper than the surface. Calculations using differential PIXE may be fitted with several depth profiles: in Table 6 we give two possible profiles. One is computed with no copper at the surface and then a maximum concentration in depth.

If we suppose that the first layer is copper free, it should contain 60% Au and 40% Ag (profile 1) and have a thickness of 2.75 μm. In this hypothesis, the Cu content in the bulk must be 7.5%. This situation is unphysical and does not fit with XRF measurements performed on the same artefact. If we take, from the bulk copper, the observed concentration values obtained by grazing XRF (minimum absorption of Cu Kα x-rays), the calculation of the Cu profile from the whole series of PIXE measurements from 2.2 to 3.2 protons gives a Cu concentration increasing from 1.5% at the surface up to 3.3% at 4 μm in depth. The density measurement is in agreement with these

Table 4. Analysis of the pectoral (2.2 MeV) (Figure 3).

Impact	Cu (%)	Ag (%)	Au (%)
1	2.7	37.6	59.7
2	2.6	40.1	57.3
3	2.3	39.1	58.6
4	2.1	39.9	58
5*	1.8	41.4	56.8
6	2.1	40.7	57.1
7	2.2	40.3	57.5
8	2.4	40	57.6
9	2.5	40.2	57.3
10	2.1	39.2	58.7

* Region selected for in-depth scan by increasing proton energy (see Table 5).

Table 5. Mesoamerican pectoral (impact 5). Apparent Cu concentration with increasing proton energy.

E_p (MeV)	Cu PIXE value (%)
2.2	1.79
2.3	1.88
2.4	1.89
2.5	1.95
2.6	1.94
2.7	1.96
2.8	1.98
2.9	2.07
3.0	2.06
3.1	2.14
3.2	2.16

Table 6. Depth profiles computed with data of Table 5.

Profile 1 (first approach)		
Layer 1	2.75 μm	60% Au + 40% Ag
Bulk	∝	7.5% Cu + 52.5% Au + 40% Ag
Profile 2 (refined approach)		
Layer 1	1.5 μm	1.5% Cu + 58.5% Au + 40% Ag
Layer 2	2.5 μm	2.5% Cu + 57.5% Au + 40% Ag
Bulk	∝	3.3% Cu + 56.7% Au + 40% Ag

determinations by differential PIXE. The depletion of copper at the surface cannot be understood by a depletion gilding procedure used by ancient Ameridian goldsmiths: this last procedure was used in Antiquity for jewellery items containing a large concentration of copper. Besides, natural wearing leading to the selective elimination of Cu from the surface cannot be accepted for the explanation of the measured depth profile because the concerned thickness (up to several microns) is too large. The shape of the Cu profile could be due to modern cleaning using acidic agents.

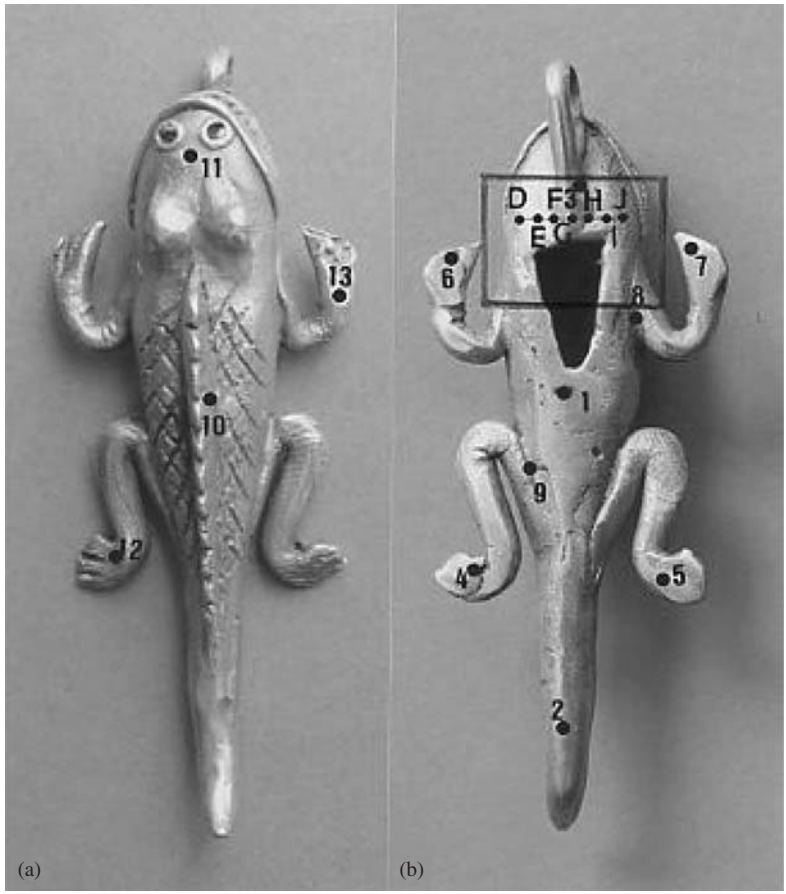

Figure 4. (a) Regions of non vacuum PIXE measurements on the zoomorphic pendant (rear). The corresponding values are listed in Table 7. (b) Regions of non vacuum PIXE measurement on the zoomorphic pendant (front). The scanned region with a microbeam is shown in the rectangle (region 3).
(This figure is presented in the signature in colours at the end of this volume, Appendix, pg. 318)

The PIXE results at various proton energies give a proof that the use of PIXE at one single proton energy to study complex matrices cannot be satisfactory.

An external beam set up was used to carry out non vacuum PIXE analyses in several regions of a zoomorphic pendant. The proton energy was 2.4 MeV at the sample surface and the beam diameter was 0.5 mm. The regions of measurements are shown in Figure 4(a) and (b). From those results, we can conclude that the mean elemental composition is quite uniform, but the gold content is higher in the front than in the rear. Wear may have given rise to modification at the rear.

As the apparent gold composition determined by PIXE in vacuum increases when the incident proton energy is decreased, one concludes that the matrix is non-homogeneous and is enriched in gold at the surface. To characterize this inhomogeneity of gold alloys a combined analysis of differential PIXE and RBS was used. The beam energy was varied from 800 keV to 2.6 MeV and the elemental depth profile was determined by comparison between the experimental Cu Kα/Au Lβ yield ratios as a function of the beam energy and the calculated ratios from a proposed layered matrix. Successive trials with various layer compositions were compared with experimental PIXE and RBS spectra to achieve the best agreement. The depth profile determined by this method indicates that the gold content decreases from 80 to 45% in a depth up to 0.5 μm below the surface. In the same

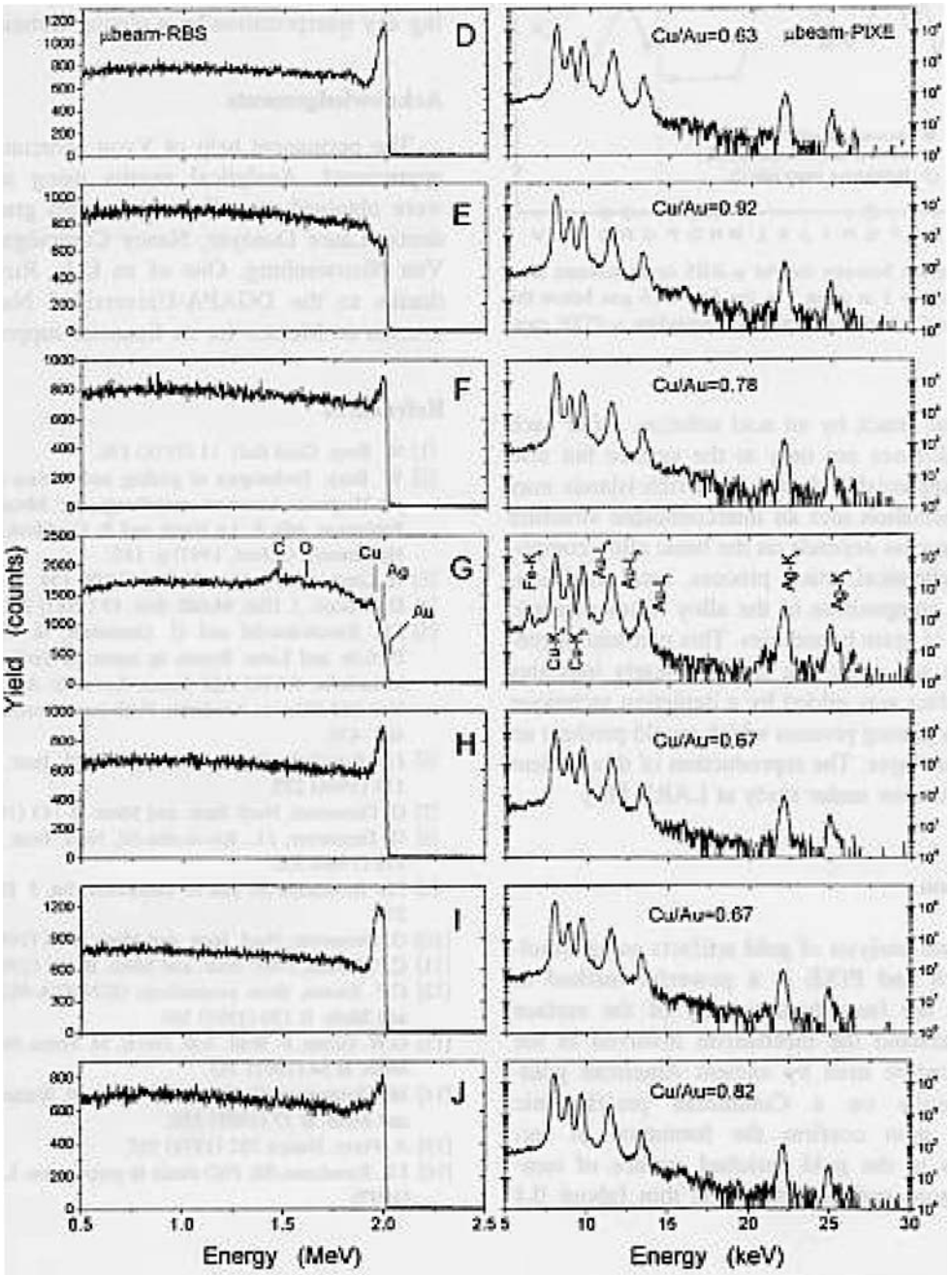

Figure 5. Microbeam RBS and PIXE spectra corresponding to the impacts D–J. Cu/Au PIXE ratio decreases when the gold concentration at the surface is higher (RBS spectra, points D, H and I).

depth, silver and copper contents ranges from 5 to 14% and from 15 to 41%, respectively. The gold enrichment at the surface is not uniform and in general the thickness of the gold enriched layer is higher in the front than in the back of the item.

If the apparent Cu and Au concentrations fluctuate from place to place when the beam is scanned along the surface, the use of a microbeam is sometimes recommended to improve the investigation.

Table 7. Elemental composition determined by non vacuum PIXE (2.4 MeV) and microbeam PIXE (2 MeV) for the zoomorphic pendant. The regions of measurements are shown in Figures 4 and 5. The accuracy on each determination is 2% for Au and 5% for Ag and Cu.

Impact	Cu (%)	Ag (%)	Au (%)
Non vacuum PIXE (700 μm diameter beam)			
1	35.6	18.6	
2	34.3	18	
3	34.1	14.9	
4	26.5	22	
5	34.8	22.5	
6	31	20	
7	35.8	14.7	
8	32.2	22.5	
9	31.2	19.7	
10	23.7	22.8	
11	24.5	21.3	
12	15.9	30.3	
13	18.4	25.2	
μ-PIXE (10 μm diameter beam)			
D	34.6	11	54.4
E	41.1	14.7	44.3
F	38.3	12.7	49.1
G*	–	–	–
H	34.7	14.1	51.2
I	35.7	11.3	53
J	40.3	10.8	48.9

* Impact where RBS indicates that the gold alloy contains a thick inclusion and then where the composition cannot be determined by using only PIXE results.

A combination of RBS and PIXE may help us to determine the elemental composition and the lateral and depth homogeneities.

The LARN's proton microprobe (10 μm diameter) was used to carry out scannings in several regions of the pendant. Typical proton beam currents were 3–4 nA. The time of irradiation at each point was about 15 min. For RBS, particle detection is made with an annular detector at a backscattering angle of 178°. The energy resolution is 12 keV. For PIXE, a LEGe detector was set at 135° relative to the beam direction. x-rays pass through a Mylar window (10 μm thick) before reaching the detector. RBS and PIXE spectra are collected simultaneously. For quantitative analysis a reference sample containing all the elements of interest is used.

In the insert of Figure 4 we show several points in the scanned region and some of the impact points on the artefact. The corresponding RBS and PIXE spectra are shown in Figure 5. We observe that the gold rich region in the sample is not uniform, its thickness and the amount of gold in the region changes from one impact point to another one and depth elemental profile is clearly observed in the RBS spectra. In some cases the impact points correspond to microregions where inclusions are present: light elements (C, O) signals are present in RBS spectra and Fe x-rays are observed in the corresponding PIXE spectra (i.e. point G).

Relative elemental composition measured by μ-PIXE (Table 7) is given by the Cu/Au ratio at each impact point. Simultaneously, the Au concentration determined at the corresponding impact point by μ-RBS in the first 0.15 μm is measured. This depth corresponds to the region where the RBS gold signal does not interfere with silver surface signal. We observe that the PIXE Cu/Au ratio decreases when the RBS Au surface composition increases. There is a clear correlation between

both sets of results. Moreover, impacts where the Au surface content increases correspond to microregions of larger thicknesses of gilding. The mean values of the μ-PIXE measurements at the points D to J (50.5% Au, 13.9% Ag, 37% Cu) agree with the non vacuum PIXE measurement in the corresponding region of the artefact (impact 3).

Depletion gilding involves annealing of the alloy and chemical attack by an acid solution. After each step, gold diffuses not only at the surface but also into some appreciable depth. Gold rich-islands may grow by nucleation into an interconnected structure. This process depends on the basic alloy composition, the chemical attack process, local modifications in the composition of the alloy in microscopic regions and in grain boundaries. This non-homogeneity in depth and along the surface clearly indicates that the artefact was gilded by a depletion technique and not by a plating process which would produce an homogeneous layer.

4 CONCLUSION

PIXE at various incident proton energies and microbeam analysis of gold artefacts using simultaneous RBS and PIXE are powerful methods to characterize the (non)-homogeneity of the surface and to understand the mechanism involved in the gilding procedure used by ancient American goldsmiths. Results on pre-Hispanic items confirm the formation of microstructures in the gold enriched surface of tumbaga. The gold enriched region may involve thicknesses in the micron range but the gold content enrichment is progressive from the bulk to the surface and do not exhibit a sharp interface with the bulk.

This explanation is only valid for low gold concentration in the bulk. For high gold bulk concentrations, the measured copper depletion at the surface is only due to wearing processes.

REFERENCES

Demortier, G. & Morciaux, Y. 1994. *Nucl. Instr. and Meth. in Phys. Res,* B85, 112–117.

Demortier, G. 1999. *Nucl. Instr. and Meth. in Phys. Res,* B150, 520–531.

Ruvalcaba-Sil, J.L. & Demortier, G. 1996. *Nucl. Instr. and Meth. in Phys. Res,* B113, 275–278.

Ruvalcaba-Sil, J.L. & Ortiz E., *Non destructive study of a gold pendant from Oaxaca, Mexico, using PIXE and RBS techniques*, British Archaeological Reports (in press).

Ruvalcaba-Sil, J.L. & Demortier, G. 1997. *Nucl. Instr. and Meth. in Phys. Res,* B130, 297–302.

Cultural Heritage Conservation and Environmental Impact Assessment by Non-Destructive Testing and Micro-Analysis – Van Grieken & Janssens (eds)
© 2005 Taylor & Francis Group, London, ISBN 90 5809 681 5

Investigation of a novel conservation procedure for historical documents

Ewa Bulska & Barbara Wagner
Warsaw University, Faculty of Chemistry, Pasteura, Warszawa, Poland

ABSTRACT: The aim of this work was to evaluate the efficiency of a new conservation treatment diminishing the iron-gall ink corrosion of the paper of historical manuscripts. The investigated conservation strategy was based on the iron complex formation as well as solid–liquid extraction of iron compounds from the paper. Various ligands, which are known to form stable complexes with iron, were chosen. The efficiency and rate of extraction was investigated for $FeCl_3$ as well as for iron compounds present in the iron-gall ink solution. The oxidation state of residual amount of iron in the paper as well as possible migration of metal ions after extraction was also evaluated. At last but not least the accelerated aging of the paper exposed to the conservation treatment was applied in order to ensure that the proposed procedure does not influence the paper itself. Most of the work was performed with the use of model samples, which were intentionally prepared to mimic the properties of real historical items. All these investigations were done with the aid of modern instrumental analytical techniques.

1 INTRODUCTION

Libraries around the world have to collect, store and preserve books, manuscripts and written documents to assure a common and long-term access to the cultural heritage collections (Porck & Teygler 2000). Paper however is considered to be a delicate matter and should be kept in a specific environment. It should be stored in cool, dark and relatively dry storage rooms, avoiding temperature and humidity fluctuations, as well as air pollutants and micro organisms (Johanssen et al. 2000, Gurnagul et al. 1993). It should be stressed however that the influence of these external conditions depends significantly on the quality of the paper itself. A composition of the paper has been changed several times over the centuries and different components could play a crucial role in on-going aging processes. Therefore the composition of the paper should be taken into account while any conservation treatment is undertaken to prolong life of historical books and documents. Some treatments can be applied in automatic way for a large number of objects. This kind of collective activity is called a "mass conservation", and it can be applied in a particular situation, when conservators deal with collection affected by common phenomena (Lienardy & Van Damme 1990, Wittekind 1994, Liers & Schwerdt 1995). One of the essential problems assisting library collection is the acidity of the paper which can be successfully solved by a mass deacidification. The problem of paper acidification is of special importance for all collections including books printed on paper from the XIXth century, when it begun to be sized with the use of acid aluminium sulphate. Special collections should not be submitted to any mass treatment, because they include rare, unique, or exceedingly valuable items. Such objects should be treated carefully and individually by conservators with the full awareness of potential side-effects of the conservation treatment and handling as well as full respect of the special needs of protected materials.

In recent years growing attention has been put to analyse and support the conservation of works of art (Schreiner & Grasserbauer 1985, Sistach Anguera 1996, Whitmore & Bogaard 1994, Bicchieri & Pepa 1996, Wunderlich 1996). Manuscripts are among the works of art, which are known to be endangered by several destructive processes (Schreiner & Grasserbauer 1985, Sistach

Anguera 1996, Whitmore & Bogaard 1994, Bicchieri & Pepa 1996, Wunderlich 1996, Van Gulic & Kersten-Pampiglione 1994). Historical manuscripts were commonly written with iron-gall inks, which were basically produced by mixing aqueous solutions of iron (II) sulphate with gallotannin-containing extracts of gallnuts (Wunderlich 1996, Van Gulic & Kersten-Pampiglione 1994). It was found out that most of ancient iron-gall inks contain an excess of iron, partly present as iron (II) ions. This form of iron could take part in redox reactions catalysing the oxidation of cellulose. The process, known as iron-gall ink corrosion, leads to losses in mechanical strength of the paper (Sistach anguera 1996, Wunderlich 1996, Van Gulic & Kersten-Pampiglione 1994, Neevel 1995, Neevel & Reissland 1997, 1998).

Taking above into consideration, it could be concluded that several phenomena are responsible for the degradation of cellulose, among which acid-catalysed hydrolysis and metal-catalysed oxidation are the most important ones in the case of written documents. These two processes may undergo simultaneously, therefore the conservation treatment developed to diminish the unwanted destruction of the paper should be based both on the removal of an excess of iron and neutralising acids. Several successful deacidification methods have been applied, not only for the purpose of mass conservation but also for the conservation of individual items (Barry & Fields 2000). It was found however that when only deacidification was applied to the documents written with iron-gall ink, the treatment was not sufficient to achieve the expected protection of the paper. The presence of ink causes the metal-catalysed oxidation which can undergo independently from acid hydrolysis and therefore a special conservation strategy should be developed when the iron-gall ink corrosion was found to be a reason for the degradation of the paper (Neevel & Reissland 1998, Neevel 2000, Kolar & Strilc 2000).

The deterioration process of historical manuscripts and drawings written with iron-gall ink is known as iron-gall ink corrosion and has been widely described in the literature concerning paper conservation (Neevel 1995, Neevel & Reissland 1998, Bannik et al. 1981, Hey 1981, Fuchs et al. 2000, de Feber et al. 2000). The on-going phenomenons caused by substances used for the production of the inks have been already mentioned above. According to old-time recipes, iron-gall inks were produced by mixing an aqueous solution of vitriol (iron (II) sulphate) and extracts from gallnuts (a swelling on a plant caused by an insect laying its eggs) containing gallotannins (Wunderlich 1996, Van Gulic & Kersten-Pampiglione 1994, Neevel & Reissland 1998). It was suggested by Wunderlich that the actual ink was formed after an air oxidation of iron (II) to iron (III), followed by the formation of complexes with gallic acid (Wunderlich et al. 1996, 1991, Krekel 1999). The colour of inks originates from the complexes created by iron (III) ions with gallic acid and complexes of iron (II) with pyrogallol (Krekel 1999). Both organic compounds were identified in the solution of extracts of gallnuts. An excess of iron ions present in the ink, apart from that present in the form of colourful complexes, can be very active and promote the catalytic degradation of cellulose (Neevel 1995, Neevel & Reissland 1997). As most historical inks were prepared with an excess of iron sulphate comparing to gallic acid or pyrogallol, after years or even centuries the ink deposited on the paper may still contain substantial amounts of active iron ions. It should be also stressed that in the presence of moisture, sulphate ions (originated from iron sulphate) could turn into sulphuric acid, which could be present in the ink as well. This phenomenon gave rise to the first explanation of the corrosion process regarded as the main reason for the degradation of paper would be acid hydrolysis of cellulose caused by sulphuric acid present in iron-gall inks (Sitach anguera 1996, Neevel & Reissland 1997). If so, the application a deacidification treatment should distinctly diminish the corrosion of paper. Unfortunately, this was not a case and commonly applied deacidification was not sufficiently effective to stop iron-gall ink corrosion of the manuscripts. In consequence, the presence of iron and other transition metal ions present in ink, was consider to be a possible reason of corrosion via the catalytic oxidation of cellulose which can proceed independently from acid hydrolysis (Neevel 1995, Neevel & Reissland 1998, Kolar & Strilc 2000, Calvini & Gorassini 2002). It was postulated by Neevel that Fe(II) ions can catalyse the cellulose oxidation in historical documents according to a way described for Fenton-like reactions (Neevel 1995, Neevel & Reissland 1998). Although the phenomenon of iron-gall ink corrosion occurring in written ancient documents was investigated by various research groups, no truly successful

conservation treatment for hindering the degradation of paper was developed (Neevel & Reisland 1997, 2000, Kolar & Strilc 2000).

Investigations concerning historical drawings and documents written with iron-gall ink are very important but also very difficult because of the non-reproducible properties of particular investigated item. The strategy towards an effective conservation procedure should include the detailed chemical and physical investigations of the object. The results obtained after such particular investigations should be considered as a base for the selection of the potentially effective conservation treatment, which in fact has to be always adapted to the specific situation (Wagner et al. 2001, Bulska et al. 2001, Wagner & Bulska 2003). Here the role of chemists is crucial as it is essential to apply those analytical methods which offer specific information about the investigated object (Wagner et al. 2001, Wagner & Bulska 2003, Adams et al. 1997, Bulska et al. 2001, Coupry et al. 1994, Wehling et al. 1999). Although various methods have been used in this field, it is essential that while dealing with unique documents or any objects having artistic or historical value, non-invasive and non-destructive methods have the priority (Neevel & Reisland 1998, Adams et al. 1997, Proost et al. 2004, Budnar et al. 2001). When the destructive phenomena have been evaluated and understood, the next step should be directed to developing the whole conservation treatment procedure. During this stage of the work the concentration and pH as well as time of application of the needed solutions should be considered. At last but not least the possible side effects have to be observed or even excluded by the investigation of the properties of the treated paper exposed to the accelerated aging. All of those investigations in fact could only be performed with a large number of identical objects, what is only possible when model samples are used.

The aim of this study was to investigate the behaviour of various iron species deposited on the paper support, when the sample was immersed into a solution of organic ligands. The undertaken investigations were performed in order to evaluate the usefulness of the chosen chemical treatment according to the requirement of conservation of ancient objects. The importance of the performed studies comes out from the particular opportunity to use samples, which were designed to model historical manuscripts written with iron-gall ink. These models were constructed according to results of previous investigations performed for real documents endangered by iron-gall ink corrosion (Proost et al. 2004, Wagner et al. 1999, 2001). Our studies were stimulated by the co-operation with the Polish National Library (Warsaw, Poland) where a number of manuscripts are endangered by corrosion processes.

2 REQUIREMENTS FOR CONSERVATION TREATMENT

The condition of paper in written documents is directly influenced by the state of cellulose, the main component of it. As it was mentioned before, metal-catalysed oxidation is one of the phenomenons, which can influence the stability of the paper. This process proceeds parallel to acid hydrolysis; which can be slowed down by any of known deacidification treatment. None of them however was sufficient to slow down the degradation of cellulose caused by iron-gall inks. Therefore the conservation treatment of ancient manuscripts endangered by ink corrosion should combine both activities: (i) neutralising acid, and (ii) performing the inactivation of active transition metal ions. Apart from iron, the main component of iron-gall ink, other elements (Cu and Mn) were expected to be present in ink and able to accelerate reactions leading to the degradation of cellulose.

Taking the above into consideration it could be predicted that the effective conservation strategy against iron-gall ink corrosion should include following processes:

- binding *active transition metal ions* into a persistent complex in paper;
- removing the excess of *active transition metal ions* from the paper;
- removing excess of *active ions* partially and binding the residual active ions in the form of stable compounds that would not accelerate degradation processes.

All of those processes should undergo in the neutral or slightly alkali environment, to prevent the paper from acid hydrolysis. The complexing compounds which could be potentially applied

for the developed conservation treatment of manuscripts endangered by iron-gall ink corrosion should fulfil various pre-requirements. The list of preliminary expected properties was constructed according to the assumption that iron was the most important element to be removed from the written document. Compared to iron, both copper and manganese are present in much lower concentration; therefore the deactivation of iron ions was found to be the most essential. Therefore the first criterion is that pre-selected compounds should form stable complexes with iron ions, however less stable than colourful compounds of this element, which are present in iron-gall inks, so the colour of the ink would be not affected. These iron complexes, preferable colourless, should be dissolved in water or water/alcohol mixture in order to be easily washed-out from the paper. The complexing ligands should be stable in a broad range of pH. They should also be neutral for the paper-support and, last but not least, be easy to prepare and apply. The conservation procedures should therefore be based on the complexation of an excess of iron followed by extraction of the iron complexes from paper into the washing solution.

When searching for the candidate's complexing ligands, one of the criteria was the possibility to block all available coordination sites of the iron ions, thus preventing the reaction leading to the formation of very active hydroxyl radicals. (Graf et al. 1984, 1987) proposed few ligands, which could be used for deactivation of catalytic activity of iron ions. Among the described ligands, the most promising was phytic acid, which was then used by Neevel in the scientifically developed conservation treatment for ancient manuscripts written with iron gall ink (Neevel 1995, 2000, Neevel & Reissland 1998). The effect of phytates applied in aqueous or non-aqueous solutions, at different pH, was studied. The procedure, which was found to have a beneficial effect on the paper exposed to ink corrosion, included the immersion of samples into the solution of phytates followed by their deacidification. Such a treatment consisting of two steps was necessary, as the original pH of the phytates solutions was not sufficiently high to provide the simultaneous deacidification of the paper. Besides the necessity to undergo additional post-complexation deacidification treatment, the low solubility of phytates is a great disadvantage of using them. As a consequence, the white deposits on the paper surface were noticed after the treatment (Neevel 2000, Kolar & Strilc 2000). Therefore a searching for other ligand was found justified and the aim of this paper was to perform detailed investigation toward the effective conservation treatment based on the deactivation of active iron ions.

3 SELECTION OF LIGANDS

The following complexing ligands were investigated:

(1) Potassium–magnesium salt of phytic acid ($C_6H_{15}O_{24}P_6KMg$) (Sigma-Aldrich Chemie GmbH, Hungary);
(2) Acetylacetone ($C_5H_8O_2$) p.a. (Fluka Chemie AG, Switzerland);
(3) Dibenzoylmethane ($C_{15}H_{12}O_2$) (Fluka Chemie AG, Switzerland);
(4) Deferoxamine mesylate ($C_{25}H_{48}N_6O_8{\cdot}CH_4O_3S$) 95% (TLC) (Sigma-Aldrich Chemie GmbH, Hungary);
(5) Diethylenetriaminepentaacetic acid ($C_{14}H_{23}N_3O_{10}$) (Sigma-Aldrich Chemie GmbH, Hungary).

The aqueous solutions of all listed compounds were prepared in double distilled water in the concentrations of 0.001, 0.005 and 0.01 mol L^{-1}. The water/ethanol solutions of diethylenetriaminepentaacetic acid, potassium–magnesium salt of phytic acid and deferoxamine mesylate were prepared in the concentration of 0.005 mol L^{-1}. The pH value of the respective ligands solution was monitored and when it was required, the pH of the solution was adjusted by adding powdered $Ca(OH)_2$.

Using the complexing compounds listed above several experiments were provided in different conditions in order to select the most efficient procedure, which could be recommended as a possible chemical treatment for ancient manuscripts. The experiments were performed for different concentration of the compounds, all in various pH starting from that obtained directly

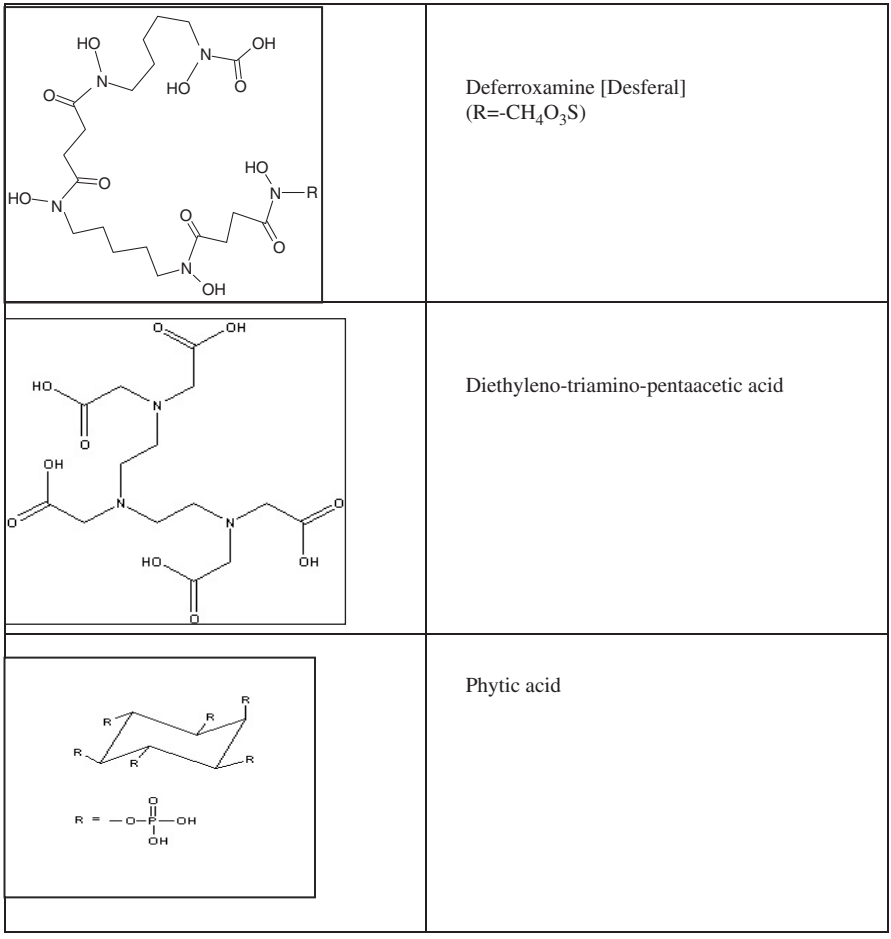

Figure 1. The chemical structure of selected complexing ligands.

Table 1. Standard stability constants for complexes with Fe(II) and Fe(III).

Ligand	Abbreviation used	Log β	
		Fe(II)L	Fe(III)L
Diethylenetriaminepentaacetic amid	DTPA	16.0	27.5
Deferoxamine	DFO	10.0	30.7
Phytic acid	PHY	18.2	29.3
Acetyloacetone	ACAC	4.0	9.5

after dissolution of the respective compounds in water, ending at pH = 9. When it was found appropriate the water or water/ethanol solutions were used.

All complexing ligands, presented in Figure 1 were selected because of their ability to block all available coordination sites of the iron ions and because of their high stability constants for complexes with iron ions, which are listed in Table 1. Phytic acid was selected because it was proved to have a beneficial effect in deactivation of iron ions (Neevel 1995, Neevel & Reissland

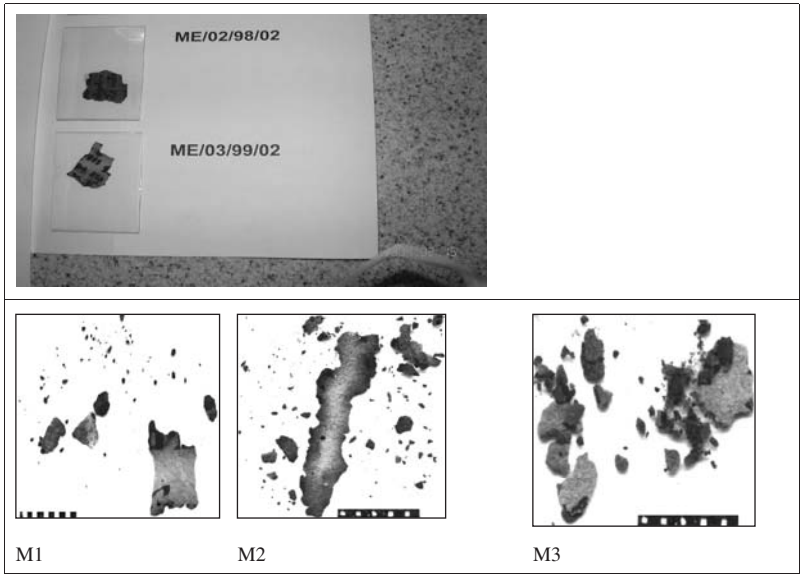

Figure 2a. Example pieces of the real manuscripts donated for the investigation: upper picture: part of the collection of the ancient samples; lower picture: example pieces of the manuscripts M1, M2 and M3.

1998). Deferoxamine mesylate, known as Desferal^{TM}, was tested as it is used in medicine as renal excretion complex used for removal of Fe^{3+} and Al^{3+} in patients with chronic renal failure/acute iron poisoning. Diethylenetriaminepentaacetic amid is used in paper industry and is stable in slightly basic solutions.

4 DESCRIPTION OF THE INVESTIGATED SAMPLES

The detailed investigations devoted to evaluation and verification of a novel conservation treatment is not possible to be performed with the used of samples taken from real artefacts. The reason for such clearly expressed rule is very simple: the real artefacts are always very valuable and unique. The only possible way to proceed necessary studies is to mimic the properties of the real objects with specially designed model samples. Therefore the first step of this project was to examine the example manuscripts, which indicated visible degradation due to iron-gall ink corrosion. For this purpose selected objects from the Polish National Library (Warsaw, Poland) were used. A visual observation of all selected items shows that nearly all manuscripts revealed the first signs of the ink corrosion process which are given by the formation of brown edges in the vicinity to the ink and the appearance of a brown colour at the backside of the page. Some parts of the chosen manuscripts were even more destructed, because with the time paper gradually became more and more brittle. It is well known that iron-gall ink corrosion finally leads to a complete disintegration after several hundreds years of storage, what could be observed in selected volumes. Three different documents from the XVIth century collection were accepted by conservators to impart micro-samples of mass around 0.8 mg for the purpose of these studies. In order to supply information about both written and non-written parts of the same manuscript we were searching for samples where only fragment of the letter was visible, which means that also the surface which was not covered by ink could be characterized. Examples of fragments available for analysis are shown in Figure 2a. In this work three different ancient manuscripts (label as M1, M2 and M3) were investigated.

M1 – “Meditationes passionis Domini nostri Iesu Christi”, a manuscript (see Figure 2b) dated back to the beginning of the 16th century (BN BOZ.1113, National Library of Poland, Warsaw).

Figure 2b. Manuscript "Meditationes, passionis Domini nostri Iesu Christi" exposed to iron-gall ink corrosion.
(This figure is presented in the signature in colours at the end of this volume, Appendix, pg. 318)

According to the hypothesis of art historians, the manuscript could be one of the copies of Meditationes among many others that were written in the monastery. Some parts of the text are written in Latin while others are written in Polish.

M2 – "Ewangelii Tetr" (BN 2648, National Library of Poland, Warsaw).

M3 – "Trebnik" (BN 2686, National Library of Poland, Warsaw).

Both manuscripts M1 and M2 were dated back to the 16th century with a text written in Old Church Slavonic language.

5 PHYSICAL AND CHEMICAL CHARACTERISATION OF ANCIENT SAMPLES

The decision concerning an effective conservation procedure should be based on a detailed characterisation of the chemical and physical properties of the work of art of interest (Adams et al. 1997, Wagner et al. 1999, 2001). For this purpose we used the samples collected by conservators during their work. A multi-method approaches was successfully used, with the aid of scanning electron microscopy (SEM); electron probe micro analyser (EPMA); X-ray fluorescence spectrometry (XRF); graphite furnace atomic absorption spectrometry (GF AAS); inductively coupled plasma mass spectrometry (ICP MS); X-ray absorption near edge structure (XANES); Mössbauer spectroscopy; molecular spectrometry (UV-Vis); laser ablation ICP MS (LA ICP MS). The list of the applied methods with their performance is collected in Table 2.

The investigation of the morphology of the cellulose fibres over the corroded and non-corroded area of the manuscript page was performed by SEM. When the non-corroded area was considered, all fibres were intact, with visible density of the material. In opposite, over the corroded area compressed and broken fibres together with ink particles were clearly seen on the SEM micrograph. Then the content of major elements over the both investigated area (corroded and non-corroded) was examined by energy-dispersive XRF. Searching for the elements responsible for the corrosion processes, the main attention was focused on the possible differences in elemental composition on both parts of the manuscript: written and unwritten areas. Because of the limited lateral resolution of XRF, the obtained data are related to the average concentration over the surface of around 2 cm^2.

Table 2. Performance of applied analytical methods for physical and chemical investigation of ancient manuscripts and model samples.

Investigated parameter	Available and used methods	
Topochemical investigation of surface structure	SEM	EPMA
Major elements distribution on the surface	XRF	
Concentration of trace elements in micro-samples	GF AAS	ICP MS
Valency state of iron	Mössbauer spectroscopy	XANES
Efficiency of metal extraction	UV-Vis	GF AAS
Migration of elements over the paper surface	LA ICP MS	

The most pronounced difference among both investigated areas (corroded and non-corroded) was found in the case of Fe, Cu, Hg, Zn, S, and Pb, while other elements (Ca, Mg, Na, K, Si, P, Al, Cl) were present at the same concentration level. Then special attention was focused on iron, copper and sulphur, as those elements were expected to be responsible for iron-gall ink corrosion. EPMA is the method of choice when better lateral resolution is required; therefore it was used for the more detailed studies of the surrounding of the single written character. The preliminary observation was done in a back-scattered electron mode, in order to select the area exposed for further inspection. Then over the selected area, the elemental maps for Fe, Cu and S were made by registered the respective X-ray spectra at each beam position. By examining those data one can conclude that the ink residue was characterized by high concentrations of Fe and Cu, while S was nearly uniformly distributed over the investigated area. The characteristic distribution of Fe and Cu is well explained by the composition of the ink. In the case of S the only explanation of such a distribution could be the ability of this element to migrate over the paper support when the relative humidity of the environment is elevated. The specific distribution of Fe and Cu over the ink layer was confirmed also by the investigation done with LA ICP MS. In archaeometry a micro-destructive feature of LA ICP MS was found to be a great advantage in many applications, obviously unless especially precious historical objects are considered. Otherwise LA ICP MS offers many analytical possibilities: it allows not only bulk and isotopic analysis of micro-samples, but studying a lateral distribution of selected elements on the sample surface and reconstructing their depth profiles in sub-surface domains as well. In the case of the investigated samples the laser shots evaporate the minute amount of the material over the defined path, starting outside of the ink border, passing over the ink layer and ending again outside of the inked area. The significant difference in signal intensity between the inked area and non inked area was in good agreement with the results obtained with EPMA mapping.

Among analytical methods mentioned above, only XRF could be considered as quantitative, but in the case of performed investigation it was limited to provide only semi-quantitative information for the major elements. In order to obtain the quantitative information in respect of trace elements two very sensitive techniques were applied: GF AAS and ICP MS. In both cases the requirement was to use the minute amount of the materials. For this purpose the micro-samples were cut off from the previously collected samples of manuscript, distinguishing by the presence of the iron-gall ink visible on the paper surface. Again, the samples with visible ink residues were characterized by significantly higher concentration of iron and copper. The average content of Fe and Cu over the inked area was around $30\,mg\,g^{-1}$ and $15\,mg\,g^{-1}$, respectively. For comparison, the average content of Fe and Cu over the non-inked area was around $3\,mg\,g^{-1}$ and $1.5\,mg\,g^{-1}$ respectively. This information was used to imitate the ancient manuscript by model samples.

The last but not least it was of crucial interest to investigate the content of both iron oxidation states: Fe(II) and Fe(III) in ancient manuscripts. Mössbauer spectroscopy and XANES were applied for this purpose, both methods capable to measure the ratio and distribution of Fe(II) and Fe(III) over the surface of the ancient manuscript. In all samples the significant amount of Fe(II) can be still visible, even after few centuries of the ink deposition. The results of average Fe(II) content in the analyzed samples are shown in Table 3. The results from Mössbauer spectroscopy represent the

Table 3. The results of Fe(II) content (in % of the total iron) by XANES and Mössbauer spectroscopy for the investigated manuscripts M1, M2 and M3.

Evaluation of Fe(II) content [%] by:	M1	M2	M3
XANES	46	24	8
	55	29	7
	40	30	8
	52	12	5
	55	11	3
XANES average	48	21	6
Mössbauer spectroscopy	52	15	7

bulk area of the investigated samples, as the results from XANES represent mean value obtained from measurements performed in different points over the same investigated area.

6 DESIGNING OF THE MODEL SAMPLES

The purpose of designing the model samples was to mimic real ancient objects in order to perform the detailed investigation without necessity of taking any sample from artefacts. The working hypothesis was put forward to solve the problem of different iron species present in real iron-gall inks. The assumption was made, that a home-made iron-gall ink solution deposited onto the paper support mimic inked areas of ancient manuscripts, while $FeCl_3$ solution deposited onto the paper support mimic only free (active) iron ions. The support for investigated model samples, chosen according to Whitmore and Bogaard, where a Whatmann chromatographic paper, made of cotton fibres, was used. In order to obtain two types of model simulating the phenomenon occurring in real artefacts (later referred as type "A" or "Fe") the set of the paper circles (Ø = 6 mm) was cut-off from the sheet of Whatmann paper and 5 μL of respective solutions was deposited on the surface. Two types of solutions were used to create models: (i) for samples "A" the solution of a home-made iron-gall ink prepared according to the described procedure; (ii) for samples "Fe" the aqueous solution of $FeCl_3$ containing 0.6 g L^{-1} of iron, were used. All samples were exposed to IR lamp for 15 minutes and then stored separately in closed vessels (á 1.5 mL).

One of the requirements for model samples was the necessity to choose the proper kind of paper, which could give good repeatability of sampling. The paper should not have fillers, thus chromatographic paper Whatmann No. 1, made of cotton fibbers, was selected. Thanks to its uniform thickness it was possible to cut off the paper dots of the same size, with almost the same mass. Care was also taken to minimise the contamination of the paper and for this purpose a laboratory made titanium punch was used to cut out the samples. Each sample, punched out from the Whatmann paper, was weighted on the analytical balance. The reproducibility of sampling was satisfactory, the average mass for 10 replicates was 2.55 mg ± 0.01 mg (RSD = 2.3%).

Iron-gall ink solution: the home made iron-gall ink solution was prepared by mixing 4.20 g of ferrous sulphate, 4.86 g of tannin and 3.14 g of gum Arabic. In order to reflect the composition of the ink from the manuscript M1 the blue vitriol (copper sulphate) was also added in the amount as to get the final concentration of copper to be around half of the concentration of iron. All components were dissolved in 100 mL of double distilled water and allow reacting for 24 hours, before being filtered.

7 INVESTIGATION PERFORMED WITH MODEL SAMPLES

As it was described above, the model samples were designed to mimic the selected properties of the real manuscript and were used to investigate the behaviour of various iron species present in ancient iron-gall ink. The investigation was focused on both, the influence of complexing agent solutions

during the extraction of iron species present in the model samples and on the influence of the extraction solution on the paper itself. The rate and efficiency of iron-complex formation in the investigated solutions were investigated by UV-Vis spectrometry. The amount of iron washed-out from the paper during extraction, either in the form of complexes or in a form of ions, was simultaneously determined directly in the solution by GF AAS. In order to obtain the complete picture of the process occurring during the contact of the paper samples with complexing agent solutions after extraction, the residual amount of iron on the paper was determine by ICP MS. Then the ratio of Fe(II)/Fe(III) was evaluated by both, XANES and Mössbauer spectroscopy. In order to exclude the possibility of migration of transition metals ions over the paper surface, out of the inked area, the LA ICP MS was used. At least but not least the artificial aging was applied for selected model samples exposed to particular treatment and the investigation of the characteristic parameters of the paper was performed.

In order to investigate the extraction efficiency of iron from paper, each sample (type "A" or "Fe") was immersed for 20 minutes into the freshly prepared complexing agent solution. During the extraction process, measurements at the maximum absorbance of expected iron complex (by UV-Vis) and at 248.3 nm of iron atomic line (by GF AAS) were done every 20 seconds (within first minute), every minute (within next 4 minutes) and then every 5 minutes. Measurements of the concentration of iron complexes were performed directly in the solution and the aim of this experiment was to evaluate the rate and efficiency of the complex formation. Determination of the total iron content in the solutions during the whole extraction process was performed by sampling of 100 μL of the solution from the reaction vessel and introducing it into the graphite furnace for AAS measurements.

The expectation was to use such a treatment conditions where it could be possible to achieved high effectiveness of the extraction of iron from $FeCl_3$, while iron being bonded with ink colourful compounds remain without any visible change of the ink's colour. Moreover, the applied solutions should not influence the paper material neither by destroying the cellulose structure nor by colouring the surface of the paper.

In the first attempt the investigation were performed with three ligands: deferoxamine (Desferal); dibenzoylmethane (DBM); acetylacetone (ACAC), because they have a broad absorbance band over the 390–600 nm, allowing applying UV-Vis for measuring iron complex formation. The spectra of the investigated ligands with iron (added as $FeCl_3$ or as gall-ink solution) were recorded in the range of 390–700 nm. The wavelengths for maximum absorbance were used for further measurements of the content of the iron-complex in the solution during the whole extraction procedure. The results of both measurements (by UV-Vis and GF AAS) are shown in Figure 3. Every point represents the mean of absorbance values for three independent samples.

From GF AAS measurements it was found that nearly 100% of iron deposited onto the paper dots as $FeCl_3$ could be washed-out by acetylacetone and deferoxamine solutions. For both compounds, the plateau has been achieved within 10 minutes. In the case of dibenzoylmethane solution, the rate of the investigated process was much slower. The respective curve for $FeCl_3$ as well as for iron-gall ink solutions have not reached plateau even after 30 minutes. Additionally, the efficiency of iron-complex formation within this time was less then 50% for $FeCl_3$.

From UV-Vis measurements it was found that the lowest extraction efficiency was achieved when dibenzoylmethane (DBM). Moreover, this ligand caused irreversible colour change in the paper. Therefore it was concluded that dibenzoylmethane has no value for the conservation of ancient written objects and was withdrawn from further investigations.

When deferoxamine solution (Desferal) was used, the efficiency of iron-complex formation was above 80%. When comparing with the data from GF AAS measurements it is clear that iron bound with compounds present in gall ink is nearly completely washed-out from the paper by the solution of deferoxamine. This was also evident from the visual observation of the paper samples after 30 minutes of extraction, as the weakness of the colour of the ink was indisputable. This means that within the applied conditions it was not possible to distinguish between two forms of iron which were of interest.

In contrast to dibenzoylmethane and deferoxamine, in that stage of the project, acetylacetone solution shows the most pronounced difference between the behaviour of both investigated forms

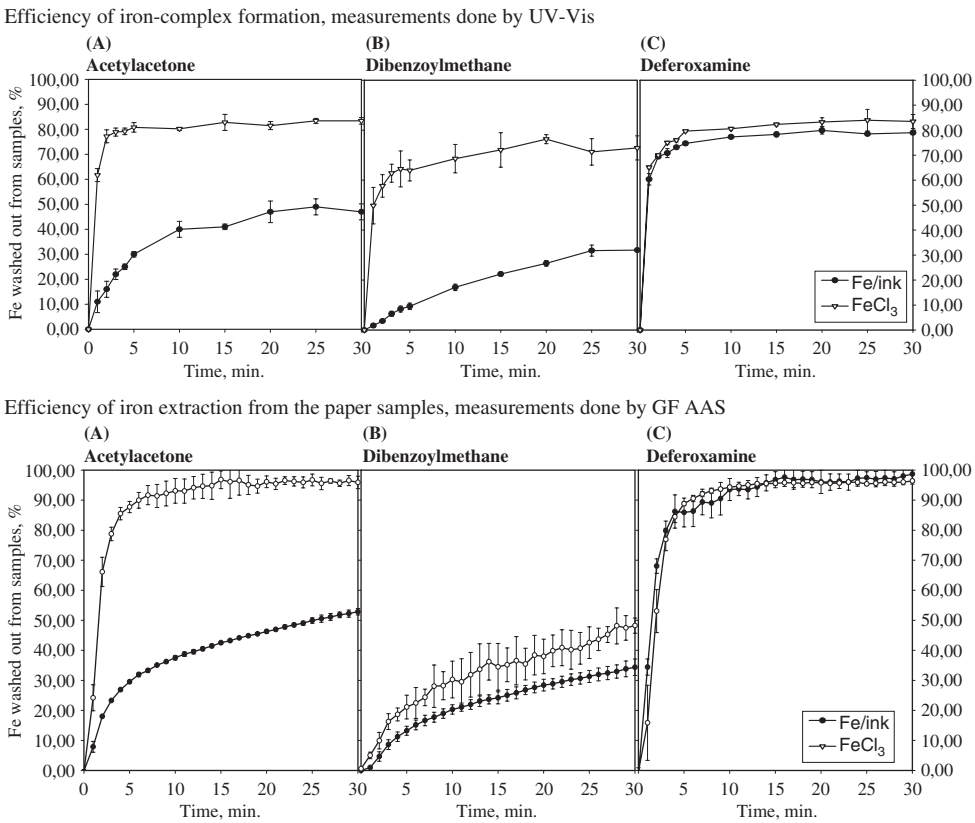

Figure 3. Efficiency of iron-complex formation (UV-Vis) and iron extraction (GF AAS) from the model samples by the ligand solutions: A – acetylacetone; B – dibenzoylmethane; C – deferoxamine. The model samples were used: (— • —) with iron-gall ink; (— ∇ —) with $FeCl_3$.

of iron. This leads to the conclusion that the process of iron-acetylacetone complex formation is not competitive to iron-complex present in iron-gall ink. In fact, after 30 minutes of extraction from the samples with deposited iron-gall ink, the colour of the ink reminds unchanged. Besides those positive conclusions, the main objective was that acetylacetone is not able to occupy all of the available coordination sides of iron, so it was apparently left aside.

Then more attention was focused for the use of diethylotriaminepentaacetic acid (DTPA), and to compare its efficiency with deferoxamine mesylathe (Desferal) and phytic acid (PHY). The problems was that by using the robust conditions it turn out, that the use of DTPA lead to influence the color of the iron-gall inks, even during the first 10 minutes of treatment, what means that the efficiency of extraction of iron from the inked samples was too high. As DTPA is known to block all available coordination sides of iron ions, even considering the preliminary results, most research was focus on the use of DTPA in order to develop suitable conditions to decrease the efficiency of extraction of iron from the iron-gall ink without decreasing the efficiency of extraction of iron from the model samples “Fe”. The effort was made to evaluate the influence of various concentrations of the complexing agent solutions, within the pH range, on the extraction efficiency. In order to compare the selected ligand with that described previously, the phytic acid treatment was also investigated and compared. The reason for such comparison was that phytic acid described by Neevel (Neevel & Reissland 1997, 1998) is undoubtedly the most popular ligand used for conservation purposes. However, only Fe can be inactivated by this compound, while other

transition metal ions (Cu, Mn) present in the iron gall ink can still catalyze degradation of paper support in historical documents.

The efficiency of iron extraction from model samples "Fe" and "A" with the use of desferoxamine mesylathe, potassium–magnesium salt of phytic acid and diethylenetriaminepentaacetic acid at varied concentration (0.01, 0.005 and 0.001 mol L^{-1}) and pH 7, 8 and 9, was then investigated. As some ancient iron-gall inks were found to be soluble in water, the use of the water/ethanol solution was tested. After all detailed investigation it was found that the solution of 0.005 mol L^{-1} diethylenetriaminepentaacetic acid (pH = 8.6) could be judged as the best ligand among the tested compounds in respect to defined requirements. The efficient extraction of active iron ions from model samples "Fe", almost without touching that part of the iron which is present in the form of colourful compounds in ink was achieved. The use of phytic acid offers also satisfactory distinguish of extraction efficiency for both forms of iron represented by models "Fe" and "A", but the pH of the solution was not sufficiently high to perform the simultaneous deacidification of the paper. In that respect, DTPA offers the effective extraction of active iron ions in slightly alkali conditions, what means that no deacidification post-treatment is needed. Moreover, DTPA form stable complexes also with copper and manganese, which is not the case of phytic acid. At least but not least DTPA is as well soluble in water or in water/ethanol solution, therefore could be also applied for the manuscript sensitive to the water treatments. Before recommending the developed procedure for conservation purposes, the awareness came into view whether the migration of metal ions within the paper area occurs after extraction, what could lead to spreading of the corrosion as a consequence of such treatment. For this purpose the use of LA ICP MS was found to be ideal.

8 MIGRATION OF METALS OVER THE PAPER

As an output of described investigation the application of DTPA aqueous solution (pH = 8.6) was found to be advantageous, mainly because it allows the simultaneous extraction and complexation of Fe, Cu and Mn in a slightly alkaline environment. The proposed procedure was found to be efficient also when water/ethanol solutions were used, what is of special importance when dealing with documents sensitive for water. LA ICP MS (Laser Ablation Inductively Coupled Plasma Mass Spectrometry) has been used to investigate the distribution of Fe, Cu and Mn within the line written with iron gall ink and in the close vicinity to it. The aim of the performed investigation was to check whether the migration of chosen elements out of the line written with iron gall ink is possible during extraction. For this purpose three original samples of mediaeval manuscripts (M1, M2 and M3) have been analyzed before and after treatment by aqueous solution of DTPA (c = 0.005 mol L^{-1}, pH = 8.6). It was important to prove that the possibility of Fe, Cu or Mn migration due to proposed conservation procedure can be excluded.

The measurement was perform with LA ICP MS, as it was described previously for the investigation of the profiles of iron and copper distribution over the inked line. After the first measurement, the sample was immersed into the DTPA aqueous solution and subjected to extraction for 5 minutes. Sample, which was taken out from the solution was dried and subjected to the next laser ablation. The second line was selected in a distance less than 1 mm from the first one.

Signals intensity registered during the first and the second measurement were combined on one graph for each element respectively, therefore changes in the signals intensity can be easily compared (Fig. 4). As it was expected, the content of all elements over the inked area decrease after extraction and what was important for the evaluation of the usefulness of the proposed conservation procedure, no signal broadening was noticed, what means that no migration of Fe, Cu or Mn over the paper was provoked by the DTPA solution. It was of great importance to notice, that not only for the model samples, but also for ancient objects the colour of the paper and the hue of the ink remained unchanged. Regarding the conservation requirements, the exclusion of the migration proved by performed investigation, became a strong argument for the proposed treatment. It could be concluded that after the DTPA treatment the phenomenon of iron gall ink corrosion is strongly diminished and restricted to the inked area of manuscripts.

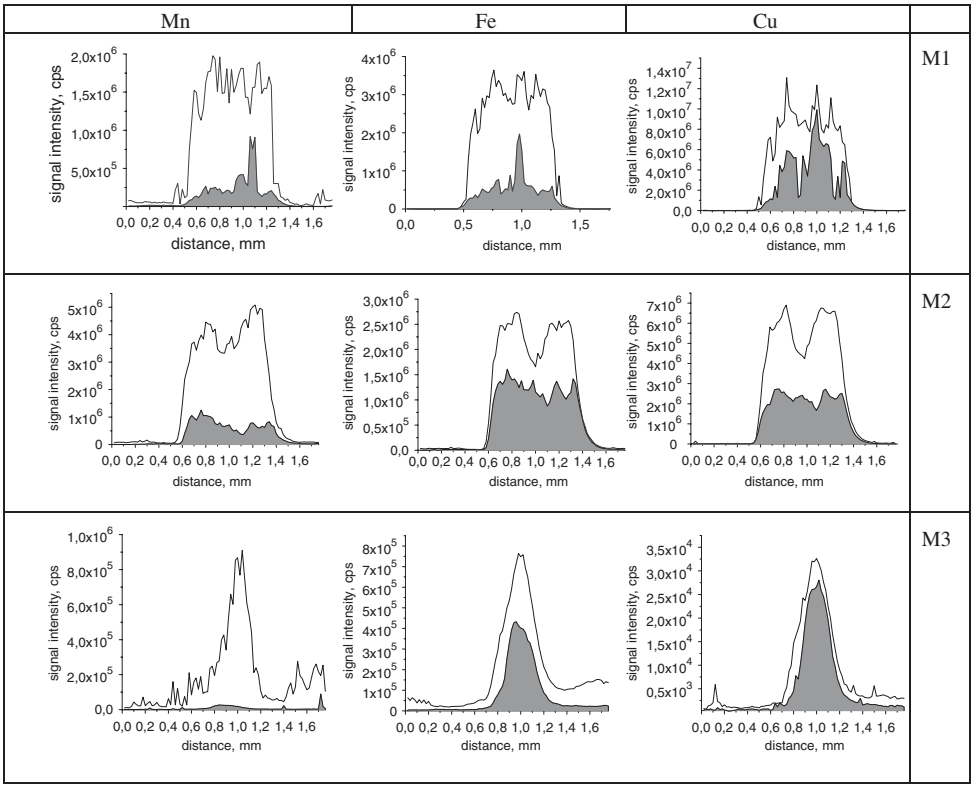

Figure 4. Signal intensity of LA ICP MS measurements over the inked line on the manuscript surface. Non-filled curves represent the result for the original samples; grey filled curves represent the results after treatment of the samples with DTPA solutions.

9 EXAMINATION OF THE CONTENT OF FE(II) AFTER EXTRACTION

As the catalytic degradation of the cellulose requires the presence of Fe(II), it was interesting to investigate, not only the efficiency of the total iron extraction but the efficiency of specific extraction of those active Fe(II) ions. Therefore the oxidation stage of iron present in the model samples with deposited home-made ink was performed by XANES and Mössbauer spectroscopy after these samples have been subjected to DTPA extraction. For this purpose the set of model samples was extended and besides the Whatmann No 1 paper, known to have no sizing, also two types of sized paper were used: paper from the 19th century and contemporary copy paper. The amount of sizing determines the degree of the soaking of the paper with deposit ink droplet. From all performed measurements it can be concluded that the prepared model samples with deposited ink contains significant amount of Fe(II) in the range from 5% to 30%. In order to evaluate the efficiency of extraction treatment, the experiments were executed by XANES for model samples before and after treatment using aqueous solution of DTPA ($c = 0.005\,\mathrm{mol\,L^{-1}}$, $pH = 8.6$). The obtained results proved that in applied conditions significant decrease of the Fe(II) content was achieved. The effectiveness of the extraction, related to Fe(II) depends on the pH of the DTPA solution. At $pH = 5$, still up to 9% of iron was found in the form of Fe(II), while at $pH = 9$ in fact no Fe(II) was detected, what means that the proposed conservation treatment is sufficient to decrease the amount of unwanted Fe(II) from the paper with deposited iron-gall ink.

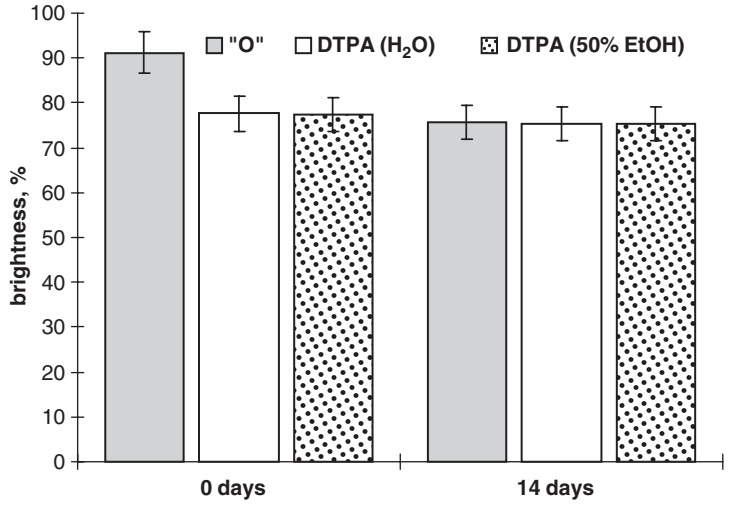

Figure 5. Evaluation of brightness of paper after artificial ageing. Non-treated paper "O"; washed at aqueous solution of DTPA "DTPA (H_2O)"; washed at ethanol solution of DTPA "DTPA (50% EtOH)".

10 EVALUATION OF THE CHARACTERISTIC PARAMETERS OF THE PAPER UNDER THE ACCELERATED AGING CONDITIONS

The investigations of the characteristic paper parameters are the subject of various national and international standards. These tests are used routinely in paper industry for the purpose of quality control, but also are useful in a conservation department for the evaluation of the usefulness of the any novel procedure intended for conservation purposes. It was found important to apply some of those tests for the model samples used in this work, to evaluate the possible influence of the proposed conservation procedure on the stability of the paper. For this purpose samples of offset paper were exposed for accelerated aging for 14 days (at 80°C and relative humidity of 65%) (Standard PN-93/P-501, PN-93/P-50174/01 (ISO 5630/1:1991), PN-93/P-50174/02 (ISO 5630/2:1985), PN-93/P-50174/03 (ISO 5630/3:1986), PN-93/P-50131, PN-83/P-50133, PN-76/P-50169, PN-84/P-50109). Selected tests of paper resistance for rupture, ultimate elongation (ultimation at rupture), breaking length and tearing resistance were performed before and after 3, 7 and 14 days of aging. Additionally, several samples were exposed to the influence of the xenon lamp in Xenotest 105S. The lightness and yellowish of the paper was then evaluated (Standard 46 PN-76/P-50169). Besides various mechanical parameters and optical properties of paper, pH of aqueous extracts from paper was measured (Standard 47 PN-84/P-50109). As an example, the results of the measurements of the brightness of paper before and after artificial aging for non-treated as well as for paper exposed for the contact with aqueous or water/ethanol solution of DTPA is shown in Figure 5. All other results of performed tests were as well satisfactory and the application of DTPA solutions was judged as safe for the paper support.

The investigation of optical and mechanical properties of the samples treated with both water and water/ethanol solutions of DTPA also proved that such a treatment does not influence the properties of the paper.

11 SUMMARY

The investigation towards the new conservation procedure for ancient documents exposed to the iron-gall ink corrosion was performed. The applied treatment uses the complexation agents, which could be efficient for the extraction of the active transition metal ions deposited on the paper with

ink. When numbers of experiments were required, the model samples designed as to mimic the selected properties of the ancient items were used.

The best behaviour in respect to defined pre-requirements for the conservation procedure was found for diethylotriaminepentaacetic acid used at pH = 8.6. In this case the best selectivity between two forms of iron was observed: DTPA was found to form the stable complexes with iron introduced as $FeCl_3$, but was not sufficient to displace iron from the gall ink compounds. Moreover copper and manganese could be extracted simultaneously. The residual amount of iron was only in Fe(III) oxidation stage, which was proved by the measurements with the aid of XANES. The performed experiments with LA ICP MS excluded the possible migration of the metal ions during the extraction. At last but not least the executed investigation of the characteristic parameters used in quality control for paper after acceleration aging of the model samples exposed to the conservation treatment proved that the proposed procedure is safe in respect of the paper itself.

ACKNOWLEDGEMENTS

The authors want to express their thanks to the Conservation Division of Manuscripts of the National Library of Poland for supporting us with original paper samples used for investigation. We wish to thank Prof. A. Hulanicki and Prof. H.M. Ortner for many valuable discussion and critical remarks during all stages of the project and Prof. W. Wegscheider for his support. We thank Prof. K. Janssens for his interest in this project and for common work on XANES investigation. We also thank T. Meisel, M. Heck and B. Stahl for their help with ICP-MS (T.M.), XRF (M.H.) and Mössbauer (B.S.) measurements.

REFERENCES

Adams, F., Adriaens, A., Aerts, A., de Raedt, I., Janssens, K. & Schalm, O. 1997. *J. Anal. Atom. Spectrom.*, 12, 257.

Banik, G., Mairinger, F. & Stachelberger, F. 1981. *Restaurator*, 1/2, 71

Barry, B. & Fields, J. 2000. The Iron Gall Ink Meeting Postprints, A.J.E. Brown (ed.), Newcastle, pp 83–88.

Bicchieri, M. & Pepa S., *Restaurator*, 17, 165 (19964).

Budnar, M., Vodopivec, J., Mandó, P.A., Lucarelli, F., Casu, G. & Signorini, O. 2001. *Restaurator*, 22, 228.

Bulska, E., Wagner, B. & Sawicki, M.G. 2001. *Mikrochim. Acta*, 136, 61.

Calvini, P. & Gorassini, A. 2002. *Restaurator*, 23, 205.

Coupry, C., Lautie, A., Revault, M. & Dufilho, J. 1994. *J. Raman Spectrosc.*, 25, 89.

de Feber, M.A.P.C., Havermans, J.B.G.A. & Defize, P. 2000. *Restaurator*, 21, 204.

Fuchs, R., Hahn, O. & Oltrogge, D. *Restauro*, 2, 116.

Graf, E., Mahoney, J.R., Bryant, R.G. & Eaton, J.W. 1984. *Biol J.. Chem.*, 259, 3620.

Graf, E., Empson, K.L. & Eaton, J.W., 1987. *Biol J.. Chem.*, 262, 11647.

Gurnagul, N., Howard, R.C., Zou, X. & Uesaka, T., Page D.H. 1993. *Pulp J. Paper Sci.*, 19, J160.

Johanssen, A., Kolseth, P., Lindqvist, O. 2000. *Restaurator*, 21, 117.

Kolar, J. & Strilc, M. 2000. The Iron Gall Ink Meeting Postprints, Ed. A.J.E. Brown, Newcastle, pp 135–138.

Krekel, C. 1999. *International J. Forensic Documents Exam*., 5, 54.

Lienardy, A. & Van Damme, P. 1990. *Restaurator*, 11, 1.

Liers, J. & Schwerdt, P. 1995. *Restaurator*, 16, 1.

Neevel, J.G. 1995. *Restaurator*, 16, 143.

Neevel, J.G. & Reissland, B. 1997. Proc. Workshop on Iron Gall Ink Corrosion, Van der Windt Ed. H., Amsterdam, pp 37–46.

Neevel, J.G. & Reissland, B. 1998. *Pap. Cons. News*, 85, 10.

Neevel, J.G. 2000. The Iron Gall Ink Meeting Postprints, A.J.E. Brown (ed.), Newcastle, pp 125–135.

Porck, H.J & Teygler, R. 2000. Preservation Science Survey, Council on Library and Information Resources, Wasington, D.C.

Proost, K., Vincze, L., Janssens, K., Gao, N., Bulska, E., Schreiner, M. & Falkenberg, G. 2003. *X-Ray Spectrom*., 32, 215.

Proost, K., Janssens, K., Wagner B., Bulska, E. & Schreiner, M. 2004. Nuclear Instruments and Methods in Physics Research; Section B-beam Interaction with Materials and Atoms, 213, 723.
Schreiner, M. & Grasserbauer, M. 1985. *Fresenius Z. Anal. Chem*, 322, 181.
Sistach Anguera, M.C. 1996. *Restaurator*, 17, 117.
Van Gulik, R. & Kersten-Pampiglione, N.E. 1994. *Restaurator*, 15, 176.
Wagner, B., Garboś., Bulska, E. & Hulanicki, A., 1999. *Spectrochim. Acta Part B*, 54, 797.
Wagner, B., Bulska, E., Meisel, T. & Wegscheider, W., 2001a. *J. Anal. At. Spectrom.,* 16, 417.
Wagner, B., Bulska, E., Hulanicki, A., Heck, M. & Ortner H.M. 2001b. *Fresenius J Anal. Chem*., 369, 674.
Wagner, B. & Bulska, E., 2003. *Anal. Bioanal. Chem*., 375, 1148.
Wagner, B., Bulska, E., Stahl, B., Heck, M. & Ortner, H.M. 2004. *Anal. Chim. Acta*, in print.
Wagner, B. & Bulska, E., 2004. *J. Anal. At. Spectrom.* DOI:10.1039/B408384A.
Wehling, B., Vandenabeele, P., Moens, L., Klockenkamper, R., von Bohlem, A. van Hooydonk, G. & De Reu M., 1999. *Microchim. Acta*, 130, 253.
Whitmore, P.M. & Bogaard J. 1994. *Restaurator*, 15, 26.
Wunderlich, C.H., Weber R. & Bergerhoff G. Z. 1991. *Anorg. Allg. Chem*., 598/599, 371.
Wunderlich, C.H. 1996. *Restauro*, 6, 414 Wittekind J. 1994. *Restaurator*, 15, 189.

Cultural Heritage Conservation and Environmental Impact Assessment by Non-Destructive Testing and Micro-Analysis – Van Grieken & Janssens (eds)
© 2005 Taylor & Francis Group, London, ISBN 90 5809 681 5

Can x-ray computed tomography contribute to cultural heritage and stone conservation through the non-destructive monitoring of deterioration and restoration processes?

P. Jacobs & V. Cnudde
Department of Geology and Soil Science, Ghent University, Belgium

ABSTRACT: Indoor but especially outdoor objects of cultural and aesthetical value are often exposed to deterioration. In order to be successful and durable, their restoration needs careful preparation based on an in-depth knowledge of the various physical, chemical and biological corroding processes that operate both on the macro- and the micro-scale. Non-destructive research techniques (ndt) represent a powerful tool to monitor the deterioration processes affecting these cultural heritage (CH) objects. Computed x-ray (micro)tomography (CT and μCT) is based on the attenuation of x-rays passing through a rotating object, allowing 3D-reconstruction of internal structures or phenomena and characterisation of material composition. From this visualisation and quantification, assumptions can be made about the governing deterioration mechanisms. Departing from well-known model conditions, predictions should become possible about the nature and the effectiveness of the proposed restoration techniques. The deterioration of natural building stones monitored with CT and with μCT seems to be governed by rock (petrophysical) properties like porosity and pore interconnectivity. Promising new applications of this ndt-research in the CH-domain will be explored.

1 INTRODUCTION

Computed x-ray Tomography (CT) is a radiological imaging technique. CT was first developed in Great Britain by Hounsfield in 1972 and revolutionised medical radiology by producing anatomical images of high accuracy and clinical detail.

Conventional x-ray radiography (e.g. chest x-rays) views an object from only one angle. Shadows from irradiated matter along a ray path are superimposed on one another. All attenuation information is averaged together in a way that localised regions with a small attenuation contrast are obscured.

By comparison, CT-scanners generate cross-sectional image slices through the study object (Fig. 1). An x-ray tube and a set of detectors revolve around the object, producing projections at many different angles. Cross-sectional images reconstructed by a back-projection algorithm in the scanner's computer, are displayed on a cathode-ray-tube monitor. Attenuation differences as small as 0.1% can be measured accurately within an interior region of 2 mm^2. As the sample is moved through the scanner, 3D CT-images in any plane can be reconstructed from sequential cross-sectional slices.

1.1 *Physical principles of x-ray attenuation*

The basic physical parameter quantified in each pixel of a CT-image is the linear attenuation coefficient μ, assuming a well-collimated beam and a monochromatic x-ray source (1):

$$I/I_0 = \exp(-\mu h) \quad (1)$$

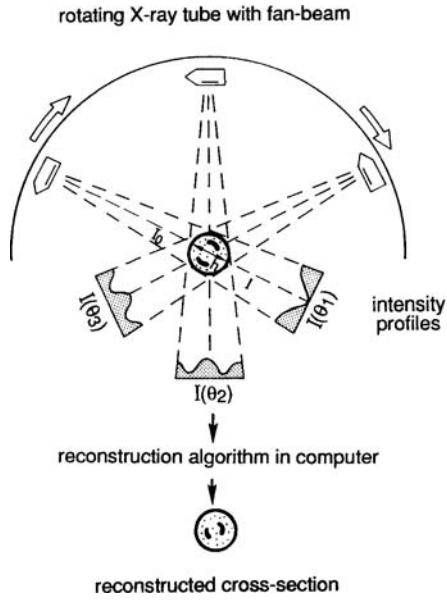

Figure 1. Principle of x-ray computed tomography (CT).

where I_0 is the incident x-ray intensity and I is the intensity remaining after the x-ray passed through a sample with thickness h.

The linear attenuation coefficient μ depends on both electron density (bulk density) ρ and atomic number Z (2):

$$\mu = \rho\,(a+bZ^{3.8}/E^{3.2}) \qquad (2)$$

where a represents the nearly energy-independent Klein-Nishina coefficient and b is a constant. The first term in (2) stands for the Compton scattering, predominant at x-ray energies above 100 keV (where medical CT-scanners normally operate). The second term accounts for photoelectric absorption, which is more important at x-ray energies well below 100 keV.

1.2 *CT-techniques*

First-generation scanners developed in 1972 used a single pencil-beam x-ray source and detector arrangement, while 2nd-generation improved image quality by using multiple detectors in a translate/rotate configuration. In third-generation scanners source and detectors rotate together around the object in rotate-only fan-beam geometry. In the actual 4th-generation, the source rotates within a fixed ring of high-efficiency detectors.

The 2nd- to 4th-generation medical CT-scanners have adequate x-ray energy and dose for petrophysical investigation and material characterisation. Remote processing of the digital image information allows computation of physical properties from the basic attenuation data, together with 3D-display, interactive colour graphics, and concurrent display of CT-animations and numerical simulations.

CT-attenuation data are normally presented in an internationally standardised scale called Hounsfield units, defined by air at −1000 HU and by water at 0 HU, each unit thus representing a 0,1% change in tomographic density. For CT-measurements on (polymineralic) rocks, it is more convenient to calibrate on standards (such as fused quartz with a bulk density of 2.20 g/cm^3), resulting in a calibration curve that allows corrections for artefacts (such as beam hardening).

The new 4th-generation scanners (a.o. Siemens Somatom+) produce CT-scans allowing high-resolution 3D x-ray imaging (approximate optimal pixel size: 100 μm × 100 μm) and data storage on tape for further image analysis. Optimal scanning operation conditions of samples require all parameters be kept constant during all experiments: scanning at 137 keV, with a scan slice of 1 mm, a zoom factor of 8.5 and the highest image resolution of 512 × 512 pixels. The measured Hounsfield values for every pixel vary between −1000 HU and 3000 HU, and are visualised on a CRT-monitor screen by 256 grey intervals.

2 PREVIOUS APPLICATIONS OF CT IN THE CULTURAL HERITAGE DOMAIN

The non-destructive character of the CT-method was applied to monitor the degradation of three different types of natural building stones under varying conditions of physical weathering and biological deterioration (Jacobs et al. 1995). The Mid-Eocene (Tertiary) Balegem grey-yellowish fine grained, fossiliferous and sometimes cavernous carbonaceous sandstone (calcarenite) has been widely used as a natural building stone in Gothic and Renaissance buildings in the County of Flanders and in the Duchy of Brabant (Belgium). Carrara marble samples are of the Michelangelo variety (locality of Massa Carrara, Italy). Pozzolana mortar samples provided by the Instituto de Ciencias de la Construccion, (Madrid, Spain), consisted of a calcium hydroxide (lime)/natural pozzolana/sand mixture in a 1:1:2 weight ratio and a 1:1 water/lime ratio. Scans of blank samples were compared with scans of physically and biologically deteriorated samples. Qualitative visual inspection of the images was complemented by quantitative statistical analysis (spectral distributions with parameter analysis; cluster analysis).

2.1 *Results*

CT-analysis results indicate an average tomographic density of 1050 HU for pozzolana mortar, 2100 HU for Balegem calcarenite and 2430 HU for Carrara marble. Visual inspection of the CT-images revealed that only physical weathering by wet freeze-thaw cycles notoriously influenced the bulk density of the mortar samples. In case of biological deterioration (through algae and cyanobacteria, black fungi or bacteria) HU tomographic density values largely differ from values of untreated or physically weathered samples (Fig. 2). This suggests that physical weathering enhances bioreceptivity by creating or increasing secondary porosity through internal mass migration caused by dissolution and consequent precipitation of soluble rock building components (Jacobs et al. 1995, 1996).

Short physical deterioration cycles apparently do not affect medium- to high-density rock types. Clustering of HU-tomographic density values of Regions-Of-Interest (ROI) detail cementation and macro- and micro-porosity characteristics of porous low- to medium-density rock types (like mortar and calcarenites). CT proved to be a powerful and promising tool for the non-destructive qualitative and quantitative assessment of artificial methods of restoration (like sand blasting and resin impregnation techniques) of decaying natural building stones (Jacobs et al. 1995, 1996).

But the analysis results also clearly indicated that medical CT-scanners operate at resolutions that are critical for the study of material characteristics like grain size and micro-porosity (100 μm or less), that are vital for the assessment of deterioration processes. Any progress in this field will therefore largely depend on future resolution improvement of scanner techniques. It is expected from preparatory tests that x-ray computed micro-tomography (μCT) will match these requirements.

3 X-RAY COMPUTED MICRO-TOMOGRAPHY (μCT)

As the resolution of medical CT-scanners is of the order of 0.1 mm at the best, they can hardly be considered as microscopes. With the arrival of compact microfocus x-ray tubes, slow-scan CCD-cameras and powerful microcomputers, desktop x-ray microtomographs can be constructed with a

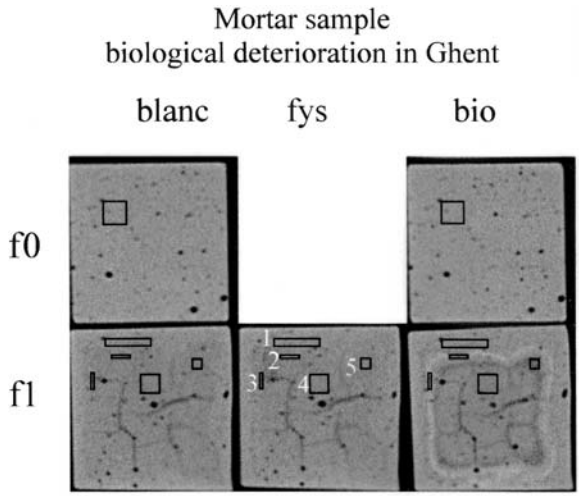

Haunsfield values in ROI (in HU)

f0	1023		1019	
	1029	1000	1036	1
	1007	957	1417	2
f1	946	906	1388	3
	931	903	906	4
	919	911	651	5

Figure 2. CT-scans of mortar samples after physical and biological deterioration. Hounsfield values refer to attenuation in boxed Regions-of-Interest (ROI, numbered).

resolution in the order of microns (Sassov & Van Dyck 1997). These microtomographs offer a great potential for new applications to look inside the 3D-microstructure of opaque biological or material objects under ambient conditions, without any need for specimen preparation, staining, etc.

3.1 *Principles*

The desktop x-ray microscope-microtomograph consists of a microfocus tube, a precision specimen manipulator, an x-ray TV-camera and a Pentium computer for instrumental control and tomographical reconstruction. The x-ray microfocus tube (10 μm focal spot size) is a compact sealed tube that operates at 7 W power with energies up to 70 keV. The non-cooling x-ray CCD-camera is based on a sensor with on-chip integration possibilities and thermal noise compensation. The x-ray image is converted into light by a high-resolution phosphor layer coated onto a plastic film. With a typical integration time of 200–500 ms per frame, this camera produces a near 'real-time' image onto the computer screen. The image format for shadow projections and reconstructed cross-sections consists of 256 × 256, 512 × 512 or 1024 × 1024 pixels. The total acquisition time ranges from 60 sec at low resolution to 2 min at high resolution. The reconstruction time (on a Pentium 200 computer e.g.) ranges from 5 sec per cross-section at low resolution to 1 min per cross-section at high resolution. Reconstruction is based on a convoluted back-projection algorithm. The signal/noise ratio is improved by filtering with a Hamming spectral window (parameter 0.54). The maximum diameter of the object is 60 mm. A spatial resolution of up to 10 μm can be obtained. It should be noted that in case of large objects, the resolution is determined by the number of pixels in the CCD-camera and the number of viewing angles rather than by the focus of the x-ray tube.

The reconstructed information can be presented as object cross-sections or as pseudo 3D-images with possibilities for 'software rotation and cutting'. A special 3D-viewer based on Liquid Crystal

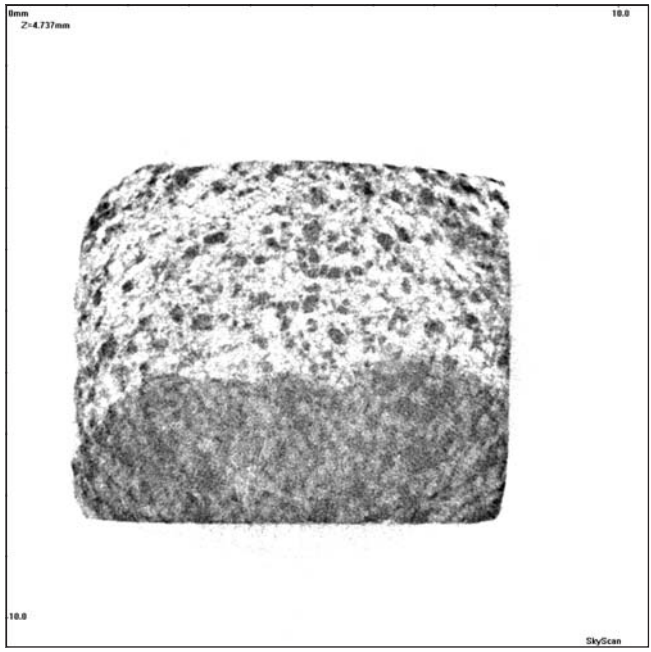

Figure 3. μCT-scan of porous Mesozoic arenitic limestone (light) restored with artificial rock (dark) that consists of a powder mixture of epoxy and arenitic limestone. Skyscan μCT-scan; scale 10 mm; pixel resolution about 12 μm.

Shutters can be used for stereoscopical presentation of the internal object structure as a 'virtual reality'-image on the screen. All software operates under Windows 95 or 2000. It is interactive and user-friendly, and supports image and cross-section printing as half-tone images by any Windows-supported printer and image export in .BMP format. The desktop x-ray microtomograph used in this study is a Skyscan 1072.

3.2 *Advantages and limitations of the new μCT*

The dramatic improvement of resolution down to 10 μm offers a broad range of new applications, inaccessible to medical CT-scanners so far. As both physical and biological deterioration processes operate on a scale of tens of microns, they are expected to fall within the range of resolution of the μCT. This implies that μCT should be able to visualise e.g. micropores or cracks (of about 100 μm) and large individual grains (like quartz or calcite of about the same size in polymineralic rocks). Moreover, all porosity related processes operating in the same range of size, would be accessible for non-destructive μCT-research. This would bring assessment of surface conditions (like roughness and pitting) and processes of adhesion or adsorption (e.g. with resins) in pores within reach (Fig. 3), provided the tomographic density differences between the constituent object parts be large enough to be detected by the μCT.

In contrast with the improved resolution of the μCT, its power of non-destructive quantification of material characteristics is still underexploited. So far, the newly developed μCT-technique has paid little or no attention to the elaboration of quantitative measuring techniques, like internal calibration or standardisation of measured tomographic density values, as it is the case with medical CT-scanners. In order to be able to use μCT for material characterisation through measurements of rock and object properties, it will be of paramount interest to objectively quantify the data acquisition through a series of standardised internal (system related) and external procedures.

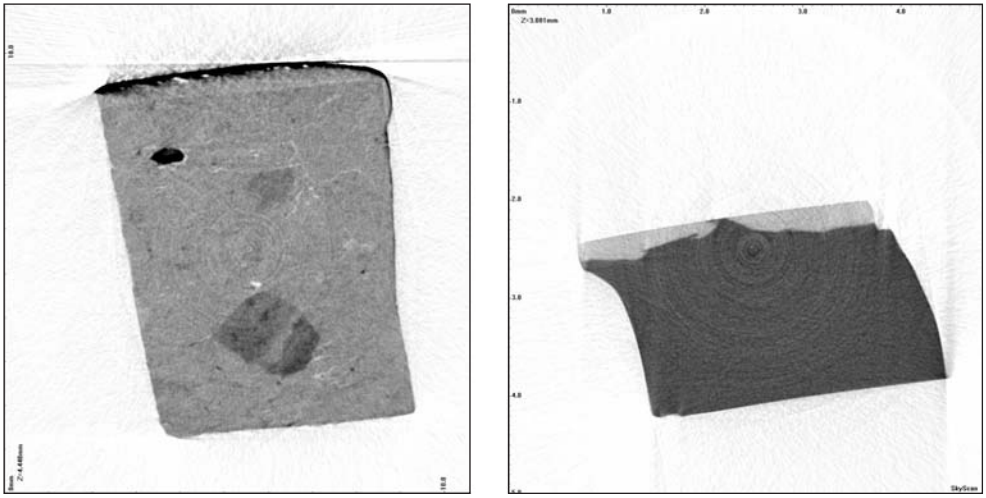

Figure 4. μCT-scans of (left side) a ceramic with high-density compounds (dark grey) and cracks (light grey) in the matrix and with a two-layer enamel at the top; (right side) a glass with a light-grey corrosion layer at the top.

3.3 *Deterioration studies of natural building stones monitored with μCT*

In deterioration studies, it is crucial to have an idea about the penetration depth of the corrosion phenomena and on their nature. Therefore it is important to undertake detailed studies on models that underwent weathering under known conditions. These simulations enable to characterise the various deterioration types and their history through their corrosion signature like weathering depth, change of material properties (e.g. dissolution and consecutive precipitation of neoformations like on Figure 2) or material condition (porosity changes or presence of newly formed cracks, …). This applies for a wide range of materials as demonstrated in the scan on the right side of Figure 4 where hemispherical corrosion phenomena of a hitherto unknown nature are detected in an ancient glass type (in fact with a chemical composition comparable to sandstone) (see also Römich et al. 2003, this volume).

The detailed knowledge of these deterioration phenomena is a prerequisite to any restoration action. Weathered samples of the object should previously have been studied to assess the effectiveness and durability of the planned restoration technique. In this respect, the non-destructive character of the CT- and μCT-technique plays a prominent role as it allows for continuous monitoring throughout the whole deterioration and restoration process. The penetration depth of a resin for consolidation applied on a weathered natural building stone can be visualised and measured through changes in the grey value of scan images from carefully selected ROI. Software manipulation can reconstruct the spatial distribution of the restoration product within the sample's interior and thus verify to what extent the product has promptly invaded zones-under-threat. Comparison of adequately positioned scans of samples before and after treatment enable to assess the porosity changes induced by the impregnation process. As all deterioration and restoration processes are porosity-governed, conditions like pore interconnectivity (or permeability) and surface roughness will influence and determine the success rate of the impregnation procedure. Thanks to the knowledge of characteristics of the natural building stones (like porosity and permeability) and of the restoration product (like in particular its viscosity), it should become possible to adapt the product application according to the needs imposed by maximum restoration effectiveness. The restoration sector would largely benefit from this predictive nature of the μCT-research as it would enable manufacturers and restorers to modulate their products and application techniques in function of scientifically-supported guidelines or needs.

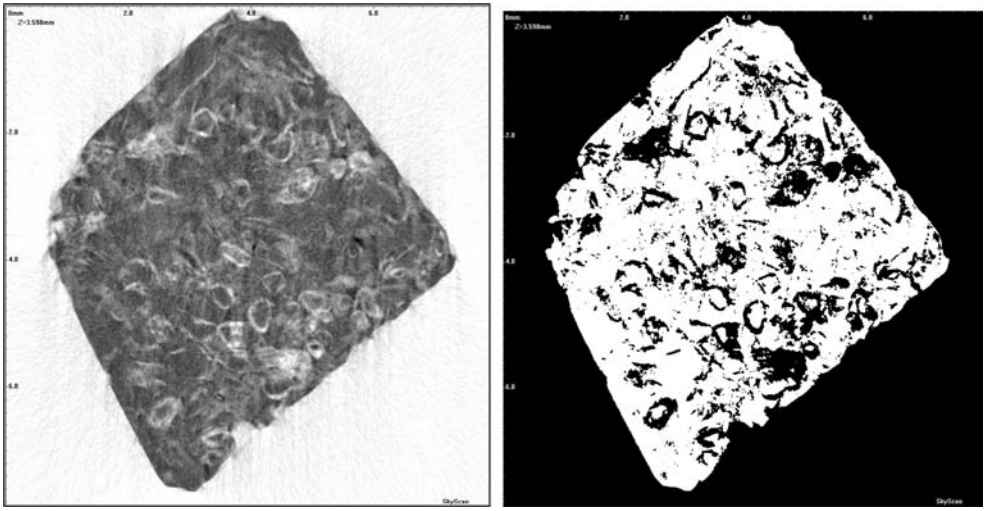

Figure 5. Left: μCT-cross-section of a Belgian natural building stone (Grandcourt limestone, Lower Eocene, Tertiary). Right: Two-phase black and white image of the same cross-section.

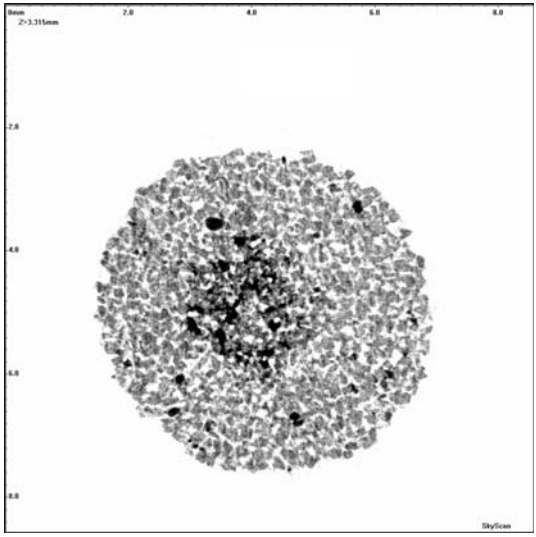

Figure 6. Original grey-scale image of sandstone of Bray (Palaeocene, Tertiary, Belgium) within the centre iodine-solution represented by darker parts.

By applying homemade software, 2D- (distance, angle, perimeter, area, etc.) and 3D-dimensions (partial and total porosity, number of objects, equivalent diameter, etc.) can be measured. Figure 5 shows a cross-section of a Belgian natural building stone (limestone of Grandcourt, Lower Eocene, Tertiary), which contains fine organic debris and ooliths. After image segmentation material and porosity can clearly be distinguished from one another (Fig. 6).

After this segmentation porosity percentage, pore-size distribution, grey-value histogram, … can also be calculated from the 3D-image that is reconstructed from the original cross-sections. These techniques can be used to determine the exact location where weathering occurred. By cross-sectioning samples with μCT, porosity changes can be monitored and visualisation of the weathering depth is possible.

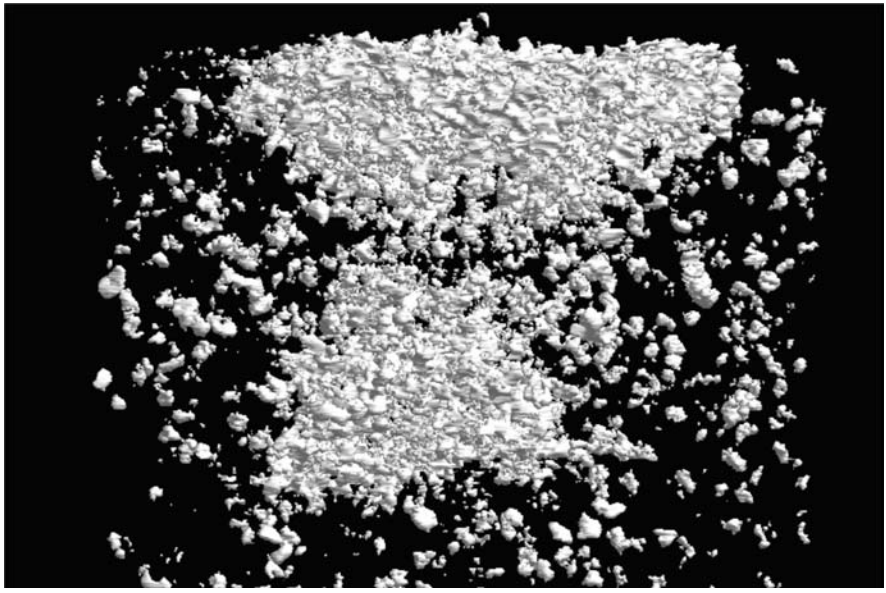

Figure 7. 3D-visualisation of the iodine-solution in the centre of the sandstone of Bray.

The application of restoration products on a weathered stone will induce differences in grey values due to porosity changes. These products will cause an increase in the number of darker grey values due to the replacement of pixels representing empty pore space (and thus low attenuation) by pixels representing pore space filled with restoration products. This increase will enable to visualise how deep these products penetrated into the rock's interior. To increase the contrast between the original rock material and the restoration products, it might be necessary to dope the latter with heavy metals.

Porosity and pore-size distribution play an important role in the durability of rocks. When porosity increases, natural building stones will become more prone to weathering because harmful solutions can penetrate into the pores (Clifton 1980). The pore-size distribution plays an even more important role, the finest pores being decisive. A consolidant that reduces the size of large pores but without blocking them completely can be even more harmful.

Because the rock sample can be scanned before and after treatment, porosity changes due to consolidation can be determined. Figure 6 shows a cross-section of a sandstone impregnated with a iodine-solution. The dark region in the centre of the cross section clearly delineates the volume the solution has migrated into. The 3D-profile of the sample (Fig. 7) clearly illustrates how the iodine-solution invaded the sandstone and the impregnation depth of the iodine-solution can easily be determined. By doping waterrepellents with bromo-silane in a low concentration the localisation of the waterrepellents becomes visible. This enables to characterise in 3D the impregnation depth and the exact localisation of the product inside the stone.

Stone consolidation can be a risky intervention because it mostly is an irreversible process that can cause harmful side effects. Due to these shortcomings a decision whether or not to undertake a consolidation action is a difficult one. However, stone consolidation sometimes is inevitable because of stone decay and of lost cohesion in the exposed surfaces down to a certain depth. A major characteristic of natural building stones is that every rock type has its own petrophysical properties and thus may react differently on certain products. Therefore it is almost impossible that one single product will fulfil all restoration expectations for all types of natural building stones at the same time. If a building or a monument has to be treated with consolidation products, it is useful to analyse and monitor with microtomography a sample specimen taken from the building wall. This should allow to determine depth of weathering and to obtain information on the penetration

depth through comparison of the various possible consolidation products, in order to enable a best choice of product to obtain durable restoration.

4 CONCLUSIONS

CT-scanning is a rapid, non-invasive, quantitative imaging technique with excellent 3D-resolution, useful for petrophysical and fluid- or gas-flow analysis with few restrictions on the type of sample or design of experiments, as medical CT-scanners operate at energies appropriate for research on different rock types. For petrophysical studies, CT provides images of either density or effective atomic number. The images yield porosity, fracture patterns and quantification of complex mineralogy, allowing characterisation of both siliciclastic and carbonaceous rocks and visualisation of macropores and internal fabric. Image analysis of tomographic density contrasts provides clues for comparison of measurement data.

Resolution improvement, data transfer and software manipulation with 4th-generation medical scanners made the study of petrophysical aspects of weathering processes of natural building stones a promising subject for CT-application, provided the attenuation differences of the density-related lithologic changes be great enough.

The development of a new generation of desktop x-ray computed microtomographs (μCT) dramatically improved the resolution with a factor of at least one order of magnitude, bringing within reach the micro-scale at which deterioration and restoration processes operate. These processes largely depend on material properties like porosity and pore interconnectivity (or permeability), and thus largely influence weathering and penetration depth. μCT-research therefore offers a wide range of applications in the Cultural Heritage domain in general and in the built environment in particular through the monitoring of processes active at the micro-scale.

The major advantage of microtomography is its non-destructive character. Samples can be examined in detail by determining their porosity and pore-size distribution. Not only 3D-reconstruction of pores is possible without destroying the specimen, but also monitoring the penetration of resins, eventually doped with heavy-metal compounds to allow better detection. Scanning of samples before and after application of resins enables comparison of images with image-analysis programmes. In this way treatment results are easy to predict or to assess. Also 3D-models of selected relevant features can be created, based on a set of horizontal cross-sections with a small vertical spacing.

The determination of the penetration depth of restoration products used to consolidate or to protect natural building stones from weathering is crucial if the application of conservation products is planned. Every type of natural building stone has its own characteristics and each rock type reacts differently on the various products available on the market. If the penetration depth and the effectiveness of a certain product have to be determined, then the technology of microtomography offers a large potential of application.

Reconnaissance experiments conducted on ceramics and on glass samples demonstrated the large potential of the μCT-technique outside the natural building stone sector thanks to its non-destructive character, thus providing it with a predictive nature to optimise restoration results and products and their applicability. Careful use of this μCT-technique with respect for its limitations (-and preferentially in combination with other non-destructive research techniques like NMR or others-) will contribute to the fundamental knowledge of the operational mechanisms of deterioration processes. This will ultimately lead towards a better understanding and definition of the required restoration.

REFERENCES

Clifton, J.R. 1980. *Stone Consolidating Materials – A Status Report.* National Bureau of Standards Technical Note 1118. Washington DC: US Government Printing Office.

Jacobs, P., Sevens, E. & Kunnen, M. 1995. Principles of computerised X-ray tomography and applications to building materials. *The Science of the Total Environment* 167: 161–170.

Jacobs, P., Sevens, E. & Kunnen, M. 1996. Computerized X-ray tomography (CT): a potential non-destructive research tool for building stone characterisation. In Marcel De Cleene (ed.) *Interactive physical weathering and bioreceptivity study on building stones, monitored by Computerized X-ray Tomography (CT) as a potential non-destructive research tool. Protection and Conservation of the European Cultural Heritage Research Report No 2*: 207–252. Brussels: European Commission.

Jacobs, P., Sevens, E., Vossaert, P. & Kunnen, M. 1997. Non-destructive monitoring of interactive physical and biological deterioration of building stones by computerized X-ray tomography. In P. Marinos, G. Koukis, G. Tsiambaos & G. Stournaras (eds), *Engineering Geology and the Environment* 3163–3168. Rotterdam: Balkema.

Römich, H., López, E., Mees, F., Jacobs, P., Cornelis, E., Van Dyck, D. & Doménech Carbo, T. 2003. Microfocus X-ray computed tomography (mCT) for archaelogical glasses. *This volume*.

Sasov, A. & Van Dyck, D. 1998. Desktop x-ray microscopy and microtomography. *Journal of Microscopy* 191: 151–158.

Cultural Heritage Conservation and Environmental Impact Assessment by Non-Destructive Testing and Micro-Analysis – Van Grieken & Janssens (eds)
© 2005 Taylor & Francis Group, London, ISBN 90 5809 681 5

Microclimate measurements in the Cour Marly, Louvre Museum

D. Camuffo, A. Bernardi, F. Becherini & E. Pagan
CNR-Institute of Atmospheric Sciences and Climate, Padova, Italy

R.A. Lefèvre
LISA, Université Paris, Créteil, France

ABSTRACT: Field surveys have been carried out in the Cour Marly in order to know more about the local microclimate and the movement of the air masses, in relation with the potential impact on conservation. The surveys have been made in the heart of the summer and the winter, when the cooling and the heating systems are operating at the maximum power. During the summer, the Cour is cooled with slits that distribute forced air from the conditioning system. However, warm air penetrates through the corridor in the underground level, forming an uprising flow on the eastern part. During the day-time, the glass ceiling acts as a green-house and entraps the warm air that forms a hot layer topped below the roof. During the night-time, the glass roof cools more and more, and the air coming into contact with it cools too, becomes denser and sinks. In the winter, a natural layering is formed, with warm air at the top floor and cool at the underground one. However, in the afternoon, warm air from the corridor enter the underground level and rises up forming a convective cell. In the summer, cold air conditioned, and in the winter hot air is exchanged between the Cour and the medieval sculpture exhibition rooms through open windows and doors. Paradoxically, the solar radiation is a source of variability less important compared with the other ones, included the system which controls the indoor temperature and humidity.

1 INTRODUCTION

The Cour Marly exhibits marble and limestone sculptures originating from the gardens of the Marly Castle built by Louis XIV near Versailles. The shape is nearly rectangular and the main edge is parallel to the Seine River, mainly oriented east to west, or more precisely rotated 20° clockwise. The Cour, located in the Richelieu Aisle of the New Louvre Museum, Paris, was obtained by closing with a vaulted glass roof a courtyard (Fig. 1). The Cour is divided into three floors connected with stairs. The top floor is C shaped and is surrounded by the French sculpture rooms, V-XVIII century, which is at the same level. Air is freely exchanged through open doors and windows connecting the Cour with the sculpture rooms. The medium floor (ground level) is Y shaped and surrounds the lowest floor (underground level), which is rectangular. In the eastern side, four doors connect the underground level of the Cour with the corridor which leads to the main entrance hall under the main glass pyramid. The Cour has several plants, and the microclimate should fit the needs of people, plants, and statues and should be safe against deterioration processes of different nature, i.e. physical, chemical and biological (e.g. Thomson 1978, De Guichen 1984, Fielden 1994, Camuffo 1998). In particular, the plants, with leaves, humid earth and fertilisers, are a favourable habitat for the growth of micro-organism which may potentially infect the Museum. Fortunately, the situation is kept under control but, prudentially, it is better to know in advance the convective motions and the diffusive potential within this area. For this reason, the study of the Cour was included in a survey to some major European museums, performed within the European project AER (Brimblecombe et al. 1999, Camuffo et al. 1999, 2001, 2002, Sturaro et al. 2003).

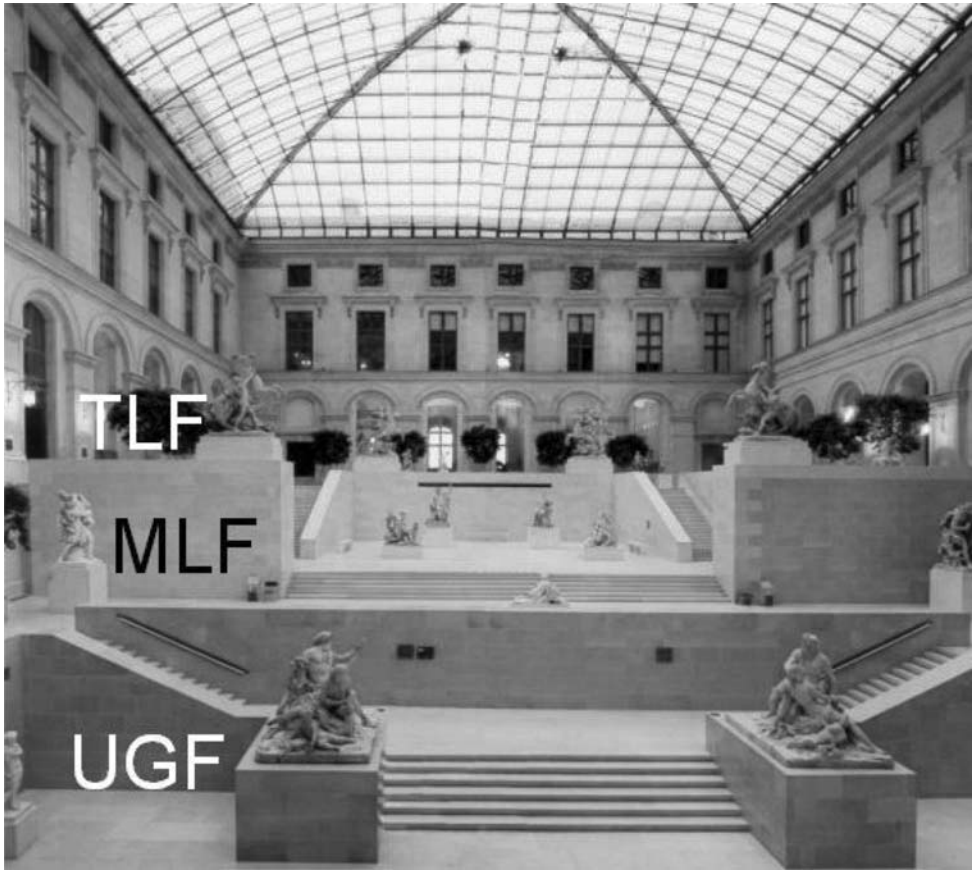

Figure 1. The Cour Marly, in the Richelieu Aisle, viewed from the eastern side. The Cour is covered with a glass ceiling, and is divided into three main floors connected by stairs, i.e.: the Underground Floor (UGF), the Medium Level Floor (MLF) and the Top Level Floor (TLF). The UGF is the smallest one, is rectangular and is connected to a corridor which joins the entrance under the pyramid. The MLF is Y shaped, and is subdivided into two parts by some steps, visible in the mid. On the southern, western, and northern sides, the lower part of the MLF surrounds the UGF and the upper part is surrounded by the TLF. The TLF is C shaped and is connected to the mediaeval French sculpture section. Each floor has statues, plants, and slits for the emission of hot/cold air.

Two campaigns, one in the summer (August 1994) and one in the winter (February 1995) were carried out in order to know the microclimate of the Cour and the dynamics of the indoor air masses. The following variables were observed: air temperature, relative humidity, specific humidity, dew point, air stability from vertical temperature profiles, air movements and fluctuations. Air pollution measurements were taken both inside and outside by the University Paris XII and the results are discussed in another paper (Lefèvre et al. 2003).

The experimental apparatus for the microclimate survey consisted of: (i) a vertical chain of psychrometers for continuous automatic recording of temperature and humidity profiles; (ii) an automatic measurement of the air speed fluctuations, recorded with a hot wire anemometer; (iii) a manual mapping (every two hours) of the temperature and humidity on the horizontal cross sections of the Cour, observing the air temperature and humidity in 51 points at 1.5 m from the floor level. Therefore, the maps showing the humidity and temperature distribution in the Cour do not refer to measurements made in the same plane, but to three different levels, one per each floor. The method

for the ambient diagnostic (Camuffo 1998) was made with manual mapping of air temperature and relative and specific humidity in a horizontal cross section of a room.

2 DATA ANALYSIS

2.1 *Penetration of the solar radiation*

The solar radiation penetrates through the glass roof and falls either on the walls or the floors. When the walls are hit, their surface is heated as well as the air coming in to contact with the hot spots. This warm air immediately rises, but the ascent is stopped by the glass roof, or by a cushion of other warmer air entrapped below the roof. In practice, this situation has no important direct impact on the statues. Different is the case when the solar radiation falls on one or more of the three floors, directly warming the statues and the soil, thus generating convective motions. As large particles tend to undergo a gravitational separation and accumulate near the soil (Reist 1984), eventually depositing and sticking on it, convection generates resuspension, mixing and dispersion in the room of these particles which otherwise would sediment.

The spots of the solar beams on the three floors have been calculated using the astronomical formulae which give the position of the sun in the sky in terms of solar height and azimuth (Robinson 1966, Kondratyev 1969). The intercepts of the solar beams with the architectonic features of the Cour were then calculated, as already made for the Giotto or the Sistine Chapels (Camuffo & Schenal 1982, Camuffo & Bernardi 1995). In the summer, in the early morning, when the sun is still low, the floor is in the shadow. At 9 a.m. the sun appears above the eastern wall and the beams reach the west half of the Cour, both top and medium floor (i.e. the upper part, just in front in Figure 1). After, the rotation of the sun displaces the radiation to the north side (i.e. the right side in Figure 1) of the top and then the medium floors. The sun drops below the western wall without reaching the lowest level. In the winter, the sun never reaches the floors.

2.2 *Summer survey*

In the summertime, when the Museum is cooled by a centralised system, the field survey has shown a daily cycle in the atmospheric variables, but also some features that remain more or less the same from the morning to the evening. The vertical profile of the air temperature (T) shows a natural layering, i.e. temperature level increasing with height, except for the eastern side for the contribution of the underground floor (Fig. 2). In the underground floor, the temperature is determined by the penetration, through four doors, of warm air coming from the corridor, which is connected with the entrance hall. The up-rise of warm air determines a convective motion and a very unstable situation. This warm current, during its ascent meets the two ending parts of the two lateral aisles of the top level floor, generating two localised maximums of T. The maximum in the south aisle (on the left) is reinforced by the advection of warm air through a door which leads to an internal staircase to upper floors. The temperature maximum in the north aisle (on the north) is reinforced by the solar heating which reaches this area from the mid morning to the early afternoon.

The coldest air is found in the top floor, in the western side, emitted by the air conditioning system through slits on the floor. The cold air spreads along the floor for its higher density. In the course of the day, the minimum temperature remains in the western side, but sometimes is found in the northern side, depending on the leakage of cold air from the exhibition rooms on the back.

The specific humidity (SH) was little affected by the presence of visitors, as they have been never too much densely concentrated during the survey, and the room is so large and tall, and the exchange rate so fast, that breathing and transpiration did not alter too much the ambient values. This parameter was used as a tracer, showing the paths of the air masses. In practice, the SH showed that air penetrated from the underground corridor, varied with the concentration of people and in the corridor had values much more elevated than in the Cour, where it was dissipated. The relative humidity (RH) had a distribution which mainly reflected the distribution of T, which was much more marked and well defined.

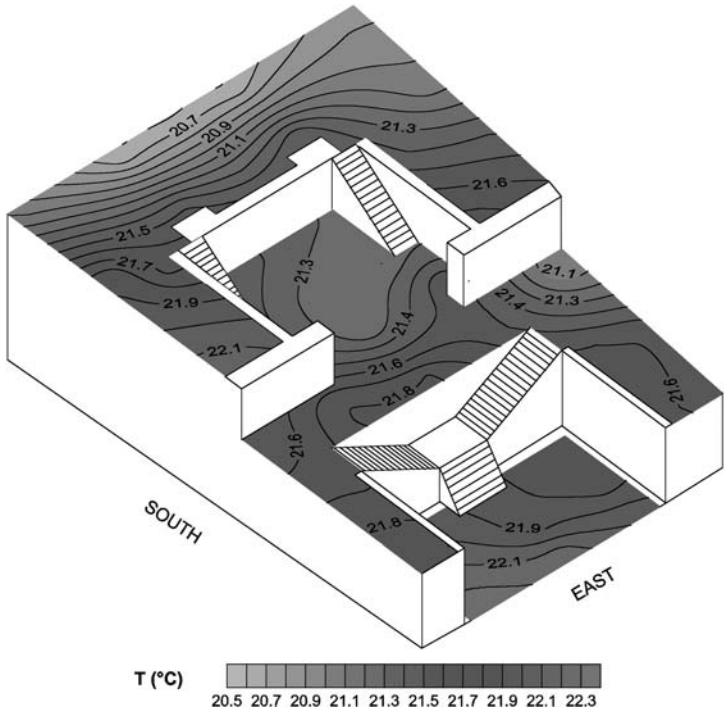

Figure 2. Distribution of the air temperature in the Cour Marly, measured 1.5 m above each floor, the 11 August 1994, 9.00 a.m.
(This figure is presented in the signature in colours at the end of this volume, Appendix, pg. 319)

2.3 *Winter survey*

In the winter, the temperature distribution was different. In the morning and the early afternoon, the underground floor was colder and the top warmer, showing a natural layering of the air (Fig. 3). However, this stable configuration was perturbed in some parts. Warm air was found in the edge of the medium floor, in the south side (left in Fig. 3). The anomaly was a local perturbation due to the presence of a statue just on the flow of hot air from the floor slit. Temporary inflows of warmer, or colder air from the adjacent exhibition rooms were sometimes visible in the top floor. In the afternoon, the situation changed and was more similar to the one already described for the summer. The highest temperature was found in the underground floor, for the warm air from the corridor that leads to the entrance hall. Local departures were due to the variability of the central heating system.

The specific humidity was variable in time and space, but with some common features per each floor in which the Cour is divided. The RH mainly ranged between 40 and 60%. This span would be too large for a general purpose conservation room, but is acceptable for the case of the Cour Marly which only contains stone statues.

2.4 *Indoor air stability*

The vertical profile of the air temperature was measured between the medium and top floor, using four psychrometers at the heights 0.2, 2.2, 3.8 and 6.0 m from the Medium Level Floor, being representative of the situation above the Medium and the Top Level Floors. In the summertime, the profile always showed atmospheric layering (for the cold air released by slits on the floor), which was attenuated for some mixing in the top of the profile especially during the mid daytime. This mixing was favoured by the convective updraft generated over the east floor and the suction of the internal staircase which joins the upper floors of the museum. The daily range was some 2°C

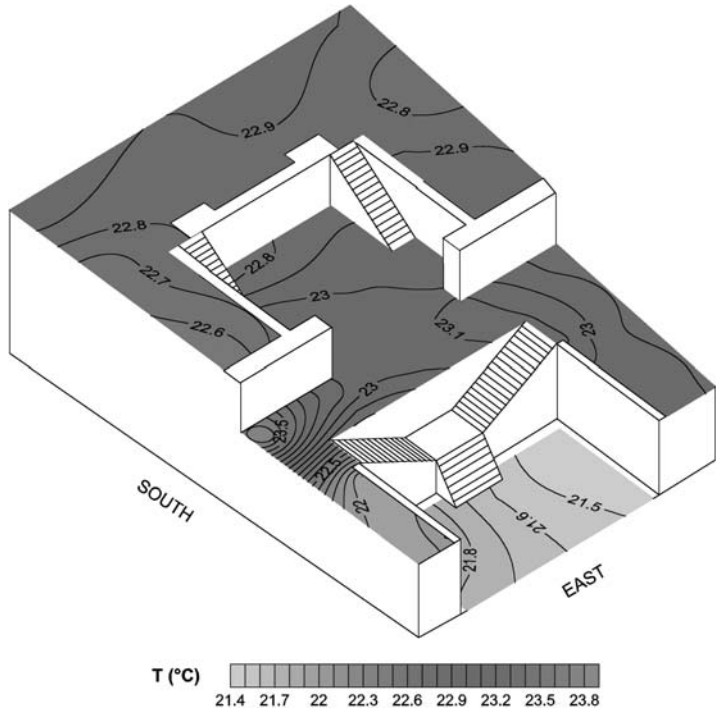

Figure 3. Distribution of the air temperature in the Cour Marly, measured 1.5 m above each floor, the 17 February 1995, 12.
(This figure is presented in the signature in colours at the end of this volume, Appendix, pg. 319)

and followed the external meteorological forcing. The T minimum was around 7.00 a.m. and the maximum around 16.00.

In the wintertime, the vertical temperature profile showed an unstable situation, with warmer air near the floor (hot air is released from slits in the floor) and colder air near the top, the two intermediate levels often having similar values for air mixing. The daily cycles were substantially determined when the operation of the heating system passed from the daytime power to the less powerful night time regime. The central system was unable to strictly control a steady level in RH, and daily cycles of the order of 10% were found.

The previous comments about the temperature measurements gave a first idea about the atmospheric stability, but this information is incomplete of the destabilising effect of the air movements and the generated turbulence. In order to get a more complete description of the existing turbulence including the dynamic state of the air, the measurements of the vertical temperature profile and those of a hot wire anemometer have been combined to compute the Högström ratio S (Högström 1964), used in micrometeorology. This ratio is defined as

$$S = \frac{\overline{\frac{dT}{dz}}}{\langle u \rangle^2}$$

where the numerator is the vertical temperature gradient and its sign determines the sign of S, i.e. typically $S > 0°C\,s^2\,m^{-3}$ for stable temperature layering, $S < 0°C\,s^2\,m^{-3}$ for unstable atmosphere and $S = 0°C\,s^2\,m^{-3}$ for isothermy which practically coincides with neutrality in the case of small height differences, as in indoor environments. The denominator introduces the destabilising effect

of the second power of the mean air speed <u> where the brackets <> indicate the average value. The greater the air speed the greater the destabilisation effect, the greater the turbulence and the lower S. On the other hand, the lower the air speed, the greater the dominance of the temperature profile, the smaller the turbulence and the greater S. In still air $<u> = 0\,m\,s^{-1}$ and $S = \infty°C\,s^2\,m^{-3}$. The temperature gradient was found by considering the vertical temperature profile. In order to measure the typical state of the room, the average difference between the top two levels was used as they were under less influence of the heat given out by the visitors.

During the summer campaign the average values found were: $<dT/dz> = 0.5°C\,m^{-1}$ and $<u> = 0.1\,m\,s^{-1}$, and $<S> = 50°C\,s^2\,m^{-3}$; the lowest value of S, corresponding to the highest value of u was $S = 1°C\,s^2\,m^{-3}$. During the winter campaign the following was found: $<dT/dz> = -0.2°C\,m^{-1}$ and $<u> = 0.0\,m\,s^{-1}$, and $<S> = -\infty°C\,s^2\,m^{-3}$; the peak value of S, corresponding to the highest value of u, was $S = -5°C\,s^2\,m^{-3}$. This parameter, measured between the Medium and Top Level Floors, shows that in summer the thermal stability tends to attenuate the air turbulence, whereas in winter the superadiabatic profile tends to generate convection and turbulent mixing. However, the absolute value of S in winter is small, showing that the instability is modest, not far from neutrality.

3 CONCLUSIONS

The measurements have evidenced that, although the indoor microclimate is controlled in both temperature and humidity, it varies daily and seasonally, being mainly forced by four dominant factors: (i) inflows of cool/hot air from the central system outlets, (ii) exchanges of air through the four doors which connect the bottom floor of the Cour with the corridor, (iii) exchanges of air with the exhibition rooms of medieval sculpture as well as the internal staircase, (iv) solar radiation from the glass ceiling and the nocturnal cooling of the ceiling.

A very common feature in this, and many other Museums, is that the microclimate was essentially based on human well being and business hours. In the summertime, the cooling system tends to counteract the natural daily cycle and in theory this operation tends to reduce the width of the cycles. However, in the winter, the daytime heating is regulated powerful during the business time, reaching a temperature level higher compared with the night time one. It would be better to keep the same level day and night. Paradoxically, the solar radiation, although not negligible, is a source of variability less important compared with the other ones, in particular the system which controls the indoor temperature and humidity.

Both winter heating and summer air conditioning are accomplished with inflows of air from long horizontal slits sited at the edges of the floor and on the walls. The high speed of the airflow facilitates the mixing with the ambient air up to a distance of two or three metres from the outlets. During the summertime the cold air generates atmospheric layering and stability, and the colder and denser air tends to descend to the lower levels of the Cour flowing along the staircases or jumping over the parapets. During the winter, the warm air injected into the Cour tends to rise vertically, forming convective cells and generating instability. However, the instability locally generated by the heating/cooling system, is generally modest, as measured in the Medium and Top Level Floor.

The four doors at the underground level allow free air exchanges between the Cour and the corridor. When the corridor is colder, cold air enters the Cour and forms a cold lake of stable air in the bottom layer. When the corridor is warmer, the hot air enters, gains buoyancy and rises immediately, generating a strong instability on the eastern side above the Underground Floor. This warm updraft rises until it is stopped at a certain height by warmer air layer layered below the hot glass roof, or by the roof itself. Whatever is the level where the vertical motion stops, at that level the air flow diverges horizontally and forces a general sink, or other colder air sinks, closing the cellar motion. The presence of warmer air found at the bottom floor and of colder one on the top floor shows a very unstable situation, so that air is continually moving to reach an equilibrium which is impossible to attain until the forcing factors remain active.

During the day-time and during the night-time, the glass ceiling has two opposite effects. When the solar radiation enters the Cour, the glass acts as a green-house and entraps the warm air that forms a hot layer topped below the roof. In addition, in summer, when the sun is higher on the horizon and solar beams reach the floors, hot spots are found which generate a secondary convection. During the night-time, the glass roof cools more and more, and the air coming into contact with it cools too, becoming denser and sinking. As the roof is shaped as a cloister vault, the cooled air flows along the vaults and sink flowing along the four walls.

Cold air conditioned in the summer, and hot air in the winter, are exchanged between the Cour and the medieval sculpture exhibition rooms through open windows and doors. These inflows constitute a factor of uncontrolled variability. However, the statues in the Cour are not sensitive to these fluctuations.

ACKNOWLEDGEMENTS

The study was conducted on request of Prof. J.R. Gaborit, of the Sculpture Department, Louvre Museum. The authors want to thank Miss Sally Gamble, University College, London, who actively participated to the data analysis during a stage at the Padova University. Travel expenses have been jointly covered by the French-Italian bi-lateral project 'Galileo' and the CNR. Instruments have been purchased in the framework of the Environmental programme of the European Commission, DGXII, contract N°: ENV4-CT95-088 (AER) for the safeguard of our cultural heritage in museums. The problem of heating historical buildings and churches in particular, is being carried out under the project FRIENDLY HEATING (Contract EVK4–2001–00007) which changes heating strategy, i.e.: to heat people, not the entire room.

REFERENCES

Brimblecombe, P., Blades, N., Camuffo, D., Sturaro, G., Valentino, A., Gysels, K., Van Grieken, R., Busse, H.J, Wieser, M., Kim, O. & Ulrych, U. 1999. The indoor environment of a modern museum building, the Sainsbury Centre for Visual Arts, Norwich, UK, *Indoor Air*, 19, 146–164.

Camuffo, D. 1998. *Microclimate for Cultural Heritage*. Amsterdam: Elsevier, 428 pp.

Camuffo, D. & Bernardi, A. 1995. The Microclimate of the Sistine Chapel. Special issue, joint edition European Cultural Heritage Newsletter on *Research*, 9, 7–33 and *Bollettino Geofisico*, 18 (2), 7–33.

Camuffo, D. & Schenal, P. 1982. Microclima all'interno della Cappella degli Scrovegni: scambi termodinamici tra gli affreschi e l'ambiente, pp. 107–209 in: *Ministero dei Beni Culturali ed Ambientali: Giotto a Padova, special issue of Bollettino d'Arte*, Rome: Poligrafico dello Stato.

Camuffo, D., Brimblecombe, P., Van Grieken, R., Busse, H.J., Sturaro, G., Valentino, A., Bernardi, A., Blades, N., Shooter, D., De Bock, L., Gysels, K., Wieser, M. & Kim, O. 1999. Indoor Air Quality at the Correr Museum, Venice, Italy, *The Science of the Total Environment*, 236, 135–152.

Camuffo, D., Van Grieken, R., Busse, H.J., Sturaro, G., Valentino, A., Bernardi, A., Blades, N., Shooter, D., Gysels, K., Deutsch, F., Wieser, M., Kim, O. & Ulrych, U. 2001. Environmental monitoring in four european museums. *Atmospheric Environment* 35/1001, pp S127–S140.

Camuffo, D., Bernardi, A., Sturaro, G. & Valentino, A. 2002. Microclimatic conditions inside the Pollaiolo and Botticelli Rooms in the Uffizi Gallery, Florence. *Journal of Cultural Heritage*, 3, 155–161.

De Guichen, G. 1984. *Climate in Museums*. ICCROM, Rome.

Fielden, B.M. 1994. *Conservation of Historic Buildings*, Oxford: Butterworth.

Högström, U. 1964. An experimental study on atmospheric diffusion. *Tellus*, 16 (2), 205–251.

Kondratyev, Y. 1969. *Radiation in the Atmosphere*. New York: Academic Press, 912 pp.

Lefèvre, R.A., Sinet, I., Bernardi, A. & Camuffo, D. 2003. Characterisation of airborne particulate matter in the Louvre Museum, Paris (in preparation).

Reist, P.C. 1984. *Introduction to Aerosol Science*. New York: MacMillan, 299 pp.

Robinson, N. 1966. *Solar Radiation*, Amsterdam: Elsevier, 347 pp.

Sturaro, G., Camuffo, D., Brimblecombe, P., Van Grieken, R., Busse, H.J., Bernardi, A., Valentino, A., Blades, N., Gysels, K., Deutsch, F., Wieser, M. & Buczolits, S. 2003: Multidisciplinary environmental monitoring at the Kunsthistorisches Museum, Vienna: *Journal of Trace and Microprobe Techniques*, 21 (2), 273–294.

Thomson, G. 1986. *The Museum Environment*. London: Butterworths, 293 pp.

Cultural Heritage Conservation and Environmental Impact Assessment by Non-Destructive Testing and Micro-Analysis – Van Grieken & Janssens (eds)
© 2005 Taylor & Francis Group, London, ISBN 90 5809 681 5

Innovative techniques for the characterisation of encrustation on Pentelic marble from the Parthenon

P. Maravelaki-Kalaitzaki
Ministry of Culture, 25th Ephorate of Prehistoric & Classical Antiquities Chania, Crete, Greece

ABSTRACT: Samples of Pentelic marble from the Acropolis in Athens covered with encrustation have been studied with the aid of several analytical techniques in order to identify the alteration products. The encrustation examined is formed on the marbles: (a) as products of the interaction between the stone surface and atmospheric pollutants (black crusts, $>200\,\mu m$), (b) from treatments conducted in the past for aesthetic and/or protective purposes (orange-brown patina in Parthenon, 100–150 μm thick) and (c) from a brown plaster on the Erechtheion consisting of lime, siliceous sand and inorganic earth pigments ($\sim$100 μm thick). Elemental in-depth profiles of polished sections of samples have been obtained by means of a scanning electron microscope coupled with energy dispersive x-ray analysis (SEM-EDS) and the laser induced breakdown spectroscopy (LIBS). A novel Hyper-spectral imaging (HySI) system, capable of acquiring images in the spectral range 380–1000 nm has also been employed for the non-destructive characterization of the colored samples. X-ray diffraction (XRD) and infrared spectroscopic studies (FTIR) reveal calcium oxalates only in the Parthenon patinas. In the black crusts, the S, Fe, Si and Al SEM-EDS and LIBS profiles exhibit a significant decrease with depth, thus expressing decreasing contamination within the alteration layers, since these elements originate from atmospheric pollution and deposition. The patina samples show homogeneous distribution of Fe, Si and Al both in the chromatic layer and inside (up to a depth of 300 μm from the surface), implying that these elements originate from sources other than environmental loading. The combination of the results of the above-mentioned techniques together with the historical documentation from archives of the Committee for the Preservation of the Acropolis Monuments, leads to the conclusion that alkali silicates have been applied for the preservation of the Parthenon marbles in the past.

1 INTRODUCTION

Black crusts, ranging in thickness between 200 μm and several mm, are formed on historic monuments by the combined action of physico-chemical phenomena (Amoroso & Fassina 1983). Monochromatic layers originating from treatments conducted in the past were observed on several ancient Greek monuments. These layers, called patina layers, resemble homogeneous and extensive coatings ($\sim$150 μm thick), variously colored from brown to orange, over sheltered and rain-washed marble surfaces. Patina layers are also very frequently encountered on Southern European monuments (Lazzarini & Salvadori 1988).

The marble surfaces of the south wall of the Parthenon were covered, on a large scale, with an orange-brown smooth layer perfectly adhering to the substrate. The term "skin of the marble" as proposed by Prof. Arch. M. Korres, will also be used to describe this patina layer (Bouras & Korres 1983). The skin of the marble is generally in a good conservation state and is better preserved on areas of the western and eastern walls of the Parthenon, where less weathering phenomena occur than those observed on the northern and southern parts.

Another brown layer has been observed in limited areas of the Acropolis monuments, e.g. at the Erechtheion, with different macroscopic characteristics from the patina. This brown layer has also been considered in comparison with the skin of the marble.

This study aims at characterizing black crusts and monochromatic layers from the Parthenon, Acropolis, in Athens. The employment of non-destructive or micro-destructive techniques, capable of being performed in-situ, has also been taken into consideration in gaining insights into both the origin and conservation state of the encrustation. The main objectives are to study the patinas under present environmental conditions and to increase our knowledge of their origin.

2 EXPERIMENTAL

Samples with black crusts and patinas, exposed to different micro-environmental conditions were collected from the 1st, 2nd and 3rd columns of the south wall of the Parthenon. Areas partially protected from run-off exhibit a relatively uniform orange coating or black crusts, which become darker the more sheltered the conditions.

The samples were analyzed by applying classical petrographical, mineralogical and chemical techniques in order to obtain different sets of information on the encrustation, as follows:

- Optical microscopy (OM, Zeiss Jenapol-U polarization microscope, for transmitted or reflected light, equipped for microphotography) was performed on polished and thin cross sections, in order to characterize the sequence of layers, the encrustation/marble interface and the macro- and microstructure.
- X-ray diffraction (XRD, PW1710 automatic x-ray diffractometer) of powder scratched from the encrustation was used to determine the mineral phases. CuKα radiation (monochromatised by a high-resolution graphite monochromator) was used with automatic grate, flashing counter and digital recorder. The accelerating voltage and the electric current at the Cu anode were 40 kV and 30 mA, respectively. The scanning speed of the goniometer ($2\theta^\circ\ s^{-1}$) and the scanning step ($\Delta 2\theta^\circ$) were 0.005 and 0.025, respectively.
- Scanning electron microscopy with energy dispersive x-ray analysis (SEM-EDS, Philips 515) facility provided information on the mineral morphology, crystal size, chemical composition and neo-formed phases. The samples were examined and analyzed at 25 KV, working distance 23 mm and tilt angle 20 degrees. An x-ray Si(Li) detector, with resolution 160 eV at 5.45 KeV, was used for the collection of x-ray spectra. Cross sections of the samples before the SEM examination were mounted in polyester resin and polished.
- Fourier-transform infrared spectroscopy (FTIR) was employed to determine the inorganic and organic compounds present in encrustation. FTIR spectroscopy was performed with a Perkin Elmer system 1000. Samples were mixed with KBr and pressed to obtain a pellet with the aid of a vacuum hydraulic press. The spectra were recorded with a spectral resolution of $4\ cm^{-1}$ and 250 consecutive scans were added and averaged before Fourier transform, in order to obtain good signal-to-noise ratio. All spectra were collected in the absorbance mode. As background, the spectrum of the KBr pellet was used.
- Laser Induced Breakdown Spectroscopy (LIBS) was used to probe the relative concentrations of key elements associated with the formation of alteration layers in various depths. The experiments have been carried out at the Laser Laboratory of FO.R.T.H., in Heraklion, Crete, Greece. The methodology and the basic experimental setup of LIBS have been described in detail elsewhere (Anglos 1997, Maravelaki 1997). In the present study the output of a nanosecond Q-switched Nd:YAG laser operating at its fundamental wavelength (1064 nm) was focused by means of a planoconvex lens ($f = +100$ mm) on the sample surface inducing the formation of a micro plume. The emission was analyzed in a 0.32 m flat field spectrograph (TRIAX-320) with a grating of 600 grooves/mm (spectral resolution 0.04 nm) and the LIBS spectrum was recorded on an Intensified Charge Coupled Device (ICCD) detector (Andor Technologies). The detector was gated by means of a pulser in order to discriminate the atomic emission from the continuum background present. Delay time of 1 μs and gate time of 0.5 μs were used in the measurements reported herein. The laser energy density (fluence) employed in the experiments was $7\ J/cm^2$. The pulse to pulse energy variation throughout all measurements performed, was no more than

±5%. It has to be noted that the sample was placed approximately 2 cm in front of the focal point and a relatively wide spot (ca. 1 mm) was used in the LIBS measurement in order to obtain a representative average of the material composition. In this way, the adventitious contribution of local microscopic in-homogeneities due to, for example, inclusions of small particles, was minimized.

Emission spectra were recorded separately for each one of successive laser pulses, and were subsequently analyzed. In this particular study, in view of the actual use of LIBS data in the rapid analysis or in monitoring laser cleaning of encrustation, we tried to employ relatively simple criteria such as spectral intensity ratios for probing changes in relative concentrations. This approach allows the use of simple, and therefore fast algorithms for the on-line control of material removal in a way, which does not slow down the cleaning process. For the plots that show the LIBS relative intensity versus depth from surface, the standard deviation of LIBS intensity was calculated by measuring three identical series of adjacent areas on the sample surface. The overall standard deviation in the relative intensities of the detected elements was estimated to be up to 40% for the black crust and 30% for the patina layers. This relatively high standard deviation is mainly attributed to the in-homogeneity of the encrustation throughout the surface of the sample.

A mechanical profile meter (Perthometer S5P, Mahr-Perthen) was used to measure the extent of material removal upon ablation. It has to be noted that the etch depth per laser pulse is not constant given the variation of the material absorptivity across the encrustation. For this reason depth measurements were made following irradiation of the crusts with 2, 4, 6 etc laser pulses (up to a depth of ca. 320 μm) in order to properly correlate the encrustation thickness with the LIBS depth profile data. In the profile meter the stylus is free to move in a vertical plane and is drawn by the tracer along a measuring path so as it senses the state of the surface. The movements of the stylus tip are transferred to an electrical measuring value converter, where they are changed to electrical measured values portraying the traced profile.

A novel Hyper Spectral Imaging System (HySI) developed at FORTH-instruments by C. Balas (Balas 2003), featuring a notably improved spectral and spatial resolution (380–1000 nm), was also employed in this study. The hardware of the HySI system comprises an imaging detector coupled with a special imaging monochromator, while both are interfaced with personal computer and controlling units. The results of the employment of the HySI in the identification and visualization of monochromatic layers from Parthenon are also discussed herein.

3 RESULTS AND DISCUSSION

3.1 *Black encrustation*

The black crusts occur in areas sheltered from rain where dry decay phenomena prevail. Generally they exhibit an anomalous relief with high friability. FTIR and XRD analyses of black crusts reveal gypsum, residual calcite, silicates, potassium nitrate, iron oxides, mica flakes, quartz and numerous organic constituents in low concentration. The examined crusts, according to the optical microscopy study consist of two successive alteration layers. The inner (100 μm thick) is characterized by the presence of micro- to cryptocrystalline gypsum, while the outer (of thickness >200 μm) by lamellar gypsum, black microparticles, deposits of dust and salt crystals. The inner layer of gypsum, as a result of the sulphation mechanism, has empty cavities and residual particles of calcite, representing the remains after the calcium ions (Ca^{2+}) migration outward from such sites as the cleavage planes and the intergranular boundaries (Skoulikidis & Papakonstantinou 1981).

SEM-EDS analysis of the atmospheric aerosol embedded within the outer layer of dendritic crust reveals several spherical, porous and smooth particles within the samples. These originate from combustion processes, as well as atmospheric and soil-dust deposition. All these particles play an active role in the damage processes affecting stone, since the elemental carbon and the transition metal oxides content contribute to the catalytic oxidation of atmospheric gaseous SO_2 and to the sulphation of calcium carbonate (Elfving et al. 1994).

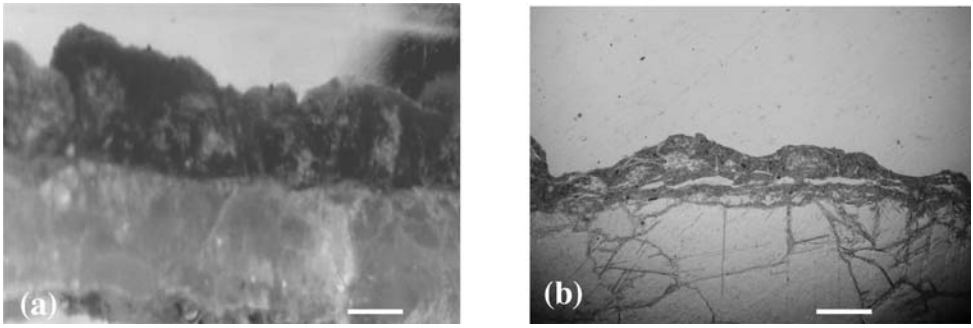

Figure 1. Polished (a) and thin (b) cross sections of patinas (bar = 150 μm) under the polarizing microscope (a: pol. //, 150 *X*, reflected light, b: pol. //, 200 *X* transmitted light).
(This figure is presented in the signature in colours at the end of this volume, Appendix, pg. 320)

3.2 *Patinas*

In general the marble covered with the uniform brown skin appeared well preserved and with no signs of decay in conjunction with the patina. XRD and FTIR analyses carried out on the patina samples showed the presence of: calcium oxalates, monohydrated (whewellite) and dihydrated (weddelite), calcium phosphate, gypsum originating from air pollution along with quartz and feldspars coming from the deposition of wind-borne particles on surfaces. The first finding of calcium oxalate was recorded in 1853 by J. von Liebig (Liebig 1853), who noted the presence of a new mineral, named "thierschite" in samples from the Parthenon. Further analyses indicated the samples to be mainly composed of dried vegetable material, probably lichens and embedded microcrystals of whewellite (Frondel 1962).

Different hypotheses concerning the origin of oxalates have been advanced. According to previous studies reported in the literature, calcium oxalates: (a) can be precipitated from oxalic acid secreted by microorganisms, such as lichens or blue algae which colonize the monuments and/or, (b) can be products of transformation of previous treatments performed with organic substances such as oil, waxes, mono-bicarboxylic acids, egg, etc., used for the protection or polishing of the stone (Fassina 1989).

The results of microscopic analysis indicate that the patina has a uniform thickness and, because of its microcrystalline nature and the presence of organic matter between crystals, it has a protective effect on the marble surface, as indicated by the low amounts of gypsum identified in patinas. Only through those points where the layer is broken mechanically or biologically may water penetrate into the rock and produce expansion when adsorbed by the clay minerals of the matrix. Figure 1 depicts polished (a) and thin (b) cross sections of patinas with the patina layer of approximately ~150 μm thick on the marble, under the polarizing microscope.

The studied samples show in some cases both the mono- and di-hydrated form of calcium oxalate. The weddelite was detected in samples located in areas unaffected by the washing effect of running water. Low humidity levels favour the occurrence of weddelite, even though it is less stable than the whewellite (Manganelli del Fá et al. 1989). Therefore, in samples sheltered from the rain the two oxalates can coexist. In areas experiencing effective washout, however, only whewellite has been detected. Figure 2 illustrates the FTIR spectra of different patina samples with the presence of weddelite (a), whewellite (b) and both of them (c). The identification of the oxalates is based on the different ν_{11} symmetric CO_2 stretching vibrations of weddelite, whewellite and their mixture, obtained at 1327, 1314 and 1319 cm^{-1}, respectively (Petrov & Soptrajanov 1975). In the same Figure the presence of calcite (CO_3^{2-} bend at 877, asymmetric stretch at 1435, and bend at 712 cm^{-1}), alumino-silicates (Si-O stretching vibration at 900–1100 cm^{-1}) and apatite (ν_3 antisymmetric PO_4^{-3} stretching at 1096, 1036 cm^{-1} and ν_4 PO_4^{3-} bend at 605, 475 cm^{-1}) is also evident (Farmer 1974).

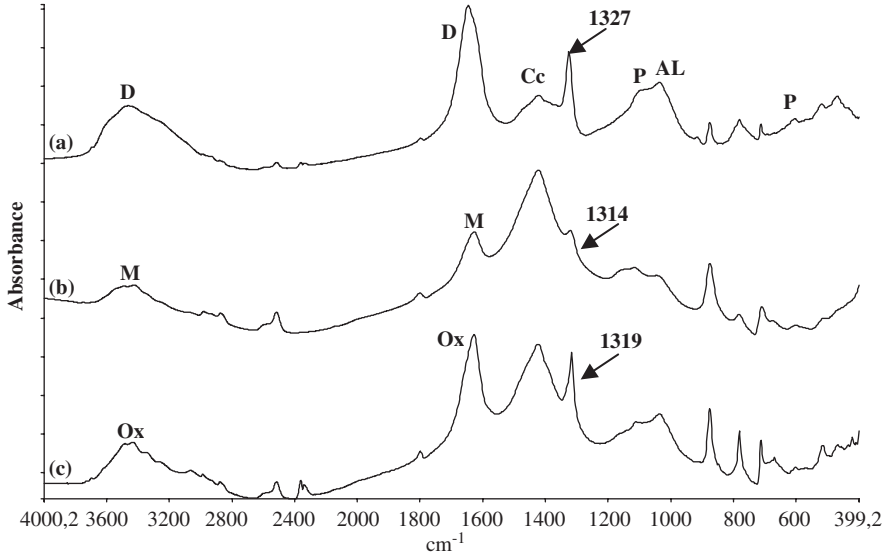

Figure 2. FTIR spectra of patinas from the Parthenon with: (a) weddelite (D), (b) whewellite (M) and (c) weddelite and whewellite (Ox), Cc: calcite, P: calcium phosphate, AL: alumino-silicates.

In the author's opinion patinas are artificial and should be attributed to old protective treatments applied to the surface of the Acropolis monuments. Evidence for this is the absence of any biological remains and the appearance of the patina as a smooth paste homogeneously covering the marble. When the origin of patina is found to be a biological or natural kind, the contact between the stone and the patina is gradual and a intermeshing of both surfaces occurs. Phosphorus (approximately 8%, see Table 1) and calcium oxalates have been linked to the application of milk-derived and calcium caseinate-based protective treatments (Ransome 1856). The transformation of calcium caseinate could occur, due to micro organisms present in the medium or by other soil micro organisms deposited on the surface of the monuments at a later stage. The colour in the patinas can be explained by the presence of iron contained in ochre, since the Pentelic marble does not itself contain enough iron-ore impurities to form coloured patinas, by leaching out and concentrating on the surface. Indeed, a small amount of brown ochre may have been added to reduce the brightness of the coating (Ransome 1856).

3.3 *Monochromatic layers from the Erechtheion*

The orange-brown layers located on the Erechtheion consist of calcite, alumino-silicates, iron oxides and gypsum, as evidenced by XRD and FTIR studies. In these layers, oxalates and phosphorous are absent. In Figure 3a the infrared spectrum of the orange layer of the Erechtheion was reported along with its cross section under the polarizing microscope (Fig. 3b). In the infrared spectrum of this layer aluminosilicates and gypsum prevail with characteristic absorptions at 1033 and 1115 cm^{-1}, respectively. An optical microscopy study of cross sections of samples reveals an encrustation with a homogeneous thickness of $\sim$100 μm, in which airborne particulate was incorporated. The orange layer resembles a fine plaster, which was intentionally applied and mainly composed of calcite with siliceous aggregates and ochres of orange and brown colour.

3.4 *Results of SEM-EDS and LIBS analyses*

SEM-EDS quantitative analyses of the black crusts, patina samples and orange layers from the Erechtheion, as well as of un-weathered Pentelic marble are shown in Table 1. Each concentration

Table 1. Quantitative analysis of encrustation (black crusts, patinas and orange coatings from the Erechtheion) and fresh Pentelic marble and enrichment factor analysis of layers of encrustation vs. un-weathered marble and soil-dust (Ti as indicator element).

% Oxides	Al_2O_3	SiO_2	P_2O_5	SO_3	Cl_2O_5	K_2O	CaO	Fe_2O_3	TiO_2	MgO
Pentelic marble	0.30	0.33	<0.01	<0.01	<0.01	0.12	98.5	0.11	0.03	0.53
Patina at 100 μm	4.72	28.5	6.51	3.22	0.33	1.64	51.1	3.12	0.20	0.74
SD (No samples = 8)	(±0.17)	(±1.31)	(±0.94)	(±1.43)	(±0.05)	(±0.05)	(±1.11)	(±0.61)	(±0.02)	(±0.05)
EF/marble*	2	14	975	480	45	2	<1	5	1	<1
EF/soil-dust**	1	2	87	197	44	2	36	5	1	1
Patina at 200 μm	5.17	21.5	10.21	0.97	0.23	1.71	55.0	4.62	0.11	0.53
SD (No samples = 8)	(±0.21)	(±1.01)	(±1.23)	(±0.11)	(±0.05)	(±0.04)	(±1.23)	(±1.12)	± 0.01)	(±0.06)
EF/marble	5	22	3060	291	60	5	<1	14	1	<1
EF/soil-dust	3	3	272	119	59	5	77	14	1	1
Black crust at 100 μm	3.07	8.27	0.72	35.74	0.33	1.62	46.0	3.03	0.52	0.71
Sd (No samples = 7)	(±0.34)	(±1.26)	(±0.04)	(±1.56)	(±0.08)	(±0.56)	(±2.09)	(±0.21)	(±0.05)	(±0.03)
EF/marble	1	2	42	2142	18	1	<1	2	1	<1
EF/soil-dust	<1	<1	4	879	18	1	13	2	1	<1
Black crust at 200 μm	3.62	10.1	1.94	33.4	0.13	1.23	47.3	2.03	0.22	0.31
SD (No samples = 7)	(±0.32)	(±2.07)	(±0.65)	(±2.09)	(±0.03)	(±0.42)	(±2.45)	(±0.12)	(±0.02)	(±0.02)
EF/marble	2	5	285	5006	15	2	<1	3	1	<1
EF/soil-dust	1	1	25	2054	15	1	33	3	1	<1
Erechtheion at 100 μm	5.69	15.9	0.72	8.33	0.14	1.15	64.3	3.15	0.21	0.43
SD (No samples = 4)	(±1.18)	(±2.13)	(±0.21)	(±1.67)	(±0.02)	(±0.74)	(±1.89)	(±0.65)	(±0.07)	(±0.09)
EF/marble	3	8	105	1245	15	2	<1	5	1	<1
EF/soil-dust	1	1	9	511	15	2	45	5	1	1

$$* \text{EF/marble} = \text{EFcrust(X)} = \frac{\text{(X/Ti)crust}}{\text{(X/Ti)marble}} \quad ** \text{EF/soil-dust} = \text{EFcrust(X)} = \frac{\text{(X/Ti)crust}}{\text{(X/Ti)/soil-dust}}.$$

value corresponds to an analyzed area of 30×200 μm, which resulted from the analyses of 5 successive areas of 30×40 μm parallel to the surface of the sample and at the designated depths. Therefore the values of Table 1 can be considered as average values for the total areas of the 30×200 μm with standard deviations calculated to be about: 25% for the crusts and 15% for the patina layers. It is apparent that these standard deviations represent the natural in-homogeneity of the encrustation. The analytical contribution to this is low and varies from 5% for MgO and CaO to 0.2% for Al_2O_3.

From the results reported in Table 1 it becomes evident that the encrustation at 100 μm of depth from surface have higher concentrations of S, Si, Fe and Al relative to a depth from surface of 200 μm. Phosphorus, however, shows the higher values in the inner part of patinas. The enrichment factor analyses of the above layers of crusts versus the un-weathered marble and soil-dust composition (using Ti as indicator element) are also reported in Table 1 (Sabbioni 1995). The elements showing enrichment factors lower or close to 1, have an origin that must be attributed either to the un-weathered marble or to the soil-dust deposition.

The results show that in black crusts Ca and Mg mainly originate from the un-weathered marble. Si and Al are certainly due to the soil-dust deposition, while Fe, P, Cl and S originate from other

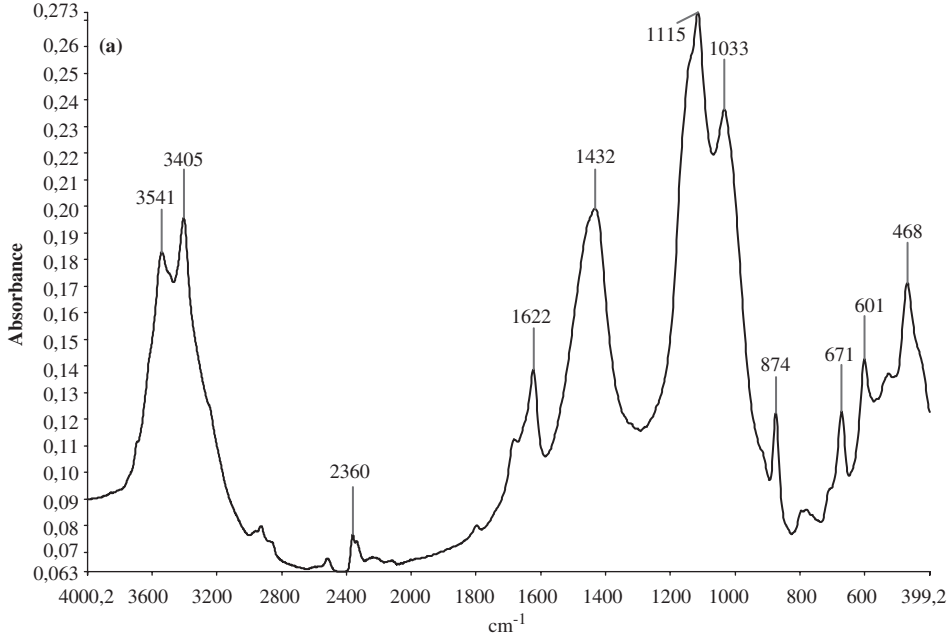

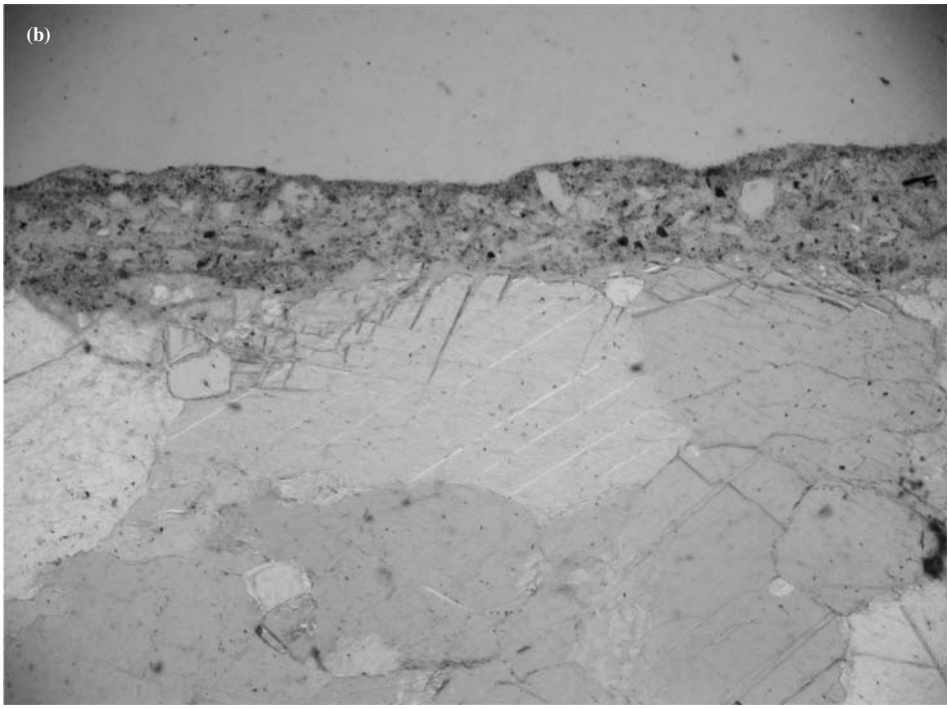

Figure 3. (a): FTIR spectrum of orange layer from Erechtheion, with calcite (1432, 874 cm^{-1}), gypsum (3541, 3450, 1622, 1115, 671, 601 cm^{-1}) and alumino-silicates (1033, 468 cm^{-1}); (b): Cross section of the same sample, where the presence of plaster with orange and brown ochres is evident (pol. //, 100 *X*).
(This figure is presented in the signature in colours at the end of this volume, Appendix, pg. 320)

sources, such as atmospheric pollution. In the inner part of patinas Si, Al, Fe, K and P show higher enrichment factors than those of the outer patinas, orange layers and black crusts. This variation results from the different genesis of patinas, orange layers and black crusts; in the latter two, elements of soil-dust deposition and environmental pollution have been incorporated into the crust matrix. In the patinas, however, the application of products containing compounds with the enriched elements had occurred.

Selected LIBS spectra obtained within the encrustation at different pulse numbers (corresponding to depth from the surface) and on un-weathered marble, are shown in Figure 4a. In the spectral range employed (230–330 nm), emission lines confirm the presence of the marble constituents Ca and Mg, as well as Fe, Si and Al of the main contamination elements (Maravelaki et al. 1997, 2001 and references therein). For a better presentation of the spectra, the absolute intensities of the individual spectra have been normalized with respect to the intensity of the Ca II line at 315.21 nm. This choice relies on the relatively stable concentration of calcium across the encrustation in relation to the other detected elements (see values of Table 1) and on a necessary differentiation of all LIBS spectra in a meaningful way.

According to the mechanical profile meter measurements the second, fifth and seventh pulse correspond to a depth from the surface of 80, 260 and 380 μm, respectively (Fig. 4a). Emission from Fe II, Si I and Al I is present up to a depth of 320 μm, thereafter reaching barely detectable values. The LIBS emission spectrum at 380 μm resembles that of the un-weathered marble. The absence of Fe II, Si I and Al I in the emission spectrum of the un-weathered marble confirms that these elements originate from atmospheric pollution. Magnesium and calcium originate from marble, as also indicated by the enrichment factor analysis. Sulphur lines are not detectable in the spectral range employed in this work.

The depth profiles of calcium, silicon, aluminium, iron and sulphur obtained by SEM-EDS and LIBS analyses, are compared in Figures 4b and c. In particular, Figure 4b shows the % concentrations of Fe, Si, Al and S relative to the Ca detected by SEM-EDS in relation to the different depths from the surface. Likewise Figure 4c depicts the variation in the relative intensity of selected LIBS emission lines for Fe II (274.8 nm), Si I (288.2 nm) and Al I (308.2 nm) with respect to the Ca I line (at 300.8 nm). This is expressed as a function of depth, obtained by probing the sample with successive laser pulses (Maravelaki et al. 1997, 2001 and references therein). Normalization is done with respect to emission from Ca, as this is the major component in all samples examined.

The in-depth SEM-EDS quantitative chemical composition of the black crust exhibits considerable variability. At a depth of 160 μm from the surface, the SEM-EDS profiles of Fe, Si and Al show a maximum value, the S profile a minimum one, and after this point they decrease in-depth (Fig. 4b). It can be assumed, that at this depth a aggregation of deposited alumino-silicates occurs. The LIBS profiles of Fe, Si, and Al show maximum values in the range of 100 to 200 μm, followed by a decreasing trend (Fig. 4c).

Even though the analyses were performed in adjacent areas of the same sample, certain discrepancies between the SEM-EDS and LIBS profiles are observed and can be attributed most likely to lack of homogeneity of dendritic crusts concerning both encrustation thickness and chemical composition. Nevertheless, both techniques clearly indicate the thickness of the alteration layers, which is correlated to the optical microscopy observations. In this crust, the internal alteration layer consisting of micro-crystalline gypsum and calcite, starts at a depth of 200 μm from the surface. This is marked by the constant content of S, as detected by SEM-EDS, and the decrease or elimination of the other contamination elements as indicated by both techniques.

LIBS spectra have been recorded for fifteen consecutive pulses in the spectral range of 230 to 330 nm on the patina samples. Figure 5a shows the LIBS emission spectra of patina samples obtained after a layer removal of 70, 140, 200 and 300 μm corresponding to second, sixth, ninth and fifteen laser pulses, respectively. These show atomic emission lines of Si I, Fe II, Mg II, Mg I, Ca I, Al I and Ca II. Emissions from Fe II, Si I and Al I are present in all the analysed area (depth of ~300 μm from the surface). Figures 5b and c show the SEM-EDS profiles of Fe, Si, Al and S and

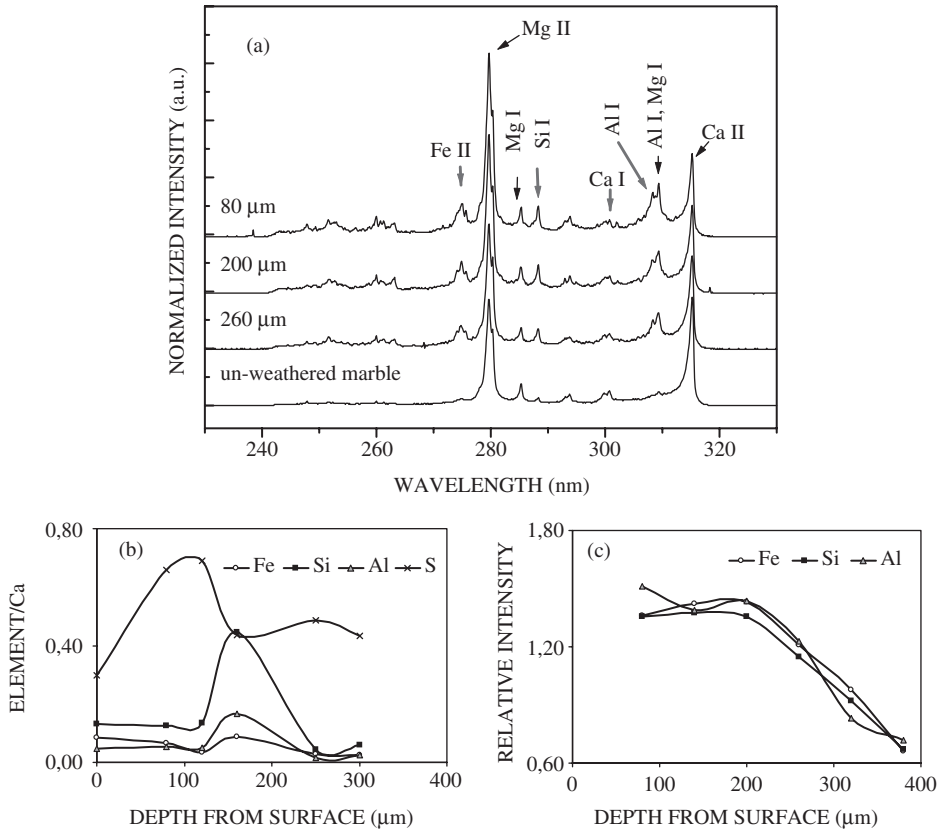

Figure 4. (a) The LIBS spectra of the ablated material from a black crust at different depths from the surface and un-weathered Pentelic marble, normalized to the intensity of Ca II line at 315.2 nm, (b) Relative elemental concentrations of Fe, Si, Al and S with respect to Ca detected by SEM-EDS and (c) Relative intensities of atomic emission lines for Fe II (274.8 nm), Si I (288.2 nm) and Al I (308.2 nm) with respect to the Ca I line (at 300.8 nm) obtained by LIBS vs. depth from the surface, for the black crusts.

the LIBS profiles of Fe, Si and Al, respectively, obtained in the previous analyzed area of the patina samples. The Fe, Si, Al and S SEM-EDS profiles are quite uniform up to depth of 300 μm from the surface, indicating that the patina has a relatively stable composition in this area (Figure 5b). Furthermore, the observed high concentrations and enrichment of Fe, Al and Si in the range from 150 up to 300 μm of depth from the surface (see Table 1) suggest that these elements originate from sources other than atmospheric deposition, such as past conservation treatments consisting of compounds rich in Fe, Al and Si (Lazzarini & Salvadori 1988).

In the LIBS analysis, however, the Si I, Fe II and Al I profiles show a decreasing trend up to a depth of 150 μm, keeping their intensities in significant and practically constant values for the next analyzed crust (Figure 5c). According to the results of the thin section study in optical microscopy, the patina shows a thickness of approximately 150 μm. The decreasing trend of the LIBS elemental profiles is associated with the area of the patina, while in the area below the patina constant intensities of the analyzed elements were observed. Conclusively, the profiles of Fe, Si and Al obtained in both techniques compare only after a depth of 150 μm from the surface. A possible explanation for this differentiation between LIBS and SEM-EDS profiles may be related to the different composition of patina compared to black crusts, which in turn determines the laser-substrate interaction (Maravelaki et al. 2001).

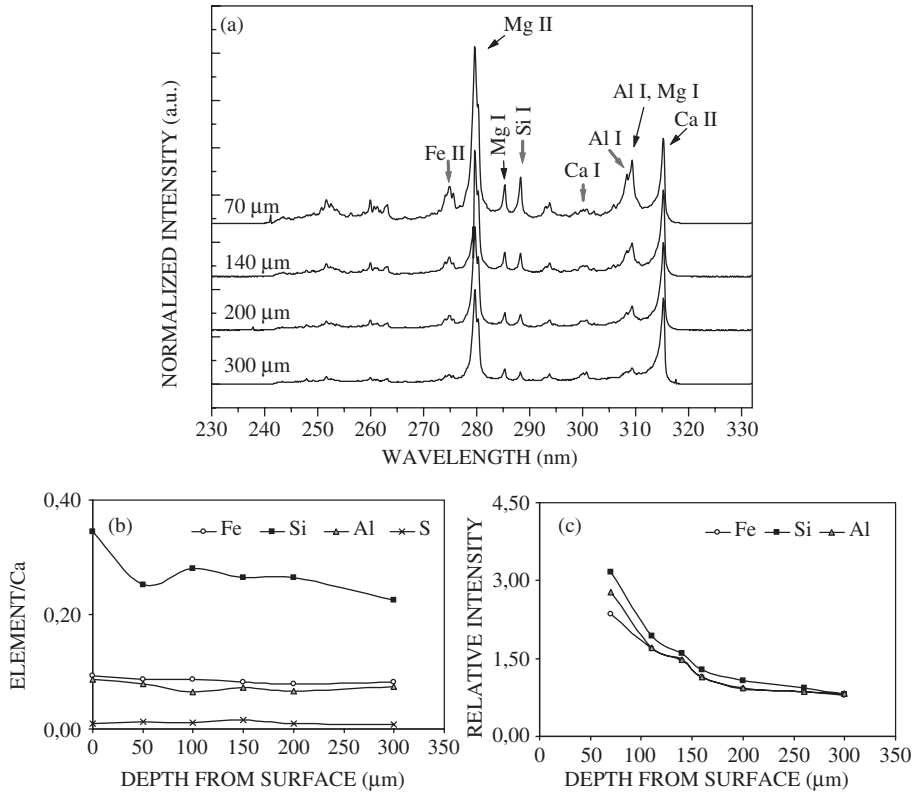

Figure 5. (a) The LIBS spectra of the ablated material from a patina at different depths from the surface, normalized to the intensity of Ca II line at 315.2 nm, (b) Relative elemental concentrations of Fe, Si, Al and S with respect to Ca detected by SEM-EDS and (c) Relative intensities of atomic emission lines for Fe II (274.8 nm), Si I (288.2 nm) and Al I (308.2 nm) with respect to the Ca I line (at 300.8 nm) obtained by LIBS vs. depth from the surface, for the patinas.

3.5 *Results of the hyperspectral imaging analysis*

Figure 6 illustrates a series of selected spectral images of monochromatic layers from the Acropolis monuments, three with patina from the Parthenon (A, B and C) and the fourth (D) with the brown coating from the Erechtheion. It can be clearly seen that the patina samples show no significant visual differences in the examined spectral images. However, wavelengths shorter than 520 nm are absorbed differently by part of the Erechtheion layer as it appears darker than the rest. This differentiation in wavelengths longer than 520 nm becomes progressively indistinguishable.

In all the examined spectral images, the presence of various compounds and the in-homogeneity of this coating become evident, since constituents absorb differently, a finding that has not been recorded in the patina samples. These findings indicate that by exploiting the spectral characteristics and differences between the examined coatings one or more spectral bands can be determined, thus indicating the best result. This analytical method contributes towards distinguishing chromatic layers of homogeneous structure, such as patinas, and in-homogeneous coatings resembling plasters consisting of calcite and sand, such as those applied on the Erechtheion.

3.6 *General considerations*

Microscopic examination of the cross-sections of patina samples showed the existence of a thin brown layer of optically isotropic material on the underlying stone. x-ray maps of the outer 70 μm

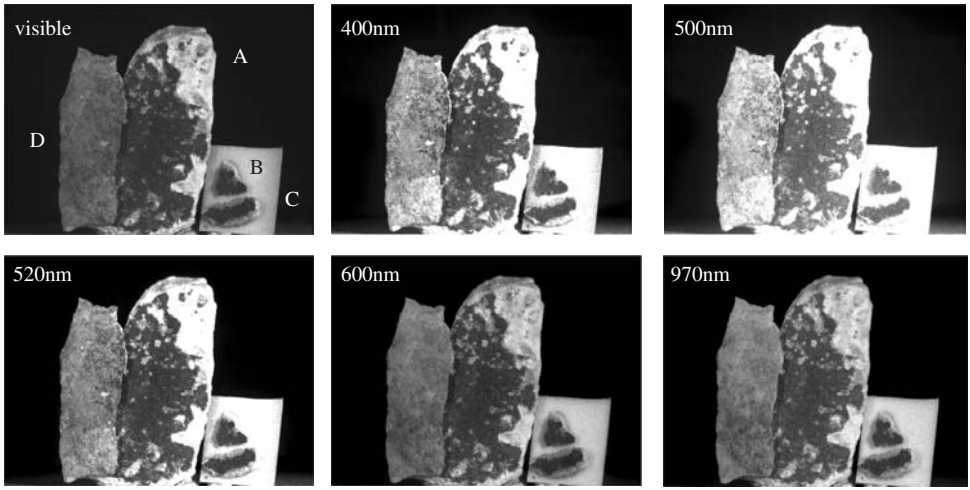

Figure 6. Selected spectral images of monochromatic layers from the Acropolis monuments, with patina from the Parthenon (A, B and C) and an orange coating from the Erechtheion (D). In the wavelengths shorter than 520 nm, part of the orange coating (D) appears light, while patinas (A, B and C) show no differences in all the spectral images.
(This figure is presented in the signature in colours at the end of this volume, Appendix, pg. 321)

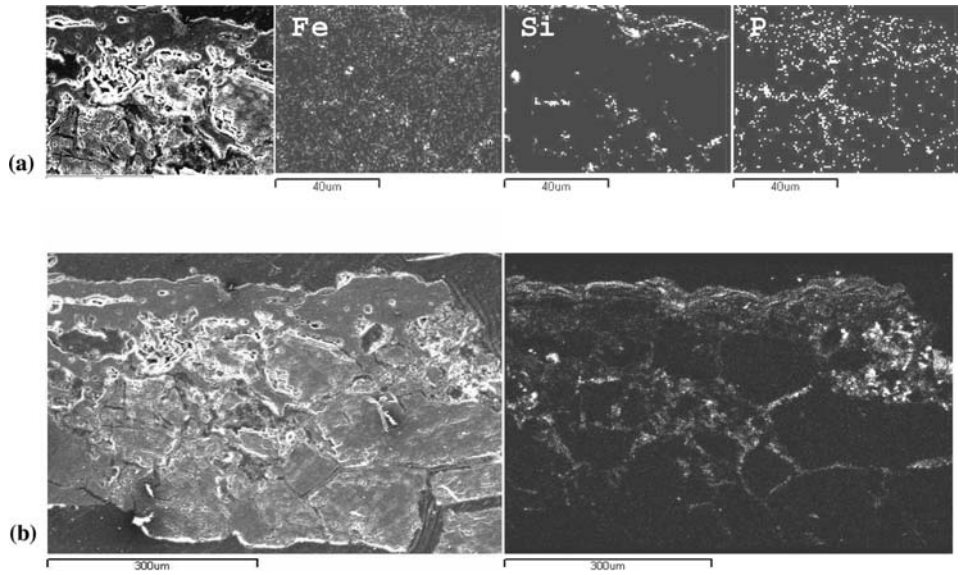

Figure 7. (a) x-ray maps showing the distribution of Fe, Si and P on a patina sample (bar = 40 μm) and (b) x-ray map of silicon in all the analyzed area (bar = 300 μm).

of the patina (Fig. 7a) show a uniform distribution of Fe confirming thus, that iron was intentionally added to the applied treatment in order to reduce its brightness. Si and P, as illustrated in Figure 7, are similarly distributed both in the outer 30 μm and the inner 40 μm of the patina.

Figure 7b illustrates the Si x-ray maps in all the previously analyzed area of approximately 300 μm of thickness. This distribution indicates that Si is present not only in the area of patina (the outer 100 μm) but also occurs around the calcite crystals located in the area below the chromatic

layer of patina. This leads to the assumption that Si originates not only from the deposition of wind-borne dust and/or the presence of inorganic earth pigments, but also from silicon-based treatments, which result in the occurrence of Si around the calcite crystals.

Combining the results of the above mentioned analytical techniques with the optical microscopy study the following conclusions can be drawn:

1. The patina samples from the Parthenon represent remnants of previous treatments and differ from the brown layers of the Erechtheion regarding their composition, microstructure and spectral imaging characteristics.
2. In the patina samples different compounds, such as oxalates, phosphorous and silicon are related to different treatments. Oxalates and phosphorous may be associated with decomposition products of organic matter intentionally applied to the surface for aesthetic and/or protective purposes. These findings are in agreement with previous studies carried out on samples located on other areas on the Parthenon by Papakonstantinou (1994) and Kouzeli et al. (1989).

This study is more focused on the silicon presence and its origin, which constitute one of the most relevant aspects of this study. The high amounts of silicon, its considerable enrichment in the inner part of marble and distribution around the calcite crystals exclude a unique origin from the air-borne particulates deposited on the marble. Otherwise, neither the existence of silicon in the inner parts of patina nor its occurrence around the crystals of calcite in the area below the patina can be explained. Furthermore, the enrichment factors of silicon in the patinas compared with those of black crusts and the Erechtheion layers support the hypothesis of an application of a silicon-based product, presumably to ensure the impermeability of the marble surface. Archive studies of documents of the Committee for the Preservation of the Acropolis Monuments confirm this hypothesis. These documents report on a proposal for a pilot application of alkali silicates, according to the method “silicatisation des pierres”, as proposed by the French chemist Frédéric Kuhlmann in 1873 (Mallouxou-Tufano 1998). No other information about any eventual application has been recorded in the archives.

4 CONCLUSIONS

In order to characterize the encrustation on Pentelic marble from the Parthenon, several specific features principally related to the gradient in the relative concentration of contamination elements were taken into account. In performing SEM-EDS and LIBS analyses of the black encrustation on Pentelic marble, two alteration layers were identified. In the studied samples, the external layer ranging in thickness from 100 to 200 μm consists of varied concentration alumino-silicates, gypsum and particulates, as indicated by the gradients both of S concentration and Fe II, Si I and Al I relative intensities. The internal layer, of ∼100 μm of thickness, is almost homogeneous in composition characterized by a stable quantity of S, as well as limited presence of Fe II, Si I and Al I emission.

In patina-samples both techniques reveal rather stable values of Fe, Si and Al below the patina layer of approximately 150 μm in thickness. Low concentrations of S occur over all the analyzed area. The innovation presented here is the use of LIBS as a means of in-situ quick compositional characterization of black crusts and patinas providing the stratigraphic trends in the emissions of elements originating both from environmental pollution and previous treatments.

HySI enables the contrast enhancement between compounds in the multi-layer encrustation based on their spectral differences. The ability to tune the imaging wavelength enables selective imaging of the different chromatic layers, since the absorption coefficient of the compounds is in general, wavelength dependent. In this study a differentiation in the absorption was recorded between brown-orange homogeneous patinas and brown plasters applied to the Erechtheion. The use of this imaging technology for the recognition of the encrusted layers contributes to the discrimination of the chromatic layers.

The elemental composition and enrichment factor analysis of encrustation reveals its origin, since the studied encrustation has been similarly affected by environmental conditions. The high enrichments of Si, P and Fe on the patinas indicate an origin from sources other than the environmental loading. Based on all the above-mentioned analyses and on historical documentation from archives of the Committee for the Preservation of the Acropolis Monuments, the use of alkali silicates has been proven for the preservation of the Parthenon marbles.

ACKNOWLEDGEMENTS

The author is grateful to the Central Archaeological Council and the Committee for the Preservation of the Acropolis Monuments for permitting sampling from the Parthenon and publication of this study. She is indebted to Emeritus Prof. Th. Skoulikidis and E. Papakonstantinou (Committee for the Preservation of the Acropolis Monuments) for many helpful discussions and suggestions. She wishes also to thank Dr. V. Kilikoglou (Laboratory of Archaeometry, National Center for Scientific Research "Demokritos") for facilities in SEM-EDS analysis, Prof. C. Balas, Dr. V. Zafiropulos, Dr. D. Anglos and Prof. K. Fotakis (Foundation for Research and Technology Hellas, Institute of Electronic Structure and Laser-FO.R.T.H.-I.E.S.L.) for facilities in LIBS analysis, as well as A. Scala and Prof. G. Sabatini (Sienna University, Environmental Science Department, Institute of Environmental Geochemistry and Conservation of Stone Cultural Heritage) for the preparation and the study of the thin sections.

REFERENCES

Amoroso, G. & Fassina, V. 1983. *Stone Decay and Conservation. Materials Science Monographs* 11, Amsterdam: Elsevier.

Anglos, D., Couris, S. & Fotakis, C. 1997. Laser diagnostics of painted artworks: laser induced breakdown spectroscopy of pigments. *Applied Spectroscopy* 51: 1025–1030.

Balas, C., Papadakis, V., Papadakis, N., Papadakis, A., Vazgiouraki, E. & Themelis, G. 2003. A Novel hyperspectral imaging apparatus for the non-destructive analysis of objects of artistic and historic value. *J. of Cultural Heritage* 4(S1): 330–337.

Bouras, X. & Korres, M. 1983. *The Restoration of the Parthenon*, Athens.

Elfving, P., Panas, I. & Lindqvist, O. 1994. Model study of the first steps in the deterioration of calcareous stone. III. Manganese and iron mediated sulphation of natural stone. *Applied Surface Science* 78: 373–384.

Farmer, V.C. 1974. *The Infrared Spectra of Minerals*, London: Mineralogical Society Monograph 4.

Fassina, V. 1989. Le pellicole ad ossalato – Lo stato delle conoscenze attuali. In: *The oxalate Films: Origin and Significance in the Conservation of Works of Art; Proc. Intern. Symp., Milan, 1989*. Milan: Centro CNR Gino Bozza.

Frondel, C. 1962. Thierschite (= whewellite). *American Mineralogist* 47: 786–790.

Kouzeli, K., Beloyannis, N., Tolias, C. & Doganis, Y. Monochromatic layers with and without oxalates on the Parthenon. In: *The oxalate Films: Origin and Significance in the Conservation of Works of Art; Proc. Intern. Symp., Milan, 1989*. Milan: Centro CNR Gino Bozza.

Lazzarini, L. & Salvadori, O. 1988. A reassessment of the formation of the patina called scialbatura. *Studies in Conservation* 34: 20–26.

Liebig, J.V. 1853. Ueber den Thierschit. *Liebig Annal. Chemie Pharm.* LXXXVI: 113–115.

Mallouxou-Tufano, F. 1988. *The Restoration of Ancient Monuments in Greece (1834–1939). The work of the Archaeological Society at Athens and the Greek Archaeological Service.* Athens: Library of the Archaeological Society at Athens.

Manganelli del Fa', C., Camaiti, M., Borselli, G. & Maravelaki, P., Variazione del grado di idratazione dell'ossalato di calcio in funzione delle condizioni termoigrometriche. In *The Oxalate Films: Origin and Significance in the Conservation of Works of Art; Proc. Intern. Symp., Milan, 1989*. Milan: Centro CNR Gino Bozza.

Maravelaki, P., Zafiropulos, V., Kilikoglou, V., Kalaitzaki, M. & Fotakis, C. 1997. Laser-induced breakdown spectroscopy as a diagnostic technique for the laser cleaning of marble. *Spectrochimica Acta B* 52: 41–53.

Maravelaki-Kalaitzaki, P., Anglos, D., Kilikoglou, V. & Zafiropulos, V. 2001. Compositional characterization of encrustation on marble with laser induced breakdown spectroscopy. *Spectrochimica Acta* B 56: 887–903.
Papakonstantinou, E. 1994. *Physical-Chemical Observations of the West Frieze of the Parthenon, Study for the Restoration of the Parthenon.* Athens: Ministry of Culture, Committee for the Preservation of the Acropolis Monuments.
Petrov, I. & Soptrajanov, B. 1975. Infrared spectrum of whewellite. *Spectrochimica Acta* 31(A): 309–316.
Ransome, F. 1856. Stone Artificial, Stone Colouring, Stone Preserving. British Patent 2267.
Sabbioni C. 1995. Contribution of atmospheric deposition to the formation of damage layers, *The Science of the Total Environment* 167: 49–55.
Skoulikidis, Th. & Papakonstantinou-Ziotis, P. 1981. Mechanism of sulphation by atmospheric SO_2 of the limestones and marbles of the ancient monuments and statues. *Br. Corrosion J.* 16: 63–69.

Cultural Heritage Conservation and Environmental Impact Assessment by Non-Destructive Testing and Micro-Analysis – Van Grieken & Janssens (eds)
© 2005 Taylor & Francis Group, London, ISBN 90 5809 681 5

New insights on the chemical nature of stone yellowing produced after laser cleaning

Maria Gaviño & Bernardo Hermosin
Instituto de Recursos Naturales y Agrobiologia, CSIC, Apartado, Sevilla, Spain

Veronique Vergès-Belmin & Witold Nowik
Laboratoire de Recherche des Monuments Historiques, Champs-sur-Marne, France

Cesareo Saiz-Jimenez
IRNAS, CSIC, Avda Reina Mercedes, Sevilla, Spain

ABSTRACT: Laser cleaning of stone monuments is nowadays a procedure widely used in restoration. However, one of the criticisms to the method is the controversial yellowing of the stone. In this paper, we present evidence that aliphatic and aromatic carboxylic acids and phenols, which are components of a yellow fraction isolated from black crusts, are not affected by Nd:YAG 1064 nm laser irradiation. We deduce that these water soluble compounds, which always impregnate the stone surface underneath black crusts, cannot be removed by the laser beam when the crust is eliminated. This means that, at least, part of the yellowish aspect after laser cleaning, is linked to these remaining compounds.

1 INTRODUCTION

Air pollution results in the deposition of a variety of organic and inorganic compounds on the surface of historic monuments. The most common form of deposit is the so-called black crust, which is formed by the sulphation of stones and consists of gypsum, carbonaceous particles, calcite, quartz, etc. (Saiz-Jimenez 1993). Black crusts cover marbles, limestones, sandstones, granites, terracota statues in urban environments, and have been observed on bronze statues, tiles, bricks, and glass windows as well. Cleaning interventions including mechanical cleaning, washing methods and poultices containing chemical agents have been used for removal of the crusts, but usually they also affect to the underlying materials.

Laser cleaning of stone monuments and statues is nowadays a procedure widely used in restoration. Research has shown that a Q-switched Nd:YAG laser is capable of removing black encrustations resulting from atmospheric pollution in a variety of materials without damage to the underlying stone (Cooper 1998, Lanterna & Matteini 2000). The laser provides 8 ns pulses of near infrared (1064 nm) radiation which are preferentially absorbed by the stone soiled layers. This gives rise to a rapid increase in surface temperature of the black crust which can lead to removal of the material (Cooper 1998).

Yellowing after laser cleaning was hypothesized to be due to the uncovering of a layer existing below the soiling. In fact, when limestone or marble sculptures were cleaned, yellowish calcium oxalate residues are often revealed beneath gypsum black crusts (Vergès-Belmin & Bromblet 2000). Moreover, stones and terracotta statues may contain brownish residues of oxidized organic matter below a black crust and laser cleaning will keep this coloration (Larson & Cooper 1996). Cooper (1998) reported that the laser appeared to be unable to remove the greasy component from soiling on a stone sculpture, but rather caused it to yellow. In some other cases, yellowing was assigned

to the presence of iron-rich spheres of 100–200 nm arising from the transformation of hematite (Klein et al. 2001).

Vergès-Belmin & Dignard (2003) reported that the discoloration of black crusts is linked to the use of a low fluence and only a limited part of the crust is removed – probably the black carbon soot – through a vaporisation process, without any action on the other components of the soiling (other yellowish oxidized organic compounds, mineral particles, etc.).

In this paper we studied the composition of the organic compounds present in the black crusts from the basilica of Saint Denis, France. We were able to separate such components in different fractions by column fractionation and one of the fractions resulted to be yellow. Herewith we report the effect of Q-switched YAG laser irradiation on the black crusts and we present evidences that laser irradiation do not affected to the yellow fraction. We discuss the chemical nature of the yellow fraction to the light of the obtained data.

2 MATERIALS AND METHODS

The black crusts used in this study were collected from the basilica of Saint Denis, France, located in the Paris suburbs, in an area heavily submitted to industrial pollution until the sixties (Plate 1a, see at the end of the article). Saint Denis basilica is considered a good representative of early Gothic architecture. Many original forms of the Gothic style are found in this basilica such as the cross rib vault and flying buttresses, which represented structural innovations.

The basilica originated as a small chapel at the graveyard of Saint Denis in the 5th century. After the 7th century, under the Merovingian era Saint Denis became the royal abbey church. The third basilica of Saint Denis was rebuilt in 775 of Carolingian era. Abbot Suger built the western façade and the chancel between 1137 and 1144. It is said that the nave, including the upper part of the choir and transept, was reconstructed probably by Pierre de Montreuil and others from 1231 to 1281. In 1805, Saint Denis began to be restored by Napoleon. The architect François Debret, indulged his own taste in repairing and refurbishing the building between 1815–1846. Viollet-le-Duc restored the basilica from 1846 to 1870. In 1998 the portal of the north transept was cleaned using a Q-switched YAG laser by the company Groux S.A. A yellowing effect associated to laser cleaning appeared in the stone (Plate 1 b), similar to that reported for other French cathedrals cleaned with laser (Bromblet et al. 2003). This yellowing was also noticed in laser cleaning of stone pieces irradiated in the laboratory (Plate 1 c).

Saint Denis black crusts were collected on the walls and vaults of a limestone arch, located on a terrace at the top of the west front of the monument. Samples were ground in an agate mortar before laser irradiation. Three cycles of laser irradiation were carried out on the crushed crusts through the glass cover of a petri dish, to avoid powder lose. After each cycle, the black crust powder was homogenised. Laser irradiation produced a colour change in the powder (Plate 1 d). All the cleaning tests reported here were performed with a Q-switched YAG laser from B.M. Industries, model NL102, fitted with an articulated arm and a specific hand piece for stone cleaning purposes. The main characteristics of this laser were: wavelength 1064 nm, range of power density 55 to 131 MW/cm^2, pulse duration 8 ns, pulse frequency 1–20 Hz. This kind of laser was used on many French monuments (Vergès-Belmin & Dignard 2003).

For solvent extraction, 20 g of black crusts were ground in an agate mortar and extracted in a Soxhlet apparatus with dichloromethane-methanol (2:1) during 70 h. The extracts were evaporated under vacuum at low temperature (below 40°C) and redissolved in dichloromethane-methanol (2:1). The resulting extract was chromatographied using a silica column, eluting with hexane (fraction I), hexane-dichloromethane (1:1) (fraction II), dichloromethane (fraction III), and finally with methanol (fraction IV). Fraction IV had a yellow to red-brown colour, depending on the concentration. The chemical composition of fractions I to IV were reported elsewhere (Gaviño et al. 2003).

TMAH thermochemolysis was accomplished as described by Saiz-Jimenez et al. (1994). Briefly, a few mg of sample were deposited in a Curie-point small hollow ferromagnetic cylinder (temperatures 300 or 590°C) and wetted with 5 µl of a 25% w/w methanolic solution of TMAH.

The cylinder was slightly dried with a N_2 flow and immediately inserted in the pyrolyser. The analysis was performed in a Fisons instrument GC 8000/MD 800, using a 30 m × 0.25 mm TRB-5HT column (film thickness 0.1 μm), to which a Fischer 0316 Curie-point pyrolyser was coupled. The GC oven was programmed from 50°C to 280°C, at a rate of 5°C min^{-1}. This temperature was held for 100 min and then to 310°C at 20°C min^{-1}, where the final temperature was held for 2 min.

In the analytical procedure used in this work, the carboxylic acids were recovered as the corresponding methyl esters and the hydroxyls as methoxyls. Throughout this paper they are referred to as acid and hydroxyls, their original forms, rather than as derivatised methyl esters and methoxyls. No attempt was made to identify all compounds but the most abundant or representatives, therefore, the lists of compounds were undoubtedly incomplete.

3 RESULTS AND DISCUSSION

Laser yellowing has been reviewed recently (Vergès-Belmin & Dignard 2003, Zafiropulos et al. 2003). In the literature it has been reported that black crust can be discoloured, but not removed in certain conditions. This was associated to the energy used. Fluences lower than 1000 mJ/cm^2 are sufficient for eliminating black crust layers. The lowest fluence able to eliminate the black crusts seems to be about 600 mJ/cm^2 (Vergès-Belmin & Dignard 2003). In our laser test we applied 800 mJ/cm^2, enough to produce a cleaning effect, similar to those black crusts on monuments.

Formation of black crusts using diesel soot on a limestone was carried out under laboratory conditions. It was observed that after many cycles of wetting and drying a light brown to dark yellowish colour, due to a soluble fraction, was present on the limestone surface, beneath the induced black crusts. This fraction could be the responsible of the yellowing of the stone after laser cleaning, because it cannot be removed at the fluences used, as it was tested in the laboratory. In fact, the yellow fraction was deposited on an alabaster probe and left for solvent evaporation. Once dried, the probe was laser irradiated, in the same conditions used for monument laser cleaning, with no apparent colour change (Plates 1 e, f). Therefore, the research was directed to the isolation and study of this yellow fraction.

The yellow fraction was isolated using column fractionation and resulted to be soluble in methanol. This fraction, as deduced from TMAH thermochemolysis and gas chromatography-mass spectrometry study, was mainly composed of fatty acids, benzenepolycarboxylic acids and aliphatic dicarboxylic acids (Fig. 1, Table 1).

Recently, it has been reported the finding of water soluble organic compounds formed by soot oxidation. This water soluble fraction contains polycarboxylic acids and it was suggested that the structure of these compounds is analogous to that of naturally occurring macromolecular polyacidic compounds humic and/or fulvic acids (Decesari et al. 2002). These results were considered consistent with previous findings concerning the presence of water soluble macromolecular humic-like substances in atmospheric aerosol samples (Havers et al. 1998). According to the data herein reported, unpublished data from our laboratory, and literature data, polycarboxylic acids are present in soots and because its solubility migrate into the stone matrix, beneath the black crusts deposit, thus forming a yellow layer which seems not to be affected by laser cleaning.

In a separate experiment, the ground black crusts from Saint Denis basilica had a grey to light grey color. After irradiation it was observed that the powder adopted a pale yellowish brown color (Rock-Color Chart 1984) as observed in Plate 1 d. Figure 2 shows the TMAH thermochemolysate of the black crusts, before and after laser irradiation. Major series of compounds found in both samples were fatty acids, benzenepolycarboxylic acids, aliphatic dicarboxylic acids, and alkanes. Other series of compounds were phenols, polycyclic aromatic hydrocarbons and a few nitrogen derivatives (Table 2).

Figure 3 shows the mass fragmentogram of fatty acids (m/z 74) from the black crusts, before and after laser irradiation. Figure 4 presents the mass fragmentogram of benzenepolycarboxylic acids (m/z 136 + 163 + 221 + 279 + 337) under similar treatment. No differences were found in these classes of compounds before and after laser irradiation, which indicates that laser cleaning did

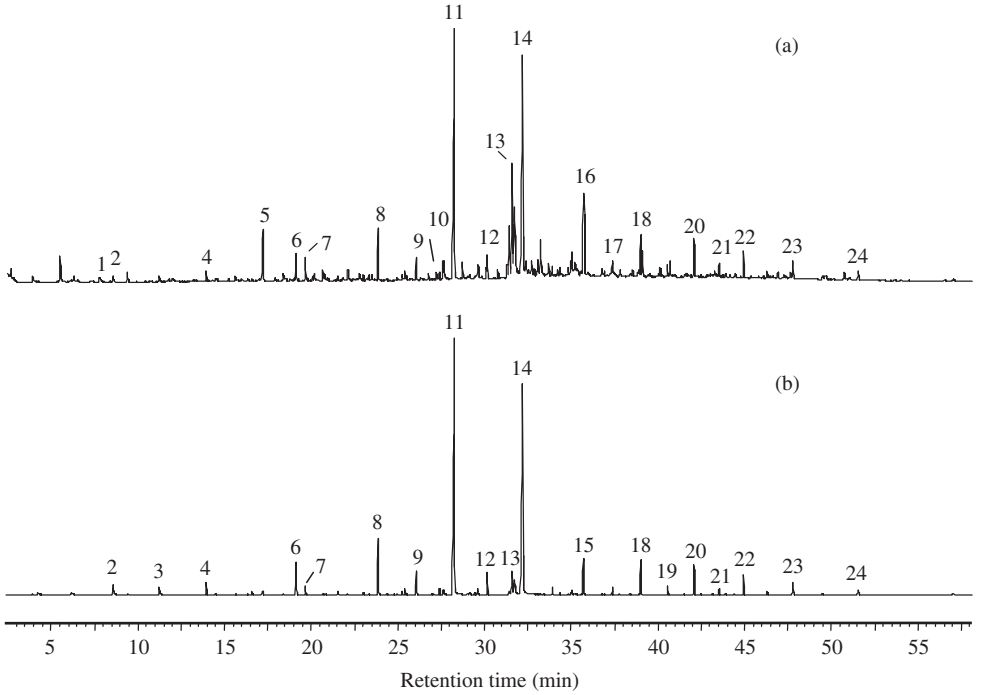

Figure 1. TMAH thermochemolysate of the yellow fraction isolated from Saint Denis black crusts. (a) TIC chromatogram. (b) Mass fragmentogram of fatty acids (m/z 74). Peak identification refers to Table 1.

Table 1. Major compounds identified in Figure 1.

Peak	Compound	Peak	Compound
1	Benzoic acid	13	*n*-Octadecenoic acid
2	*n*-Octanoic acid	14	*n*-Octadecanoic acid
3	*n*-Nonanoic acid	15	*n*-Eicosanoic acid
4	*n*-Decanoic acid	16	Dehydroabietic acid
5	1,2-Benzenedicarboxylic acid	17	*n*-Heneicosanoic acid
6	*n*-Dodecanoic acid	18	*n*-Docosanoic acid
7	1,9-Nonanedioic acid	19	*n*-Tricosanoic acid
8	*n*-Tetradecanoic acid	20	*n*-Tetracosanoic acid
9	*n*-Pentadecanoic acid	21	*n*-Pentacosanoic acid
10	*n*-Hexadecenoic acid	22	*n*-Hexacosanoic acid
11	*n*-Hexadecanoic acid	23	*n*-Octacosanoic acid
12	*n*-Heptadecanoic acid	24	*n*-Triacontanoic acid

not affect these carboxylic acids-containing compounds. Similar laser irradiation on the isolated yellow fraction deposited onto an alabaster matrix showed no changes with respect to aliphatic and aromatic carboxylic acids nor colour changes (Plates 1 e, f).

Bromblet et al. (2003) reported that laser cleaning usually achieves a homogeneous removal of the black crust (whatever its thickness), uncovering a yellowish stone surface which corresponds to the epigenic gypsum layer due to sulphation. From our studies it could be suggested that the yellowish colour of the uncovered epigenic gypsum layer is due to yellow organic compounds derived from soot and/or black crusts, as already supposed by Vergès-Belmin & Dignard (2003).

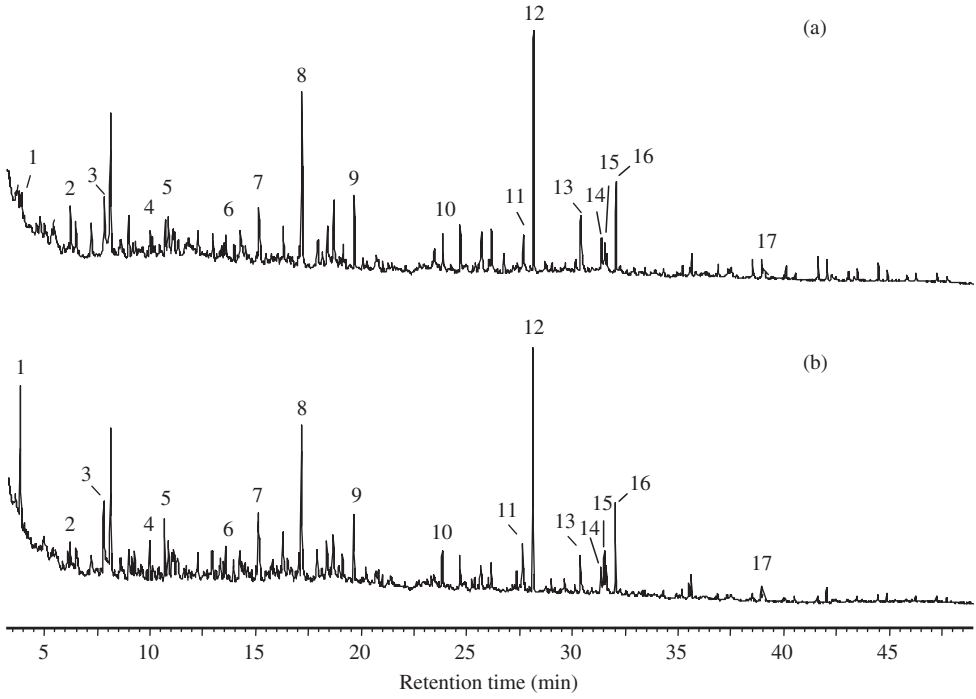

Figure 2. (a) TMAH thermochemolysate of Saint Denis black crusts. (b) The same after laser irradiation. Peak identification refers to Table 2.

Table 2. Major compounds identified in Figure 2.

Peak	Compound
1	Ethenylbenzene
2	2-Butenedioic acid
3	Benzoic acid
4	Naphthalene
5	Methylbenzoic acid
6	1,3-Dimethoxy-2-hydroxybenzene
7	1,3-Dimethoxy-4-hydroxybenzene
8	1,2-Benzenedicarboxylic acid
9	1,9-Nonanedioic acid
10	*n*-Tetradecanoic acid
11	*n*-Nonadecane
12	*n*-Hexadecanoic acid
13	Fluoranthene
14	Pyrene
15	*n*-Heneicosene
16	*n*-Octadecanoic acid
17	*n*-Docosanoic acid

As a matter of fact, we have shown that these compounds are not reactive to the laser irradiation, and thus may remain unaltered on the epigenic gypsum layer after crust elimination. Abrasive methods, which are not selective, generally remove totally or partially the epigenic layer, thus removing also the yellow compounds that lay on its surface or impregnate it.

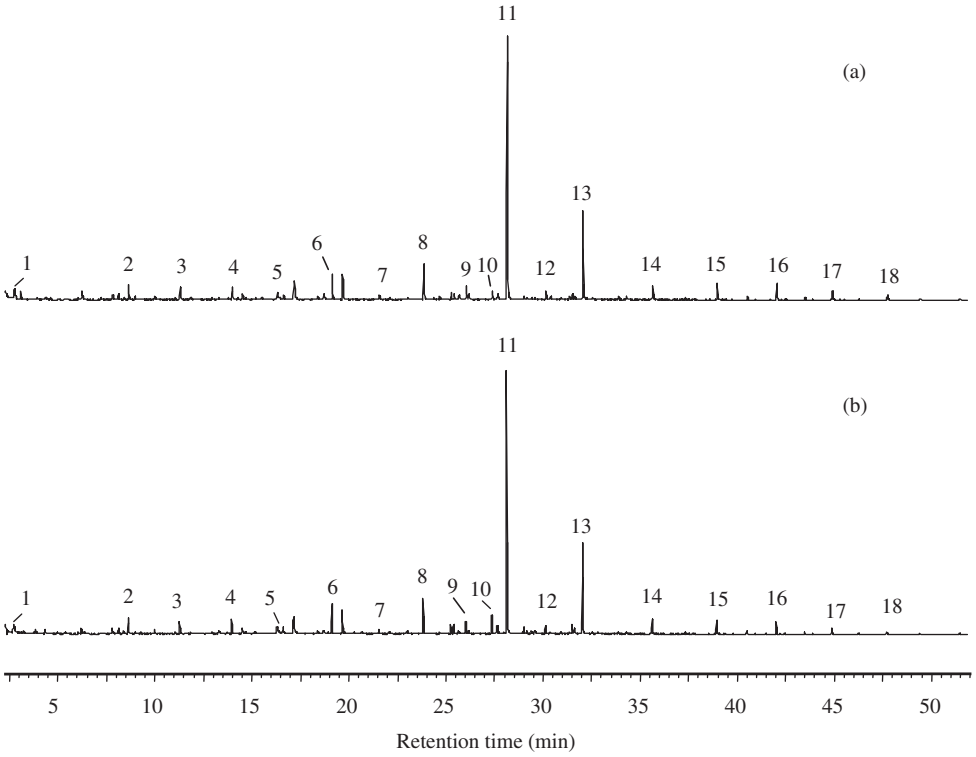

Figure 3. TMAH thermochemolysate of Saint Denis black crusts. (a) Mass fragmentogram of fatty acid (m/z 74). (b) The same after laser irradiation. Peak identification refers to Table 3.

Table 3. Major compounds identified in Figure 3.

Peak	Compound
1	*n*-Pentanoic acid
2	*n*-Octanoic acid
3	*n*-Nonanoic acid
4	*n*-Decanoic acid
5	*n*-Undecanoic acid
6	*n*-Dodecanoic acid
7	*n*-Tridecanoic acid
8	*n*-Tetradecanoic acid
9	*n*-Pentadecanoic acid
10	Methylpentadecanoic acid
11	*n*-Hexadecanoic acid
12	*n*-Heptadecanoic acid
13	*n*-Octadecanoic acid
14	*n*-Eicosanoic acid
15	*n*-Docosanoic acid
16	*n*-Tetracosanoic acid
17	*n*-Hexacosanoic acid
18	*n*-Octacosanoic acid

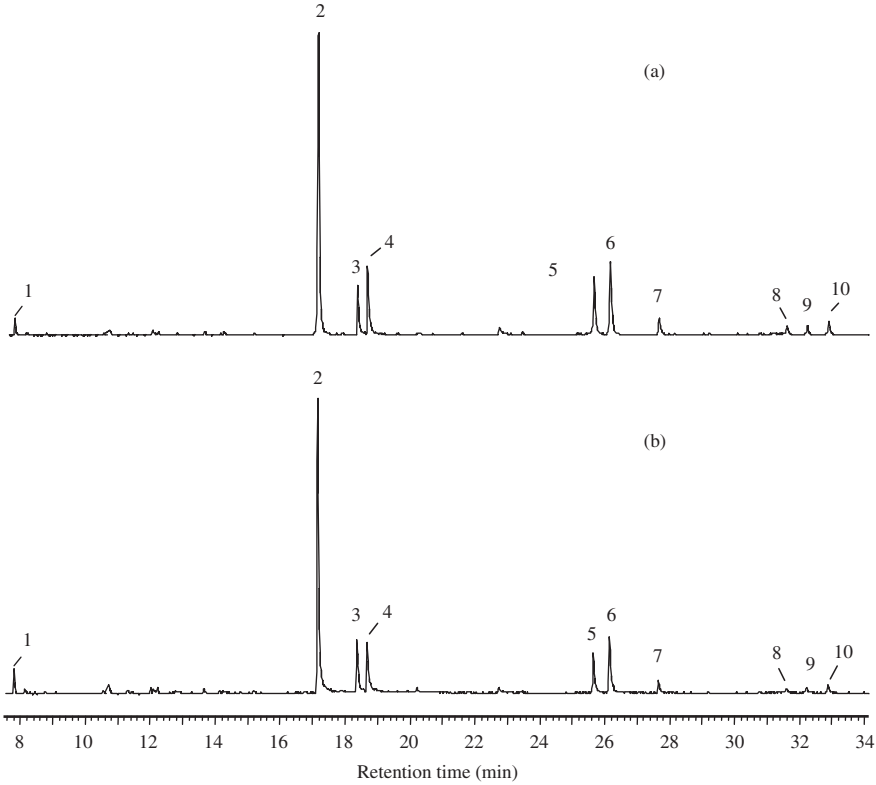

Figure 4. TMAH thermochemolysate of Saint Denis black crusts. (a) Mass fragmentogram of benzenepolycarboxylic acids (m/z 136 + 163 + 221 + 279 + 337). (b) The same after laser irradiation. Peak identification refers to Table 4.

Table 4. Major compounds identified in Figure 4.

Peak	Compounds
1	Benzoic acid
2	1,2-Benzenedicarboxylic acid
3	1,4-Benzenedicarboxylic acid
4	1,3-Benzenedicarboxylic acid
5	Benzenetricarboxylic acid
6	Benzenetricarboxylic acid
7	Benzenetricarboxylic acid
8	Benzenetetracarboxylic acid
9	Benzenetetracarboxylic acid
10	Benzenetetracarboxylic acid

4 CONCLUSIONS

A yellow fraction composed of aliphatic and aromatic carboxylic acids and phenols is present in soot and black crusts. The solubility of this fraction permit it to migrate into the stone matrix, beneath the black crusts deposit. Laser cleaning can remove elemental carbon and other compounds present in the black crusts due to rapid increase in surface temperature and the ejection of material

by vaporisation and rapid thermal expansion. Once the black layers has been removed further pulses are harmlessly reflected away by the stone surface. Therefore, neither the yellow layer present in the stone surface nor the classes of compounds forming it are affected by laser irradiation, which is a plausible explanation for the yellowing on stone materials after laser cleaning.

ACKNOWLEDGEMENTS

This work was supported by the European Commission (project EV4K-CT2000-00029), the French Ministry of Culture (subvention de recherche chapitre 6698 20, exercice 2001) and MCyT, project BTE2001-1277.

REFERENCES

Bromblet, P., Labouré, M. & Orial, G. 2003. Diversity of the cleaning procedures including laser for the restoration of carved portals in France over the last 10 years. *J. Cult. Heritage* 4: 17s–26s.

Cooper, M.I. 1998. *Laser Cleaning in Conservation: An Introduction.* Oxford: Butterworth-Heinemann.

Decesari, S., Facchini, M.C., Matta, E., Mircea, M., Fuzzi, S., Chughtai, A.R. & Smith, D.M. 2002. Water soluble organic compounds formed by oxidation of soot. *Atmos. Environ*. 36: 1827–1832.

Gaviño, M., Hermosin, B., Vergès-Belmin, V., Nowik, W. & Saiz-Jimenez, C. 2003. The composition of the black crusts from Saint Denis basilica, France, as revealed by gas chromatography-mass spectrometry. *J. Separ. Sci*. (in press).

Havers, N., Burba, P., Lambert, J. & Klockow, D. 1998. Spectroscopic characterization of humic acid-like substances in airborne particulate matter. *J. Atmos. Chem*. 29: 45–54.

Klein, S., Fekrsanati, F., Hidenhagen, J., Dickmann, K., Uphoff, H., Marakis, Y. & Zafiropulos, V. 2001. Discoloration of marble during laser cleaning by Nd:YAG laser wavelengths. *Appl. Surf. Sci*. 171: 242–251.

Lanterna, G. & Matteini, M. 2000. Laser cleaning of stone artefacts: a substitute or alternative method? *J. Cult. Heritage* 1: 529–535.

Larson, J. & Cooper, M. 1996. The use of laser energy for cleaning architectural terracotta decoration. In: *Architectural Ceramics, their History, Manufacture and Conservation*: 92–100. London: James & James.

Rock-Color Chart 1984. Boulder: Geological Society of America.

Saiz-Jimenez, C. 1993. Deposition of airborne organic pollutants on historic buildings. *Atmos. Environ.* 27B: 77–85.

Saiz-Jimenez, C., Hermosin, B. & Ortega-Calvo, J.J. 1994. Pyrolysis/methylation: a microanalytical method for investigating polar organic compounds in cultural properties. *Int. J. Environ. Anal. Chem*. 56: 63–71.

Vergès-Belmin, V. & Bromblet, P. 2000. Le nettoyage de la pierre. *Monumental:* 220–273. Paris: Editions du Patrimoine.

Vergès-Belmin, V. & Dignard, C. 2003. Laser yellowing, myth or reality? *J. Cult. Heritage* 4: 238s–244s.

Zafiropulos, V., Balas, C., Manousaki, A., Marakis, Y., Maravelaki-Kalaitzaki, P., Melesanaki, K., Pouli, P., Stratoudaki, T., Klein, S., Hildenhagen, J., Dickmann, K., Luk'Yanchuk, B.S., Mujat, C. & Dogariu, A. 2003. Yellowing effect and discoloration of pigments: experimental and theoretical studies. *J. Cult. Heritage* 4: 249s–256s.

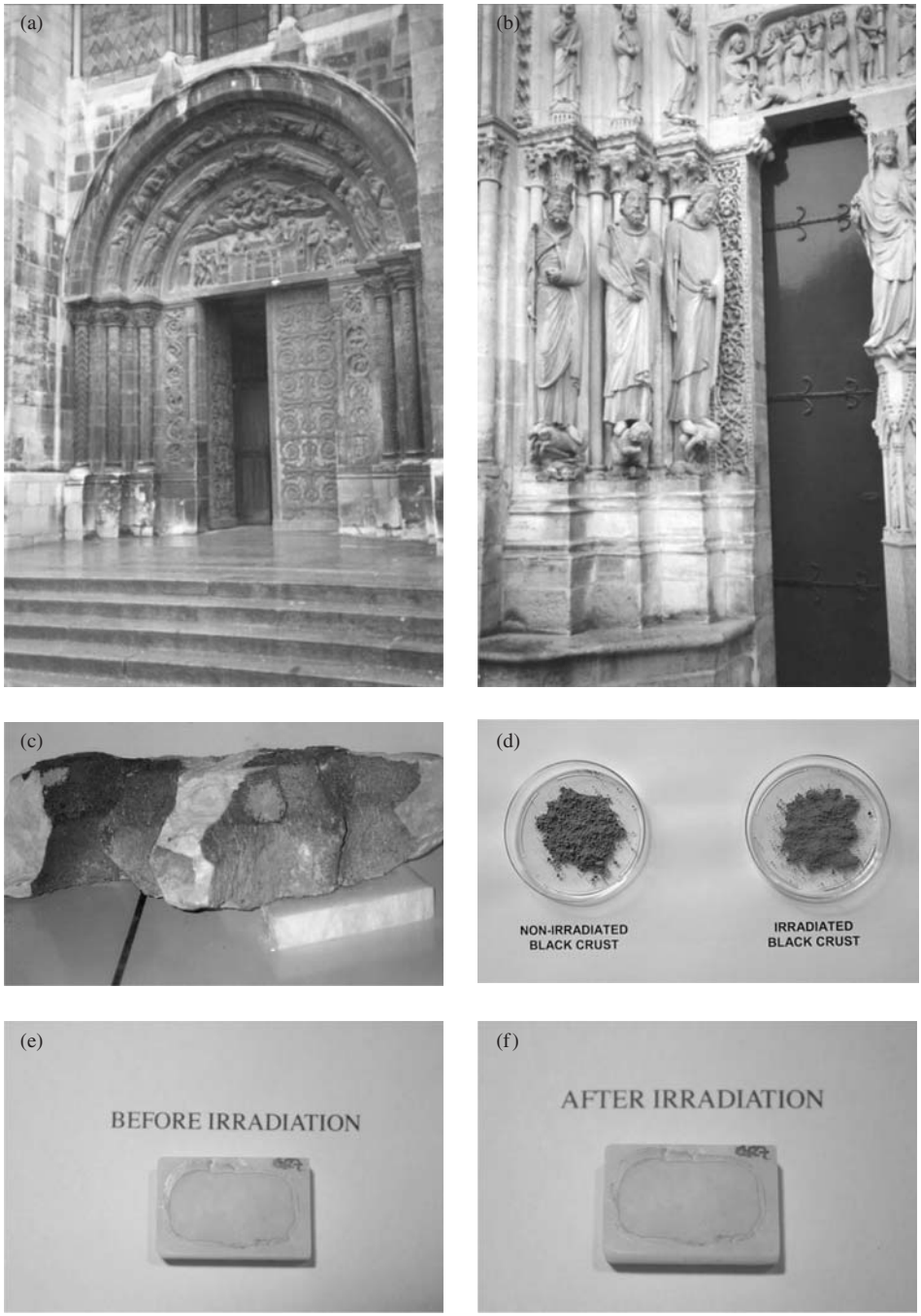

Plate 1. (a) Saint Denis basilica: one of the three portals of the western façade covered with black crusts. (b) Saint Denis basilica, portal of the northern transept. The larger statues and ornaments along the door have been laser cleaned. The tympanum, vaults and stone elements behind and underneath the large statues have been cleaned by water-based and/or abrasive methods. (c) Limestone piece with black crusts after laser irradiation at the laboratory. (d) Ground black crusts before and after laser irradiation. (e) Yellow fraction extracted from black crusts and deposited on an alabaster probe. (f) The same after laser irradiation.
(This plate is presented in the signature in colours at the end of this volume, Appendix, pg. 322)

Cultural Heritage Conservation and Environmental Impact Assessment by Non-Destructive Testing and Micro-Analysis – Van Grieken & Janssens (eds)
© 2005 Taylor & Francis Group, London, ISBN 90 5809 681 5

Dyes and pigments: ten open questions for conservation science

N.S. Baer
Conservation Center, Institute of Fine Arts, New York University, New York, USA

ABSTRACT: In over three decades of teaching conservation science to students at the Conservation Center of the Institute of Fine Arts, the author has prepared a range of assignments whose primary goal is to develop in the student the ability to critically evaluate the scientific literature relevant to the conservation and study of artistic and historic artefacts. Among these assignments have been those that require students to conduct a literature search for a specific dye or pigment, and on the basis of that search, to define the most important open research question related to the selected material, e.g. dates of first and last use, technique of manufacture, conservation of the pigmented surface, identification, etc. In recent years, a five-minute poster presentation has been an additional requirement. Selected results are presented together with typical assignments.

1 INTRODUCTION

The curriculum (http://www.nyu.edu/gsas/dept/fineart/ifa/index_chan.htm) of the Conservation Center includes in the first two years a general introduction to the materials of art and archaeology: their structure, manufacture, properties, analysis, degradation, and conservation. Though student undergraduate preparation includes two years of laboratory science, most commonly, general and organic chemistry, many areas of interest must be taught on the assumption of no significant background knowledge. Since the focus of the teaching at the Conservation Center is the training and education of practicing conservators rather than the training of conservation scientists, one seeks in teaching to develop skills of critical thinking, so that our graduates can evaluate with confidence the literature of conservation, recognizing weaknesses in experimental design, gaps in knowledge, and limitations of analytical techniques. The availability of such electronic data bases as AATA and CHIN permits the student to gain an overview of a topic of interest efficiently. A typical course assignment might be the evaluation of product literature with critical assessment of the application of standard test methods, for example those of the Technical Association of the Pulp and Paper Industry (TAPPI), to treatment materials and methods commonly used in paper conservation.

A virtue of a literature review assignment beyond the vital skills of critical thinking, is the possibility to introduce subjects that do not readily lend themselves to the lecture format, e.g. the properties of individual solvents commonly used in conservation practice. As discussed previously (Baer 2001), by assigning each student a specific solvent and the task of developing a risk analysis for that solvent in conservation practice, a large number of solvents can be reviewed and the results distributed and discussed in the format of a poster presentation to the class. The solvent assignment also introduces the student to the principles of risk assessment and risk management.

2 PIGMENT DYE AND INK LITERATURE ASSIGNMENTS

The first of the literature search assignments designed both as an introduction to the scientific literature and as a means to collect data, involved a survey of the changing exposure standards for commonly used solvents. The author had begun to apply risk assessment and risk management to conservation issues in 1983–1984 when he held a Guggenheim Fellowship (Baer 1984, 2001).

New York University, Institute of Fine Arts, Conservation Center
Materials of Art and Archeology I and III

Assignment: Pigments

1. From the list of pigments given below, select one. Each researcher is to select a different pigment.
2. Prepare a bibliography of five [5] references in which your pigment is discussed. Simple citations of occurrence are not acceptable. You may wish to conduct a CHIN search in connection with this assignment.
3. In a brief statement of ca. 100 words, define the most important research question relating to your selected pigment [conservation, technology, provenance, first use, identification, etc.].

1. Azurite	6. Lead-tin yellow	11. Scheel's Green
2. Bitumen	7. Mars red	12. Silver
3. Bone black	8. Mars yellow	13. Terre verte
4. Chalk	9. Maya blue	14. Tin white
5. Cobalt green	10. Orpiment	15. Vandyke brown

Figure 1. Typical literature search assignment with emphasis on inorganic pigments.

An early assignment asked the students to trace the evolution of threshold limit values (TLVs) for solvents by consulting the multiple editions of Sax's monumental Dangerous Properties of Industrial Materials. That rather simple assignment, initially given in 1986, has become a more formal risk management study considering risks to the conservator, the artefact, and the environment (Baer 2001). The many positive aspects to this literature-based approach suggested its expansion to the subject of pigments, where once again one had an ever-growing literature and many individual study subjects.

2.1 *Inorganic pigments*

Any inquiry involving a specific pigment begins logically with the three compendia under the common title, Artists' Pigments: A Handbook of their History and Characteristics. Feller (1986), Roy (1993) and FitzHugh (1997) each edited a volume in which virtually all reliable information available at that time for a group of ten pigments or pigment pairs was published in a standard format. The inspiration for this project was Rutherford John Gettens who began the series of articles in Studies in Conservation that would form the basis of the volume edited by Roy with an article on azurite and blue verditer. Earlier, he collaborated with George L. Stout to publish the influential reference work, Painting Materials: a Short Encyclopedia (1942). Two later significant reference works were based on a study of documentary sources (Harley 1982) and laboratory investigations (Schramm & Hering 1989).

These books, while essential references for the conservator and the conservation scientist, suffer from being frozen in time. Rapid advances in analytical capability, allowing complete characterization of samples of negligible size have made it essential that these most valuable reference works be supplemented with a thorough search of the conservation and scientific periodical literature. In Figure 1, a typical literature research assignment with emphasis on inorganic pigments is shown. The focus of this assignment is the identification of those research questions that remain open.

2.2 *Organic dyes, pigments and inks*

Given that by tradition, subject matter for the core curriculum of the Conservation Center in one year emphasizes inorganic materials followed by an emphasis on organic materials the next year,

New York University, Institute of Fine Arts, Conservation Center
Materials of Art and Archeology II and IV

Assignment: Organic Dyes, Pigments, and Inks

1. From the list of organic dyes, pigments, and inks given below, select one. Each researcher is to select a different dye, pigment, or ink.
2. Prepare a bibliography of five [5] references in which your selection is discussed. Simple citations of occurrence are not acceptable. You should conduct a CHIN search in connection with this assignment, indicating the raw number [no correction for duplicates] of citations offered.
3. In a brief statement of some 100-150 words, define the most important research question relating to your selected material [e.g. conservation, first use, identification, technology of production].

1. Alizarin	6. Fustic	11. Madder red	16. Safflower
2. Asphaltum	7. Gamboge	12. Mummy	17. Sepia
3. Bistre	8. Indian yellow	13. Pink	18. Turmeric
4. Brazil wood	9. Indigo	14. Prussian blue	19. Verdigris
5. Cochineal	10. Logwood	15. Quercitron	20. Woad

Figure 2. Typical literature search assignment with emphasis on organic pigments, dyes, and inks.

it was appropriate to assign a literature search for organic pigments, dyes and inks in the organic year. A typical assignment with this emphasis is depicted in Figure 2.

2.3 *Open research issues for inorganic pigments*

In Figure 3, summary statements taken from student responses to the assignments are compiled. The reader will observe that while there are eleven statements, the title of this paper refers only to ten open questions for conservation science. Soon after the assignment was given for the first time, the remarkable series of Raman microscopy studies on pigments, e.g. Clark & Gibbs (1997) began to appear, answering the question, "How does one differentiate among orpiment, realgar and pararealgar."

2.4 *Evaluation of literature research resources*

To illustrate the ever expanding nature of the literature reporting on dyes and pigments as found in works of art and archaeology, students were asked to conduct a new survey in order to test the validity of the statements of open research questions (see Figure 4). They were also asked to evaluate the relative importance of the standard reference works, data bases, and the seemingly omniscient Google search engine.

3 EPILOGUE

The author has employed student assistants in the task of compiling a bibliographic data base http://www.nyu.edu/gsas/dept/fineart/ifa/faculty/baer.htm. Many of the items in that data base are references originally cited in student papers. The complete bibliography is available on-line including a section devoted to dyes and pigments.

The growing trend towards poster presentation at professional meetings suggests that the students would gain useful experience by presenting the results of various assignments in the form of five-minute poster presentations. A selection of the posters, chosen for either artistic presentation,

Inorganic Pigments: Research Statements

1. Cadmium Yellow: What is the cause of discoloration of the early cadmium yellows. Is it due to impurities associated with manufacture.
2. Chalk: How does one best identify the type of chalk and associate it with a specific source.
3. Cobalt Green: Though discovered in 1780, it is not mentioned in the literature till 1835. What is in fact the first date of use in painting.
4. Emerald Green: How does on best identify it in paintings for use in authentication.
5. Ivory Black: How does one distinguish ivory black from other blacks, esp. bone black.
6. Lead-tin Yellow: How can one use lead-tin yellow in the authentication of paintings.
7. Lead White: What is the mechanism of degradation [oxidation] of lead white in wall paintings.
8. Mars Yellow: What synthetic processes were used in its production and how do the differing methods of manufacture affect the end product.
9. Orpiment: How does one differentiate among orpiment, realgar, and pararealgar.
10. Red Lead: What is the cause of degradation of the pigment's hue from orange-red to brown black and can it be reversed.
11. Vermillion: Can one reverse the blackening of the pigment on exposure to light.

Figure 3. Open research questions identified by students on the basis of literature reviews.

New York University, Institute of Fine Arts, Conservation Center
Materials of Art and Archeology I

Inorganic Pigments: Research Question Evaluation Assignment

Below are listed in alphabetical order eleven pigments and a paraphrase of one or more student statements as to the most important research question associated with that pigment. The primary data used in that assessment were produced in a CHIN search. For your assigned pigment, answer the following three questions.

I. Based on a review of the literature, in a brief essay of ca. 250 words, either support or reject the statement. If you reject the statement, you are to replace it with an alternative research question. Your position is to be supported with 3-5 references.

II. In responding to the statement of Part I, consult CHIN, Google, the three "Pigment Handbooks" edited by R. L. Feller, A. Roy, and E. West FitzHugh, respectively, and "Artists' Pigments c. 1600-1835," by R. D. Harley. In a brief statement of ca. 50-100 words, indicate which of the three pathways, i.e. CHIN, Google, or library volumes was most helpful and why.

III. The Infrared and Raman Users Group [IRUG] maintains a web site at www.IRUG.org. Similarly, I. M. Bell, R. J. H. Clark and P. J. Gibbs of the Department of Chemistry at University College London, maintain a web-based Raman Spectroscopy Library of Natural and Synthetic Pigments [pre-1850]. Based on an examination of these sites, briefly indicate whether you consider Laser Raman Spectroscopy to be a suitable tool for the identification of your pigment in easel paintings, illuminated manuscripts, or wall paintings.

Figure 4. Typical assignment for the evaluation of the results of student findings on pigment research questions.

humour, or technical content is presented in an Appendix. In some cases, the reader is asked to imagine the artful use of colour in the original.

Student Pigment Posters (see below, at the end of this chapter, in the following order)	
Bitumen by Isabelle Duvernois	(2000)
Bone Black by Julie DesChamps	(2000)
Chalk by Beth Edelstein	(2000)
Emerald Green by Lauren Fly	(2002)
Mummy by Caitlin O'Grady	(2002)
Lead-Tin Yellow* by Joanne M. Klaar	(2002)
(*This poster is also presented in the signature in colours at the end of this volume, Appendix, pg. 323)	

ACKNOWLEDGEMENTS

The author takes great pleasure in acknowledging the efforts of the students whose work product was the inspiration for this report. He also gratefully acknowledges the generosity of the Hagop Kevorkian Fund in its support of the student assistants who worked on the bibliographic project.

REFERENCES

Baer, N.S. 1984. Risk assessment as applied to the setting of solvent toxicity limits. In *Adhesives and Consolidants. Preprints of the Tenth International IIC Congress 1984.* Paris, France: 26–31. London: International Institute for Conservation.

Baer, N.S. 2001. Risk management, value and decision-making. *The Paper Conservator* 25: 53–58.

Clark, R.J.H. & Gibbs, P.G. 1997. Identification of lead (II) sulfide and pararealgar on a 13th century manuscript by Raman microscopy. *Cem. Commun.* 1003–1004.

Feller, R.L. (ed.) 1986. *Artists' Pigments: A Handbook of their History and Characteristics*. Volume 1. Washington: National Gallery of Art.

FitzHugh, E.W. (ed.) 1997. *Artists' Pigments: A Handbook of Their History and Characteristics*. Volume 3. Washington: National Gallery of Art.

Gettens, R.J. & FitzHugh, E.W. 1966. Azurite and blue verditer. *Studies in Conservation* 11: 54–61.

Gettens, R.J. & Stout, G.L. 1942. *Painting Materials: a Short Encyclopedia*. New York: D. Van Nostrand

Harley, R.D. 1982. *Artists' Pigments c. 1600–1835: A Study in English Documentary Sources. Second Edition*. London: Butterworth Scientific.

Roy, A. (ed.) 1993. *Artists' Pigments: A Handbook of Their History and Characteristics.* Volume 2. Washington: National Gallery of Art.

Schramm, H.-P. & Hering, B. 1989. *Historische Malmaterialen und ihre Identifizierung*. Berlin: VEB Deutscher Verlag der Wissenschaften.

Isabelle Duvernois
Materials of Art and Archeology I & III
Prof. N.S. Baer
December 11,2000.

PIGMENT RESEARCH
BITUMEN

ABSTRACT:
A geologically modified organic material, bitumen, also known as asphaltum, is the product of the distillation of crude natural petroleum. The composition of this dark brown or black product constituting the useful part of the raw material can vary and is chemically fairly complex. It was widely used in the 17th, 18th, and 19th centuries. Although it is generally recognized to be a remarkably poor drying pigment, research has shown widely different opinions upon the nature of this instability. Some explained the doomed nature of the pigment in relation to the various media and additive incorporated into the paint, while others guaranteed that careful selection of the hardest and brittle kind heated at high temperature for a very long time, and later ground with drying oil, would yield a paint that neither cracks nor moves on the canvas.

REFERENCE:
White, Raymond. "Brown and Blake Organic Glazes, Pigments and Paints." *National Gallery Bulletin 10* (1986): 58-71.

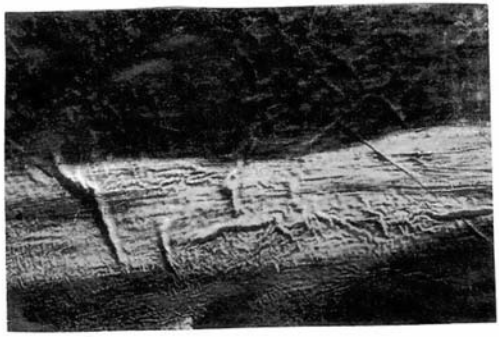

Illustration taken from Knut Nicolaus, *The Restoration of Paintings* (1999), showing the creasing in the paint layer caused by the slipping of an upper layer of paint over a lower layer, such as bitumen, that has not yet dried properly.

Julie DesChamps
Presentation
11 December 2000
Dr. Norbert Baer

BONE BLACK

ABSTRACT:Bone black, a warm, deep black pigment made from charred animal bones, is composed of carbon, calcium phosphate, and calcium carbonate. Recent research has focused on the identification of bone black in works of art using various analytical methods, such as SEM-EDS, neutron activation autoradiography, XRF, and optical microscopy.

REFERENCE:
Garret, M. D. "Carbon Black Pigments." In *Pigment Handbook*, ed. Temple C. Patton, vol. I, p. 740-2. (New York: John Wiley and Sons, 1973.

Bone black is found throughout Rembrandt's oeuvre, often in conjunction with other pigments for the dark backgrounds or costumes in his paintings. In this cross section from Portrait of Philips Lucasz of 1635, the artist mixed lead white with bone black to create the tone of the sitter's gray left sleeve. This layer appears above a chalk ground and imprimitura. (See Bomford, David et al. Art in the Making: Rembrandt. London: National Gallery Publications, 1988. p. 57)

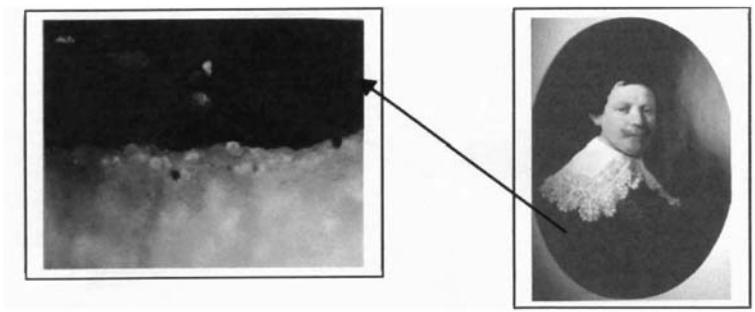

Bone black also formed the main pigment of sketchy underdrawings used by Van Dyck, Rembrandt, and other artists to define the composition of the painting. Since radioactive phosphorus, P-32, a component of bone black, can be detected by neutron activation autoradiography, sketches below the paint surface that are executed in bone black can be found. Below is an autoradiographic study of St. Rosalie by Van Dyck, which revealed a self portrait of the artist. (See Ainsworth, Maryan, et al. Art and Autoradiography, New York: The Metropolitan Museum of Art, 1982.)

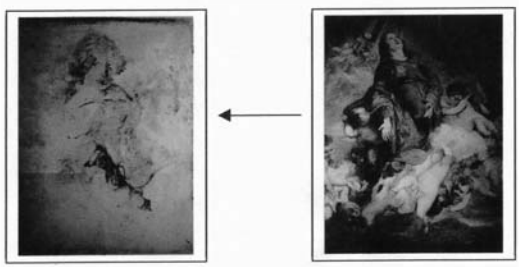

BETH EDELSTEIN
Materials and Technology
December 11, 2000
Presentations – Pigments

Pigment Handout: Chalk

While the word "chalk" technically relates to one particular form and source of calcium carbonate, the mineral exists in a number of forms, many of which are important materials in art and architecture. It is valuable for the conservator to recognize these different forms when considering issues of preservation and authentication of an art object.

1. Calcium carbonate, $CaCO_3$:
   - Historically important artists' material
   - Used as pigment, bulking agent, in preparatory layers, and as a polishing compound
   - Most stable mineral form is calcite
2. Types of calcium carbonate used in artistic production:

	Source	Preparation	Uses
Marble/ Limestone	Naturally occurring mineral deposits. Marble is metamorphosed limestone, recrystallized calcite.	Ground into powder	Pigment; filler or bulking agent
Chalk 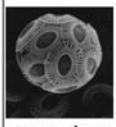 coccosphere 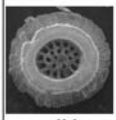 coccolithus	Naturally occurring deposits of a soft, porous, friable rock, largely composed of fossil remains of unicellular algae. These remains consist primarily of coccoliths (see illustration), minute calcareous platelets that make up the shell of the living organism. The presence of coccoliths is the primary identifying characteristic of chalk.	The chalk is weathered, ground under water, washed, and allowed to settle into strata; the uppermost stratum is the finest, and so on. Also known as whiting, English white, Paris white.	Pigment, though due to low refractive index has low hiding power in oil medium paints. Ground layer, mixed with animal glue, particularly in northern Europe. Abrasive, for polishing gold and silver.
Synthetic $CaCO_3$	Also called precipitated chalk; derived as by-product of various chemical industries.	Carbon dioxide from the burning of lime (CaO) is combined with a lime slurry to form the carbonate. Other methods exist as well.	Basis for pastel crayons. Filler and pigment for paper. Used in manufacture of printing inks, plastics, and rubber.
Lime white	Calcium hydroxide, $Ca(OH)_2$	When $CaCO_3$ is heated, CO_2 is driven off to leave CaO, which reacts vigorously with water to produce $Ca(OH)_2$; reaction can be controlled to result in a fine white powder. When water is added, it forms a paste or putty, called slaked lime.	Slaked lime used in building mortars; combines with CO_2 in air to re-form $CaCO_3$. Aged slaked lime was used as a pigment in fresco painting, *bianco sangiovanni*.
Shell white	Mollusk shells, which are nearly pure calcium carbonate.	Dried, pulverized, and levigated in water tanks.	Pigment, often in Japanese ukiyo-e paintings.

Lauren Fly
Materials in Art & Archaeology I
Third Assignment
Baer
9 December 2002

EMERALD GREEN

HISTORY

Research into the production of emerald green was begun in the early 19th-century by two different individuals. Wilhelm Sattler, working in Schweinfurt, Germany with the help of pharmacist Friedrich Russ, began investigation into the pigment's synthesis in 1814. The second man credited with the discovery of emerald green is Ignaz von Mitis. Mitis first discovered copper acetoarsenite, the chemical compound from which emerald green is derived, between 1798 and 1812. By 1814 Mitis, working in Vienna, had successfully manufactured the pigment on a small scale.[1]

Emerald green achieved immediate commercial popularity. Its most appealing characteristic was that it provided the artist with a bright, brilliant, pure green color with a wide variety of applications. It was soon being marketed under a range of names, mainly determined by its place of production. These names include Mitis, Paris, Schweinfurt, and *vert Véronèse*. It was particularly popular with French impressionists and post-impressionists, who favored the kind of brilliantly luminous palette it exemplified. Important artists who made use of emerald green include Joseph Turner, Eduoard Manet, Claude Monet, Camille Pisarro, Paul Cézanne, Georges Seurat, Gustave Moureau, Vincent van Gogh, and Paul Gauguin.[2]

Emerald green continued to be used by artists until the 1960's, although because of its high toxicity it was marketed as a pesticide in the United States until the 1980's.[3]

METHODS OF PRODUCTION

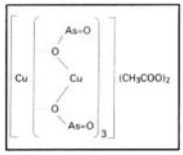

There are two reactions that can be used to prepare emerald green :

Acetate Method

$6NaAsO_2 + 4Cu(CH_3COO)_2 \rightarrow 3Cu(AsO_2)_2{\cdot}Cu(CH_3COO)_2 + 6CH_3COONa$

Sulfate Method

$4CuSO_4 + 6NaAsO_2 + 2HCH_3COO + Na_2CO_3 \rightarrow 3Cu(AsO_2)_2{\cdot}Cu(CH_3COO)_2 + 4Na_2SO_4 + H_2O + CO_2$

METHODS OF IDENTIFICATION

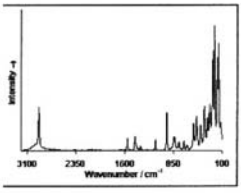

Emerald green is readily identifiable through the standard means of pigment analysis: XRD, XRF, optical microscopy, etc. However, the developing field of laser Raman spectroscopy offers an intriguing new possibility for detecting the use of emerald green in easel paintings, wall paintings, and illuminated manuscripts. Emerald green has a firmly established, clearly visible spectrum when examined with laser Raman spectroscopy, as seen to the left.[4] Laser Raman spectroscopy is an ideal method of analysis for this pigment, as it is also non-destructive, and when used with fiber optics, can be adapted to various media. For example, the laser can be focused via fiber optics through the varnish of an easel painting. Thus, the painting's surface can remain intact throughout the examination.

---

[1] Michael A. Bayard and Inge Fielder, "Emerald Green and Scheele's Green," in *Artists' Pigments: A Handbook of Their History and Characteristics*, vol. 3 ed. Elizabeth West Fitzhugh (Washington, D.C.: National Gallery of Art), 222.
[2] Ibid., 223-4 and 256-64.
[3] Ibid., 225.
[4] Ian M. Bell, Robin G.H. Clark, and Peter J. Gibbs. "The UCL Raman Spectroscopy Library of Natural and Synthetic Pigments (pre-1850 AD) *The Department of Chemistry, University College London* 29 May 1998. 25 November 2002 http://www.chem.ucl.ac.uk/resources/rama/speclib/html.

CAITLIN O'GRADY
Materials of Art and Archaeology IV
Assignment 3: Organic Pigments
Prof. Norbert Baer
Class Handout
8 April 2002

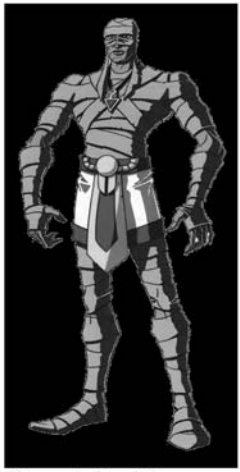

Figure 1: Possible source of Mummy Brown

Mummy (or Egyptian) Brown

CHEMICAL CHARACTERIZATION

The characterization of Mummy Brown varies according to the availability of materials (Woodcock 1996, White 1986, Gettens and Stout 1966); but consists primarily of natural resins (conifer, mastic, gum arabic) used in mummification, proteinaceous materials and linen cloth fragments.

USES

Mummy brown is typically used as a glaze in drying oils and can also be used in watercolors.

ABSTRACT: Mummy Brown, a popular pigment manufactured from Egyptian mummies during the mid-eighteenth and nineteenth centuries, varies widely in content and is difficult to identify. Mummy Brown will cause some cracking or crocodiling when mixed in drying oils, but not as much as bitumen or asphaltum. Therefore, identification of Mummy Brown in oil paintings should be feasible based on its overall state of conservation, as well as the presence of polysaccharides,
proteinaceous materials and textile fibers in the pigment sample. Research into the further characterization and identification of Mummy Brown, as well as the chemistry of its drying qualities should identify the reasons for cracking.

Grinding up mummy bones for paint. The process is rather a lengthy one, and is done on a granite slab with a large flat-faced stone.

Figure 2: Preparing Mummy Brown pigment. From "Body Colour: The Misuse of Mummy," *The Conservator* 20 (1996): 89.

Single Most Important Source
White, Raymond. "Brown and Black Organic Glazes, Pigments and Paints," *National Gallery Technical Bulletin* 10 (1986): 58-71.

Joanne M. Klaar
December 9, 2002
New York University, Institute of Fine Arts, Conservation Center
Materials of Art and Archaeology III

Lead-Tin Yellow

Lead-Tin Yellow I - Pb_2SnO_4
Lead-Tin Yellow II - $PbSnO_3$ or $Pb_2(Sn, Si)O$

QUESTION OF THE DAY: HOW CAN ONE USE LEAD-TIN YELLOW IN THE AUTHENTIFICATION OF PAINTINGS?

The use of what we term lead-tin yellow (both type I and II) in painting appears to have been limited to the 13th c. through 1750.[1] Its use waned in the second half of the 18th c., and fell out of favor after that.[2] In 1940 the pigment was reintroduced by a scientist from the Doerner Institute in Munich, and can currently be found on the market today.[3]

http://webexhibits.org/pigments/indiv/overview/pbsnyellow.html

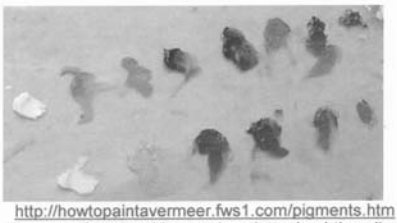

http://howtopaintavermeer.fws1.com/pigments.htm
Pigments found on Vermeer's palette, lead-tin yellow on bottom left

The small window of dates allows one to use lead-tin yellow as an authentification tool, as paintings from the 19th and 20th c. do not commonly contain it. However, it is important to note that one may have been able to procure the pigment from places which still held it in stock or left over from another time. Similarly, the reintegration of lead-tin yellow onto the palette in the 1940s may also be an issue in forgeries, as it is now easier to replicate a painting of the 13th c. to 1750.[4] Finally, in light of the recent research of the regrouping of yellow pigments, it may be necessary to reexamine many of the paintings to determine the presence of tin and reconsider the nomenclature of these pigments in the past.

The small window of dates allows one to use lead-tin yellow as an authentification tool, as paintings from the 19th and 20th c. do not commonly contain it. However, it is important to note that one may have been able to procure the pigment from places which still held it in stock or left over from another time. Similarly, the reintegration of lead-tin yellow onto the palette in the 1940s may also be an issue in forgeries, as it is now easier to replicate a painting of the 13th c. to 1750.[5] Finally, in light of the recent research of the regrouping of yellow pigments, it may be necessary to reexamine many of the paintings to determine the presence of tin and reconsider the nomenclature of these pigments in the past.

Best of all, Laser Raman Spectroscopy is a suitable method for identification of lead-tin yellow in easel paintings, illuminated manuscripts, or wall paintings!

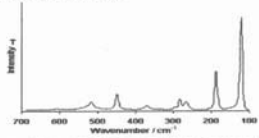

http://www.chem.ucl.ac.uk/resources/raman/pigfiles/leadtin1.html
Lead-tin yellow I Raman spectra

[1] http://webexhibits.org/pigments/indiv/history/pbsnyellow.html
[2] Kuhn, H. "Lead-Tin Yellow" 83-112 in Artist Pigments: A Handbook of Their History and Characteristics vol. 2, Roy, A. ed., National Gallery of Art, Washington D.C., 1993. 86
[3] *ibid*, 85
[4] *Ibid.*, 86
[5] *Ibid.*, 86

(This poster is presented in the signature in colours at the end of this volume, Appendis, pg. 323)

Cultural Heritage Conservation and Environmental Impact Assessment by Non-Destructive Testing and Micro-Analysis – Van Grieken & Janssens (eds)
© 2005 Taylor & Francis Group, London, ISBN 90 5809 681 5

Analysis of paint layers by light microscopy, scanning electron microscopy and synchrotron induced x-ray micro-diffraction

B. Hochleitner & M. Schreiner
Institute of Humanities, Sciences and Technologies in Art, Academy of Fine Arts, Vienna, Austria

M. Drakopoulos, I. Snigireva & A. Snigirev
ESRF – European Synchrotron Radiation Facility, Grenoble, France

ABSTRACT: Light microscopy (LM) and scanning electron microscopy (SEM) in combination with energy dispersive x-ray microanalysis (EDX) were used for the characterization of the structure of the paint layers of a specimen taken from a mural painting. The sample consisted of 7 layers in total, whereby a thin layer of pure gold was suspected to be the uppermost layer. The sequence of the various paint layers as well as the distribution of the elements present in the pigments could be obtained from the cross-sectioned specimen. Additionally, synchrotron induced x-ray micro-diffraction analysis (XRD) enabled the identification of the crystalline structure of the pigments used for the painting. Traversing the sectioned sample through a focused x-ray beam with a size of 2 μm allows microscopic resolved analysis of the crystalline constituents within the diverse paint layers. By this, it is possible to attribute the usage of various pigment minerals within the paint layers, even including a 2 μm thick gold layer at the surface.

1 INTRODUCTION

Knowledge of the composition of the originally used pigments in works of art is of great importance for the restoration and conservation of such objects (Fuller & Lewis 1988, Kittel 1960). Various analytical techniques can be applied in order to gain information concerning their material composition, i.e. about the pigments used in paintings, polychromed sculptures or illuminated manuscripts (Schreiner 1995, Gettens & Stout 1966, Matteini & Moles 1990). This gained information allows in most cases the classification of this work or the correlation with a special period or a certain artist (Feller 1986, Roy 1993, West FitzHugh 1997).

The most common way to analyze a work of art is the preparation of a cross-section on properly sampled specimens, where the sequence of all layers is preserved (Kühn 1988). The examination of the cross-section by light microscopy and UV-fluorescence microscopy provides frequently sufficient information about the structure of the paint layers, grain size and grain size distribution of the various pigments as well as varnish layers or organic binding media (Banik et al. 1982). However, for the identification of individual pigments present in the various paint layers additional investigations of the cross-section are necessary. Scanning electron microscopy (SEM) combined with energy-dispersive x-ray microanalysis (EDX) has been used widely to obtain information about the elements present in the pigments as well as their distribution in the different layers (Hanlan 1975, Mantler et al. 2000). Single pigments can be identified by comparing their color and elemental composition with standard materials known to be used in the present or past for painting artifacts.

However, many inorganic materials and some of the most interesting pigments can occur in different crystalline structures (Kirk & Raymond 1978, Ullmann 1979, PDF 2000). $CaCO_3$ - chalk,

which has been often used as filler in the ground layer, e.g. can occur in the modification of calcite as well as aragonite (Schramm & Hering 1988). Therefore, x-ray diffraction analysis has been proved to be a valuable tool for the examination of the paint layers too. With common XRD it is rather difficult to carry out those investigations of specific pigments, as the thickness of the paint layers is in the range of several tens micrometers or even below. Therefore, synchrotron induced x-ray micro-diffraction was used in the present work, where the step scan resolution can be much smaller than the thickness of the paint layers. The combination of SEM/EDX analysis and x-ray micro-diffraction has proved to be suitable for the identification and characterization of the composition of this cross-section.

2 EXPERIMENTAL METHODS

A specimen taken from a mural painting of the Baroque periods could be employed for the investigations. The specimen was embedded with a particular orientation in a transparent resin, ground and polished with SiC-paper up to 4000 mesh perpendicular to the paint layers. Highly polished layers are required for an informative microscopic investigation and flawless photographs. For analyzing this sample three different methods were applied.

2.1 *Light microscopy*

Analysis with the light microscope (Leitz, Orthoplan) was performed by using polarized light and the dark field reflectance technique. With this method it is possible to gain information about the thickness of the cross-section and the structure of the paint layers. Furthermore, this method yields information about the grain size and grain size distribution of the used pigments. This information is a useful indication for the way of manufacturing the painting, since modern pigments have uniform distribution of their grain size whereas hand ground colouring matters are strongly heterodisperse.

2.2 *SEM/EDX analysis*

In addition to the light microscopic images SEM analysis of the same cross-section was carried out with a Philips XL 30 ESEM microscope without coating the specimen, although the materials in the paint layers as well as the embedding material are electrically non-conducting. Energy dispersive x-ray microanalysis in the SEM (EDAX Phoenix) was used for qualitative analysis of the elements present in the pigments as well as for x-ray mappings yielding to the distribution of the elements in the different paint layers.

2.3 *X-ray micro-diffraction*

For this purpose a micro-diffraction facility installed at a beamline at the European Synchrotron Radiation Facility (ESRF) in Grenoble, France was used. The central quality of the synchrotron induced x-ray radiation is the minute source from which the radiation is emitted, and the small solid angle into which the radiation is confined. At a distance of several ten meters from the source an intensive x-ray beam displaying a cross-section of around 1 mm^2 is attained. This gives the possibility to collect the majority of the beam with the x-ray optical elements, which typically have apertures of a few hundred micrometer diameter.

In particular, compound refractive x-ray lenses (CRL) (Snigirev 1996, Lengeler 1999) are used, which focus x-rays in a similar manner as glass-lenses would do with visible light. The focal spot is a demagnified image of the x-ray source, imaged by the CRL. The value of demagnification can be directly derived from the geometrical properties of the imaging set-up, by ray-tracing methods usually applied in geometrical optics. The demagnification value is the ratio between the source-lens distance and the lens-sample distance. This setup benefits from the large distance of the

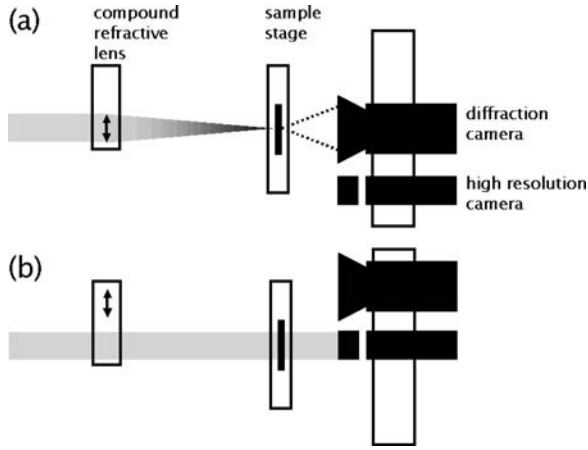

Figure 1. Experimental set-up for micro-diffraction, at beamline ID22, ESRF, Grenoble. The monochromatic x-ray beam enters from the left. (a) is the set-up in diffraction mode, (b) shows the alignment mode.

experimental station from the storage ring, being 42 m, which is made possible because of the slowly diverging x-ray beam. With a typical lens-sample distance of one meter it is possible to get a demagnification ratio in the order of 40. The effective source size is of 50 μm vertical and 600 μm horizontal, and consequently a focal spot of 1–2 microns in the vertical direction and 15 microns in the horizontal direction is achieved at sample location. Thus, it is possible to perform x-ray scanning microscopy with micrometer resolution, if the scanning direction is chosen to be vertical. The use of a monochromator device located in the beam path between source and sample helps to select the desired x-ray wavelength by means of x-ray diffraction on Si single-crystals. Here a wavelength of 0.620 Å is selected, with a relative bandwidth of $1.4 \cdot 10^{-4}$.

The focusing of x-rays with CRL is particularly advantageous for the recording of diffraction signals. Diffraction is measured by observing the angular distribution of x-ray radiation scattered by the sample. Thus, the angular divergence of the incoming beam will account for the resolution of the experiment. Because the aperture of the CRL is small in comparison to the focal length, the lens provides a small divergence in the incoming beam of only 0.2 mrad. This value translates into a relative accuracy in the determination of crystalline lattice spacing in the order of 10^{-3}. This value is exceedingly sufficient to distinguish diffraction patterns arising from different mineral species which are envisioned for analysis.

A scheme of the instrumental set-up used is shown in Figure 1. Basically, two modes come into operation. The micro-diffraction mode (Fig. 1a) has the CRL inserted, and the diffraction pattern is then collected by means of a two-dimensional x-ray camera behind the sample. At the chosen wavelength the diffracted intensities from the relevant crystalline lattice spacing values are confined within an angular cone of 90° opening angle. For recording the diffraction patterns, the diffraction-camera with an active diameter of 100 mm is located at a few cm distance from the sample (Fig. 2).

The diffraction spectrum analyzed at a later stage is obtained by summing up all intensities belonging to the same diffraction angle and plotting the so obtained intensity distribution versus diffraction angle.

For the second operation mode the lens and diffraction camera are removed and instead a high-resolution x-ray camera is placed directly behind the sample (Fig. 1b). Illuminated by the plane x-ray beam, the radiogram of the paint layers is obtained (Fig. 7b). Primarily, this high resolution imaging mode is used to align the sample in respect to the focused beam position, which can be made with an accuracy of 2 μm. However, the different attenuation within diverse paint layers can yield some approximate knowledge about their mean density.

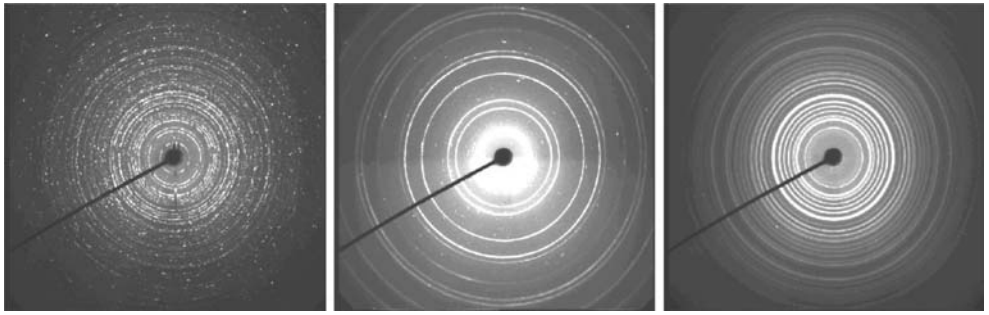

Figure 2. X-ray micro-diffraction. Experimentally obtained powder diffraction patterns from different positions across the paint layers. Position number 20, 60, and 90 (from left to right, referring to numeration scheme of Figure 7).

As both modes are performed in transmission geometry, the sample was sectioned into a 300 μm thick slice, prior the x-ray experiment.

The complete micro-diffraction analysis was accomplished by step-wise moving the section across the focused beam in steps of 4 μm. The paint layers were oriented horizontally, parallel to the larger beam-dimension, thus allowing to traverse the layers with a beam-size limited resolution of around 2 μm. In-between each step a diffraction-pattern is recorded, with an acquisition time of 2 s. The diffraction signal arises from a sample volume which is defined by the lateral beam-dimensions, i.e. $2 \times 15\ \mu m^2$, and the sample thickness, which was 300 μm. After 160 steps, the beam passed through all seven layers and 160 diffraction spectra were collected, which are representative for the crystalline composition of the sample. Finally, the diffraction spectra were processed in order to eliminate instrumental parameters like wavelength λ or diffraction angle 2Θ. By applying Bragg's law for 1st order diffraction ($\lambda = 2d \cdot \sin\theta$) the abscissa was converted into the lattice spacing d. This makes the data comparable to the tabulated values from similar compounds.

In practical terms, the measurements were evaluated by analyzing crystalline phases by means of a search/match program. In order to identify unknown sample constituents, it was necessary to compare the measured diffraction spectra with a collection of tabulated spectra of known compounds. For this purpose, the collection by the International Centre for Diffraction Data (ICDD 2000), the Powder Diffraction File (PDF 2000), was available.

Using this method it is possible to identify pigments with a crystalline structure. However, amorphous dyes and binding media can not be identified.

3 RESULTS AND DISCUSSION

In general paintings are made by mixing pigments with a liquid binding medium (e.g. animal glue or linseed oil). After applying a layer of paint, it is dried and other layers are added as needed (Mantler & Schreiner 2000). A final coating mainly made of natural resin normally protects the painting and is responsible for the visual quality of the optical depth.

3.1 *Light microscopic examination*

The gained information by light microscopy and UV-fluorescence microscopy concerns the sequence and the thickness of paint layers and distribution of the pigments (Wülfert 1999). Figure 3 depicts a light-optical micrograph of the cross-section of the specimen investigated. The thickness of all paint layers is about 500 μm. The different layers can be seen clearly, although the gold layer, which should be on top (Fig. 3), can hardly be detected at this magnification (approximately 100×).

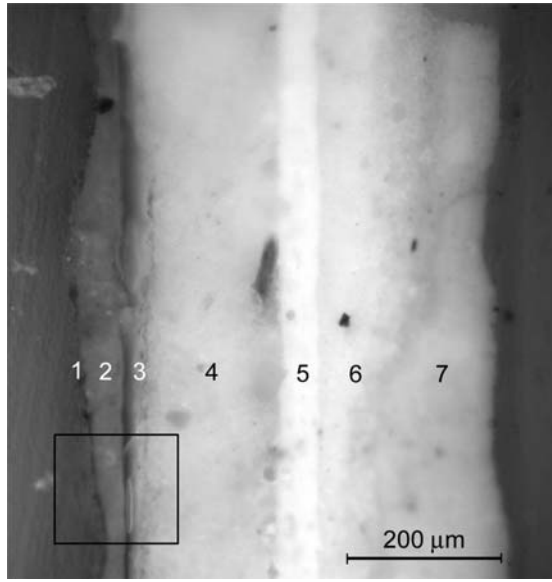

Figure 3. Cross-section of the paint layers of a specimen taken from a golden part in a mural painting.

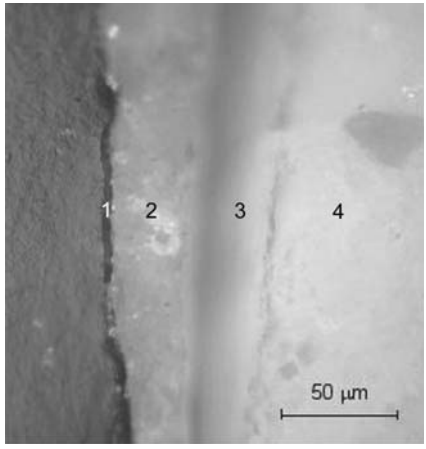

(a) Light microscopic image

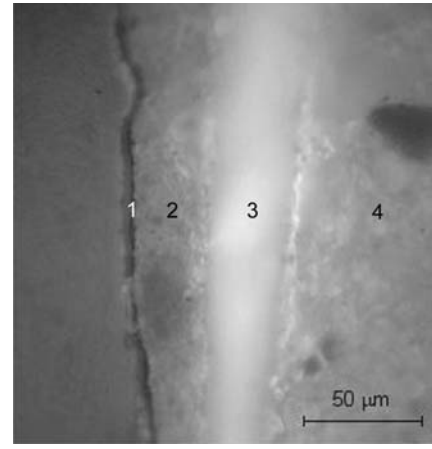

(b) UV-fluorescence micorscopic image

Figure 4. Detail of the paint layers in Figure 3.

With a higher magnification of about 400× the gold layer (layer 1) can be seen in Figure 4 as a thin dark layer on the left side of the layer 2 (red/orange layer). Both, the light microscopic (Fig. 4a) as well as the UV-microscopic image (Fig. 4b) show the surface layer as a non-continuous thin layer clearly due to its high metallic reflectance of the visible light and the total absorption of the UV radiation.

The light microscopic images in Figure 3 and Figure 4a yield to the structure of the different paint layers, where 7 layers can be determined: The surface layer (layer 1) is the gold layer followed by a red/orange layer (layer 2) clearly visible in Figure 4a. Layer 3 is a thick layer transparent in the visible light (Fig. 4a) and showing a bright bluish fluorescence in the UV-fluorescence microscope, which indicates the presence of natural resin. Underneath layer 3 is a thick yellow paint layer (layer

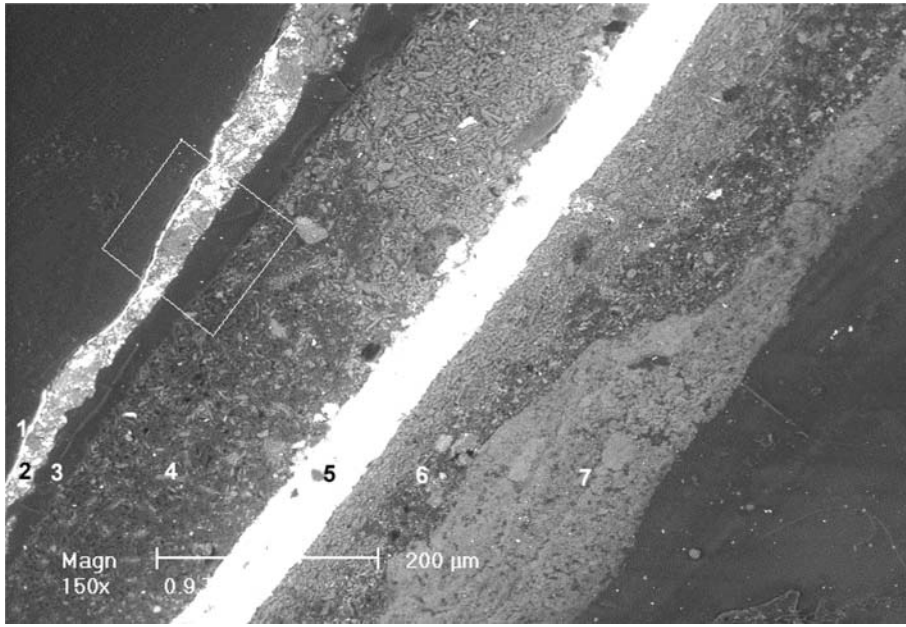

Figure 5. Backscattered electron (BSE) image of the cross-section in Figure 3.

4), followed by a thin white layer (layer 5) as shown in Figure 3. Layer six and seven are of white colour with a light touch to yellow and grey, where the transition between these two layers seems to be very unsteady.

3.2 *SEM analysis*

The backscattered electron image in Figure 5 clearly reveals the structure of the paint layers due to the atomic numbers of the elements present in the pigments. Layers containing pigments of heavy elements such as lead present in lead white, appear bright; those containing primarily elements with medium or low atomic numbers are dark. This information may already serve as a hint for the identification of the elements present and hence the pigments used for the various layers. Additionally, in the various layers also single pigment grains are clearly visible surrounded by the binding medium, which consists mainly of an organic material with C and H (low atomic numbers) as main constituents.

Figure 5 shows a backscattered electron image at a magnification of 150× with all the 7 layers determined by light microscopy. The gold layer is visible as a thin bright line due to the high amount of backscattered electrons. Layer 2, identified with light microscopy as a red/orange layer, shows bright pigment grains between darker areas, which point to heavy elements in this layer. Layer 3 is dark followed by layer 4 in light grey. Layer 5 appears very bright, which indicates elements with high atomic numbers. Layer 6 and 7 can be separated in this image too.

3.3 *EDX analysis*

The second step in the characterization of the individual paint layers is qualitative x-ray microanalysis usually carried out by means of energy dispersive analysis yielding the simultaneous display of all elements except H and He. Additionally, a more detailed information about the distribution of the main elements can be achieved by x-ray mappings. As an example, in Figure 6a the BE-image of a selected domain of the cross-section is depicted with the corresponding distribution of the elements Au (b), Ba (c), Ca (d), Pb (e) and C (f).

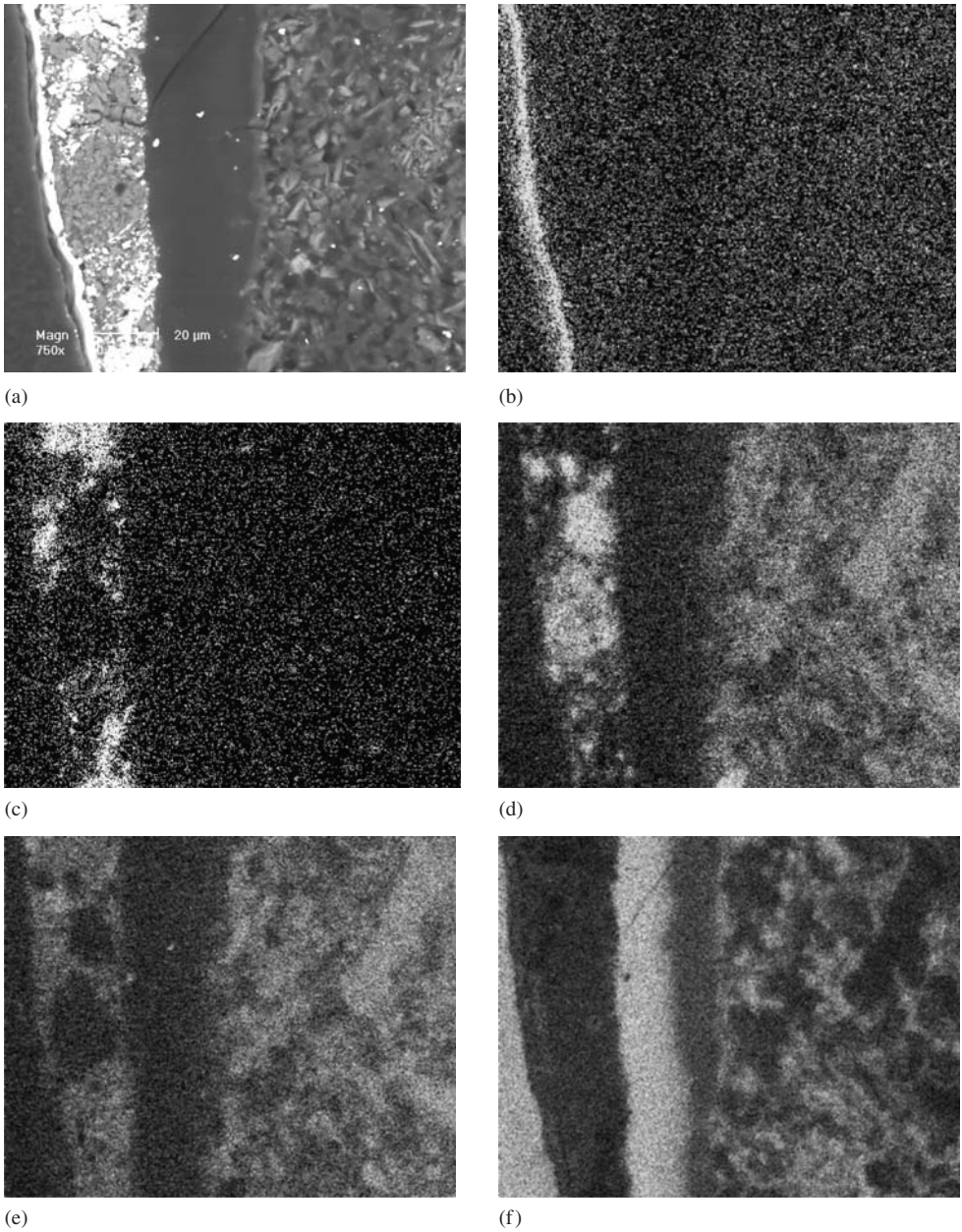

Figure 6. BE image of a detail of the cross-section of the specimen in Figure 5 (a), with the corresponding elemental distributions of Au M-line (b), Ba L-line (c), Ca K-line (d), Pb M-line (e) and C K-line (f).

With these elemental distribution images the main elements in the different layers could be correlated with the pigments used for the paint layers. Table 1 shows the results of the element distribution in combination with the analysis by optical microscopy.

Figures 6b–f show that the first layer consists of Au, which confirms the surface layer to be of gold. In layer 2 the main elements are Ba and Ca, with some S and/or Pb. In this case it is not possible to distinguish between these two elements due to the coincidence of the S K-lines (2.31 keV) with

Table 1. Results of the element distribution images.

Layer	Appearance of the layer in light microscopy	Elements determined with EDX analysis
1	Yellow	Au
2	Red/orange	Ca, Ba, S and/or Pb
3	Transparent	C
4	Yellow	C, Ca, S and/or Pb
5	White	Ca, S and/or Pb
6	White (yellowish)	Ca
7	White (grey)	Ca

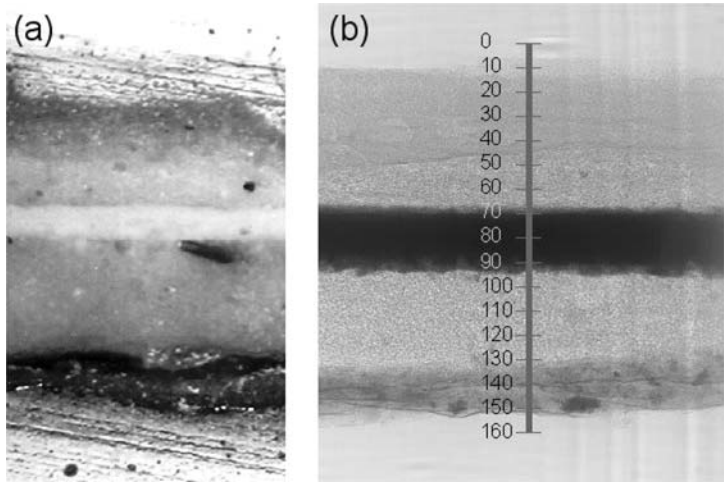

Figure 7. Optical image (a) and corresponding x-ray radiogram (b) of the specimen with the paint layers used for the synchrotron x-ray micro-diffraction. The vertical line in Figure (b) indicates the alignment of the micro-diffraction scan, with 160 individual points.
(This figure is presented in the signature in colours at the end of this volume, Appendix, pg. 321)

the Pb M_α-line (2.35 keV), which could not be separated with the energy dispersive system with a resolution of approximately 160 eV. Ca as well as S and/or Pb are also the main constituents of the layers 4 and 5, whereas in layer 3, which appears transparent in the light microscope, only C could be detected. In layer 7 only Ca could be determined.

With the information of the elements present in the pigments of the various layers, it is possible to suppose the materials used for these layers. In order to gain structural information to identify the crystalline composition of the pigments, x-ray micro-diffraction is performed.

3.4 *X-ray micro-diffraction*

For the positioning of the individual paint layers during the x-ray diffraction a radiogram of the specimen illuminated with the plane beam was recorded as shown in Figure 7b. The complete scan, as indicated by the vertical line, consisted of 160 single points, separated by 4 μm. The lead containing and thus strong absorbing paint layer turn up dark against the less absorbing Ca containing layers (Fig. 7b).

All 160 diffraction spectra are displayed in a contour plot in Figure 8. Although this way of displaying the data is not appropriate to accurately identify individual crystalline phases, it brings onto view the continuous assembly of all subsequent paint layers by crystalline matter.

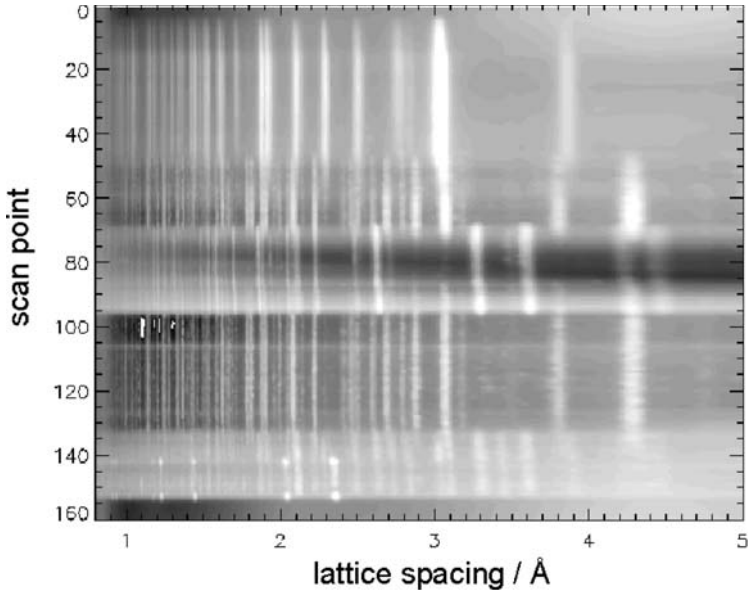

Figure 8. X-ray micro-diffraction. Contour plot of all 160 diffraction spectra subsequently measured across the paint layers. Diffraction angles are replaced by the according crystalline lattice spacing values. Bright grey values indicate high intensity.

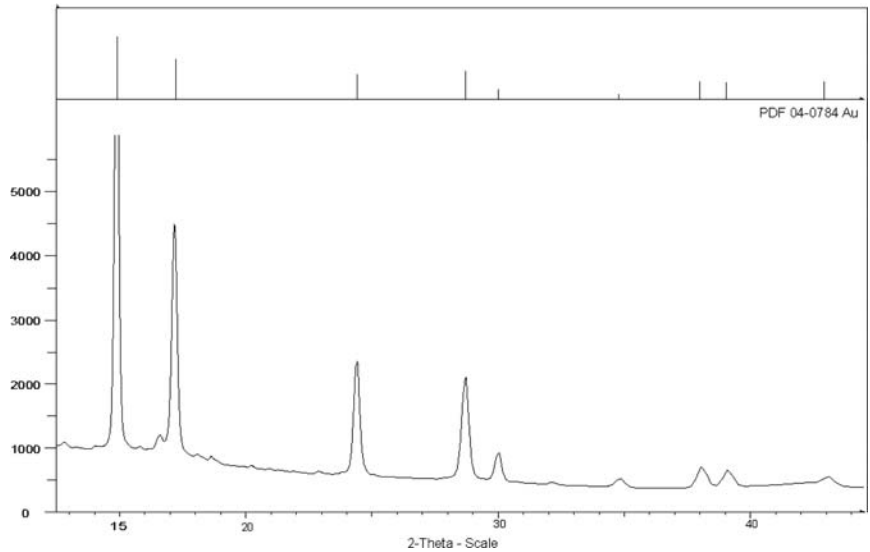

Figure 9. X-ray micro-diffractogram of the gold layer, layer 1, identified by the ICDD-database as Au.

Because of the small scan interval of 4 μm enough spectra of each layer are available for the crystalline identifications of the pigments in the paint layers. This line scan also shows the continuous transition between the various layers, which could be clearly separated by this analytical technique. Although the surface layer is a very thin gold layer, it could be found with the micro-XRD and identified by the ICDD-database, as shown in Figure 9.

Table 2. Results of x-ray micro-diffraction.

Layer (color)	Phases identified
1 (yellow)	Au
2 (red/orange)	$BaSO_4$, $CaCO_3$
3 (transparent)	
4 (yellow)	$2PbCO_3 \cdot Pb(OH)_2$, $CaSO_4 \cdot 2H_2O$
5 (white)	$2PbCO_3 \cdot Pb(OH)_2$, $CaSO_4 \cdot 2H_2O$
6 (white/yellowish)	$CaSO_4 \cdot 2H_2O$
7 (white/grey)	$CaCO_3$

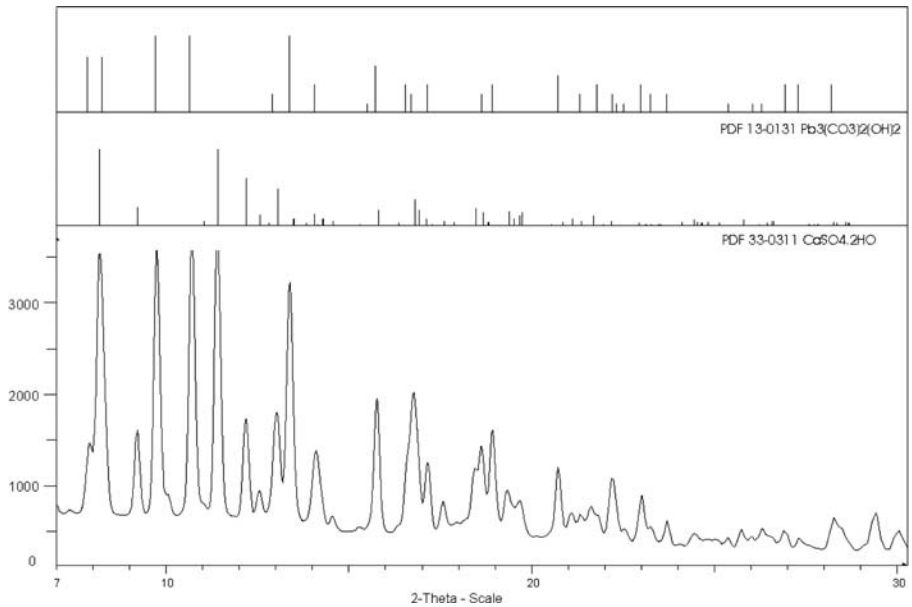

Figure 10. Diffractogram of layer 4, identified by the ICDD-database as lead white ($2PbCO_3 \cdot Pb(OH)_2$) and gypsum ($CaSO_4 \cdot 2H_2O$).

The results of the x-ray micro-diffraction of the other layers are summarized in Table 2 as well as in the Figures 10 and 11. In layer 2, which contains the elements Ca and Ba with some S and/or Pb (Table 1) a mixture of $BaSO_4$ and chalk could be identified. In the layers 4–6 mainly gypsum was identified by x-ray micro-diffraction, whereby in layer 4 and 5 also some lead white could be found (Fig. 10). In the SEM/EDX only C was registered for layer 3, which shows the bright fluorescence in the UV-fluorescence micrograph (Fig. 4b). The result of gypsum in this layer obtained by x-ray micro-diffraction can only be explained by the presence of gypsum in the neighbouring layer 4. Figure 11 depicts that calcite ($CaCO_3$) was used as ground material (layer 7).

4 CONCLUSIONS

With synchrotron induced x-ray micro-diffraction new perspectives for analyzing paint layers could be demonstrated. With this method it is possible to identify the pigments used exactly by their crystallographic structure and not only by their main elements, as the other methods (e.g. SEM/EDX) work with. Because of the great variety of inorganic pigments containing similar main elements it is

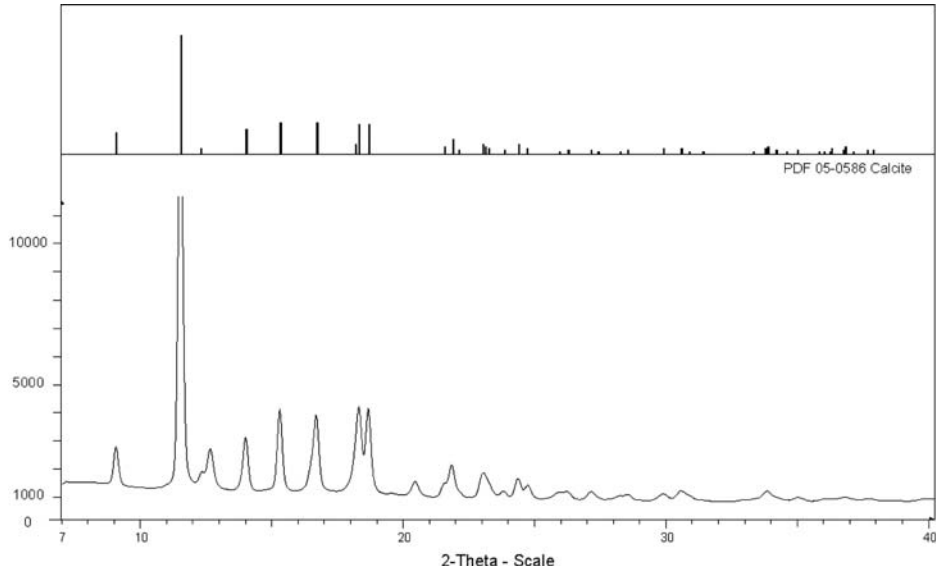

Figure 11. Diffractogram of layer 7, identified by the ICDD-database as calcite ($CaCO_3$).

now much easier to find the appropriate compound. However, for a clear interpretation of the materials used in paint layers a combination of light and UV-fluorescence microscopy, scanning electron microscopy combined with energy dispersive x-ray microanalysis and x-ray micro-diffraction yields to a high degree of information.

ACKNOWLEDGEMENTS

The authors express their sincere thanks to Dipl. Ing. Michael Melcher for carrying out the SEM/EDX analysis.

REFERENCES

Banik, G., Schreiner, M., Mairinger, F. & Stachelberger, H. 1982. Scanning Electron Microscopic Investigation of Cross-Sections taken from Paint Layer Specimens. *Praktische Metallographie*, Stuttgart, Dr. Riederer Verlag GmbH., Band 19, H.2, 104–108.

Feller, R.L. 1986. *Artists' Pigments – A Handbook of their History and Characteristics*, *Volume 1*. New York: Cambridge University Press.

Fuller, C. & Lewis, P. 1988. *Pigment Handbook*, New York: John Wiley & Sons.

Gettens, R.J. & Stout, G.L. 1966. *Painting Materials: a Short Encyclopaedia*. New York: Dover Publications.

Hanlan, J. 1975. The Scanning Electron Microscope and Microprobe. *Application to Conservation and Historical Research.* Venedig: ICOM, 4th Triennal Meeting, Reprints 75/4/3.

ICDD, 2002. International Centre for Diffraction Data, 12 Campus Boulevard, Newtown Square, PA.

Kirk-Othmer & Raymond, E. 1978. *Encyclopedia of Chemical Technology*. New York: John Wiley & Sons.

Kittel, H. 1960. *Pigmente – Herstellung, Eigenschaften, Anwendung*. Stuttgart: Wissenschaftliche Verlagsgesellschaft mbH.

Kühn, H. 1988. *Handbuch der künstlerischen Techniken*. Stuttgart: Reclam jun. GmbH.

Lengeler, B., Schroer, C., Tümmler, J., Benner, B., Richwin, M., Snigirev, A., Snigireva, I. & Drakopoulos, M. 1999. J. Synchrotron Rad. 6 1153–1167.

Matteini, M. & Moles, A. 1990. *Naturwissenschaftliche Untersuchungsmethoden in der Restaurierung.* München: Georg D.W. Callway GmbH & Co.

Mantler, M., Schreiner, M. & Schweizer, F. 2000. *XRD in the Museum*. Industrial Application of X-Ray Diffraction. New York, Basel: Marcel Dekker, 621–658.
Mantler, M. & Schreiner, M. 2000. X-ray fluorescence spectrometry in art and archaeology. *X-Ray Spectrom.* 29, 3–17.
PDF, 2000. Powder Diffraction File – Joint Commitee on Powder Diffraction Standards. Swarthmore
Roy, A. 1993. *Artists' Pigments – A Handbook of their History and Characteristics*, *Volume 2*. New York: Cambridge University Press.
Schramm, H.P. & Hering, B. 1988. *Historische Malmaterialien und ihre Identifizierung.* Graz: VEB Berlin/Akademische Druck- und Verlagsanstalt.
Schreiner, M. 1995. *Naturwissenschaften in der Kunst.* Vienna: Böhlau Verlag.
Ullmann, F. 1979. *Enzyklopädie der technischen Chemie*, Band 18 – Pigmente. Weinheim: Verlag Chemie GmbH.
West FitzHugh, E. 1997. *Artists' Pigments – A Handbook of their History and Characteristics, Volume 3*. New York: Cambridge University Press.
Wülfert, S. 1999. *Der Blick ins Mikroskop: Lichtmikroskopische Methoden zur Untersuchung von Bildaufbau, Fasern und Pigmenten*. Ravensburg: Ravensburger Buchverlag.

Cultural Heritage Conservation and Environmental Impact Assessment by Non-Destructive Testing and Micro-Analysis – Van Grieken & Janssens (eds)
© 2005 Taylor & Francis Group, London, ISBN 90 5809 681 5

From Giotto to De Chirico: analysis of paintings with portable EDXRF equipment

R. Cesareo
Dept. of Mathematics and Physics, University of Sassari, Sassari, Italy

A. Castellano, G. Buccolieri & S. Quarta
Dept. of Material Science, University of Lecce, Lecce, Italy

M. Marabelli, P. Santopadre & M. Ioele
Central Restoration Institute, Rome, Italy

G.E. Gigante & S. Ridolfi
Dept. of Physics, University of Rome "La Sapienza", Rome, Italy

ABSTRACT: Energy-dispersive x-ray fluorescence (EDXRF) analysis is particularly suited to analyse paintings, because of its non destructive manner and multi-elemental capacity. Interestingly, it can be conducted with portable equipment. The mean penetration of incident and secondary radiation has the same order of magnitude as the pigments thickness;

EDXRF-analysis of paintings generally provides the following informations:

– possible presence of elements on the surface due to pollution (sulphur, chlorine);
– identification of the elements and pigments, used by the artist;
– identification of previous restored areas, detected by the presence of "modern" elements;
– such as titanium, zinc, cadmium, selenium, etc;
– identification of fraudolent submissions.

Recently the famous "Chapel of the Scrovegni" painted by Giotto in Padua in 1303–05 was analysed in detail to obtain all the information as described above, and, more specifically, to determine the superficial presence of sulphur due to pollution and to control its removal. Further the golden haloes were studied in details.

As another example of application of EDXRF-analysis, 11 assumed paintings of De Chirico (1888–1978) were recently analysed to create a basis of comparison with 15 paintings positively identified as authentic.

1 INTRODUCTION

Energy-dispersive x-ray fluorescence (EDXRF) analysis is a highly valuable technique for the study of works of art, because it is non destructive, multi elemental, simple and relatively inexpensive (Cesareo 1988).

For these reasons EDXRF is a very popular analytical technique in the field of "archaeometry" (Cesareo 1997), even though there are various types of laboratory equipment dedicated to archaeometry, as well as portable equipment.

Portability of EDXRF equipment is, of course, extremely useful and almost mandatory in many cases, such as analysis of frescoes, large paintings, bronzes, brasses, gold alloys, etc., located in museums, churches, excavations, etc. (Cesareo et al. 2000a). In fact, only in a few cases it is possible to study a work of art outside its normal location and for these instances portable equipment is of the utmost importance.

There are a wide variety of materials that can be studied by using a portable EDXRF apparatus: to list a few, paintings and frescoes, alloys, ceramics, illuminated manuscripts and papers, enamels, stones and marbles. This type of portable equipment is beneficial in its diversity of applications, such as, instances in which a qualitative analysis is sufficient (for example the individuation of a pigment in a painting) and others in which a quantitative approach is required (for example in the case of alloys).

EDXRF analysis generally involves an area of mm^2, and a thickness between μm and a few mm. Therefore the analysis is superficial and dependent on the surface conditions. In some cases "capillary collimators" are employed, to focus the radiation into an area approximately 0.01 mm^2 (Janssens 2001). Due to reduced analysed thickness, EDXRF analysis is representative of the bulk composition only for homogeneous samples. EDXRF analysis is specifically suited for analysis of pigments in any type of paintings. In this particular case only a semi-quantitative analysis was required, and the penetration of the radiation was of the same order of magnitude of the pigment's thickness.

From the analysis of paintings, following information may be deduced:

a. the effects of pollution on the surfaces, generally indicated by the presence of sulphur or chlorine; the first element may be present, mainly as gypsum ($CaSO_4$) at the surface of monuments, frescos etc. due to burning of wood, cokes, gasoline, during the centuries. Gypsum produces blackening and heavy damages; chlorine, as NaCl, is sometimes present in works of art close to the sea;
b. the identification of "modern" restoration areas, is indicated by the presence of elements such as zinc, titanium, chromium, cadmium, selenium and others; for example titanium, as titanium white (oxide) was systematically employed starting from 1918, and zinc, as zinc white, starting from about 1870;
c. the characterisation of the pigments commonly used by the artist;
d. the identification of fakes, for example on the basis of points b and c.

In this paper a review is presented of recent applications of portable EDXRF equipment for analysis of paintings, from Giotto in the Chapel of the Scrovegni (painted in the years 1303–1305) and De Chirico (1888–1978). In the chapel of the Scrovegni, the above outlined points a. to c. were emphasised, and the golden haloes were systematically analysed.

In the case of De Chirico, 26 paintings were examined, including 11 of which were of uncertain attribution, possibly fraudulent. This last hypothesis was in fact confirmed by EDXRF-analysis, based on an in-depth comparative analysis of the pigments used by the artist (point c) with the authentified De Chirico paintings.

2 THEORETICAL BACKGROUND

When radiation from a x-ray tube penetrates the pigments of a fresco or of a painting, it is absorbed along its path. A fraction of the energy of the absorbed photons is converted into fluorescent photons of the various elements, and some of them, according to the thickness of the involved layers, reach the surface of the fresco and are detected.

In the case of a fresco, the deepest layer is indicated by the plaster. Superimposed is the preparation, and above that one or more pigment layers. In the case of a painting, the deepest layer is given by the canvas or wood. Superimposed is the preparation, and above one or more pigment layers.

As an example, in the case of Giotto's haloes in the chapel of the Scrovegni the complexity of the x-ray spectra indicated the presence of various pigment layers below the golden leaf. Each layer behaves as a thin layer (Cesareo 1988); elements are visible, such as strontium, coming from the deepest layer, which corresponds to the plaster. In the hypothesis of a sequence of thin layers, fluorescent counts Na from a generic element a may be written in the form:

$$N_a \propto N_0 \, k \, \omega_a \, \sigma_{ph.a} \, m_a \, A_i \qquad (1)$$

where:

- N_0 is the incident photon flux;
- k is an overall geometrical and detector factor;
- ω_a is the fluorescent yield;
- $\sigma_{ph.a}$ is the cross section of element a for photoelectric effect;
- m_a is the mass per unitary area of element a in the sample.
- A_i gives the attenuation of incident and output radiation if element a is in the internal layer j.

A_i is given by:

$$A_i = \exp[-\Sigma_i^{j-1} \mu_i(E_0)x_i] \exp[-\Sigma_{j-1}^{1} \mu(E_{ph.a})\, x_i] \quad (2)$$

where:

- $\mu_i(E_0)$ and $\mu(E_{ph.a})$ is the attenuation coefficient of the i-th layer at incident energy E_0 and fluorescent energy $E_{ph.a}$ respectively;
- x_i represents the thickness of the i-th layer.

In the case of thin layers, elements from the various layers will be visible by EDXRF-analysis. The attribution to the correct layer is in many cases possible, especially when heavy elements are present in a layer and L-lines of these elements (gold, mercury, lead) are clearly visible. In these cases the approximate thickness of the pigment may be calculated through the calculation of auto attenuation, so as the thickness of a super imposed pigment or metal layer.

For example the ratio $R = L_\alpha/L_\beta$ of a heavy element of thickness x changes by auto attenuation in the following manner (Cesareo 2000b):

$$R = R_0 \{[(\mu_0+\mu_2)/(\mu_0+\mu_1)]\,(1-\exp-[(\mu_0+\mu_1)\rho x])/(1-\exp-[(\mu_0+\mu_2)\rho x])\} \quad (3)$$

where:

- R_0 is the ratio $R = L_\alpha/L_\beta$ for an infinitely thin thickness; R_0 depends on its theoretical value and on the detector efficiency at the two energy values of L_α and L_β radiation (Cesareo, 2000a).
- μ_0, μ_1, μ_2 are the mass attenuation coefficients (in cm^2/g) at incident energy and at energy of L_α and L_β radiation respectively; in the case of incident Bremsstrahlung radiation the energy of incident radiation is not well defined, and an approximate mean value should be defined;
- ρ is the physical density of the sample (in g/cm^3);
- x is the thickness of the sample (in cm).

Differential attenuation of L_α and L_β x-rays of a heavy element a (for example lead) by another heavy element b (for example gold, as in the golden haloes of the Chapel of the Scrovegni) is given by:

$$[L_\alpha/L_\beta]_a = [L_\alpha/L_\beta]_{a0} \exp-([\mu_2-\mu_1]\rho x \quad (4)$$

where:
$[L_\alpha/L_\beta]_{a0}$ represents the L_α/L_β ratio (for example of lead) simply auto attenuated.

The term $(\mu_2 - \mu_1)$ is positive for example for gold attenuation, because of the gold edges, and negative for example for tin.

The measured L_α/L_β ratio for a heavy element in a pigment is finally depending on two effects: a. the auto attenuation in the pigment containing this element and b. the attenuation in a superimposed pigment or metal layer.

Figure 1 shows the attenuation coefficients of gold, lead and tin versus energy, and Figure 2 the ratio $R = L_\alpha/L_\beta$ for lead L-lines attenuated by a gold leaf or by a tin sheet. Examples will be discussed later, concerning both pigments employed by Giotto and by De Chirico, where the above discussed cases will be present.

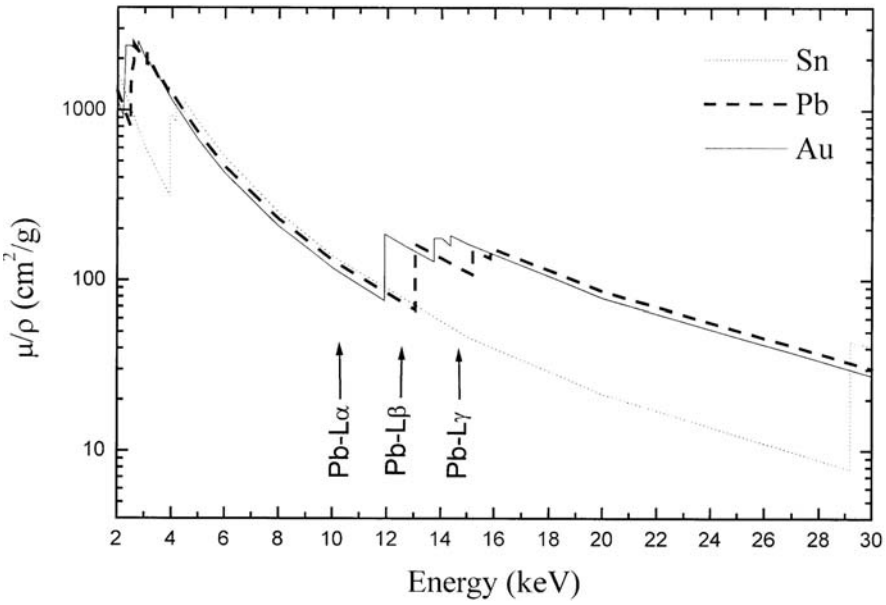

Figure 1. Attenuation coefficient of gold, lead and tin versus energy, showing that Pb-L_β are more absorbed than Pb-L_α X-rays by Au, less absorbed by Sn.

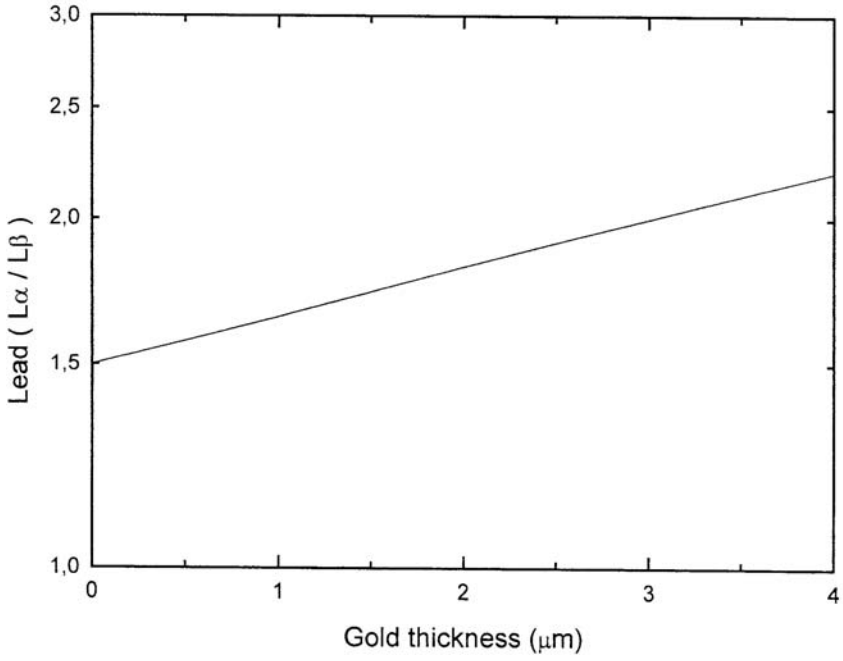

Figure 2. Ratio L_α/L_β of lead lines attenuated by a gold leaf versus Au thickness x, following Eq. (4).

It should be observed that the above described differential attenuation effects is quantitatively evident for L-X rays of heavy elements, but are also present in the case of K-X rays. However this effect is much more reduced both for low-Z elements (calcium, iron, copper), because K-lines are very close in energy, and for medium-Z elements (tin) because the attenuation coefficient is very slowly changing.

3 EXPERIMENTAL SET-UP

For analysis of low atomic number elements (sulphur, chlorine, argon, potassium, calcium) a portable EDXRF-equipment was assembled, composed of a Ca-anode x-ray tube working at about 6 kV (Cesareo 1999) (Fig. 3).

In this case the incident radiation is composed of the Ca-K lines at 3.7 keV, and of Bremsstrahlung radiation extending up to 6 keV. This radiation is able to excite in a very efficient manner sulphur, and also calcium can be excited, but only by the last and smaller tail of the Bremsstrahlung radiation.

Alternatively, also a Pd-anode x-ray tube was employed, working at 4–6 kV (Cesareo 2000b). In this case the incident radiation is composed of the Pd-L lines at 2.9 keV and of the Bremsstrahlung radiation. Also in this case sulphur is excited in a very efficient manner, while, on the contrary, calcium is excited only by the last and smaller part of the Bremsstrahlung spectrum

In both cases an AMPTEK thermoelectrically cooled Si-PIN detector was employed, having a beryllium window of 25 μm, an energy resolution of 200 eV at 5.9 keV and coupled to a pocket AMPTEK multi channel analyser (AMPTEK 2003)

For analysis of all elements with atomic number Z higher than that of silicon approximately (including therefore elements from sulphur to calcium, however excited with low efficiency), i.e. analysis of pigments from both Giotto's Chapel of the Scrovegni, and De Chirico paintings, a portable EDXRF-equipment was employed, composed of a small size, low weight W-anode Oxford x-ray tube, working at 30 kV and 10–50 μA (Oxford Anal. Systems 2003) and a small size, thermoelectrically cooled AMPTEK detector.

Si-PIN detector having a Be-window of 75 μm, with an energy resolution of 200 eV at 5.9 keV and a pocket AMPTEK multi channel analyser (Fig. 4). For analysis of the 14 true De Chirico paintings, a thermoelectrically cooled Si-drift detector from EIS was employed, having an energy resolution of 150 eV at 5.9 keV (Fiorini 1998). The x-ray output from the W-anode x-ray tube is composed of a Bremsstrahlung radiation, with a photon intensity starting from about 4–5 keV, having a maximum at about 10 keV and decreasing up to 30 kV. The order of magnitude of the fluorescence excitation efficiency was approximately the same from elements from iron to lead, a factor of 4–5 less for calcium and of 20 for sulphur (Cesareo 2000).

Both x-ray tube and detector were placed as close as possible to the painting, for increasing the geometrical efficiency of the system, but without touching it. This corresponds to x-ray tube and detector at a distance of about 5–10 mm from the painting, each at an angle of about 20° with respect to the painting normal. An area of approximately 3–5 mm^2 was irradiated, varying with the distance. A typical measuring time of about 100–200 s is generally needed to obtain a x-ray spectrum with a sufficiently good statistics.

4 RESULTS

4.1 *Determination of sulphur in frescos and especially in Giotto's frescoes in the Chapel of the Scrovegni in Padua.*

Superficial sulphur in monuments and frescos, mainly in the form of gypsum ($CaSO_4$), are the indicators of pollution. It can be often found on the surface of frescoes and monuments, producing black colouring and damages (Laurenzi Tabasso 1992). These elements, and especially sulphur must be removed to avoid extensive damage

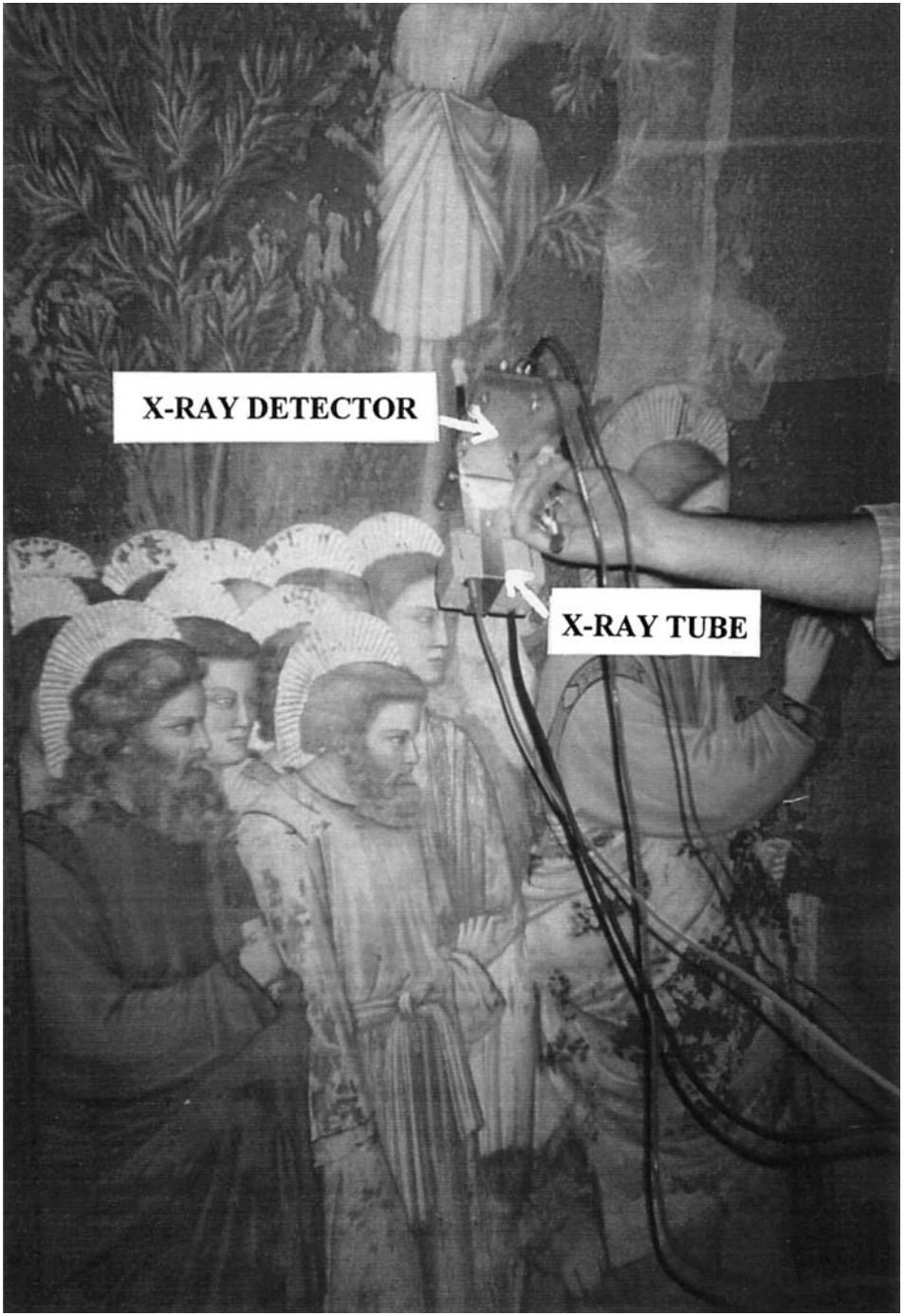

Figure 3. Equipment for sulphur and chlorine analysis, composed of a Ca-anode x-ray tube working at 6 kV and 0.1 mA, and a thermoelectrically cooled Si-PIN detector.
(This figure is presented in the signature in colours at the end of this volume, Appendix, pg. 324)

Figure 4. Equipment for analysis of elements from 1 to 30 keV employed in the Chapel of the Scrovegni in Padua, composed of a W-anode 30 kV, 0.3 mA x-ray tube and a thermoelectrically cooled Si-PIN detector. (This figure is presented in the signature in colours at the end of this volume, Appendix, pg. 325)

Sulphur and chlorine were analysed with the apparatus as shown in Figure 3. By using the Ca-anode x-ray tube the minimum detection limit for sulphur is 0.1% in 100 s measuring time, at 3SD from the background. By using the Pd-X ray tube the MDL is approximately the same. When both S and Cl are present, then the Ca-anode apparatus is much better for chlorine, because the separation between Cl-lines and exciting peak is greater in the first case.

The following frescoes were analysed during the process of restoration carried out by the "Istituto Centrale del Restauro" in Rome.

a. frescos attributed to Pomarancio in the church of S. Stefano Rotondo in Rome, which was under restoration by the "Istituto Centrale del Restauro" of Rome. A large number of areas were analysed in which three typical situations were detected: a. in non-restored areas, sulphur was found everywhere at concentrations up to about 12%; b. in areas that were simply sponged with a proper solution, sulphur was found at concentrations between 2% and 4%; c. in areas accurately treated to remove pollution layers, no sulphur was found (Castellano 1997).
b. frescos of Piero della Francesca in the Church of S. Francesco, Arezzo, where sulphur was detected in all areas (Castellano 1999);
c. frescos of Domenichino in the Nolfi Chapel in the Cathedral of Fano, sulphur was detected in all areas, except in those that were restored;
d. ancient roman frescos in the Church of S. Clemente, Rome. In this church both the ancient fresco in the mithraic school and the fresco in the lower basilica were analysed; large quantities of sulphur were detected in the lower basilica, at the upper level, close to the outside air. No sulphur was detected in the mithraic school, which is on the upper level close to the outside air. No sulphur was detected in the Mithraic School (located underground in an isolated area) although for the red pigment, in which S and Hg were detected, showing the presence of cinnabar, not of pollution.

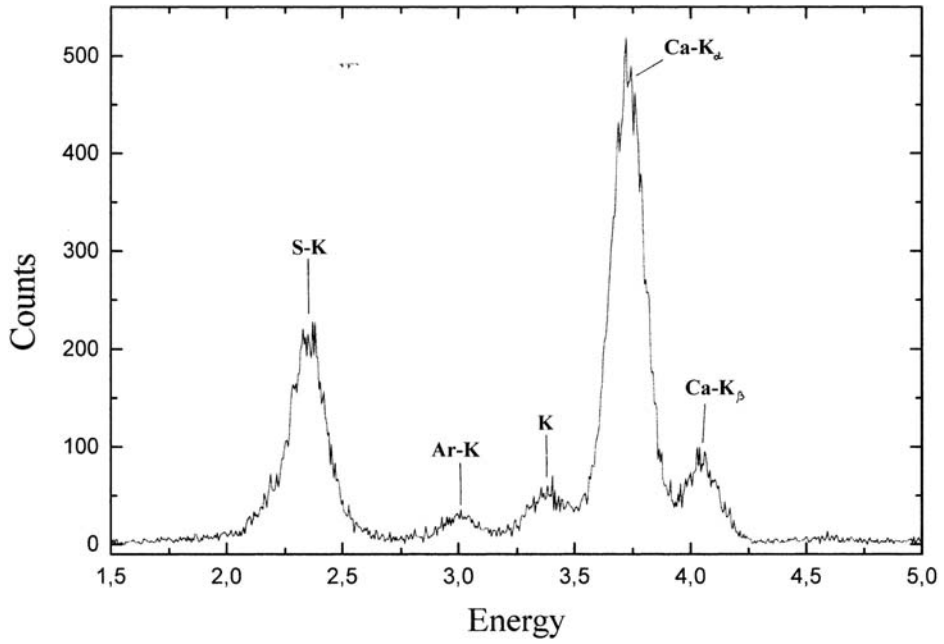

Figure 5. X-ray spectrum of an area of the last judgement (flame on the top left) of the Chapel of the Scrovegni obtained with the equipment shown in Figure 4. The x-ray peaks of S, Ar, K and Ca are visible.

e. the famous frescos by Giotto in the "chapel of the Scrovegni" in Padua were systematically analysed in July and September 2001, and again in January 2002, in about 300 points, before, during and after restoration, in order to detect the possible presence of sulphur and to test various cleaning procedures. Concerning this last example, as described in Section 2, sulphur was determined with two different types of equipment: one using the Ca-anode x-ray tube, the second one using the Pd-anode working at low voltages, to selectively excite Pd-L lines. The fresco-pigments were analysed with the same Pd x-ray tube working at about 10 kV, and with a W-X ray tube working at 30 keV.

The following results were obtained:

– sulphur was detected everywhere, at a concentration level from about 1% to about 10%, depending on the exposition and on the underlying pigment, possibly due to porosity; sulphur content for example was lower in the case of azurite pigments, higher in the white and green pigments; the use of the Ca-anode x-ray tube (Fig. 5) gave rise to a "cleaner" spectrum with respect to the Pd-L x-ray tube, but the counting rates are much lower, due to the much larger window of the Ca-anode tube;
– the S-cleaning process was of great importance to the restoration of the frescoes and was continuously monitored with the EDXRF portable equipment. Various cleaning procedures were carried out, and the S-content is reported in Figure 6. The use of a cleaning process based on ion-exchange resins gave the best results, compatibly with the requirement to not touch the pigments lying below;
– chlorine was detected only once, in an area that was possibly recently cleaned with a chlorine solution;
– titanium was detected in many white areas, indicating recent restoration.

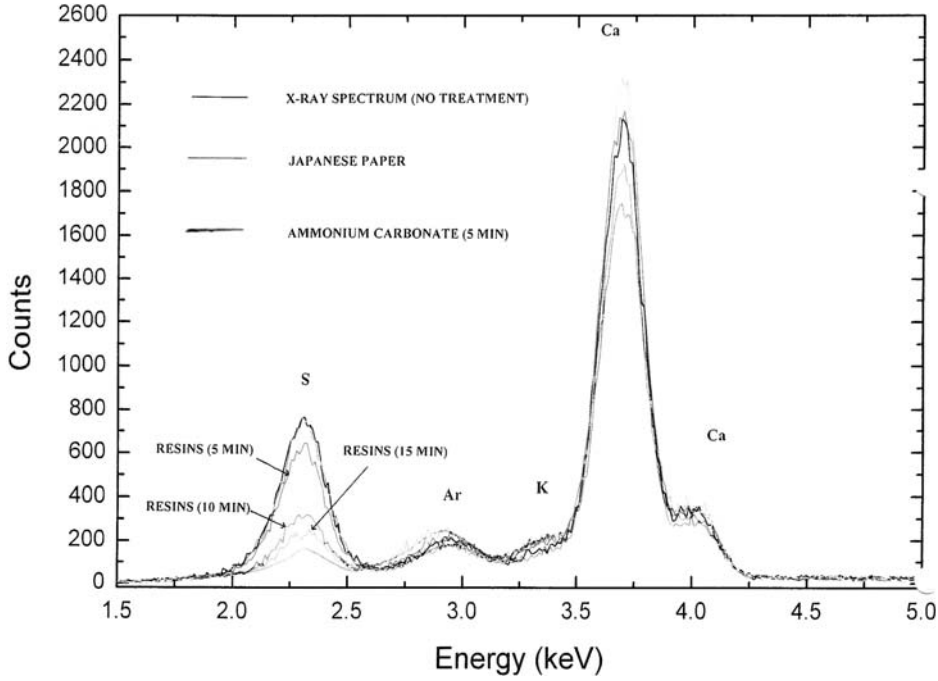

Figure 6. Sulphur x-ray peak and its partial remotion as a function of cleaning procedure in the Chapel of the Scrovegni. The use of Japanese paper gives no effects, while ammonium carbonate produces the maximum removal, but partially affects the pigments.

4.2 *Analysis of Giotto's haloes in the Chapel of the Scrovegni*

About 30 haloes were analysed, many of them golden and in good conditions, while others damaged, and others completely black (Cesareo 2003, Ieole 2002).

An x-ray spectrum of a good condition golden halo compared with the x-ray spectrum of a black halo is shown in Figure 7. From left to right fluorescence peaks are visible due to the following elements:

- gold M-lines at 2.1 keV;
- sulphur K-lines at 2.3 keV, due to pollution effects;
- lead M-lines at 2.34 keV;
- argon K-lines, at 2.95 keV, due to the presence of this element in air;
- tin L_α lines, at 3.45 keV, present in the black halo only;
- calcium K-lines, at 3.7 keV;
- iron K_α and K_β lines, at 6.4 and 7.06 keV;
- nickel K_α and K_β lines, at 7.5 and 8.3 keV, due to background effects in the x-ray tube;
- copper K_α and K_β lines, at 8.04 and 8.94 keV;
- tungsten L-lines, at 8.35, 9.8 and 11.3 keV respectively, due to the x-ray tube anode;
- gold L-lines, at 9.67, 11.5 and 13.4 keV, present in the golden halo only;
- silver K-lines, at 22.1 and 25.2 keV, mainly due to fluorescence effects in the detector;
- lead L-lines, at 10.5, 12.6 and 14.8 keV;
- strontium K_α lines, at 14.15 keV;
- tin K_α and K_β lines, at 25.2 and 28.7 keV respectively, present in the black halo only.

There are several cases of peaks overlap: sulphur K with lead M, tin L with calcium K, gold L_α with tungsten L_β.

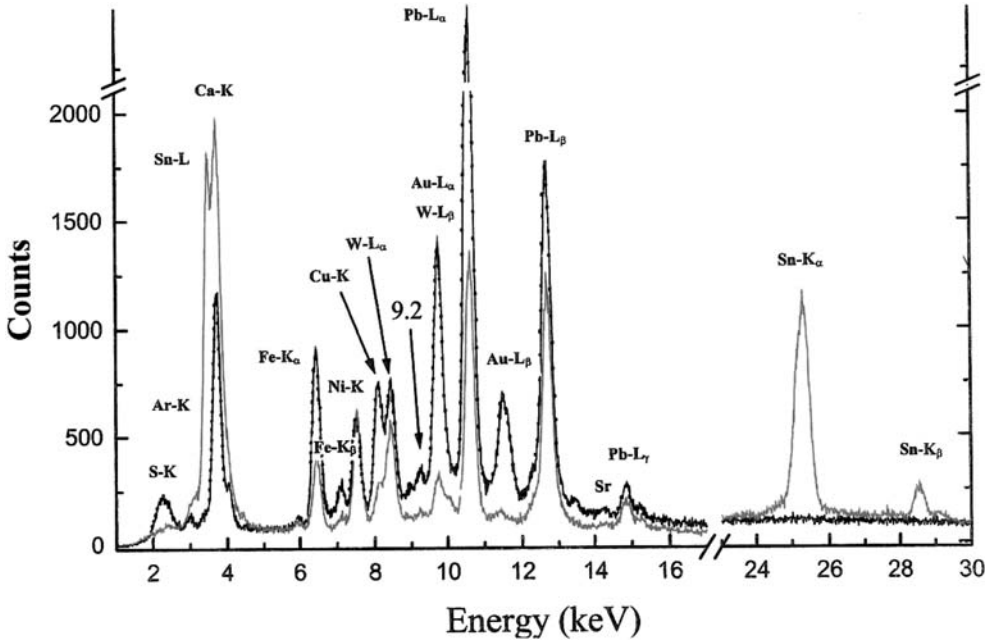

Figure 7. X-ray spectrum of a golden halo (dotted) and a black halo (red) in the Chapel of the Scrovegni.

X-rays of elements argon, nickel, tungsten and silver are due to the x-ray tube anode (W), or to the interaction of the x-ray beam with the detector (Ag), air (Ar), tube material (Ni), the other x-lines are related to the fresco pigments and/or to the plaster. However, they must be assigned to the proper layer. The ratio of the x-rays of all elements with respect to gold L-x-rays and the Pb (L_α/L_β) ratio were first calculated, according to Eq.(4) (Table 1). If an element belongs to the gold alloy, typically composed of gold, silver, copper, lead and iron, then its ratio with respect to gold should remain approximately constant.

From the mean values of these ratios it may be deduced that no one of the elements essentially belongs to the gold alloy, although it cannot be excluded that a small amount of these elements could belong to it. Therefore, the gold employed by Giotto most probably is of high purity. This conclusion was confirmed by the EDXRF analysis on a small fragment of gold from a halo.

The lead should belong to the "second layer", because it appears at the surface where gold is partially damaged. This point is confirmed from results shown in Table 1, where it may be observed that lead/gold ratio does not varying too much. In this hypothesis of a gold leaf superimposed to a layer of a lead containing pigment (possibly minium or white lead), the Pb-L lines should be attenuated in a different manner by the gold leaf, as discussed in Section 2. This effect is, in fact, clearly visible in Figure 8, where the x-ray spectrum of a golden halo is compared with a black one, in which the contemporary presence of tin and lead is apparent (in this case a tin sheet is superimposed to the white lead pigment). The different attenuation of Pb-L_α and Pb-L_β lines by gold and tin is clearly visible.

By plotting the attenuation coefficients of gold, lead and tin (Cesareo 2003) (Fig. 2), it may be calculated that Pb-L_β lines are more attenuated with respect to Pb-L_α lines when crossing a gold leaf, less attenuated when crossing a tin sheet.

Considering these effects for all gold haloes in good conditions, the mean thickness of the gold layer may be calculated, which turns out to be:

$$1.6 \pm 0.5 \mu m$$

Table 1. $Pb(L_\alpha/L_\beta)$ ratio and ratio of the intensity of elemental x-rays with respect to gold intensity for golden haloes.

Sample n.	$Pb(L_\alpha/L_\beta)$	$Pb\text{-}L_\alpha/Au\text{-}L_\beta$	Fe/Au	Cu/Au
245	1.78	4.2	2.2	0.6
248	1.9	11.8	1.0	2.4
294	1.71	6.4	3.9	2.2
302	1.67	7.1	1.8	1.8
207	1.85	3.7	5.0	2.0
208	1.85	2.7	6.5	7.4
209	1.87	3.9	12.4	0.9
346	1.80	3.4	4.4	0.7
227	1.80	3.5	3.4	0.7
228	1.67	4.4	8.0	0.8
348	1.74	3.4	3.7	0.6
236	1.65	7.4	3.3	1.1
238	1.65	10.4	4.7	0.6
239	1.77	6.9	2.6	0.5
240	1.66	6.4	1.9	0.5
242	1.70	4.2	2.1	0.3
246	1.65	3.8	2.4	2.4
295	1.77	6.0	4.8	1.2
296	1.65	6.5	6.4	1.3
310	1.74	6.7	2.2	1.5
319	1.8	8.0	2.5	0.18
320	1.79	3.6	3.9	0.2
246	1.71	3.9	5.2	1.7
Mean values	1.75 ± 0.08	5.6 ± 2.2	4.1 ± 3.0	1.3 ± 1.4

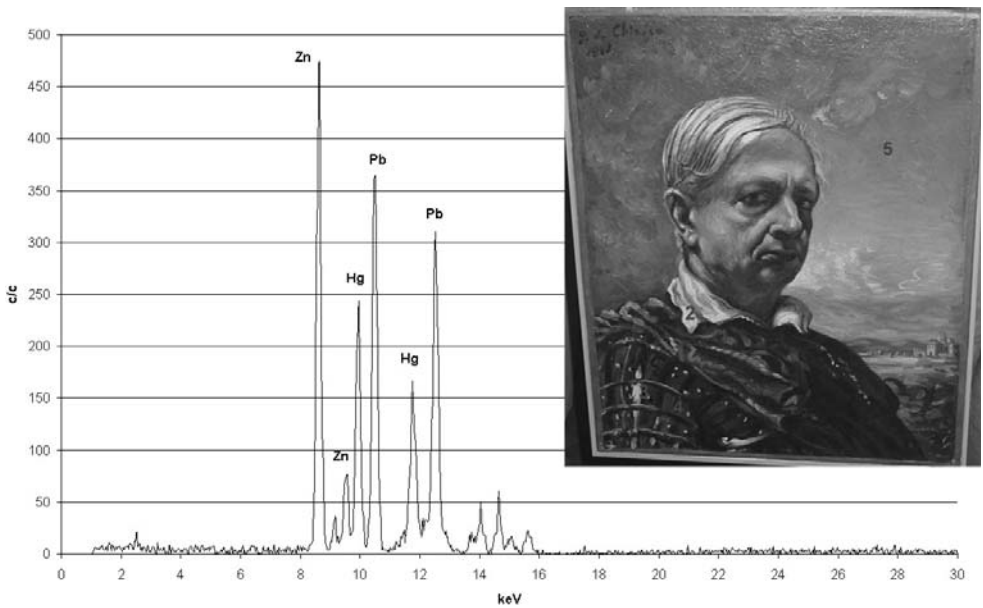

Figure 8. X-ray spectrum of a red area of the painting "self portrait" by De Chirico, painted around 1968.

This result is confirmed by other techniques, such as SEM-EDS and XRD (Ioele 2002). It may be concluded that the gold leaf is extremely thin and of relatively constant thickness (minimum and maximum values: 1 μm and 2.3 μm, respectively). Calculating the total area covered by the gold haloes, the total amount of gold employed by Giotto in the Chapel of the Scrovegni can be approximately evaluated as:

$$m_{Au} = 540 \pm 170\,g$$

The thickness of the layer of the pigment containing lead can be calculated from the Pb/Au counts ratio and from the Au-thickness as being about 6 ± 2 μm Pb-equivalent, corresponding, of course, to a much larger thickness of the pigment.

Complicated is the attribution of copper to the correct layer. Looking at the x-ray spectra of irradiated areas, it turns out that x-rays of copper are clearly more intense when the halo is superimposed to an azurite background, which is at a deeper layer than lead. Excluding these cases, from Table 1 the calculated ratio Cu/Au will be lower and also more constant $\approx (0.6 \pm 0.2)$. It is therefore reasonable that Cu-X rays come both from the azurite and from a layer between the lead containing pigment and gold (may be Cu-resinate employed to glue the gold leaf on the white lead preparation). From the ratio Cu/Au ≈ 0.6 it turns out that the copper equivalent thickness of the glue between lead and gold is of about 0.9 ± 0.3 μm.

Considering now the Cu-K lines from the azurite layer, which can be identified by the much higher intensity, they are attenuated by the lead + gold sheet, but the K_α line is more attenuated, giving rise to a K_α/K_β ratio of about 8.5 instead of the "normal" value of 6.4. This effect can be observed in a few x-ray spectra where the Cu-lines are sufficiently clean. The Cu-equivalent thickness of azurite can be calculated as being about 5 μm.

Calcium, iron and strontium could come, at least partially, from the deepest layer: the plaster. In this hypothesis Ca, Fe and Sr-K lines should be attenuated by lead carbonate, copper and gold, giving rise to an attenuation factor of about 10^6, 35 and 3 respectively. In the case of Calcium this attenuation seems to be too high to give reasonable Ca-counts in the x-ray spectra. Calcium should be, therefore, also present at the surface of the fresco, possibly as $CaSO_4$. This hypothesis is confirmed by x-ray spectra obtained with a x-ray tube working at 5 kV, where the penetration of incident radiation is extremely reduced. In those spectra large peaks of sulphur and calcium are present (see Figure 5).

Also the attenuation factor for iron seems to be too high, and the ratio of K_α/K_β, in the few cases in which it could be calculated, seems to be not compatible with the hypothesis of iron coming only from the plaster. May be iron is also present in a non identified more superficial layer, mixed with other pigments.

Strontium is a minor component of the plaster. In fact the peak of this element is present in almost all x-ray spectra of the fresco, at higher levels when iron or copper pigments were employed by Giotto over the plaster, and at lower levels in the case of golden haloes, when the Sr-K photons cross Pb + Au, or Sn + Pb layers.

Seven haloes are black, and contain high quantities of lead, but no gold. Besides that, the x-ray spectra are quite similar to those of golden haloes. The ratio Pb-L_α/Pb-L_β is ≈ 1.57, which corresponds to a Pb-L_α/Pb-L_β ratio affected by auto attenuation only. The golden leaf was possibly lost.

Two additional haloes are black and also similar, and contain high quantities of both lead and tin. Also in these cases, besides lead and tin, the x-ray spectra are similar to those of golden haloes. The ratio Pb-L_α/Pb-L_β is about 1.1, corresponding to the situation of a tin layer superimposed to one of white lead. The thickness of tin, calculated from the Pb-L_α/Pb-L_β ratio turns out to be about 13–15 μm. This result is confirmed by SEM-EDS and XRF (Ioele 2002).

4.3 *Analysis of paintings by De Chirico*

Giorgio De Chirico (1888–1978) was the inventor of the "pittura metafisica" (metaphysical painting), a unique and enigmatic style which served as the precursor to many artistic movements including Futurism and Surrealism. His cartoon-like dreamscapes, featuring classical statues, Italian piazzas, sinister shadows, geometrical objects remind one of childhood drawings, but with a

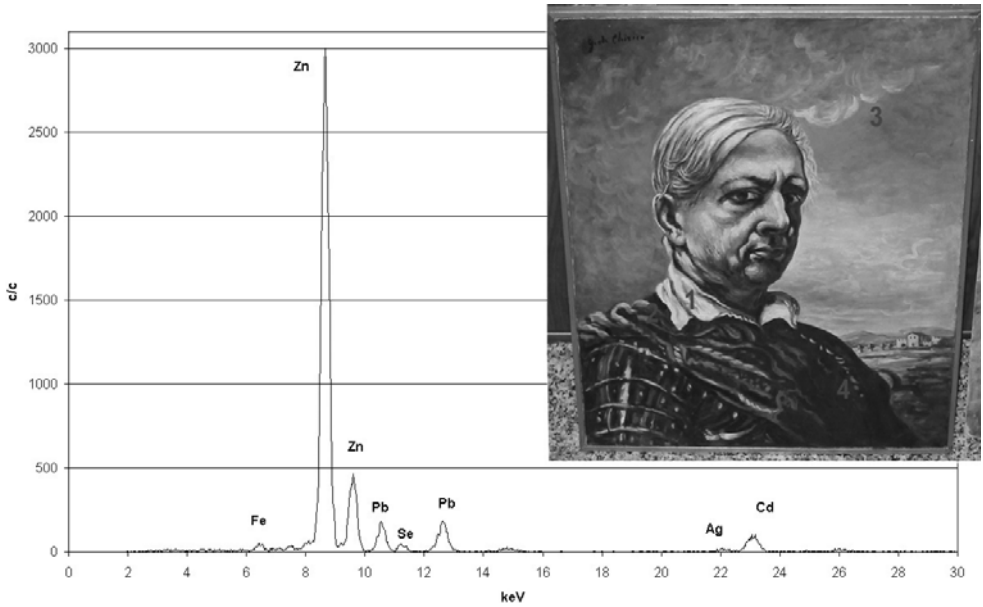

Figure 9. X-ray spectrum of a red area of the painting "self portrait" of suspect attribution to De Chirico.

menacing edge. The bright golden yellows and turquoise blues attract the eyes, and the unexpected juxtapositions of architecture and objects capture the imagination. De Chirico was a very prolific artist and during his long life he produced thousands of paintings. Also for this reason there are many copies, imitations and fakes of De Chirico.

15 oil-paintings completed from his last period were analysed to identify the pigments typically employed by the artist in this period (De Chirico 1983). These paintings were systematically analysed by EDXRF with an equipment as described in Section 3.

These paintings have all a similar composition. The "fingerprint" of them is:

– a preparation made with a mixture of lead white and zinc white;
– a systematic use of lead-based pigments, not only for the preparation;
– the red colours based on the use of cinnabar (HgS);
– a rare or completely absent use of organic pigments.

A typical painting with corresponding analysed points and x-ray spectra is shown in Figure 8.

11 oil-paintings supposedly painted by De Chirico also in his last period were analysed in the same manner as the authentified De Chirico paintings, to identify the pigments typically used by the painter and to establish if these pigments are similar or different from those employed by De Chirico (1983). It was verified that all paintings seem to have a similar composition, signifying that they were, in any case, painted by the same artist. The "fingerprint" of these paintings is the following:

– a preparation made with zinc oxide;
– almost absence of lead;
– the red colour systematically made with cadmium red;
– a very frequent use of organic pigments and/or of an organic protective varnish.

A typical painting of this type, showing the analysed points and related x-ray spectra is shown in Figure 9.

The deduction concerning the use of organic pigments and varnishes (containing no element which can be analysed by x-ray fluorescence analysis) was deduced mainly by a highly reduced

intensity of several x-ray peaks and by an alterated $R = L_\alpha/L_\beta$ ratio of lead. Examining in a general way the values of this ratio, it may also be deduced that the oil pigments layer employed by De Chirico is much thicker than the fresco layer employed by Giotto in the Chapel of the Scrovegni. Excluding the gold haloes, the $R = L_\alpha/L_\beta$ mean ratio for lead in the Chapel of the Scrovegni is 1.6 ± 0.2, while in the case of the true De Chirico paintings the same mean ratio is given by 1.15 ± 0.25. The difference is given, as observed above, by a thicker thickness of oil based pigments and by the possible presence of varnish at the surface.

The two paintings clearly appear to be made by two different artists. Comparing then all the results of the authentified and unauthentified De Chirico paintings, they seem to be very different. The 11 paintings assumed to be De Chirico are, in fact, with high probability fakes.

ACKNOWLEDGEMENTS

This work was partially supported by the Consiglio Nazionale delle Ricerche, Programma Finalizzato "Beni Culturali". The authors also like to thank Prof. Giovanna Dalla Chiesa for the discussions about the De Chirico paintings.

REFERENCES

AMPTEK Inc., 6 De Angelo Drive, Bedford, MA 01730-2204 USA.

Castellano, A. & Cesareo, R. 1997. A portable instrument for energy-dispersive x-ray fluorescence analysis of sulfur. *Nucl. Instrum. and Methods in Phys. Res. B* 129: 281–285.

Castellano, A. 1999. Unpublished work.

Cesareo, R. 1988. Photon induced x-ray emission. In R. Cesareo (ed.). *Nuclear Analytical Techniques in Medicine: 19–119.* Amsterdam: Elsevier.

Cesareo, R., 2000b. X-ray physics; *Suppl. Nuovo Cimento.* 19: 1–214.

Cesareo, R., Castellano, A., Fiorini, C., Gigante, G.E., Iwanczyk, J.S., Longoni, A., Pantazis, J.A., Pena Chapas, J.L. & Rosales, M.A. 1997. Thermoelectrically cooled semiconductor detectors for portable EDXRF equipments. *Proc. SPIE, S. Diego, CA, 31 July-1 August*, 3115: 274–283.

Cesareo, R., Castellano, A., Buccolieri G. & Marabelli, M. 1999. A portable apparatus for EDXRF-analysis of S and Cl in frescoes and stone monuments. *Nucl. Instrum. Methods B* 155: 326–330.

Cesareo, R., Gigante, G.E., Castellano A. & Iwanczyk, J.S. 2000a. Portable systems for energy-dispersive x-ray fluorescence. In R.A. Meyers (ed.). *Encyclopedia of Analytical Chemistry:* 1–12. New York: J. Wiley & Sons.

Cesareo, R., Cappio Borlino, C., Stara, G., Brunetti, A., Castellano, A., Buccolieri, G., Marabelli, M., Giovagnoli, A.M., Gorghinian, A. & Gigante, G.E. 2000b. A portable energy dispersive x-ray fluorescence apparatus for the analysis of sulphur and chlorine in frescoes. *J. Trace and Microprobe Techniques* 18: 23–33.

De Chirico G., 1983: Piccolo trattato di tecnica pittorica. 3rd Edition. Milano: Scheiwiller.

Fiorini, C. & Longoni, A. 1998. Application of a new non cryogenic x-ray detector in portable instruments for archaeometric analysis. *Rev. Sci. Instruments* 69: 1523–1528.

Ioele, M., Marabelli, M., Santopadre, P., Cesareo, R., Castellano, A. & Verità, M. 2002. L'utilizzo delle lamine metalliche nella Cappella degli Scrovegni. *ICR Internal Report.*

Janssens, K. 2001. Use of microscopic XRF for non-destructive analysis in art and archaeometry; In *Proc. 16th Int. Conf. on x-ray Optics and Microanalysis; Vienna*, *2–6 July 2001*, 44–48.

Laurenzi Tabasso, M. & Marabelli, M. 1992. *Il degrado dei monumenti in Roma in rapporto all'inquinamento ambientale*. Viterbo: BetaGamma.

Oxford Analytical Systems Division, 2003; 275 Technology Circle, Scotts Valley, CA 95066 USA.

Cultural Heritage Conservation and Environmental Impact Assessment by Non-Destructive Testing and Micro-Analysis – Van Grieken & Janssens (eds)
© 2005 Taylor & Francis Group, London, ISBN 90 5809 681 5

Corrosion of bronze in outdoor environments

Susan I. Sherwood
Center for Technology & Innovation, Inc. Endicott, NY, USA

ABSTRACT: More than a century of observations has linked atmospheric chemicals with increased bronze corrosion. The UN/ECE dose response function for bronze, derived from observations of short-term exposure of standard coupons, compares well with in situ measurements of long-term corrosion of the series of 50+ *Hiker* statues in the U. S. Kitson's *Hikers* are attractive as corrosion monitors because of the fixed geometry and reasonably consistent alloy chemistry, their wide distribution and the long period over which distribution took place. Both mapping and profiling techniques make it possible to conduct longitudinal studies of the evolution of corrosion. Of ongoing interest is the potential of the moulding technique to record changes in corrosion with time and to document the effects of bronze conservation treatments.

1 HISTORICAL PERSPECTIVE

By the mid-1800s, it had become apparent that the range of materials sensitive to pollution included outdoor bronzes, copper roofs, iron, some building stones, textiles, leather and paper (Brimblecombe 1987). In 1864, corrosion and metal samples were collected from 10 bronze monuments in Potsdam, Berlin, Munich and Ausburg to determine why the desirable green patina did not always form (Magnus 1864). Magnus found that bronzes developed a dark-coloured copper-sulphur corrosion film instead of copper hydroxides (green malachite) if they were exposed to sulphur-containing air, either from a "sulphur-spewing factory" or large scale introduction of brown coal for heating. A few decades later, differential marble decay was measured in British cities and country graveyards in the late 1800s. Marble disintegration in cities was found to be "an exaggeration of the normal rate. Slabs … with sufficiently projecting architrave to keep off much of the rainfall, retain their inscriptions legible for a century or longer. Where the marble has been less screened from rain, the rapidity of waste has been sometimes very marked" (Geike 1880).

The "greening" or *verdigris* patina formation on copper roofs is a well-known corrosion phenomenon. Copper ions interact with the environment to form a sequence of mineral corrosion products that conclude in a chemical composition reflective of the integrated exposure. The rate of copper loss appears to be dependent on rain chemistry and volume (Cramer et al. 2002). Vernon and Whitby (1929) observed that *verdigris* samples from rural copper roofs were composed of copper hydroxides, as compared with samples from urban roofs dominated by copper sulphates and samples from seaside roofs dominated by copper chlorides. In the Northeastern US, the "greening" rate of copper roofs was estimated to be 10–14 years for the period from 1900–1932 when ambient urban SO_2 of more than 100 $\mu g/m^3$ were common (Freeman and Kirby 1932). Increased rates of "greening" were also documented in Copenhagen. In the 1930s, roofs became green in 20–30 years, compared with 10 years to greening in the 1950s and 8 years in the 1960s. The acidity of Copenhagen's rain observed in 1944–1945 was pH 6 to 8, compared with pH 4 to 5 in 1965 (Schmidt 1970).

An excellent overview of copper and bronze corrosion chemistry vis à vis pollution was published by Graedel (1987) and Graedel et al. (1987).

2 HISTORIC PATINATION PRACTICE IN THE US

Bronze alloys used in outdoor sculpture are among the most corrosion resistant metals. [1]Bronze is a copper-tin alloy in a roughly 10:1 ratio; the cost of bronze decreases with decreasing copper content. The typical alloy for statuary bronze in the United States is nominally 85% copper, 5% tin, 5% zinc, and 5% lead, sometimes referred to as 85-three-5 (American Society of Metals 1961). Nonetheless, outdoor bronzes left uncoated form dark or black corrosion films in sheltered, unwashed areas, while rain-washed surfaces exhibit pitting and green streaks. In the late 19th and early 20th c, the atmospheric corrosion of bronze was considered a process that could be managed for aesthetic purpose. In 1917, C. A. Fullerton, General Manager for Architectural Bronze, The u Company, described the situation as follows.

Most new bronze work is artificially coloured. A piece of bronze fresh from an acid bath – chemically clean – is a bright, reddish, golden yellow. Immediately it is exposed to atmospheric influence it begins to oxidize and darken. This process continues in varying degrees of rapidity – subject to atmospheric and actinic(sic) condition – from two to eight years, when it attains its ultimate natural patina and becomes practically a dead black. This colour will change with the weather at times, is affected by all sorts of atmospheric conditions, and it is absolutely impossible to say what the ultimate colour of a piece of bronze placed in a certain locality will be; you can only guess at it.

With such an uncertain and interesting medium, we can only start it out right. Manifestly, on a job of any magnitude going through a shop, it would be next to impossible to retain a natural even colour, as a portion of the work that might be finished up today would have a month's start on the piece finished a month from today. We therefore adopt the expedient of artificially oxidizing or aging the bronze with chemicals, to the colour selected, then holding the colour by waxing or lacquering the work. In this way we give all the parts of a job an even start. After that it is a matter of time or care. The wax or lacquer eventually wears off and the metal grows darker and richer until the natural ultimate colour is attained. This ultimate colour can be controlled to an extent and beautified by care and attention, like the colouring of a meerschaum pipe, and the most beautiful and gratifying results can be obtained. (*Monumental News* 1917, 568–569).

An excellent review of the history of bronze patination is found in Weil (1985). The range of patina colours for available for finishing early 20th century bronzes by Gorham were described as follows (see Plate 1 below, at the end of this chapter), as follows:

The name "Statuary" is applied to the simplest of the Gorham patina formulas because it is that most used on exterior monuments and easily yields to the beautifying influences of time.

No. 34 "Light Statuary". Bronze oxidized with a diluted bath of hydrosulphide of ammonia. It does no more than soften the glitter of the new metallic surface, leaving time to do the rest.

No. 35 "Medium Statuary". This colour is obtained as above except that the bath solution is stronger. A conservative color, rich when sunlit and safe for all decorative purposes.

No. 36 "Dark Statuary". Somber in tone. A splendid background for polished letter faces. Recommended where contrast is desired, as in signs, etc.

These patinas are permanent with reasonable care. Bronze should occasionally be gone over with a cloth moistened with beeswax dissolved in turpentine (Gorham 1927).

These early 20th c. Gorham patinas are very similar to Hughes and Rowe's Formula 1.68 that instructs that the object be brushed or immersed several times in a 1.6% solution of ammonium sulphide until the desired colour is achieved (Hughes & Rowe 1982).

[1] Bronze is a copper-tin alloy in a roughly 10:1 ratio; the cost of bronze decreases with decreasing copper content. The typical alloy for statuary bronze in the United States is nominally 85% copper, 5% tin, 5% zinc, and 5% lead, sometimes referred to as 85-three-5 (American Society of Metals, 1961).

Table 1. Copper corrosion at NAPAP test sites (NAPAP, 1993).

NAPAP Test site	Annual acidity pH	SO_2 annual average $\mu m/m^3$	Overall corrosion rate Mm/year	Sulphur related corrosion (%)	Acidity related corrosion (%)	All other corrosion Factors (%)
Newcomb, NY	4.36	4.4	$0.37 \pm .14$	10	25	65
Washington, DC	4.21	27.2	$0.83 \pm .19$	38	25	37
Steubenville, OH	4.06	56.5	$0.88 \pm .29$	57	20	23

3 QUANTIFYING CORROSION RATE FACTORS

Researchers in Europe, Japan, and the US have intensively studied the relative contribution of air pollution to copper corrosion rates for more than 25 years (e.g. Baboian & Cliver 1986, Brown et al. 1977, Doktor & Woznik 2002, Drayman-Weisser 1992, Ericsson & Johansson 1986, Fitz & Kucera 1999, Katou et al. 1982, Leidheiser 1971). Late 20th c. observations in the US attribute 20–25% of copper corrosion to rain acidity (Cramer et al. 2000), as shown in Table 1. Copper corrosion rates at the Newcomb, NY site in the Adirondacks are less than half those found in the urban sites in Steubenville, OH and Washington, DC, where sulfur oxides plays a dominant role in enhanced urban copper corrosion. A comparative study of copper, brass and bronze alloys found that copper corrosion rates are 50–100 times faster than corrosion of brass, and that bronze corrosion is even slower (Franey 1988).

The sulphur content of corrosion films, often called "patinas," documents pollution's role in bronze corrosion. Lins & Power (1991) found that both wet and dry atmospheric deposition play important roles in bronze corrosion. Dry deposition of sulphur and nitrogen supplies reactive cations and anions to the outer zone of corrosion films. With increasing acidity, the rate of copper sulphate removal by rain is enhanced, thus increasing both the corrosion of bronze statuary surfaces and the staining of adjacent stone and masonry materials. Removal of copper stains from stone is one of the more difficult tasks facing conservators, suggesting that this secondary effect of pollution may be non-trivial.

A dose response function proposed for cast bronze by the UN/ECE Program (Fitz & Kucera 1999, Tidblad et al. 1999, Stöckle & Krätschmer 1999) quantifies the relationship among these factors: rain volume, relative humidity, airborne SO_2, acid and chloride concentrations, as follows:

$$\text{Mass loss of bronze (in g/m}^2) = [0.26\,[SO_2]^{0.44} * RH\ *\ \exp^{(+0.060T-11)*}t^{0.86} + [0.0028\,\text{Rain}\,[H+] + [0.0043\,\text{Rain}\,[Cl-] * t^{0.76}].$$

where
SO_2 = annual avg. concentration, $\mu g/m^3$
RH = relative humidity, %, annual avg.
T = annual avg. temperature, degrees C
t = time, years
Rain = rainfall, mm, annual avg.
H^+ = precipitation acidity in mg/l, annual avg.
Cl^- = chloride concentration in rain, mg/l, annual avg.
(Equation 9.13b; Tidblad et al. 1999).

To illustrate the scale of bronze corrosion, loss calculations were made for the urban and rural sites in the Northeastern and Midwest United States (see Table 2). The damage metric is bronze thickness loss, in grams/year, also specified as loss of metal thickness in μm/year.[2] Bronze thickness loss

[2] Using a density of 2.8 g/cm^3, mass loss was converted to thickness loss (Stöckle & Krätschmer 1999). A mass loss of 3 grams/square meter from cast bronze is equivalent to a corrosion layer 1.07 μm deep. By comparison, a typical piece of paper is 100 μm thick.

Table 2. Cast bronze corrosion rates in the US estimated w/ UNECE dose response function (Tidblad, et al., 1999). Sample calculations using environmental data from 1997–2001, except as noted).

Location	Rain mm	Cl mg/l	H+ mg/l	SO_2 $\mu g/m^3$	Bronze loss $\mu m/yr$	Time to 0.1 mm loss (yrs)
Data source	NADP, NYDEC	NADP, NYDEC	NADP, NYDEC	CASTNet NYDEC, EPA Table 4–1		
Dyken Pond, rural NY	963.6	0.127	0.035	4.19	1.86	54
Greater Albany, NY	830.2	0.164	0.044	18.3	3.25	31
West Point, NY	712.7	0.284	0.040	11.7	2.67	37
Buffalo, NY	936	0.200	0.037	16.7	3.13	32
Chicago, IL	989.6	0.203	0.021	24.7	3.50	29
Bondville, rural IL	854.4	0.164	0.024	6.3	2.02	50
Indiana Dunes, rural IN	1127	0.164	0.021	6.3	2.06	48
Purdue Center, rural IN	824.9	0.160	0.028	10.8	2.53	40
St. Louis. MO	1225	0.186	0.026	20.2	3.34	30

is a measure of surface recession that assumes a uniformly deep corrosion across the exposed surface, rather than pitting, where corrosion proceeds intensely in specific areas. For illustration purposes, the time it would take for a fully exposed bronze surface to recede the thickness of one sheet of paper (0.1 mm) was also computed for these locations. This damage threshold of 0.1 mm is arbitrary and the probable error on the estimate is in excess of the computed differences.[3]

Based on the UN/ECE dose response function, bronze loss rates of 1.8–3.5 μm/year were estimated for urban and rural areas in the Midwest and New York. The Midwest sites offer a range of SO_2 exposures similar to New York, but with generally lower rain acidity and higher rain volume (Gatz 1991).

These estimates are in keeping with long-term corrosion measured on 50+ replicate bronze statues across the country, discussed below (Meakin & Sherwood 1992; Sherwood 1995). The regional corrosion rate from the 1920s to the 1990s of 26 unconserved *Hiker* statues in the Northeast and Mid-west averaged 3.4 μm/year, with a standard deviation of 1.0 μm/year. *Hiker* statues in Schenectady (1921) and Troy (1925), two urban areas near Albany, NY, exhibited annual corrosion rates of 2.4 μm/year, based on exposures of 60+ years.[4]

4 HIKER STUDY – IN SITU MEASUREMENT OF MONUMENTAL CORROSION

4.1 *Experimental conditions*

The Gorham Bronze Company cast Theo Ruggles Kitson's *Hiker* figure more than 50 times between 1921–1963. Each time Gorham used the same pattern to sand cast about 1,000 pounds of statuary bronze. Metallurgically, the replicates are very consistent – dense, fine-grained alloys of between 88% and 90% copper with few detectable casting flaws. The figures were cold-patinated medium statuary brown and varnished. Kitson *Hikers* are found in nearly every climate zone in the continental US. Before 1939, the preponderance of *Hikers* were dedicated in northeast; later statues were almost all deployed in southern and western states. Early *Hikers* have seen pollution levels rise and fall dramatically, peaking in the 1970s. All the *Hikers* pre-date the air pollution reductions resulting from the Clean Air Act of 1970. Kitson's *Hikers* are attractive as corrosion monitors

[3] Error in these estimates is unknown, but may be as high as ±0.5 μm, suggesting that small site-to-site differences should be evaluated with caution.

[4] A third Hiker statue nearby in Cohoes (1921) was conserved prior to the Hiker corrosion study. The corrosion, including metal loss from cleaning, yielded an annualized rate of 2.8 μm/year.

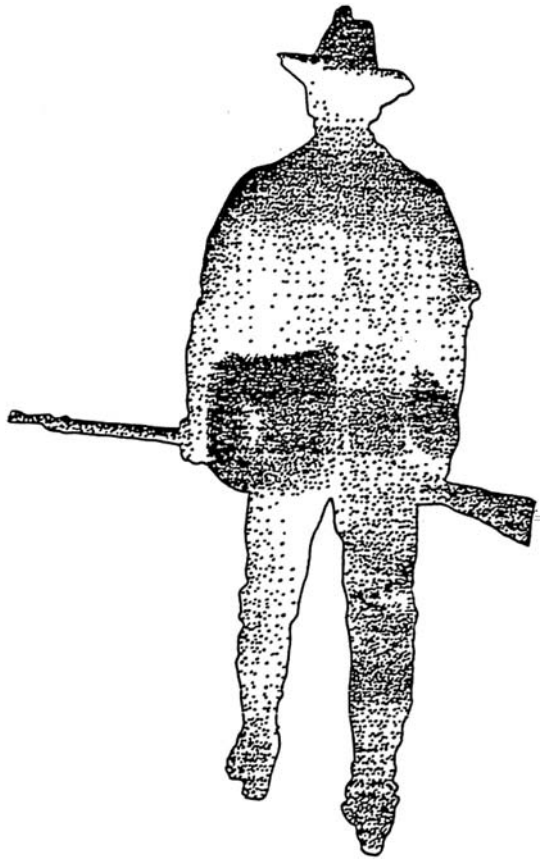

Figure 1. *Hiker Study*: composite corrosion map. 25 *Hiker* statues.

because of their fixed geometry, reasonably consistent alloy chemistry, their wide distribution, and long period of exposure.

4.2 *In situ corrosion measurement methods*

Corrosion was measured in two ways – the areal extent was mapped and the texture of the bronze surface was moulded and profiled. The hydrology of *Hiker* corrosion is remarkably diagnostic. There is a consistent general pattern of bronze corrosion for rain-washed versus sheltered surfaces (Doktor & Woznik 2002). This consistency, which is independent of a shape's complexity, is illustrated in a composite map of green corrosion on 25 replicate bronze statues of the *Hiker* that have been exposed to a range of environment for at least 25 years. (Sherwood et al. 1990a, Meakin & Sherwood 1992). (Fig. 1)

Dental moulding putty, vinyl polysiloxane, was used to make very precise replicas of corroded bronze surfaces, allowing the investigator to transfer the "metal" into the laboratory for detailed analysis without damage to the statues. A profilometer was used to quantify the pit depth and surface roughness of the moulds. This instrument draws a fine probe across a surface, generating a plot of surface elevation as a function of position along a line. For the *Hiker* moulds, a line was traced about 12 mm in length with a vertical discrimination of 0.001 mm. All profiles were taken on the mould immediately below the front sight, which is about 25 mm in length, and within 2–3 mm above or below the front vertical surface of the gun barrel. The digitally stored profiles provide a precise and

Table 3. Standard deviation of pit depth for 16 statues.

Statue	Mean depth of 4 Profiles (mm)	Std. deviation 4 profiles	St.dev./Mean (%)
Baltimore	0.195	0.027	14
Birmingham	0.106	0.034	32
Columbia	0.108	0.041	38
Dayton	0.153	0.053	35
Elmira	0.204	0.088	43
Knoxville	0.078	0.013	17
Memphis	0.163	0.048	29
Meriden	0.253	0.033	13
Morristown	0.110	0.021	19
New Bedford	0.151	0.046	30
Providence	0.335	0.017	5
Sacramento	0.096	0.024	25
Shamokin	0.225	0.054	24
Toledo	0.156	0.028	18
Tuscon	0.068	0.016	24
Wichita falls	0.086	0.029	34
		Mean	25

repeatable measure of the surface roughness. Tests were conducted to determine the dimensional stability of the mould material itself; over one year the dimensions were stable to $<0.5\%$.

The precision of the measurements was evaluated by examining multiple profilometer traces from 16 moulds, that included the full range of *Hiker* roughnesses from 0.07 to 0.33 mm. For each of these moulds, the standard deviation of the pit depth from the set of 4 profiles was computed and expressed as a percentage of the mean pit depth (Table 3). The variability, measured as a standard deviation, ranges from 5 to 38% with a mean value of 25%. In view of the factor of three difference between smoothest and roughest surfaces, a measurement tolerance of about $\pm 25\%$ is quite adequate to allow meaningful comparisons between *Hikers.*

The full capability of surface profiling for monitoring both corrosion and conservation has yet to be realized. First order effects such as the impact of sand blasting or chemical cleaning are immediately evident, and the moulding technique may be used for quality-control and long-term monitoring of conservation treatments. Equally important second order effects may also be measured by surface profiling. For example, how is the bronze corrosion rate influenced by cleaning, lacquering, and waxing? Observation of bronze surfaces over time can be supplemented by this quantitative measure of microscale texture. The readily available, easy-to-use, medium cost dental moulding is a technique that should be considered for 21st century conservation tool kits.

The moulding profile technique is also a tool to track environmental progress. Precise measurements of metal loss taken systematically over time can be the basis for corrosion rate determinations. With this technique, bronze corrosion rates and the chemistry of the atmosphere can be monitored in parallel. In principle, reduction in sulphur emissions since the 1960s in the US and Europe should be detectable as reduction in bronze corrosion, although these gains have to some extent been offset by increases in the amounts of oxides of nitrogen. Eventually we should be able to quantitatively respond to the question – does cleaner air mean more durable bronze statuary? For the foreseeable future, outdoor bronzes will be exposed to a variety of corrosive agents, deposited as particles, gases, and in rain. At present, an annual program of maintenance is the most satisfactory means of extending the life of outdoor bronzes in contemporary atmospheres.

4.3 *Hiker corrosion trends*

The general trend of pit depth with the age of the statue is clearly shown in Figure 3, a plot of maximum pit depth against the dedication year.

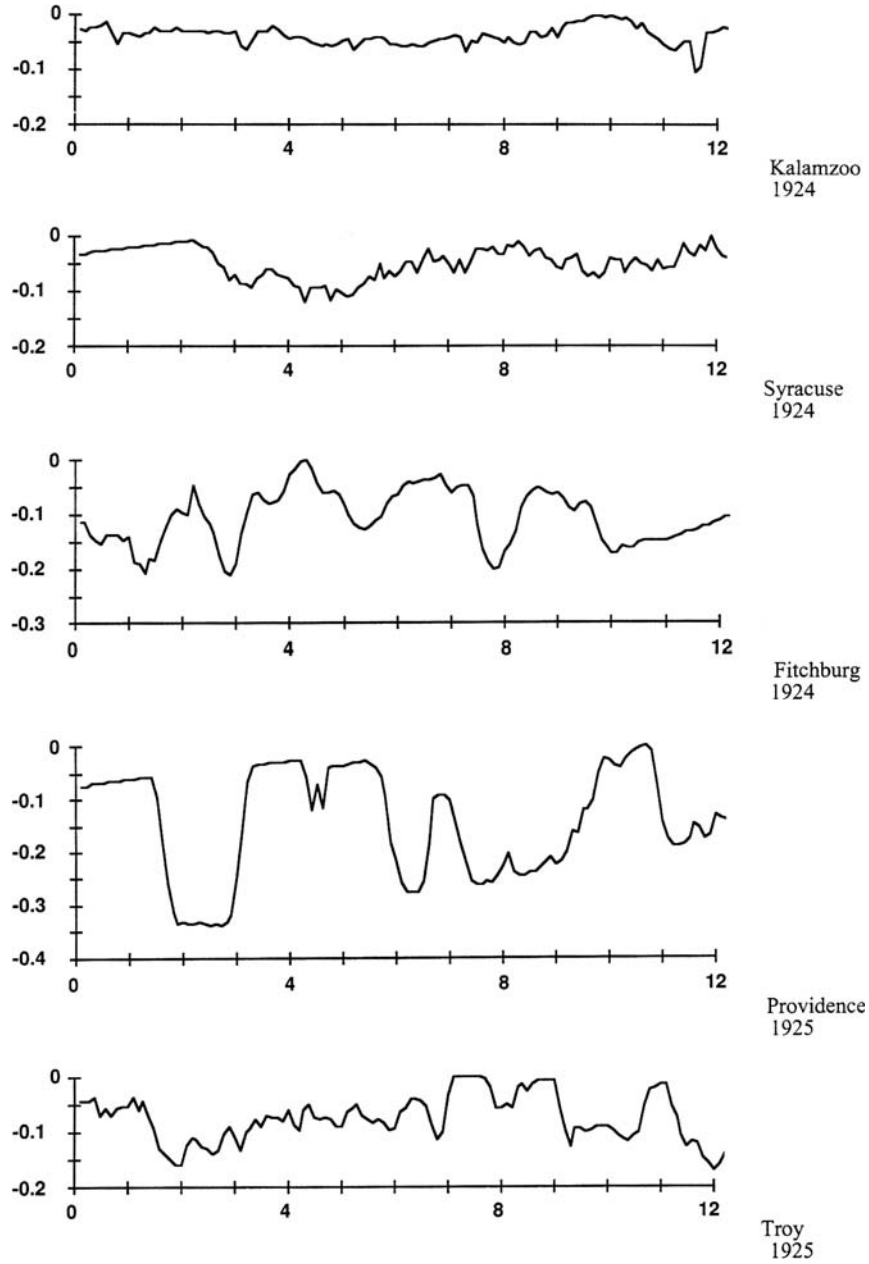

Figure 2a. Older *Hikers. Hiker Study*: sample corrosion profiles.

A similar trend was found in the relationship between surface roughness and dedication year. This similarity between indicates a relationship between surface roughness and maximum pit depth but this has not been explored in detail. Rain exposure is a key factor in metal loss as measured by pit depth. The strong influence of rain, measured either as total volume or total number of rain days (>0.1), on pit depth is illustrated in Figure 4. All the *Hikers* in dry climates show a pit depth of 0.10 mm or less, irrespective of years of exposure. At the other extreme, the most corroded *Hikers* show depths of about 0.30 mm. This range and the scatter in Figures 3 and 4 reveals that

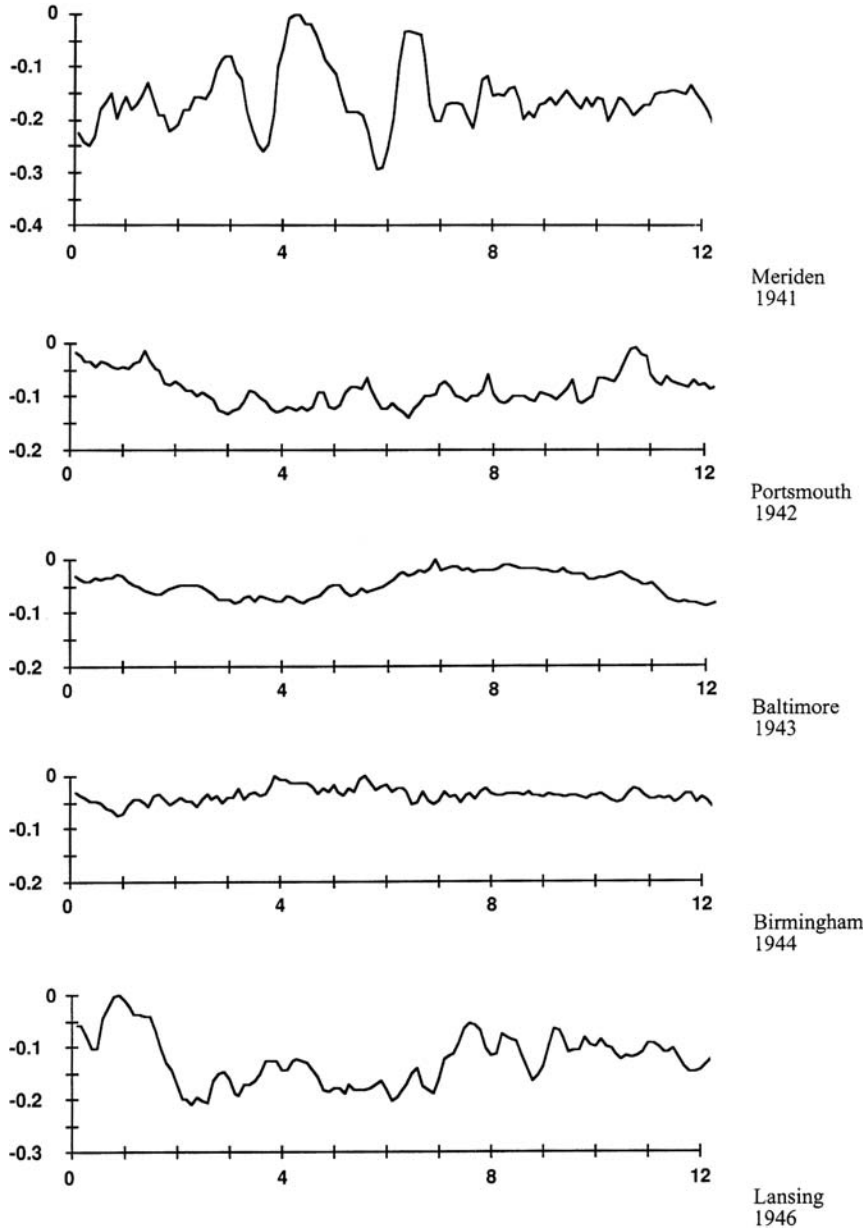

Figure 2b. Older *Hikers. Hiker Study*: sample corrosion profiles.

neither age nor exposure to rain alone explains the degree of corrosion measured by maximum pit depth. This scatter indicates that other strong effects, in particular arising from air pollution and treatments, including vandalism and its repair. Despite the uncertainty in estimating lifetime SO_2 exposures, the relationship between SO_2 and maximum pit depth is stronger than that for rain exposure. (Fig. 5)

The 1920s *Hikers* located in rainy cities with heavy industry show corrosion rates nearly double the average for the era. i.e., Providence (1925, pit depth 0.33 mm), Chicago (1926, pit depth 0.35 mm), and Everett (1927, pit depth 0.39 mm). For this subset of *Hikers*, it appears that density

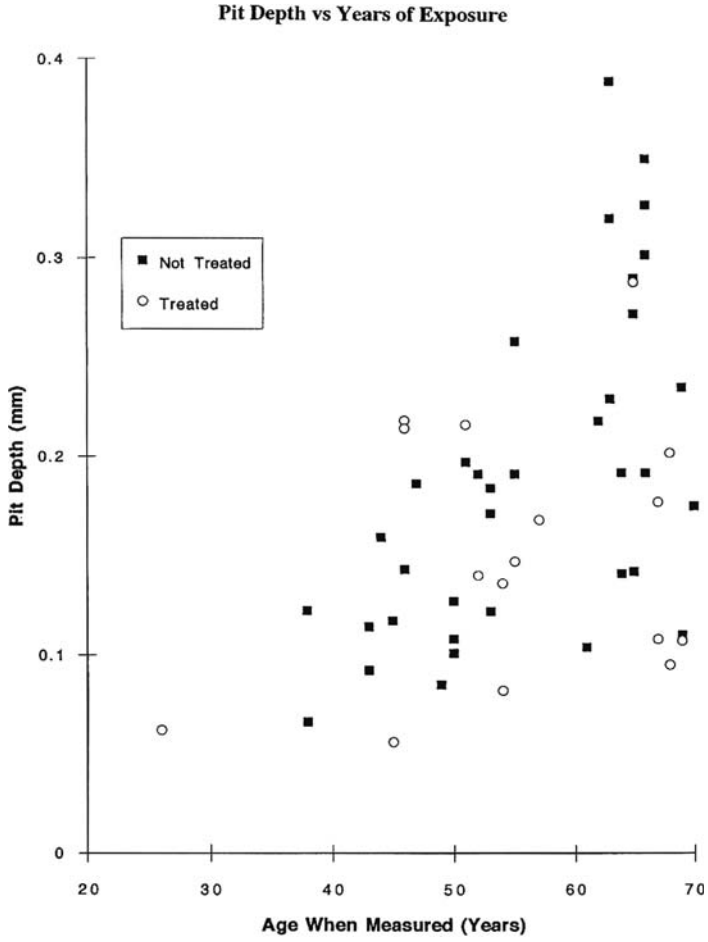

Figure 3b. *Hiker Study:* maximum pit depth versus dedication year.

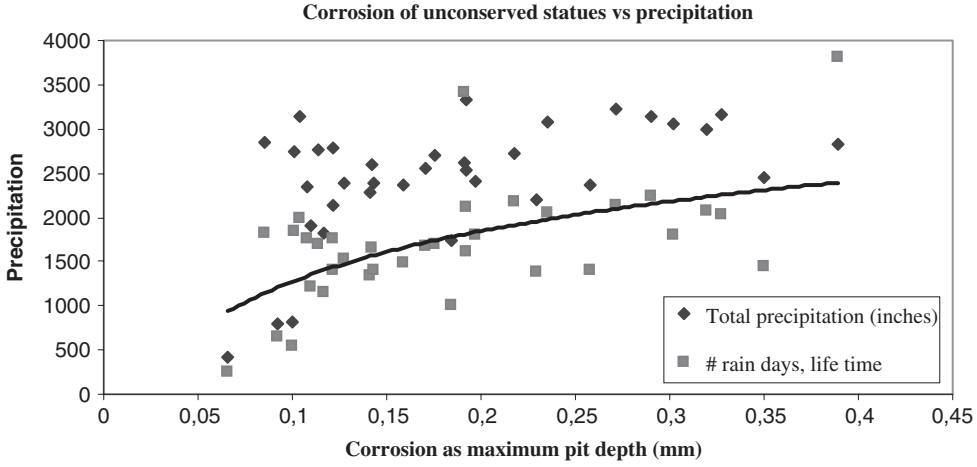

Figure 4b. *Hiker Study*: lifetime precipitation versus maximum pit depth.

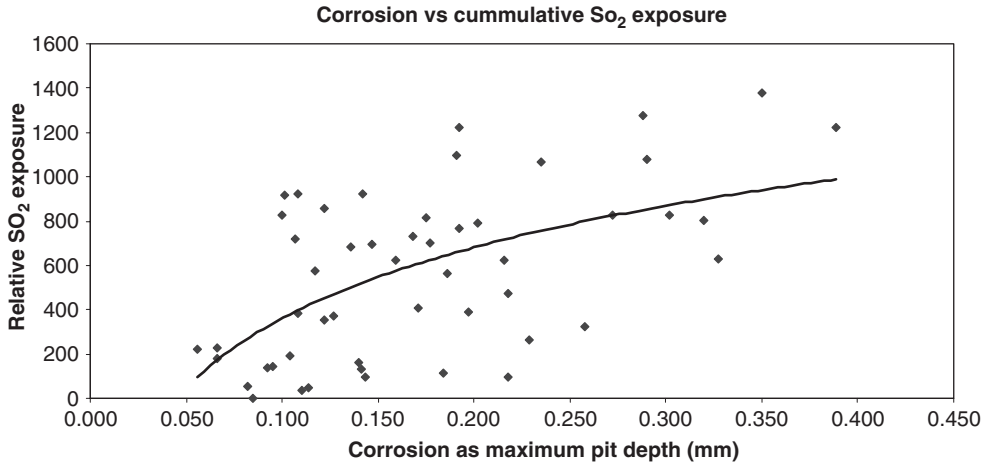

Figure 5b. *Hiker Study*: estimated SO_2 exposure versus maximum pit depth.

of industry rather than urban population is more telling; from 1920 to 1950, Everett's population was under 50,000, Providence's about 250,000, and Chicago more than 3,000,000. Chicago and Providence are two of the most industrialized *Hiker* cities; only Baltimore and Los Angeles also had more than 1,000 manufacturers at their industrial peaks. Everett (1927, pit depth 0.39 mm) and Lynn (1923, pit depth 0.29 mm) are close to central Boston, exposed to elevated SO_2 concentrations in the mid-1970s.

The untreated *Hikers* from the 1920s near Albany help illustrate the incremental role of industry within a small city. Pit depths are about half those observed in highly industrial areas described above. The Schenectady *Hiker* (1921, pit depth 0.18 mm, 2.4 μm/year is located in a park in the suburban area west of the city, while the Troy statue (1925, pit depth 0.19 mm; 2.4 μm/year) stands in a college campus not far from the industrial section along the Hudson. The Cohoes statue also stood in an industrial centre since 1923 (pit depth 0.20 mm, 2.8 μm/year), but because it was cleaned to a "penny bright" surface in the early 1980s, the surfaces are not strictly comparable. Until the World War II, industry prospered in the Albany area; Cohoes specialized in textiles and Troy was a noted 19th century steel producer.

The younger *Hikers* dedicated in the 1940s and 1950s are located in a broader range of exposures than the "rust-belt" concentration of the early *Hikers,* including most of the statues in coastal and desert exposures. Similar to their older neighbours, *Hikers* in manufacturing cities in the East Coast megalopolis evidence higher corrosion rates compared with statues in areas with less population and industry – compare Meriden, Connecticut (1941, pit depth 0.26 mm) and Cambridge, Massachusetts (1947, pit depth 0.16 mm) with Knoxville (1940, pit depth 0.08 mm) and Kansas City (1947, pit depth 0.12 mm).

5 CONSERVATION CONSIDERATIONS

Unlike stone, there are preservation methods to control environmental damage to outdoor bronzes (Naude 1985, Montagna 1995, Montagna 2001). However, once severe corrosion and extensive pitting has occurred, it can be difficult to restore the original lustre of bronze sculptures. Protecting outdoor bronze sculptures depends on maintaining a protective coating of lacquer or wax or a combination of both. Prior to application of a coating, bronzes are generally thoroughly cleaned; the method and extent of cleaning varies widely between conservators. In the 1980s the approach to bronze conservation of cleaning with walnut shell blasting or gentle scrubbing followed by coating with lacquer and/or wax gained favour. Highly aggressive cleaning with sand or glass bead blasting and attack with strong chemicals were at the same time losing favour. A general observation from the

Hiker profiles is that conservation changes the shape of the surface profile, and in a characteristic manner. Sandblasted surfaces tend to exhibit sharp points, while waxed surfaces show gently curved topographies. Corrosion control coatings involving wax require renewal seasonally or annually, while lacquer coatings can typically be left for 3–5 years before maintenance is needed (Montagna 2001). More durable coatings are being developed by several European research groups, including heteropolysiloxanes by Roemich and colleagues.

Bronze conservation solutions, although relatively straightforward, can be costly. In the United States in the late 1980s, the average cost of initial conservation was $7,500 per bronze figure, with an associated annual maintenance cost of $1,100 (Sherwood et al. 1990b). Adjusted for 2002[5] the typical cost of conserving a single figure, life-size bronze statue averaged about $10,000, up to $15,000 for sculptures in difficult locations. Annual maintenance costs are typically $1,500 ± $500 per figure, depending on accessibility and regularity of treatment.

ACKNOWLEDGEMENTS

This paper represents the collective thought and efforts of a research group at the University of Delaware who considered corrosion of the *Hikers* for a decade under a cooperative research agreement between the University and the National Park Service: U. Delaware faculty John Meakin, Thomas Meirding, David Ames, and then art history doctoral candidates Dennis R. Montagna and Michael Panhorst.

REFERENCES

American Society of Metals. 1977. *Source Book on Materials Selection.*, Vol. II. Metals Park, OH: American Society of Metals.

Baboian, R. & Cliver, E.B. 1986. *Corrosion on the Statue of Liberty*. Parts 1–5. Material Performance 25: 74–83.

Brimblecombe P. (ed.). 1994. The Balance of Environmental Factors Attacking Artifacts. John Wiley & Sons Ltd., London.

Brimblecombe, P. 1987. The Big Smoke – *A History of Air Pollution in London since Medieval Times.* Londen: Methuen.

Brown, B.F., Burnett, H.C., Chase, W.T., Goodway, M., Kruger, J. & Pourbaix, M. 1977. *Corrosion and Metal Artifacts – A Dialogue between Conservators and Aracheologists and Corrosion Scientists.* Washington, DC: National Bureau of Standards.

Cramer, S.D., Matthes, S.A., Covino, Jr.B.S., Bullard, S.J. & Holcomb, G.R., 2002. Environmental factors affecting the atmospheric corrosion of copper. In: H.E. Townsend (ed.), *Outdoor Atmospheric Corrosion.* American Society for Testing and Materials, Philadelphia, pp. 245–264.

Cramer, S.D., Matthes, S.A., Holcomb, G.R., Covino, Jr.B.S. & Bullard, S.J., 2000. Precipitation runoff and atmospheric corrosion. In: *Corrosion/2000*. Houston: NACE International.

Doktor, A. & Woznik, E. 2002. Results from the Multi-Pollutant Programme: Corrosion attack on copper and cast bronze after 4 years of exposure (1997–2001). Munich: Bavarian State Department of Historical Monuments.

Drayman-Weisser, (ed.) 1992. Dialogue/89- The Conservation of Bronze Sculpture in the Outdoor Environment: A dialogue among Conservators, Curators, Environmental Scientists, and Corrosion Engineers. Houston: NACE International.

Ericsson, P. & Johansson, L.G. 1986. The role of NO_2 in the atmospheric corrosion of different metals. 10th Scandanavian Corrosion Congress. Houston: NACE International.

Fitz, S. & Kucera, V. 1999. The UN/ECE Material Exposure Programme: Aim and Scope. *Quantification of Effects of Air Pollutants on Materials.* Berlin, Umweltbundesamt (Federal Environmental Agency), pp. 5–10.

Fitz, S. 1999. *Quantification of effects of air pollutants on materials.* Berlin: Umweltbundesamt (Federal Environmental Agency), pp. 5–10.

[5] Consumer Price Index for January 1990, 127.4, and January 2002, 177.1.

Freeman, J.R.Jr.K.P.H. 1932. Metals and Alloys, 3: 190.
Gatz, D.F. 1991. Urban precipitation chemistry: a review and synthesis. *Atmospheric Environment*, 25B: 1–15.
Geike, F.R.S. 1880. Rock weathering as illustrated in Edinburgh churchyards. *Proceedings of the Royal Society of Edinburgh*, 10: 518–532.
The Gorham Co. 1927. *Bronze Tablets by Master Craftsmen.* New York: Gorham.
Graedel, T.E. 1987. Copper patinas formed in the atmosphere – II. A qualitative assessment of mechanisms. *Corrosion Science*, 27: 721–740.
Graedel, T.E., Nassau, K. & Franey, J.P. 1987. Copper patinas formed in the atmosphere – I. Introduction. *Corrosion Science*, 27: 639–657.
Hughes, R. & Rowe, M. 1982. *The Colouring, Bronzing and Patination of Metals.* London: The Crafts Council.
LaQue, F.L. & Copson, H.R. 1963. Corrosion resistance of metals and alloys. New York: Reinhold Publishing Corp. Lins, A. & Power, T. 1991. The corrosion of bronze monuments in polluted urban sites: a report on the stability of copper mineral species at different pH levels. D.A. Scott, J. Podany & B. B. Considine, (eds) *Ancient and Historic Metal Conservation and Scientific Research.* Marina del Rey: Getty Conservation Institute, pp. 119–151.
Katou, T.K., Akiyama, K. & Kadakura, T. 1982. Analysis of air pollution by verdigris components, *Scientific Papers on Japanese Antiques and Art Crafts*, 27: 18–28.
Leidheiser, H. Jr. 1971. The corrosion of copper, tin and their alloys. New York: John Wiley and Sons.
Magnus, G. 1864. The influence of bronze composition on the formation of an attractive, green patina. *Dingler Polytechnisches Journal*, 172: 371–376.
Meakin, J.D. & Sherwood, S.I. 1992. Corrosion of monumental bronzes. *Proceedings of the 1992 U. S. Environmental Protection Agency and Air and Waste Management Association International Symposium on Air Toxics and Air Pollution.* Pittsburgh: PA, AWMA.
Montagna, D.R. 2001. Bronze conservation in the United States at the dawn of the new century. Jeanne-Marie Teutonico and John Fidler. Monuments and the Millennium; *Proceedings of a Joint Conference Organised by English Heritage and the United Kingdom Institute for Conservation.* London: James & James Ltd, pp. 128–137.
Naude, V.N. 1985. *Sculptural Monuments In an Outdoor Environment*, Philadelphia: Pennsylvania Academy of the Fine Arts.
Schmidt, M. 1970. Observations on natural patination of copper. *J. Institute of Metals*, 98: 238.
Sherwood, S.I. 1992. The greening of American monuments: The role of atmospheric chemistry in the corrosion of outdoor bronze. In: Draman-Weisser, (ed.) 1992. Dialogue/89- *The Conservation of Bronze Sculpture in the Outdoor Environment: A dialogue among Conservators, Curators, Environmental Scientists, and Corrosion Engineers.* Houston: NACE International, 33–72.
Sherwood, S.I., 1995. Kitson's *Hikers* capture a half-century of corrosion history. *CRM Bulletin*,18: 23–25.
Sherwood, S.I., Gatz, D.F., Hosker, Jr.R.P., Davidson, C.I., Dolske, D.A., Hicks, B.B., Langmuir, D., Linzey, R., Lipfert, F.W., McGee, E.S., Mossotti, V.G., Schmiermund, R.L. & Spiker, E.C. 1990a. *Processes of Deposition to Structures*. National Acidic Precipitation Assessment Program, Washington, D.C.
Sherwood, S.I., Lipfert, F.W., Daum, M.L., Chase, S.B., Panhorst, M.W., Smith, E.A., Alderson, C.R., Jenkins, R.V., Miller, D.E., Montagna, D.R., Pendergrass, P.S. & Zimmt, W.S. 1990b. *Distribution of Materials Potentially at Risk to Acid Deposition.* National Acidic Precipitation Assessment Program, Washington, D.C.
Spence, J.W., Lipfert, F.W. & Katz, S. 1992. The effect of specimen size and orientation on the atmospheric corrosion of galvanized steel. *Proceedings of the 1992 U. S. Environmental Protection Agency and Air and Waste Management Association International Symposium on Air Toxics and Air Pollution.* Pittsburgh: PA, AWMA.
Stöckle, B. & Krätschmer. 1999. Quantification of effects of air pollutants on copper and bronze. S. Fitz. *Quantification of Effects of Air Pollutants on Materials.* Berlin: Umweltbundesamt (Federal Environmental Agency).
Tidblad, J., Mikhailov, A.A. & Kucera, V. Unified dose-response functions after 8 years of exposure. S. Fitz. *Quantification of Effects of Air Pollutants on Materials.* Berlin, Umweltbundesamt, pp. 77–86. 1999.
Vernon, W.H.J.W.L. 1929. Open-air corrosion of copper, a chemical study of the surface patina. *J. Institute of Metals*, 42: 181.
Weil, P.D. Patina, a historical perspective artistic intent and subsequent effects of time, nature and man. Naude, V. N. *Philadelphia: Pennsylvania Academy of the Fine Arts*, pp. 21–27. 1985.

COLOR

The surface of a new bronze casting is more or less garish in color. Exposure to the atmosphere causes a gradual change, the surface becoming a rich brown or sometimes a delicate green. The brown tones are the result of oxidization by the air—the green hues are produced by the minute quantities of salts in rain water. These salts attack the surface of the metal, forming basic salts of copper, the air then converting them into basic copper carbonate. The latter is green in color and is found in nature as malachite. This beautiful natural coloring is known as patina or Aerugo Nobilis (noble rust).

The patina of antique bronzes, long buried in the ground, varies with the nature of the soil or because of contiguous materials. Thus, the marshy and peaty soils between Rome and Naples have imparted a low olive tone to the bronzes found there. Contact with iron will cause a rusty tint. Volcanic soils act strongly on the metal, as does the nitrous soil of Egypt, leaving the surface rough and in many instances blistered and distorted out of form. In some examples more frequently afforded by the dry climate of upper Egypt and Greece, the surface of these bronzes is left purely metallic and free from oxidization. This is also the case with many bronzes which have been constantly beneath fresh water as, for instance, the weapons dredged from the bed of the Thames.

The natural patina of an antique bronze cannot be faithfully imitated. It has, however, been the practice from early times to color the metal chemically by processes which are kept as precious secrets by their discoverers. The beauty and variety of the artificial patina imparted by the Japanese to their admirably finished work in bronze is noteworthy.

Research and much experiment in the Gorham laboratories have developed formulas for a wide variety of patina.

The color of any metallic surface is a combination of local and reflected colors. No photo engraving process can faithfully illustrate the subtle beauties of these delightful accidental combinations. The chart on the opposite page is offered, therefore, only as a suggestion and comprises colors in more general use.

KEY TO COLOR CHART

No. 34. Light Statuary. Bronze oxidized with a diluted bath of hydrosulphide of ammonia. It does no more than soften the glitter of the new metallic surface, leaving time to do the rest.

No. 35. Medium Statuary. This color is obtained as the above except that the bath solution is stronger. A conservative color, rich when sunlit and safe for all decorative purposes.

No. 36. Dark Statuary. Sombre in tone. A splendid background for polished letter faces. Recommended where contrast is desired, as in signs, etc.

The name "Statuary" is applied to the simplest of Gorham patina formulas because it is that most used on exterior monuments and easily yields to the beautifying influences of time.

No. 33. Soixante Quinze. So called for its resemblance to the color of the French field ordnance of the late war. This patina is obtained by what is called the "Burnt" process, being the application of various chemicals with fire. In effect it is the natural antique coloring process stimulated by heat.

No. 17. Sepia (Burnt Process). A rich brown patina.

No. 37. Green Gold. Bronze treated to cause a light green oxide in the modeling depths and waxed to protect the surface from further oxidization. This is not considered a permanent color for out-of-doors bronze, but with occasional care will hold for years. A bright and rich color for any interior use.

No. 25. Pontine (Burnt Process). A neutral green, inspired by the beautiful patina of antique bronzes unearthed near Naples.

No. 27. Maremma (Burnt Process). A warm green, also inspired by natural antique patina on bronzes excavated from marshy and peaty soil near Rome.

No. 31. Della Robbia (Burnt Process). A beautiful bluish green patina.

No. 16. Verde Antique (Burnt Process). Like the patina of Pompeian bronzes, rough and mottled blue and green. This is not recommended for bronzes delicately ornamented.

These patinas are permanent with reasonable care. Bronze should occasionally be gone over with a cloth moistened with beeswax dissolved in turpentine.

Plate 1a. “Bronze Patina Colors”, The Gorham Company, 1927.

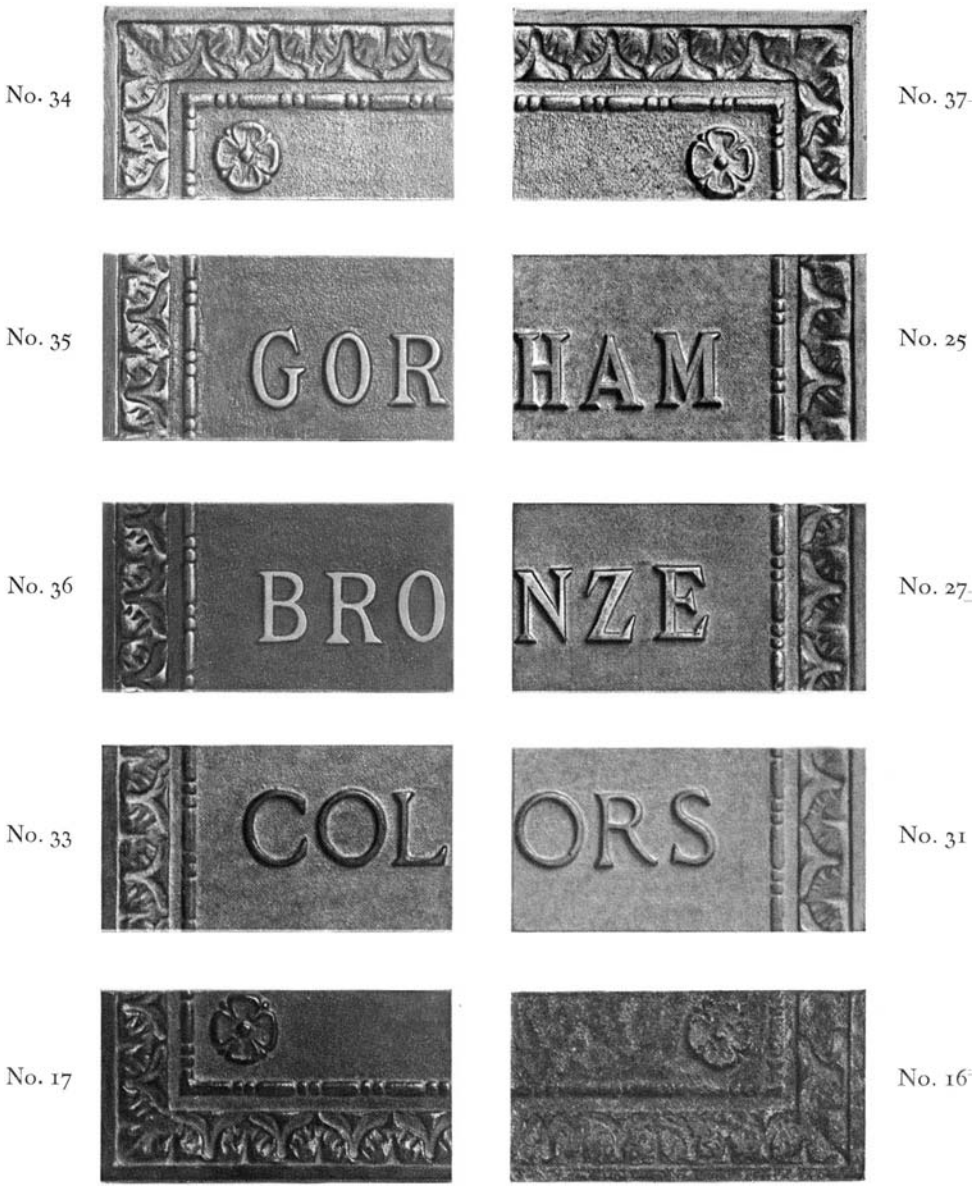

Plate 1b. "Bronze Patina Colors", The Gorham Company, 1927.
(This plate is presented in the signature in colors at the end of this volume, Appendix, pg. 326)

Cultural Heritage Conservation and Environmental Impact Assessment by Non-Destructive Testing and Micro-Analysis – Van Grieken & Janssens (eds)
© 2005 Taylor & Francis Group, London, ISBN 90 5809 681 5

Endangered glass objects identified by ion beam analysis

C. Neelmeijer & M. Mäder
Forschungszentrum Rossendorf e.V., Dresden, Germany

ABSTRACT: Art objects of glass are subjected to ageing processes even under air conditioning of museums. Glass surfaces are decomposed and sometimes their transparency is considerably reduced. This is the consequence of chemical processes which take place between the silicate network and the humidity of the ambient atmosphere. In particular, potassium-calcium-silica glasses are affected. Degradation takes place via ion exchange reactions where potassium and calcium are leached out and hydrogen-bearing species are incorporated into the silicate structure. Endangered glass objects of museums should be indicated by means of non-destructive composition analysis. Simultaneous use of the ion beam methods PIXE, PIGE and RBS at a non-vacuum facility proves ideal to determine both the corrosion state of the glass surface and the composition of the glass bulk. The results allow recommendations to museums regarding demands of special storage conditions. Art scientists may deduce details on the glass provenience or on special manufacturing technologies.

1 INTRODUCTION

Glass surfaces are subjected to corrosion. This is due to environmental effects attacking the glass network (Römich 1999). Thus, unique glass objects of our cultural heritage may be abandoned to advanced deterioration as a consequence of improper long-term storage. As known, the resistance of glass against humidity and harmful substances depends sensitively on the individual composition (Scholze 1982). It is the well-tuned balance of so-called glass network formers and glass network modifiers which protects a historic piece against natural impairment (Doremus et al. 1983). However, glass work of former times could consider glass corrosion only to a lesser extent. Glass makers were much more oriented to manage their production with the available standard of kiln. Therefore, glass compositions were given by technological premises, in particular by an expedient melting temperature. In this regard it is remarkable that coloured windows of medieval churches often show the typical degeneration effect of opacity. Sometimes, crusts of corrosion products are observable excluding any non-destructive analytical work (Schreiner 1988). Of course, windows are extremely exposed to weathering whereas pieces of art in museums obtain comparatively ideal conditions due to air conditioning. Even there, the chemical processes of deterioration go ahead into the depth. For a glass of individual composition the future state of preservation will depend on the individual storage conditions, i.e. temperature, humidity and atmospheric pollutants.

It is the aim of natural scientists to develop objective analytical procedures which allow to identify critical objects of potential glass disease already in advance. Preventive check-ups of valuable pieces shall help to clarify both the present status of glass surface ageing and the necessity of special storage conditions in order to retard progressive damage phenomena (Rayn 1993). This article presents a current project making use of the combination of ion beam based analytical methods. Non-destructive analysis is essential that can be assured by working at an external proton beam, i.e. a proton beam on air. The equipment is illustrated in the last chapter. This paper attaches importance to explain characteristic signals from the measured spectra and specific sets of data that can be applied by the analyst to decide on glass corrosion and chemical resistance. Results of model experiments are discussed mainly. Finally they will be confronted with recent first findings from authentic ancient glass stored in a museum.

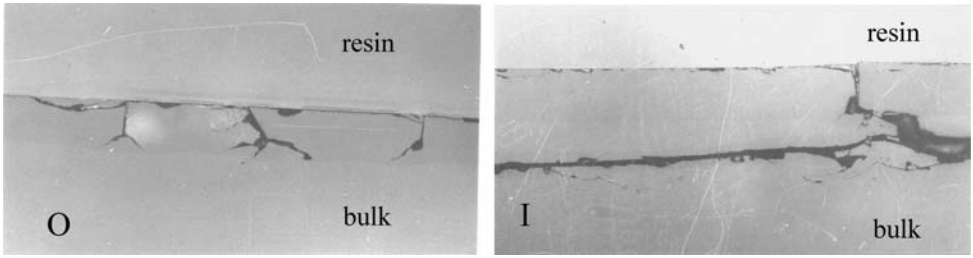

Figure 1. Cross section of a historic glass shard, early 18th century, archived in the museum "Staatliche Kunstsammlungen Dresden/Germany, Kunstgewerbemuseum Pillnitz". O – less affected outer side, I – strongly deteriorated inner side. The total width of each photo corresponds to 530 μm.

2 GLASS DISEASE

Glass corrosion caused by environmental attacks is a serious problem especially in the case of non-replaceable historic works of art. Contrary to damaged paintings, destroyed glass surfaces cannot be rebuilt by restoration work. When exposed to the humid atmosphere glasses may lose both their transparency and stability (Schreiner 1991). This is because of compositional changes in the surface region promoting the formation of micro-cracks. It depends on the storage conditions whether this initial alteration extends to a network of cracks penetrating deeper and deeper into the glass bulk. Such progressing processes are demonstrated in Figure 1 showing the microscopic view of a cross section prepared from a potash-lime-silica glass of the early 18th century. Obviously, the curved shard is the rudiment of a glass vessel. Its exterior, in permanent contact with air, shows less damage compared to the degenerated interior. Probably the inner surface was in temporary contact with water. Thus, enhanced strain caused an expansion of initial vertical cracks into the horizontal direction. Clods have been formed which partially are removed by flaking.

The chemistry of glass deterioration is explicitly described in the literature (Adams 1984). Break down of chemical bonds in the glass network, induced by humidity, is followed by subsequent leaching of mainly alkali ions (Na, K) but also alkaline earth (Ca). Created dangling bonds are saturated by the ionic components of water. With increasing time the reaction front penetrates deeper into the glass material forming a near-surface leached region, i.e. the gel layer. Such layers can grow up to a thickness of some hundred microns, and they consist mainly of remaining SiO_2, see also Chapter 4. Mechanical stress produced by this process causes the formation of initial cracks. As a consequence, further penetration of aqueous components is more and more in favour increasing both the depth and the branching of cracks. Changing environmental conditions, e.g. alternating humidity and temperature, give rise to alternating swelling and shrinking of corrosion products inside the cracks. Mechanical stress, as a consequence thereof, stimulates the process of further crack initiation.

Over the decades and centuries, step-by-step these recurrent sequences of gel layer formation, cracking and flaking of glass clods may destroy susceptible treasures completely. Surface degeneration visible to the naked eye suggests already serious attack. This is the reason why instrumental early identification of endangered glass substance is of increasing demand. Once ascertained, such objects of art should be preferably stored inside controlled show-cases kept under constant and individual air conditioning. This procedure allows to embank initial corrosion processes and retards its extension in an effective manner.

3 ANALYTICAL FUNDAMENTALS

Preventive analysis of art works made from glass follows two questions: (i) to get information on the present state of surface corrosion, and (ii) to decide on the expected risk of potential surface deterioration when exhibiting the objects under normal air conditions in the museum.

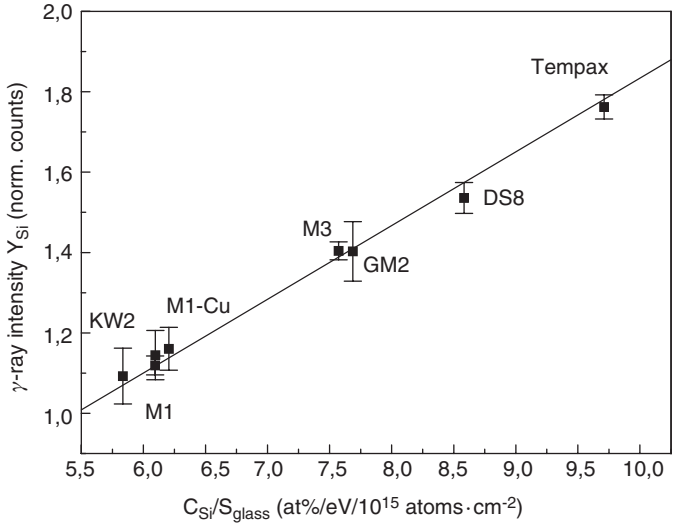

Figure 2. PIGE calibration curve for the element Si: γ-ray intensity Y_{Si} (normalised per number of incident protons) as a function of the Si concentration (at%) in glasses of known composition represented by the marks, see also (Mäder 2002). For a given composition specific stopping powers S_{glass} can be obtained from a physical data base (Ziegler et al. 1985).

3.1 *The basic idea*

Starting from a simple potash-lime-silica glass this matter consists of the network former SiO_2 and the network modifiers K_2O and CaO. Concentrations of silicon, potassium and calcium in intact homogeneous material can be easily specified by PIXE – Particle induced x-ray emission (Johansson et al. 1995): protons penetrate into the solid as a straight line beam, and the "hit atoms" emit their characteristic x-radiation. If the glass surface is modified as the result of leaching phenomena, the detected PIXE spectra do no longer represent the real original glass composition. This is especially due to the fact that the main intensity of the low-energy Si K-radiation ($E_x = 1.74$ keV) originates predominantly from the modified near-surface region. Those Si-K x-rays emitted from the unaffected bulk are already strongly attenuated after passing a corrosion top layer of about 10 microns thickness. However, PIXE is straight suited to measure the concentration of silicon just within this altered surface region.

There is a second technique of ion beam analysis (IBA) which allows to determine the silicon concentration of the thick but underneath glass bulk: particle induced Gamma-ray emission (PIGE) which is based on nuclear reactions producing γ-rays. In the case of silicon the $^{28}Si(p,p_1\gamma)^{28}Si$ reaction is used and the intensity of the $E_\gamma = 1779$ keV line is measured (Kiss et al. 1985). This characteristic radiation of high energy E_γ penetrates hundreds of microns without attenuation. The PIGE information depth in glass is about 40 μm (for Si and 4 MeV protons), and it is limited by the decreasing γ-ray production with decreasing proton energy due to the proton slowing down in the solid.

As can be seen in Figure 2 the concentration of silicon atoms in the glass bulk can directly be deduced from the measured yield of the 1779 keV γ-ray line. Here, S_{glass} – the stopping power – is a parameter which joins the individual composition of each glass standard applied for generating this graph. The analyst knows that $S_{glass} \sim 3$ eV/10^{15} at/cm^2 is an acceptable first approximation (Ziegler et al. 1985). The PIGE method is also useful and indispensable for quantitative registration of the other light glass components like the oxides of sodium ($E_\gamma = 440$ keV), magnesium ($E_\gamma = 1369$ keV) and aluminium ($E_\gamma = 1014$ keV). Concentrations of these elements in relation to silicon can be obtained easily by relating the intensity of the corresponding γ-ray line to the

intensity of $E_\gamma = 1779$ keV from silicon. The glass standards mentioned in Figure 2 are useful also for this part of calibration. For glass examination by IBA the use of PIGE, simultaneously to PIXE, is mandatory because just the combination of both techniques guarantees a complete analysis, i.e. the detection of heavier plus light elements.

Even for an unaffected glass surface, relative concentration values given by PIXE analysis only may be wrong. This is due to strong attenuation of Si x-radiation by "PIXE non-visible" light elements, e.g. Na from soda-lime-silica glass. The PIXE-PIGE alliance gives the correct result. The calculation of elemental concentrations starts from the measured γ-ray yields making use of the PIGE calibration curves and $S_{glass} = 3$ eV/10^{15} at/cm^2. After that, the corresponding PIXE spectrum is evaluated taking the PIGE result as an initial matrix. It is supposed that oxygen fits the stoichiometric rules of elemental oxides. Finally, the stopping power S_{glass} is improved by feeding the tables of Ziegler et al. (1985) with the derived concentration values. Improved S_{glass} has the consequence of improved light element concentrations given by PIGE (see Figure 2 for Si) etc. The correct concentrations are obtained if the self-consistent procedure yields stable stopping power values.

Focusing the attention now on the identification of a corroded glass surface the following strategy becomes evident: simultaneous measurement using PIXE plus PIGE and subsequent comparison of the concentrations deduced for silicon, see also (Mäder et al. 1998). In the case of non-affected glass the result $C_{Si}(PIXE) = C_{Si}(PIGE)$ is expected. If the concentrations of potassium and calcium in the near surface network are lowered due to leaching, this situation will be indicated by $C_{Si}(PIXE) > C_{Si}(PIGE)$, i.e. by an enhanced silicon concentration recorded by the surface sensitive PIXE method. For thin corrosion layers ($d < 2\,\mu m$) experiments prove this effect to be small. Hence, the silicon atoms from the unaffected glass bulk contribute predominantly to the measured in-depth integral yield $Y_{Si}(PIXE)$. Under these circumstances the K-shell x-ray intensities of potassium and calcium ($E_x = 3.31$ and 3.69 keV, respectively) represent the glass bulk quiet well. The situation obtained for anymore thicker corrosion layers ($d < 6\,\mu m$) are discussed below.

3.2 *Level of knowledge*

Glasses of definite composition (model glass) were molten at both the Academy of Fine Arts Vienna (Schreiner, Austria: glasses termed "M") and the Federal Institute for Materials Research and Testing Berlin (Müller et al. Germany: glasses termed "KW"). The specified samples were polished for ion beam analysis. Combined studies of PIXE and PIGE made sure that the nominal elemental concentrations could be verified by IBA. In this connection it was of special interest to scrutinize that the concentrations of silicon given by PIXE and PIGE agree within the frame of the experimental errors.

In a next cycle the model glasses were exposed to step-by-step artificial leaching. For this purpose the glass surfaces were treated in aqueous solutions of hydrochloric acid. Corresponding chemical procedures were provided by Schreiner (Academy of Fine Arts Vienna, Austria) and Römich (Frauenhofer Institute for Silicate Research, Würzburg, Germany). Modified layers of different thickness could be produced by this controlled technique. Figure 3 compares PIXE and PIGE spectra as gained from the model glass termed M3 (60 SiO_2, 15 K_2O, 25 CaO, numbers are gew%). After a 195 hours chemical treatment drastic losses of K and Ca are visible from the reduction of the corresponding x-ray peak intensities (see Figure 3, left), whereas the x-ray intensity of Si increases by a factor of 1.7 indicating the growing surface region of silicon enriched material. The Si γ-ray intensity (see Figure 3, right) shows only a slight increase ($\sim$10%). The latter confirms that the total PIGE information depth is large compared to the thickness of the leached surface layer.

Figure 4 compares the Si concentration values deduced from the PIXE and PIGE spectra as a function of the measured corrosion layer thickness. For PIXE two regions can be distinguished in this graph: (i) the proportional region, $d < 6\,\mu m$, where the leached layer plus the unaffected glass bulk contribute to the PIXE signal, and (ii) the region of saturation in the case of thicker corrosion films. The corresponding PIGE curve imparts that corrosion top layers $d < 3\,\mu m$ do not falsify the Si concentration value of the bulk glass as given by PIGE. Figure 4 makes clear that the

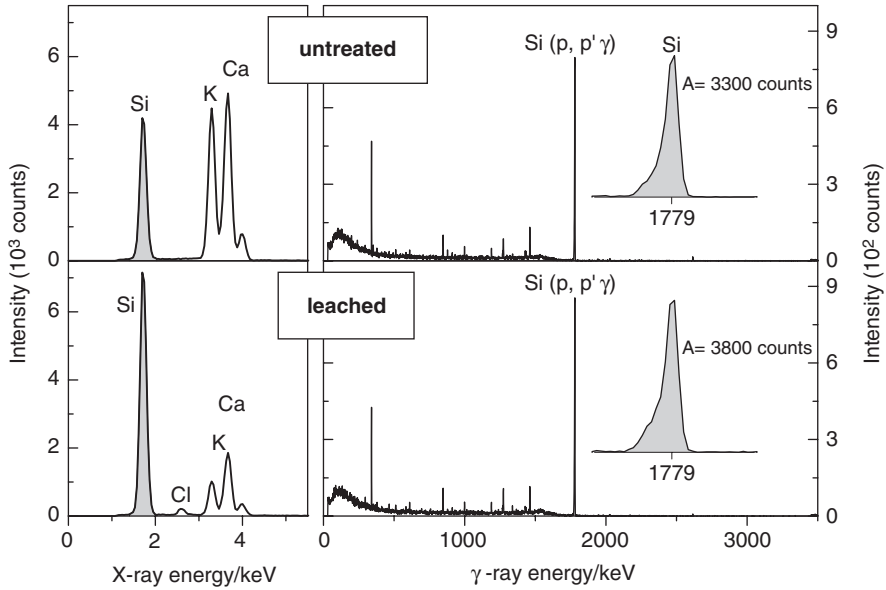

Figure 3. PIXE (left) and PIGE (right) spectra obtained from M3 glass at $E_p = 3.9$ MeV proton energy before and after 195 h treatment in 0.1 n HCl, see text. For exact evaluation the Si γ-ray lines are given as zoom (compare the peak areas A).

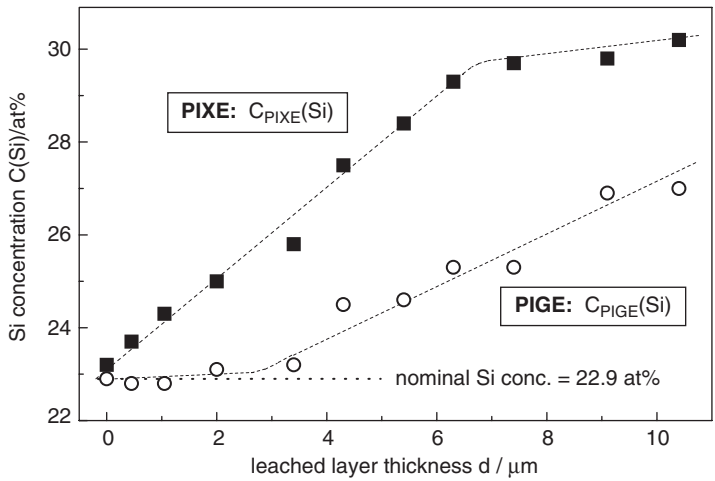

Figure 4. Si concentrations for M3 glass (at% deduced from PIXE and PIGE measurements) in dependence on the thickness of the surface region modified by leaching, see text.

concentration ratio $C_{PIXE}(Si)/C_{PIGE}(Si)$ is a potential indicator for the corrosion state of slightly aged glasses as found in museums, see also (Mäder et al. 1998).

Thicker corrosion layers are discernible from additional RBS – Rutherford backscattering spectrometry (Chu et al. 1978) – a technique which informs about depth dependent characteristics close to the object surface. Protons are detected after "reflection" from top/underneath atoms, i.e. protons without/with energy loss in the glass. Figure 5 compares RBS spectra from glass M3 before and after controlled leaching. As can be seen from this figure, two effects appear if the leached region

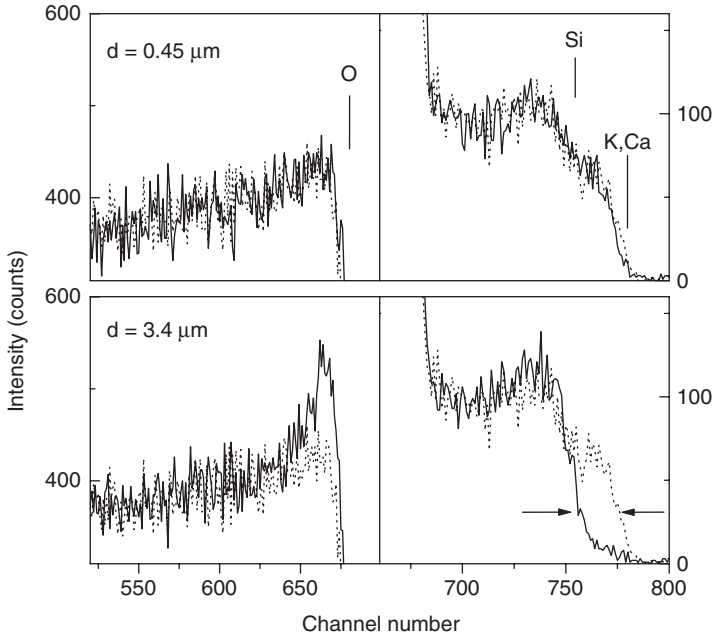

Figure 5. RBS spectra obtained from leached M3 glass: Regions of interest show the increase of both (i) shift of the surface signal from K + Ca and (ii) oxygen surface signal for increasing thickness of the leached layer. For comparison spectra of the untreated glass are given by broken lines.

surpasses a critical value around $d \sim 2\,\mu m$, namely (i) a shift of the highest-energy edge towards lower energies becomes obvious, and (ii) the near surface oxygen signal raises, see Figure 5. With increasing thickness of the corrosion layer both effects increase, and they origin from one and the same process: progressive leaching of K and Ca. Potassium and calcium atoms are no longer present directly on the surface, and the detected protons loose energy before and after backscattering from K and Ca (i). At the same time the grown concentration of SiO_2 gives rise to an increased RBS signal from oxygen and silicon (ii). It is the consequence of physical laws that this rise is only visible for oxygen. In addition, the replacement of leached K and Ca by penetrating O (and H) atoms from the humid surrounding amplifies the increase of the oxygen RBS signal. Thus, the Figure 5 specifies a further sign indicating the glass surfaces to be covered by a corrosion layer of $d > 4\,\mu m$, see also (Mäder 2002).

Testing model glass allows getting detailed information on the corrosion layer intrinsic effects. This is because cross sections can be prepared in order to conduct depth dependent studies using secondary electron microscopy (SEM) accompanied by energy dispersive x-ray analysis (EDX). Figure 6 shows corresponding results gained from the leached near-surface region of glass M3. The measurements were done by Woisetschläger (Technical University of Vienna, Austria). Here, SEM clearly visualises the modified surface – note the formation of clods framed by vertical and horizontal cracks as already known from Figure 1. Both, the decreased number of K and Ca atoms and the increased concentration of Si become visible by depth-resolved EDX. It is of importance to mention that the combination of RBS and SEM allows to determine the density of the affected region which was found to change from 2.6 g/cm^3 (virgin glass) to 1.4 g/cm^3 (leached glass) in the case of glass M3.

As already mentioned above, the leached glass components are replaced by hydrogen and oxygen and/or H and O containing cations/anions. Therefore it is of interest to get an idea of the concentration of embedded hydrogen atoms. This is possible by making use of the $^1H(^{15}N, \alpha\gamma)^{12}C$ nuclear resonance reaction at 6.385 MeV resonance energy of the impinging ^{15}N ions (Lanford

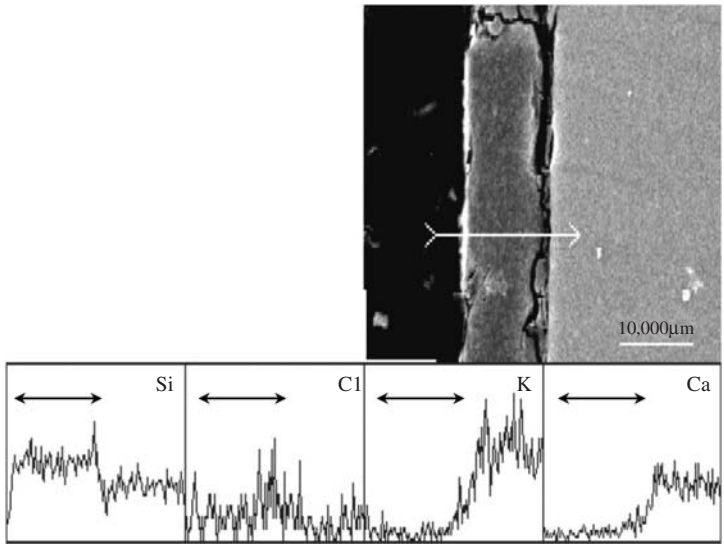

Figure 6. SEM micrograph of an embedded polished cross-section of glass M3 after 195 h treatment in 0.1 N HCl. The layer sequence (white arrow from left to right) is: resin – leached layer – glass bulk. Elemental line scans (below) were taken by means of EDX (black arrows mark the leached layer).

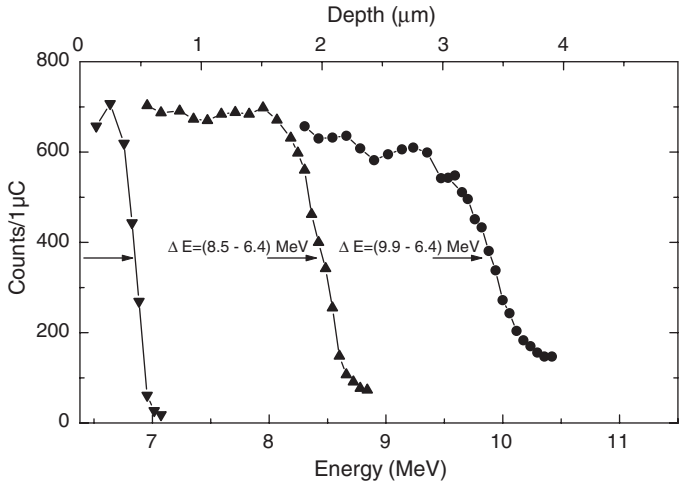

Figure 7. Hydrogen depth profiles from M3 glass treated in 0.1 n HCl for different times. The nuclear resonance reaction $^{1}H(^{15}N, \alpha\gamma)^{12}C$ was used in the vicinity of 6.4 MeV.

et al. 1976). Figure 7 presents the H depth profiles measured from leached M3 glass by gradual increasing the ^{15}N incidence energy. The plateau of the γ-ray intensity as a function of depth indicates a homogeneous distribution of hydrogen atoms. After calibration by suitable standards, the absolute plateau intensity tells the analyst that the H concentration amounts to $C_H \sim 10$ at% in the present case. Corresponding values gained from model glasses of different composition confirm that $C_H = 10$ at% is a representative overall-value for artificially leached glass (Mäder 2002). It is also obvious from Figure 7, that the thickness of a corrosion layer is represented by the decline of the corresponding H depth profile. For obtaining a depth scale the physicist makes use of the

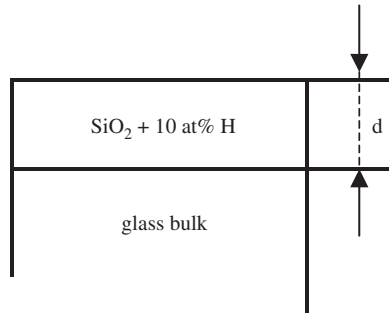

Figure 8. Glass bulk covered by the leached layer (schematically): This image serves as a model for PIXE simulation of Si x-radiation emitted from both glass bulk plus leached region.

^{15}N ion energy loss in the H-containing region. This is given by the difference – maximum incident energy at half of the plateau intensity minus resonance energy (~6.4 MeV) at the glass surface. This energy loss (in keV) can be related to the total thickness of the leached layer (in nm) as given by SEM(EDX).

It is necessary to remember that the detailed knowledge gained from extensive SEM/EDX measurements and hydrogen depth profile studies required the preparation of small glass samples. Such a procedure is excluded from non-destructive analysis of intact works of art. Therefore, model glasses (potassium-calcium-silica) of different composition were subjected to systematic investigations including both artificial leaching and the complete analytical characterisation as described above. From this it could be generalised that the modified glass surface region consists of $SiO_2 + 10$at% H where the network modifiers K and Ca are almost completely leached out. Further research on naturally aged glass will improve this initial model description.

4 APPLICATION

Regarding corrosion, most endangered glass is plain K_2O-CaO-SiO_2 glass of low SiO_2 concentration (<65 gew%), see Schreiner (1991). The primary classification of an unknown glass is given by a qualitative inspection of the measured PIGE and PIXE spectra. Thus, additives of network stabilising components (Scholze 1977), i.e. glass formers like B_2O_3, P_2O_5, GeO_2, As_2O_3 but also network formers like Al_2O_3 and PbO, are directly detectable. Note that colouring agents, e.g. CuO in green glass, cause higher glass resistance as well.

The results described above make possible to develop an initial strategy for deducing the real bulk composition of a glass even though modified by minor surface corrosion, i.e. a thickness of the leached layer $d < 3\ \mu m$, for details see Mäder (2002) and Figure 5. From a single IBA measurement (PIXE-PIGE-RBS) such museum objects should be characterised by

(i) no signal shift and no increased surface signal for oxygen in the RBS spectrum, but
(ii) $C_{Si}(PIXE) > C_{Si}(PIGE)$.

Figure 8 illustrates the image used for further PIGE and PIXE data processing: the original glass bulk of interest is covered by a thin leached layer (density $\rho = 1.4\ g/cm^3$) consisting of SiO_2 that contains 10 at% of hydrogen. This model implicates that

(a) the PIGE evaluation gives the correct concentration value C_{Si} for silicon in the glass bulk, and
(b) the PIXE spectrum, though modified due to the near-surface composition changes, gives a useful first approximation for the concentration ratio C_K/C_{Ca} of the adjacent elements K and Ca in the undisturbed glass bulk.

Table 1. Concentration (gew%) of elements in leached ($d \sim 2\,\mu m$) glass M3: nominal values and the result of ion beam analysis. For comparison, the last column gives the PIXE result as obtained without consideration of a modified surface region.

Element	Nominal value	IBA result	PIXE*
Si	28.1	28.4	31.5
K	12.5	12.2	10.9
Ca	17.8	17.5	14.0
O	41.7	41.9	43.6

* Assumption of homogeneous material.

A commercial PIXE soft-ware (Maxwell et al. 1989) allows to simulate the total x-ray intensities obtained from both the glass bulk plus the top layer specified above. Present calculations premise that the glass bulk is composed of $100\% = C_{SiO_2} + C_{K_2O} + C_{CaO}$ for potash-lime-glass. Step-by-step, the thickness d of the top layer ($SiO_2 + H$, see Figure 8) is varied and the ratio C_K/C_{Ca} is corrected until the simulated x-ray intensities $Y_{Si}(d)$, $Y_K(d)$ and $Y_{Ca}(d)$ fit the measured values at one and the same top layer thickness d.

4.1 *Example*

Glass M3 treated for 10 hours in 0.1 n HCl gets a leached surface layer of about 2 μm thickness. As expected, the RBS spectrum does not yet show any enhancement of the oxygen surface signal. Supposing undisturbed and homogeneous glass, straight evaluation of both PIGE and PIXE spectra results in $C_{Si}(PIXE) = (25.0 \pm 0.5)$ at% and $C_{Si}(PIGE) = (23.1 \pm 0.5)$ at%. From this difference the presence of a silicon-rich surface layer has to be accepted. Initially, PIXE simulation verifies the intensities of the measured Si, K and Ca peaks in the x-ray spectrum only when a different thickness d of the corrosion top layer ($SiO_2 + 10$ at% H, $\rho = 1.4\ g/cm^3$) is inserted: $d(Si) = 1.5\,\mu m$, $d(K) = 2.25\,\mu m$, $d(Ca) = 0.75\,\mu m$. The contradictory thickness values for the individual elements now require corrections of the initial C_K/C_{Ca} ratio as given by PIXE. Gradual improvement leads to the good agreement: $d(Si) = 1.5\,\mu m$, $d(K) = 1.65\,\mu m$, $d(Ca) = 1.6\,\mu m$. Table 1 compares the final results with the M3 nominal concentration values. As can be seen from this table, the complete IBA result (PIGE + PIXE) taking surface modification into account (compare Figure 8) fits the nominal concentrations of all the glass constituents. On the contrary, deviations remain in the case of simple PIXE analysis assuming a homogeneous undisturbed glass matrix.

5 OUTLOOK – MODEL AND REALITY

Any time accelerating simulation of slowly-processing natural glass corrosion represents a rough and questionable procedure. This is especially true if well-preserved glass objects from museums are under consideration instead of church windows which have been exposed permanently to alternating weather conditions. Less aggressive chemistry, i.e. at typical humidity in rooms of minor acid gaseous concentration, might dissolve the weakest oxygen bonds only. This idea is born from very recent studies on authentic museum glass of the 18th century. The foot of a goblet was analysed on both sides (i) the exposed upside and (ii) the concaved bottom side protected as a consequence of normal positioning. PIXE measurements show comparable intensity ratios $Y_X(Ca)/Y_X(Si)$ from x-radiation of calcium and silicon. On the contrary, the relative intensity of potassium $Y_X(K)/Y_X(Si)$ drops by a factor of four when analysing the foot upside (i) instead of the bottom (ii). Obviously, water soluble K_2O components were dissolved and K is leached from the upside glass surface. This process seems to be suppressed in the case of the protected bottom. In contrast to model glass M3

treated in diluted HCl (see Table 1), natural ageing of the archived historic goblet did apparently not attack the water resistant CaO network modifier. The latter finding will be finally clarified after improving the procedure of non-destructive bulk composition analysis described above. In order to upgrade the image of natural corrosion layers further experiences from originally aged glass are necessary. For instance, the concentration of water molecules incorporated during/after the leaching process may depend on sequenced periods of more wet and more dry surrounding stimulated by fluctuations of temperature. Soft long-term leaching of the glass network might allow relaxation processes which possibly stabilise a favoured silicate frame.

Current studies on museum glass of the early 18th century will allow widespread investigation. This is due to the availability of fragments: (1) a disease-ridden potash-lime-silica glass of surprisingly high SiO_2 but very low CaO concentration, and (2) a visually well-preserved PbO containing potash-lime-glass of sufficient SiO_2 concentration but high concentration of K_2O compared to CaO, see also Table 2. It is remarkable that glass (1) of about 77% SiO_2 could not withstand glass disease (see Figure 1). This is interpreted as due to the 12% K_2O in contrast to 2% CaO only. Remember, that addition of K_2O loosens the SiO_2 network, hence lowers the melting point, whereas CaO serves for higher water insolubility. For glass (2) it is the addition of 5% PbO that improves the stability of the 63% SiO_2 network. Until now, a first analytical overview of the fragments (1,2) bulk was obtained by ion beam analysis from the fractures. Beyond it, the fragments will be used to get special insights in order to qualify ion beam based investigation for non-destructive analysis of the glass bulk of unique originals when surface-corroded under real condition.

Table 2. Composition of two historic glasses (1) and (2), values in gew%, as determined by means of external proton beam analysis, see text.

	Na_2O	MgO	Al_2O_3	SiO_2	K_2O	CaO	TiO_2	MnO	Fe_2O_3	As	PbO
Glass 1	0.7	0.2	0.6	77.5	12.1	1.9	0.1	0.2	0.1	–	–
Glass 2	0.3	–	0.2	63.4	20.7	4.3	–	0.1	0.1	1.9	5.1

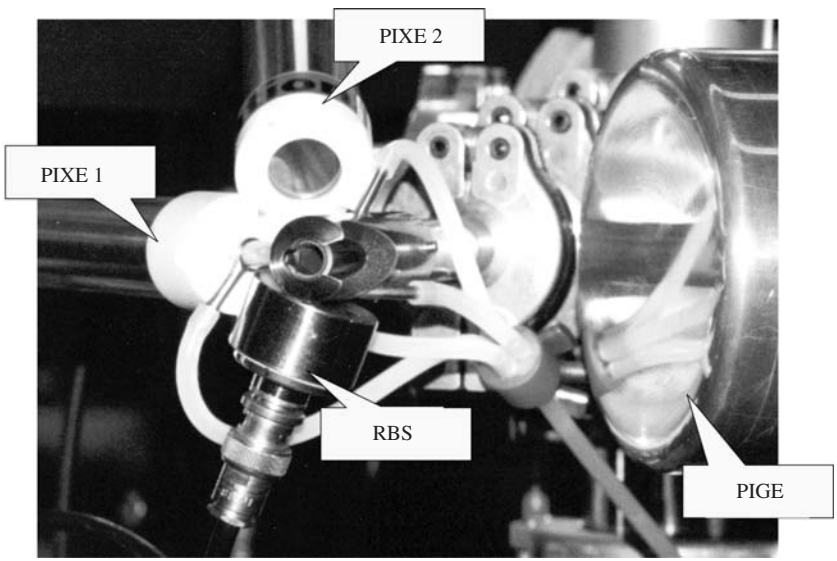

Figure 9. Rossendorf external beam set-up: four detectors are arranged around the beam exit pipe which is flushed by helium gas (see feed lines). Objects are positioned directly on air. The large-volume Si(Li) detector (PIXE 2) serves for sensitive analysis of heavier elements.

6 EXTERNAL BEAM EQUIPMENT

Protons of 4 MeV energy leave the vacuum tube by passing through a thin ($\sim$2 μm) metallic foil. The Rossendorf external beam facility joins an efficient multiple detector set-up at low distances from the beam spot on the object (Neelmeijer 1996). This arrangement allows simultaneous measurements and it ensures sufficient radiation intensities at low proton currents ($\sim$200 pA on a 1 mm^2 spot). Figure 9 shows the beam exit pipe where the detectors are placed around in backward directions. The analytical problems mentioned above make mainly use of both the Si(Li) x-ray detector (PIXE 1) and the Ge γ-ray detector (PIGE). In addition, a special surface barrier detector records the spectrum of "reflected" protons, RBS – Rutherford backscattering spectrometry (Chu et al. 1978). The projectiles are backscattered from atoms at the glass surface and from atoms underneath after loosing portions of energy. In particular, the measured RBS spectrum informs on peculiarities relating to the very near surface region. The inner of the exit pipe is flushed with helium (flexible tubes in Figure 9) in order to avoid both slowing down of protons and attenuation of x-rays on air. During analysis the object is arranged directly in front of the exit pipe. Exact and reproducible positioning is guaranteed by means of a motor-driven manipulator.

ACKNOWLEDGEMENTS

The authors wish to express their special gratitude to M. Schreiner and W. Müller for essential hints and numerous fruitful discussions. The helpful cooperation of H. Römich, M. Schreiner and I. Beatus during artificial ageing of model glass samples is gratefully acknowledged. The authors would like to thank R. Aniol and M. Rossner for careful sample preparation. SEM(EDX) studies were kindly carried out by G. Woisetschläger. Hydrogen analysis was helpfully supported by D. Grambole and F. Herrmann. Special thanks are expressed to the "State Art Collection of Dresden, Kunstgewerbemuseum Pillnitz" for the open minded interest to study objects of their collection. This work was supported by BMBF under contract 03NE9RO1-7.

REFERENCES

Adams, P.B. 1984. Glass corrosion: A record of the past? A predictor of the future? *Journal of Non-Crystalline Solids 67*: 193–205

Chu, W.-K., Mayer, J.W. & Nicolet, M.-A. (eds) 1978. *Backscattering Spectrometry*. New York: Academic Press

Doremus, R.H., Mehrotra, Y., Lanford, W.A. & Burman, C. 1983. Reaction of water with glass: influence of a transformed surface layer. *Journal of Materials Science 18*: 612–622

Johansson, S.A.E., Campbell, J.L. & Malmqvist, G.K. (eds) 1995. *Particle-Induced X-Ray Emission Spectrometry (PIXE)*. New York, Chichester, Brisbane, Toronto, Singapore: John Wiley & Sons, Inc.

Kiss, A.Z., Koltay, E., Nyako, B., Somorjai, E. & Anttila, A. 1985. Measurements of relative thick target yields for PIGE analysis on light elements in the proton energy interval 2.4–4.2 MeV. *Journal of Radioanalytical and Nuclear Chemistry, Articles, 89*: 123–141

Lanford, W.A., Trautvetter, H.P., Ziegler, J.F. & Keller, J. 1976. New precision technique for measuring the concentration versus depth of hydrogen in solids. *Applied Physics Letters 28*: 566–568

Maxwell, J.A., Teesdale, W.J. & Campbell, J.L. 1989. The Guelph PIXE software package. *Nuclear Instruments and Methods B43*: 218–230

Mäder, M., Grambole, D., Herrmann, F., Neelmeijer, C., Schreiner, M. & Woisetschläger, G. 1998. Non-destructive evaluation of glass corrosion states. *Nuclear Instruments and Methods B136–138*: 863–868

Mäder, M. 2002. Zerstörungsfreie Charakterisierung historischer Glasobjekte mittels Ionenstrahlen. *Thesis*. Technische Universität Dresden, Germany

Neelmeijer, C., Wagner, W. & Schramm, H.-P. 1996. Depth resolved ion beam analysis of objects of art. *Nuclear Instruments and Methods B118*: 338–345

Rayn, J., McPhail, D., Rogers, P. & Oakley, V. 1993. Glass deterioration in the museum environment. *Chemistry Industry*: 498–501

Römich, H. 1999. Historic glass and its interaction with the environment. In N.H. Tennent (eds), *The Conservation of Glass and Ceramics*: 5–14. London: James and James
Scholze, H. 1977. In *Glas – Natur, Struktur und Eigenschaften*. Berlin, Heidelberg, New York: Springer
Scholze, H. 1982. Chemical durability of glasses. *Journal of Non-Crystalline Solids 52*: 91–103
Schreiner, M. 1988. Deterioration of stained medieval glass by atmospheric attack. *Glastechnische Berichte 61*: 197–204
Schreiner, M. 1991. Glass of the past: the degradation and deterioration of medieval glass artifacts. *Microchimica Acta*: 255–264
Ziegler, J.F., Biersack, J.P. & Littmark, U. (eds) 1985. *The Stopping and Range of Ions in Solids*. New York: Pergamon Press. Use also http://www.research.ibm.com/ionbeams/SRIM/

Cultural Heritage Conservation and Environmental Impact Assessment by Non-Destructive Testing and Micro-Analysis – Van Grieken & Janssens (eds)
© 2005 Taylor & Francis Group, London, ISBN 90 5809 681 5

Trace elements fingerprinting using accelerators and ICP-MS: circulation of gold from the 6th century BC to the 12th century AD

M.F. Guerra
Centre de recherche et de restauration des musées de France, MR CNRS, Palais du Louvre, Paris, France

ABSTRACT: The aim of this paper is to give an overview of the main characteristics and applications of the analytical techniques used to study the circulation of gold in the Past. Accelerator base techniques such as the combination of PIXE, PIXE-XRF and PIGE and activation analysis as well as ICP-MS in liquid mode and with laser ablation were used in this work. The combination of the concentrations of the measured trace elements is used to identify the gold supplies and their provenance. The loss of information on the characteristic trace elements of gold after refining, melting and alloying are cited. The possibilities and limitations of the techniques are shown through three examples concerning different historical periods. Gold coins, nuggets and foils fabricated from the 6th century BC to the 12th century AD in the Mediterranean basin and in Asia were analyzed.

1 GOLD IN THE PAST

Gold can be found in primary deposits – in quartz veins, with pyrites and arsenopyrites and as tellurides – as well as in secondary deposits, named placers (Morteani 1995). The secondary deposits, which are formed by natural phenomena such as the erosion of the primary deposits, provided most of the gold sources of the past. This fact is evidenced by different legends and myths such as those of king Midas and of Jason and the Golden Fleece.

Secondary deposits are easily exploited by Man. For example, alluvial gold can be obtained by simple panning and washing. We can still remember the recent gold rushes of Serra Pelada in Brazil, of Sierra Nevada in the United States of America and of Ballarat in Australia. Panned gold consists on dust and pellets but also nuggets of very different dimensions. Some nuggets can be rather big. For example, the *Welcome Stranger* found in Australia, state of Victoria, weighted 78 kg and contained 71 kg of gold (Herrington et al. 1999).

Gold is in general associated with silver and copper. For example, alluvial gold may contain up to 40% of silver but less than 1% copper (Antweiler & Sutton 1970, Raub 1995, Chapman et al. 2002). Depending on the type of ore very different elements are associated with gold, such as inclusions of galena, pyrite, chalcopyrite and arsenopyrite (Chapman et al. 2002). Alluvial gold undergoes also the association with other alluvial ores such as cassiterite (tin oxide), accumulation with heavy elements such as platinum and can still be panned together with iron and iron-titanium oxides, the so-called black sands. In some states of Brazil alluvial gold is also associated with diamonds.

The presence of gold in Nature as a native metal together with its ductility and malleability enabled the fabrication of objects by simple hammering. Before heating metallurgy Man could produce simple gold objects such as beads and foils. This assumption is illustrated by the objects from the 5th millennium BC found in a burial at Varna, in Bulgaria (Eluère & Raub 1991).

Metallurgy brought on casting but also refining and purification (see for the refining techniques Craddock et al. 1998). Techniques such as cupellation, cementation, parting, mercury amalgamation among others were applied to gold ores. As soon as Man could separate gold from the other

metals he could obtain very pure gold. The first gold objects being fabricated with natural gold alloys their color depended on the composition of the natural gold, called electrum. The refining techniques allowed the goldsmith to fabricate a wide range of gold-silver-copper alloys according to the colors (more copper for red gold, more silver for pale gold and so on) and of the properties required.

The beginning of gold processing is not well known. The use of cupellation and parting was archaeologically identified in the archaeological remains of the 6th century BC refinery of Sardis (Craddock 2000). The use of fabricated instead of natural electrum at that time was recently confirmed by the determination of the composition of contemporary gold coins struck by king Croesus in Lydia (Craddock et al., in press).

Information on the manufacturing technologies used by Man in the Past as well as on the origin of gold can be obtained by determining the composition of an archaeological object (Guerra & Calligaro 2003). The main elements of the gold alloys can be measured by a certain number of analytical techniques. These measurements leading to the study of different properties of the alloys and different manufacturing techniques. For example, we can consider by the analysis of gold alloys the study of the debasement of a coinage or the soldering and platting of a certain object. Nevertheless, the identification of the gold provenance is not an easy task. A certain ore contains specific elements or isotopes connected to its geological formation. In general provenancing is made through the determination of the combination of the concentrations of the characteristic trace elements or of the lead isotope ratios present in the final object. This latter technique is hardly perform in the case of objects fabricated with secondary gold. In fact, lead being absent or present at very low concentrations in this type of deposits.

The characterization of a gold used in the fabrication of a set of objects, the identification of the changes of gold supplies and the identification of the origin and the provenance of the metals are constrained in the case of art and archaeology to the determination of the elemental composition. However, we must note that the refining techniques demand high temperatures which means that several elements are susceptible to oxidation and loss by evaporation from gold or absorbed by the cupel with the consequent loss of information on the original metal (Craddock 2000). Another difficulty comes from the unknown geological chemistry. If the chemical composition of the ores might be available for recent gold mines, such as those exploited in South America after the 16th century and still those more recently exploited in the United States of America, those exploited during the Antiquity and sometimes in the Middle Ages are exhausted and any geological samples is available for analysis.

In most cases, suggestions on the identification of the provenance of a gold can only be advanced by using its chemical composition and statistical analysis. When statistical analysis is applied to the concentrations of several characteristic trace elements of gold, several chemical groups can be formed (Gondonneau & Guerra 2002). Well documented objects from known archaeological contexts are analysed in order to define those chemical groups. If those chemical groups can be associated with a provenance, objects matching those groups are said to be fabricated with the same gold.

2 ANALYTICAL TECHNIQUES

The studies on ancient gold provenancing require the development of analytical techniques measuring, with good limits of detection, a large number of trace and ultra-trace elements. In the case of archaeological and art objects, those techniques are as far as possible non-destructive.

The non-destructiveness of the accelerator based techniques led to the rather common use in archaeology of ion beam techniques (IBA). A wide range of analytical methods is provided to the archaeological scientist by the different particles accelerators, van de Graaff, cyclotrons, and also by the latest synchrotrons. The good detection limits allowing the study of a large number of questions. Slightly destructive, the techniques based on an inductively coupled plasma (ICP) provide better detection limits. Quite often coupled to an atomic emission spectrometry (ICP-AES),

when associated to mass spectrometry (ICP-MS) the detection limits are improved and the size of the sample is quite reduced. The necessary sample can still be reduced by coupling laser ablation (LA) to ICP-MS.

The high accuracy and sensitivity of mass spectrometry allows the measurement of isotope ratios either by coupling it to a thermo ionisation (TIMS) or, in order to reduce the size of the sample, to the quite recent multi-collector ICP (Niederschlag et al. 2003). As referred in the previous chapter, the isotope ratios and the combination of trace and ultra-trace elements contents are characteristic of a certain geological formation and so of the provenance of gold.

All the techniques referred in this work are based on particle accelerators or on mass spectrometry. The accelerator base techniques consider only incident beams of protons. According to their energy, either nuclear reactions or atomic phenomena are concerned. We remark that other particles might be used to study particular questions or particular elements of gold.

2.1 *Nuclear activation analysis*

Nuclear activation with a proton beam issued from a cyclotron (PAA) was first developed by P. Meyers in the 1960s (Meyers 1969) for the analysis of gold coins. However, the set-up used in this work for a beam of 12 MeV was developed in 1983 by J. Poirier (Poirier 1983) also for the analysis of gold coins. At 12 MeV protons produce in the sample almost only (p,n) nuclear reactions which minimizes the interferences. The radioisotopes produced by the 2 μA beam impinging on the gold samples can be measured by γ-ray spectrometry. When a 3 mm lead sheet is interposed between the object and the detector, γ-ray spectrometry can be performed immediately after irradiation. The γ-rays at about 300 keV emitted by the isotopes formed by (p,n) reactions on gold being absorbed. Quantitative calculations are made by using the flux monitoring technique and the Ricci & Hann mean σ method (Ricci & Hann 1965 and 1967).

This technique measures major and minor elements as well as about 10 significant trace elements in gold with limits of detection in the ppm level. The range of protons in gold is of about 0.2 mm, but 50% of the total measured γ-rays come from the first 50 μm (Beauchesne et al. 1988). For low quality alloys the elimination of copper from the surface by oxidation might be important. However, in the case of thin heterogeneous layers their contribution to the final result is insignificant.

This technique is usually used for the analysis of coins, which means small objects with a diameter from 5 mm to 5 cm (Guerra & Barrandon 1998). The set-up is not adapted to the analysis of objects with less than 2 mm and more than 5 cm diameter and with very different shapes. In addition to the induction of radioactivity, point analysis cannot be performed and very thin objects like foils, thinner than the proton range, can hardly be analysed. However, for gold alloys PAA has in general better detection limits than IBA techniques.

2.2 *IBA techniques: PIXE, PIGE and PIXE-XRF*

Particle induced x-ray emission (PIXE) uses a 3 MeV proton beam issued from a van de Graaff accelerator and has been used for the analysis of gold since the 1970s (for example Ferreira & Gil 1981, Demortier 1986; see also Guerra 1998, Dran et al. 2000). In our configuration two Si(Li) detectors allow the measurement by x-ray spectrometry of major, minor and about 10 important trace elements. One of the detectors has a 1 mm lead collimator and measures major elements while the other with a 75 μm Cu filter to absorb the Au-lines measures trace elements. With a 20 nA current the limits of detection reach 10 to 90 ppm for elements of atomic number between 20 and 60 and 100 to 300 ppm for atomic number higher than 75 (Guerra & Calligaro, in press). With a 30 μm external beam, PIXE analyses objects of very different sizes and shapes and performs point analysis, surface mapping and depth profiling (Calligaro et al. 1996, 2000, Demortier & Ruvalcaba Sil 1996).

PIXE being a near-surface technique (5 to 17 μm analyzed depth for an incident beam of 3 MeV protons) the results might be influenced by possible copper elimination from the surface.

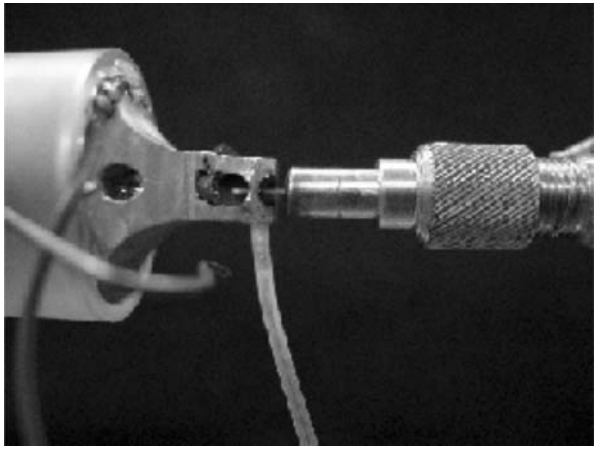

Figure 1. Experimental PIXE-XRF set-up for the measurement of platinum in gold in the AGLAE accelerator installed in the Louvre Museum. The proton beam impinges on an arsenic target and the object is placed at an angle of 45° with the beam.

To overcome this problem, γ-ray lines (produced deeper in the sample, about 27 μm for an incident beam of 3 MeV protons) are simultaneously measured by PIGE.

Particle induced γ-ray emission (PIGE) uses a 3 MeV proton beam issued from a van de Graaff accelerator. The copper, silver and gold γ-rays (energies between 115 and 991 keV), having a more important range than the x-rays emitted by the same elements, give information on the deeper layers of the object. PIGE is a nearly bulk analysis for thin objects. The range of 3 MeV protons in gold is of about 30 μm. The contribution of the possible heterogeneous surface to the total composition is negligible as for PAA. For a small set of gold alloys the results obtained by activation analysis and PIGE showed a good agreement (Guerra & Calligaro, in press).

This technique uses the same beam characteristics as PIXE and a 30% efficiency HPGe detector placed at 45° from the beam (Calligaro et al. 2000). The variation of the incident energy may be use to produce elemental depth profiles. PIGE can also be used to produce surface elemental mappings simultaneously with PIXE by mechanically moving the sample under the fixed beam. However, having poor limits of detection for a gold matrix (about 1000 ppm for copper, silver and gold), PIGE can only be applied to the measurement of major elements in gold.

PIXE induced x-ray fluorescence (PIXE-XRF) uses a 3 MeV proton beam issued from a van de Graaff accelerator and high currents (1–2 μA). The proton beam impinging on a thick primary target produces x-ray lines which are used to excite the target (Demortier 1986). The constituent of the primary target is chosen in order to emit an x-ray radiation of such an energy that, without exciting the major element of the target, the one or two trace elements with atomic number immediately below the major element are excited. In general, this technique is used either to analyze fragile objects which cannot be warmed-up under a particle beam (like paper) or when a good limit of detection (ppm level) is necessary for the measurement of a specified element (Bertrand et al. 2002).

In our case this technique was developed for the specific measurement of platinum in gold (Guerra & Calligaro 2003 and Guerra et al., in press). The set up uses the quasi-monochromatic x-ray radiation emitted by a primary target of arsenic (see Fig. 1). The Si(Li) detector has a zinc absorber of 25 μm. Quantitative evaluation is performed by subtraction of the atomic resonant Raman scattering (Karydas & Paradellis 1997) and the Rayleigh scattering in gold. By exciting platinum lines without exciting gold lines, the limit of detection attains about 80 ppm instead of 1000 ppm by PIXE with a filter of 75 μm of zinc (Guerra & Calligaro, in press). However, we must be aware that for each primary target this technique can only measure with good detection limits one or two elements in a sample.

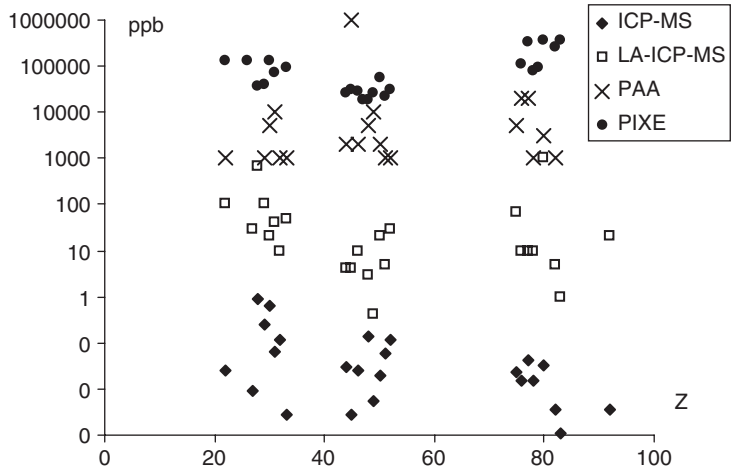

Figure 2. Limits of detection measured for a group of elements in gold routinely by PIXE (PIXE-XRF for Pt), LA-ICP-MS and ICP-M and with optimized conditions by PAA.

2.3 *ICP-MS*

The measurement of trace elements in gold can also be performed by mass spectrometry. In this work we used inductively coupled plasma mass spectrometry in two different methods of sample introduction: liquid mode (ICP-MS) and laser ablation (LA-ICP-MS).

In laser ablation mode we used the development of Gondonneau & Guerra 1999 with a Fisons PlasmaQuad PQXS combined with a 2 mJ pulsed VG Nd:YAG laser working on Q-switched mode and in the UV wavelength with a shot frequency of 6 Hz. Acquisition was performed using pick jumping mode, 10.24 ms dwell time, 60 s acquisition time after 10 s of pre-ablation and 3 by 3 raster scan pattern. Craters are of about 40 μm diameter and 130 μm depth, corresponding to a weight of about 1 μg per ablation. With $AuAr^+$ ion as internal standard the limits of detection range from 10 ppb to 1 ppm if we consider the high purity NBS gold standard SRM685 to produce a "gold plasma". However, if we only consider the blanks corresponding to the argon plasma, the limits of detection are improved by a factor of about 10 (Gondonneau & Guerra 1999).

In ablation mode ICP-MS gives hardly quantitative results particularly for major elements. The linearity of the signal depending on the laser pulse type. Being a relative technique, the scarcity of solid gold standards with a large spectrum of trace elements complicates the quantitative evaluation.

In liquid mode we used the development by Gondonneau et al. 2001 on a Fisons PlasmaQuad PQXS. The optimization of the analytical parameters was done in order to minimize the drilled sample to be dissolved. Acquisition was performed using pick jumping mode, 10.24 ms dwell time and 30 s acquisition time. For 2 mg samples limits of detection vary from 0.01 to 10 ppb. Using indium as internal standard we obtained for gold samples a good agreement between measured and certified concentrations. Even if slightly destructive, this technique employs standards which are fabricated by combining different standard solutions. Silver being lost during dissolution, major elements must be measured by another technique, such as μ-XRF or PIXE, before dissolution of the sample.

In Figure 2 we can observe the limits of detection for a large number of trace elements measured routinely in gold samples by PIXE (by PIXE-XRF for Pt), LA-ICP-MS and ICP-MS and in optimized conditions by PAA.

3 HISTORICAL EXAMPLES

The study of the circulation of gold is carried out by means of the combination of the information given by the analysis of the objects and by the historical documents (Guerra 2000a). According to

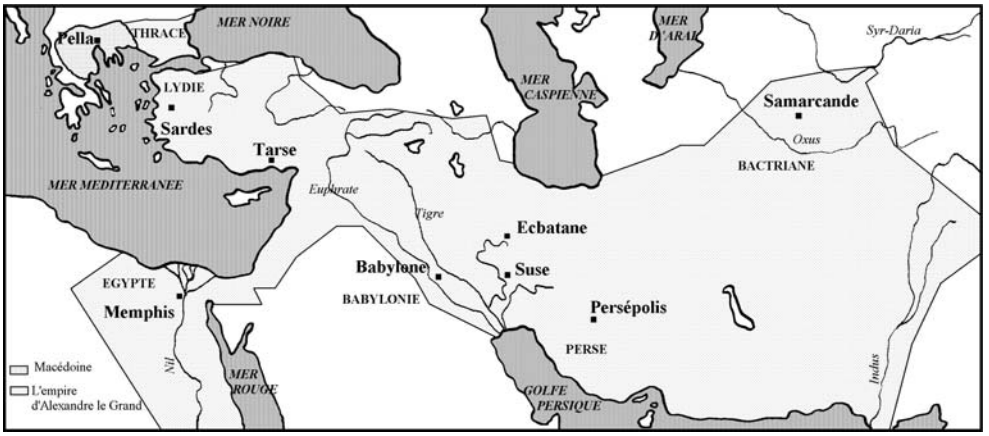

Figure 3. The empire of Alexander the Great (356–323 BC).

the considered periods or regions and the known written sources, analyses can provide more or less information about the Past. In fact, the relationship between the composition of a gold alloy and an historical event must be found. The interpretation of the use of one or another gold supply and the identification of the provenance of the metal depends on the available historical information. In general, the analytical results concerning the more recent periods are more easily interpreted than the analytical results obtained for objects from very ancient times.

To illustrate how far the elemental analysis of gold objects can give information on the Past according to the historical period and the type of analyzed object, we expose in this work three different examples. The first example concerns the circulation of gold in the 4th century BC in the empire ruled by Alexander the Great. The second example shows the main changes of gold supplies in the whole Arabian Empire from the 7th to the 12th century AD. At last, the third example considers the identification of the origin of the gold from the tombs of one rather unknown nomad tribe living from the 3rd century BC to the 2nd century AD in the Ordos region, present Mongolia.

For the first two applications we analyzed coins, quite regular and thick objects, as well as a group of nuggets with very different weights (from a few mg to 2 grams). For the third application thin gold foils of 30 to 60 μm thickness and very variable size were analyzed. The analysis of such different objects fabricated by such different civilizations shows the possibilities and limitations of the techniques described above. Those limitations are usually associated to the type of analyzed object, to the importance of the known historical sources and to the questions to be solved.

3.1 *The gold of Alexander the Great*

Alexander III of Macedonia, known as Alexander the Great, lived between 356 and 323 BC. Son of Philip II of Macedonia, Alexander the Great assembled a big army in order to conquer the territories situated in Asia Minor. Very quickly his empire became a vast territory comprising the regions from Macedonia to the Indus and from Egypt to the Oxus, including the ancient Achaemenid empire (see Fig. 3).

The conquest of such an empire and the payment of the soldiers required a certain amount of money. Alexander the Great struck gold coins, called staters. These coins were already struck in Macedonia by Alexander as well as by his father Philip II. It has been suggested by many scholars the use of the Achaemenid treasures to strike those staters in the mints of Asia Minor. However, this assumption has never been proved.

The wealth of the Achaemenid kings came from the taxes. The historical sources refer to the taxes paid by the satrapies, the different districts of the Empire, and cite the enormous treasures accumulated since Cyrus the Great (559–530 BC) in the Achaemenid palaces. Those taxes being paid with different products such as gold.

Figure 4. Stater issued by Alexander the Great at Sardis (reference BnF 363).

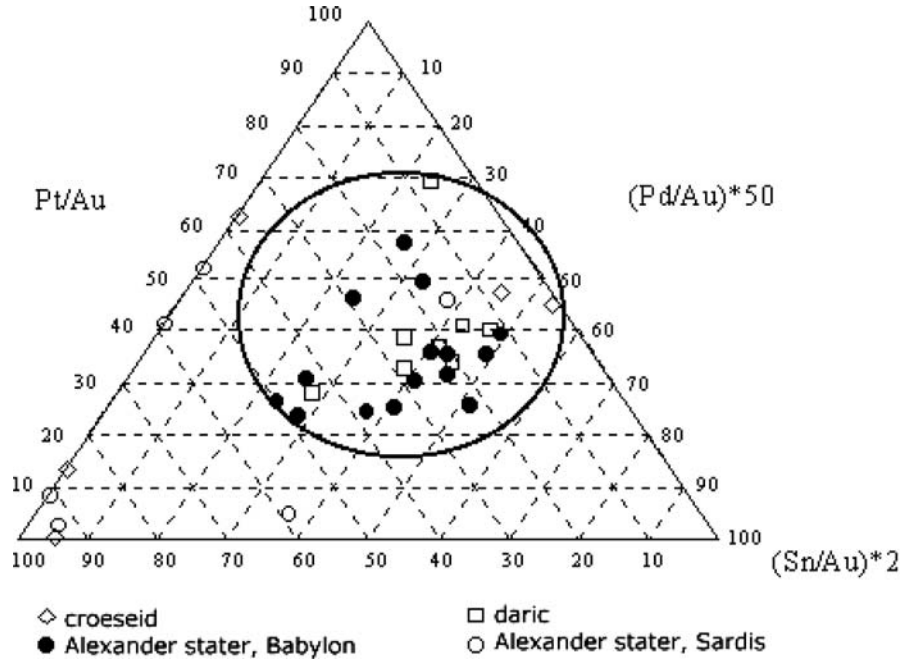

Figure 5. Characteristic trace elements normalized to the gold content for the coins struck in Asia Minor by Croesus, by the Achaemenid kings and by Alexander the Great.

In order to validate the assumption of the use by Alexander the Great of the Achaemenid treasures to strike staters (see Fig. 4) we analyzed by PAA a group of coins fabricated in the Asiatic mints of the empire. In that group we considered in addition to the staters some darics. The daric, issued since the reign of Darius I (522–486 BC) in Babylon and in Sardis, was the Achaemenid gold coin replaced under Alexander the Great by the stater. We can imagine the re-melt of the ancient gold coinages of Asia Minor to fabricate the new ones.

In Figure 5 (Gondonneau et al. 2002) we can observe the ratio of tin, platinum and palladium in ppm to the gold content in percent for the coins struck in Sardis and Babylon by Alexander the Great and the Achaemenid kings. We also represented in Figure 5 a small number of croesids, the gold coins struck by king Croesus in Sardis. These coins are used as a reference for Lydian gold. In fact, we could assume that the coins issued in Sardis could have been fabricated with gold coming from Mount Tmolus and river Pactolus. These alluvial placers and mines are said to be the sources of gold of the famous king Croesus who lived in the 6th century BC. We note that in 547 BC Lydia is conquered by the Achaemenids and the croesid is replaced by the Achaemenid gold coin, the

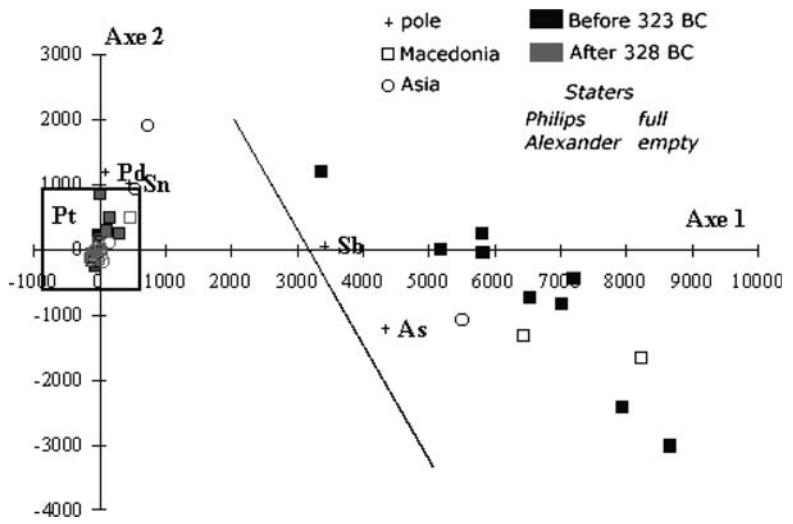

Figure 6. Statistical analysis for platinum, palladium, arsenic, antimony and tin on the staters struck by Alexander the Great in Asia and in Macedonia and by his father Philips II in Macedonia.

daric. The coins struck in Babylon, situated in the Eastern part of the empire, could have been struck with a different gold.

The high contents of platinum and tin for the croesids and most of the staters issued by Alexander the Great in Sardis represented in Figure 5 can be explained by the use of alluvial gold. Platinum and tin being among the characteristic elements of alluvial gold, the dispersion is justified by the exploitation of different panning regions during different periods. We note that if these coins appear dispersed in the ternary graphic, all the other coins fit together in one single group.

In the graphic of Figure 5 any difference is observed between the gold struck in Sardis and the gold struck in Babylon. The absence of chemical groups for the coins struck under Alexander could be explained by the use of one same mixture of gold under Alexander the Great and the Achaemenid kings. If we consider the texts of Herodotus (III, 96) about the gold and the silver received by the Achaemenid king as payments of the taxes, we can conceive but not certify the re-use of the Persian treasures to strike the staters (Briant 1996).

We could imagine the arrival of this gold in Macedonia. In order to verify this possibility we also analyzed by PAA some staters struck in Macedonia by Alexander as well by his father, Philips II.

When we try to separate the gold struck in Asia from the gold struck in Macedonia, we observe in Figure 6 two chemical groups (Gondonneau & Guerra 2000). These groups are obtained by a statistical analysis applied to the platinum, palladium, arsenic, antimony and tin contents measured in the coins. The first group, characterised by the absence of platinum and palladium, contains the staters struck before 323 BC. The second group, characterised by the higher contents of platinum palladium and tin, contains the staters struck after 328 BC. We can suggest that the first group was fabricated with an alluvial gold while the second group was fabricate with a primary gold. A change of supply is observed after the death of Alexander the Great.

If we consider the coins classification by G. Le Rider in 1977 we notice that this scholar established the suspension of the staters issuing between 328 and 323 BC. This suspension is revealed in Figure 6 by the change of the chemical composition of the coins. We cannot identify the provenance of the gold. Pliny in his Natural History, book 34, cites the mines of Mount Pangaeus, exploited since 357 BC. However, they were certainly exhausted in 328 BC. Healy suggesting the exploitation after 323 BC of mines such as that of Scapte-Hyle and the alluvion sources of the Hebrus (Healy 1978). We can only suggest the replacement of a primary gold by a secondary one.

The identification of the 328–323 BC suspension of striking together with the characterisation of the metals used before and after that suspension allow to date hitherto non datable coins.

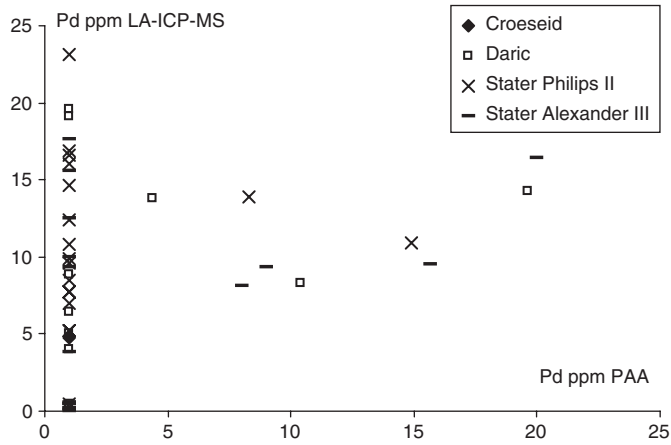

Figure 7a. Palladium contents obtained by PAA and LA-ICP-MS on the same group of coins struck in Macedonia and Asia Minor.

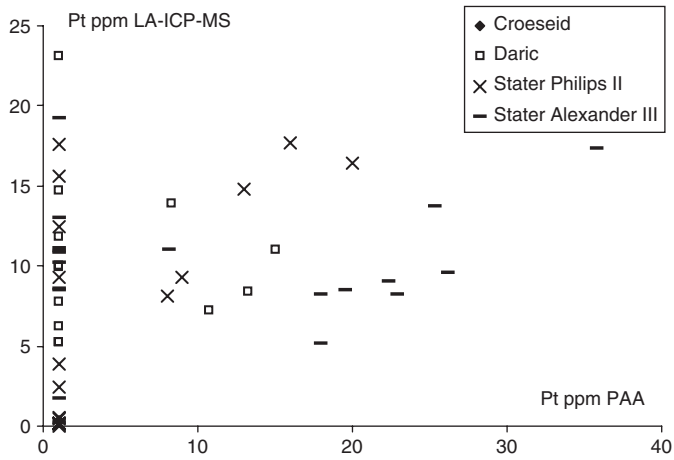

Figure 7b. Platinum contents obtained by PAA and LA-ICP-MS on the same group of coins struck in Macedonia and Asia Minor.

If the elemental analysis using the PAA technique defined two chemical groups for the coins issued before and after the death of Alexander, we are unable to identify the provenance of the gold. Furthermore, we were unable to differentiate the gold struck in the different mints. In fact, for the coins issued under Alexander the Great we cannot distinguish between the Macedonian and the Asian gold. We could not also distinguish the minted gold of Sardis from the gold struck in Babylon.

In order to measure a larger number of elements with better detection limits, we performed LA-ICP-MS on a group of staters struck in Macedonia and Asia. The compositions thus obtained showed equivalent concentrations for all the trace elements except for gallium and bismuth. The Macedonian staters having about 10 times more gallium and 100 times more bismuth than the Asiatic staters. This could indicate the use of two different gold source if we could rely on the quantitative results obtained by LA-ICP-MS. However, as shown in Figures 7 a and b for palladium and platinum, the trace elements concentrations measured for one same group of coins by LA-ICP-MS do not match those measured by PAA. The concentrations obtained by the two

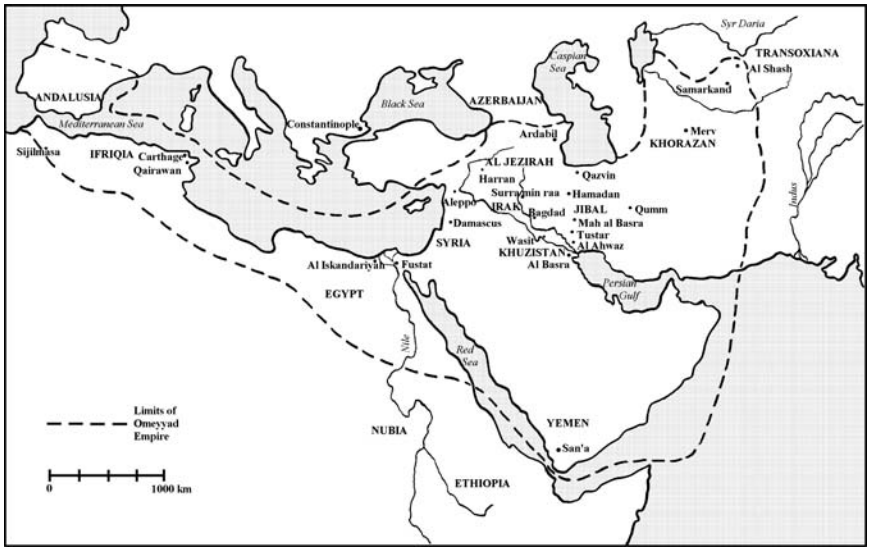

Figure 8. The Ummayad empire at the beginning of the 8th century.

techniques for each element in the same coin may differ by a factor of 5 to 10. We can say that in the case of gold alloys their rather low melting points together with problems related to ablation and sample transportation make ICP-MS hardly quantitative when coupled to the laser ablation of our set-up (Guerra & Calligaro, in press). This lack of linearity depends on the laser and could be improved as discussed by Gondonneau et al. 2001.

3.2 *The Muslim empire*

The conflicts opposing the Byzantines to the Sassanians from the 6th century to the beginning of the 7th century contributed to the expansion of the Arabs. Between the death of Mahomet in 632 AD and 732 AD they conquered an enormous territory from the Iberian Peninsula to the Syr Daria, represented in Figure 8. From the economical point of view we can consider two main periods in this empire: the first from 661 to 750 corresponds to the centralized Ummayad power ruling from the capital Damascus, while the second from 750 till 1258 corresponds to the clearly decentralized Abbassid power ruling from Baghdad, the new capital of the empire. With one language and one religion the Arabic empire became one of the biggest economical powers that ever existed in the Mediterranean world.

During about five centuries the internal struggles in the empire gave the power to very different dynasties as referred in Table 1. According to the period concerned, one or another dynasty conquered or lost the control of certain regions. Such a vast territory contained a large number of sources of wealth among which a certain number of gold sources. Some documents refer to the exploitation of the ancient mines of Nubia, Red Sea, Ethiopia, Yemen among others, but Islam when we consider the texts of the Arabian geographers the most important economical event of seems to be the discovery of the West African gold in ancient Sudan (present Ghana, Mauritania, Mali, …) (Gondonneau & Guerra 2002). The control of one or another region gave access to the control of the caravan routes of gold.

At the beginning of the conquest, the Arabs, as soon as they conquered a territory they started to strike coins. According to the region, heir first coins were typologically similar to the Byzantine or to the Sassanian coins, with a legend containing the words of the Prophet. The first gold coin of Arabian type, the dinar (Fig. 9), with no figures, appeared under the Ummayads, after the reform

Table 1. The Islamic dynasties cited in this work with the corresponding periods of reign and the main controlled regions.

Dynasty	Dates (AD)	Main regions
Ummayad	661–750	Near-East, North Africa
Abbassid	750–1258	Near-East, Egypt
Midrarid	771–976	North Africa
Aghlabid	800–909	North Africa
Tulunid	868–905	Egypt (Near-East)
Ikhshidid	934–968	Egypt
Fatimid	909–1171	North Africa, Egypt (Near-East)
Zirid	972–1167	North Africa
Almoravid	1061–1147	North Africa, Spain
Almohad	1147–1269	North Africa, Spain

Figure 9. Abbassid dinar issued in 294 H in Damascus (reference BnF L1075).

of Abd al-Malik in 695. The dinar became the dominant specie of the Mediterranean world and was used in all the commercial exchanges. Due to this large commercial network, the source of gold is often very difficult to determine.

In order to follow the circulation of gold in such a big empire, the first question to solve concerns the gold used to mint the first coins. As already cited, these coins were typologically similar to those minted in the conquered regions. However, were they struck with a new gold or just with an alloy obtained by re-cycling of the previous coins? To answer this question we analyzed a group of coins corresponding to the periods just preceding and following the conquest.

In Figure 10 we reported the ratios of palladium and platinum contents in ppm to gold concentration in percent for the coins struck in North Africa by the Byzantines (in Carthage) and in Spain by the Visigoths (southern Iberian mints) before the Islamic expansion as well as the coins struck immediately after the conquest by the first Arabian dynasty (Gondonneau & Guerra 2002, Guerra & Roux 2000, Gondonneau et al. 2000, Guerra 2000b). We can observe in this figure that the first Arabic coins, those called Arab-Latin (Muslim legends written with Latin characters), were certainly struck by recycling of the preceding Byzantine and Visigothic coins.

We can assume that the same procedure of re-cycling the previous coins to strike the first Arabian coin could have been used all over the empire. In order to validate this assumption we analyzed some Byzantine and Arabian gold coins struck in the Near and Middle-East.

Figure 11 (Gondonneau & Guerra 2002) presents the ratios of palladium and platinum contents in ppm to gold content in percent for the coins struck in the North of Africa and in the Near and Middle East during, as in the case of Figure 10, the periods immediately before and after the conquest. We can observe exactly the same re-cycling phenomena of the preceding Byzantine coins.

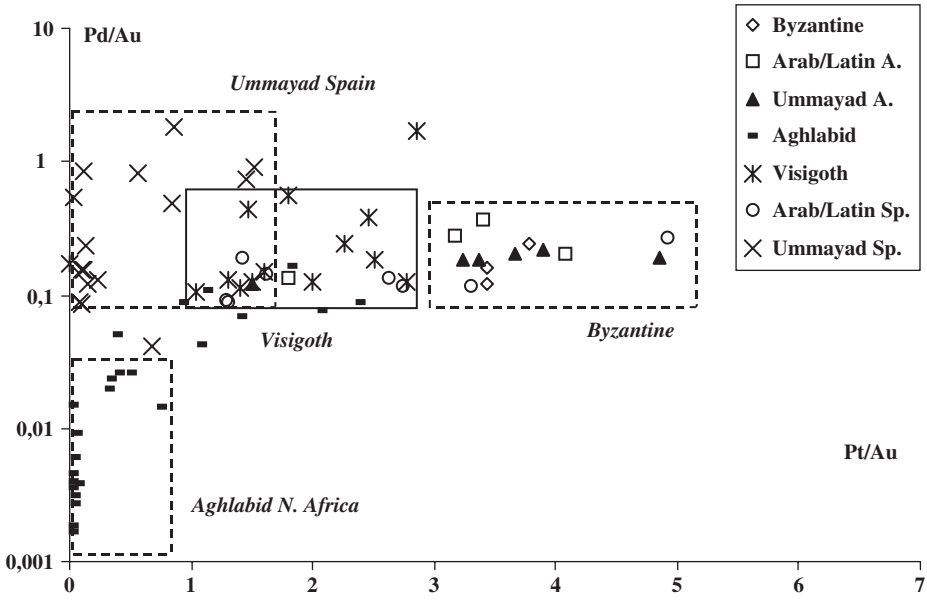

Figure 10. Ratio of platinum and palladium contents in ppm to gold concentrations in % for the coins struck in North Africa and Spain immediately before and after the Arabic conquest. The coins from North Africa are noted "A" and the coins from Spain are noted "Sp".

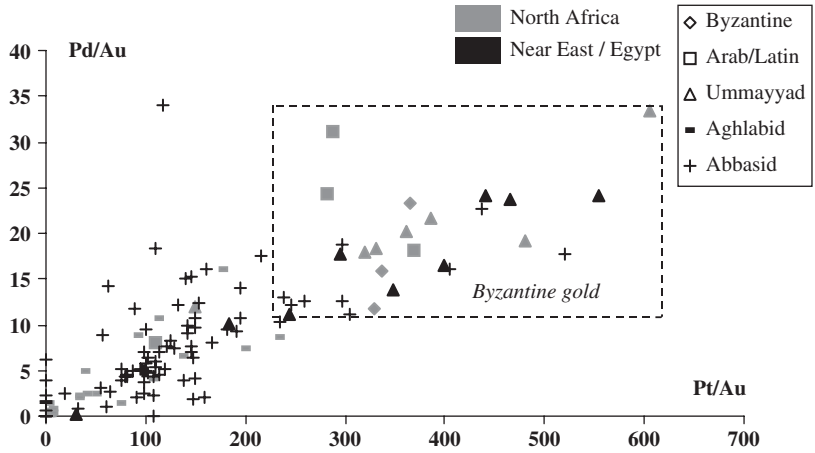

Figure 11. Ratio of platinum and palladium contents in ppm to gold concentrations in % for the coins struck immediately before and after the Arabic conquest in Near and Middle East and in North Africa.

We can thus state that the gold supplies change in all the mints of the Arabic empire around 750 AD. We could prove that this statement is also applied to the silver supplies of the same regions (Gondonneau & Guerra 2002). In conclusion, all the precious metals supplies changed in the Islamic empire when the centralized Ummayyad government was replaced by the decentralized Abbasid one.

In order to define where the new gold comes from, we analyzed a large number of coins issued by the different main mints of the empire. Figure 12 shows the results of a statistical analysis applied to the platinum, palladium, tin, antimony and gallium contents measured by PAA for the gold coins

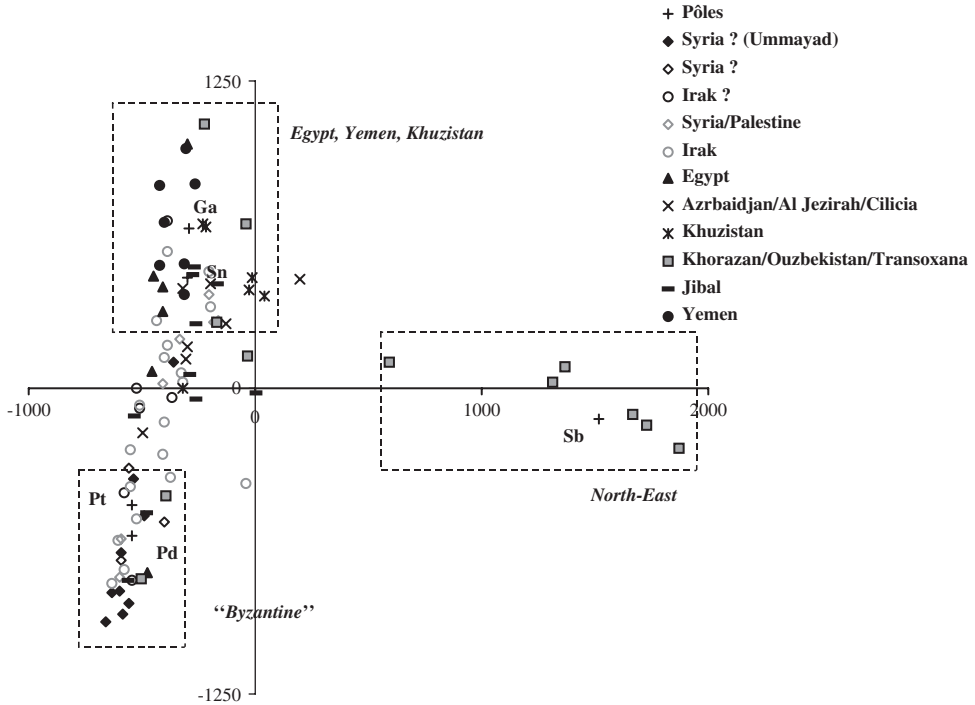

Figure 12. Result of the statistical analysis for platinum, palladium, gallium, antimony and tin on the dinars struck in Near and Middle East. (?) corresponds to the coins without a mint name usually attributed to Damascus and Baghdad.

struck in the Near and Middle East, where the sign (?) corresponds to the coins without a mint name but which can be attributed by the written sources to Damascus and Baghdad (Gondonneau & Guerra 2002). In Figure 12 we can identify three different gold supplies. The first group corresponds to a gold with high platinum and palladium contents and contains the coins fabricated by the recycling of the Byzantine gold. The second supply corresponds to a gold characterized by higher gallium and tin contents which slowly replaces the preceding Byzantine gold in Egypt, Yemen and Khuzistan. This gold certainly comes from Sudan and the Red Sea mines. The third and last supply corresponds to a gold with higher antimony contents struck in the Khorazan and the Transoxana, the north-eastern mints of the empire. This gold could be local, exploited in the Transoxana or in the more Eastern regions.

The same type of study was done for the North African coins. That study was carried out by considering one dynasty who reigned all over the African territories, the Fatimids (909–1171 AD). We reported in Figure 13 (Gondonneau & Guerra 2002) the results of a statistical analysis applied to the platinum, palladium, tin, zinc, arsenic and gallium contents measured by PAA for the gold coins struck in Egypt and in North Africa by the Fatimids as well as the gold coins struck in North Africa by the Midrarids (771–976 AD) and the Zirids (972–1167 AD). In addition to these coins, we also consider in Figure 13 the coins struck by one African dynasty, the Almoravids (1061–1147 AD). This Muslim dynasty controlled the gold caravan routes of West Africa and reigned also over Spain (Roux & Guerra 2000 and Guerra & Roux 2002).

We can observe that the Fatimids used two different gold sources. In Egypt they struck what we can call an Egyptian gold with higher palladium and platinum contents and certainly coming from Nubia and the mines of the Red Sea. In North Africa they struck a different gold which is characterized by higher concentrations of gallium and zinc. In spite of that, some of the North African coins were minted with a gold showing the same characteristics of the Egyptian gold.

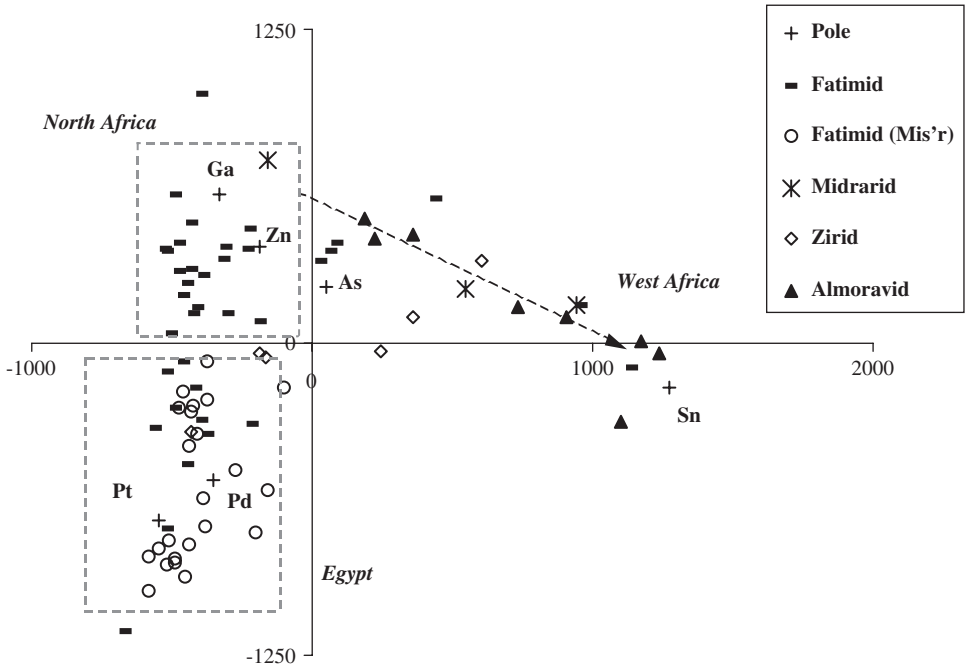

Figure 13. Result of the statistical analysis for platinum, palladium, gallium, zinc, antimony and tin contents on the dinars struck in Near East and North Africa by the Fatimids. North African Midrarid, Zirid and Almoravid dinars were also included.

This means that the Fatimids could have imported gold from Egypt to mint a part of their North African dinars. This issue does not seem to confirm the expected importance of the West African mines. This could however be related to a possible interruption of the gold supplies provided by the western caravan routes during a short period of time.

Under the Almoravids, the Midrarids and the Zirids we observe the use of a new gold. This might be the famous gold of the Arabian geographers coming from the West Africa mines. In fact, these dynasties only had access to the western caravan routes of Africa.

To verify the assertion on the use of the West African gold to strike the North African dinars we analyzed a set of 25 modern nuggets from Ivory Coast, Ghana and Mali weighing between 2 mg and 2 g (Guerra 2002). In order to measure trace elements, ICP-MS in liquid mode was performed on most nuggets. The solutions were prepared by M. Cowell in the research laboratory of the British Museum (Gondonneau et al. 2001). A group of 8 bigger nuggets was analyzed by PAA.

As ICP-MS allows the determination of a large range of elements we just considered in Table 2, the average concentrations of the most characteristic elements of gold measured by both techniques. These results show the very low contents of trace elements in gold. The composition of these nuggets is compared with the composition obtained by PAA for eight Almoravid dinars struck in Sijilmasa. The Sijilmasa mint was situated on the most important North African gold caravan route coming from the West African mines. The similarity of the composition found for both the nuggets and the dinars takes us to conclude that the new gold reaching the western mints of the Islamic empire can be identified as the West African gold.

3.3 *The gold of the Xiongnu*

The Xiongnu lived in the Asian part of the Great Eurasian steppe from the 3rd century BC to the 1st century AD (Pirazzoli 1982). Very little is known about this people. Only one chapter of the

Table 2. Average contents of trace elements in ppm on a group of 8 Almoravid dinars analyzed by PAA and a group of 25 gold West African nuggets analyzed according to their size by PAA and ICP-MS.

Element	Almoravid coin	Nugget ICP-MS	Nugget PAA
Sb	1	5	1
Pt	1	0.5	1
Pd	1	0.3	1
Zn	57	13	36
Te	1	0.6	2

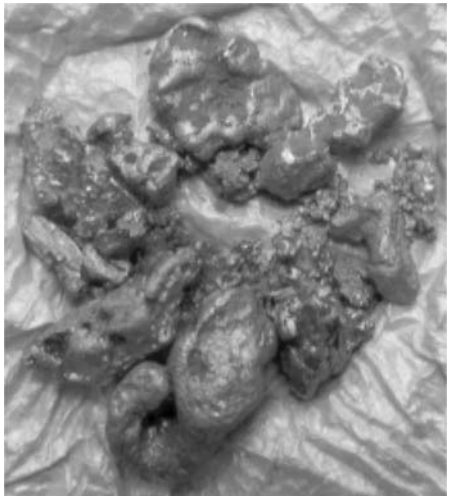

Figure 14. A group of nuggets and pellets from Ivory Coast analyzed for this work.

book "Records of the Grand Historian" written by the Han historian Sima Qian (145 to 90 BC) (Watson 1983) shortly describes this pastoral nomadic people of horseback hunters who did not practice agriculture.

Powerful warriors, the Xiongnu made a large number of incursions in China killing many Chinese soldiers every year. For a wide period they became the first powerful steppe empire along the China's frontier. Between 209 and 128 BC the Xiongnu tribal confederation occupied a large territory from the Yellow river to the North of Siberia, from the Xingjian to the Manchuria as shown in Figure 15 (Kessler 1994).

The excavations led since 2000 by the French Archaeological Mission in Mongolia in the imperial necropolis of Gol Mod in the Arhangay, north-west of Mongolia (Fig. 15), revealed a large number of very different social rank tombs. Among those tombs, tomb labeled 1 revealed to be similar to tomb number 6 of Noin Ula. Discovered in 1925 by an archaeological Russian team, tomb number 6 of Noin Ula is the tomb of the Xiongnu emperor Wushuliu, who died in 13 AD.

Tomb 1 of Gol Mod corresponds to a burial with a horse chariot. The archaeologists found in that tomb a profusion of objects of very high quality. If this tomb is not yet chronologically attributed, the only carbon 14 measurement made on a piece of wood from the coffin indicated a burial between 20 and 50 AD (date communicated by C. Moulherat, sub-director of the excavation). This date suggests that tomb 1 could be the burial of emperor Yu, or Wudadihou or Punu. All the other tombs, among which one from an important personage labeled 79, showed up less important remains.

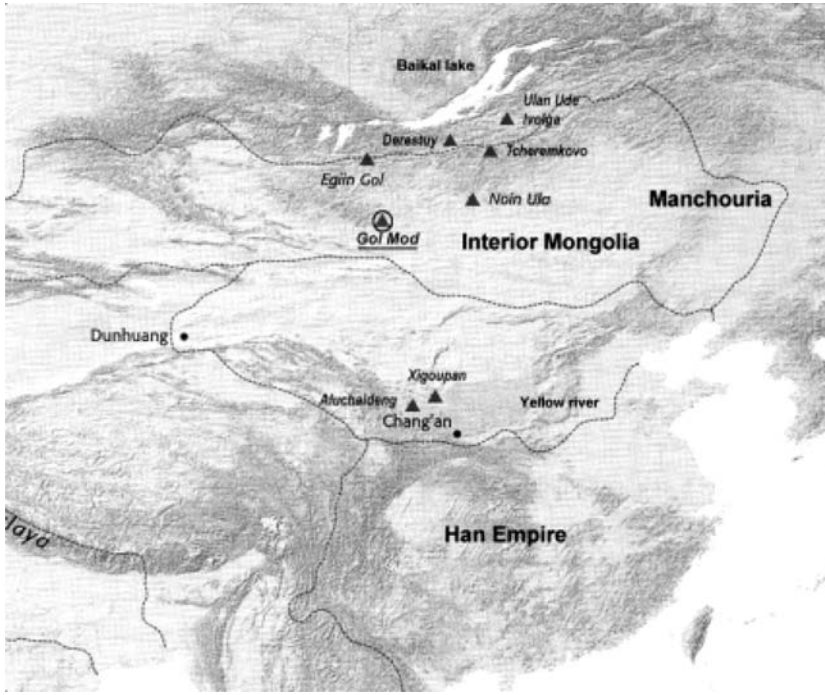

Figure 15. Situation of the necropolis of Gol Mod in the Arhangay, Mongolia (based on map of the French Archaeological Mission in Mongolia, 2002).

The wood coffin of tomb 1 is covered with gold stripes and quatrefoils, characteristic of the Chinese artwork. The re-creation of this decoration is illustrated in Figure 16. The other tombs of Gol Mod revealed only either gold quatrefoils or gold stripes. The typically Chinese gold decoration fits together with other objects of Chinese typology found in the tomb. However, the Xiongnu lived close to the Altai mountains known by their geological wealth. The Altai region could have provided the necessary raw material to produce the gold foils. In order to find out if the gold foils were imported or made *in situ*, a set of about 50 gold stripes and quatrefoils from the two main tombs (1 and 79) were analyzed. Because the stripes and quatrefoils have 30 to 60 μm thickness and are very different in sizes and forms, the combination of PIXE, PIGE and PIXE-XRF in external beam was employed (Guerra et al, in press).

The results obtained by PIXE and PIGE for the major elements of the gold foils (gold, silver and copper) from both the imperial (number 1) and the important personage (number 79) tombs, are reported in Table 3. We can observe that tomb 1 presents a better alloy than tomb 79 and that the copper contents are very low for both tombs. We compared the composition of the Xiongnu gold foils with the composition of two contemporary Chinese gold plaques from the Guimet Museum (Paris). Table 3 shows that the base alloy of the Chinese plaques is of better quality than the quatrefoils of tomb 79 but of lower quality than the stripes and quatrefoils of tomb 1.

We could also identify high quantities of iron and tin in the gold foils. In Figure 17 we can observe that the highest values were found for tomb 79 (Guerra 2002). These results, together with the low copper contents, seem to indicate the use of a local alluvial gold certainly slightly processed. As already indicated above, alluvial gold undergoes the association with other alluvial ores such as tin oxide (cassiterite), the accumulation with heavy elements such as platinum and are usually panned with iron and iron-titanium oxides, the so-called black sands.

The use of alluvial gold in this region is not surprising. In fact, near the site of Noin Ula alluvial gold was exploited till recent times. We can assume that the region around the Altai mountains was

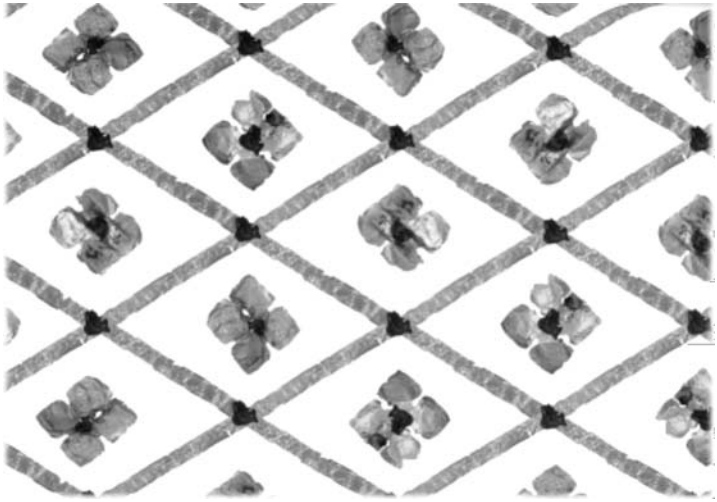

Figure 16. Reconstruction of the gold decoration of the coffin of tomb 1 of Gol Mod (photo D. Bagault).

Table 3. Average values and standard deviation of the major elements measured by PIGE for the different analyzed foils of tombs 1 and 79 as well as for the two Chinese objects.

Reference	Type	Au(%)	Ag(%)	Cu(%)
Tomb 1	Total			
	average	96.1	3.5	0.21
	σ	1.8	1.6	0.16
	Quaterfoils			
	average	94.9	4.6	0.33
	σ	0.9	0.8	0.11
	Stripes			
	average	97.4	2.3	0.09
	σ	1.6	1.5	0.10
Tomb 79	Quaterfoils			
	average	89.7	9.6	0.21
	σ	0.6	0.4	0.04
Chinese	C1			
	average	92.5	6.7	0.8
	σ	0.2	0.2	0.1
	C2			
	average	91.6	7.7	0.7
	σ	0.2	0.1	0.1

rich in placers. We can cite the placers of the district of Transbaikal already referred by De Launay (De Launay 1913) as well as those cited in the work of Guachin Dejidma who recorded a large number of secondary gold deposits in Mongolia (Dejidma 2001).

The few gold remains from the gold decoration of two satellite tombs of Gol Mod showed even higher variability for tin and iron contents. The analysis by scanning electron microscopy of three foils from those tombs revealed grains of iron oxide as well as a few inclusions of tin oxide, which could be identified by their composition as cassiterite inclusions. These inclusions are of different type. One example is given in Figure 18. At present we cannot affirm the use of gold either melted under oxidising conditions or just sintered (Raub 1995). However, our results tend to show that gold

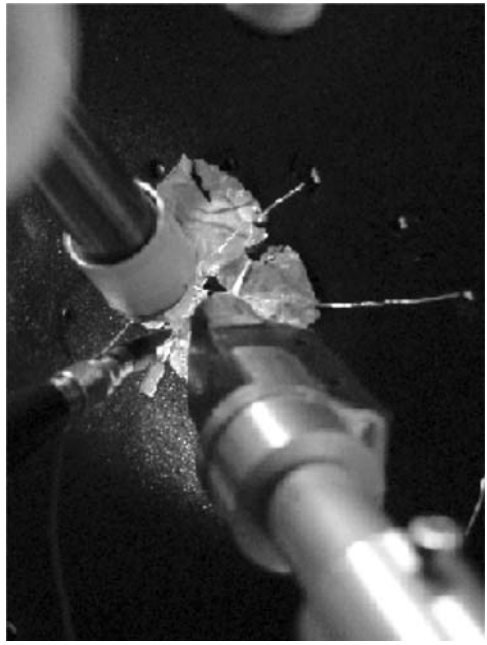

Figure 17. PIXE-PIGE set-up for the analysis of the Xiongnu gold foils (photo J. Salomon and M.F. Guerra).

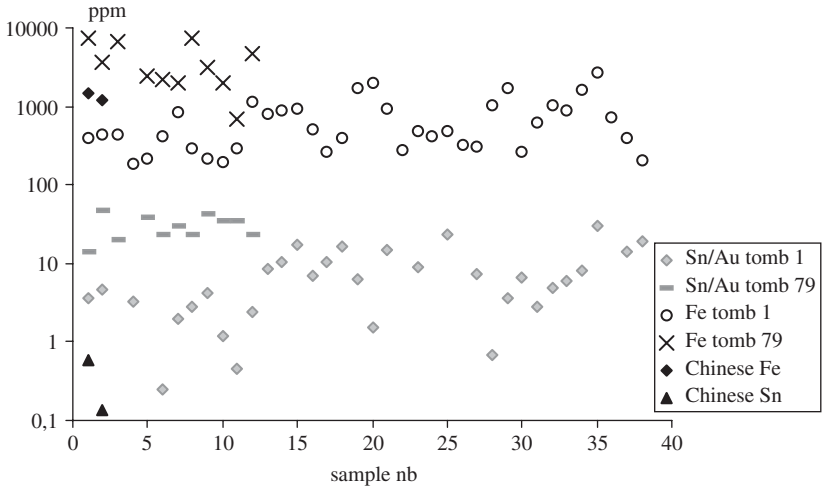

Figure 18. Tin and iron contents measured by filtered PIXE in the Xiongnu foils and the Chinese objects. Tin is normalized to the gold content.

processing depends on the type of tomb. Further analysis by SEM will elucidate the manufacturing technologies used in the fabrication of the gold decoration of the coffins of Gol Mod.

If we consider the other trace elements for both tomb 1 and tomb 79, we can observe that palladium has an average concentration of 34 ± 16 ppm for tomb 1 and 68 ± 17 ppm for tomb 79, which could reinforce the assumption of the use of a different gold. However, we can also conceive that distinct panning regions were exploited or, as the Gol Mod necropolis was occupied during a

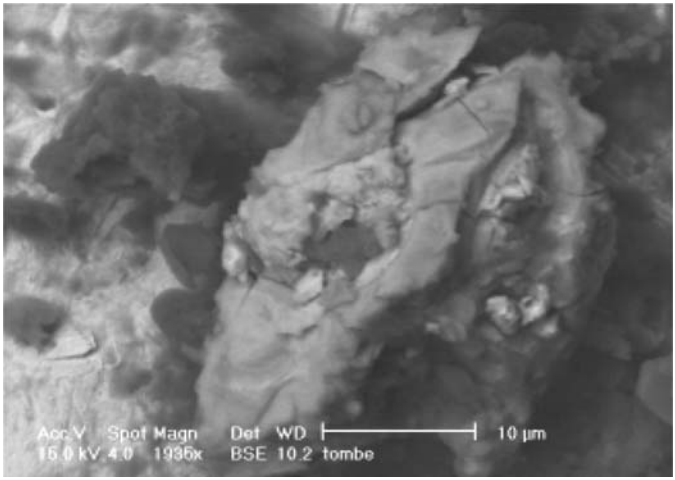

Figure 19. Grain of cassiterite observed by SEM on a gold stripe from one of the satellite tombs of Gol Mod.

long period, that a large lapse of time went through between both burials. The same problem exists for the satellite tombs. New carbon 14 dates will clarify this last conjecture.

For the two Chinese gold plaques Figure 17 shows that iron and tin are present at lower contents than in the Xiongnu foils, while palladium has an average composition of 48 ± 12 ppm. This seems to denote a different gold processing and maybe also another origin for the Chinese objects. A few analyses by PIXE-XRF were recently performed on both the Xiongnu foils and the Chinese plaques to determine platinum (Guerra & Calligaro 2003). These analyses seem to corroborate the use of different gold sources or different panning regions. Further analysis by PIXE-XRF and by ICP-MS in liquid mode will give new information on these gold objects.

4 CONCLUSION

The analytical techniques to be performed on gold objects must be chosen according to the type and morphology of the objects and to the historical questions concerned. One technique or if necessary a combination of techniques must be selected to study the circulation of gold and try to identify the provenance of the metal.

The three historical applications exposed in this work showed the increasing difficulty to infer the circulation of gold when the historical sources are sparse. This is the case of the Xiongnu people. At present the archaeological remains are almost the only information we have about that civilization time.

Among the three examples exposed in this work, the most successful application from the provenance point of view is undoubtedly the one that concerns the Muslim dynasties. We could identify for all the Islamic empire several changes of gold supplies and suggest the origin of the minted metal. We must note that for this period, among many other features, the caravan routes are known and several gold mines are revealed by the Arabian geographers. Furthermore, the coins themselves provide a large number of clues such as the mint name and the date of issue.

When the coins are struck in antiquity, such as those dating from the time of Alexander the Great, much less information is provided by the coin itself. Their classification is based on typological and metrological criteria as well as on the historical sources. We must remark that, for example, G. Le Rider proposed the functioning in Macedonia of two mints to strike the staters: Pella and Amphipolis. Other authors suggest the existence of a third mint. If the results obtained for those coinages are quite important from the numismatic point of view we were unable to attribute a

provenance to the two chemical groups revealed by the analysis. Lack of written sources and loss of information on the trace elements by re-melting of the original metals are the main causes of the non-success of provenancing.

When very few documents exist on an historical period it is important that objects undergo analysis. However, the analysis must as far as possible be completely non destructive. If we consider objects of diversified sizes and forms, PIXE/PIGE analyses associated with those by PIXE-XRF seem to be the best arrangement. However, it may happen that the information required cannot be totally obtained by those techniques. The detection limits might be too poor for certain elements which occur at very low concentration levels. In this case other analytical techniques should be performed on the objects or on a sub-set of the objects. When a small drilling is available, ICP-MS in solution mode, with its multi element capability and sub $ng.g^{-1}$ detection limits, overcomes many of the problems associated with the determination of certain elements contents. In addition to that, the number of objects submitted to drilling for ICP-MS analysis can be minimized. Their choice being based on the results obtained with the non destructive techniques.

ACKNOWLEDGEMENTS

The author is grateful to all the persons from the research teams involved with the works presented in this paper: Alexandra Gondonneau, Hélène Nicolet, Corinne Roux, Michael Cowell, Francisco Magro, Carlos Costa and Patrick Girard for the study of the coinages of Alexander the Great and of the Arabs; Thomas Calligaro, Joseph Salomon, Jean-Claude Dran and Christophe Moulhérat for the Xiongnu gold. The author is also grateful to the Bibliothèque national de Paris, to the Archaeological French Mission in Mongolia, to the Guimet Museum and to the CERI and IRAMAT CNRS laboratories.

REFERENCES

Antweiler, J.C. & Sutton, A.L. 1970. Spectrochemical analyses of native gold samples, *U.S.G.S. Report GD-70-00.3*: 1–28.

Beauchesne, F., Barrandon, J.N., Alves, L., Gil, F.B. & Guerra, M.F. 1988. Ion beam analysis of copper and copper alloy coins. *Archaeometry* 30: 187–197.

Bertrand, L., Calligaro, Th., Dran, J.C., Dubus, M., Guerra, M.F., Moignard, B., Salomon, J. & Walter, Ph. 2002. Développement expérimental d'une ligne PIXE-XRF pour les matériaux du patrimoine. *J. Phys. IV France* 12: 359–364.

Briant, P. 1996. *Histoire de l'Empire Perse. De Cyrus à Alexandre.* Paris: Fayard.

Calligaro, T., MacArthur, J.D. & Salomon, J. 1996. An improved experimental setup for the simoultaneous PIXE analysis of heavy and light elements with a 3 MeV proton external beam. *Nucl. Instrum. Meth.* B109-110: 125–128.

Calligaro, T., Dran, J.C., Ioannidou, E., Moignard, B., Pichon, L. & Salomon, J. 2000. Development of an external beam nuclear microprobe on the Aglae facility of the Louvre museum. *Nucl. Instrum. Meth.* B161-163: 328–333.

Chapman, R., Leake, B. & Styles, M. 2002. Micro chemical characterization of alluvial gold grains as an exploration tool. *Gold Bulletin* 35: 53–65.

Craddock, P. 2000. Historical survey of gold refining. Parts 1 and 2. In A. Ramage & P. Craddock (eds), *Kings Croesus' Gold*: 27–71. London: The Trustees of the British Museum.

Craddock, P., Meeks, N., Cowell, M.R., Middleton, A., Hook, D., Ramage, A. & Geçkinli, E. 1998. The refining of gold in the Classical World. In D.Williams (ed.) *The Art of the Greek Goldsmith*: 111–121. London: British Museum Publications.

Craddock, P., Cowell, M.R. & Guerra, M.F. in press. Controlling the Composition of Gold and the Invention of Gold Refining in Lydian Anatolia. *Anatolian Metal II* Germany: Der Anschnit.

Dejidmaa, G. 1999. Preliminary table of placer gold deposits and occurrences of Mongolia. In W.J. Nokleberg, V.V. Naumova, M.I. Kuzmin & T.V. Bounaeva. *Project on Mineral Resources, Metallogenesis, and Tectonics*

of Northeast Asia Institute of Geology and Mineral Resources, Open-File Report 99–165. Denver: U.S. Geological Survey.
De Launay, L. 1913. *Gîtes minéraux et métallifère*. In Ch. Béranger (ed) tome 3. Paris and Liège: Librairie Polytechnique.
Demortier, G. 1986. Characterisation of gold jewellery items by NRA, PIXE, PIGE and PISXRF in non-vacuum and milliprobe and vacuum milliprobe assemblies. In G. Furlan, P. Cassola Guida & C. Tuniz (eds), *New Paths in the Use of Nuclear Techniques for Art and Archaeology*: 48–64. Singapore: World Scientific Publishing Co Pte Ltd.
Demortier, G. & Ruvalcaba Sil, J.L. 1996. Differential PIXE analysis of Mesoamerican jewellery items. *Nucl. Instrum. Meth.* B 118: 352–358.
Dran, J.C., Calligaro, T. & Salomon, J. 2000. Particle-induced x-ray emission. In E. Cilibert & G. Spoto (ed.), *Modern Analytical Methods in Art and Archaeology*, Chem. Analysis 155: 135–166. Chichester: Wiley-Interscience.
Eluère, C. & Raub, C.J. 1991. New investigations on early gold foil manufacturing. *Archaeometry'90*: 45–54. Berlin: Birkhäuser.
French Archaeological Mission in Mongolia 2002. Connaissance des Arts, Hors-Série:177. Paris : Société Française de Promotion Artistique.
Ferreira, G. & Gil, F.B. 1981. Elemental analysis of gold coins by PIXE. *Archaeometry* 23: 189–199.
Gondonneau, A. & Guerra, M.F. 1999. The analysis of gold by ICP-MS with an UV laser. Application to the study of the gold currency of the Muslim West Africa. In S. Young, A. Pollard, P. Budd & R.A. Ixer (eds), *Metals in Antiquity*. BAR International Series 792: 262–270.
Gondonneau, A., Roux, C., Guerra, M.F. & Morrisson, C. 2000. La frappe de l'or à l'époque de l'expansion musulmane et les mines de l'ouest de l'Afrique: l'apport analytique. In B. Kluge & B. Weisser (eds), *XII. Internationaler Numismatischer Kongress Berlin 1997*, Akten II: 1264–1274. Berlin: Staatlichen Museen zu Berlin–Preussischer Kulturbesitz.
Gondonneau, A. & Guerra, M.F. 2000. L'or perse à travers l'analyse de monnayages antiques et médiévaux. *Rev. d'Archéométrie* 24: 27–38.
Gondonneau, A., Guerra, M.F. & Cowell, M.R. 2001. Searching for the provenance of gold. The methodology of gold analysis by ICP-MS: first developments. In *Archaeometry'2000*, CD-ROM, University of Mexico.
Gondonneau, A. & Guerra, M.F. 2002. The circulation of precious metals in the Arabic Empire: the case of the Near and the Middle East. *Archaeometry* 44: 473–599.
Gondonneau, A., Nicolet-Pierre, H. & Guerra, M.F. 2002. The Persian and Macedonian gold from Darius to Alexander the Great. *BAR International Series* 1043(II): 369–374.
Guerra, M.F. 1998. The analysis of archaeological metals. The place of XRF and PIXE in the determination of technology and provenance. *X-Ray Spectrometry* 27: 73–80.
Guerra, M.F. & Barrandon, J.N. 1998. Ion beam activation analysis with a cyclotron. In W.A. Oddy & M. Cowell (eds), *Metallurgy in Numismatics 4*, SP 10: 15–34. London: Royal Numismatic Society.
Guerra, M.F., Sarthre, C.O. & Gondonneau, A. 1999. Precious metals and provenance enquiries using LA-ICP-MS. *Journal of Archaeological Science* 26: 1101–1110.
Guerra, M.F., Calligaro, T., Dran, J.C., Moulherat, C. & Salomon, J. in press. Development of the PIXE-PIGE-PIXRF association for the analysis of the gold from the First Empire of the Steppes. *Geoarchaeological and Bioarchaeological Studies*.
Guerra, M.F. 2000a. The study of the characterisation and provenance of coins and other metalwork using XRF, PIXE and Activation Analysis. In D.C. Creagh & D.A. Bradley (eds), *Radiation in Art and Archaeometry*: 378–416. Amsterdam: Elsevier Science.
Guerra, M.F. 2000b. Em busca da origem do ouro dos Visigodos através dos seus elementos traço. In M.C. Hipólito, D.M. Metcalf, J.M.P. Cabral & M. Crusafont i Sabater (eds), *Homenagem a Mário Gomes Marques*: 223–251. Sintra: Instituto de Sintra.
Guerra, M.F. 2002. Ancient gold and modern techniques: identification of gold supplies from Croesus to Mahomet using accelerators and ICP-MS. In R. van Grieken & K. Janssens (eds), *Non-destructive Testing and Microanalysis for the Diagnostics and Conservation of the Cultural and Environmental Heritage; Proceedings of Art 2002*, Antwerp, 2–6 June 2002 Antwerp: University of Antwerp. cd-rom.
Guerra, M.F. & Roux, C. 2002. L'or de la Péninsule Ibérique de l'Invasion à la Reconquista. *Rev. d'Archéométrie* 26: 219–232.
Guerra, M.F. & Calligaro, T. 2003. Gold objects from the cultural heritage: studies on manufacturing technology and provenancing. *Meas. Sci. Tech.* 14: 1–11.
Guerra, M.F. & Calligaro, T. in press. Gold traces to trace gold. *J. of Archaeological Sciences.*

Karydas, A.G. & Paradellis, T. 1997. Measurement of KL and LM resonant Raman scattering cross sections with a proton-induced x-ray beam. *J. Phys B: At. Mol; Opt. Phys.* 30: 1893–1905.
Healy, J.F. 1978. *Mining and Metallurgy in the Greek and Roman World*. London: Thames and Hudson.
Herrington, R., Stanley, C. & Symes, R. 1999. *Gold*. London: The Natural History Museum.
Raub, C.J. 1995. The metallurgy of gold and silver in prehistoric times. In G. Morteani & P. Northover (eds), *Prehistoric Gold in Europe*: 243–260 Berlin: Kluwer Academic Publishers.
Kessler, A.T. 1994. *Empires Beyond the Great Wall: The Heritage of Ghenghiz Khan*. Los Angeles: Natural History Museum.
Le Rider, G. 1977. *Le monnayage d'argent et d'or de Philippe II frappé en Macédoine de 359 à 284*. Paris: Le Bourgey.
Meyers, P. 1969. Non-destructive activation analysis of ancient coins using charged particles and fast neutrons. *Archaeometry* 11: 67–84.
Morteani, G. 1995. Mineral economics mineralogy, geochemistry and structure of gold deposits. In G. Morteani and P. Northover (eds), *Prehistoric Gold in Europe*: 97–113. Berlin: Kluwer Academic Publishers.
Niederschlag, E., Pernicka, E., Seifert, Th. & Bartelheim, M. 2003. The determination of lead isotope ratios by multiple collector ICP-MS. *Archaeometry* 45(1): 61–100.
Pirazzoli-t'Serstevens, M. 1982. *La Chine des Hans. Histoire et Civilisations*. Fribourg: Office du Livre S. A.
Poirier, J. 1983. *Contribution à l'analyse de l'or antique. Application aux monnayages du monde méditerranéen du IIe au XVI siècles*, PhD thesis. France: University of Orléans.
Ricci, E. & Hann, R.L. 1965. Theory and Experiment in Rapid, Sensitive Helium-3 Activation Analysis. *Analytical Chemistry* 37: 742–748.
Ricci, E. & Hann, R.L. 1967. Sensitivities for Activation Analysis of 15 Light Elements with 18-MeV Helium-3 Particles. *Analytical Chemistry* 39: 794–797.
Roux, C. & Guerra, M.F. 2000. La monnaie almoravide: de l'Afrique à l'Espagne. *Rev. d'Archéométrie* 24: 39–52.
Watson, B. 1993. *Translation of Records of the Grand Historian by Sima Qiam*, New York: Columbia University Press.

Cultural Heritage Conservation and Environmental Impact Assessment by Non-Destructive Testing and Micro-Analysis – Van Grieken & Janssens (eds)
© 2005 Taylor & Francis Group, London, ISBN 90 5809 681 5

Assessment of air pollutant levels in some European museums and churches

V. Kontozova, Z. Spolnik, A. Worobiec, R. Godoi & R. Van Grieken
Department of Chemistry, University of Antwerp, Antwerpen, Belgium

F. Deutsch
Flemish Institute of Technological Research (VITO), Integral Environmental Studies, Boeretang, Mol, Belgium

L. Bencs
Research Institute for Solid State Physics and Optics, Hungarian Academy of Sciences, Budapest, Hungary

ABSTRACT: Problems concerning the preserving of the cultural heritage for future generations are often connected to atmospheric pollution. Danger can derive from pollutants originating from outside, e.g. NO_2, SO_2, O_3 and particulate matter, but also from inside generated pollutants, e.g. acetic acid and soot particles. This research was focused on two museums in Belgium and four cathedrals in Europe. Indoor and outdoor gaseous and particulate pollutants have been investigated by means of ion chromatography, spectrophotometry, x-ray fluorescence spectrometry and electron microscopy.

The investigation in the museums showed that the exposure of works of art to outdoor pollutants can be reduced significantly by placing them in showcases. Indoor pollutants originating from the artworks themselves or the construction material of the showcase can accumulate and further deteriorate or corrode the pieces of art. Sometimes this adverse effect of the showcase even exceeds its advantage.

The investigations in the cathedrals showed that the management plays an important role in the formation and distribution of particles. Visitors introduce dust into the churches which is further resuspended subsequently. Also religious activities (incense, candles) and the heating systems can be a source of pollution inside the church.

1 INTRODUCTION

Airborne pollutants exhibit a wide range of adverse effects on objects connected to our cultural heritage. Both gaseous and particulate air pollutants are responsible for deteriorating processes. Some of these pollutants encountered in indoor atmospheres have their main sources in the outdoor environment and enter mainly via air exchange. Other pollutants are, in contrast, mainly produced indoors. For an integrated assessment, concentrations of pollutants and their sources have to be investigated along with possible ways of deterioration of the objects of art.

In the framework of several EU and local projects, levels of air pollutants have been measured in two museums in Belgium and four churches throughout Europe. The main subject of interest in the museum studies was the influence of gases on works of art exposed in exhibition galleries and in showcases. The exposure of objects of art in showcases is, besides security reasons, mainly done to protect the objects of art against contamination by dust particles (Nazaroff 1991), and deterioration by gaseous pollutants (De Santis 2001, Brimblecombe 1990, Shaver 1983, Hisham 1991). The studies in the churches were related to the influence of gaseous and particulate air pollutants on stained glass windows and to the effect of heating systems.

In this work some examples are given for the diversity of problems connected to the influence of air pollutants on objects of art in the light of these different case studies on museums and churches in Europe. Gaseous and particulate air pollutants were investigated indoors and outdoors these museums and churches. The obtained results show that very different situations can be encountered and no universal advice can be given to conservators. Nevertheless some basic and often reoccurring problems in indoor environments could be identified.

1.1 *Gaseous air pollutants*

1.1.1 *Outdoor pollutants*

The most dangerous gaseous air pollutants with mainly outdoor sources are sulphur dioxide (SO_2), nitrogen dioxide (NO_2) and ozone (O_3). These gases are mainly from anthropogenic origin. The main sources of sulphur dioxide are oil and coal burning. Nitrogen dioxide is mainly emitted by road traffic and by industrial combustion processes. Ozone in contrast is a secondary pollutant which is formed in the atmosphere from reactions between non-methane volatile organic compounds (NMVOC's) and nitrogen oxides under influence of sunlight. NMVOC's both from anthropogenic sources (e.g. combustion processes, traffic) and from natural sources (mainly isoprene from vegetation) play an important role in ozone formation. These gases enter the indoor environment via the air exchange between outdoor and indoor air.

SO_2 deposits very fast on surfaces and is oxidized via different pathways to sulphates or sulphuric acid. This goes along with a drastic decrease of the pH-value (acid attack). Nitrogen dioxide has also the tendency to deposit on surfaces and can be transformed to nitrates, which also can react acidicly. Ozone is a very strong oxidant, destroying especially organic material (e.g. dyes).

1.1.2 *Indoor pollutants*

Since recently, also formic acid (HCOOH) and acetic acid (CH_3COOH) are assumed to be dangerous for certain objects of art, containing e.g. copper, lead or calcareous material. Measurements inside museum showcases showed that these acids can accumulate and reach high concentrations (Gibson et al. 1997, Tétreault & Stamatopoulou 1997, Tétreault et al. 2003, van Bommel et al. 2001, Ryhl-Svendsen & Glastrup 2002). Most of the showcases are made of wood and/or composite materials as MDF (Medium Density Fiberboard), considered as sources for volatile organic compounds with low molecular weight. Hence, these organic acids can be emitted directly into the showcase.

1.2 *Particulate air pollutants*

1.2.1 *Outdoor pollutants*

Atmospheric particulate matter plays a significant role for the state of conservation of various cultural heritage objects. The deposition of aerosol particles causes not only soiling and blackening of the object's surface, but the deposited particles can further chemically react with the surface and lead to weathering and destruction of the precious objects of art. These particles also enter the indoor environment mainly with the air exchange.

1.2.2 *Indoor pollutants*

Particles from outdoors include soil dust, sea salt, fly ash, soot, etc. Particulate matter can also originate from sources located indoors. In churches the burning of candles and incense are considered as an important source of soot and other organic particles, which cause blackening of the indoor surfaces. The layer of deposited soot additionally comprises a medium for enhanced adsorption of pollutant gases. Another type of indoor generated particles derives from the deterioration of walls. In limestone buildings, they consist mostly calcium carbonate as main compound.

2 APPLIED SAMPLING AND ANALYTICAL TECHNIQUES

2.1 *Gaseous pollutants*

Sampling for all the above mentioned gases was performed by means of diffusion tubes. For sampling times of up to one week, radiello® diffusive samplers (Fondazione Salvatore Maugeri, Padova, Italy) were used. For long term sampling, passive samplers from Gradko International Ltd. (Winchester, England) were used. For NO_2, SO_2, formic and acetic acid measurements by radiello® samplers, a polyester microfiber cartridge coated with triethanolamine (TEA), and for O_3 a cartridge filled with 4,4′-dipyridylethylene coated silica gel was utilized. For NO_2, SO_2 and O_3, the experimentally measured sampling rates from Fondazione Salvatore Maugeri, Padova, Italy were adopted. For acetic and formic acid the sampling rates were calculated from the diffusion coefficients of these compounds and the experimentally measured effective geometric constant of the radiello® diffusion tubes.

The determination of the formed nitrite, nitrate, sulphite, sulphate, formate and acetate was carried out using a DX-120 ion chromatograph equipped with an autosampler AS50 (both Dionex, Sunnyvale, CA, USA). For the separation an AG14-4 mm guard column and an AS14-4 mm analytical column were used. The flow-rate was set to 1.2 ml/min. The eluent contained a mixture of 3.5 mM Na_2CO_3 and 1 mM $NaHCO_3$ for the determination of nitrite, nitrate, sulphite and sulphate. For the determination of formate and acetate, 2 mM $Na_2B_4O_7$ was used as eluent. All ions were detected by suppressed conductivity using the self-regenerating suppresser ASRS-ULTRA. From the detected amounts of ions, the concentrations of the gases were calculated. The concentration of the 4-pyridylaldehyde, formed during ozonolysis of the 4,4′-dipyridylethylene, was determined by UV/VIS-spectrophotometry at a wavelength of 430 nm, using a double beam spectrophotometer (UVIKON 930, Kontron Instruments). From the 4-pyridylaldehyde-concentration, the concentration of O_3 in the air was calculated.

2.2 *Particulate pollutants*

For the collection of bulk aerosol samples, Nuclepore® filters of 0.4 μm pore-size and 47 mm diameter were used within a Millipore filter-unit connected to a low-volume vacuum pump (flow rate 40 l min^{-1}). The average sampling time was 24 hours.

Energy-dispersive X-ray fluorescence analysis (EDXRF) of the bulk samples was performed on a Tracor Spectrace 5000 EDXRF instrument. It uses a low power Rh-anode X-ray tube (17.5 W). The characteristic X-ray radiation was detected by a Si(Li) detector. For determining high-Z elements (starting from K), an accelerating voltage of 35 kV and a current of 0.35 mA were used. The acquisition time was set to 10000 s. Low-Z (from Al to Cl) elements were measured at 10 kV and 0.35 mA with an acquisition time of 4000 s. The measured intensities were converted into elemental concentrations by the application of the AXIL program (Analysis of X-ray spectra by a non-linear Iterative Least-squares) code (Vekemans et al. 1994).

For the collection of size-segregated aerosol samples, a 9-stage Berner cascade impactor was applied. In the present experiments, stages 3–8 with cut-off diameters of 0.25, 0.5, 1, 2, 4 and 8 μm, respectively, were used. Si wafers and Ag foils were chosen as collection substrates. Advantages and disadvantages of these kinds of substrates for single particle analysis by EPMA have been discussed by Szalóki et al. (2001) and Worobiec et al. (2003). The Si wafers were used to collect the finest particles (cut-off diameters of 0.25 and 0.5 μm, corresponding to stages 3 and 4, respectively). The particles collected with cut-off diameters of 1–8 μm (stages 5–8) were deposited on Ag foils.

The size-segregated samples were analysed by an electron probe microanalyser (EPMA, JEOL 733, Tokyo, Japan) equipped with an ultra-thin window Si(Li) detector (Oxford) under two different conditions. The two smallest stages of the Berner impactor used in this experiment (3 and 4) were measured manually with an accelerating voltage of 10 keV and a beam current of 1 nA. The measurement time of one particle was 20 s. For each sample, one hundred single particles were measured. The samples deposited on Ag foils were analysed by using an automatic mode. The

accelerating voltage and the beam current were the same as mentioned above. The measurement time for one single particle was here taken as 10 s. Mostly 300 particles were measured for each sample. To avoid beam damage of the analysed particles, cooling of the sample holder by liquid nitrogen was applied (Szalóki et al. 2001, Worobiec et al. 2003). Such measurement conditions are suitable particularly for the determination of low-Z (starting from C) elements. The obtained characteristic X-ray spectra from the low-Z elements EPMA were evaluated by non-linear least squares fitting using the AXIL program (Vekemans et al. 1994). The semi-quantitative elemental composition of the particles was calculated with an iterative approximation method based on Monte Carlo simulations (Ro et al. 1999, Osán et al. 2000, Szalóki et al. 2000).

The large data sets from low-Z EPMA were treated by statistical methods. The particles analysed on each impactor stage (from 100 to 300 particles) were classified by Hierarchical Clustering Analysis (HCA) (Bondarenko et al. 1996). In this way the analysed particles were divided into different clusters, based on their compositional similarity and their relative abundance in the sample. An overall analysis of the most important particle types allows determining the main sources responsible for soiling and blackening of objects displayed within the churches.

3 INVESTIGATIONS IN MUSEUMS

3.1 *Sampling*

The concentrations of NO_2, O_3, SO_2, formic acid and acetic acid were measured in two museums in Belgium: the Musical Instrument Museum (MIM) in Brussels (see Figure 1) and the Plantin-Moretus Museum (PMM) in Antwerp. In the MIM, a unique collection of about 1,500 musical instruments from all over the world, from antiquity to the 20th century, is exposed both in display cases and (unprotected) in the galleries. The PMM is situated in the old printing works of Christoffel Plantin and Balthasar Moretus, which were the most important book publishers in Europe in the seventeenth century, reflecting the significance of Antwerp as a centre of humanism and science.

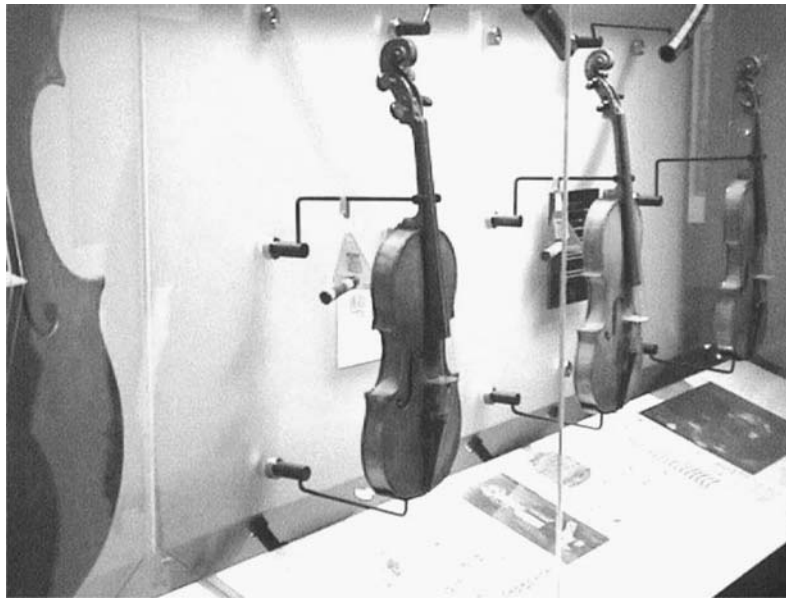

Figure 1. Sampling with diffusion tubes inside a museum showcase in MIM.
(This figure is presented in the signature in colours at the end of this volume, Appendix, pg. 327)

The house is preserved with the authentic furniture and equipment for printing books. This museum owns a fascinating collection of printing plates and early books, partly displayed in showcases.

Sampling was performed by means of radiello® diffusion tubes as described in 2.1. The exposure time of the cartridges was one week in both museums. Samples were taken outside the museums, in the exhibition galleries and inside the showcases. In both museums, the showcases are not hermetically sealed; some air exchange through small slits is possible.

3.2 *Results and discussion*

3.2.1 *Musical Instrument Museum (MIM)*

3.2.1.1 NO_2, O_3 and SO_2

In the MIM, 13 samples were taken. Figure 2 shows the results obtained for NO_2. The first 5 samples from the left (Italy, Tympani, Gamelan orchestra, Brussels and Bagpipes) show results obtained inside the specific showcases. Sample 6 (Reserve) is taken from the depot of the museum, which consists of a big cabinet with separated compartments to store instruments. The samples 7 to 10 (Intermidii, Mechanical instruments, Antwerpen and Small organs) show the concentrations in different sections of the exhibition gallery. The last three samples (Outside air inlet, Outside street 1 and Outside street 2) were taken from the outside air near the air-inlet of the heating, ventilating and air conditioning (HVAC)-system or in the direction of two streets adjacent to the museum.

The concentrations of NO_2 were around 35 $\mu g/m^3$ in the outside air. In the exhibition galleries the NO_2-concentration was approximately the same as outside (medium value 33 $\mu g/m^3$). In the depot, the concentration of NO_2 was slightly reduced (28 $\mu g/m^3$). However, inside the showcases, the NO_2-concentration was significantly reduced (10 $\mu g/m^3$). These results show that NO_2 enters the museum with the outside air and that there are no strong sources inside the museum. The showcases have only a small air exchange with the air in the galleries; hence, the concentration decreases because of deposition of the NO_2.

The concentration of O_3 in the outside air was approximately the same as the concentration of NO_2 (35 $\mu g/m^3$). In contrast to the latter, the O_3-concentration was reduced significantly in the exhibition galleries (1 $\mu g/m^3$). Inside the showcases, the concentration was very low (0.4 $\mu g/m^3$). This can be explained by the high reactivity of O_3. Already in the galleries, almost no O_3 was found anymore.

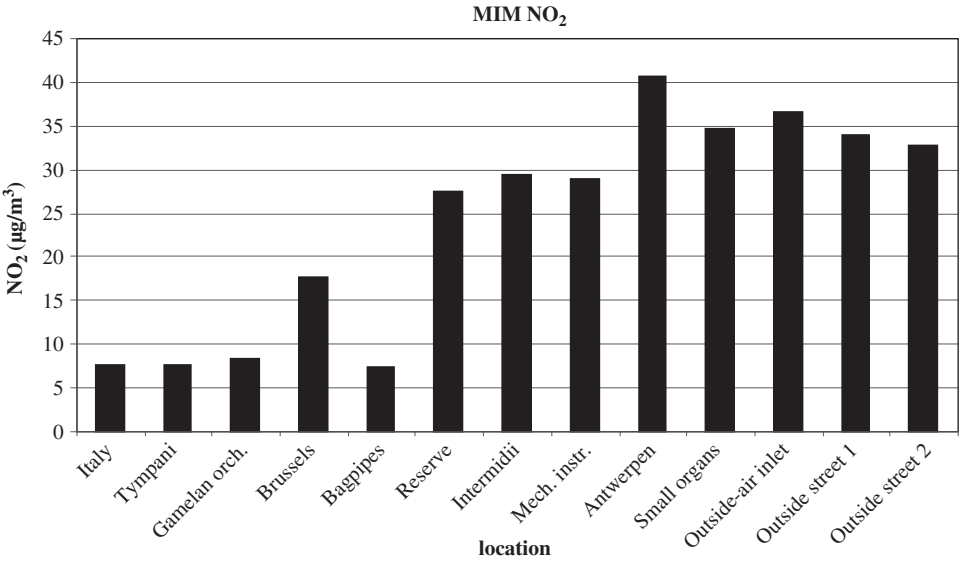

Figure 2. NO_2-concentrations in the Musical Instrument Museum (Italy – Bagpipes = showcases; Intermidii – Small organs = exhibition gallery; Reserve = store room).

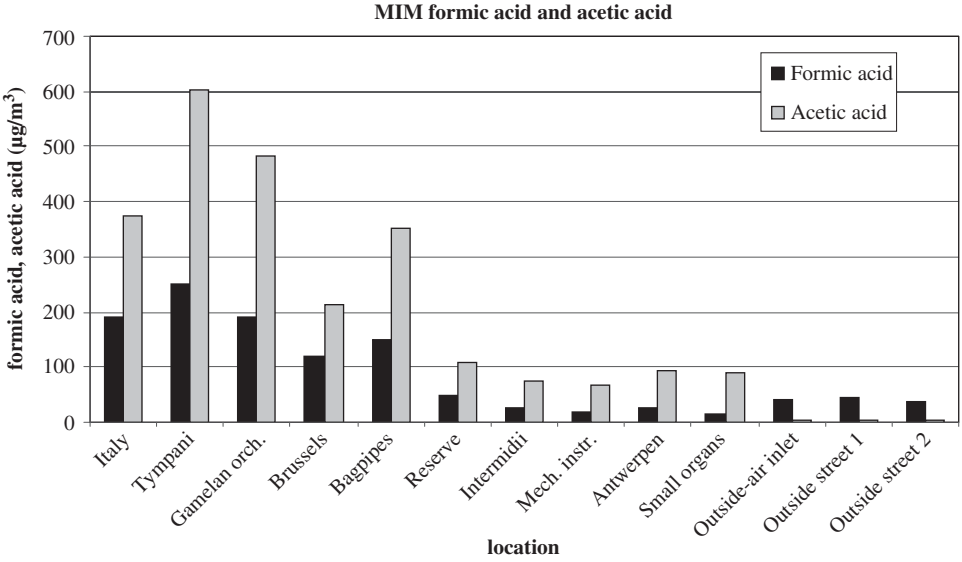

Figure 3. Concentrations of formic and acetic acid in the Musical Instrument Museum (Italy – Bagpipes = showcases; Intermidii – Small organs = exhibition gallery; Reserve = store room).

SO_2 was only detected in the outside air (1.4 µg/m^3). In the galleries or inside the showcases, the concentration of SO_2 was below the detection limit of 0.1 µg/m^3. This shows that also SO_2 is deposited and that there are no important SO_2-sources within the museum.

3.2.1.2 Formic acid and acetic acid

On the contrary, the concentrations of formic acid and acetic acid show a completely different picture. In the outside air, concentrations of 42 µg/m^3 for formic acid and 4 µg/m^3 for acetic acid were detected. In the galleries, the concentration of formic acid was only half of the outdoor-value (21 µg/m^3), whereas the concentration of acetic acid was clearly higher in comparison to the concentration in the outside air (82 µg/m^3). Within the showcases, the atmosphere was significantly enriched with the two acids, especially with acetic acid. Medium concentrations of 180 µg/m^3 for formic acid and of 400 µg/m^3 for acetic acid (with a maximum value of 604 µg/m^3) were detected (Figure 3).

From literature it is known that these acids are emitted from wood. Because the walls of the showcases in MIM are made from Medium Density Fiberboard (MDF), which is an improved version of chipboard, and also most of the musical instruments are wooden, the detected high concentrations of organic acids, especially acetic acid, are explainable. As it seems from the results, the acids accumulate inside the showcases.

3.2.2 *Plantin-Moretus Museum (PMM)*

3.2.2.1 NO_2, O_3 and SO_2

In the PMM in Antwerp, 16 samples were taken. Figure 4 shows the results for NO_2. Samples 1 to 8 (from the left) were taken from different showcases with books and printing plates made of copper, steel and wood. Samples 9 to 13 show the concentration in the different exhibition rooms with authentic furniture. The samples 14 and 15 were taken from the depot of the museum (with a large collection of old books). The last sample was taken from the garden of the museum.

The concentration of NO_2 was at 49 µg/m^3 in the outside air. In the different rooms the NO_2-concentrations lay between 23 and 34 µg/m^3. Inside the showcases the NO_2-level was strongly reduced to values between 0.1 and 14 µg/m^3 with an average value of 4 µg/m^3. Hence, the

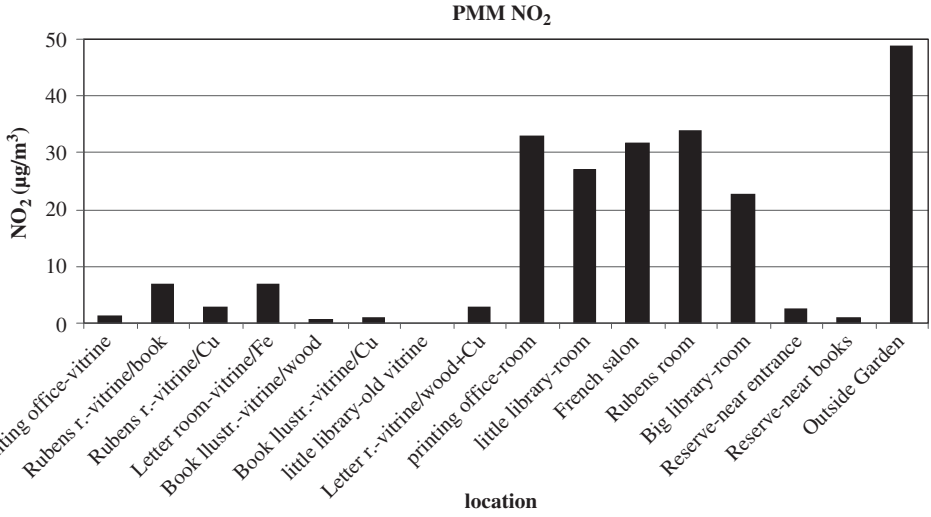

Figure 4. NO_2-concentrations in the Plantin-Moretus Museum (Printing office-vitrine – Letter room-vitrine = showcases, Printing office-room – Big library = exhibition gallery; Reserve = store room).

NO_2-concentrations were, like in MIM, reduced inside the museum and especially inside the showcases, but in the PMM this decrease was stronger.

For O_3 an outdoor concentration of 24 $\mu g/m^3$ was obtained. In the different rooms the medium O_3-concentration lay at 1.2 $\mu g/m^3$ and within the showcases at 1.0 $\mu g/m^3$. These results correspond to the results obtained in MIM and show that the O_3-concentrations inside the museum buildings were generally low.

The SO_2-concentration in the garden of the PMM was at 8 $\mu g/m^3$, i. e. significantly higher than the outdoor concentration at the MIM. Therefore, inside the museum, concentrations above the detection limit, but still very low values, were measured. Both in the rooms and within the showcases, a medium value of 0.5 $\mu g/m^3$ was detected.

3.2.2.2 Formic acid and acetic acid

Like in MIM, the concentrations of formic acid and acetic acid show a completely different picture in comparison with the concentrations of NO_2, O_3 and SO_2. In the outside air, a concentration of 42 $\mu g/m^3$ for formic acid and of 9 $\mu g/m^3$ for acetic acid was detected (Figure 5). These concentrations are comparable to the ones obtained in Brussels. In the different rooms of the PMM the concentration of formic acid (25 $\mu g/m^3$) is again reduced in comparison to the outside air, whereas acetic acid (106 $\mu g/m^3$) is significantly enriched. Within the showcases different levels of organic acids were found, reaching from 16 to 438 $\mu g/m^3$ for formic acid and from 113 to 3215 $\mu g/m^3$ for acetic acid. The average values were 154 and 1137 $\mu g/m^3$ for formic acid and acetic acid, respectively. In the PMM, the walls of the showcases are made of wood, so emissions of organic acids are to be expected. Additionally, in some showcases wooden printing plates and books are displayed, which can also be sources of organic acids.

3.3 *Conclusions*

An important difference between the two investigated museums is, that in MIM, an HVAC-system is operating, causing a higher ventilation rate in the galleries than in PMM. There, only occasionally windows are opened to get fresh air into the galleries. This is also reflected by the indoor concentrations of the gases: in spite of a higher outdoor NO_2-level at the PMM, the indoor concentration of NO_2 is lower than in the MIM.

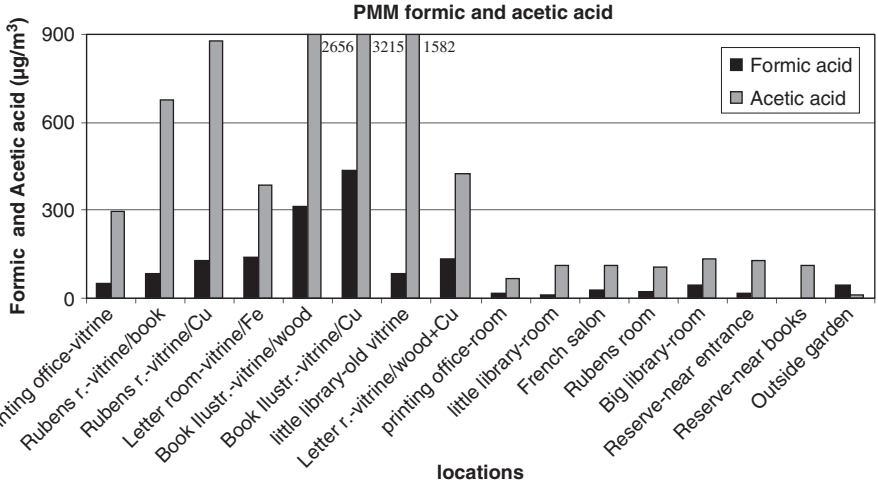

Figure 5. Concentrations of formic acid and acetic acid in the Plantin-Moretus Museum (Printing office-vitrine – Letter room-vitrine = showcases, Printing office-room – Big library = exhibition gallery; Reserve = store room).

The concentrations of O_3 and SO_2 measured in both museums do not represent any danger for the works of art. NO_2 was found even in the showcases, however in significantly reduced amounts in comparison to the outside atmosphere and to the air in the galleries. The detected high concentrations of especially acetic acid can cause corrosion to metal surfaces of the works of art.

Generally, these results confirm that the display cases protect the objects of art from dangerous outdoor pollutants (like NO_2, O_3 and SO_2), but, on the other hand, they accumulate dangerous compounds (like formic and acetic acid) emitted by the showcases themselves or by the works of art. Depending on which pollutants are especially dangerous for the works of art, the storage in showcases can improve, but also deteriorate the conditions for conservation.

4 INVESTIGATIONS IN CHURCHES

Several European projects were devoted to study the air quality and its effects on different cathedrals and churches of importance for our cultural heritage. The EU-project "VIDRIO" has the aim to determine conditions to prevent weathering of ancient stained glass windows which have been provided with protective glazing. The EU-project "Friendly Heating" is dedicated to a multi-disciplinary investigation of the influences of two different heating systems on preserved works of art in the church of Rocca Pietore in the Italian Alps. Another case study was carried out in the St. Martinus Cathedral in Weert in the Netherlands. Here, the chemical composition, size distribution and abundance of aerosol particles was determined, to find out which particles are responsible for the blackening and soiling of the works of art displayed within the cathedral and to verify the possible sources responsible for these processes. The investigated churches can be separated in two groups; churches in big, polluted cities and churches situated in small towns or villages. The location of the church plays definitely an important role in the deterioration processes. Via air exchange, outdoor pollutants enter the churches and accelerate the deterioration of the indoor environment.

Similar sampling procedures and analytical techniques were employed in each of the following studies.

4.1 *Important churches with stained glass windows*

Medieval stained glass used as window panels in cathedrals, churches and historic buildings has been exposed over hundreds of years to different environments: a less aggressive environment

on the inside, a more aggressive one on the outside. By examining the glasses of a window, different deterioration levels can be observed. The stages of deterioration can be grouped into few main situations, according to the type of glass and environments (Salem 1998). As a result, the atmospheric corrosion of glass, weathering, depends on several factors including glass composition, heat treatment, surface characteristics, type, climate and exposure time. Recently, atmospheric constituents, gaseous and particulate pollutants, have been identified as one of the main cause of weathering of these glasses (Salem 1998, Verità et al. 2000, Schreiner et al. 1984, Fernandez 1996). The chemical degradation is the consequence of the progressive attack of the glass surface exposed to the weathering conditions. The deposition of particles can initiate and consequently lead to deterioration of these panels. Much of the damage can be caused when punctual chemical reactions are initiated between compounds present in the aerosol particles and the glass surface, mainly when the surface becomes wet. Several chemical compounds can be considered as threatening for the preservation of stained glass. For instance, soot can cause significant soiling, corrosion and visual degradation and constitutes, together with organic compounds and dust particles, a medium for the adsorption and incorporation of damaging gases like SO_2 or NO_2 and of salts to build up a corrosion crust.

4.1.1 *Sampling*

In the framework of the EU project VIDRIO, measurements were performed in the Basilica Saint-Urbain in Troyes and in the Sainte Chapelle in Paris, both in France. The Basilica Saint-Urbain is built in Flamboyant style with the help of Pope Urbain IV from Troyes. The basilica has a fine set of renovated stained glass windows from the 13th century.

The Sainte Chapelle is included in UNESCO's World List of Cultural Heritage. This small gothic chapel has been built by Louis IX to house relics from the Holy Land believed to be the Crown of Thorns and part of the True Cross. The stained glass windows which surround the entire upper floor date from the 12th century.

Both cathedrals possess stained glass windows with and without protective glazing. Sampling was always performed at a protected and an unprotected window, as well as in- and outdoors in order to compare the different conditions and their effects on the stained glass windows.

Passive diffusion tubes were used for sampling of in- and outdoor gaseous pollutants (NO_2, SO_2 and O_3) as shown in Figure 6. The results showed that the diffusion tubes are able to detect pollutant concentrations down to around 0.5 $\mu g/m^3$. Because of their small size and their independence from electricity, sampling can even be performed inside the interspace between the protective glazing and the ancient stained glass panels.

Aerosol particles were collected as mentioned in section 2.2. The samplings were performed always indoors and outdoors of the churches, close to the investigated windows. Several sets of bulk and size-resolved aerosol samples were taken at each location. Additionally, particles were collected, with size-resolution from the interspace by means of an impactor.

4.1.2 *Results and discussion*

The results obtained at the Sainte Chapelle in Paris and the Basilica Saint-Urbain in Troyes show that the outside gaseous pollutants are present in the churches to different extents (Figure 7). Generally, NO_2, SO_2 and O_3 have their main sources (traffic, combustion processes, photochemical reactions in the atmosphere) outside the churches. They enter the churches with the exchanged (outside) air and deposit/react in the indoor atmosphere.

The results for O_3 for the two churches are rather comparable. Outdoor concentrations were significantly higher than the concentrations indoors, which stayed low at all locations. The outdoor SO_2-concentrations were in the range of 2 $\mu g/m^3$ (Saint-Urbain) and 7 $\mu g/m^3$ (Sainte Chapelle). Indoors, much lower concentrations were observed: below 1 $\mu g/m^3$ (Sainte Chapelle) and below 0.7 $\mu g/m^3$ (Saint-Urbain). The fact that, inside the two churches, these low concentrations of SO_2 were detected, does not mean that SO_2 does not form any problem in the indoor environment. It adsorbs quickly to surfaces and reacts under formation of dangerous sulphuric acid. Hence, the low observed concentrations comprise the SO_2 which did not adsorb yet to the surfaces, e.g. to

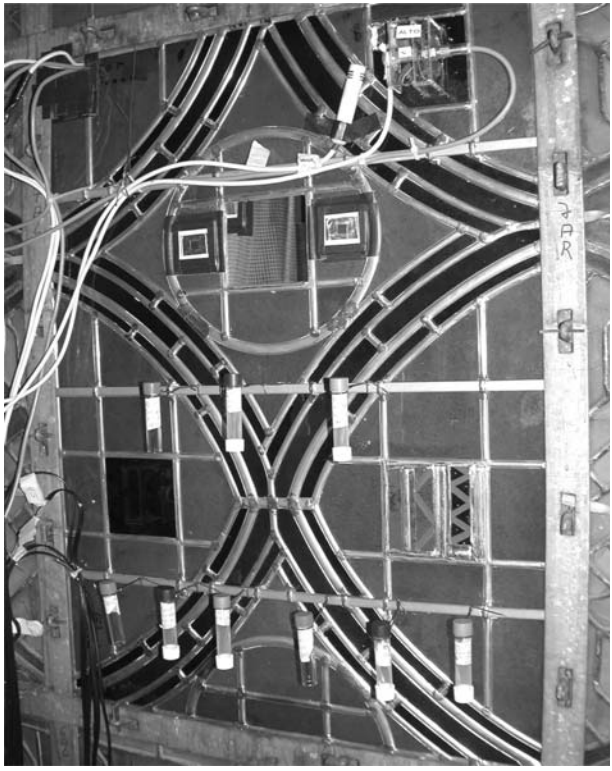

Figure 6. Diffusion tubes and equipment for microclimatic measurements, installed on a stained glass window panel.
(This figure is presented in the signature in colours at the end of this volume, Appendix, pg. 326)

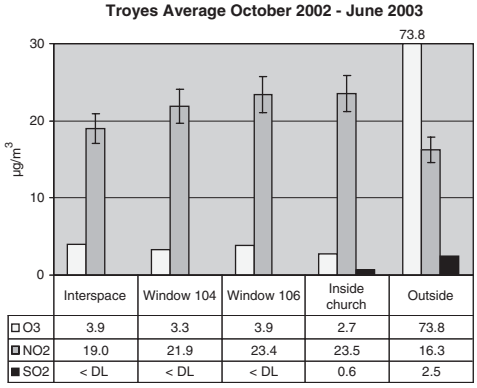

	Interspace	Window 104	Window 106	Inside church	Outside
O3	3.9	3.3	3.9	2.7	73.8
NO2	19.0	21.9	23.4	23.5	16.3
SO2	< DL	< DL	< DL	0.6	2.5

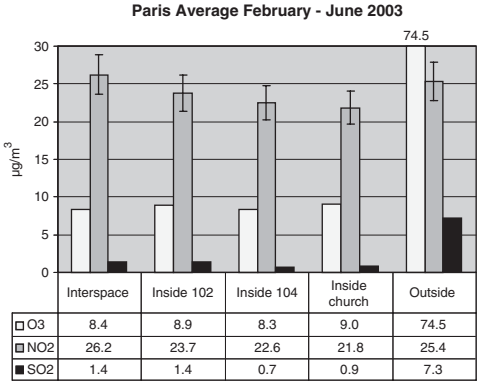

	Interspace	Inside 102	Inside 104	Inside church	Outside
O3	8.4	8.9	8.3	9.0	74.5
NO2	26.2	23.7	22.6	21.8	25.4
SO2	1.4	1.4	0.7	0.9	7.3

Figure 7. Average gas concentrations in the Basilica Saint-Urbain and the Sainte Chapelle.

the glass. In Troyes, at all sampling locations close to the ancient windows and also inside the interspace, the SO_2-concentrations lay below the detection limit. The results for NO_2 in the Sainte Chapelle show that the concentrations outside and inside the church were the same within the error interval. No significant differences between outdoor and indoor concentrations could be observed. NO_2-concentrations in Troyes in the indoor environment were on average slightly higher

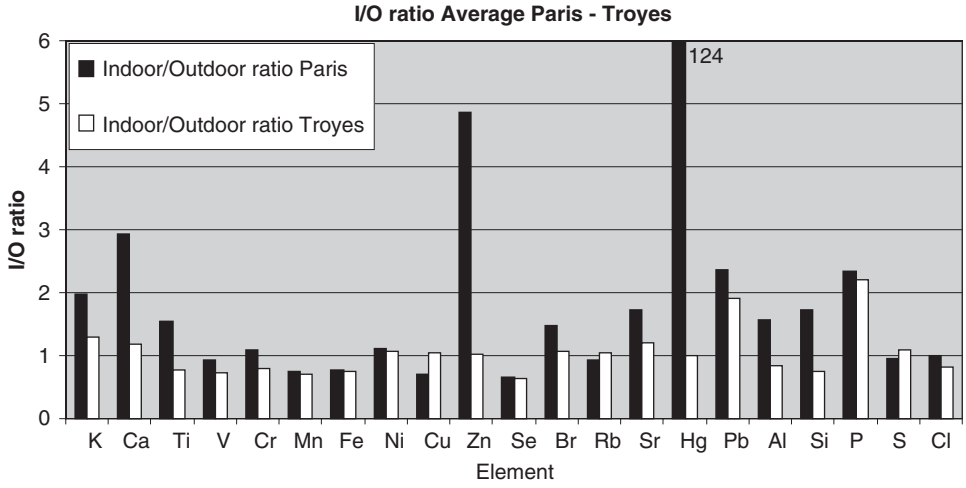

Figure 8. Indoor/Outdoor elemental ratios for bulk aerosols in the Sainte Chapelle (Paris) and in Saint-Urbain (Troyes).

than outdoors. This observation can be connected with the burning of candles inside the Basilica Saint-Urbain.

The results of the bulk particle analysis of the samples from Sainte Chapelle show that, during the sampling campaigns, the following investigated elements were enriched in the indoor air in comparison to the concentrations obtained for the outdoor air: K, Ca, Ti, Cr, Ni, Zn, Br, Hg, Pb, Al, Si, P and Cl. The elements that are typically found in samples dominated by contributions from soil and stone-deterioration (Al, Si, K and Ca) showed inside the Sainte Chapelle concentrations of a factor of 1.5 or higher than in the outside air (Figure 8).

Only some of the transition metals showed higher abundances in the outdoor air (V, Mn, Fe and Cu). An explanation for this observation can probably be given by the high number of visitors present in the Sainte Chapelle. The visitors enter the church and introduce with them rather large amounts of particles from outside on their clothes and shoes into the Sainte Chapelle. Inside the building, the particles can be released and are subsequently continuously resuspended by the visitors, when they walk around, looking at the stained glass windows. The air volume inside the Sainte Chapelle is not very large, so particles can accumulate and finally show higher concentrations in the indoor environment. Some of the elements possibly also have indoor sources.

The results from the Basilica Saint-Urbain in Troyes show that the following elements were enriched in the indoor air in comparison to the outdoor air: K, Ca, Pb, P and S. Many more elements than in the Sainte Chapelle had higher concentrations outdoors: Ti, V, Cr, Mn, Fe, Se, Al, Si and Cl. These are nearly all transition metals, but also soil-derived elements like Al and Si. While, only few elements were enriched indoors in comparison to the outdoor air in Troyes, in Paris most elements were enriched indoors. The main reason for this lies certainly in the high number of visitors in the Sainte Chapelle. The basilica in Troyes is mainly visited only during church ceremonies.

The element content of the size-fractionated aerosol particles was investigated by thin-window EPMA followed by numerical clustering to classify chemically similar particles into certain particle types. Elemental concentrations were calculated for each individual particle. In order to determine possible sources of the aerosol and the possible chemical interactions between gaseous and particulate pollutants, the particles were classified into groups using the chemical data obtained by EPMA.

The results for the particles sampled in the Sainte Chapelle show that the small particles (0.5–1 μm) from indoors were dominated by aluminosilicates (Al-Si), while outdoors, also particles containing organic material together with Al-Si and biogenic particles showed quite

high abundances. The particles with sizes between 1 and 2 μm indoors were mainly Al-Si-particles, biogenic particles, other organic particles and particles rich in Na and S. In the outdoor air, exactly the same groups were found. The particles with sizes between 2 and 4 μm showed the broadest spectrum regarding their composition. Indoors, Al-Si-particles, organic and organic + Al-Si-particles were most abundant, while in the outdoor environment, biogenic and Na-S-rich particles were dominating.

In the Basilica Saint-Urbain in Troyes, the small particles (0.5–1 μm) from inside the church contained mostly Al-Si and calcium carbonate, and also C-rich and biogenic particles were quite abundant. The particles of this size-fraction from outdoors contained mainly Al-Si, calcium carbonate and particles rich in C-N-O. The particles with sizes between 1 and 2 μm from indoors were mainly particles rich in C-N-O, calcium carbonate and organic particles. The corresponding particles from outside were Ca-rich- and calcium carbonate particles. The particles with sizes between 2 and 4 μm indoors contained mainly calcium carbonate and organic compounds. The corresponding particles sampled outdoors were dominated by organic, Al-Si, C-N-O-rich, and biogenic particles.

Generally, it is important to notice that only low amounts of C-rich particles were found inside the Sainte Chapelle. This type of particles can blacken the windows and form additionally a medium for the adsorption of dangerous gases. Hence, its presence would certainly be disadvantageous. In contrast, the most abundant particle types (Al-Si, biogenic and Na-S-rich) do not represent a particular threat to the windows; they will of course soil the windows, nevertheless. Inside the Basilica Saint-Urbain in Troyes, in contrast, C-rich particles were found in all investigated size-classes, probably due to candle burning. This fact can represent a threat to the stained glass windows.

Concerning the particles, the influence of the protective glazing has to be evaluated carefully. The interspace is flushed with indoor air, containing rather high concentrations of particles in the case of the Sainte Chapelle. The deposition on the ancient glass will depend on the air flow characteristics and the microclimatic conditions in the interspace which are very different of those inside and outside the Sainte Chapelle.

4.1.3 *Conclusions*

The sampling of pollutant gases and particles with diffusion tubes, filter membranes and impactors and the subsequent physico-chemical bulk- and micro-analysis of the obtained samples give useful results for the assessment of the threatening of the stained glass windows by air pollutants. The chosen approach to combine various sampling and analysis methods for different gases and different components of the particulate matter together seems to deliver a comprehensive picture about the various kinds of air pollutants affecting the stained glass windows.

The investigation showed significant differences for the concentrations of SO_2 and O_3 between the indoor and outdoor air of the Sainte Chapelle in Paris and the Basilica Saint-Urbain in Troyes. At all locations, the indoor SO_2- and O_3-concentrations were much lower than the concentration in the outside air. This means that, for these two dangerous pollutants, the main threat to the stained glass windows comes from the outside air. Unprotected windows are attacked by rather high ozone-concentrations on the outside of the windows, while the inside is exposed to much lower concentrations.

In the cases where a protective glazing is installed, the ancient panels are completely isolated from the outside air. The interspace is flushed with inside air. Hence, the ancient panels are effectively protected against high outside SO_2- and O_3-levels. This is certainly a great advantage of the protective glazing.

NO_2 is not as reactive air pollutant as SO_2 or O_3, so the decrease of the NO_2-concentration in the indoor air in respect to the outdoor concentration cannot be expected to be as high as for SO_2. In fact, in the Sainte Chapelle no reduction at all was observed, maybe because of the extensive air ventilation. In Troyes as in Paris the indoor and outdoor NO_2-levels were approximately the same.

In the bulk particles collected at the Sainte Chapelle in Paris higher particulate concentrations were found for all elements in the indoor air, probably because the many visitors inside the quite small church introduce and resuspend particles. In terms of conservation of the stained glass

windows, this means that the protective glazing (on the outside of the windows) leads to a higher load of particles containing the investigated elements, because inside air is re-circulated through the interspace. Especially in the interspace this could lead to a higher deposition of these particles on the ancient panels with possibly damaging effects for the glass.

Single-particle analysis using low-Z EPMA is an efficient tool for the characterization of various kinds of environmental particulate matter. Atmospheric particles as calcium sulphate, sodium and calcium carbonate, sodium nitrate, carbonates, biogenic organics, soot, aluminosilicate among others were classified in separate groups in the aerosol samples collected.

The concentrations of the air pollutants inside and outside the two churches are quite different and the observed indoor concentrations were often higher than the outdoor concentrations, suggesting the existence of important indoor sources, e.g. of soot in the Basilica Saint-Urbain, and/or of effective ways of transport of dust from the outdoor to the indoor environment, e.g. by the visitors in the Sainte Chapelle.

4.2 *St. Martinus Cathedral in Weert, the Netherlands*

EDXRF and EPMA techniques were used to analytes bulk aerosol and single particle samples collected at the St. Martinus Cathedral in Weert (The Netherlands), both in the indoor and outdoor air. The aim of our research was to determine the chemical composition, size distribution and abundance of aerosol particles responsible for blackening and soiling of the works of art displayed within the cathedral and to verify the possible sources responsible for these processes.

4.2.1 *Sampling*

The samples were collected at five locations inside the church (S1-S5) and one sample was taken outside (S6).

4.2.2 *Results and discussion*

The results of the bulk analysis are comparable with the data of the bulk analysis from the Basilica Saint-Urbain in Troyes. The concentrations for almost all analytes were outdoors significantly higher than the indoor concentrations. Indoor/Outdoor ratios for K, Ca, Ti, Mn, Cu, Pb, Al and Si are below 1. This means that the main sources of these elements are located outside of the church. For Zn and S the Indoor/Outdoor ratio reaches 1 in some locations (Figure 9).

The S concentrations were rather similar at all locations including outdoor. In general, the indoor concentration of particulate S was the highest, compared to all other elements.

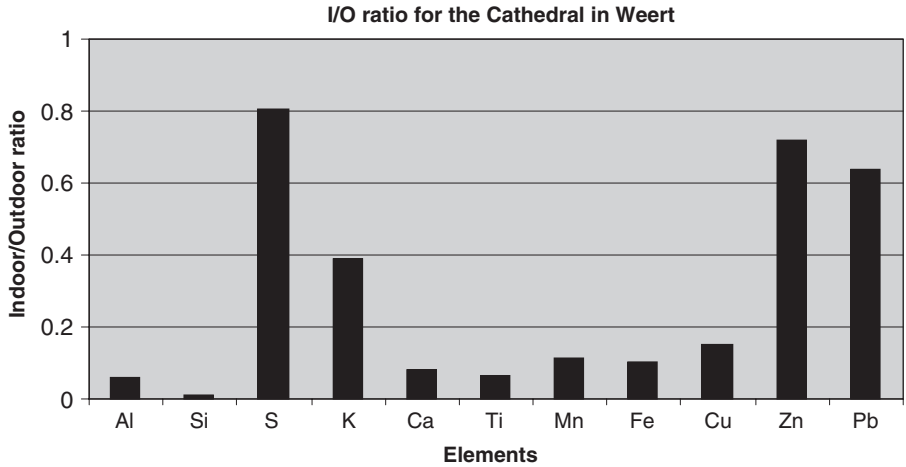

Figure 9. Indoor/Outdoor ratios for bulk elements in the St. Martinus Cathedral in Weert.

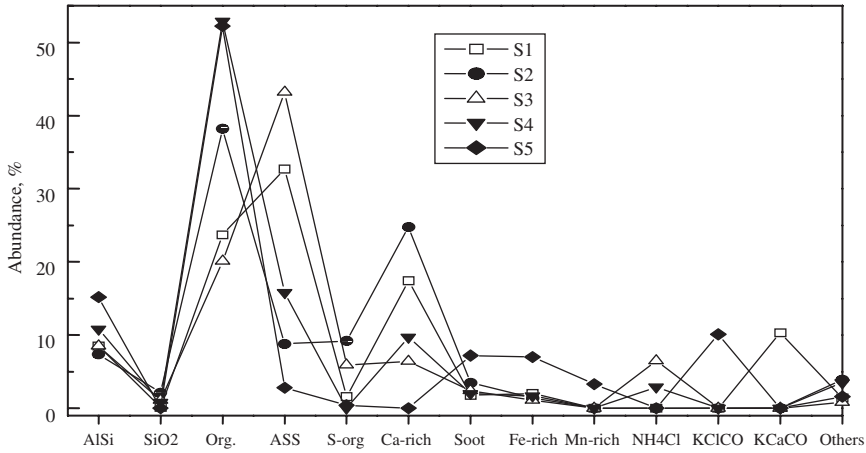

Figure 10. Overview of the most important particle types inside the Cathedral in Weert, shown is the relative abundance (%).

From the performed EDXRF analysis of the bulk aerosol samples, we can conclude that the sources of all determined elements (starting from Al) are situated outside the cathedral, with S as a possible exception.

The most abundant individual particles in the cathedral (Figure 10) were organic particles and particles considered as aged sea salt (ASS: NaCl that has had time to react with S-compounds and turned into Na-S-Cl rich particles) or organics enriched with Na. The set collected in a more isolated place near the central exit (S3) contained less organic particles.

The particles containing Na with low-Z elements were dominant there. Other large groups of particles found in all sets were alumosilicates agglomerated with organic material and Ca-rich particles. K-Ca-C-O-containing particles, which were abundant in the fraction with cut-off diameter of 1 μm of set S1 were not found in other sets.

Since only one set of samples was collected at each location, some kinds of particles could appear randomly. It is known that organic material, especially soot, causes soiling or blackening and constitutes a medium for the adsorption and oxidation of some gases. Unfortunately, the specification of organic particles cannot be determined by EPMA. This means that organic particles determined in different sets and stages can contain various organic materials from different sources. Some of them can be introduced from outdoors like the ones observed at location S3; others can be created inside the cathedral like in locations S1, S2 and S4. Burning candles and incense can be considered as examples of internal sources. As there were no burning candles near the central door (S3) and this part is isolated from the main part of the cathedral, the organic particles found in set S3 originated mostly from outside.

These particles consisted of other kinds of organic material not leading to soiling or blackening of the ceiling to such a degree as the organic particles originated from candles and incense. The confirmation is that the ceiling near the central exit (S3) is clean compared to the ceiling of the main part of the cathedral. The second reason of the soiling of the ceiling inside the cathedral is that the organic particles originated from the candles and incense as well as introduced from outdoor can be moved up by the rising air warmed by the under-floor heating and can be deposited on the ceiling of the church causing its blackening. Since near the central door (S3) no heating takes place, there is no upward air stream transporting particles to the ceiling.

4.3 *Mountain church in Rocca Pietore, Italy*

A possible negative effect of occasional heating during the cold season on artworks in churches is of practical importance for conservation purposes. The assessment of the influence of two

different kinds of heating systems on the generation of particulate and gaseous matter responsible for blackening, soiling and deterioration of precious artworks presented in the church was the research topic of the EU project called "Friendly Heating". The small church of Rocca Pietore, located in the Italian Alps at 1143 m above sea level, was chosen as a model in this study. The church has some artworks preserved in it, the most valuable being a wooden, carved and painted triptych by R. Potsch dating from 1518. Moreover, this church had a diesel oil-fueled hot-air heating system that is widely used in mountain regions. The hot air was blown from two grid diffusers at a height of 4 m above the floor, which provoked an undesirable turbulence of the temperature and velocity fields, i.e., large driving forces that can be responsible for the deposition of particles on the cold surfaces of walls and works of art. The above mentioned hot-air blowing heating system was recently substituted by a modern one consisting of electrically heated pews and electrically heated carpets near the altar.

The primary aim of our work was to characterize the bulk chemical composition of indoor and outdoor aerosols, as well as the size distribution, chemical composition and abundance of single particles responsible for blackening and soiling of the works of art displayed within the church, and to point out the influence of the two heating systems on these deterioration processes. Moreover, the level of some relevant gaseous pollutants was also monitored inside and outside the church.

4.3.1 *Sampling*

Aerosol samples for the EDXRF and EPMA analysis methods were collected at various locations inside the church under two different conditions: when the heating system was switched on for periods of 1.5 h (hot-air blowing heating) and 3 h (new electrical heating) during the sampling period, and when it was switched off. For the comparison of the indoor and outdoor air pollutants, several samples were collected outside nearby the church.

4.3.2 *Results and discussion*

The results of the EDXRF analysis obtained for the two heating systems are shown in Table 1.

For the hot-air blowing heating system (January 2003) several trends were observed.

- The Ca and Si concentrations were not dependent on the operation of the heating system. They were always significantly higher indoors than outdoors, thus the existence of an internal source of Ca and Si can be assumed, e.g. the resuspension of deposited soil dust by church visitors or by the heating system. We suppose that Ca inside the church originates from the deterioration of the walls, which can also be provoked by the hot air blowing from the heating system.
- The concentrations of K, Zn and Al inside when the heating was on exceeded those when the heating was off (introduced from the air-tube and the fuel-chamber).
- The S concentration outside was higher than inside. However inside concentrations were found to be higher when the heating was switched on than those when it was switched off.

The hot-air blowing heating system can be considered as an important factor for the resuspension of particulates as well as for the deterioration of the plastered walls (additional internal source of Ca).

For the new electrical heating system (January 2004) also several tendencies were found:

- The concentrations of Al, K, Ca, Cl, Fe, Si and Ti in the samples collected outside the church and in the samples collected inside when the heating was switched on were significantly higher than those in samples collected inside without heating. It is assumed that the sources of these pollutants are situated outside the church and the heating system just resuspends them. This is confirmed by the fact that the concentrations of the mentioned elements found on the filters collected near the organ, with the heating system switched on, were significantly lower than those found near the altar. Since the organ is relatively far away from the heated benches and the carpets, probably a lower amount of resuspended particles can reach this location.
- The concentrations of S found outside were higher or equal to those measured inside, independent on the heating operation. Hence the source of this dangerous pollutant is also situated outside the church. There is no exact dependency of the S concentration on the heating operation. Switching on the new heating system did not increase the concentration of S inside the church.

Table 1. Concentration of elements with the corresponding standard deviation (±SD) in bulk aerosol samples (ng/m^3) inside and outside the church in Rocca Pietore, Italy, determined by EDXRF.

Sample (month)	Al	Si	S	Cl	K	Ca	Fe	Zn	Pb
Outside1 (Jan. 2003)	14 ± 6	31 ± 8	150 ± 30	61 ± 16	100 ± 20	90 ± 20	22 ± 5	7 ± 1	1.3 ± 0.1
Outside2 (Jan. 2003)	13 ± 5	26 ± 7	330 ± 70	31 ± 9	110 ± 20	30 ± 10	18 ± 4	9 ± 2	1.4 ± 0.1
Outside1 (Jan. 2004)	9 ± 7	20 ± 7	140 ± 40	110 ± 30	120 ± 4	130 ± 5	26 ± 1	9 ± 1	2.0 ± 0.3
Outside2 (Jan. 2004)	0	70 ± 19	89 ± 24	450 ± 116	70 ± 3	730 ± 20	39 ± 1	4 ± 1	0.7 ± 0.3
Outside3 (Jan. 2004)	9 ± 9	80 ± 22	130 ± 30	390 ± 100	110 ± 5	890 ± 30	57 ± 2	8 ± 1	2.0 ± 0.4
Altar,on[1] (Jan. 2003)	27 ± 8	86 ± 20	150 ± 30	44 ± 13	140 ± 30	200 ± 40	20 ± 5	16 ± 3	1.4 ± 0.1
Altar,off[2] (Jan. 2003)	12 ± 5	41 ± 10	110 ± 20	63 ± 17	95 ± 20	200 ± 40	20 ± 4	6 ± 1	1.2 ± 0.1
Altar,on[1] 1(Jan. 2004)	70 ± 30	200 ± 50	110 ± 30	180 ± 50	170 ± 80	870 ± 30	94 ± 3	14 ± 1	4.0 ± 1.0
Altar,on[1] 2(Jan. 2004)	100 ± 30	260 ± 70	79 ± 23	320 ± 80	160 ± 70	1400 ± 40	107 ± 3	12 ± 1	2.4 ± 0.5
Altar,off[2] (Jan. 2004)	16 ± 7	22 ± 6	84 ± 23	14 ± 5	100 ± 3	100 ± 3	11 ± 1	6 ± 1	0.6 ± 0.2
Organ,on[1] (Jan. 2003)	24 ± 7	39 ± 10	110 ± 20	100 ± 30	170 ± 30	120 ± 20	21 ± 4	12 ± 2	1.2 ± 0.1
Organ,off[2] (Jan. 2003)	16 ± 6	40 ± 10	80 ± 19	42 ± 12	90 ± 20	160 ± 30	18 ± 4	7 ± 1	1.1 ± 0.1
Organ,on[1] (Jan. 2004)	41 ± 13	84 ± 22	76 ± 21	74 ± 20	100 ± 4	360 ± 10	43 ± 2	7 ± 1	1.7 ± 0.2
Organ,off[2] (Jan. 2004)	15 ± 8	24 ± 7	84 ± 24	22 ± 8	130 ± 4	105 ± 4	13 ± 1	9 ± 1	0.9 ± 0.3

[1] The heating was switched on for 1.5 (3.0) hours.
[2] The heating was switched off during the whole sampling time.

The new heating system can be considered as a resuspending factor of the particulate material originating from outside. Soil dust from boots of people penetrates inside the heating elements placed at the bottom of the benches through metallic nets. The electrical carpet placed near the altar can play the same role. Compared to the old heating system, the concentrations of almost all elements significantly decreased to a very low level when the new heating system is switched off. There is no permanent deterioration of the walls inside the church by the new heating system. Since usually the new heating is switched on for 30 min before service and for less than 1 h during service itself, it is clear that the new heating system provokes resuspension only during a short time.

The results obtained from the single particle analysis performed by EPMA for both heating systems are presented in Figure 11, for the altar (front; ground level) and organ (backside; 4 m above the ground level).

When the old heating system was active, the obtained EPMA results show that Ca-C-O-rich particles (range 1–4 μm, stage 5, 6 and 7) were significantly abundant inside the church. The abundances were strongly determined by the sampling place. Due to the hot air blowing, the relative humidity and temperature vary abruptly. This leads to permanent deterioration of the plastered walls causing an additional internal source of Ca-rich particles. The old heating system also causes transport and resuspension of particulate matter (especially soil dust particles) in the total volume of the church. These particles can cause soiling, although they are not chemically active. High

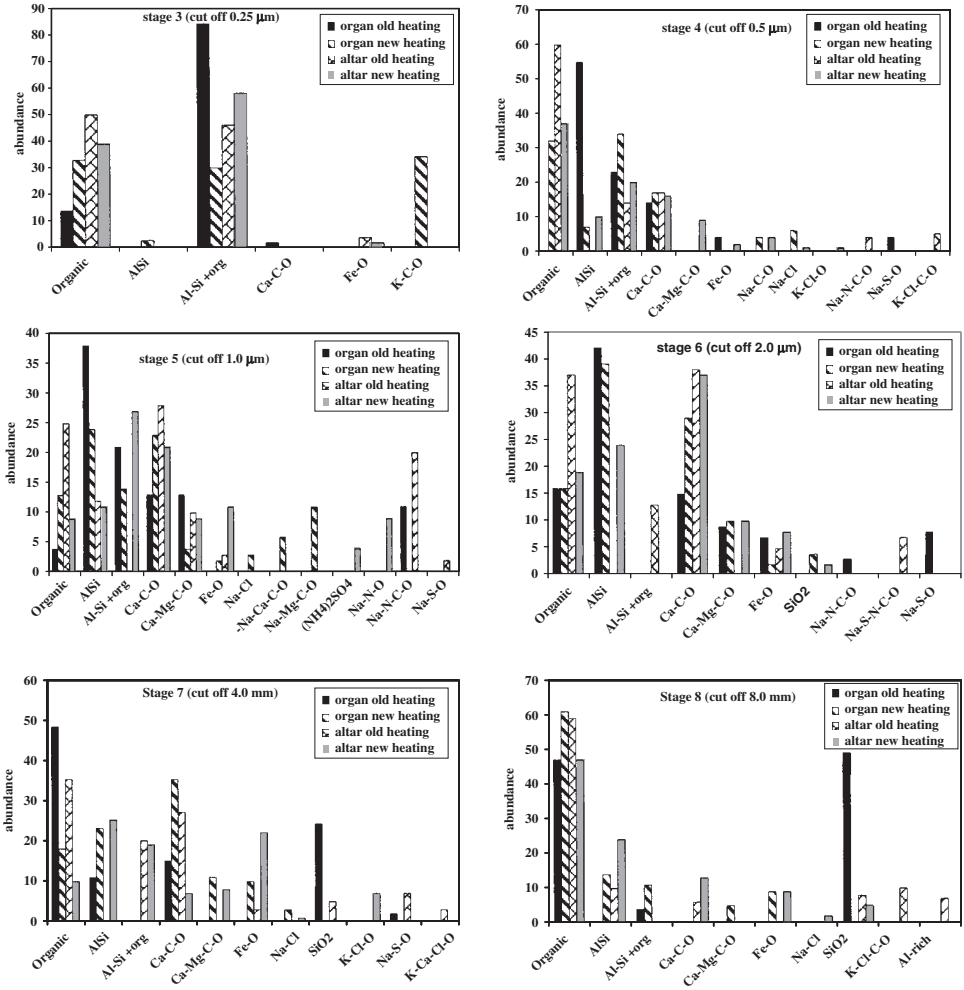

Figure 11. Comparison of abundance of single particles collected near the organ and near the altar for both heating systems.

abundance of organic matter inside the church was also found. This kind of particles is probably created inside by the heating system and can cause soiling of the works of art.

The EPMA results obtained when the new heating system was installed show the following trends: More intensive resuspension of the particles was observed, but only in the case of the ground level. Ca-rich particles were more abundant but only in the samples collected near the altar, probably because of the resuspension by the electrical carpet of particulate matter from the floor.

Near the altar organic matter was less abundant than in the case of the old heating system, but more abundant in samples collected near the organ.

The results of the gaseous pollutants obtained in the church of Rocca Pietore show the same trend as the results determined for the churches in France. The concentration of O_3 was lower inside (1.1 and 0.05 $\mu g/m^3$) than outside (43 and 13 $\mu g/m^3$). SO_2 was detected neither inside nor outside the church. The NO_2-concentrations observed inside the church exceeded significantly those in the samples collected outside (see Figure 12).

Consequently, the existence of an internal source of NO_2 caused by the combustion of diesel oil in the fuel-chamber of the old heating system can be assumed. However, the NO_2 concentration

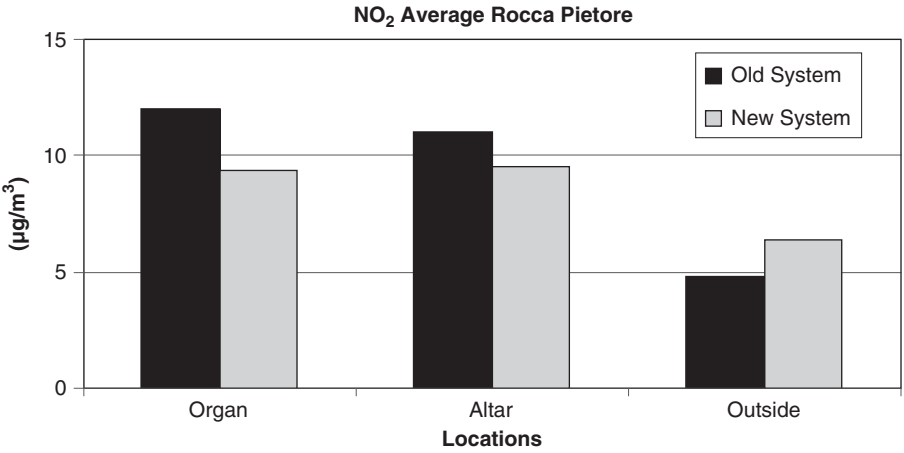

Figure 12. NO_2-concentrations in the church of Rocca Pietore for both heating systems.

determined inside after the electrical heating system had been installed was still somewhat higher than that found outside, but their ratio (1.5) was lower compared to that obtained for the old heating system (2.5). Still some small amounts of NO_2 is formed or accumulated inside the church. Likely, the inadequate airing of the building together with the daily fluctuation of the density of the local traffic in the village contributes to the ingress of NO_2 and its accumulation inside the church.

ACKNOWLEDGEMENT

Special thanks are due to Mia Awouters and the staff of the Musical Instrument Museum in Brussels as well as to Pierre Meulepas and the staff of the Plantin-Moretus Museum in Antwerp for their interest in this work and their assistance during the measurement campaigns. We greatfully acknowledge the financial support by the University of Antwerp through an ASPEO project and of the EU through the VIDRIO (contract No. EVK4-CT-2001-00045) and Friendly Heating (contract No. EVK4-CT-2001-00067) projects. One of the authors (L. Bencs) acknowledges the support of the NATO Scientific Fellowship Program under the project number of 4016/NATO/03.

REFERENCES

van Bommel, M., van Elst, B. & Broekens, F. 2001. Emission of organic acids from wooden construction materials in a small test chamber; preliminary results of optimisation of the Solid Phase Micro Extraction technique. *Abstracts of the 4th meeting of the Indoor Air Pollution Working Group, National Museum of Denmark, Copenhagen, November 8th–9th 2001*.

Brimblecombe, P. 1990. The composition of museum atmospheres. *Atmos. Environ. B-Urban Atmosphere* 24, 1–8.

Bondarenko, I., Treiger, B., Van Grieken, R. & Van Espen, P. 1996. IDAS: A Windows based software package for cluster analysis. *Spectrochim. Acta* 51B, 441–456.

De Santis, F., Fino, A., Vazzana, C. & Allegrini, I. 2001. Monitoring of atmospheric pollutants by passive sampling for the protection of historic buildings and monuments. *Annali di Chimica* 91, 759–765.

Fernandez Navarro, J.M. 1996. Procesos de alteración de las vidrieras medievales. *Mater. Construcción* 46, 5–25.

Gibson, L.T., Cooksey, B.G., Littlejohn, D. & Tennent, N.H. 1997. A diffusion tube sampler for the determination of acetic acid and formic acid vapours in museum cabinets. *Anal. Chim. Acta* 341, 11–19.

Hisham, M.W.M. & Grosjean, D. 1991. Sulfur-dioxide, hydrogen-sulfide, total reduced sulfur, chlorinated hydrocarbons and photochemical oxidants in southern Californian museums. *Atmos. Environ.* 25, 1497–1505.

Nazaroff, W.W. & Cass, G.R. 1991. Protecting museum collections from soiling due to the deposition of airborne particles. *Atmos. Environ.* 25, 841–852.

Osán, J., Szalóki, I., Ro, C.U. & Van Grieken, R. 2000. Light element analysis of individual microparticles using thin-window EPMA. *Mikrochim. Acta* 132, 349–355.

Robbiola, L. 2003. Corrosion of copper and lead by formaldehyde, formic and acetic acid vapours. *Studies in conservation* 48, 237–250.

Ro, C.U., Osán, J. & Van Grieken, R. 1999. Determination of low-Z elements in individual environmental particles using windowless EPMA. *Anal. Chem.* 71, 1521–1528.

Ryhl-Svendsen, M. & Glastrup, J. 2002. Acetic acid and formic acid concentrations in the museum environment measured by SPME-GC/MS. *Atmos. Environ.* 36, 3909–3916.

Salem, A.A. 1998. Analytical investigations on gaseous corrosion of silicate glasses using scanning electron microscopy, energy dispersive x-ray and x-ray diffraction analyses. *Glass Technol.* 39, 111–116.

Schreiner, M., Stingeder, G. & Grasserbauer, M. 1984. Quantitative Characterisation of surface-layers on corroded medieval window glass with SIMS. *Fresenius J. Anal. Chem.* 319, 600–605.

Shaver, C.L., Cass, G.R. & Druzik, J.R. 1983. Ozone and the deterioration of works of art. *Environ. Sci. Technol.* 17, 748–752.

Szalóki, I., Osán, J., Worobiec, A., de Hoog, J. & Van Grieken, R. 2001. Optimization of experimental conditions of thin-window EPMA for light-element analysis of individual environmental particles. *X-Ray Spectrom.* 30, 143–155.

Szalóki, I., Osán, J., Ro, C.U. & Van Grieken R. 2000. Quantitative characterization of individual aerosol particles by thin-window electron probe microanalysis combined with iterative simulation. *Spectrochim. Acta* 55B, 1017–1030.

Tétreault, J. & Stamatopoulou, E. 1997. Determination of concentrations of acetic acid emitted from wood coatings in enclosures. *Studies in Conservation* 42, 141–156.

Tétreault, J., Cano, E., van Bommel, M., Scott, D., Dennis, M., Barthes-Labrousse, M.G., Minel, L., Verità, M., Falcone, R., Vallotto, M. & Santopadre, P. 2000. Study of the weathering mechanisms and chemical composition of ancient mosaic tesserae. *Rivista della Staz. Sper. Vetro* 6, 33–44.

Vekemans, B., Janssens, K., Vincze, L., Adams, F. & Van Espen, P. 1994. Analysis of X-ray spectra by iterative least squares (AXIL): New developments. *X-Ray Spectrom.* 23, 278–285.

Worobiec, A., de Hoog, J., Osán, J., Szalóki, I., Ro, C.U. & Van Grieken, R. 2003. Thermal stability of beam sensitive atmospheric particles in electron probe microanalysis at liquid nitrogen temperature. *Spectrochim. Acta* 58B, 479–496.

Cultural Heritage Conservation and Environmental Impact Assessment by Non-Destructive Testing and Micro-Analysis – Van Grieken & Janssens (eds)
© 2005 Taylor & Francis Group, London, ISBN 90 5809 681 5

A survey of the recent use of x-ray beam methods for non-destructive investigations in the cultural heritage sector

K. Janssens
Centre for Micro- and Trace Analysis, Department of Chemistry, University of Antwerp, Belgium

ABSTRACT: An overview is presented of the use of microscopic x-ray fluorescence, x-ray absorption and x-ray diffraction methods for non-destructive analysis of materials and artefacts from the cultural heritage field during the last five years. Both the use of x-ray beams generated by means of x-ray tubes, operated either in the laboratory or on-site, and produced in synchrotron radiation storage rings, is covered.

1 INTRODUCTION

Objects and monuments of culturo-historical significance are made in a wide variety of materials (metals, ceramics, glass, various igneous and sedimentary rocks, textile, leather, wood, horn, parchment, paper, ...) and usually exhibit a fairly complex three-dimensional structure and a heterogeneous chemical composition. Especially in the case of artefacts of precious nature (e.g., jewellery, weaponry, religious objects) these objects often:

- are composed of various materials (e.g., Au/Ag alloy artefacts adorned with gemstones),
- consist of a base material covered with one or more layers of pigmentation (e.g., polychrome wooden statues, easel paintings, illuminated manuscripts) or
- show significant (surface) alteration due to burial or atmospheric exposure (e.g., bronze statues, silver coins, …) (Pollard & Heron 1996).

Next to the requirement that the method(s) of analysis that are employed to assess the material state of such objects/materials are as non-destructive as realistically possible, in most cases, preference is then given to methods that are able to yield information on well-defined areas of the artefacts in question (Creagh & Bradley 2000). Sometimes, these areas are microscopically small; in other cases, a lateral resolution of 1 mm^2 suffices.

Accordingly, for the study, the conservation and the restoration of materials and artefacts of culturo-historical value, there is a well-defined need for analytical methods that are able to provide information on :

- the chemical nature/composition of selected parts of cultural heritage artefacts and materials in order to elucidate their provenance
- the state of alteration (on the surface and/or internally) of objects as a result of short, medium and long term exposure to particular environmental conditions
- the effect/effectiveness of conservation/restoration strategies during and after application.

According to Lahanier et al. (1986), the ideal method for analyzing objects of artistic, historic or archaeological nature should be:

(a) non-destructive, i.e., respecting the physical integrity of the material/object. Often valuable objects can only be investigated when the analysis does not result in any (visible) damage to be object. Usually this completely eliminates sampling or limits it to very small amounts;

(b) fast, so that large numbers of similar objects may be analyzed or a single object investigated at various positions on its surface; this property is very valuable since this is the only way of being able to discern between general trends in the data and outlying objects or data points;
(c) universal, so that by means of a single instrument, many materials and objects of various shapes and dimensions may be analyzed with minimal sample pre-treatment
(d) versatile, allowing with the same technique to obtain average compositional information but also local information of small areas (e.g., mm to micron-sized) from heterogeneous materials;
(e) sensitive, so that object grouping and other types of provenance analysis can be done not only by means of major elements but also by means of trace-element fingerprints, and
(f) multi-elemental, so that in a single measurement, information on many elements is obtained simultaneously and more importantly, so that also information is obtained on elements which were not initially thought to be relevant to the investigation.

While many (micro) analytical methods fulfil several, but usually not all of the requirements described above, it is obvious that in the cultural heritage field, the analytical techniques should preferably be non-destructive or micro-destructive. Non-destructive techniques allow analytical information to be obtained with no damage to the sample or (in some cases) to be artefacts in question. When micro-destructive methods are used, all visible damage is avoided and the objects under examination remain esthetically unimpaired (Ciliberto & Spoto 2000). The possibilities to use these type of methods is of enormous advantage when sampling is not feasible or when fragments used for analysis need to be put back in the original location at the end of the investigation. Among the truly non-destructive methods, the spectroscopies based on ultraviolet, visual and infra-red radiation can be counted, as well as the x-ray based methods.

In recent years, partially driven by the increasing importance of high-tech materials of complex micro structural nature and mainly as a result of miniaturization of components (radiation sources, radiation guide tubes, detectors), a number of portable and/or microscopic versions of established analytical methods have come into existence. Such methods are well suited for inspection and/or analysis of objects of great cultural value as measurements can be made on site (e.g., pigment identification in frescoes) thus eliminating the need to sample or even move the objects out of their normal surroundings (e.g., a museum, an archaeological site). Thus, most of today's major museums dispose of one or more (trans) portable instruments for high spatial resolution examination of the artefacts in their collection.

Next to being useful for analysing the cultural heritage artefacts themselves, such techniques are also employed in support studies, where under controlled laboratory circumstances, e.g., the deterioration of building materials (mortar, sandstone, ...) under the influence of rain, exposure to solar radiation, pollution gases, ... is examined.

X-rays were discovered by W.C. Röntgen in 1878 and were first considered to be a mysterious type of radiation with properties very different from electromagnetic radiation in the ultraviolet, visual and infra-red range of the spectrum: Röntgens first experiments suggested that x-rays could not reflected, refracted or polarized but instead penetrated fairly deeply into materials, apparently without causing harm or other (permanent) changes. Although it is now well documented that x-rays exhibit analogous characteristics as the radiation of longer wavelengths and that high doses of this type of radiation on (biological) tissues can effectively induce discolorations and other damages, irradiation of inorganic materials with x-rays is general considered not to cause them any harm. Thus, next to being used for radiographic purposes x-rays are also very frequently employed for compositional and for structural analysis of cultural heritage materials.

A well-established method of quantitative element analysis is x-ray fluorescence analysis (XRF), which is based on the ionization of the atoms of the material being investigated by an energetic beam of primary x-rays. The characteristic radiation that is emitted by the ionized atoms upon relaxation contains information on the nature and the abundance of the elemental constituents present.

Since XRF meets a number of the requirements of the 'ideal method' for non-destructive analysis of cultural heritage materials (Lahanier et al. 1986.), analysis of objects of artistic and/or archaeological value with conventional XRF is fairly common; it is in fact one of the most often

applied methods for obtaining qualitative and semi-quantitative information on the materials these objects are made of (Johansson & Campbell 1988). Several textbooks cover the fundamental and methodological aspects of the method and its many variants (Van Grieken & Markowicz 2002). In the specific context of non-destructive analysis of (often) irregular and/or heterogeneous materials, the use of conventional XRF for reliable quantitative analysis is severely hampered by the fact that the irradiated area usually is large. This prevents the separate analysis of details of decorations, distinct features etc. Also, the irradiation geometry and sample surface are usually non-ideal and/or not well-defined, possibly introducing systematic errors in the quantification. Using smaller x-ray beams can circumvent some of these limitations. In such as case, motorized sample movement allows to extend the local analysis capability towards two-dimensional imaging of certain elements on the surface of artefacts. Since many objects of artistic and/or archaeological nature are fairly large and bulky (e.g., statues, oil paintings, vases, treasury objects), recently available instrumentation that can accommodate objects of various shapes and is able to operate in air atmosphere is very useful.

X-ray diffraction (XRD) makes use of the coherent scattering of x-rays by atomic electron clouds and the constructive interference that takes place between rays scattered by regularly spaced series of atoms. The orientation and relative intensity of the reflexes contain information on the crystallographic structure of the materials being studied. Via the use of appropriate data bases, XRD allows to qualitatively identify the compounds present and quantitative determine their relative abundance in case a mixture of the latter is under scrutiny. More detailed information on this method may be found in many excellent reference texts (Hammond 1997, Sands 1994, Guinier 1994, Bish & Post 1990, Young 1993).

With the advent of more powerful x-ray sources called synchrotrons, also other forms of x-ray spectroscopy, requiring highly monochromatic primary radiation of which the energy or wavelength may be continuously varied, have come into use. Notably some of the forms of x-ray absorption spectroscopy (XAS) are proving themselves to be useful for non-destructive characterization of cultural heritage materials while these sources also have significantly stimulated the development of the microscopic equivalents of XRF and XRD. During XAS experiments, the probability of interaction of highly monochromatic x-ray beams of which the energy is continuously varied across an absorption edge of the element of question is directly or indirectly measured. The resulting XAS spectra contain information on the local order around and the chemical state of the central atomic species. Information on the theory, techniques, and applications of XAS can be found in Koningsberger and Prins (1988), Stern (1988) and Durham (1988) describe in a relatively brief form the theory of EXAFS and XANES spectroscopies. Applications of XAS in materials and earth sciences are summarized by Wong (1986) and Brown et al. (1988). By means of XAS it is possible to obtain information on the chemical state of specific (inorganic) constituents of a material without the necessity that the constituent in question needs to be present at the minor to major level of concentration or needs to be part of a crystalline lattice, as in the case of XRD.

In what follows, after briefly describing the principle of the methods and outlining the instrumentation employed for the investigations, a selected number of cases studies highlighting the above-described types of investigations are outlined. Depending on the nature of the investigation and on the type of information required, one or more of the various forms of x-ray analysis are employed. In several books (Ciliberto & Spoto 2000, Creagh & Bradley 2000, Tsuji et al. 2004) and special journal issues (Selin 2000), several other collections of similar cases studies can be found.

2 X-RAY METHODS

2.1 *X-ray fluorescence analysis*

X-ray fluorescence spectrometry (XRF) (Van Grieken & Markowicz 2002) typically uses a polychromatic beam of short wavelength/high energy photons to induce the emission of longer

wavelength/ lower energy characteristic lines in the sample to be analyzed. Modern x-ray spectrometers may use either the diffracting power of a single crystal to isolate narrow *wavelength* bands (wavelength dispersive XRF – WDXRF) or an energy-selective detector may be employed to isolate narrow *energy* bands (energy dispersive XRF – EDXRF) from the polychromatic radiation (including characteristic radiation) that is produced in the sample.

Because the relationship between emission wavelength and atomic number is known, isolation of individual characteristic lines allows the unique identification of an element to be made and elemental concentrations can be estimated from characteristic line intensities. Thus this technique is a means of material characterization in terms of chemical composition.

Wavelength dispersive XRF instrumentation is almost exclusively used for (highly reliable and routine) bulk-analysis of materials, e.g., in industrial quality control laboratories. In the field of energy-dispersive XRF instrumentation, next to the equipment suitable for bulk analysis, several important variants have evolved in the last 20 years. Both total reflection XRF (TXRF) and microscopic XRF (μ-XRF) are based on the spatial confinement of the primary x-ray beam so that only a limited part of the sample (+support) is irradiated. This is realized in practice by the use of dedicated x-ray sources, x-ray optics, and irradiation geometries.

2.1.1 *Microscopic XRF*

The basic measuring strategy of microscopic x-ray fluorescence analysis (μ-XRF) is illustrated in Figure 1. This micro analytical variant of bulk EDXRF is based on the localized excitation and analysis of a microscopically small area on the surface of a larger sample, providing information on the lateral distribution of major, minor and trace elements in the material under study. Essentially, a beam of primary x-rays with (microscopically) small cross-section irradiates the sample and induces the emission of fluorescent x-rays from a micro-spot. A suitable detector system collects the fluorescent radiation that carries information on the local composition of the sample. When the sample is moved either manually or under computer control in the x-ray beam path, either spot analyses, line-analysis or image collection is possible.

The difficulties in the exploitation of this method reside with the production of sufficiently intense x-ray beams to allow for sensitive micro analysis. Techniques to do this have only recently appeared; in the past, x-rays were considered to be notably difficult to focus into beam of small dimensions. Variants on the basic mode of operation either reside with the method employed for x-ray beam concentration/focussing or with the source type employed: conventional x-ray tubes

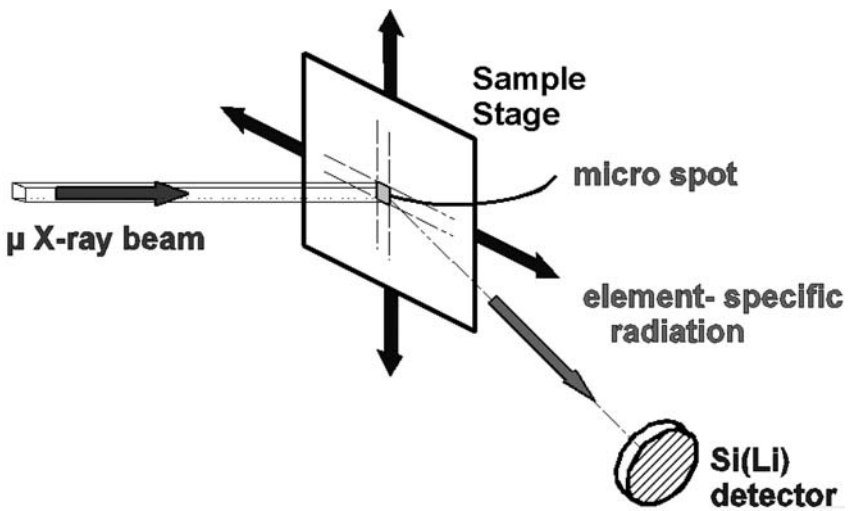

Figure 1. Principle of μ-XRF.

or synchrotron radiation sources. Especially the increased performance of compact and relatively inexpensive x-ray focusing devices and in particular the development of (poly) capillary x-ray focusing optics, permitting x-ray beams to be focused to below 10 μm diameter spots, has made the development of μ-XRF possible.

Mono- and polycapillary x-ray optics (Janssens et al. 1998, Dabagov et al. 1995) are very frequently used in μ-XRF instruments since they are compact, robust and relatively inexpensive optical elements. In almost all laboratory μ-XRF apparatus either capillary optics or pin-hole apertures are employed for focusing or collimating the polychromatic spectrum emerging from a micro-focus x-ray tube. Capillary optics have the additional advantage of being 'non-imaging optics', indicating that the diameter of the x-ray micro beams they generate is largely independent of the size of the x-ray source employed. Generally, polycapillary optics produce beam sizes in the range 10 to 50 μm while operating efficiently in the 5–25 keV range. A more detailed treatment of their characteristics can be found elsewhere (Gao & Janssens 2004).

At synchrotron μ-XRF setups, also more sophisticated types of optics are is use: Compound Refractive Lenses (CRL), (Simionovici et al. 2004), Fresnel Zone Plates (FZP), (Lai et al. 1992) and curved mirror systems are examples of the latter (Yanagihara & Yamashita 2004). These imaging optics are capable of producing x-ray beams with submicron dimensions but can only be used at synchrotron sources such as the European Synchrotron Radiation Facility (Grenoble, France).

When the appropriate type of x-ray optics is used in combination with x-ray tubes, absolute detection limits in the pg area can be obtained for thin samples by means of μ-XRF. In massive samples, relative detection limits of around 10 ppm have been reported for transition elements. At synchrotron facilities, the capabilities of the μ-XRF method (both regarding spot sizes and detection limits) are significantly better: fg to ag-level absolute detection limits are obtained with beams as small as 0.5–2 μm in diameter. By the use of monochromatic beams of polarized radiation, optimal peak-to-background ratios in the resulting EDXRF spectra can be obtained, resulting in relative detection limit values in the 10–100 ppb range in biological materials. The application of μ-XRF to a great variety of problems and materials has been described, including geochemistry, archaeology, industrial problems and environmental studies (Janssens et al. 2000). Especially the fact that quantitative data on (trace) constituents can be obtained at the microscopic level without sample damage is of use in many different circumstances.

2.1.1.1 *Laboratory μ-XRF*

Though suitable for trace-level micro-analysis of organic materials (e.g., paper, pigments dispersed in a organic binder), offering (sub) ppm level detectability for many elements (Adams et al.1998) or of silicate-rich materials such as pottery or glass, the high primary intensity of synchrotron micro beams usually is not compatible with the XRF analysis of metallic materials (e.g., artefacts made in bronze, iron, silver, gold or alloys of these metals). Laboratory μ-XRF can be conveniently used for this purpose. Another strong point of laboratory μ-XRF is the possibility to perform local (quantitative) analysis on objects whose size, shape or nature is incompatible with the vacuum and the small sample enclosures employed by most conventional micro analytical techniques such as EPXMA and μ-PIXE. In this respect, μ-XRF offers similar possibilities to external-beam PIXE (Johansson & Campbell 1988), but in some cases with a better lateral resolution.

Even for smaller objects (such as, e.g., coins), which might be analyzed as a whole in conventional XRF apparatus, the use of a small beam instrument offers advantages. A small x-ray beam permits to analyze an object at various locations, e.g., to verify that all parts of a statue are made of the same material, or to investigate the homogeneity of the material used. XRF on curved or otherwise non-flat surfaces can lead to errors in the quantification (especially for metallic materials) (Milazo & Cicardi 1997); with a small beam, it is in general easier to select locations on an object which resemble more closely to the ideal, flat and polished surface normally required for reproducible quantitative measurements. In case corroded objects are under investigation, only a small area of the (altered) surface needs to be removed in order to expose the underlying original material.

Several commercial companies offer laboratory μ-XRF instruments, including EDAX and Horiba. In Figure 2, photographs of the exterior and interior of the EDAX Eagle instrument are

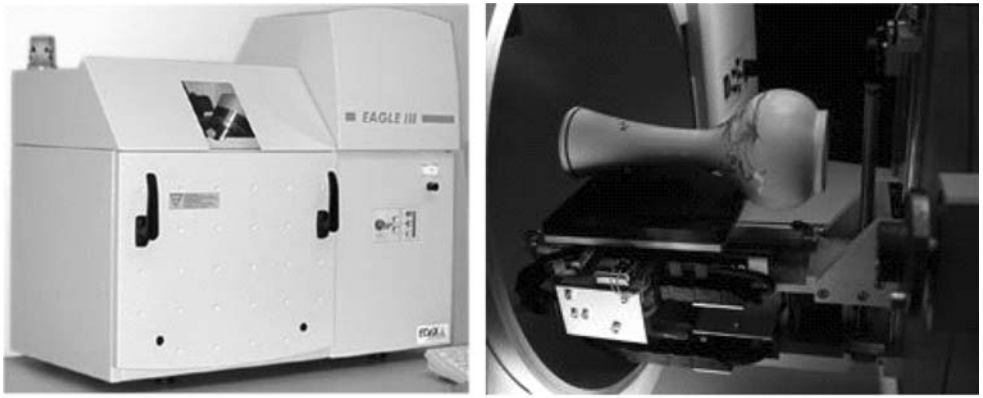

Figure 2. Photograph of (a) the exterior and (b) the inside of the Eagle vacuum chamber, showing the positioning of an artefact on the motorized stage (shown retracted). By means of a camera, the interior can be observed when the vacuum chamber is closed.

shown. The heart of this spectrometer is a 40 W Mo or Rh anode micro-focus x-ray tube that can be interfaced to a monocapillary collimator or polycapillary lens, yielding x-ray beams in the range 20 μm to 3 mm. x-rays are detected with a 80 mm^2 Si(Li) detector. This instrument is available with a large vacuum chamber in which medium-sized artefacts (up to 25 × 20 × 9 cm in size) can be analyzed without encountering practical problems.

2.1.1.2 *Portable/in situ μ-XRF*

A recent direction in μ-XRF instrument development is the construction of compact and/or portable small-beam instruments, consisting for example of an air-cooled mini-focus x-ray tube, a compact optical element for beam focussing/collimation and a Peltier-cooled energy-dispersive detector. Such instruments, offering beams of 50–200 μm cross section, are very useful for *in situ* investigations of archaeological and artistic materials, i.e., in the museum, gallery or archaeological site they normally are present.

In some cases, the spectrometer can be as simple as a compact x-ray tube equipped with a collimator tube, defining the x-ray beam to ca. 1–2 mm diameter, an optional beam filter and a small pin-diode detector attached to the side of the tube. Such a system can be very useful for *in situ* analysis of bronze statues (Vittiglio et al. 1999, Moioli & Seccaroni 2000). Other systems make use of drift chamber detectors (Fiorini et al. 1997, Fiorini & Longoni1998).

Bronk et al. (2001) have described the design of a mobile spectrometer for microscopic x-ray fluorescence with the requirements of archaeometry in mind. The ARTAX instrument offers non-destructive and sensitive multi-elemental analysis, a sub-mm resolution with the possibility of working outside the laboratory (see Figure 3). The spectrometer consists of an air-cooled, low-power molybdenum tube, a polycapillary x-ray lens that focuses the beam to ca 100 μm, a silicon drift detector, a CCD camera, and three light diodes for sample positioning. The motor-driven measurement head is fixed on a x, y, z-flexible tripod support which can be assembled and dismantled within minutes. The detection limits of this device are in the range of 10 μg/g for transition elements in glass. Open helium purging in the excitation and detection paths enables the determination of elements down to sodium, thus avoiding vacuum conditions or a size-limiting sample chamber. To demonstrate the potential of ArtTAX in the field of art and archaeology, a selection of qualitative and quantitative results on pigment, metal, glass, and enamel analyses were presented (Bronk et al. 2001).

Bichlmeier et al. (2001, 2002) and Vittiglio et al. (2004) have described another compact micro-XRF instrument, consisting of a similar set of compact components and applied it to the analysis

Figure 3. The ARTAX μ-XRF spectrometer, mounted onto a flexible support, allowing easy positioning of the device in front or above large artefacts.

of noble metals objects (such as coins, burial artefacts and statuettes in bronze and brass), multi-coloured beads and 20th century decorate glass objects and pigmented materials of various nature (18th C. illuminated parchments various manuscripts from the 13th to the 19th C. prepared with ferro-gallic ink.).

2.1.1.3 *Polychromatic synchrotron μ-XRF*

In Figure 4a the schematic lay-out of number of different μ-XRF spectrometers that make use of synchrotron radiation are shown. The capabilities of some of these spectrometers is limited to elemental microanalysis while by means of other facilities, elemental analysis can be combined with other types of x-ray spectroscopy such as μ-XANES and μ-XRD.

The experimental setup used for polychromatic synchrotron μ-XRF measurements installed at Beamline L of the HASYLAB (Hamburg, Germany) synchrotron laboratory are schematically depicted in Figure 4a. The bending magnets of this storage ring produce a white spectrum that contains appreciable amounts of very energetic photons (above 60 keV), something which is not the case at many other synchrotron facilities, such as e.g., the National Synchrotron Light Source (NSLS, Upton, NY, USA).

The beam that originates from the storage ring is first collimated down to ca. $100 \times 100\,\mu m^2$ by motorized cross-slits before entering a straight glass capillary. The latter is mounted onto a motorized XY$\theta\varphi$-stage for alignment to the beam. Usually, straight borosilicate glass capillaries

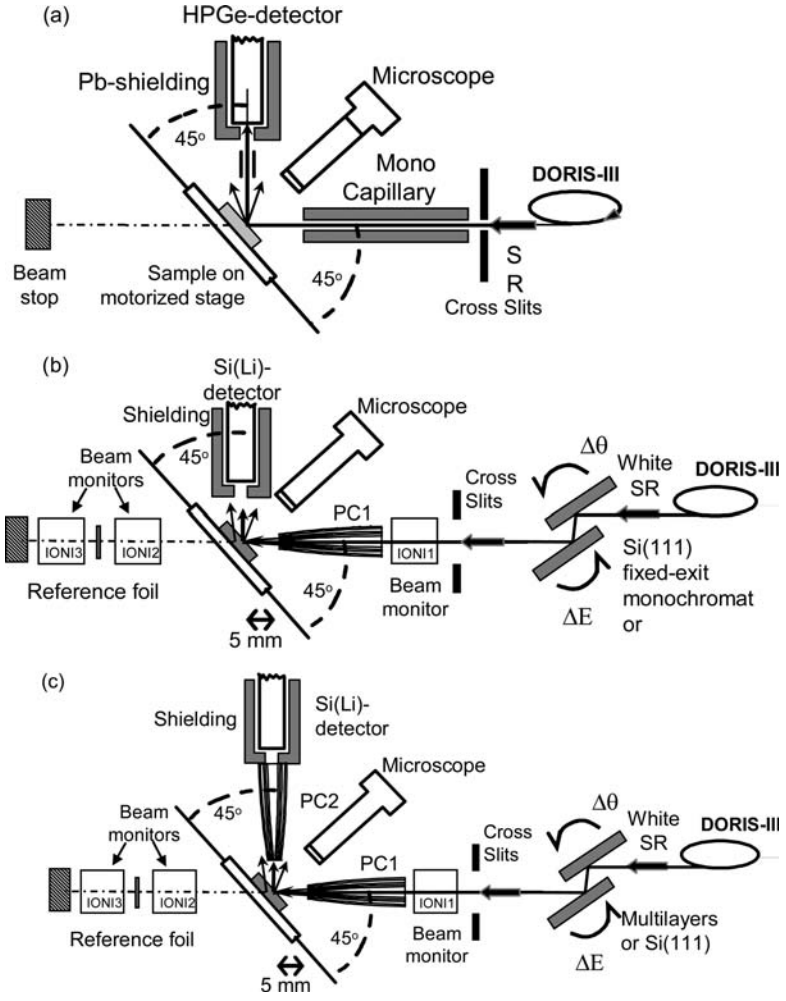

Figure 4. Schematics of (a) a polychromatic μ-SRXRF spectrometer, (b) a combined μ-SRXRF and μ-XANES facility employing monochromatic excitation and (c) a confocal μ-XRF excitation geometry, making use of pink-beam excitation. These instruments are in operation at Beamline L, HASYLAB, (DORIS III storage ring), Hamburg, Germany.

of inner diameter 10–50 μm are employed for micro beam formation (Janssens et al. 1996); the capillary-sample distance is typically of the order of a few mm. The sample itself is mounted onto a motorized XYZθ-stage, allowing it to be moved in increments of 1 μm and 0.1° resp. The sample surface plane is vertical and oriented at 45° to the incoming micro beam and is also in the focal plane of the long distance optical microscope which is placed horizontally. Fluorescent signals are detected by a HPGe (high-purity germanium) solid-state detector; the latter is located at a distance of 5–7 cm from the sample and is shielded by a Ta/Pb enclosure. The detector collects the fluorescent and scattered radiation in a solid angle of ca. 0.001 steradians. The vertical position of the detector is such that it is exactly in the (horizontal) plane formed by the storage ring and the micro beam. Since the HPGe detector is oriented at 90° to the micro beam in the plane of maximum linear polarization, the XRF spectra which are collected in this way feature optimal peak-to-background ratio's as the scatter-induced continuum background is reduced in intensity (Vincze et al. 1995). Behind the sample, an ionization chamber is placed to monitor the transmitted beam intensity; a similar monitor can be placed in the beam path between slits and capillary (not shown in Figure 4a).

During conventional μ-XRF measurements, involving point analyses, line scans or two-dimensional (2D) mapping, the sample is moved through the beam by means of the motorized stage (in the XYZ directions) so that the appropriate locations on the surface are irradiated; the rotation stage (θ stage with vertically oriented rotation axis) normally is only useful during tomographic measurements (Vincze et al. 1999). Correlated stage movement and spectrum acquisition allows the collection of $n_x \times n_y$ individual XRF spectra (n_x, n_y = number of pixels in horizontal and vertical direction of the image) which during or after the acquisition can be processed to yield (net) elemental maps, line profiles or area/phase-specific sum spectra of the irradiated material. By means of appropriate calibration models, the latter can be converted into quantitative images or local composition values (Janssens et al. 1997). The analytical characteristics of this facility are described more in detail elsewhere (Knöchel & Haller 1996). A special feature of this experimental facility is the fact that K-line XRF measurements can be performed on the elements ranging from K (Z = 19) to Pb (Z = 82) because of the high energy components of the white beam. In the transition metal range, fg-level absolute detection limits in thin samples and ppm-level relative detection limits in thick organic or silicate-based samples are obtained while for the lanthanides, equivalent values are situated around 10 fg and 5–10 ppm resp. within 1000 sec of irradiation time (Janssens et al. 1998). Next to the high intensity of the synchrotron beam, the high sensitivity over an extended element range is also the consequence of the fact that in SR-XRF spectra, a reduced background level is observed. This is the result of the polarized character of the radiation and the fact that the XRF is detected in the plane of the synchrotron ring (see Ref. Vincze et al. 1999 for details). A disadvantage of the use of the strongly penetrating primary and fluorescent radiation is that the analytical signals in thick samples can originate from extensive depths (e.g., for REE, this can be up to several mm in glass samples), hereby reducing the effective lateral resolution of the technique in one direction. This blurring effect can be avoided by employing thin samples.

2.1.1.4 *μ-XRF and μ-XANES using tuneable monochromatic excitation*

In the setup shown in Figure 4b, a narrow energy-band is selected from the continuum by means of a fixed-exit Si<111> monochromator (Falkenberg et al. 2001). After passing cross-slits, the monochromatic beam is demagnified by a polycapillary lens. What is shown in Figure 4b&c are so-called polycapillary half-lenses, suitable for focussing of (quasi-parallel) synchrotron radiation. An important feature of this type of lens is the large beam acceptance area, typically several square millimetres in size. This permits to capture a large fraction of the photons in the impinging beam, resulting in a high throughput and gain factor. When the orientation of the monochromator crystals is kept constant, μ-XRF measurements with monochromatic excitation can be performed. This excitation form results in XRF spectra with very low background levels, leading to relative detection limits situated in the 0.1–10 ppm range and at the 0.1–1 fg level in thin samples. The increase in flux density is of such a magnitude that it becomes possible to perform μ-XANES measurements at a second generation synchrotron bending magnet source where a very significant part of the initial beam is lost in the monochromatization process (Vincze et al. 2002, Proost et al. 2003).

2.1.1.5 *Confocal μ-XRF and μ-XANES in monochromatic and pink-beam mode*

A striking difference between μ-XRF and micro-analytical methods such as electron probe x-ray micro analysis (EPXMA), secondary ion microscopy (SIMS) and laser-ablation inductively-coupled mass spectrometry (LA-ICP-MS) is that x-ray photons of sufficient energy can penetrate very deeply into the material being analyzed. Since this penetration depth can be one to several orders of magnitude higher than the diameter of the focused x-ray beam, often a degradation of the lateral resolution is observed (Janssens 1993, 2000) when samples thicker than the beam size are investigated. In fact, rather than measuring the lateral distribution of the elemental constituents at the surface of the materials, a two-dimensional projection of the three-dimensional distribution of these constituents in the sample is obtained.

This penetrative characteristic of x-ray beams is employed to advantage in XRF tomography experiments, where through the measurement of a series of the aforementioned projected

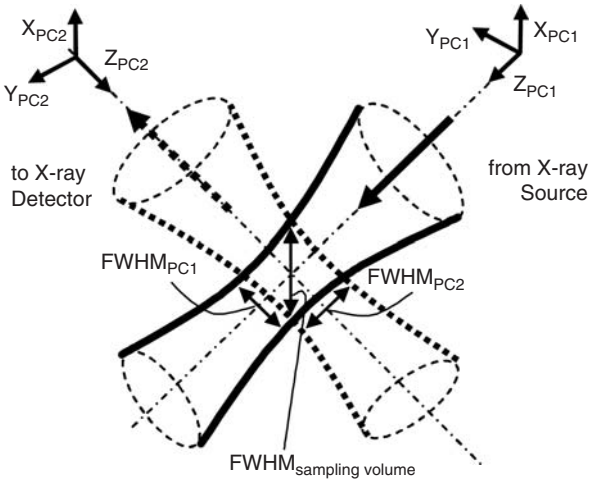

Figure 5. Detail of the intersecting waists of two polycapillary lenses aligned perpendicularly relative to each other in the same horizontal plane.

distributions under various angles and the use of appropriate mathematical back projection algorithms (Vincze et al. 2002, Hansel et al. 2002)., it is possible to perform three-dimensional elemental analysis in a non-destructive manner. Since this method involves rotation of the sample over 180° or 360° relative to the primary beam, it is limited to the investigation of relatively small objects, typically of dimensions of a few mm.

Figure 4c shows the same arrangement as that of Figure 4a–b, but in this case, instead of one optical element (PC1, to focus the primary beam), a second optic (PC2) is placed between sample and detector. The polycapillary half-lens PC1 focuses (quasi-)parallel radiation that enters the wide end of the device into a focal spot that is situated ca 5 mm outside the narrow end of the lens. Between the lens end and the focal spot, the resulting x-ray beam is strongly convergent, while after the focus, it is strongly divergent. Around the focal spot, the primary x-ray beam has a narrow 'waist', as schematically shown in Figure 5. At a primary energy E_0 of 21 keV, the diameter of the waist is ca 10 μm. The narrow part of the waist extends in both directions for several hundreds of μm before significantly getting broader. Similarly, secondary radiation emitted by the sample atoms in the direction of the detector will pass through lens PC2 only when their point of origin is situated in the waist associated with PC2.

Thus, when the two lenses are situated perpendicular to each other in one plane, in such a way that the intersection of the two waists form a cube-like volume, only fluorescent signals generated in this volume will reach the detector. Within the limits imposed by (a) the absorption of the radiation in the sample and (b) by the free distance to the end of the lenses, it is possible to arbitrarily position this micro volume within an material being investigated. This method is henceforth denoted confocal μ-XRF. When combined with energy scanning, also confocal μ-XANES measurements can be performed in this arrangement. The spatial resolution obtained with such an arrangement are dependent on the energy of the primary and of the fluorescent radiation being employed and are situated in the 10–40 μm range (Bjeoumikhov & Chevalier 1998, Janssens et al. 2004, Kanngießer et al. 2003).

Since the introduction of the second lens before the detector causes the detected net count rate to decrease by a factor 10 or more, instead of using the highly monochromatic form of excitation required for x-ray absorption spectroscopy studies, also 'pink-beam' mode can be employed. In this case, the Si<111> crystals of the monochromator are replaced by a pair of multilayer-coated reflectors. These reflectors select a relatively wide energy band ($\Delta E/E \approx 10^{-2}$) out of the excitation spectrum, leading to a primary beam intensity that is ca. 30–50 times higher than is the case of monochromatic excitation.

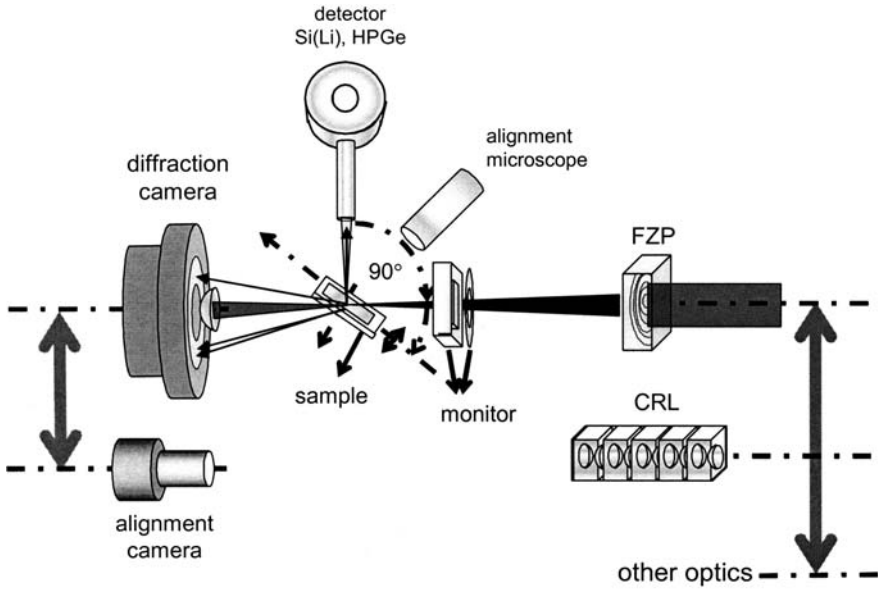

Figure 6. Schematics of a combined μ-SRXRF, μ-SRXRD setup at ESRF ID18F.

2.1.1.6 *Combined μ-SRXRF and μ-SRXRD*

At undulator beamlines of 3rd generation synchrotron facilities, only photons within specific energy-bands (undulator harmonics) are produced with which it is possible to perform combined μ-SRXRF/μ-SRXRD experiments. In Figure 6, a schematic of the experimental arrangement at ESRF ID18F is shown (Somogyi et al. 2001.). After the monochromator, the beam is focussed onto the sample by means of a Compound Refractive Lens (CRL); an additional pin-hole is used to reduce the scatter background in the sample area and to define the beam in the horizontal direction. In this manner, beam sizes as small as $0.5 \times 0.9\ \mu m^2$ can be obtained. Also with other optics, such as pairs of curved mirrors, beam sizes of these sub microscopic dimensions can be produced.

Next to energy-dispersive x-ray detector, at right angles to the primary beam, behind the sample, a wide angle x-ray diffraction camera can be placed. This camera allows to record the diffracted beams generated in the sample up to a scattering angle 2θ of ca 40°. By scanning a sample through the beam, simultaneously local composition information (from the generated XRF spectrum) as well as structural information (from the two-dimensional diffraction pattern) can be recorded.

2.1.2 *Total-reflection XRF*

When x-rays impinge upon an (optically) flat material under a very small angle (typically a few mrad), i.e., nearly grazing the surface, total external reflection occurs. This means that instead of penetrating the material, the x-ray photons will only interact with the top few nm of the material and then be reflected. Material that is present on top of the reflecting surface will be irradiated in the normal manner, and will interact with both the primary and the reflected x-rays. The major difference between conventional EDXRF and TXRF therefore is the excitation geometry. In the standard case of EDXRF the angle between the primary incident radiation and the sample is 45° while the detector is placed normal to the incident beam so that the angle between sample and detector is also 45°. The principle set-up of TXRF is shown Figure 7. As is the case for micro-XRF, TXRF measurements are also performed at synchrotron radiation sources, where the additional advantages associated with high intensity, the parallel nature and the polarized character of the radiation lead to improved performance.

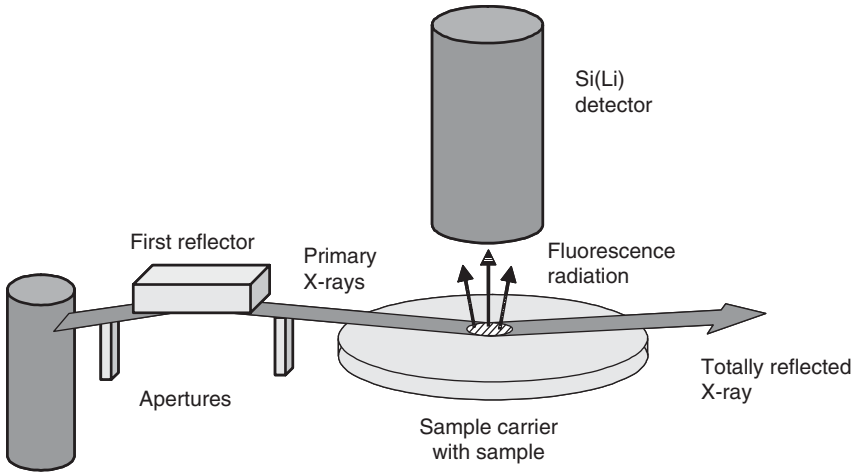

Figure 7. Schematic layout of a TXRF spectrometer.

The main advantages of TXRF are:

(a) The background caused by scattering of the primary radiation on the substrate is reduced.
(b) The fluorescence intensity is doubled as the primary and reflected beams pass through the sample giving efficient excitation.
(c) The distance between the sample on the reflector surface and the detector can be made small, thus the solid angle for detection is large.
(d) Depending on the x-ray source and the spectral modification devices, the absolute limits of detection are in the pg range for instruments employing 2–3 kW x-ray tubes and in the fg range when synchrotron radiation excitation is used.

2.1.3 *Quantitative XRF analysis*

With the exception of TXRF, all forms of x-ray fluorescence analysis suffer from matrix effects, i.e., the observed net x-ray intensity of a specific element is not only a function of the concentration of the analyte element itself but also depends of that of the other constituents. This effect is caused by the absorption of x-rays in the sample and by fluorescence enhancements when the radiation is emerging from the sample. In samples with non-ideal homogeneity, the texture and size of the particles that constitute a porous sample may significantly influence the observed x-ray signals. Thus, in XRF very frequently curved rather than straight calibration curves are obtained; only in case of the analyses of trace constituents in a constant matrix, in which the absorption and enhancement effects are constant or of very thin foil samples, in which no such non-linear phenomena occur, is the quantification of XRF signals relatively straightforward. The same applies to the quantification of TXRF data, where the equivalent of 'thin' samples is being analyzed.

Accordingly, a variety of correction and calibration models and procedures is in use in x-ray spectrometry based on (a) standard addition and dilution, (b) thin-film samples, (c) matrix dilution, (d) comparison to type standards, (e) internal standard elements and (f) mathematical corrections. A number of these procedures are destructive in nature (for example because they require dissolution of the material to be analyzed) and therefore are not always applicable to analyses of cultural heritage materials. In these situations, the so-called 'fundamental' approaches to the quantification problem in XRF are frequently employed. Here, knowledge on x-ray physics is employed to model all x-ray matter interactions in the sample in an attempt to correct for the matrix effects. Among the software packages that are available, a distinction can be made between those making use of (sometimes sophisticated) interpolation strategies between x-ray intensities derived from a large

number of standard samples strongly resembling the unknown materials (e.g., a series of Cu-containing alloys when bronzes are analyzed, a series of glass standards in the case ceramics are studied) (De Vries & Vrebos 2002) or the software models that are based on a detailed knowledge of the XRF spectrometer response to different materials (He & Van Espen 1991).

2.2 *X-ray diffraction*

When a monochromatic x-ray beam of wavelength λ is directed at a single crystal, then, as a result of constructive interference between waves that are elastically scattered by periodically spaced planes of atoms, only one or two diffracted beams may result. The angle 2θ under which the diffracted beam is observed relative to the original beam is given by Bragg's law:

$$2d \sin\theta = n\lambda$$

where d is the interplanar distance in the crystal and n is the diffraction order. When the crystal is now rotated around the impinging beam so that the angle between the diffracting planes and the primary beam remains the same, then the reflected beam will describe a cone with the crystal at its apex. The same effect can be obtained when instead of rotating a single crystal, the irradiated material consists of hundreds to thousands of very small crystals, all having a random orientation of their own. The diffracted beams are then seen to lie on the surface of several cones. A circle of film can be used to record the diffraction pattern. Each cone intersects the film giving rise to arcs on the film. For every set of crystal planes, by chance, one or more crystals will be in the correct orientation to give the correct Bragg angle to satisfy Bragg's equation. Every crystal plane is thus capable of diffraction. Each diffraction line is made up of a large number of small spots, each from a separate crystal. Each spot is so small as to give the appearance of a continuous line. If the crystal is not ground finely enough, the diffraction lines appear speckled.

This is the basis of the Debye-Scherrer or powder method of x-ray diffraction; it is probably the most commonly applied method in x-ray crystallography. The powder method is used to accurately determine the value of the lattice parameters of a crystal.

In x-ray diffraction instruments, a (quasi) monochromatic beam is normally employed to irradiate the samples, unless a form of energy-dispersive diffraction is being employed. In instruments employing laboratory sources, the wavelength of the radiation is fixed and (usually) equal to the most intense emission line of the x-ray tube anode being used.

In its simplest form, the powder diffraction camera consist of a metal cylinder at the centre of which is placed the sample (see Figure 8). Powdered material is typically glued to a glass rod with an amorphous type of adhesive. A strip of x-ray film can placed inside the cylinder with two holes punched into it: one for the primary beam to enter the camera and a second for the beam stop, diametrically opposed to the first. The camera enclosure must be light-tight and is placed in front on the x-ray beam.

When confronted with phase identification problems in the field of art and archaeometry, an additional difficulty may be the fact that only very small samples are available for analysis. Sample may be tiny single crystals or agglomerates of a few single crystals (Schreiner et al. 2004). The Gandolfi x-ray diffraction camera allows non-destructive analysis of single crystals smaller than 100 micrometers in diameter via the recording of the equivalent of a powder pattern. To obtain this pattern, a single grain or crystal is doubly rotated in the x-ray beam in order to sequentially expose all available atomic planes to diffracting positions. A schematic of the Gandolfi camera is shown in Figure 9. It closely resembles a Debye-Scherrer camera. The sample in mounted on the tip of a needle that is mounted at 45° to the camera axis Ω. The needle rotates around its own axis (Φ-rotation) as well as around the camera axis. Requiring a sample barely visible to the naked eye, this technique is capable of identifying the mineral constituents of minute samples of paint, used, e.g., by prehistoric artists or applied in very thin layers by easel painters. Recently, a Gandolfi camera equipped with an image plate detector has been developed (Otto et al. 2002).

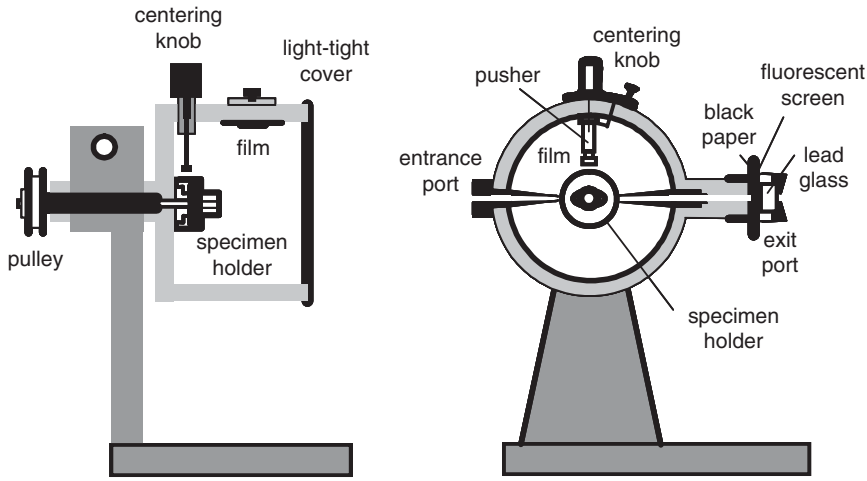

Figure 8. Apparatus for Debye-Scherrer recordings: (left) side view, (right) front view.

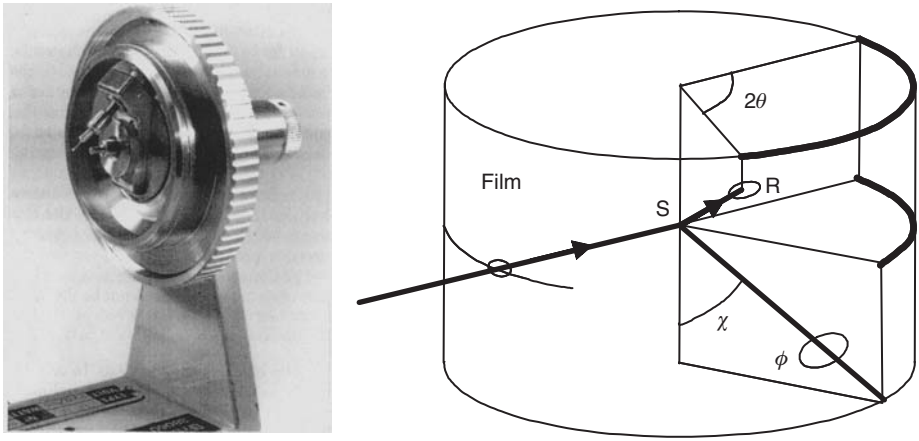

Figure 9. (left) Photograph and (right) schematic of the Gandolfi camera. The diffracted beam hits the film at R. The angle χ (which can be freely chosen in a 4-circle diffractometer) is fixed at 45° while the specimen rotates about the Ω and Φ axes.

At synchrotron beamlines, usually, either x-ray diffractometers that make use of imaging plates (i.e., laser readable and erasable x-ray sensitive surfaces), x-ray sensitive CCD cameras or Geiger/scintillator counters as x-ray detectors are employed (Salvadó et al. 2002). The latter are normally mounted in computer-controlled and commercially available 4-circle diffractometers that only require the crystal to be aligned in the x-ray beam; the instruments software will autonomously measure and refine unit-cell dimensions, record all reflections out to a maximum θ-angle and store their intensities. In combination with the use of micro-beams, often the use of a fixed CCD camera (see Figure 6), mounted behind the sample to collect diffraction signals in transmission geometry is sufficiently to perform power-diffraction data acquisition for phase identification on a local scale. In some cases, rotation and/or translation of the sample is required to collect 'powder'-like diffractograms of series of (sub) microscopic crystals, as typically encountered in stratigrafies of paint layers (Hochleitner et al. 2004).

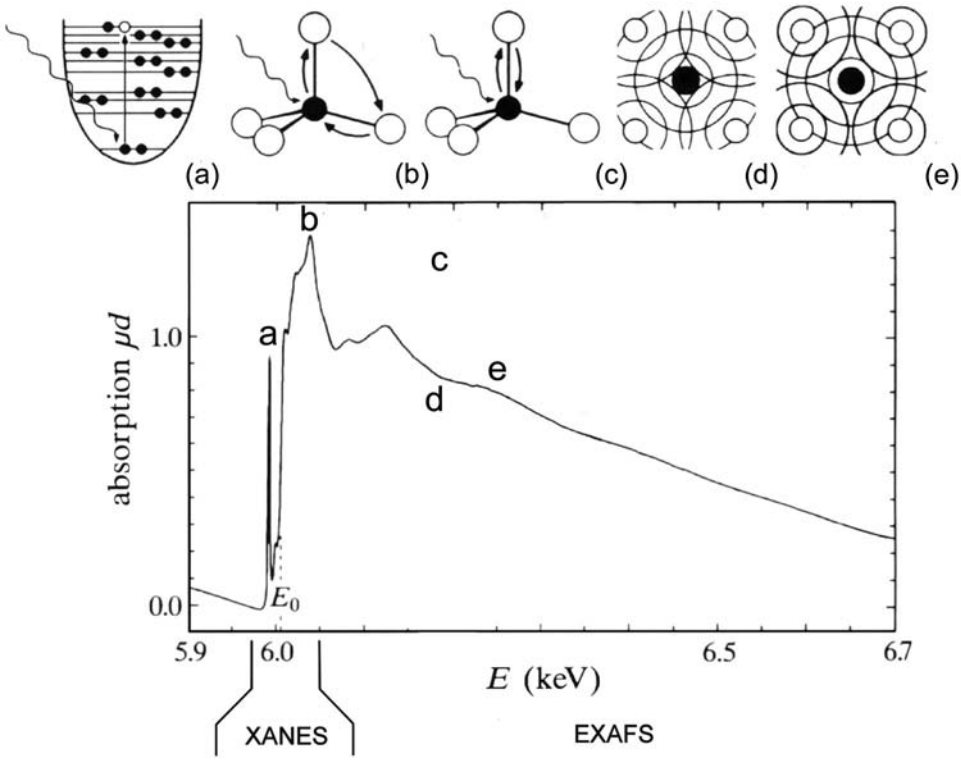

Figure 10. Cr-K edge x-ray absorption spectrum of K_2CrO_4; the physical processes leading to the different features of an x-ray absorption spectrum are indicated, as well as the XANES and EXAFS regions. (a) Pre-edge peak(s) caused by transitions to unoccupied orbitals, (b) multiple scattering peaks, (c) single scattering region showing oscillations on the absorption curve caused by (d) destructive interferences and (e) constructive interference between the outgoing and back-reflected photo-electron waves.

2.3 *X-ray absorption spectroscopy*

The mass absorption coefficient μ vs. energy curves of the elements feature sharp discontinuities, called absorption edges, corresponding to the energies required for electronic transitions from deep core levels to the vacuum level. However, when one considers in more detail the shape of the $\mu(E)$ vs. E curves in the immediate vicinity of these edges (see Figure 10), additional features become apparent. X-ray absorption spectroscopy (XAS) is a method that employs this fine structure to extract information on the chemical environment of the absorbing atom.

In an x-ray absorption experiment, a monochromatic x-ray beam is directed at the sample. The photon energy of the x-rays is gradually increased such that it traverses one of the absorption edges of the elements contained within the sample. Below the absorption edge, the photons cannot excite the electrons of the relevant atomic level and thus absorption is low. Transitions at energies E smaller than the binding energy E_0 occur only when the absorbing atoms possesses localized unoccupied (or only partially occupied) states, for example d-orbitals in the case of transition metals (see Figure 10a). When the photon energy is just sufficient to excite the electrons ($E = E_0$), then a large increase in absorption occurs known as the absorption edge. At x-ray energies higher than E_0, transitions to continuum states take place, i.e., to electronic states not localized on the absorbing atom. The resulting photo electrons have a low kinetic energy and can be backscattered by the electron shells of the atoms surrounding the emitting atom (see Figure 10c–e).

The photo electrons (with kinetic energy $E - E_0$) leaving the atoms can also be regarded as an expanding spherical wave with wavenumber k given by:

$$k = \sqrt{\frac{2m_0}{\hbar^2}(E - E_0)}$$

An x-ray absorption spectrum is typically divided into two energy regions: the x-ray Absorption Near-Edge Structure or XANES region, which extends from a few eV below an element's absorption edge to about 50 eV above the edge, and the Extended x-ray Absorption Fine Structure or EXAFS region, which extends from about 50 eV to as much as 1000 eV above the edge (Figure 10). The XANES region is also sometimes referred to as the Near-Edge x-ray Absorption Fine Structure or NEXAFS region. The range just before the edge is called the pre-edge region (see Figure 10a). The physics of the processes responsible for XANES and EXAFS spectral features is different; thus, these spectral regions provide different types of information about an element and its local environment.

XANES can provide information about vacant orbitals, the electronic configuration and site symmetry of the absorbing atom. The absolute position of the edge contains information on the oxidation state of the absorbing atom. In general, with increasing oxidation state of the central atom [e.g, Mn^o, Mn^{+2}, Mn^{+3}, …, Mn^{+7}], the absorption profiles shifts towards higher energies by a few eV per oxidation state. In the near edge region, multiple scattering events dominate (see Figure 10b). Theoretical multiple scattering calculations can be compared with experimental XANES spectra in order to determine the geometrical arrangement of the atoms surrounding the absorbing atom. Hence the technique provides complementary information to EXAFS.

The basis physical process leading to the oscillations of the absorption in the EXAFS region is the interference between the photo electron wave leaving the emitting atom with its backscattered equivalents, as pictorially represented in Figure 10b and c. Depending on the wavelength (i.e., on the energy of the ejected photo electron) of the interfering waves and on the distance between the central atom and the backscattering neighbours, the interference can be constructive, leading to a higher value for the absorption coefficient (see Figure 10b) or destructive, giving rise to a lower value for (Figure 10c) relative to the case when the central atom would not have any backscattering neighbours. The net result is a series of oscillations on the high photon energy side of the absorption edge, called the x-ray absorption fine structure (XAFS).

After transforming the energy scale of the XAS spectrum to wave numbers, the EXAFS oscillations $\chi(k)$ are isolated from the total absorption coefficient curve by fitting a 'background absorption' curve $\mu_0(k)$ to it and using the expression:

$$\chi(k) = \frac{\mu(k) - \mu_0(k)}{\mu_0(k)}$$

The different coordination shells around the absorbing atom each contribute to the total EXAFS signal. By means of a Fourier transformation, $k^n \cdot \chi(k)$ (where n is an integer, e.g., 2 or 3) the contributions can be sorted, yielding a radial distribution function (RDF) around the absorbing atom. This function shows peaks at the distance where the neighbouring atoms that cause the EXAFS oscillations are situated. The RDFs contain information on the environment of the absorbing element out to ca. 5 Å. By isolating and individually fitting the contributions to $\chi(k)$, the true interatomic distances and number of neighbouring atoms per shell can be determined.

XAS generally requires a synchrotron x-ray source for several important reasons:

– A high x-ray flux is required in an XAS experiment in order to obtain high signal-to-noise data in a reasonable time frame (of the order of 30–40 minutes per spectrum). This requirement is particularly critical if the element of interest is at low concentration in a sample. Synchrotron sources provide x-rays of five or more orders of magnitude greater flux than conventional laboratory x-ray sources.

– A broad spectral range at uniformly high flux is required because a typical x-ray absorption spectrum covers about 1000 eV. Tuneable monochromators with appropriate d-spacings can be used to scan through a broad range of energy; thus one can choose the most appropriate energy range for an experiment.
– High stability in flux, energy, and beam position is required in an XAS experiment and can be achieved with a synchrotron x-ray source.

The main advantages of XAS over those of other structural methods are its element specificity and the fact that it can be used with practically any atom in any state of organization (solid, liquid, or gas). In addition, the sensitivity of XAS can be at the tens-hundreds of ppm level of an element, so that it can be used to study the structural environment of an element at trace levels in a chemically complex matrix. These attributes coupled with its ability to provide quantitative information on interatomic distances and the number and identities of atoms in the first and, in favourable cases, the second shell around an absorber, make XAS an extremely versatile and often unique probe of an atom's local environment. The local nature of the XAS probe is both an advantage (e.g., XAS is particularly useful in studying the environment of atoms in amorphous materials where there is no long-range order and where x-ray scattering methods suffer from lack of element specificity) and a disadvantage (e.g., XAS provides essentially no information on long-range order in a solid, including cation order-disorder among non-equivalent sites in a crystal structure). Disadvantages of XAS relative to x-ray diffraction includes a limited resolution for sets of similar bond lengths and a high sensitivity to disorder.

In order to produce the highly monochromatic radiation required for x-ray absorption spectroscopy, a double crystal monochromator consists of two parallel crystals mounted on a common rotation table can be used. The mounting is such that the diffraction angle θ can be continuously varied (see Figure 4bc). The first crystal selects the wavelength (and its higher order overtones) while the diffraction at the second crystal ensures that the monochromatic beam regains a horizontal direction. In between the sample and the monochromator, x-ray focusing optics of various types can be placed in order to concentrate the x-ray beam in the horizontal and/or vertical direction. The experimental setup shown in Figure 4b allows to simultaneously record XAS data in two manners:

Absorption XAS. The most straightforward mode of operation is to directly record the intensity of a monochromatic beam before and after (a homogeneous) sample as a function of energy E by means of two ionization chambers (see IONI1 and IONI2 in Figure 4bc) and calculate the $\mu(E)$ vs. E curve:

$$\ln\left(\frac{I(E)}{I_0(E)}\right) = -\mu(E).\rho d$$

where the sample areal density $\rho\, d$ is a scaling factor that usually is normalized out.

An ionization chamber essentially consists of two isolated parallel metal plates between which a voltage (several 100 V) is applied. The electrical current flowing between the two condensator plates is proportional to the flux I of the x-ray beam that passes in between. XAS data will sufficiently signal-to-noise ratio can be obtained when (a) the absorption in the sample is not too large so that $I(E)$ and $I_0(E)$ do not differ too much and (b) the concentration of the absorbing element is high enough ($>$0.1 % w/w) so that a significant difference between $I(E)$ and $I_0(E)$ can be recorded.

Fluorescent XAS. When the sample under investigation is so strongly absorbing (or so thick) that the transmitted intensity is no longer measurable or when XAS data from a minor/trace constituent are to be recorded, instead of directly measuring the absorption, one of the signals produced as a result of photo-electric absorption can be recorded as a function of the primary energy. By means of the energy-dispersive detector, positioned at 90° to the primary beam (see Figure 4bc), the fluorescence intensity profile $I_{fl}(E)$ vs. E can be recorded. When the absorbing element is not too strongly concentrated ($<$0.1–0.5%), the normalized fluorescent intensity $I_{fl}(E)/I_0(E)$ is proportional to $\mu(E)$, provided appropriate dead-time corrections etc. are taken into account. An alternative to detection of the fluorescent intensity is to record the total electron yield (TEY), i.e. to

measure the number of (photo)electrons emitted by the sample during the irradiation as a function of the primary beam energy *E*. The TEY mode of detection is especially useful at low primary energies and when low atomic number elements are studied.

3 CASE STUDIES

3.1 *Compositional analysis of historic glass*

The composition of glass, produced from prehistoric to the modern ages has been subject to a number of distinct changes, depending on the raw materials available and the state of glassmaking technology and know-how. Thus, chemical analysis of excavated glass fragments can be very useful for gaining information on glass making technology and/or glass trade in different periods. X-ray based methods has been used extensively for analyzing this type of material (Wobrauschek et al. 2000, Jokubonis et al. 2003, Aerts et al. 1999, 2003, Hoffmann et al. 1994, 2000) next to other (trace-level) methods of (micro)analysis.

For some time now the composition of glass objects found in the European region and the Near East has been known to be very similar for the period of the Roman Empire and beyond into the 8th and 9th centuries (Sayer & Smith 1961, Velde 1990, Sanderson et al. 1984). The components of these glasses are basically sodium, and silica. Small amounts of alumina (generally near 2.5 weight percent) and calcium oxide (between 6 and 8%) are characteristically present in these glasses also. Low magnesia and potash contents (less than 1.5%) distinguish these from other sodic glass types. This Roman glass composition seems to have been in fact discovered during the Hellenistic period (Dussart & Velde 1990). Hence the small range of compositional variation of this glass produced over a long period (1000 years or more) is striking. It is reasonably well accepted now that the glass for this period was produced as a raw material somewhere in the Middle East and worked to produce finished products at various sites near to the point of their use (Henderson 1985). Several studies has been published that attempt to document the occurrence of glass with this typical Syro-Palestinian composition in various period of time and geographical locations throughout Europe. In natural high quartz sands, minor elements can be concentrated as heavy minerals. These minerals are classically used as tracers of source materials in geological research. The same approach can be used in investigating the silica components of Roman glasses. Heavy minerals in sands are those which are chemically inert under the ambient aqueous conditions of geological cycles. These minerals are iron oxides such as magnetite and iron titanates such as ilmenite, or silicates such as zircon. Other elements such as Rare Earth Elements (REE) and Y can be included in zircons or more specific REE phases such as monazite (Patyk-Karar et al. 1999).

The Celtic La Tène Culture (ca 500-0 BC) achieved highly specialized glass manufacture. Bracelets and ring-beads made out of glass were in common use at the beginning of the middle La Tène period. The art of glass working was one of the new technologies adopted by the eastern Celtic tribes (located around the upper Danube) during the second half of the third century BC. Glass jewellery appears to have been manufactured in many workshops in different places in the large area of the La Tène culture. Thus, archaeologists find it difficult to identify the workshops the artefacts originated from while there is a controversy whether or not the Celts produced the basic glass (primary workshops) or only reworked glass (secondary workshops) that was imported from Mediterranean sources. In order to investigate to what extent clues on the manufacturing technology of the glass can be derived from (variations in) its chemical composition, a series of ca 250 artefacts from the Middle and Late La Tène period (denoted LT-C1 – LT-D1, ca 250-50 BC), excavated at archaeological sites in North-Eastern Austria were analyzed by means of direct excitation EDXRF (Wobrauschek et al. 2000). Glasses of different colours, opaque or transparent, in the form of beautiful ornaments were studied; some examples are shown in Figure 11. However, most artefacts were represented by small fragments only. The Celtic glasses were on loan for the time of analysis from museums and private collections under the guarantee that no harm would be done to the objects. The main goal was to establish a reliable analytical method to achieve qualitative

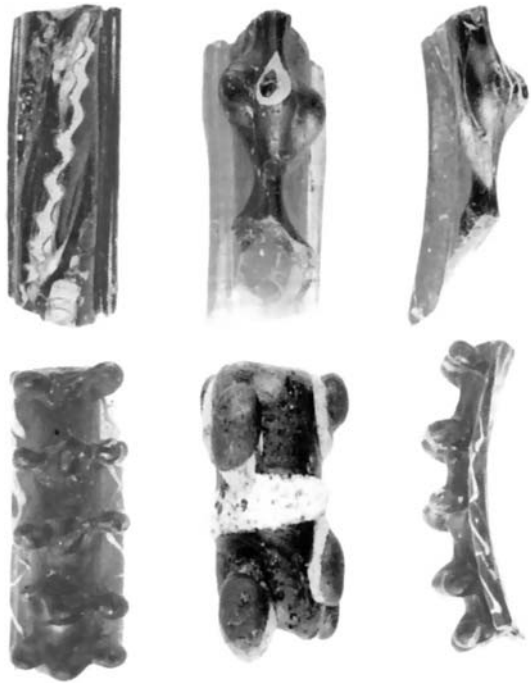

Figure 11. Fragments of Celtic glass fragments.
(This figure is presented in the signature in colours at the end of this volume, Appendix, pg. 328).

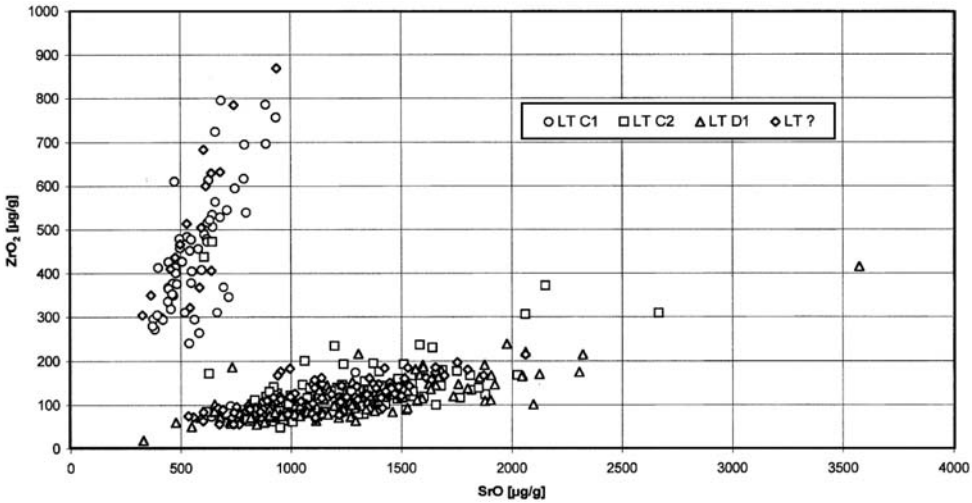

Figure 12. Zr vs Sr concentration is Celtic glass fragments of different time periods. Circles: objects of La Tene C1 period (ca 250-180 BC), squares and diamonds: La Tène C2 and D2 periods (180-50 BC) and diamonds: objects belonging to the LT C1 – LC C2 period (~250-120 BC).

and quantitative results within acceptable errors. To this effect, a special plastic sample holder was designed in which the fragments could be reproducibly positioned, exposing the desired section of the glass samples to the x-ray beam. A systematic investigation of the influence of the orientation of the sample, the height of the artefacts in the spectrometer and their surface roughness, carried

Table 1. Compositional categories found in a series of Roman glass samples from Qumrân, Israel. Uncertainties represent standard deviation of concentration in each group.

	Group 1a (n = 45)	Group 1b (n = 5)	Group 2 (n = 9)
in % w/w			
Na_2O	16.4 ± 0.4	16.3 ± 0.6	17.2 ± 0.35
MgO	0.23 ± 0.13	0.07 ± 0.13	0.01 ± 0.01
Al_2O_3	2.5 ± 0.1	2.4 ± 0.1	2.4 ± 0.3
SiO_2	69.5 ± 0.6	70.9 ± 1.6	71.7 ± 0.4
P_2O_5	0.08 ± 0.04	0 ± 0	0.02 ± 0.04
SO_3	0.16 ± 0.11	0.2 ± 0.07	0.17 ± 0.07
Cl	0.82 ± 0.07	1.06 ± 0.05	1.16 ± 0.05
K_2O	0.84 ± 0.06	0.61 ± 0.11	0.58 ± 0.12
CaO	8.41 ± 0.6	7.54 ± 0.42	5.52 ± 0.60
TiO_2	0.05 ± 0.04	0.02 ± 0.02	0.04 ± 0.04
MnO	0.43 ± 0.06	0.09 ± 0.09	0.84 ± 0.13
Fe_2O_3	0.52 ± 0.06	0.39 ± 0.13	0.33 ± 0.04
in ppm w/w			
Cr_2O_3	12 ± 12	9 ± 8	23 ± 27
NiO	7 ± 5	8 ± 8	15 ± 7
CuO	209 ± 95	83 ± 137	50 ± 43
ZnO	35 ± 19	18 ± 13	26 ± 7
Br	7 ± 11	7 ± 4	8 ± 7
Rb_2O	14 ± 4	13 ± 3	12 ± 3
SrO	637 ± 145	570 ± 137	534 ± 130
Y_2O_3	9 ± 2	8 ± 3	6 ± 1
ZrO_2	79 ± 17	59 ± 15	63 ± 16
Mo_2O_3	3 ± 2	0 ± 0	3 ± 1
SnO_2	113 ± 49	52 ± 21	56 ± 34
Sb_2O_5	354 ± 190	1 ± 1	29 ± 31
BaO	234 ± 127	151 ± 92	151 ± 59
PbO	156 ± 64	13 ± 9	17 ± 14

out with standard reference glasses, revealed that errors in quantitative analysis up to 20% relative can be made, especially for the light elements Na-Si. The historical fragments themselves are sufficiently homogeneous to permit quantitative analysis with the above-mentioned limitations. From the analysis results, it could be concluded that the Celtic glass is of the soda-lime type, the most common in the Ancient World. The elements Co, Fe, Cu and Mn were used as colorants while the use of Sb and Mn as decolourants was also noticed. To opaficy the glass, Pb and Sb additives were employed. When the quantitative results of glass fragments are considered (Jokubonis et al. 2003), Sr and Zr allow to subdivide the data into two groups, which may be associated with different sources of sand and lime.

Aerts et al. (1999, 2003) have investigate the major, minor and trace element concentrations of ca 499 samples of Roman blown glass objects found in Qumrân (Israel), Mancetter and Leister (England), Rouen (France), Trier and Cologne (Germany) and Oudenburg, Grobbendonk, Tongeren, and Maastricht (Belgium). They used a combination of EPXMA (for the major components) and μ-SRXRF (for the minor and trace constituents) to analyze these samples. In order to reduce uncertainties due to surface corrosion or contamination, in all cases, minute glass fragments were removed from the excavated objects, embedded in resin and polished flat. As mentioned above, glass from the Roman era shows a remarkable constancy in composition. This is also the case for the Qumran samples, where among the series of ca 100 analysed samples, only two to significant subgroups could be distinguished (see Table 1): group 1 has a CaO content of 8%, against 5% for group 2. This difference in composition may be related to the origin of the natron (a Na_2CO_3-rich

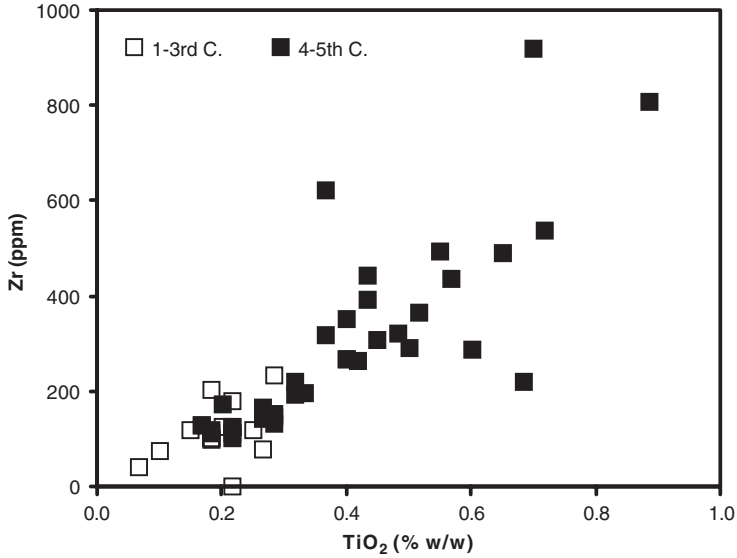

Figure 13. Relation between Ti and Zr contents of Roman glass excavated in Maastricht in different time periods.

deposit used a raw material for the glass making) or the sand that was employed. To verify the compositional homogeneity of the glass in both groups, next to EPXMA measurements, the trace composition (down to the 1–10 ppm level) of the fragments were determined by polychromatic μ-SRXRF. When also the trace concentrations are employed for performing a cluster analysis, the two groups previously found are obtained, except that within group 1 (Ca-rich), a subgroup containing 5 objects with a much lower Sb concentration is identified (group 1b). The distinction between groups 1 and 2 is more clear since in the trace-element fingerprint, significant differences in the average concentration of the elements Cu, Sn, Pb and Sb are found. All these elements are associated with the colour of the glass: Cu, Sn and Pb probably originate from bronze chips which may have been intentionally added to the glass melt to give it a green colour while Sb was used to decolorize the glass. Together, major and trace-element data indicate that the entire series of ca. 100 glass vessels found at the Qumrân site originated from one or two workshops and were probably purchased together. This information supports the hypothesis (Donceel-Voûte 1994) that at this site perfumes and ointments were manufactured on a large scale, requiring large number of small glass vessels as containers.

When the major and trace element concentration profiles of the glass samples from the German and Belgian sites are considered, again the composition typical for the Roman and post-Empire glasses found in Europe is encountered, confirming the constancy of the sources of raw materials used for glassmaking. However, in the trace element fingerprint of some 4–5th century and later specimens there is evidence of the use of a different source of silica (sand) component. As shown in Figure 13, zirconium and titanium are the discriminating elements. The data derived from 278 specimen from 1–4th century German and Belgian samples indicate a strongly homogeneous Zr and Ti content. Likewise, 62 samples from Maastricht show low Zr - Ti contents for 1–3rd century samples but 4–5th century samples show a strong trend of concomitant Ti and Zr increase. If the high values of Zr-Ti are considered to represent a new source of silica (sand) the trend from low to high content suggests that a significant amount of low Zr-Ti glass was re-cycled to form these glass objects. A similar high Ti content can be seen in analysis results reported for other but not all 4–5th century samples found in northern Europe while earlier productions show typical low Ti contents (Bezborodov 1975). Although the fusing agent for these glasses seems to have always been natron

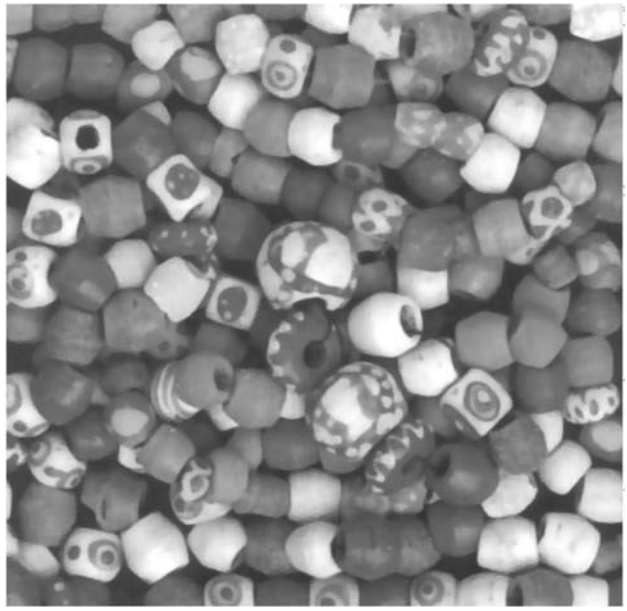

Figure 14. Glass beads recovered from Merovingian graveyards.
(This figure is presented in the signature in colours at the end of this volume, Appendix, pg. 328).

(a mineral deposit in the Nile delta) from Hellenistic times to the 9th century, a change in the silica source, indicated by variation of the Ti and Zr content, could very well reflect the results of political instability of the 4–5th century exemplified by the fragmentation of the Roman Empire into two parts.

Hoffman et al. (2000) have used a polarized EDXRF system to make an extensive study of the composition of multicoloured Merovingian Beads, found in great quantities in graves in the neighbouring sites of Eichstetten-Wanneberg and Endingen-Diehl, in the Upper Rhine region near Kaiserstuhl and the Black Forest (Germany). These sites were occupied by the tribe of the Alamani. About 300 beads from the period 570–670 AD were analyzed, showing the colours white, yellow, orange, green, blue and brown (see Figure 14). Each bead was analyzed using different secondary and polarized targets to get information on the element groups Na-V, Cr-Sr, Zr-Ba that were determined by means of the K-lines. Additionally the elements W-Bi and U were determined by means of their L-lines. For calibration of the instrument, various soda-lime and lead glass standards were employed. For the analysis, double-cone beads that offered a fairly flat surface for analysis of several mm^2 were selected. Per colour, a typical XRF spectrum was obtained, as shown in Figure 15. Also here, the glass has a soda-lime composition, with Na_2O, SiO_2 and CaO as main components, but also containing MgO, Al_2O_3, Fe_2O_3 and MnO. In a number of individual cases, next to compositional information, XRD was employed to identify the colouring agents; in the case of green or blue collared samples, no diffraction reflexes could be observed (Hoffman 1994). In the white beads, the pigments SnO_2 (and sometimes $Ca_2Sb_2O_7$) was found, in the orange Cu_2O, in the green beads CuO, SnO_2 and PbO and in the brown ones Fe_xO_y, metallic Cu, SnO_2 and PbO. When the colouring elements were stripped from the obtained compositions, in all color groups, glass with the same matrix composition, consisting of ca $18 \pm 2\%$ NaO_2, $68 \pm 3\%$ SiO_2 and $8 \pm 1\%$ CaO was encountered. By comparison of the composition measured at the surface by means of EDXRF with that obtained via EPXMA on a cross-sectioned beam, a deficit of Na_2O and an excess of Al_2O_3 was observed at the surface of the orange and brown beads. This change in composition is due to surface corrosion that took place during the storage of the beads in the soil. A comparison of the glass matrix composition with literature data on Roman, 10th–17th C.

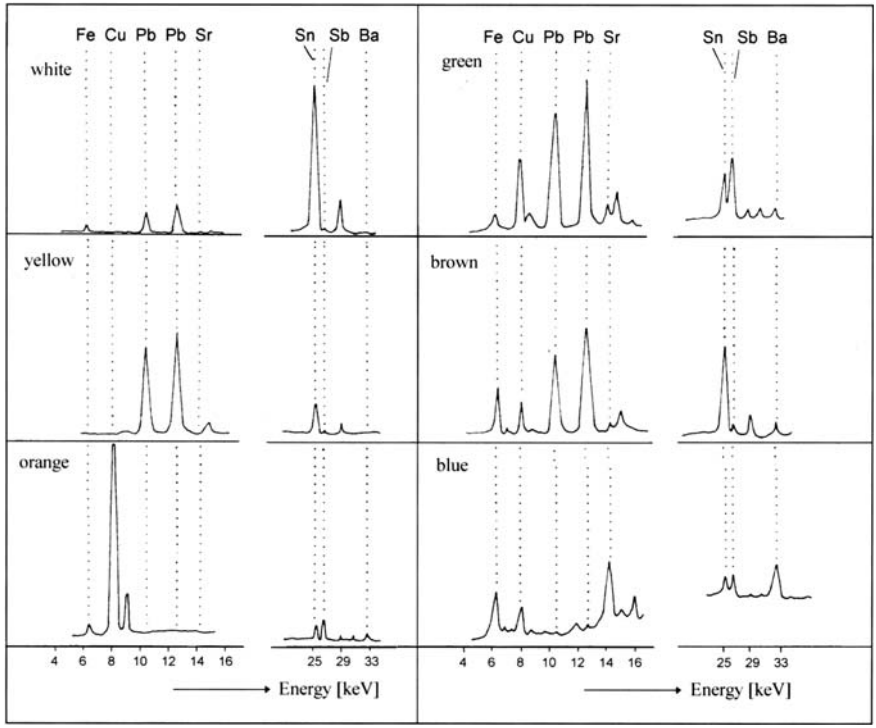

Figure 15. EDXRF spectra of glass beads of the various colour groups.

Italian and medieval French glass revealed a strong resemblance of the Merovigian beads to the antique and 10th–13th C. Italian glass. At least the same recipe and raw materials appear to have been used for the manufacture of the beads; the question whether the glassware was manufactured by the Merovigians, bought from the Romans or made with recycled Roman glass could not be answered. However, some of the encountered compositions are so complex from a chemical (e.g., redox reactions) or glass technical point of view that is difficult to believe that the Alamani possessed the requisite knowledge for obtaining such a material. The probability of accidental or empirical discovery of the effects of mixing specific components, heating them to certain temperatures and keeping stable reducing or oxidizing conditions is also most improbable in case of the Alamani.

In the early 16th C, the port of Antwerp (Belgium) was the most important one in Europe and an intense exchange of people and goods with many parts of the world took place. From 1541, an Italian dynasty of glass makers, originating from the North of Italy and in particular from Venice, started activities in Antwerp, importing and reproducing Venetian glass products. De Raedt et al. (1999, 2000, 2001) investigated the composition of a colourless 'Façon-de-Venise' glass vessels recovered from various cities in the Low Countries (such as Antwerp, Maastricht, Breda, Amsterdam) with the aim of determining the importance of the local glass production, relative to the import of vessels from Venice. Some of the vessels shapes are shown in Figure 16.

In Venice, two types of high quality transparent glass, called 'Vitrum Blanchum' and 'Cristallo' were produced. As can be seen in Figure 17a, in Antwerp, four distinct compositional groups of soda-lime glass are encountered in the 16th–17th C., next to potash and woodash based glass (not shown in the figure) (Deraedt et al. 1999). These data were obtained by means of EPXMA of minute, polished glass samples, that were removed from the archaeological fragments. Two of the four groups (marked MA and FDV) have compositions richer in CaO than the Venetian glass types and can be considered to be local production (De Raedt et al. 2000). One group (marked AVB)

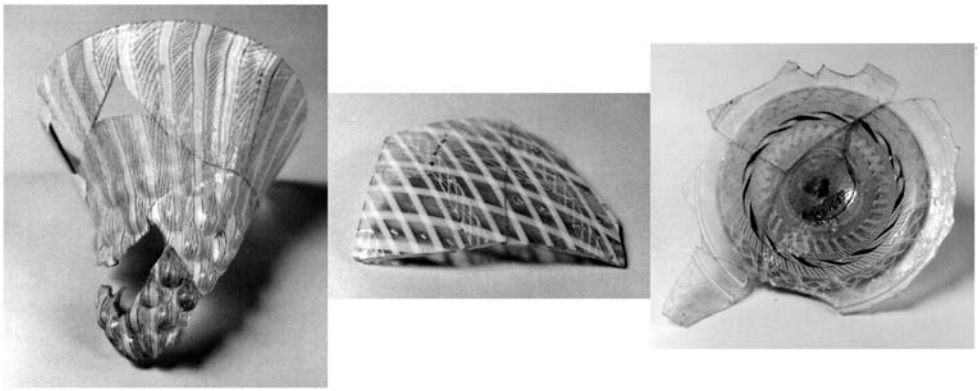

Figure 16. Photographs of some of the Façon-de-Venise vessels (belonging to the VVB group) excavated in Antwerp.

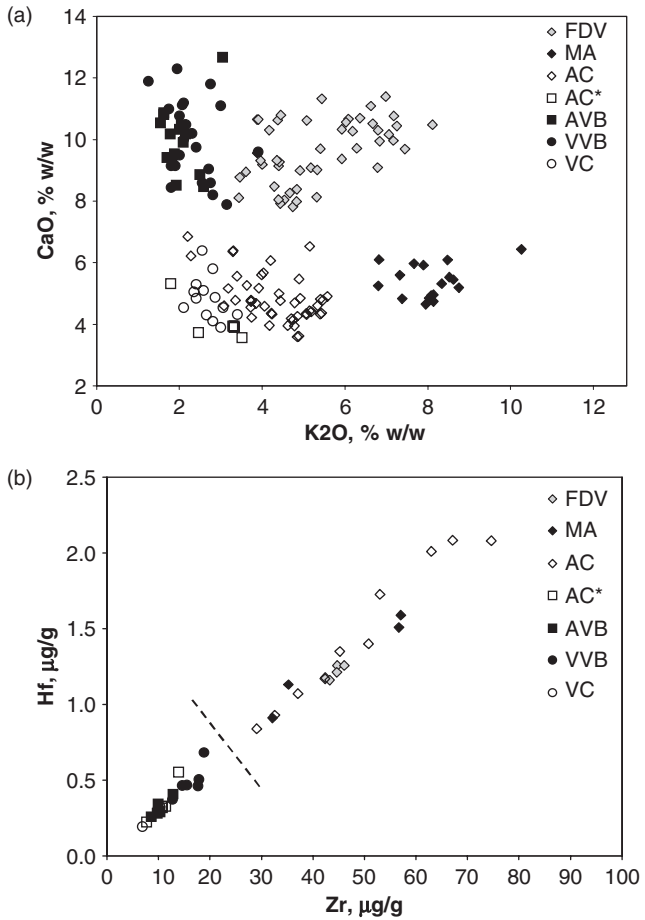

Figure 17. (a) CaO vs. K_2O content (in % w/w) of Façon-de-Venise glass vessels excavated in Antwerp (Belgium); (b) a Hf vs. Zr plot (in µg/g) allows to distinguish between Venetian and Antwerp production, resulting from differences in the silica-source.

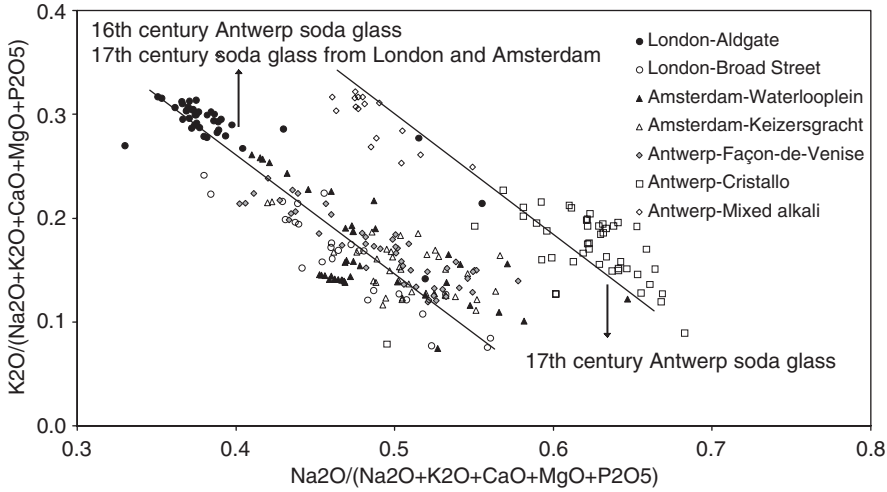

Figure 18. Flux composition plot of 16–17th C. glasses excavated in Antwerp and various neighbouring cities.

has a composition corresponding to that of Venetian Vitrum Blanchum and also shows the same trace element fingerprint. The group marked AC is similar in major composition to the Venetian Cristallo (VC) but on average is richer in K_2O and shows a trace element fingerprint that more resembles that of the other Antwerp groups than to that of the Venetian ones, as illustrated in Figure 17b (De Raedt et al. 2001). The trace element information was partially determined by means of μ-SRXRF analysis of the same glass samples used for the EPXMA analyses.

At the end of the 16th C., the Low Countries were split into an independent Northern part, with Amsterdam as its capital, while Antwerp remained part of the Habsburg empire and was cut of from trade. At this time, many artists and artisans, among which glass makers fled Antwerp to neighbouring urban centres such as London and Amsterdam. When the composition of the flux used for making the 16–17th C. glass vessels that were excavated in Antwerp, London and Amsterdam, is compared as in Figure 18 (i.e., vessels from before and after the above-mentioned political changes), it is possible to distinguish two series of compositional groups, having variable Na_2O and K_2O contents but in which the sum of these two flux constituents is more or less constant. Furthermore, it is striking to note that the glass types introduced in 16th C. Antwerp are found back in London and Amsterdam during the 17th C. while in Antwerp, other compositions were being used in that period, probably the result of restricted availability and/or increased prices of raw materials for glass making such as soda-rich ashes (De Raedt 2002).

3.2 *Pigments*

Essentially two x-ray based approaches to pigment analysis in painted works of art (oil paintings, fresco's, miniatures and illuminated manuscripts) can be distinguished: (a) the *in situ* approach where portable equipment is employed to irradiate a small part of a large artefact and (b) the *ex situ* approach where the pigmented layer(s) to be examined are sampled with minimal damage to the work of art and the resulting minute fragments or particles are examined by means of one or more techniques in specialized laboratories. For the detailed characterization of paint layer stratigraphies, traditionally small fragments are removed from oil paintings by means of a hollow needle or a fine scalpel. However, as outlined below, such a destructive procedure is not always necessary.

The pallet of inorganic pigments contains a wide range of different types with well-known chemical compositions (see Table 2). Inorganic pigments have been used for all colours of the artists' pallet because of their high colouring power and their stability against changes in temperature,

Table 2. Inorganic pigments and the key elements that can be used for their identification based on x-ray techniques (adapted from Klockenkämper et al. 2000).

Color	Pigment name	Chemical composition	Key element(s)
White	Antimony White	Sb_2O_3	Sb
	Lithophone	$ZnO + BaSO_4$	Zn, Ba
	Permanent White	$BaSO_4$	Ba
	Titanium White	TiO_2	Ti
	White Lead	$2PbCO_3 \cdot Pb(OH)_2$	Pb
	Zinc White	ZnO	Zn
	Zirconium Oxide	ZrO_2	Zr
	Chalk	$CaCO_3$	Ca
	Gypsum	$CaSO_4 \cdot 2H_2O$	Ca
Yellow	Auripigmentum	As_2S_3	As
	Cadmium Yellow	CdS	Cd
	Chrome Yellow	$2PbSO_4 \cdot PbCrO_4$	Cr
	Cobalt Yellow	$K_3[Co(NO_2)_6] \cdot 1.5H_2O$	K, Co
	Lead-tin Yellow	$Pb_2SnO_4/PbSn_{1-x}Si_xO_7$	Sn
	Massicot	PbO	Pb
	Naples Yellow	$Pb(SbO_3)_2/Pb_3(SbO_4)_2$	Pb, Sb
	Strontium Yellow	$SrCrO_4$	Sr, Cr
	Titanium Yellow	$NiO \cdot Sb_2O_3 \cdot 20TiO_2$	Ni, Sb, Ti
	Yellow Ochre	$Fe_2O_3 \cdot nH_2O$ (20–70%)	Fe
	Zinc Yellow	$K_2O \cdot 4ZnO \cdot 4CrO_3.3H_2O$	Zn, Cr
Red	Cadmium Red	$CdS + CdSe$	Cd, Se
	Cadmium Vermilion	$CdS + HgS$	Cd, Hg
	Chrome Red	$PbO \cdot PbCrO_4$	Pb, Cr
	Molybdate red	$7PbCrO_4 \cdot 2PbSO_4 \cdot PbMoO_4$	Pb, Cr, Mo
	Realgar	As_2S_3	As
	Red lead	Pb_3O_4	Pb
	Red ochre	Fe_2O_3(up to 90%)	Fe
	Vermilion	HgS	S, Hg
Green	Basic copper sulfate	$Cu_x(SO_4)_y(OH)_z$	Cu
	Chromium oxide	Cr_2O_3	Cr
	Chrysocolla	$CuSiO_3 \cdot nH_2O$	Cu
	Cobalt Green	$CoO \cdot 5ZnO$	Co, Zn
	Emerald Green	$Cu(CH_3COO)_2 \cdot 3Cu(AsO_2)_2$	Cu, As
	Guignent Green	$Cr_2O_3 \cdot nH_2O + H_3BO_3$	Cr
	Malachite	$CuCO_3 \cdot Cu(OH)_2$	Cu
	Verdigris	$Cu(CH_3COO)_2 \cdot nCu(OH)_2$	Cu
Blue	Azurite	$2CuCO_3 \cdot Cu(OH)_2$	Cu
	Cerulean Blue	$CoO \cdot SnO_2$	Co, Sn
	Cobalt Blue	$CoO \cdot Al_2O_3$	Co, Al
	Cobalt Violet	$Co_3(PO_4)_2$	Co
	Egyptian Blue	$CaO \cdot CuO \cdot 4SiO_2$	Ca, Cu, Si
	Manganese Blue	$BaSO_4 \cdot Ba_3(MnO_4)_2$	Ba, Mn
	Prussian Blue	$Fe_4[Fe(CN)_6]_3$	Fe
	Smalt	Co-glass (K_2O, SiO_2, CoO)	Si, K, Co
	Ultramarine	$Na_{8-10}Al_6Si_6O_{24}S_{2-4}$	Si, Al, Na, S
Black	Antimony Black	Sb_2O_3	Sb
	Black iron oxide	$FeO \cdot Fe_2O_3$	Fe
	Carbon/charcoal black	C (95%)	–(K)
	Cobalt Black	CoO	Co
	Ivory Black	$C + Ca_3(PO_4)_2$	P, Ca
	Manganese oxide	$MnO + Mn_2O_3$	Mn

climate and light. Each inorganic pigment is characterized by its color and by one or more constituting elements; when these key-elements are observed in the correct proportions, the pigment can be identified. Furthermore impurities can give information on the provenance and/or manner of manufacture of specific colouring materials. Since the chronological use of most pigments is known, it is possible in some cases to determine a approximate date for the genesis of painted historical objects. Due to the circumstance that some pigment appeared on artists' pallets after a certain time (post quem) or another pigment disappeared before that time (ante quem), it is possible to distinguish between original materials, restored parts or fakes (Longoni et al. 1998, Gao & Janssens 2004).

However, a number of problems render pigment identification by means of x-ray fluorescence or x-ray emission analysis alone difficult. A first difficulty derives from the fact that, as is apparent from Table 2, many pigments share key elements (e.g., the presence of the element Sb may point to the presence of antimony white or to that of Naples Yellow, that of Cu to many green or blue pigments) so that the observation of a specific element in the XRF spectrum cannot always be used as an unambiguous indication of the presence of a specific pigment. Especially in the case of Cu-containing greens and Fe-containing yellow-browns, the data provided by x-ray fluorescence or emission analysis is rather unspecific. A second problem has to do with the fact that during x-ray irradiation of artefacts that have been covered with more than one pigmented layer (e.g., varnish, ground and support layers next to one or more actual paint layers), the constituents of many (if not all) of these layers will contribute to the observed XRF spectrum. Strong x-ray lines of, e.g., a lead-white base layer may then obscure much weaker x-ray lines of the top-most layers while generally the interpretation becomes more cumbersome. Similarly, when pigments are mixed to obtain a particular color, the identification of the individual components can be rendered more difficult. In quite a few cases, however, the identification is unproblematic and the XRF method can even be used to determine the mixing ratio(s) of the original pigments. In other cases, specific measures need to be taken either (a) to increase the specificity of the analysis or (b) to limit the depth in the paint layer stack from which the signals in the XRF spectrum originate.

The use of compact portable XRF equipment for pigment identification has been described predominantly for the analysis of frescoes and ceramics (Moioli & Seccaroni 2000, Aloupi et al. 2000). With these works of art, usually a single pigmented layer covers a substrate material so that most of the observed XRF signals can straightforwardly be attributed to constituents of the collared layer. In some cases, however, also with frescoes, complicated stratigraphies can be encountered. For example, during the study of the frescoes of Giotto in the Chapel of the Scrovegni in Padova, Italy (Cesarao et al. 2004), it could be established by means of portable XRF and without any sampling that the golden haloes in these frescoes are composed of different layers: (a) a superficial layer of calcium sulphate, due to pollution, (b) an (on average) 1.6 μm thick layer of gold leaf, (c) a Cu-containing glue layer, having an equivalent Cu thickness of ca 1 μm, (d) a layer of white lead, having an equivalent Pb thickness of around 5 μm, (e) possibly a layer of azurite (Cu) and finally (f) the Fe- and Sr-containing plaster substrate. Bronk et al. (2001) have used the ARTAX spectrometer for studying the evolution of the use of pigments in enamelled objects of the 16th to the 19th C. where, e.g., the occurrence of Ni, As and Bi impurities in Co-blue enamels is indicative of a 16–17th dating of the objects while the absence of the former elements is observed in Co-blue enamel layers of objects (re)produced in the 19th C.

TXRF can be used for the analysis of minuscule amounts of pigments, removed from illuminated manuscripts by a virtually non-destructive sampling method. By means of this method, pigments from the top-most pigmented layer of (oil) paintings can be analyzed, provided the varnish layer is removed (e.g., during restoration activities) (Klockenkämper et al. 2000, Vandenabeele et al. 2000, Vandenabeele 2002).

XRD and the related method of small-angle x-ray scattering (SAXS) has been used recently to study and identify textile fibres from the Dead Sea caves (Müller et al. 2003). SRXRD has also been used to study the structure of the Maya Blue pigment (Chiari et al. 2003) and of Cu-green pigments used in the Gothic period (Salvadó et al. 2002).

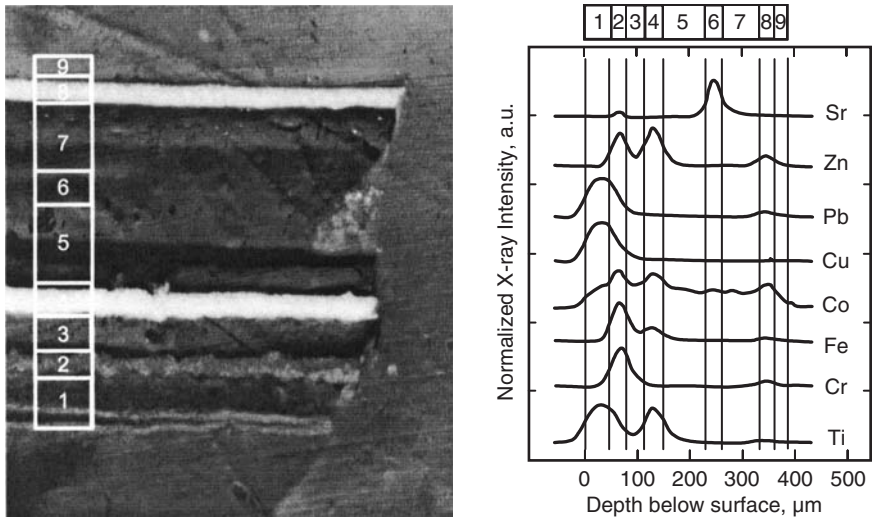

Figure 19. (left panel) (a) Car paint multilayer stack, consisting of a series of 9 (possibly 10) differently pigmented or transparent layers with thicknesses in the range 20–100 μm; (right panel) x-ray intensity depth profiles of various elements. The sample was analysed with the blue layer on top. Layer 1 (blue) can be observed to contain Ti, some Co, Cu and Pb; layer 2 (red) contains Cr, Fe, Cu, Zn and some Sr; layer 3 (black) is not associated with any strong XRF intensity; layer 4 (orange) contains Ti, Fe, Co and Zn, but less Fe and more Zn than layer 2, layers 5–7 (black) also do not show strong XRF signals, expect layer 6 that is associated with Sr and some Co; finally layer 8 (orange) shows a similar pattern as layer 4. Some of the signals originating from this deep layer (ca 350 μm deeper than the surface) are strongly absorbed by the layers on top of it. Layer 9 is a transparent varnish layer.

Analysis of paint multilayers by means of the confocal variant of μ-XRF is relatively new possibility which shows a lot of promise for application in the cultural heritage sector (Kanngießer et al. 2003); preliminary experiments on car paint multilayers, consisting of up to 9 different coatings showed that each layer could be non-destructively analyzed separately (see Figure 19). This method was also demonstrated to be applicable to quantitative analysis of complex paint layers stratigraphies encountered in 16th C. oil paintings (Smit et al. 2004).

3.3 *Lustre ware*

Pottery from the Middle Ages and Renaissance Era often is decorated with glazes showing gold and copper-coloured metallic reflections and iridescence. These effects are called lustre and consists of a metal deposition on a tin-opacified lead glaze that produces the brilliant metallic reflections of different color and iridescence (Caiger-Smith 1985).

The technique of lustre was developed by the Islamic culture in Mesopotamia, during the 9th century AD. Since Muslims were not allowed to use gold in artistic representations, a way was found to create the same effect without using real gold. It arrived in Spain during medieval times, following the expansion of Arabian culture. From there it was introduced into the centre of Italy, where it was exploited to produce polychrome lustre Renaissance pottery. Thus, lustre became one of the most important decorative techniques of the Medieval and Renaissance pottery of the Mediterranean basin.

Centuries later, the lustre is still visible thanks to the high quality of the film and its resistance to atmospheric oxidation and burial weathering. The specific optical properties of the films are the consequence of the presence of silver and copper nanoparticles, dispersed homogeneously in the glassy matrix of the ceramic glaze. To create these nanoparticles, artisans applied a mixture

of copper and silver salts and oxides, together with vinegar, ochre and clay, on the surface of previously-glazed pottery. The object was then placed in a kiln for heating to about 600°C in a reducing atmosphere. The high temperature caused the glaze to soften so that copper and silver ions could migrate into the outer layers of the glaze. In the reducing atmosphere, the ions reduced to metals which upon aggregation formed nanoparticles that gave rise to the desired colour and optical properties. Different recipes were used to obtain different luster colours, ranging from goldlike to copperlike. A red originates from the migration of copper ions and their subsequent reduction. In the case of gold shades, in principle only silver is needed, but craftsmen used both copper and silver. Researchers are still trying to find out why they used both materials and what procedure was employed, since copper needs higher temperatures than silver in order to stimulate the formation of nanoclusters. The lustre technique shows that craftsmen had an advanced technological and empirical knowledge of materials science.

Several techniques have been used to characterize the chemical and physical properties of these films. Detailed compositional information can be obtained by Rutherford Backscattering Spectrometry (RBS), while the optical properties can be investigated by optical absorption in the visible-ultraviolet region. By electron microscopy (TEM and SEM) it was possible to visualize the metallic particles present in the glaze; silver and copper nanocrystals can be well separated in TEM pictures. They are quasi-spherical, with a diameter between 5 and 100 nm. Silver nanocrystals, larger than copper ones, appear grouped together among copper crystals and close to the glaze surface.

From x-ray diffraction patterns, the crystalline phase of the particles could be derived. In order to determine the valence state of Ag and Cu and to describe the local atomic environment around the metallic species, x-ray absorption spectroscopy measurements were performed. This permitted to study the amorphous oxide phase in which the metals are present. Lustre samples of glazed Renaissance pottery (end of XV–XVI century) from Deruta and Gubbio, Italy were analysed (Padovani et al. 2003). Examples of luster pottery from these localities are on display in many important international museums, such as the Louvre Museum (Paris, France) and the Metropolitan Museum of Art, New York, USA. The lustre on the examined artefacts consists of a heterogeneous metal-glass composite film, some hundreds of nanometers thick, analogous to that present in the modern metal-glass nanostructured composites synthesized for high technology applications (Pérez-Arantegui et al. 2001, Borgia et al. 2002). It was found that in the case of red lustre, the color was mainly due to the presence of copper nanoclusters, while in the case of gold luster the color was caused by nanoclusters of silver. In the gold luster, Ag^{+}, Cu^{+} and Cu^{2+} ions are present, while in the red luster, according to the historical recipes (Kingery & Vandiver 1986, Piccolpasso 1976), the dominant ion is Cu^{+}. The nanoclusters are confined to the more external glaze while the oxidized forms are present at larger depths.

Figure 20 summarizes some of the XANES results obtained at the Cu-K edge (8979 eV). When XANES data are recorded in the fluorescence mode of detection, where the lustre layer is probed down to a depth of 50 μm, Cu appears to be predominantly present under an oxidized form (i.e., as Cu^{+} in Cu_2O, cuprite). However, if the total electron yield (TEY) mode of detection is used, where only the top 100 nm of the same lustre layer is analyzed, a different profile is obtained, showing the presence of Cu in the metallic state.

The analysis of the EXAFS spectra obtained for three red luster samples, performed in fluorescence mode, suggests the presence of copper coordinated by oxygen atoms at a distance of 1.86 Å, which is a distance very close to distance for the first shell of Cu_2O (1.85 Å). The Cu-O first shell coordination also shows a number of neighbours not very far from 2, the value shown by the Cu_2O standard.

In general, one can state that the chemical state and local environment of the Cu ions are similar to those found in copper-alkali ion exchanged silicate glass samples. This finding strongly supports the view that cluster formation is mediated by a copper- and silver-alkali ion exchange as a first step, followed by nucleation and growth of metal nanocrystals as a spontaneous process due to the super saturation of the elemental concentrations in the region where clustering occurs.

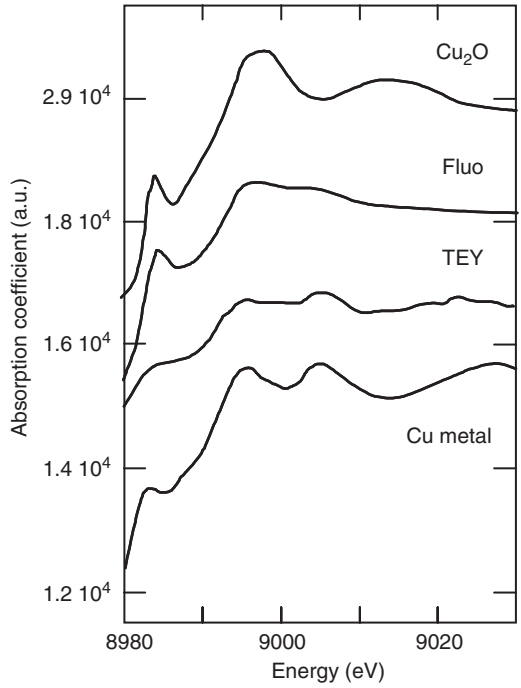

Figure 20. XANES spectra obtained in fluorescence (fluo) and total electron yield (TEY) mode of the red lustre, compared to the XANES profiles of Cu_2O and metallic Cu.

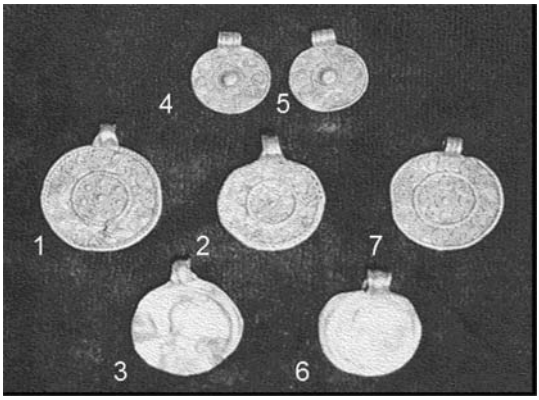

Figure 21. Series of 7 late-Roman gold medallions, fitted with attachment rings.

3.4 *Metallic artefacts*

COPRA, short for 'Compact Röntgen Analyser', is a fully-equipped μ-XRF instrument intended for easy transportation to museums and galleries. Bichlmeier et al. (2002) has used this instrument for the analysis of five golden medallions and two Roman coins (dated 550–575 AD) that were all fitted with small attachment rings (Figure 21). The questions regarding these artefacts were the elemental composition of the rings and medallions and whether different or identical gold alloys could be identified. The average compositions of the artefacts' rear sides and rings were obtained from three measurements on different spots (Table 3). The standard deviations of the Cu, Ag and

Table 3. Results of the micro-XRF analyses (wt%), average data for 3 measurements (40 kV, 0.8 mA).

	Back side				Ring			
% w/w	Fe	Cu	Ag	Au	Fe	Cu	Ag	Au
M1	1.0	0.5	8.6	90.1	1.5	1.3	8.3	88.8
M2	0.3	0.6	8.7	90.3	1.0	1.4	6.7	91.1
M3	1.5	0.4	1.2	96.9	0.9	2.4	8.6	88.0
M4	0.3	1.8	18.7	79.4	0.3	1.8	15.2	82.9
M5	0.3	1.7	18.4	79.6	0.2	2.0	15.0	83.0
M6	0.2	0.5	1.4	98.1	1.4	1.5	8.3	88.2
M7	1.4	0.6	8.1	90.3	8.5	3.0	8.8	79.9

Au concentrations were 2–8%. This relatively small uncertainty allowed the grouping of identical artefact and ring materials according to their compositions.

For example, the prominent high silver content of medallions M4 and M5 leads to the conclusion that both belong to one group; also, their composition of gold and copper match well. The composition of the bulk materials can be combined easily with the shape of the objects: Both Roman coins (Figure 21, Nos 3 and 6), the two smaller medallions with a convex projection (Figure 21, Nos 4 and 5) and the three richly ornamented, large medallions (Figure 21, Nos 1, 2 and 7) consist of the same material. Also, the attached rings of the larger medallions and of the Roman coins show identical compositions. The standard deviations of the copper, silver and gold concentrations were fairly small (2–8%), while the standard deviation of the iron concentration was about 40%. A possible explanation is that iron particles may have been be introduced mechanically into the artefacts (e.g. by hammering) and therefore are distributed inhomogeneously. For this reason, the iron concentration was not be considered further. For the gold artefacts it was assumed that the rings of medallions 1 and 2 were attached in the manufacturing process, whereas medallion 7, which shows distinct signs of mending, was repaired subsequently. The mounting of rings on the Roman coins took place in a second step of production, since the material of the bulk and of the eye do not have the same composition. This implies that the coins originally used as currency were transformed into pendants and not manufactured in one piece. There was no apparent distinction between the rings and medallions M4 and M5, so that it was not possible to determined if the rings were attached originally or subsequently. It was possible to distinguish different rings materials: those of medals M4 and M5 show the same composition, and also M1, M2, M3 and M6. Owing to this grouping it can be assumed that medallions M1 and M2 were made from the same material and therefore in the same workshop where coins M3 and M6 were modified.

The above-described studies concerned investigations of materials that could either be sampled or where the complete object could be easily brought into the laboratory. Sometimes, however, the analytical instrument must be brought to the objects. During an exhibition of ancient gold artefacts from the Iranian National Museum in the Kunsthistorisches Museum (Vienna, Austria), a number of these valuable items were analyzed *on site* by means of the COPRA instrument. The complete set-up of the instrument took ca. 45 min. 5 objects were analyzed in various places with the aim of determining the type of gold alloy they were manufactured from and in order to document possible difference in origin of these objects. The spectra data were calibrated against a series of Au/Ag/Cu standards (Ögussa, Austria). The average compositions are summarized in Table 4. Quasi-straight line calibration curves between observed x-ray intensities and the concentration of the above-mentioned elements were established. Since it concerns a metallic matrix, the obtained concentration data was normalized to 100%. Three of the objects are made in fine gold (pure Au with some Cu present) while two others are made in different Au/Ag/Cu alloys. The variability of the composition within most objects was small. In Figure. 22, a photograph taken during the irradiation of one of the artefacts (a griffin) is shown. In this case, the object is positioned before the x-ray beam by means of a manual laboratory stage. When combined with a motorized stage, the

Table 4. Average composition derived from *in situ* irradiation of five Iranian Au artefacts.

Object	Number of analysis points	Au (%)	Ag (%)	Cu (%)	Other lines (not quant.)
Lion	18	98.8	0.0	1.2	Fe
Griffin	8	99.0	0.0	1.0	Fe
Bracelet	9	99.2	0.0	0.8	K, Ca, Fe
Beaker	3	64.8	31.7	3.4	Fe
Seal	5	83.6	12.4	4.0	Fe

Figure 22. Use of the COPRA instrument for in situ (i.e., in the museum gallery) analysis of a gold artefact.

control software of the instrument allows for coordinated sample stage movement and spectrum collection, so that, e.g., element distributions along a line on the specimen surface can be recorded.

The COPRA instrument is currently installed at the Academy of Fine Arts, Vienna, Austria. Other types of cultural heritage artefacts that were investigated with it include Medieval brass and bronze burial artefacts (Cu, Zn, Sn), early 20th C. decorated glass objects (Mn, Fe, Co, Ni, Zn, Sn), daguerreotypes (Cu, Au, Ag), differently pigmented areas of 18th C. illuminated parchments (Ca, Mn, Fe, Cu, Au, Pb) and various manuscripts from the 13th to the 19th C. of the Austrian State Archives prepared with ferro-gallic ink, next to modern car paints, multi-collared beads and industrial materials (Vittiglio et al. 2004).

For the chemical characterization of corrosion compounds analysis on ancient bronze objects, De Ryck et al. (2003) have compared different micro beam techniques. They include optical microscopy, SEM-EDX, secondary ion microscopy, synchrotron-based FTIR, synchrotron-based XRD and XANES. The objective was to investigate which combination of analysis methods is most suitable for this type of investigations, taking into account aspects such as limited sampling and the ability of obtaining spatial information. These authors state that XRD in combination with optical microscopy and SEM-EDX is able to provide a complete description of the layered structure both on the elemental and on the molecular level.

3.5 *Analysis of graphic documents*

Historical objects such as documents, illuminated manuscripts and collared prints are not only valuable objects of cultural heritage but also documents of human history. The knowledge about historical materials is very important to answer archaeometrical questions and to develop and/or refine restoration and conservation concepts.

Historic inks contain, next to the constituents that are responsible for its colour (e.g., carbon/soot in bistre-type inks, Fe in ferro-gallic inks, …) also impurities of various nature. Together, these non-essential components of the inks can form a characteristic fingerprint that can provide information on the manufacturing technology of the ink or that can be used to investigate additions, alternations and or falsifications made in different inks to historical documents.

Haller and Knöchel (1996) and Mommsen et al. (1996) compared the concentrations of Cu and Pb in ink of the Gutenberg Bible to that of other early single leaf copies and books. The pioneering work with PIXE by Cahill et al. (1981, 1984) identified the (x-ray based) analysis of ink as a new research tool for the history of early printing (from the second half of the 15th century) (Kusko & Schwab 1987, Schwab et al. 1983). It is assumed that each printer/printing-office can be recognized by a specific ink-preparation as reflected in the trace element signature of the dried ink. The recipes for the ink were kept as a secret; in the 15th century, not a single specification of composition is documented (Bloy 1967).

Mommsen et al. (1996) employed a $0.5 \times 1\,mm^2$ polychromatic x-ray beam derived from the synchrotron storage ring ELSA (Bonn, Germany) for irradiating single leaves of early 15th century printed paper. Ink and paper of 22 different works from different locations in Germany, Italy and Switzerland were analyzed. The energy deposited in the paper during the measurements (300 s) was estimated to be ca. $15\,\mu W/cm^2$, i.e., about a factor 70 lower than bright sunlight.

Comparison of the spectra from paper and paper/ink combinations from page II,316 of the single leaf 42-line Gutenberg bible revealed that Ni, Cu and Pb are present in the ink at concentration levels of a few $10\,\mu g/cm^2$ while K, Ca, Ti, Mn, Fe and Zn originate from the paper base.

In six of the 22 leaves, printed areas could not be distinguished from blank areas, suggesting that the corresponding inks were prepared from mainly C-bearing material such as lampblack or soot (Bloy 1967). In some of the other inks, in addition to Ni, Cu and Pb, also K, Ca and Fe were present. On all analyzed pages except the Gutenberg leaf, the same ink composition on the recto and verso side were found. On the recto side of the Gutenberg B-42 leaf, the ink thickness was ca. 3 times larger than on the verso side, although both sides show the same Cu/Pb and Ni/Pb ratios (resp. 1.0 ± 0.5 and 0.007 ± 0.003). For the same page (II, 316) of the Harvard Gutenberg bible, by means of PIXE recto and verso Cu/Pb ratio's of 1.15 ± 0.05 and 1.44 ± 0.07 were reported (Mommsen et al. 1996, Cahill et al. 1981, Cahill et al.1984, Kusko & Schwab 1987).

For three specific printers, the constancy of their ink composition over large time intervals was tested by analyzing leaves of several books produced by them. They appear to have changed the composition of their inks fairly frequently. It therefore appears difficult to establish a definite trace element pattern specific for one printer. When only the trace elements which occur in the ink alone (and not in the paper) are considered, only Pb and Cu concentrations can be used for distinguishing between early printers.

As a result of this study, Mommsen et al. (1996) concluded that a systematic investigation of the ink composition in works printed 10 to 15 years after Gutenberg's first bible edition is needed to learn more about the early recipes for ink preparation and to find specific reasons for the presence of metallic impurities in the ink. The synchrotron based XRF method was found to be suitable for non-destructive measurements on this fragile type of material and appropriate for performing the large number of measurements required to reveal systematic trends in the composition of paper and inking.

Next to synchrotron-based XRF, also laboratory μ-XRF is an excellent technique for the analysis of valuable documents, for example to determine their authenticity. Typically, different inks, while having the same visible appearance, will have different chemical compositions. Larsson (Larsson 1991) and Stocklassa and Nillson (1992) described analysis by μ-XRF of a 500 year old Swedish

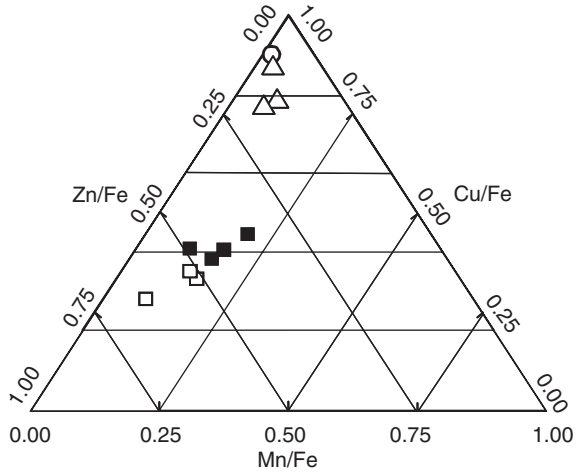

Figure 23. Analysis results of J.W. von Goethes manuscripts of Faust I and II by means of the ARTAX μ-XRF spectrometer. The two inks used in Faust I (squares) show a similar composition; the ink used for corrections to Faust I (triangles) is similar to that used for Faust II (circles).

possession letter (dated April l, 1499). The document, a sales contract for an estate, showed signs of alterations. It was suspected that the alteration was made in the 1530s, when the Swedish king restituted land back to certain nobles, who previously had been stripped of their estates by an earlier ruler. Although alteration was suspected by visual inspection (the original name of the owner had been removed by scraping), the original text was unreadable. By employing μ-XRF generated Ca and Zn-maps (a trace constituent of the original ink), the original name could be established however. In the Ca map, the (falsified) visible text was visible, featuring the family name "Gäsmestad i Böre"; in the Zn map of the same area, however, a completely different text reading "Bøtinge i Asbo" could be read. Obviously, the forger used different ink for the alteration, accounting for the change in chemical makeup.

In Figure 23, the elemental ratios Mn/Fe, Cu/Fe and Zn/Fe obtained by means of μ-XRF investigations of Goethes manuscripts of Faust I and Faust II are intercompared. Folios GSA25/XVII,2,12; GSA25,XVII,1,2; (Faust I, original and corrections) and GSA25/XVIII,5,7 (Faust II) were examined by means of the ARTAX spectrometer at the Goethe und Schiller-Archiv (Weimar, Germany), yielding fingerprint spectra of the inks. It can be observed that the two inks employed by Goethe to write Faust I have a similar composition. The ink used for the corrections to Faust I are similar to the ink employed for writing Faust II, indicating that Goethe did not modify the first part until working on the second part. These and other valuable manuscripts (e.g., music scores by Bach and Mozart) also have been examined in the context of oxidative corrosion inflicted to the paper by ferro-gallic inks (Fuchs et al. 2000).

The ARTAX spectrometer was also used to investigate the pigments used for coloration of two similar copper engravings of Albrecht Dürer (Kupferstichkabinett, Berlin, Germany) entitled "Petrus und Johannes heilen einem Lahmen" (Peter and John healing a cripple). Both 16th C. prints were collared at a later time. μ-XRF analysis revealed that one of the prints (KK Berlin Inv.-Nr. A137) was collared with pigments such as azurite (blue), malachite (green), white lead, cinnabar (red), ochre (yellow-brown), red lead, gold water colour and crayon, consistent with a coloration made in the 16th–17th C. In the second print (KK Berlin Inv.-Nr. A551), however, zinc oxide red and chromium green pigments were encountered, pointing to a coloration in the 19th century (Denker et al. 2003).

Silver point drawings belong to the most precious and rarest treasures of print collections. They were essentially created during the Renaissance and are characterized by extremely thin grey-brownish strokes on paper that had been coated before use. So far, only little chemical information

on these drawing materials could be obtained because the drawings are very delicate, and, therefore, analyses are very difficult to perform without any damage. A chemical fingerprint can be obtained by the determination of ratios of selected elements, reflecting not only the origin of the used materials but also the processing and the storage conditions. In order to precisely characterize the chemical composition of drawings by Albrecht Dürer (1471–1528) and Jan van Eyck (ca. 1395–1441), Reiche et al. (2004a, 2004b) employed synchrotron radiation induced μ-XRF.

3.6 *Mn oxidation in odontolites*

In the Middle Ages, Cistercian monks created odontolite, a turquoise-blue gemstone, by heating fossilised mastodon ivory found in 13–16 million year old Miocene geological layers next to the Pyrenees. They thought they had produced the mineral turquoise because of the resemblance of odontolite with this semi-precious stone. Odontolite was used for the decoration of medieval art objects such as the reliquary bronze crosses. Fossilised ivory and its mysterious colour change upon heating have been investigated by several naturalists and gemmologists, among them Réaumur (1683–1757). Reiche et al. (2001) investigated odontolite decorations on a 13th. C cross made in a Limoges workshop. Although vivianite, a blue-coloured iron phosphate, or copper salts were proposed to be the colouring phases, none of these minerals were found in the odontolite material. Rather, it consisted of fluorapatite, $Ca_5(PO_4)_3F$, containing trace amounts of iron, manganese, barium, lead, rare earth elements and uranium and presenting crystallites of 100 to 500 nm in size. The crystal size was about 10 times larger than that of unheated fossilised ivory and suggested that odontolite was heated at about 600°C (Reiche et al. 2000). As potential colouring agents manganese and iron were then studied. Luminescence and optical spectroscopy permitted the exclusion of iron as a colouring ion and suggested that manganese ions could be responsible for the colouration of odontolite. XAS was employed to follow changes in the local environment and the valence state of manganese on heating. XANES and EXAFS spectra were recorded at the K-edge of manganese impurities (200 to 650 ppm) in fluorapatite which is a strongly absorbing matrix at this energy (6.5 keV). An energy resolution of 0.4 eV, realized by using the a Si(220) monochromator of ESRF Beamline ID26, was used to measure the position and the intensity of the pre-edge structure of manganese. They indicate most clearly the changes in the structural environment and oxidation state of manganese. Unheated (white) fossil ivory showed Mn^{2+} ions in octahedral coordination while in the (turquoise-blue) fossilised ivory heated at 600°C and in the two odontolite samples, the major part of the manganese was found to be in the 5+ oxidation state as indicated by the pre-edge structure observed at 6541.3 eV. In addition, a comparison of the XANES spectra of heated fossilised ivory, odontolites and a reference synthetic Mn-chlorapatite indicated that the Mn^{5+} substitutes for P^{5+} at the tetrahedral sites; in such a coordination Mn^{5+} ions gives rise to an intense turquoise-blue colour.

On the basis of the XANES data (see Figure 24), it could be concluded that the transformation of white mastodon ivory into turquoise-blue odontolite involves two phenomena: (1) a fossilisation accompanied by an uptake of metal ions, specifically Mn ions (Mn^{2+}), possibly by sorption on apatite crystallites; and (2) a deliberate heating process in air above 600°C that oxidises Mn^{2+} into Mn^{5+}, which substitutes for P^{5+} in the tetrahedral site of the apatite structure. This substitution occurs during the heat-induced crystal growth of apatite. Thus, the origin of the colour change in fossilised ivory during heating could clearly be demonstrated using x-ray absorption spectroscopy and, in contrast to former hypotheses, it could be shown that odontolite owes its turquoise-blue colour to traces of Mn^{5+} ions in a distorted tetrahedral environment of four O^{2-} ions.

3.7 *Therapeutic and cosmetical chemicals of ancient Egypt*

The funerary furniture discovered in Egyptian tombs, dating from between 2000 BC and 1200 BC, provides a lot of information about the customs of everyday life in Ancient Egypt (Lucas & Harris 1963). Among these objects there was an abundance of toilet accessories: mirrors, hairpins, eyeliner

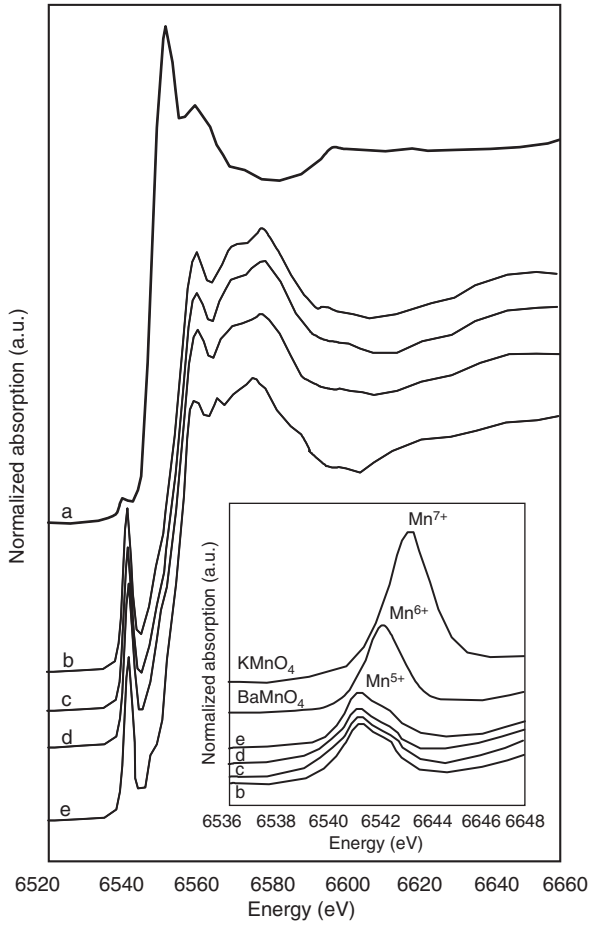

Figure 24. Mn K-edge XANES spectra of: (a) fossilised ivory; (b) 600°C heated fossilised ivory; (c,d) turquoise-blue collection odontolites and (e) synthetic apatite $Ba_5(PO_4)_{2.5}(MnO_4)_{0.5}Cl$ taken as reference mineral with Mn^{5+} in tetrahedral coordination. Inset: Pre-edge structure of tetrahedral Mn^{5+} in (b) heated fossilised ivory; in (c, d) odontolites and in (e) synthetic $Ba_5(PO_4)_{2.5}(MnO_4)_{0.5}Cl$, are observed at 0.9 eV and 1.9 eV below those of tetrahedral Mn^{6+} in $BaMnO_4$ and Mn^{7+} in $KMnO_4$, respectively.

applicators, combs or spatulas, and make-up receptacles, some of which are now preserved in the Egyptian Department of the Louvre Museum (Figure 25).

Inside these 3–4000 year old containers made of marble, alabaster, wood or reed, cosmetic powders in an exceptionally good state of conservation were found. In order to obtain information on their composition and the methods used in their elaboration, the organic fractions of the cosmetics were analyzed by chromatographic techniques and the mineral content by Scanning Electron Microscopy, FTIR spectrometry and powder XRD (Walter et al. 1999). Conventional quantitative laboratory XRD was impeded by several factors: (a) owing to the high archaeological value of the powders, only small quantities could be extracted and analyzed; (b) the as-found cosmetics are highly absorbing mixtures of lead-based compounds; (c) most mixtures contained as many as 10 phases, i.e. the resulting diffractograms display a complex series of overlapping Bragg lines. Measurements carried out at two synchrotron beamlines (ESRF BM16 and LURE DW22) were able to take advantage of the high flux, the high energy and the high resolution of the exciting radiation. The Rietveld refinement method was applied to determine the respective crystalline phase mass fractions. Taking into account the anisotropic line profile of some phases, it was possible

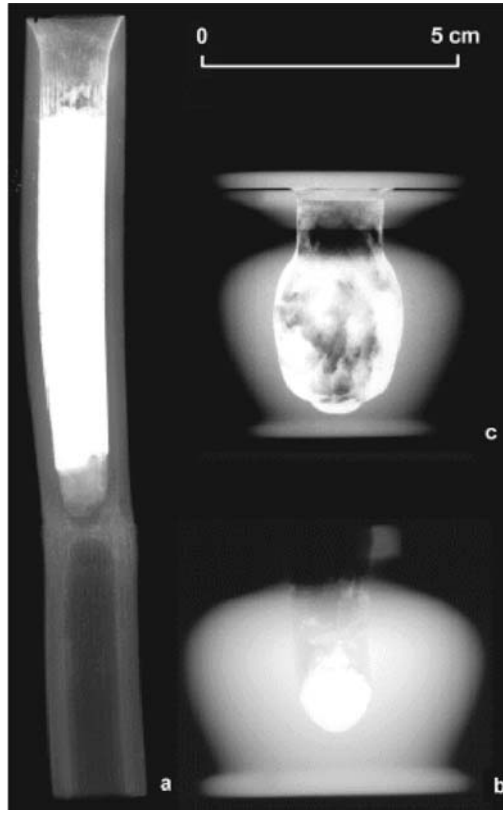

Figure 25. X-ray radiography of different make-up receptacles from the Egyptian collections of the Louvre Museum. The white areas show the distribution of the x-ray absorbing lead powders present in the make-up. (a) Reed case, still full of make-up; (b) alabaster recipient with a fabric lid; (c) alabaster recipient and cover. It contains a small amount of make-up attached on the inner wall.

to significantly improve the fit agreement factors (to less than 10%) and it was possible to detect quantities of minerals down to 0.5% (see Figure 26).

Two natural compounds bound with some animal grease were identified: crushed ore of black galena (PbS) and cerussite ($PbCO_3$). Galena is still the basic constituent of many khols traditionally used in North Africa, Asia and the Middle-East nowadays. White cerussite was added to the composition in order to obtain a grey-to-white make-up. Rietveld analysis of the XRD patterns of the mixture revealed the presence of two more white constituents: laurionite (PbOHCl) and phosgenite ($Pb_2Cl_2CO_3$). These products are very rare in nature and could not have been extracted from the mines in sufficient quantities for the preparation of the cosmetics. These products could have been formed by chemical alteration and ageing, assuming the original content of the make-up receptacles had been in contact with carbonated and chlorinated waters. However, no clear trace and no evidence of such alteration processes could be found in any of the 49 recipients.

Therefore one major conclusion of the work was that laurionite and phosgenite were intentionally manufactured by the Egyptians. The texts of Pliny the Elder and Dioscorides (first century AD) report on a number of medical recipes. In particular some of them refer to the use of lead oxide that was ground and diluted into salted and sometimes carbonated (natron) water. This wet process was mimicked in the laboratory. By maintaining the solution at a neutral pH, a slow reaction yields white precipitates of either laurionite or phosgenite. This is the first indication that wet chemistry has been practiced since 2000 BC.

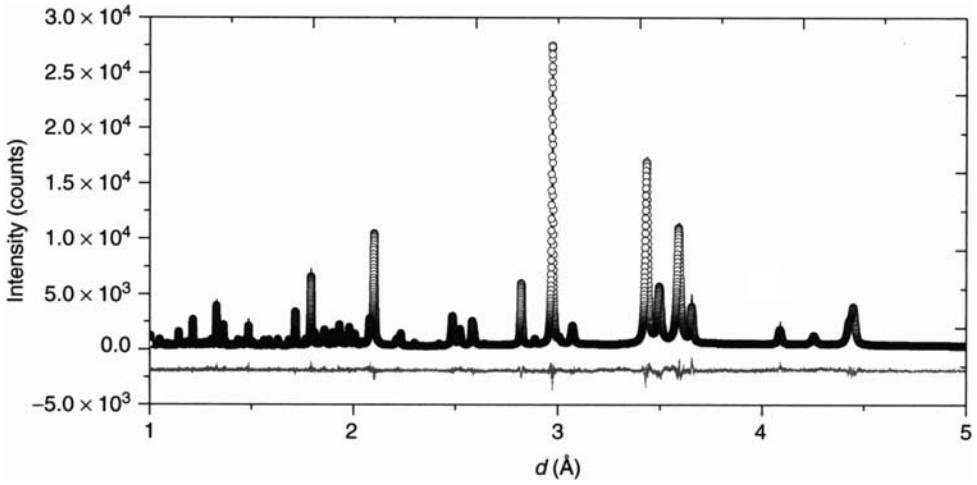

Figure 26. XRD pattern of a sample of Egyptian cosmetic powder (black curve) and Rietveld refinement. Open circles: calculated pattern on the basis of four components: black galena (PbS), cerussite ($PbCO_3$), phosgenite ($Pb_2Cl_2CO_3$) and laurionite (PbOHCl) (all white); grey curve: residual.

The reason for adding the white lead derivatives PbOHCl and $Pb_2Cl_2CO_3$ to black PbS, instead of white cerussite ($PbCO_3$) is that since the earliest periods of Egyptian history, cosmetics were not only employed for aesthetic purposes, but also for their therapeutic and magic/religious properties. Greco-Roman texts mention, e.g., that white precipitates synthesized from PbO are appropriate for eye and skin care; these lead compounds could be used as a bactericide and as a protection for the eye against exposure to the suns rays.

The width of the diffraction peak profiles also permitted to compare the strain and crystallite size in archaeological, synthetic and natural powders (Martinetto et al. 1998, Ungar et al. 2003). XRD peak breadth analysis combined with SEM observations showed that the PbS ore present in the cosmetics was ground and sorted according to grain size. The resulting granulometry of galena provided the make-up with the expected texture and its metallic brightness. By contrast the Bragg line broadening of PbOHCl and $Pb_2Cl_2CO_3$ is free from any strain: this suggests that they have been directly synthesized as fine powders and have not been prepared by crushing. In this manner, the XRD line broadening related with the crystallographic microstructure contributed to a better understanding of the origin and the process of elaboration of the archaeological powders.

The same authors also studied the effect of Pb-containing cosmetics on the structure and composition of ancient hair samples, obtained from different Egyptian mummies, by means of x-ray micro beam techniques (Bertrand et al. 2002). In native hair, the lipids as present as calcium soaps; μ-XRF and μ-XRD investigations performed at ESRF ID22 and ID13 showed that appropriate lead treatment considerably enhances the organized lipid features in hair (Bernard et al. 2003). The elemental micro-analysis of Egyptian mummy hair cross-sections, compared to native modern hair, showed a significant increase in content of specific trace elements. The observed elemental distribution across the hair sections differed noticeably between hairs originating from different mummies. X-ray fluorescence measurements of the hair of one of the mummies revealed a notable increase in calcium (146 μmol/g on average), zinc (37 μmol/g), iron (14 μmol/g) and lead (1.1 μmol/g) contents, compared to the maximum contents of these elements observed in native samples. Other trace constituents of native hair such as manganese (1.8 μmol/g), bromine (1.1 μmol/g), titanium (1.1 μmol/g) and strontium (0.62 μmol/g) also showed a significant increase. The elemental distribution across hair sections from a second mummy was found to be very heterogeneous (see Figure 27). The localization of sulphur, mainly originating from hair proteins, enables a

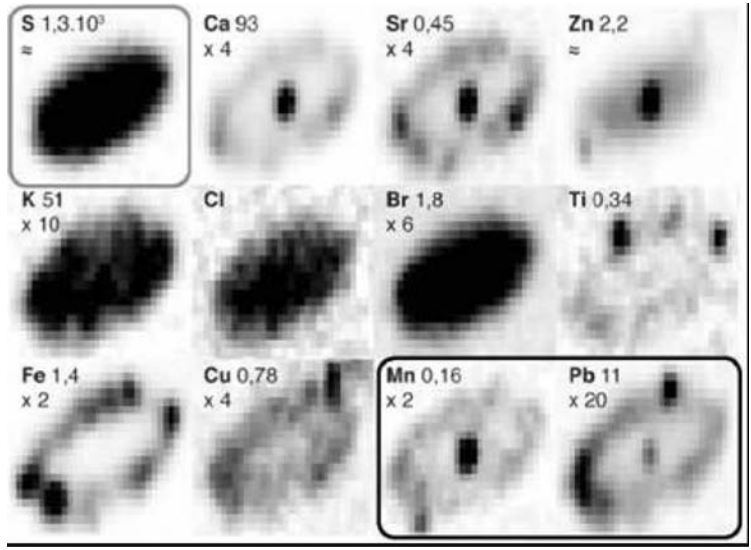

Figure 27. X-ray fluorescence maps of an Mummy hair section. The hair diameter is ca 150 μm. The elemental content (in μmol/g w/w) is indicated, followed by the ratio to average native hair trace element content.

clear visualization ion of the hair section contour. Three types of elemental distribution could be distinguished:

(a) elements such as Ca that are similarly distributed in the fibre section as in current hair;
(b) elements concentrated specifically in some of the histological zones: Mn, Zn, Pb, Sr in the medullar canal and Fe, Cu and Pb in the peripheral areas of the hair strand;
(c) elements presents as impurities, deposited on the surface of the hair strand (Ti, Zn).

Considering that natron, the dehydration and purification agent used during mummification, is a complex mixture of sodium chlorides, sulphates, carbonates and bicarbonates, as well as containing small quantities of calcium carbonate, part of the trace element load in the hair must be assumed to originate from this treatment. Significant amounts of calcium and chlorine were observed in all samples while all trace elements associated with natron of the Greco-Roman period (Ca, Sr, Br, Cl, Fe, Mg) were found to be in excess in one of the examined hair samples. Apart from these elements, a very high content of Mn and Pb in the hair strands from both mummies was observed. These elements are particularly concentrated at the hair periphery and in the medulla of one of the samples. The presence of these elements was attributed to the use of Pb-based make-up and of Mn-based hair dyes in Ancient Egypt. The specific concentration of lead, calcium and other cations within the medullar canal, where the lipids were concentrated before mummification, could be related to the saponification of hair lipids. The absorption of exogenous metal cations within the fibre may have locally increased the electronic density of the material. The diffusion of metal ions can moreover have had a structuring effect, by regularly organizing the keratins around the metal sites. This can be an explanation for the increase in contrast observed in the hair diffraction pattern.

4 CONCLUSIONS

It can be concluded that x-ray micro beam techniques offer a variety of possibilities for non-destructively compositional and/or structural analysis of cultural heritage materials. Apart from

determinations of the (local) composition, which may be performed via x-ray fluorescence analysis, also structural information on crystalline and amorphous phases can be obtained via x-ray diffraction and x-ray absorption spectroscopy. Next to standard laboratory equipment, which is not always suitable for analysis of large artefacts, open beam instrumentation is available, either under the form of compact transportable equipment for *in situ* measurements or as part of larger installations such as synchrotron facilities. Provenance analysis investigations as well as conservation studies can be executed in many cases by means of x-ray techniques.

REFERENCES

Adams, F., Janssens, K. & Snigirev, A. 1998. Microscopical x-ray fluorescence analysis and related methods with laboratory and synchrotron radiation sources. *J. Anal. Atom. Spectrom.*, 13, 319–331.

Aerts, A., Janssens, K. & Adams, F. 1999. Trace level microanalysis of Roman glass from Khirbet Qumran, Israel, *Journal of Archaeological Science*, 26, 883–891.

Aerts, A., Velde, B. & Janssens, K. 2003. Change in silica sources in Roman and post Roman glass, *Spectrochimica Acta B*, 58, 659–667.

Aloupi, E., Karydas, A. & Paradellis, T. 2000. Pigment analysis of wall paintings and ceramics from Greece and Cyprus. The optimum use of x-ray spectrometry on specific archaeological issues, *X-Ray Spectrometry*, 29, 18–24.

Bernard, L., Doucet, J., Simionovici, A., Tsoucaris, G. & Walter, P. 2003. Lead revealed lipid or lipid organisation in human hair. *Biochemica et Biophysica Acta*, 1620, 218–224.

Bertrand, L., Chevallier, P., Doucet, J., Simionovici, A., Tsoucaris, G. & Walter, P. 2002. Apport du rayonnement synchrotron à l'étude de cheveux archéologiques. *Journal de Physique* IV, 12, 237–243.

Bezborodov, M.A. 1975. Chemie und Technologie der antiken und mittelalterlichen Gläser, Mainz: Philipp von Zabern Verlag.

Bichlmeier, S., Janssens, K., Heckel, J., Gibson, D., Hoffmann, P. & Ortner, H.M. 2001. Component selection for a compact micro-XRF spectrometer, *X-Ray Spectrometry*, 30, 8–14.

Bichlmeier, S., Janssens, K., Heckel, J., Hoffmann, P. & Ortner, H.M. 2002. Comparative material characterization of historical and industrial samples by using a compact micro-XRF spectrometer, *X-Ray Spectrometry*, 31, 87–91.

Bichlmeier, S., Janssens, K., Heckel, J., Hoffmann, P. & Ortner, H.M. 2002. Comparative material characterization of historical and industrial samples by using a compact micro-XRF spectrometer, *X-Ray Spectrometry*, 31, 87–91.

Bish, D.L. & Post, J.E. (eds) 1990. *Modern powder diffraction*. Reviews in mineralogy, Vol. 2. ISBN 0-939950-24-3, 369 pp.,Washington DC, USA: The Mineralogical Society of America.

Bjeoumikhov, A.A. & Chevalier, P. 1998. *Proc. SPIE* Vol. 3444, 430–435.

Bloy, C.H. 1967. *A History of Printing Ink, Balls and Rollers* 1440–1850, London: Butterworths.

Borgia, I., Brunetti, B., Mariani, I., Sgamelotti, A., Cariati, F., Fermo, P., Mellini, M., Viti, C. & Padeletti, G. 2002. Heterogeneous distribution of metal nanocrystals in glazes of historical pottery. *Appl. Surf. Science* 185, 206–316.

Bronk, H., Röhrs, S., Bjeoumikhov, A., Langhoff, N., Schmalz, J., Wedell, R., Gorny, H.E., Herold, A. & Waldschläger, U. 2001. ArTAX – a new mobile spectrometer for energy-dispersive micro x-ray fluorescence spectrometry on art and archaeological objects, *Fres. J. Anal. Chem*., 371, 307–316.

Brown, G.E., Jr., Calas, G., Waychunas, G.A. & Petiau, J. 1988., X-ray absorption spectroscopy and its applications in mineralogy and geochemistry. In F. Hawthorne (ed) *Spectroscopic Methods in Mineralogy and Geology, Reviews in Mineralogy*: 18, 431–512, Mineralogical Society of America.

Cahill, T., Kusko, B., Eldred, R.A. & Schwab, R.N. 1984. *Archaeometry* 26, 3.

Cahill, T., Kusko, B. & Schwab, R.N. 1981. Analyses of inks and papers in historical documents through external beam PIXE techniques, *Nucl. Instr. Meth. Phys. Res. B* 181, 205.

Caiger-Smith, A. 1985. *Luster Pottery. Technique, Tradition and Innovation in Islam and the Western World*. London, UK: Faber & Faber.

Cesarao, R., Castellano, A., Buccolieri, G., Quarta, S., Marabelli, M., Santopadre, P., Ieole M., & Brunetti, A. 2004. Portable equipment for energy-dispersive x-ray fluorescence analysis of Giotto's frescoes in the Chapel of the Scrovegni, *Nucl. Instr. Meth. Phys. Res. B* 213, 703–706.

Chiari, G., Giustetto, R. & Ricchiardi, G. 2003. Crystal structure refinements of palygorskite and Maya Blue from molecular modelling and powder synchrotron diffraction, *Eur. J. Mineral*., 15, 21–33.

Ciliberto, E. & Spoto, G. (eds) 2000. *Modern Analytical Methods in Art and Archaeology*, Vol. 155, Chemical Analysis Series, Chichester: Wiley.
Creagh, D.C. & Bradley, D.A. (eds) 2000. *Radiation in Art and Archaeometry*, Amsterdam: Elsevier Science.
Dabagov, S.B., Nikitina, S.V. & Kumakhov, M.A. 1995. *Nucl. Inst. Meth. Phys. Res. B* 103, 99–105.
De Raedt, I. 2002. "Composition of 16–17th Century Facon-de-Venise Glass excavated in Antwerp and Neighbouring Cities". *PhD thesis*, University of Antwerp, Antwerp, Belgium.
De Raedt, I., Janssens, K., Veeckman, J. & Adams, F. 2000. Composition of façon-de-venise and Venetian glass from Antwerp and the Southern Netherlands, In *Annales du 14e Congrès de l'Association internationale pour l'histoire du verre, Lochem, AIHV*, p. 346–350.
De Raedt, I., Janssens, K., Veeckman, J., Vincze, L., Vekemans, B. & Jeffries, T. 2001. Trace analysis for distinguishing between Venetian and façon-de-Venise glass vessels of the 16th and 17th century. *J. Anal. Atom. Spectrom*, 16, 1012–1017.
De Ryck, I., Adriaens, A., Adams, F. & Pantos, E. 2003. A comparison of microbeam techniques for the analysis of corroded ancient bronze objects, *Analyst* 128, 1104–1109.
De Vries, J.L. & Vrebos, B.A.R. 2002. Quantification of infinitely thick specimen by XRF analysis, Chapter 5. In R. Van Grieken & A. Markowicz, (eds) *Handbook of X-Ray Spectrometry*, 2nd edition. New York: Marcel Dekker.
Denker, A., Hahn, O., Kanngießer, B., Malzer, W., Merchel, S., Radtke, M., Röhrs, S., Reiche, I. & Stege, H. 2003. Chemie der Kunst – Zerstörungsfreie Analyse von Kunst- und Kulturgütern. *MP Materialprüfung* 45 (11–12) 485–503.
Deraedt, I., Janssens, K. & Veeckman, J. 1999. Compositional distinctions between 16th century 'Façon-de-Venise' and Venetian Glass Vessels, excavated in Antwerp, Belgium, *J. Anal. Atom. Spectrom*. 14, 493–498.
Donceel-Voûte, P. 1994. Qumran revisited. *Archeologia*, 298. 24.
Durham, P.J. 1988. Theory of XANES in x-ray absorption. In D.C. Koningsberger & R. Prins (eds), *Principles, Applications, Techniques of EXAFS, SEXAFS and XANES*: 53–84. New York: John Wiley & Sons.
Dussart, O. & Velde B. 1990. La composition du verre Hellenistique en Jordanie et Syrie du Nord, *Syria,* 67 687–693.
Falkenberg, G., Clauss, O. & Swiderski, A. 2001. Upgrade of the x-ray fluorescence beamline at HASYLAB/DESY. *X-Ray Spectrom*. 30, 170–173.
Fiorini, C., Kemmer, J., Lechner, P., Kromer, K., Rohde, M & Schulein, T. 1997. A new detection system for x-ray microanalysis based on a silicon drift detector with Peltier cooling, *Rev. Sci. Instrum*., 68, 2461–2465.
Fiorini, C & Longoni, A. 1998. Application of a new noncryogenic x-ray detector in portable instruments for archaeometric analyses, *Rev. Sci. Instrum*., 69 1523–1528.
Fuchs, R., Hahn, O. & Oltrogge, D. 2000. Geist und Seele sind verwirret . . . Die Tintenfraßproblematik der Autographen Johann Sebastian Bachs, *Restauro* 106, 116–121.
Gao, N. & Janssens, K. 2004. Polycapillary x-ray optics, In K. Tsuji, J. Injuk, & R. Van Grieken (eds), *X-Ray Spectrometry: Recent Technological Advances*, 89–110. Chichester: Wiley.
Guinier, A. 1994. X-*Ray Diffraction in Crystals, Imperfect Crystals, and Amorphous Bodies*: ISBN: 0486680118, 378 pp., Dover, UK: Dover Publications.
Hammond, Ch. 1997. *The Basics of Crystallography and Diffraction, IUCr Texts on Crystallography*, No. 3: ISBN 0-19-855966-6. 249 pp. International Union of Crystallography/Oxford University Press.
Hansel, C.M., Laforce, M.J., Fendorf, S. & Sutton, S. 2002. Spatial and temporal association of As and Fe species on aquatic plant roots, *J. Env. Sci. Technol.*, 36, 1988–1994.
He, F. & Van Espen, P. 1991. General approach for quantitative energy dispersive x-ray fluorescence analysis based on fundamental parameters, *Anal. Chem*., 63, 2237–2244.
Henderson, J. 1985. The raw materials of early glass production, Oxford J. Archaeology, 4, 267–291.
Hochleitner, B., Schreiner, M. & Drakopoulos, M. 2004. Analysis of paint layers by light microscopy, scanning electron microscopy and synchrotron induced x-Ray micro-diffraction, this volume, Leiden: Balkema.
Hoffman, P. 1994. Analytical determinaton of coloring elements and their compounds in glass beads from graveyards of the Merowings time. *Fres. J. Anal. Chem*., 349, 320–333.
Hoffmann, P., Bichlmeier, S., Heck, M., Theune, C. & Callmer, J. 2000. Chemical composition of glass beads of the Merovingian period from graveyards in the Black Forest, Germany, *X-Ray Spectrom.*, 29, 92–100.
Janssens, K. 2000. Comparison to other techniques, Chapter 7. In K. Janssens, F. Adams & A. Rindby, (eds), *Microscopic X-Ray Fluorescence Analysis*. Chichester: Wiley.
Janssens, K., Adams, F. & Rindby, A. 2000. *Microscopic X-ray Fluorescence Analysis,* Chichester: Wiley.
Janssens, K., Proost, K. & Falkenberg, G. 2004. Confocal microscopic x-ray fluorescence at the HASYLAB microfocus beamline : characteristics and possibilities, *Spectrochimica Acta B*, in press.

Janssens, K., Vekemans, B., Vincze, L., Adams, F. & Rindby, A. 1996. A micro XRF spectrometer based on rotating anode generator and capillary optics. *Spectrochim. Acta*, B51, 1661–1678.

Janssens, K., Vincze, L., Adams, F. & Jones, K.W. 1993 Synchrotron x-ray microanalysis, *Anal. Chim. Acta*, 283, 89–119.

Janssens, K., Vincze, L., Aerts, A., Adams, F. & Hertogen, J. 1997. Automated segmentation of μ-XRF image sets. *X-Ray Spectrom.*, 26, 333–346.

Janssens, K., Vincze, L., Vekemans, B., Williams, C.T., Radtke, M., Haller, M. & Knöchel, A. 1998. The non-destructive determination of REE in fossilized bone using synchrotron radiation induced K-line x-ray microfluorescence analysis, *Fres. J. Anal. Chem.*, 363, 413–420.

Janssens, K., Vincze, L., Vekemans, B., Adams, F., Haller, M. & Knöchel, A. 1998. The use of ellipsoidal lead-glass capillaries for micro-focussing of highly energetic (0–60 keV) synchrotron radiation, *J. Anal. Atom. Spectrom.* 13, 339–350.

Johansson, S.A. & Campbell, J.L. 1988. *PIXE: A Novel Technique for Elemental Analysis*, Chichester: Wiley.

Jokubonis, C., Wobrauschek, P., Zamini, S., Karwowski, M., Trnka, G. & Stadler, P. 2003. Results of quantitative analysis of Celtic glass artifacts by energy dispersive x-ray fluorescence spectrometry. *Spectrochim. Acta B*58 627–633.

Kanngießer, B., Malzer, W. & Reiche, I. 3003. A new 3D micro x-ray fluorescence analysis set-up – first archaeometric applications. *Nucl. Instrum. Meth. Phys. Res. B*, 211, 259–264.

Kingery, W.D. & Vandiver, B. 1986. In *Ceramic Masterpieces. Art, Structure and Technology*, pp. 111–121. New York: The Free Press.

Klockenkämper, R., von Bohlen A. & Moens, L. 2000. Analysis of pigments and inks in oil paintings and historical manuscripts using total reflection x-ray fluorescence spectrometry. *X-Ray Spectrom.*, 29, 119–129.

Knöchel, A. & Haller, M. 1996. X-ray fluorescence analysis using synchrotron radiation (SYXRF). *J. Trace Microprobe Techn.* 14, 461–488.

Koningsberger, D.C. & Prins, R. (eds) 1988. *X-ray Absorption: Principles, Applications, Techniques of EXAFS, SEXAFS and XANES*: 3–51, New York: John Wiley & Sons.

Kusko, B.T. & Schwab, R.N. 1987. Historical Analyses by PIXE, *Nuclear Instr. Meth. Phys. Res.*, 22, 401–406.

Lahanier, Ch., Amsel, G., Heitz, Ch., Menu, M. & Andersen, H.H. 1986. *Proc. of the Intern. Workshop on Ion-Beam Analysis in the Arts and Archaeology, Pont-A-Mousson, Abbaye des Premontrés, France, February 18–20, 1985* – Editorial, Nucl. Instr. Meth. Phys. Res. B14 1.

Lai, B., Yun, B., Legnini, D., Xiao, Y., Chrzas, J., Vicaro, P.J., White, V., Bajikar, S., Denton, D., Cerrina, F., Di Fabrizio, E., Gentili, M., Grella, L. & Baciocchi, M. 1992. Hard x-ray phase zone plate fabricated by lithographic techniques, *Appl. Phys. Lett*., 61, 1877–1879.

Larsson, S. 1991. *X-Ray Microbeam Spectroscopy*, Thesis, Department of Physics, Chalmers University of Technology, S-41296 Goteborg, Sweden. ISBN 91-7032- 579-0. Göteborg, Sweden: Bibliotekets ReproService.

Longoni, A., Fiorini, C., Leutenegger, P., Sciuti, S., Fronterotta, G., Strüder, L. & Lechner, P. 1998. A portable XRF spectrometer for non-destructive analysis in archaeometry, *Nucl. Instr. Meth. Phys. Res. A*, 409, 395–400.

Lucas, A. & Harris, J.R. 1963. *Ancient Egyptian Materials and Industries*. London: Edwards Arnold Ltd.

Martinetto, P., Anne, M., Dooryhee, E. & Walter, Ph. 1998. Analysis of x-ray diffraction line profile of galena powders: a clue to some practices of mineral crushing in ancient Egypt. In *Proceedings of the 6th European Conference on Powder Diffraction* (EPDIC6), Materials Science Forum.

Milazo, M. & Cicardi, C. 1997. Simple methods for quantitative x-ray fluorescence analysis of ancient metal objects of archaeological interest, *X-Ray Spectrom.* 26, 211–216.

Moioli, P. & Seccaroni, C. 2000. Analysis of art objects using a portable x-ray fluorescence spectrometer. *X-Ray Spectrom.*, 29, 48–52.

Mommsen, H., Beier, Th., Dittmann, H., Heimermann, D., Hein, A., Rosenberg, A., Boghardt, M., Manebutt-Benz E.-M. & Halbey, H. 1996. *Archaeometry*, 38, 347.

Müller, M., Papiz, M.Z., Clarke, D.T., Roberts, M.A., Murphy, B.M., Burghammer, M., Riekel, C., Pantos, E. & Gunneweg, J. 2003. Identification of textiles from the Khirbet Qumran caves using microscopy and synchrotron radiation x-ray fibre diffraction in Khirbet Qumran et Ain Feshkha. In J.-B. Humbert & J. Gunneweg (eds), II. *Etudes d'Anthropologie, de Physique et de Chimie*., Fribourg: Academic Press.

Otto, H.H., Hofmann, W. & Schröder, K. 2002. A double-radius Gandolfi x-ray camera for the generation of powder-like diffractograms of small single crystals, using an imaging plate detector, *J. Appl. Cryst*. 35, 13–16.

Padovani, S., Sada, C., Mazzoldi, P., Brunetti, B., Borgia, I., Sgamellotti, A., Giulivi, A., D'Acapito, F. & Battaglin, G. 2003. Copper in glazes of Renaissance luster pottery: nanoparticles, ions, and local environment, *J. Appl. Phys*., 93, 10058–10063.

Patyk-Karar, N.G., Bardeeva, E.G. & Sjevelev, A.G. 1999. Titano-zirconium placers in the sedimentary cover platforms, *Episodes*, 22, 89–97.

Pérez-Arantegui, J., Molera, J., Larrea, A., Pradell, T., Vendrell-Saz, M., Borgia, I., Brunetti, B.G., Cariati, F., Fermo, P., Mellini, M., Sgamellotti, A. & Viti, C. 2001. Luster pottery from the thirteenth century to the sixteenth century: A nanostructured thin metallic film, *J. Am. Ceramic Soc*. 84, 442–446.

Piccolpasso, C. & Li Tre. 1976. *Libri dell'Arte del Vasaio*, 1557, Firenze: Edizioni all'Insegna del Giglio.

Pollard, A.M. & Heron C. 1996. *Archaeological Chemistry*, London: Royal Society of Chemistry.

Proost, K., Vincze, L., Janssens, K., Gao, N., Bulska, E., Schreiner, M. & Falkenberg, G. 2003. Characterization of a polycapillary lens for use in micro-XANES experiments, *X-Ray Spectrom.*, 32, 215–222.

Reiche, I., Berger, A., Görner, W., Merchel, S., Radtke, M., Riederer, J., Riesemeier, H. & Roth, M. Following the traces of Albrecht Dürer: analysis of silverpoint drawings by spatially resolved synchrotron-induced x-ray fluorescence analysis, *Nucl. Instr. Meth. Phys. Res B*, in press.

Reiche, I., Radtke, M., Berger, A., Ketelsen, T., Merchel, S., Görner, W., Riesemeier, H., Riederer, J. & Roth, M. 2004. Spatially resolved synchrotron-induced x-ray fluorescence analyses of metal point drawings and their mysterious inscriptions, *Spectrochim. Acta B*, in press.

Reiche, I., Vignaud, C., Calligaro, T., Salomon, J. & Menu, M. 2000. Comparative analysis of odontolite, heated fossil ivory and blue fluorapatite by PIXE/PIGE and TEM, *Nucl. Instr. Meth. B*, 161, 737–742.

Reiche, I., Vignaud, C., Champagnon, B., Panczer, G., Brouder, C., Morin, G., Solé, V.A., Charlet, L. & Menu, M. 2001. From mastodon ivory to gemstone: The origin of turquoise color in odontolite. *American Mineralogist*, 86, 1519–1524.

Salvadó, N., Pradell, T., Pantos, E., Papiz, M.Z., Molera, J., Seco, M. & Vendrell-Saz, M. 2002. Identification of copper based green pigments in Jaume Huguet's Gothic altarpieces by Fourier transform infrared microspectroscopy and synchrotron radiation x-ray diffraction, *J. Sync. Rad.,* 9, 215–222.

Sanderson, D.C.W., Hunter, J.R. & Warren, S.E. 1984. Energy dispersive x-ray fluorescence analysis of 1st millennium AD glass from Britain*, J. Archaeological Science*, 11, 53–70.

Sands, D. E. 1994. *Introduction to Crystallography*. ISBN: 0486678393. Dover, UK: Dover Publications.

Sayer, E.V. & Smith, R.W. 1961. Compositional categories of ancient glass. *Science*, 133, 1824–1826.

Schreiner, M., Fruhmann, B., Jembrih-Simburger, D. & Linke, R. 2004. X-rays in art and archaeology: an overview. *Powder Diffraction*, 19, 3–11.

Schwab, R.N., Cahill, T.A., Kusko, B.H., Eldred, R.A., Moller, G. & Dutschke, D. 1983. Cyclotron analysis of the ink in the 42-Line Bible. In *The Papers of the Bibliographical Society of America*, 77, 285–315.

Selin, E. (ed) 2000. Special Millenium Issue on Cultural Heritage, *X-Ray Spectrom.*, 29 1–129.

Simionovici, A., Schroer, C. & Lengeler, B. 2004. Parabolic compound refractive x-ray lenses, In K. Tsuji, J. Injuk, R. Van Grieken (eds), *X-Ray Spectrometry: Recent Technological Advances*: 111–131. Chichester: Wiley.

Smit, Z., Janssens, J., Proost, K. & Langus, I. 2004. Confocal μ-XRF depth analysis of paint layers, *Nucl. Instr. Meth. Phys. Res. B*, 219–220, 35–40.

Somogyi, A., Drakopoulos, M., Vincze, L., Vekemans, B., Camerani, C., Janssens, K., Snigirev, A. & Adams, F. 2001. ID18F: a new micro-x-ray fluorescence radiation facility at the European Synchrotron Radiation Facility (ESRF): preliminary results, *X-Ray Spectrom.*, 30, 242–252.

Stern, E.A. 1988. Theory of EXAFS, in x-ray Absorption. In D.C. Koningsberger & R. Prins (eds), *Principles, Applications, Techniques of EXAFS, SEXAFS and XANES*: 3–51. New York: Wiley & Sons.

Stocklassa, B., Nillson, G. & Paulson, N. 1992. paper presented at the European Conference on EDXRS, Myconos, Greece, May 30-June 6 (1992).

Tsuji, K., Injuk, J. & Van Grieken, R. (eds) 2004. *X-Ray Spectrometry: Recent Technological Advances:* ISBN 0-471-48640-X. Chichester: Wiley.

Ungar, T., Martinetto, P., Ribarik, Dooryhee, E., Walter, P. & Anne, M. 2003 Revealing the powdering methods of black makeup in ancient Egypt by fitting microstructure based Fourier coefficients to the whole x-ray diffraction profiles of galena. *Journal of Applied Physics*, 91, 2455–2465.

Van Grieken, R. & Markowicz, A. (eds) 2002. *Handbook of X-ray Spectrometry*, 2nd edition, New York: Marcel Dekker.

Vandenabeele, P., van Bohlen, A., Moens, L., Klockenkämper, R., Joukes, F. & Dewispelaere, G. 2000. Spectroscopic examination of two Egyptian masks: a combined method approach, *Analytical Letters* 33/15, 3315–3332.

Vandenabeele, P., Wehling, B., Moens, L., De Reu, M., Van Hooydonk, G., von Bohlen, A. & Klockenkämper, R. 2002. In E. Jerem and K.T. Biró (eds), *Proceedings of the 31st International Symposium on Archaeometry* (Vol. II), *BAR International Series 1043(II)*, Oxford: pp. 825–827, Archaeopress – Archaeolingua.

Velde, B. 1990. Alumina and calcium oxide content of glasses found in western and northern Europe, first to ninth centuries, *Oxford Journal of Archaeology*, 9, 105–117.

Vincze, L., Janssens, K., Vekemans, B. & Adams, F. 1999. Monte Carlo simulation of x-ray fluorescence spectra: part 4: photon scattering at high x-ray energies, *Spectrochim. Acta B* 54, 1711–1722.

Vincze, L., Janssens, K., Adams, F. & Jones, K.W. 1995. A general Monte-Carlo simulation of ED-XRF spectrometers: Part III, polarized polychromatic radiation, homogeneous samples. *Spectrochim. Acta B*, 50, 1481–1500.

Vincze, L., Janssens, K., Vekemans, B. & Adams, F. 1999. Modeling of photon scattering at high x-ray energies: experiment vs. simulation, *J. Anal. Atom. Spectrom*. 14, 529–533.

Vincze, L., Vekemans, B., Szalóki, I., Janssens, K., Van Grieken, R., Feng, H., Jones, K.W. & Adams, F. 2002. High-resolution x-ray fluorescence micro-tomography on single sediment particles. In U. Bonse Ulrich (ed), *Proceedings SPIE conference on "Developments in X-Ray Tomography*: 3, pp. 240–245. Washington: Bellingham.

Vincze, L., Wei, F., Proost, K., Vekemans, B., Janssens, K., He, Y., Yan, Y. & Falkenberg, G. 2002. Suitability of polycapillary optics for focussing of monochromatic synchrotron radiation as used in trace level micro-XANES measurements. *J. Anal. Atom. Spectrom*, 17, 177–182.

Vittiglio, G., Bichlmeier, S., Klinger, P., Heckel, J., Fuzhong, W., Vincze, L., Janssens K., Engström, P., Rindby, A., Dietrich, K., Jembrih-Simbürger, D., Schreiner, M., Denis, D., Lakdar A. & Lamotte, A. 2004. "A compact μ-XRF spectrometer for (in-situ) analyses of cultural heritage and forensic materials", *Nucl. Instr. Meth. Phys. Res. B*, 213, 693–698.

Vittiglio, G., Janssens, K., Vekemans, B., Adams, F. & Oost, A. 1999. A compact small-beam XRF-instrument for in-situ analysis of objects of historical and/or artistic value. *Spectrochim. Acta B*, 54, 1697–1710.

Walter, Ph., Martinetto, P., Tsoucaris, G., Bréniaux, R., Lefebvre, M.A., Richard, G., Talabot, J. & Dooryhee, E. 1999. Manufacturing cosmetics in ancient Egypt. *Nature* 397, 483–484.

Wobrauschek, P., Halmetschlager, G., Zamini, S., Jokubonis, C., Trnka, G. & Karwowski, M. 2000. Energy-dispersive x-ray fluorescence analysis of Celtic glasses. *X-Ray Spectrom.*, 29, 25–33.

Wong, J. 1986. Extended x-ray absorption fine structure: a modern structural tool in materials science. *Materials. Sci. Eng*. 80, 107–128.

Yanagihara, M. & Yamashita, K. Multilayers for soft and hard x-rays. In K. Tsuji, J. Injuk, R. Van Grieken (eds), *X-ray Spectrometry: Recent Technological Advances*, pp. 63–87. Chichester: Wiley.

Young, R.A. (ed) 1993. *The Rietveld method*. (IUCr Monograph on Crystallography, No. 5.), ISBN 0-19-855577-6: 298 pp. International Union of Crystallography/Oxford University Press.

Cultural Heritage Conservation and Environmental Impact Assessment by Non-Destructive Testing and Micro-Analysis – Van Grieken & Janssens (eds)
© 2005 Taylor & Francis Group, London, ISBN 90 5809 681 5

Author index

Avdelidis, N.P. 67

Baer, N.S. 159
Becherini, F. 127
Bencs, L. 245
Bernardi, A. 127
Brimblecombe, P. 11
Buccolieri, G. 183
Bulska, E. 101

Camuffo, D. 127
Castellano, A. 183
Cesareo, R. 183
Chabas, A. 77
Chryssoulakis, Y. 49
Cnudde, V. 117
Colapietro, M. 1
Cornelis, E. 37

D'Ercoli, G. 19
Daniilia, S. 49
Delegou, E.T. 67
Demortier, G. 91
Deutsch, F. 245
Doménech Carbó, T. 37
Drakopoulos, M. 171
Dyck, Van, D. 37

Gaviño, M. 149
Gigante, G.E. 1, 183
Godoi, R. 245
Grieken, Van, R. 245
Guerra, M.F. 223
Guida, G. 19

Hermosin, B. 149
Hochleitner, B. 171

Ioele, M. 183

Jacobs, P. 37, 117
Janssens, K. 265

Kontozova, V. 245

Lefèvre, R.A. 77, 127
Lombardo, T. 77
López, E. 37

Mäder, M. 211
Marabelli, M. 19, 183
Maravelaki-Kalaitzaki, P. 135
Mees, F. 37
Moens, L. 27
Moropoulou, A. 67
Munier, I. 77

Neelmeijer, C. 211
Nowik, W. 149

Pagan, E. 127

Quarta, S. 183

Ricciardi, P. 1
Ridolfi, S. 1, 183
Roemich, H. 37
Ruvalcaba-Sil, J.-L. 91

Saiz-Jimenez, C. 149
Santin, V. 19
Santopadre, P. 183
Schreiner, M. 171
Sherwood, S.I. 197
Snigirev, A. 171
Snigireva, I. 171
Spolnik, Z. 245

Vandenabeele, P. 27
Vergès-Belmin, V. 149

Wagner, B. 101
Worobiec, A. 245

APPENDIX

Signature with selected figures in colours,
from different chapters

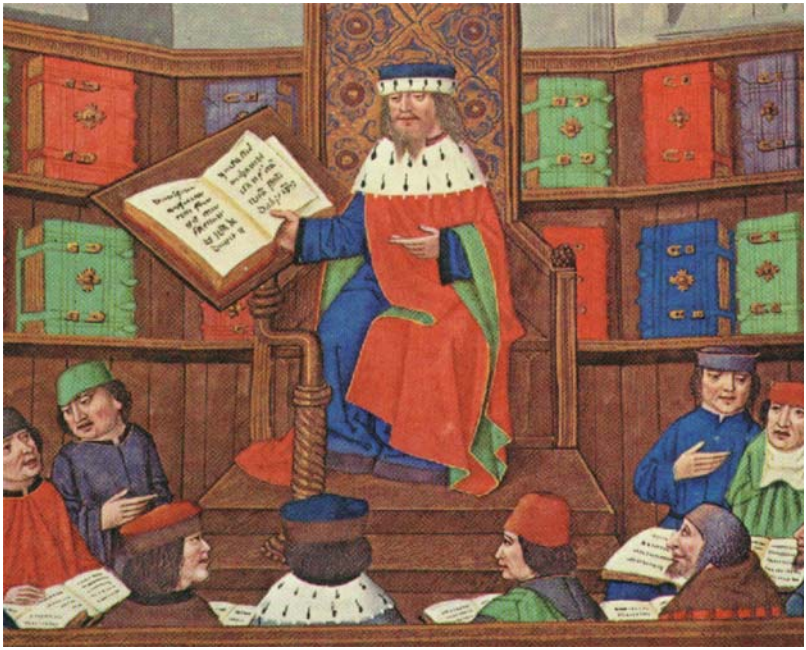

From the chapter by Vandenabeele & Moens:
Figure 1. Illustration from the Mercatellis manuscripts, showing a huge collection of books on the background. The large books were preserved in a vertical position and had ornaments in metal, in order to protect them.

From the chapter by Roemich et al.
Figure 1. Original glass, Middle Ages, excavated near Ulm, Germany. Left: Overview; the original green color is not visible. The surface is covered by a brownish corrosion layer. Right: Light microscopy; micro-cracks are covering the surface, which appears slightly iridescent.

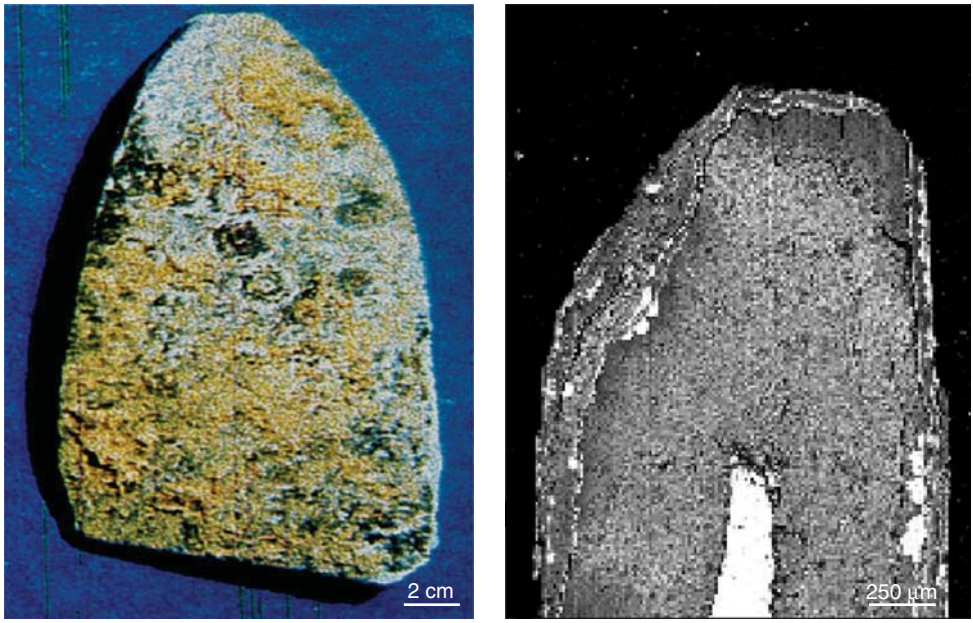

From the chapter by Roemich et al.
Figure 3. Original glass (sample number: F8 – 6), Middle Ages, excavated in Almoina (Valencia), Spain. Left: Overview; the external layer is opaque, which makes the fragment non-transparent. Right: SEM (cross-section); the thickness of the corrosion layer ranges between 100 µm and 400 µm, the remaining non-corroded bulk glass is about 100 µm thick.

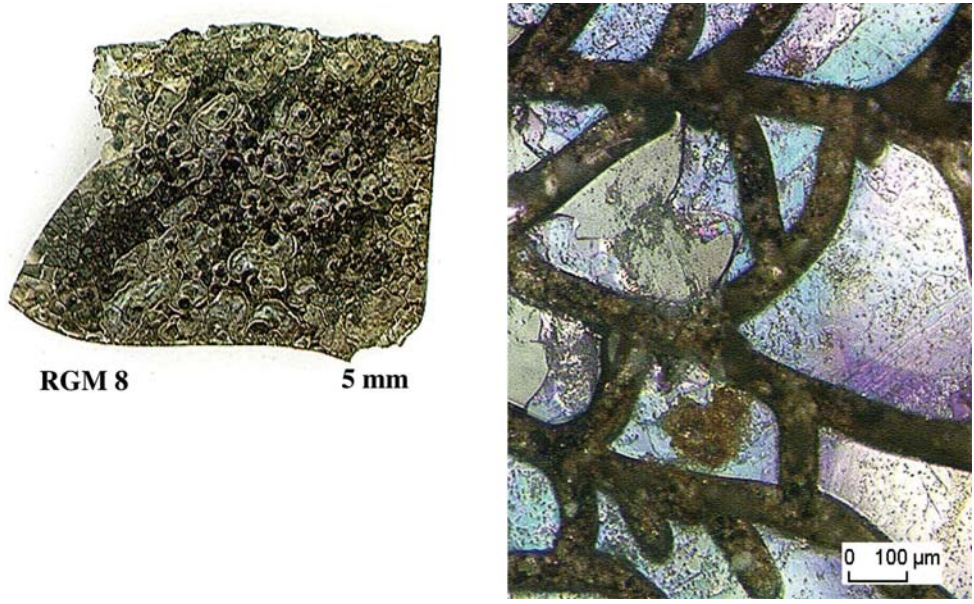

From the chapter by Roemich et al.
Figure 4. Original glass (sample number: RGM8), Middle Ages, excavated in Cologne, Germany. Left: Overview; the fragment seems to be completely corroded. Right: Light microscopy; large cracks are covering the surface, which appears opaque.

From the chapter by Chryssoulakis & Sister Daniilia
Figure 9. The Entrance of the Mother of God into the Temple. Manuel Panselinos, 1295 AD.

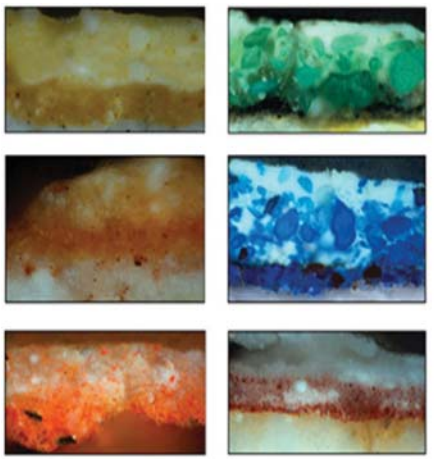

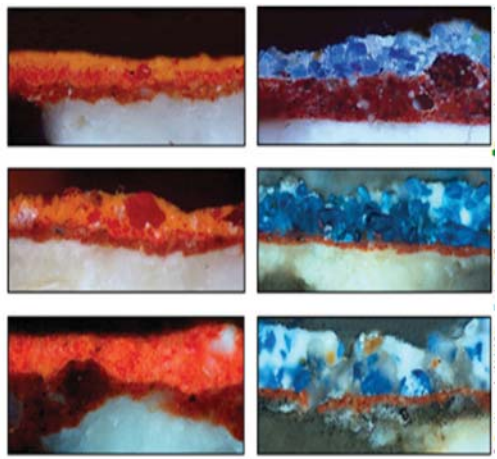

From the chapter by Chryssoulakis & Sister Daniilia
Left: Figure 10. Gradual mixing of lime white with the basic colour of underlay in order to achieve highlights gradations.
Right: Figure 11. The use of cinnabar, minium and azurite as highlights.

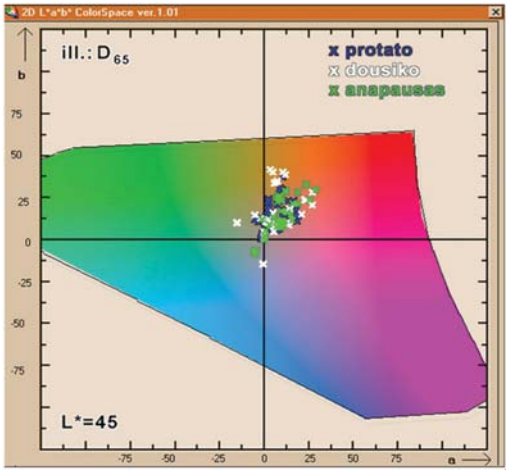

From the chapter by Chryssoulakis & Sister Daniilia

Figure 13. Colour diagram a*b*: Illustration of representative measurements taken from the three monuments (Protaton, Dousikon and Anapausas). The relatively low saturation level is apparent.

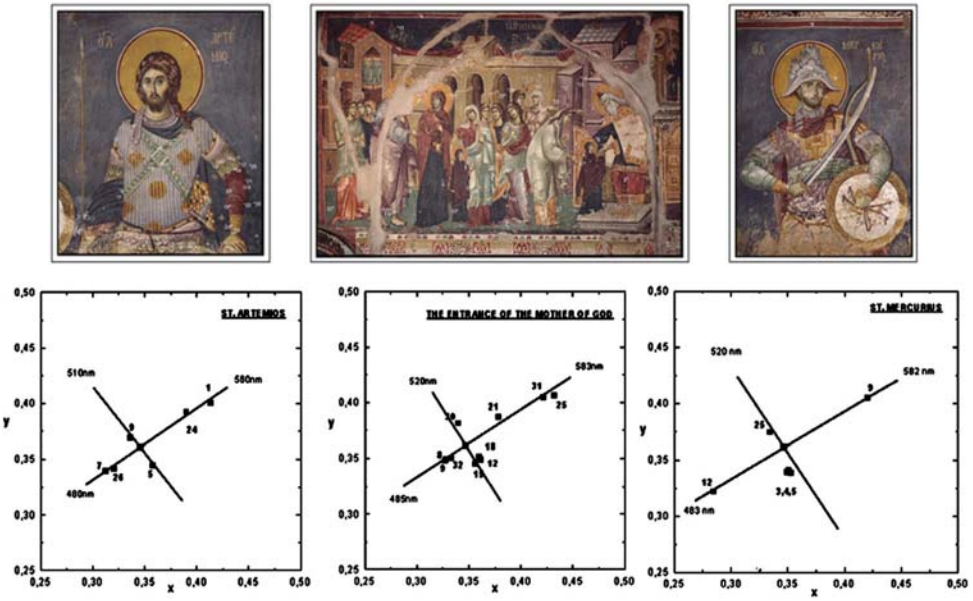

From the chapter by Chryssoulakis & Sister Daniilia

Figure 16. x, y chromaticity diagram (CIE 1931). Illustration of representative measurements of supplementary colours from isolated holy figures and from entire scenes of the Protaton church.

From the chapter by Lefèvre et al.
Figure 1. Saint John the Baptist stained glass of the Sainte-Chapelle in Paris (Window 102, panel 58). Left: viewed by transparency from the interior of the Chapel; Right: the same viewed from the exterior: gypsum black crusts develop in the parts sheltered from rain (mainly upper parts).

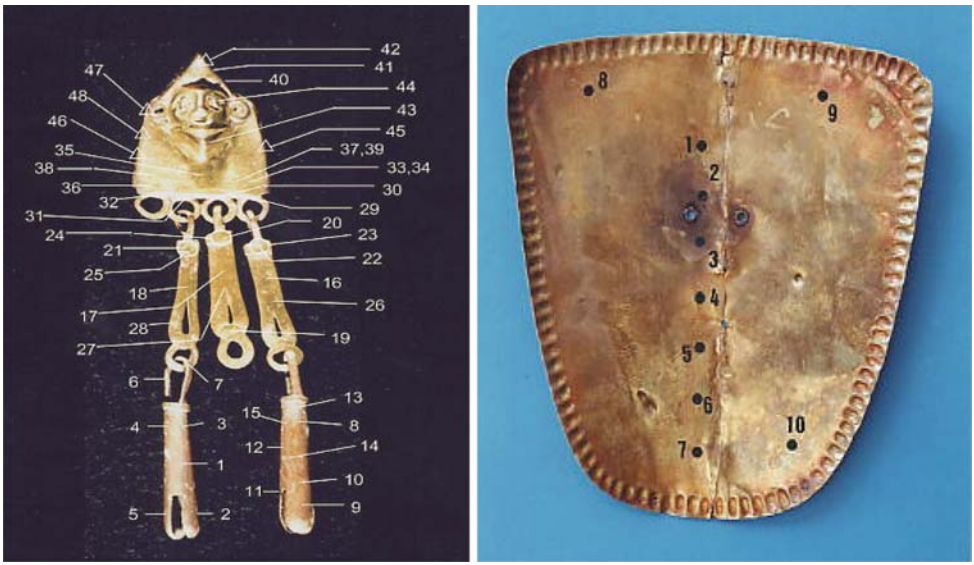

From the chapter by Demortier & Ruvalcaba-Sil
Left: Figure 2. Eagle warrior pendant (San Francisco Caxonos, Oaxaca, 1500 AD, length: 8.0 cm). Oaxacas's Regional Museum, Mexico.
Right: Figure 3. Mesoamerican pectoral (Columbia) (500–1500 AD). Weight: 37.3 gr; volume: 2.65 cm^3.

From the chapter by Demortier & Ruvalcaba-Sil
Figure 4. (a) Regions of non-vacuum PIXE measurements on the zoomorphic pendant (rear). (b) Regions of non vacuum PIXE measurement on the zoomorphic pendant (front). The scanned region with a microbeam is shown in the rectangle (region 3).

From the chapter by Bulska & Wagner
Figure 2b. Manuscript "Meditationes, passionis Domini nostri Iesu Christi" exposed to iron-gall ink corrosion.

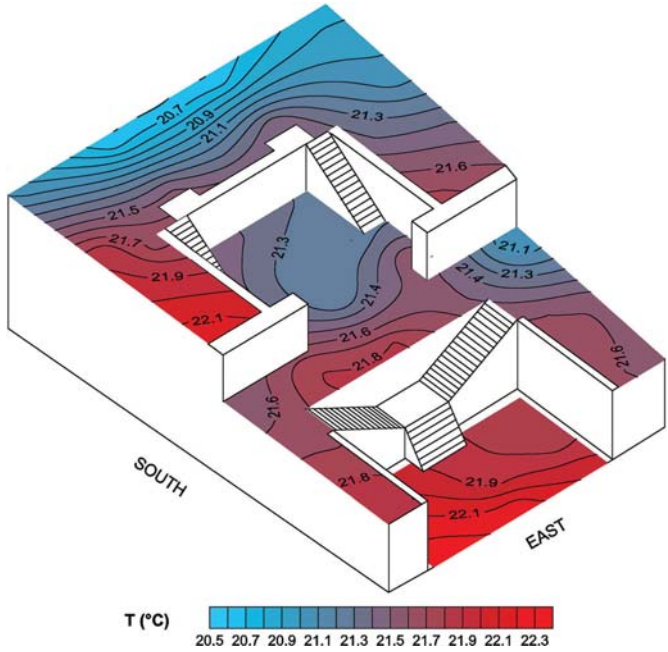

From the chapter by Camuffo et al.
Figure 2. Distribution of the air temperature in the Cour Marly, measured 1.5 m above each floor, the 11 August 1994, 9.00 a.m.

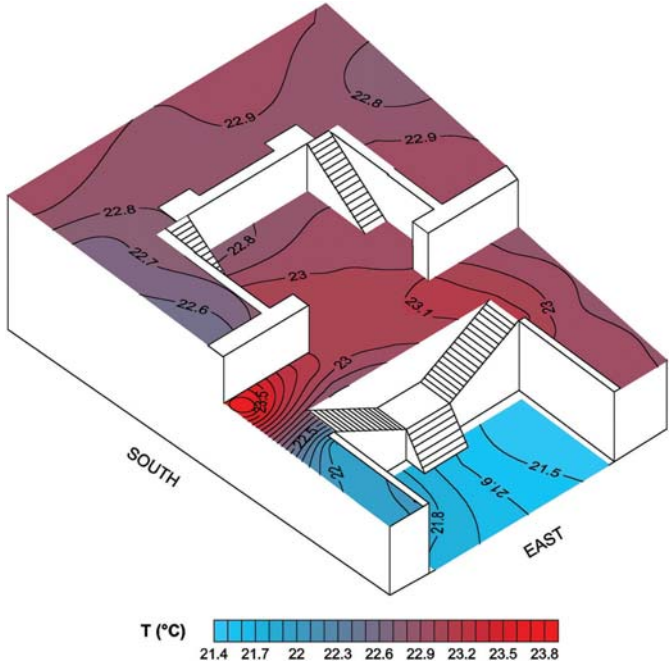

From the chapter by Camuffo et al.
Figure 3. Distribution of the air temperature in the Cour Marly, measured 1.5 m above each floor, the 17 February 1995, 12.

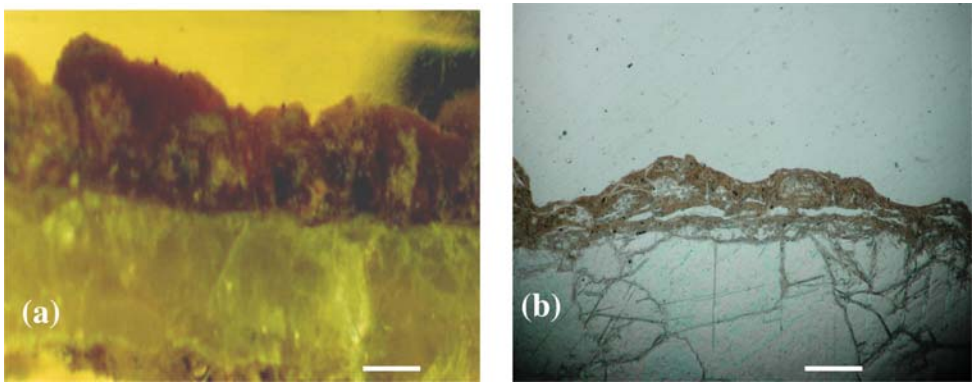

From the chapter by Maravelaki-Kalaitzaki
Figure 1. Polished (a) and thin (b) cross sections of patinas (bar = 150 μm) under the polarizing microscope (a: pol. //, 150 *X*, reflected light, b: pol. //, 200 *X* transmitted light).

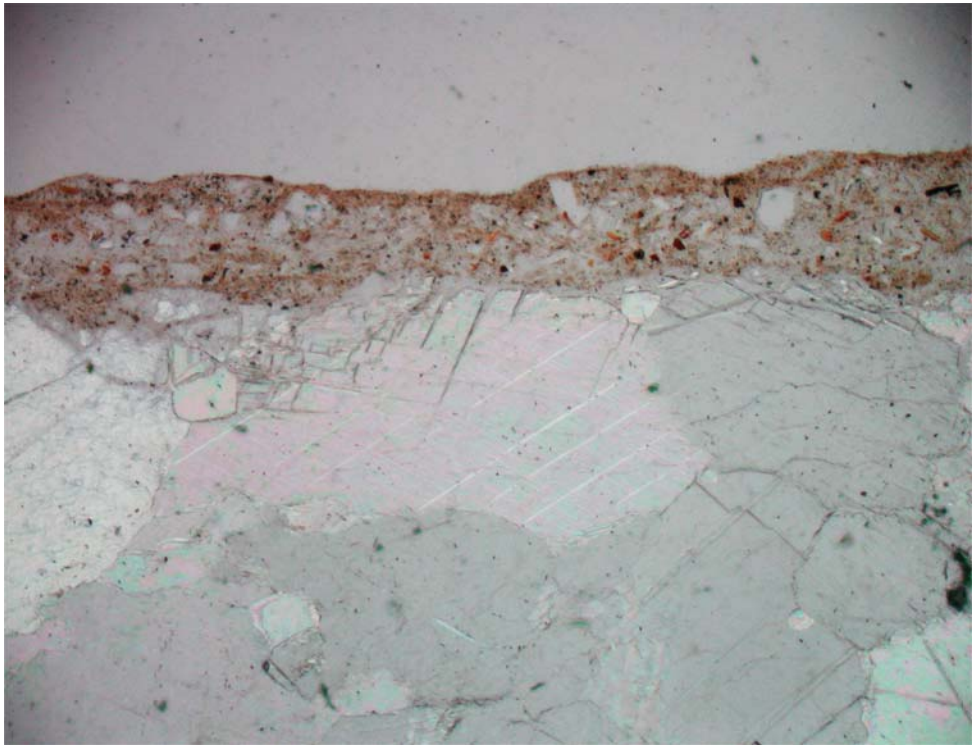

From the chapter by Maravelaki-Kalaitzaki
Figure 3. Orange layer from Erechtheion, with calcite, gypsum and alumino-silicates. Cross section of the sample, where the presence of plaster with orange and brown ochres is evident.

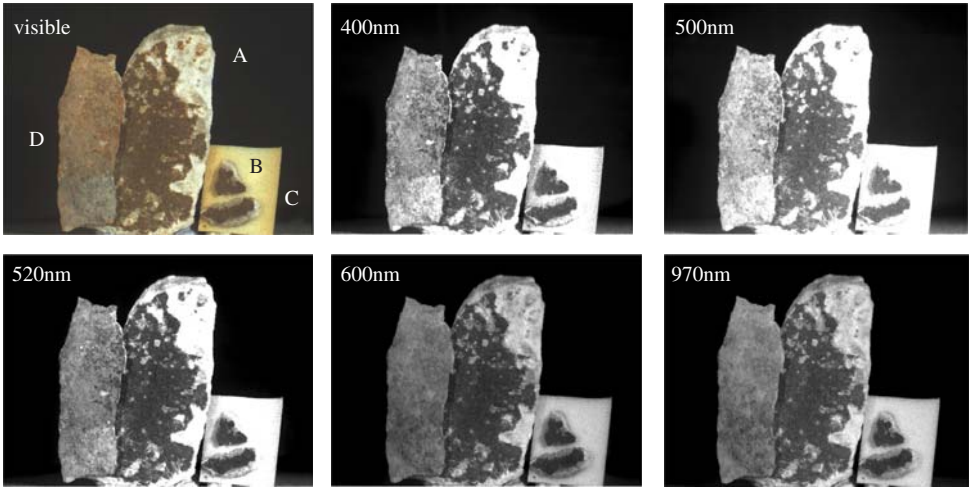

From the chapter by Maravelaki-Kalaitzaki

Figure 6. Selected spectral images of monochromatic layers from the Acropolis monuments, with patina from the Parthenon (A, B and C) and an orange coating from the Erechtheion (D). In the wavelengths shorter than 520 nm, part of the orange coating (D) appears light, while patinas (A, B and C) show no differences in all the spectral images.

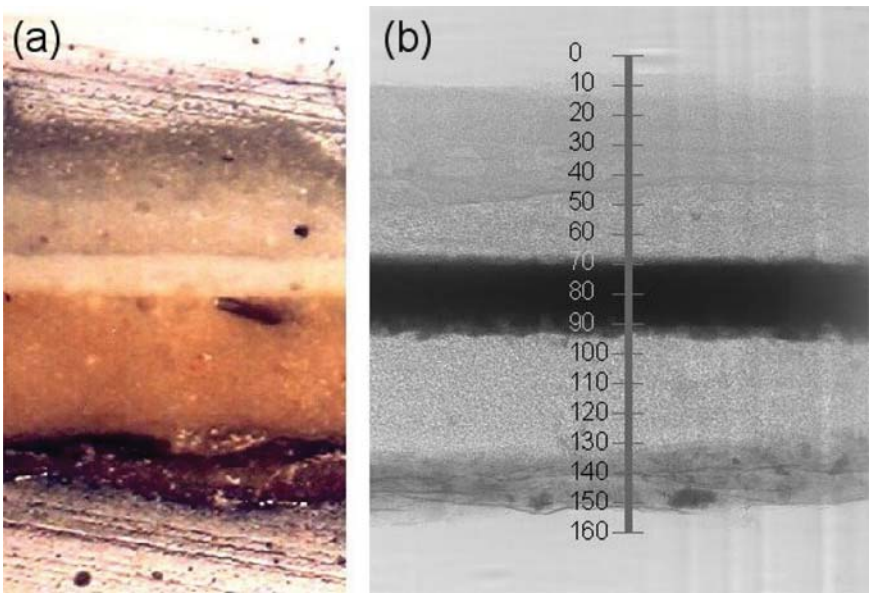

From the chapter by Hochleitner et al.

Figure 7. Optical image (a) and corresponding x-ray radiogram (b) of the specimen with the paint layers used for the synchrotron x-ray micro-diffraction. The vertical line in Figure (b) indicates the alignment of the micro-diffraction scan, with 160 individual points.

From the chapter by Gaviño et al.

Plate 1. (a) Saint Denis basilica: one of the three portals of the western façade covered with black crusts. (b) Saint Denis basilica, portal of the northern transept. The larger statues and ornaments along the door have been laser cleaned. The tympanum, vaults and stone elements behind and underneath the large statues have been cleaned by water-based and/or abrasive methods. (c) Limestone piece with black crusts after laser irradiation at the laboratory. (d) Ground black crusts before and after laser irradiation. (e) Yellow fraction extracted from black crusts and deposited on an alabaster probe. (f) The same after laser irradiation.

Joanne M. Klaar
December 9, 2002
New York University, Institute of Fine Arts, Conservation Center
Materials of Art and Archaeology III

Lead-Tin Yellow

Lead-Tin Yellow I - Pb_2SnO_4
Lead-Tin Yellow II - Pb_2SnO_3 or $Pb_2(Sn, Si)O$

QUESTION OF THE DAY: HOW CAN ONE USE LEAD-TIN YELLOW IN THE AUTHENTIFICATION OF PAINTINGS?

The use of what we term lead-tin yellow (both type I and II) in painting appears to have been limited to the 13th c. through 1750.[1] Its use waned in the second half of the 18th c., and fell out of favor after that.[2] In 1940 the pigment was reintroduced by a scientist from the Doerner Institute in Munich, and can currently be found on the market today.[3]

http://webexhibits.org/pigments/indiv/overview/pbsnyellow.html

http://howtopaintavermeer.fws1.com/pigments.htm
Pigments found on Vermeer's palette, lead-tin yellow on bottom left

The small window of dates allows one to use lead-tin yellow as an authentification tool, as paintings from the 19th and 20th c. do not commonly contain it. However, it is important to note that one may have been able to procure the pigment from places which still held it in stock or left over from another time. Similarly, the reintegration of lead-tin yellow onto the palette in the 1940s may also be an issue in forgeries, as it is now easier to replicate a painting of the 13th c. to 1750.[4] Finally, in light of the recent research of the regrouping of yellow pigments, it may be necessary to reexamine many of the paintings to determine the presence of tin and reconsider the nomenclature of these pigments in the past.

The small window of dates allows one to use lead-tin yellow as an authentification tool, as paintings from the 19th and 20th c. do not commonly contain it. However, it is important to note that one may have been able to procure the pigment from places which still held it in stock or left over from another time. Similarly, the reintegration of lead-tin yellow onto the palette in the 1940s may also be an issue in forgeries, as it is now easier to replicate a painting of the 13th c. to 1750.[5] Finally, in light of the recent research of the regrouping of yellow pigments, it may be necessary to reexamine many of the paintings to determine the presence of tin and reconsider the nomenclature of these pigments in the past.

Best of all, Laser Raman Spectroscopy is a suitable method for identification of lead-tin yellow in easel paintings, illuminated manuscripts, or wall paintings!

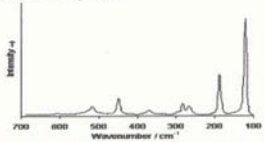

http://www.chem.ucl.ac.uk/resources/raman/pigfiles/leadtin1.html
Lead-tin yellow I Raman spectra

---

[1] http://webexhibits.org/pigments/indiv/history/pbsnyellow.html
[2] Kuhn, H. "Lead-Tin Yellow" 83-112 in Artist Pigments: A Handbook of Their History and Characteristics vol. 2, Roy, A. ed., National Gallery of Art, Washington D.C., 1993. 86
[3] *ibid*, 85
[4] *Ibid.*, 86
[5] *Ibid.*, 86

From the chapter by Bear

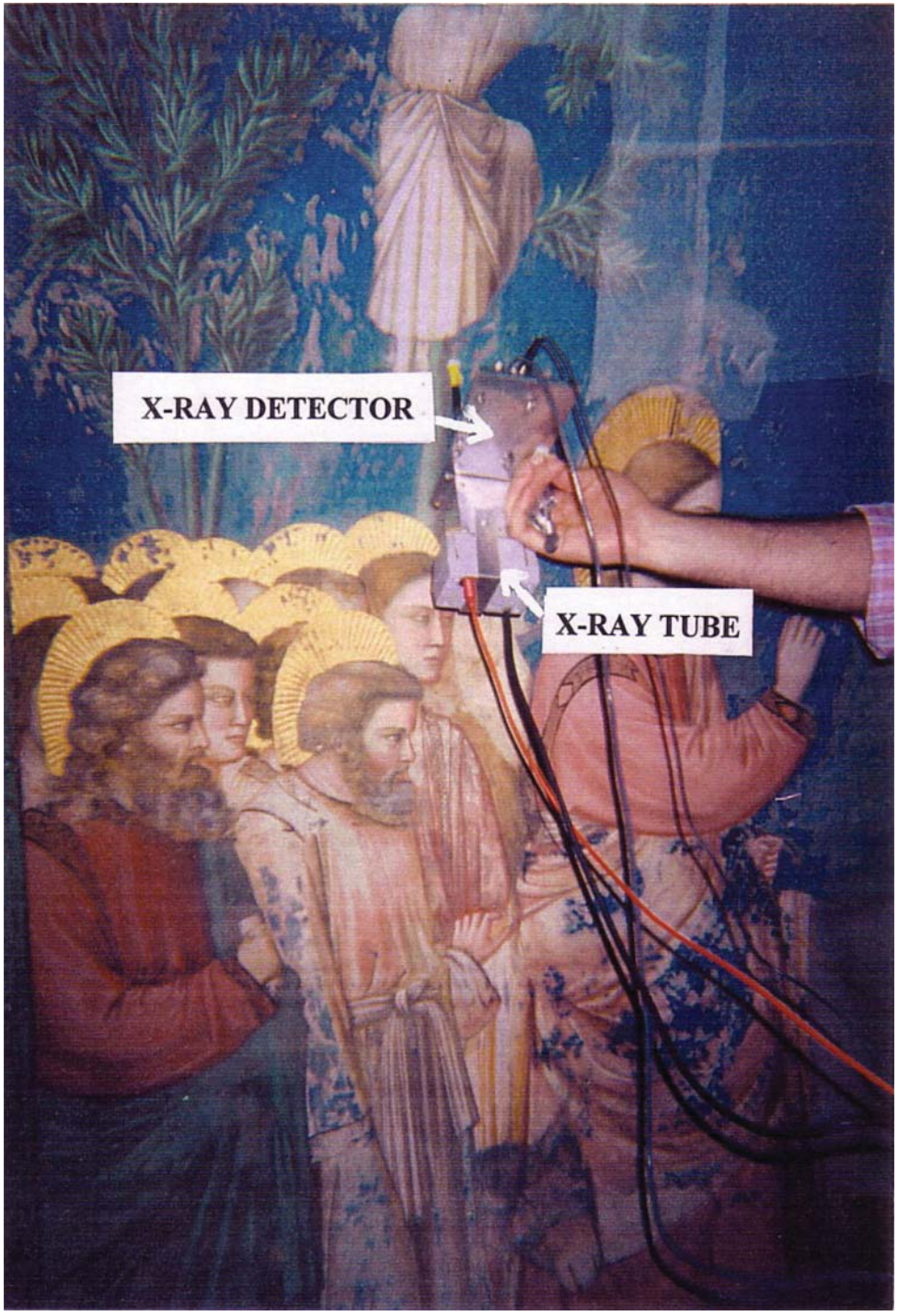

From the chapter by Cesareo et al.
Figure 3. Equipment for sulphur and chlorine analysis, composed of a Ca-anode x-ray tube working at 6 kV and 0.1 mA, and a thermoelectrically cooled Si-PIN detector.

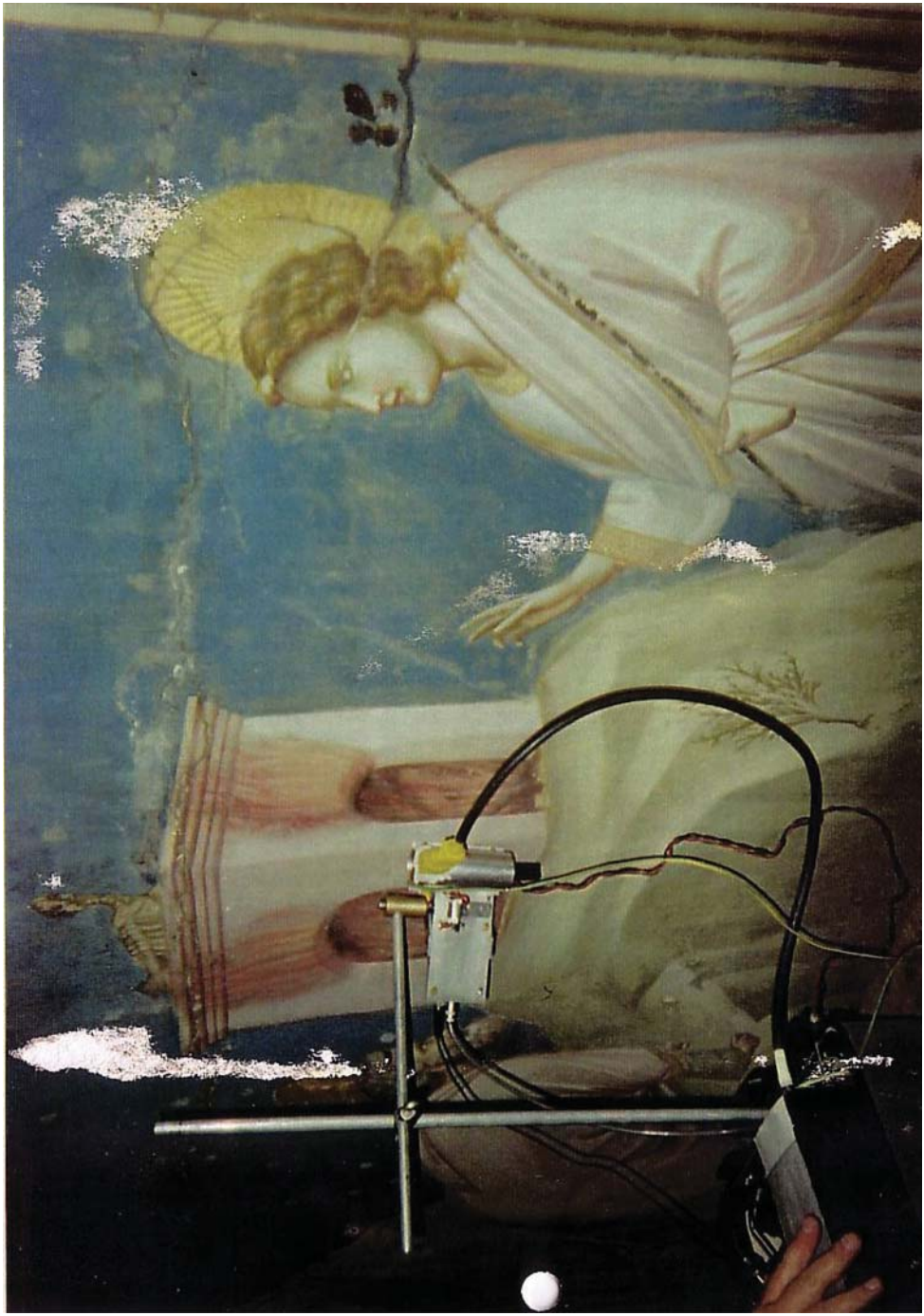

From the chapter by Cesareo et al.
Figure 4. Equipment for analysis of elements from 1 to 30 keV employed in the Chapel of the Scrovegni in Padua, composed of a W-anode 30 kV, 0.3 mA x-ray tube and a thermoelectrically cooled Si-PIN detector.

From the chapter by Sherwood
Plate 1b. "Bronze Patina Colors", The Gorham Company, 1927.

From the chapter by Kontozova et al.
Figure 1. Sampling with diffusion tubes inside a museum showcase in Musical Instruments Museum in Brussels.

From the chapter by Kontozova et al.
Figure 6. Diffusion tubes and equipment for microclimatic measurements, installed on a stained glass window panel.

From the chapter by Janssens
Figure 11. Fragments of Celtic glass fragments.

From the chapter by Janssens
Figure 14. Glass beads recovered from Merovingian graveyards.